Biologically-Inspired Systems

Atsushi Hozumi
Lei Jiang
Haeshin Lee
Masatsugu Shimomura *Editors*

Stimuli-Responsive Dewetting/Wetting Smart Surfaces and Interfaces

Springer

Biologically-Inspired Systems

Volume 11

Series editor
Stanislav N. Gorb, Department of Functional Morphology and Biomechanics,
Zoological Institute, Kiel University, Kiel, Germany

Motto: Structure and function of biological systems as inspiration for technical developments

Throughout evolution, nature has constantly been called upon to act as an engineer in solving technical problems. Organisms have evolved an immense variety of shapes and structures from macro down to the nanoscale. Zoologists and botanists have collected a huge amount of information about the structure and functions of biological materials and systems. This information can be also utilized to mimic biological solutions in further technical developments. The most important feature of the evolution of biological systems is multiple origins of similar solutions in different lineages of living organisms. These examples should be the best candidates for biomimetics. This book series will deal with topics related to structure and function in biological systems and show how knowledge from biology can be used for technical developments in engineering and materials science. It is intended to accelerate interdisciplinary research on biological functional systems and to promote technical developments. Documenting of the advances in the field will be important for fellow scientists, students, public officials, and for the public in general. Each of the books in this series is expected to provide a comprehensive, authoritative synthesis of the topic.

More information about this series at http://www.springer.com/series/8430

Atsushi Hozumi • Lei Jiang • Haeshin Lee
Masatsugu Shimomura
Editors

Stimuli-Responsive Dewetting/Wetting Smart Surfaces and Interfaces

Springer

Editors
Atsushi Hozumi
The National Institute of Advanced
Industrial Science and Technology (AIST)
Structural Materials Research Institute
Nagoya, Japan

Haeshin Lee
Department of Chemistry
KAIST
Daejeon, Korea (Republic of)

Lei Jiang
Beijing Advanced Innovation Center
for Biomedical Engineering, School of
Chemistry
Beihang University
Beijing, China

Technical Institute of Physics and
Chemistry, Chinese Academy of Sciences
Beijing, China

Masatsugu Shimomura
Chitose Institute of Science and Technology
Chitose Shi, Japan

ISSN 2211-0593 ISSN 2211-0607 (electronic)
Biologically-Inspired Systems
ISBN 978-3-319-92653-7 ISBN 978-3-319-92654-4 (eBook)
https://doi.org/10.1007/978-3-319-92654-4

Library of Congress Control Number: 2018954811

© Springer International Publishing AG, part of Springer Nature 2018
This work is subject to copyright. All rights are reserved by the Publisher, whether the whole or part of the material is concerned, specifically the rights of translation, reprinting, reuse of illustrations, recitation, broadcasting, reproduction on microfilms or in any other physical way, and transmission or information storage and retrieval, electronic adaptation, computer software, or by similar or dissimilar methodology now known or hereafter developed.
The use of general descriptive names, registered names, trademarks, service marks, etc. in this publication does not imply, even in the absence of a specific statement, that such names are exempt from the relevant protective laws and regulations and therefore free for general use.
The publisher, the authors and the editors are safe to assume that the advice and information in this book are believed to be true and accurate at the date of publication. Neither the publisher nor the authors or the editors give a warranty, express or implied, with respect to the material contained herein or for any errors or omissions that may have been made. The publisher remains neutral with regard to jurisdictional claims in published maps and institutional affiliations.

This Springer imprint is published by the registered company Springer Nature Switzerland AG
The registered company address is: Gewerbestrasse 11, 6330 Cham, Switzerland

Preface

During billions of years of evolution, living creatures have successfully acquired their astonishing surface functionalities simply by adjusting their surface structures to win the struggle for survival under harsh environmental conditions. They have established their own novel nanotechnologies based on self-assembly, e.g., “bottom-up” approaches, to fabricate complicated hierarchical structures using ubiquitous elements under mild conditions at both low temperature and pressure. Their technologies developed by evolution are completely different from those actively developed by human beings, which strongly depend on “top-down” approaches and specific elements such as rare earth metals, fluorinated compounds, semiconductor compounds, and so on. The paradigm is completely different; such material processing demonstrated by living creatures with low environmental burden is a model for us to realize a sustainable society.

Among numerous useful surface functionalities developed for practical applications, in particular surface wetting/dewetting is frequently observed in our daily lives, and the control of wetting/dewetting properties has been strongly demanded. The creation of superhydrophobic surfaces which artificially mimic lotus leaves has captured the attention of scientists and engineers over the past few decades. Extensive studies on them have been performed, ranging from basic research to demonstrations of practical applications, and almost 10,000 papers have been published on this subject alone. Recently, further requirements for useful surfaces have become apparent, meaning that surfaces are needed which can repel not only water but also low surface tension liquids (oils and organic solvents), viscous emulsions, biological fluids, and so on. Such surfaces are called superomniphobic or superamphiphobic and have been developed based on findings on superhydrophobic surfaces. In addition, dynamic rather than static surface wetting/dewetting properties, which can be triggered by various stimuli, including temperature, pH, magnetic/electric fields, solvents, light exposure, and so on, have also attracted much attention due to their applications in a variety of engineering fields.

This book is mainly focused on recent topics and trends related to stimuli-responsive wetting/dewetting surfaces based on biomimetic approaches and gives an overview of the knowledge and concepts of how to design and establish such smart artificial surfaces. It is intended for not only technical developments in a wide variety of engineering fields but also basic research on surface/interface science of biomimetics. This book is also targeted to senior undergraduate and graduate students as well as researchers and engineers who want to apply great tips from nature to their research fields. We believe that many new ideas and concepts inspired from living creatures shown in this book will be helpful for the development of our technology and daily life in the next decade and beyond.

Nagoya, Japan	Atsushi Hozumi
Daejeon, Republic of Korea	Haeshin Lee
Beijing, China	Lei Jiang
Chitose, Japan	Masatsugu Shimomura

Contents

Part I Stimuli-Responsive Dewetting/Wetting Smart Surfaces and Interfaces

Part II Practical Applications

Contributors

Jitesh Barman Department of Physics, Indian Institute of Technology Kanpur, Kanpur, Uttar Pradesh, India

Sneha Dattatreya Department of Physics, Indian Institute of Technology Kanpur, Kanpur, Uttar Pradesh, India

Gary J. Dunderdale Department of Chemistry, University of Sheffield, Sheffield, UK

National Institute of Advanced Industrial Science and Technology (AIST), Nagoya, Japan

Syuji Fujii Department of Applied Chemistry, Faculty of Engineering, Osaka Institute of Technology, Osaka, Japan

Nanomaterials Microdevices Research Center, Osaka Institute of Technology, Osaka, Japan

Raju Kumar Gupta Department of Chemical Engineering, Indian Institute of Technology Kanpur, Kanpur, Uttar Pradesh, India

Center for Nanosciences and Center for Environmental Science and Engineering, Indian Institute of Technology Kanpur, Kanpur, Uttar Pradesh, India

Linlin He Beijing Advanced Innovation Center for Biomedical Engineering, School of Chemistry, Beihang University, Beijing, China

Yuji Higaki Institute for Materials Chemistry and Engineering, Kyushu University, Fukuoka, Japan

Atsushi Hozumi National Institute of Advanced Industrial Science and Technology (AIST), Nagoya, Japan

Naoyuki Ishida Division of Applied Chemistry, Graduate School of Natural Science and Technology, Okayama University, Okayama, Japan

Daisuke Ishii Department of Life Science and Applied Chemistry, Graduate School of Engineering, Nagoya Institute of Technology, Nagoya, Aichi, Japan

Lei Jiang Beijing Advanced Innovation Center for Biomedical Engineering, School of Chemistry, Beihang University, Beijing, China

Technical Institute of Physics and Chemistry, Chinese Academy of Sciences, Beijing, China

Krishnacharya Khare Department of Physics, Indian Institute of Technology Kanpur, Kanpur, Uttar Pradesh, India

Center for NanoSciences, Indian Institute of Technology Kanpur, Kanpur, Uttar Pradesh, India

Motoyasu Kobayashi Department of Applied Chemistry, Advanced School of Engineering, Kogakuin University, Tokyo, Japan

Soo Hyeon Lee Department of Chemistry, Korea Advanced Institute of Science and Technology (KAIST), Daejeon, Republic of Korea

Haeshin Lee Department of Chemistry, Korea Advanced Institute of Science and Technology (KAIST), Daejeon, Republic of Korea

Yan Li Beijing Advanced Innovation Center for Biomedical Engineering, School of Chemistry, Beihang University, Beijing, China

Rashika Mittal Department of Chemical Engineering, Indian Institute of Technology Kanpur, Kanpur, Uttar Pradesh, India

Department of Chemical Engineering, Manipal Institute of Technology, Manipal, Karnataka, India

Takuya Ohzono Electronics and Photonics Research Institute, National Institute of Advanced Industrial Science and Technology (AIST), Tsukuba, Japan

Reeta Pant Department of Physics, Indian Institute of Technology Kanpur, Kanpur, Uttar Pradesh, India

Jai Prakash Department of Chemical Engineering, Indian Institute of Technology Kanpur, Kanpur, Uttar Pradesh, India

Mikyung Shin Department of Chemistry, Korea Advanced Institute of Science and Technology (KAIST), Daejeon, Republic of Korea

Narendra Singh Department of Chemical Engineering, Indian Institute of Technology Kanpur, Kanpur, Uttar Pradesh, India

Center for Nanosciences and Center for Environmental Science and Engineering, Indian Institute of Technology Kanpur, Kanpur, Uttar Pradesh, India

Atsushi Takahara Institute for Materials Chemistry and Engineering, Kyushu University, Fukuoka, Japan

Dongliang Tian Beijing Advanced Innovation Center for Biomedical Engineering, School of Chemistry, Beihang University, Beijing, China

Chihiro Urata Structural Materials Research Institute, National Institute of Advanced Industrial Science and Technology (AIST), Nagoya, Japan

Younseon Wang Department of Chemistry, Korea Advanced Institute of Science and Technology (KAIST), Daejeon, Republic of Korea

Erica J. Wanless Discipline of Chemistry, University of Newcastle, Callaghan, NSW, Australia

Priority Research Centre for Advanced Particle Processing and Transport, University of Newcastle, Callaghan, NSW, Australia

Grant B. Webber Discipline of Chemical Engineering, University of Newcastle, Callaghan, NSW, Australia

Priority Research Centre for Advanced Particle Processing and Transport, University of Newcastle, Callaghan, NSW, Australia

Shin-ichi Yusa Department of Applied Chemistry, Graduate School of Engineering, University of Hyogo, Hyogo, Japan

Na Zhang Beijing Advanced Innovation Center for Biomedical Engineering, School of Chemistry, Beihang University, Beijing, China

Chapter 1
Introduction of Stimuli-Responsive Wetting/Dewetting Smart Surfaces and Interfaces

Gary J. Dunderdale and Atsushi Hozumi

Abstract Functional surfaces and interfaces possessing wetting/dewetting properties which change reversibly and repeatably in response to various external stimuli have attracted considerable attention lately because of their great potential in a wide variety of engineering fields, practical applications, and basic research. Different types of these smart surfaces/interfaces, on which chemical compositions and/or surface structures can be arbitrarily controlled by different external stimuli, such as pH, temperature, light, solvent, mechanical stress, electric/magnetic fields and so on, have been successfully prepared by various methods. This chapter will give an introduction to the basic theories of surface wetting/dewetting properties, including static/dynamic contact angles (CAs), CA hysteresis, Young's, Wenzel's, and Cassie-Baxter's equations, and in addition, typical examples and applications of stimuli-responsive wetting/dewetting smart surfaces and interfaces are also described.

Keywords Static/dynamic contact angles (CAs) · CA hysteresis · Young's, Wenzel's, and Cassie-Baxter's equations · Stimuli responsive · Wetting/dewetting

1.1 Introduction

The adherence of liquid droplets to solid surfaces can lead to corrosion, deterioration, reduction of visibility, and degradation of appearance, and thereby significantly damage the safety and reliability of everyday devices and industrial equipment. For this reason, the development of surface modifications that show excellent performance in liquid removal is of high importance, with extensive

---

G. J. Dunderdale
Department of Chemistry, University of Sheffield, Sheffield, UK

National Institute of Advanced Industrial Science and Technology (AIST), Nagoya, Japan

A. Hozumi (✉)
National Institute of Advanced Industrial Science and Technology (AIST), Nagoya, Japan
e-mail: a.hozumi@aist.go.jp

A. Hozumi et al. (eds.), *Stimuli-Responsive Dewetting/Wetting Smart Surfaces and Interfaces*, Biologically-Inspired Systems 11,
https://doi.org/10.1007/978-3-319-92654-4_1

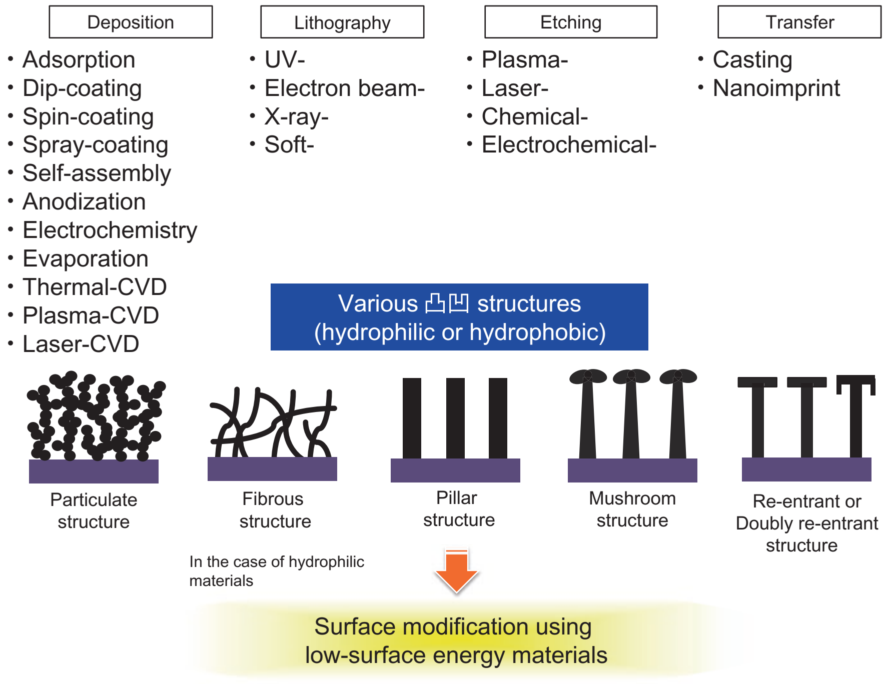

Fig. 1.1 Micro-/nano-fabrication methods and typical surface structures produced in the fabrication of man-made SLR surfaces

research on the control of adhesion and dewetting of liquid drops from solid surfaces having been reported so far. Most studies related to this research field have particularly focused on the effects of surface structures and chemical compositions on the surface wetting/dewetting properties (Onda et al. 1996; Hozumi and Takai 1997; Crevoisier et al. 1999; Chen et al. 1999; Lafuma and Quéré 2003; Gao and McCarthy 2006a; Tian et al. 2014). Many researchers have taken inspiration from Nature to achieve "superhydrophobic" surfaces, which generally display extremely large static contact angles (CAs, θ_S, greater than 150°), including lotus leaf surface and water strider's leg. Water droplets on such surfaces are unstable and can be easily moved, and needing the surface to tilt to only a small angle (low substrate tilt angles (θ_T) of less than 5~10°) before the drop rolls off. According to the Web of science®, the total number of papers of superhydrophobic surfaces is closing to 10,000 (Topic:"superhydrophobic" and "ultrahydrophobic") and more than 1000 papers have been published each year. In contrast to such skyrocketing publications on water-repellent surfaces, preparation of superoleophobic surfaces, where droplets of low-surface tension (γ) liquids such as oils can easily roll across and off the surface (exhibiting minimum θ_T for droplet motion of less than 5–10°), are rare (Tsujii et al. 1997; Tuteja et al. 2007; Zhang and Seeger 2011; Deng et al. 2012; Pan et al. 2013; Wang and Bhushan 2015; Brown and Bhushan 2016), in spite of the practical advantages they offer. In this chapter, we hereafter refer to the surfaces possessing excellent liquid-repellent properties against various kinds of liquids as super-liquid-repellent (SLR) surfaces. Such man-made SLR surfaces have been generally prepared using a variety of techniques (Fig. 1.1) (Bhushan and Jung 2011) which commonly create micro/nano hierarchical structures, which are then subsequently treated using low-surface-energy materials (for example, terminated with alkyl or perfluoroalkyl groups).

In addition to such SLR surfaces which show high θ_S values, more recently, dynamic rather than static surface wetting/dewetting properties, which can be triggered by various external stimuli, including temperature, pH, magnetic/electric fields, solvents, light exposure and so on, has also attracted much attention due to their applications in a variety of engineering fields, such as oil/water separation (Kota et al. 2012; Dunderdale et al. 2015), drug delivery (Kim et al. 2013; Qiu and Park 2001), cell encapsulation (Kim et al. 2012), microfluidic devices (Huber et al. 2003), and so on (Sun and Qing 2011). Several important review papers on the topic of stimuli-responsive surfaces and interfaces have also been reported (Lahann et al. 2003; Feng and Jiang 2006; Xia et al. 2009; Xin and Hao 2010; Guo and Guo 2016).

In this chapter, we will describe basic theories of surface wetting/dewetting properties, including static/dynamic CAs, CA hysteresis, Young's, Wenzel's, and Cassie-Baxter's equations. In addition, typical examples and applications of stimuli-responsive wetting/dewetting smart surfaces and interfaces are also described.

1.2 Fundamental Theories of Surface Wetting/Dewetting

1.2.1 Flat/Smooth Surface

It is well-known that when a liquid droplet is placed on a solid surface, it tends to form a dome shape with a certain CA, rather than fully spreading out across the surface to form a thin film. In such a case, an apparent CA can be measured between the horizontal surface and the tangential line of the liquid surface near the three-phase (liquid (L), vapor (V), and solid (S) phases) contact line (Fig. 1.2). This apparent CA (θ_S) of a liquid on a smooth/flat surface can be estimated by Young's equation Eq. (1.1).

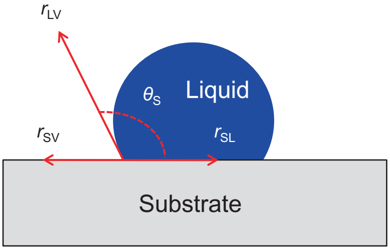

Fig. 1.2 Liquid droplet placed on a smooth/flat surface and vector representation of the three-surface tensions (γ_{LV}, γ_{SV}, and γ_{SL}) interacting on the liquid droplet

$$\cos\theta_S = (\gamma_{SV} - \gamma_{SL}) / \gamma_{LV} \tag{1.1}$$

γ_{LV}: surface tension at the L-V interface, γ_{SV}: surface tension at the S-V interface, and γ_{SL}: surface tension at the S-L interface.

A surface with a θ_S value of less than 90° is regarded as hydrophilic/oleophilic, and in particular when θ_S is close to 0°, it is called a superhydrophilic/superoleophilic surface. In contrast, a surface with a θ_S value of over 90° is regarded as hydrophobic/oleophobic, and when this value becomes larger than 150°, superhydrophobic/superoleophobic.

Superhydrophobic surfaces generally exhibit excellent liquid repellency due to the small area of contact between the drop and the surface caused by the high CA. However, there are adhesive/sticky surfaces on which water drops remain pinned to the surface regardless of the magnitude of their θ_S values (Jin et al. 2005). Rose petal surfaces are a good example; they exhibit 'superhydrophobicity', but at the same time are strongly adhesive towards water (so called "rose-petal effect") (Jin et al. 2005). In addition, such "pinning" phenomena have also been frequently observed on conventional hydrophobic glass windows and car windshields with water θ_S values of ~120°, as can be seen on rainy days even if the surface has been treated with perfluoroalkylsilanes. As is obvious from this example, it is clear that surface dewetting properties cannot be characterized by θ_S values alone, which have conventionally been used to explain this behavior. Thus, recently, to accurately characterize surface wetting/dewetting properties, measurements of dynamic wettability, advancing (θ_A) and receding (θ_R) CAs, CA hysteresis, and θ_T, have been used (Cheng et al. 2012a, b; Wong et al. 2013). Hereafter we will explain these measurements and use them to explain observed phenomena.

CA hysteresis is the mass-independent measure of the resistance to macroscopic liquid drop movement on inclined surfaces. It recognizes that in order for the gravitational force to cause a liquid drop to de-pin from a stationary position on a horizontal surface and begin sliding/rolling down an inclined surface, the shape of the liquid drop must first undergo a certain amount of deformation, as shown in Fig. 1.3.

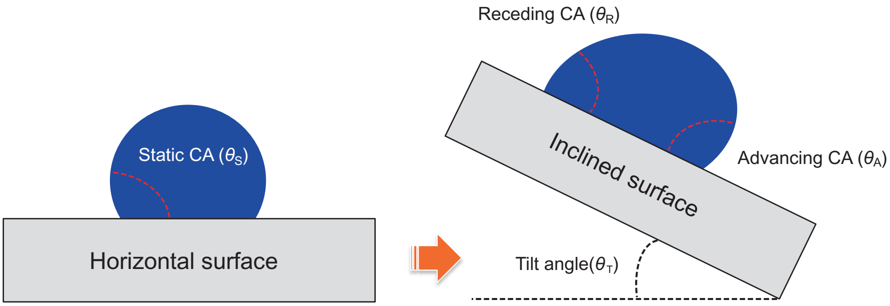

Fig. 1.3 Comparison of liquid drops on horizontal (left) and inclined (right) surfaces. The advancing CA (θ_A) indicates the maximum angle just before the droplet advances. The receding CA (θ_R) indicates the minimum angle just before the droplet recedes

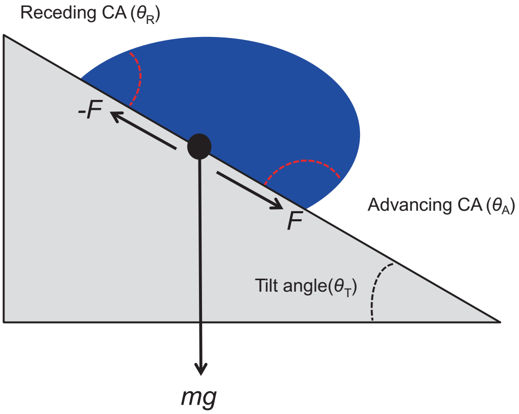

Fig. 1.4 Liquid droplet on an inclined surface. The substrate tilt angle (θ_T) indicates the angle at which the gravitational force ($F = mg \bullet \sin \alpha$) overcomes the lateral adhesion force ($-F$) and induces sliding/rolling of the liquid droplet

Assuming that the solid-liquid contact area remains constant or experiences a relatively insignificant change, this deformation from its typical spherical dome/cap shape results in an increase in the drop's liquid-vapor interfacial area. The energy associated with this increase has been described as the activation energy barrier to liquid drop motion down an inclined surface (Gao and McCarthy 2006b, 2009). From the initial horizontal position (at θ_S), the drop begins to move when its CAs at the front and back ends are capable of advancing and receding, respectively. These advancing and receding events, which occur at θ_A and θ_R, are also the maximum and minimum possible CAs, respectively, for a liquid-surface pair. CA hysteresis can be described using θ_A and θ_R, or the cosine of these values as follows:

$$\Delta\theta = \theta_A - \theta_R \tag{1.2}$$

$$\Delta\theta_{\cos} = \cos\theta_R - \cos\theta_A \tag{1.3}$$

Kawasaki and Furmidge reported that there is a relation between the mobility of probe liquids on an inclined surface and $\Delta\theta_{\cos}$ (=$\cos\theta_R - \cos\theta_A$) (Kawasaki 1960; Furmidge 1962). The gravitational force required to initiate drop movement across an inclined surface (Fig. 1.4) dependent on $\Delta\theta_{\cos}$ is described by Eq. (1.4).

$$F = mg \cdot \sin\theta_T = kw\gamma_{LV}\left(\cos\theta_R - \cos\theta_A\right) \tag{1.4}$$

m: the mass of the drop, g: the gravitational constant, α: substrate tilt angle (θ_T), k: constant that depends on drop shape, w: the width of the drop, and γ_{LV}: the L-V surface tension.

According to Eq. (1.4), $\Delta\theta_{\cos}$ (Eq. (1.3)) shows significantly stronger correlation with the resulting θ_T values of a liquid drop on a surface than with the conventional definition of CA hysteresis ($\Delta\theta$, Eq. (1.2)) (Cheng et al. 2012b). Therefore, when CA hysteresis value is small enough, a liquid drop will only require a low θ_T value to de-pin from a horizontal position and begin moving down the surface without

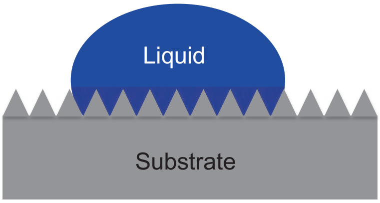

Fig. 1.5 Schematic illustration of the possible wetting state of liquid droplet placed on a chemically homogeneous rough surface (Wenzel state)

substantial deformation of its shape. Conversely, drops can remain permanently pinned to vertically oriented surfaces, regardless of their magnitude of θ_S values (even if the θ_S values are over 150°), when the CA hysteresis is significant. Actually, in many cases, the θ_S values of SLR surfaces were less influenced by surface contaminations and defects, but they have a serious influence on dynamic CAs (in particular, θ_R values decrease), affecting the sliding/rolling properties (Verho et al. 2011). Thus, the latest definition of SLR surfaces is that they display not only high θ_S values (greater than 150°), but also low $\Delta\theta$ values (less than 5–10°), and low θ_T values (less than 5–10°) for small volumes (3–5 μL) of various probe liquids, not only water but also virtually all probe liquids including low γ liquids (below 30 dyn/cm) (Kota et al. 2014).

1.2.2 *Rough Surface*

In contrast to flat/smooth surfaces, when a liquid droplet contacts a rough surface, it can adopt one of the following two configurations to minimize its overall free energy (Marmur 2003; Nosonovsky 2007), *i.e.,* the Wenzel (Wenzel 1936) or the Cassie-Baxter state (Cassie and Baxter 1944). As shown in Fig. 1.5, in the Wenzel state, the liquid droplet completely permeates into the voids on the rough surface underneath of the liquid droplet, forming a fully-wetted interface. As these voids are usually very small (<10 μm), it is not possible to measure the angle between the surface and the tangent of the liquid drop (CA) without the use of microscopy. In this case, an apparent CA is defined as the angle between the tangent of the liquid drop and the plane of the rough surface as viewed on a macroscopic scale. In this Wenzel state, this apparent CA (θ_W) is related to the real CA by Wenzel's equation Eq. (1.5) (Wenzel 1936).

$$\cos\theta_w = r \cdot \cos\theta \tag{1.5}$$

θ_W: Wenzel's CA on the rough surface, θ: CA on the smooth/flat surface of the identical material, r: the surface roughness factor (r = actual surface area/projected surface area).

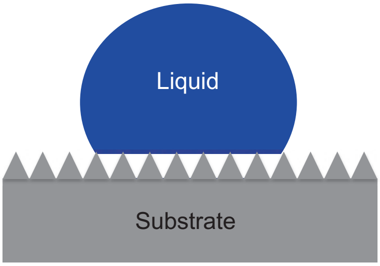

Fig. 1.6 Schematic illustration of the possible wetting state of liquid droplet placed on a chemically heterogeneous rough surface (Cassie-Baxter state)

In the Wenzel state, because r is always larger than 1, surface roughness amplifies both wetting/dewetting behaviors of materials. When the θ value is less than 90°, the θ_W value will decrease, while when the θ value is larger than 90°, the θ_W value will increase with an increase in surface roughness. However, actual droplets on the rough surfaces do not exhibit the apparent CAs (θ_W) described by Eq. (1.5), because the three-phase contact line of the liquid is frequently pinned to the surface by defects/voids from the production mechanism, resulting in an increase in CA hysteresis (Forsberg et al. 2010). The Wenzel model is also only applicable to chemically homogeneous rough surfaces, whereas in real life, many of the produced surfaces are heterogeneous.

In contrast, in the Cassie-Baxter state, when a liquid droplet is placed on a rough surface, the liquid doesn't flow into the voids of the surface, and they remain filled with air underneath the droplet, as can be seen in Fig. 1.6. Now the L-S interface is a composite interface consisting of two components, in this case, L-substrate and L-air. Moreover, the Cassie-Baxter state can also account for the effects of chemical heterogeneities of the rough surface on the apparent CA, if extra terms with different CAs are included in this composite interface. The general Cassie's equation is given by Eq. (1.6).

$$\cos\theta_C = f_1\left(\cos\theta_1\right) + f_2\left(\cos\theta_2\right) \tag{1.6}$$

θ_C: Cassie's CA of the rough surface, f_1 and f_2 are the area fractions, and θ_1 and θ_2 are CA of the flat/smooth materials 1 and 2, respectively.

In Cassie–Baxter state, for example, when f_2 component is air, and $f_1 + f_2 = 1$, $\cos\theta_2$ (=cos180°) is −1, and $f_2 = 1 - f_1$, respectively. Thus, the apparent CA (θ_{CB}) is finally given by Cassie-Baxter's equation (Eq. 1.7) (Cassie and Baxter 1944).

$$\begin{aligned} \cos\theta_{CB} &= f_1\left(\cos\theta_1\right) - f_2 \\ &= f_1\left(\cos\theta_1\right) - \left(1 - f_1\right) \\ &= f_1\left(\cos\theta_1 + 1\right) - 1 \end{aligned} \tag{1.7}$$

In contrast to the Wenzel state, high values of f_2 (air-area fraction) in the Cassie-Baxter state enhance the magnitude of the θ_{CB} values. In such a case, liquid droplet is unstable and can move smoothly without pinning on the surface.

1.3 Preparation Methods of Stimuli-Responsive Smart Surfaces and Interfaces

A wide variety of surface functionalization methods, such as electrospinning (Huang et al. 2013; Ma et al. 2016a; Wang et al. 2016a; Sarbatly et al. 2016; Tai et al. 2014; Obaid et al. 2015a; Ning et al. 2015; Ma et al. 2016b; Alayande et al. 2016; Zhang et al. 2015; Arslan et al. 2016; Obaid et al. 2015b; Fang et al. 2016; Liu and Liu 2016; Li et al. 2016a, b; Wang et al. 2015, 2016b; Che et al. 2015), surface-initiated atom-transfer radical polymerization (SI-ATRP) (Wang et al. 2015; Sun et al. 2004; Barbey et al. 2009; Jain et al. 2009; Matyjaszewski and Tsarevsky 2009; Koenig et al. 2014; Dunderdale et al. 2014), layer-by-layer (LBL) deposition (Yang et al. 2011a; Lu et al. 2013; Lim et al. 2006), self-assembly (self-assembled monolayers: SAMs) (Liu et al. 2013; Jin et al. 2011), spray-deposition (Yang et al. 2011b; Zhang et al. 2012), spin-coating (Li et al. 2009), electrodeposition (Xu et al. 2014), Langmuir-Blodgett (LB) methods (Feng et al. 2001), electrochemical deposition (Wang and Guo 2013) and so on (Wu et al. 2013; Byun et al. 2012; Wang and Zhang 2012), have been reported to prepare stimuli-responsive smart surfaces and interfaces.

Some typical examples of functionalized surfaces and interfaces showing stimuli-responsive properties are summarized in Table 1.1.

The electrospinning technique has become a versatile and effective method for synthesizing nanofibrous materials with controlled compositions and morphologies (Agarwal et al. 2013; Misra et al. 2017; Ding et al. 2010; Singh et al. 2016). In addition, electrospinning can provide other important features, such as high surface-to-volume ratio and multi-porous structures possessing unique chemical, physical, and mechanical properties by incorporating other components with ease and control (Li and Xia 2004; Ramakrishna et al. 2006; Wang et al. 2013; Bhardwaj and Kundu 2010). Because of the highly specific surface areas, interconnected nano-scale pore structures, and the potential to incorporate active chemical functionality on a nano-scale surface, electrospinning is one of the promising and cost-effective methods to prepare stimuli-responsive smart surfaces and interfaces. Various polymeric membranes and nanofibrous mats showing stimuli-responsive properties have been successfully fabricated by this method and have been widely applied for oil/water separation applications (For example, Fig. 1.7) (Huang et al. 2013; Ma et al. 2016a; Wang et al. 2016a; Sarbatly et al. 2016; Tai et al. 2014; Obaid et al. 2015a; Ning et al. 2015; Ma et al. 2016b; Alayande et al. 2016; Zhang et al. 2015; Arslan et al. 2016; Obaid et al. 2015b; Fang et al. 2016; Liu and Liu 2016; Li et al. 2016a, b; Wang et al. 2015, 2016b; Che et al. 2015). Although electrospinning is a useful technique to prepare structured smart surfaces and interfaces, the resulting structures and properties of electrospun nanofibers are considerably influenced by experimental factors, such as molecular weight (MW) and solubility of polymers, the solvent/solution properties, and external environmental conditions (Doshi and Reneker 1995; Megelski et al. 2002; Huang et al. 2003; Lee et al. 2003).

Table 1.1 Typical examples of functionalized surfaces and interfaces showing stimuli-responsive properties[a]

Stimuli	Substrate shape	Materials/chemicals	Preparation methods	References
Stress/stretch	Film	PTFE	N.A.	Zhang et al. (2004)
		Polyamide		Zhang et al. (2005)
pH	Fiber mat	PBz	Electrospinning	Liu and Liu (2016)
	Cu mesh	Cu-NPs/Au/$HS(CH_2)_9CH_3$ and $HS(CH_2)_{10}COOH$	Electrochemical deposition/self-assembly	Wang and Guo (2013)
Temperature	Si micro-convexes	PNiPAAm	SI-ATRP	Xia et al. (2009)
	RC nanofibrous membrane			Wang et al. (2015)
Light	Nanofibrous membrane	TiO_2-NPs/PVDF	Electrospinning	Wang et al. (2016b)
	Si	CF_3AZO/PAH/SiO_2-NPs	LBL deposition	Lim et al. (2006)
Magnetic field	Ni-micronails	1*H*,1*H*,2*H*,2*H*-Perfluorodecanethiol	Electrodeposition/self-assembly	Grigoryev et al. (2012)
	Structured Si	Fe_3O_4-NPs	N.A.	Cheng et al. (2012c)
Gas	Nanofibers	PMMA-*co*-PDEAEMA	Electrospinning	Che et al. (2015)
	SAM/Au	NADPA	Self-assembly/grafting	Li et al. (2014b)
Solvent	Structured PTFE	PSF-COOH/PVP-COOH	Grafting	Minko et al. (2003)
	Structured Si	PNiPAAm-*co*-Cy&AA		Wang et al. (2009)

[a] Abbreviations: *PTFE* Polytetrafluoroethylene, *PBz* Polybenzoxazine, *NPs* Nanoparticles, *RC* regenerated cellulose, *PNiPAAm* Poly(*N*-isopropylacrylamide), *SI-ATRP* Surface-initiated atom-transfer radical polymerization, *PVDF* Polyvinylidene fluoride, *CF_3AZO* 7-[(trifluoromethoxyphenylazo) phenoxy]pentanoic acid, *PAH* Poly(allylamine hydrochloride), *LBL* Layer-by-layer, *PMMA-co-PDEAEMA* Poly(methyl methacrylate)-*co*-poly(*N,N*-diethylaminoethyl methacrylate), *NADPA* *N*-(2-aminoethyl)-5-(1,2-dithiolan-3-yl) pentanamide amidine, *PSF* Pentafluorostyrene, *PVP* Poly(*N*-vinylpyrrolidone), *PNiPAAm-co-Cy&AA* Aspartic acid (AA) and cysteine (Cy) units grafted PNiPAAm

SI-ATRP is a novel approach to fabricate stimuli-responsive smart surfaces and interfaces by growing low polydispersity polymer chains on a surface (Fu et al. 2004). Responsive polymer brushes prepared by SI-ATRP have recently attracted considerable attention because of their great potential for the preparation of stimuli-responsive surfaces (Sun et al. 2004; Barbey et al. 2009; Jain et al. 2009; Matyjaszewski and Tsarevsky 2009; Koenig et al. 2014; Dunderdale et al. 2014).

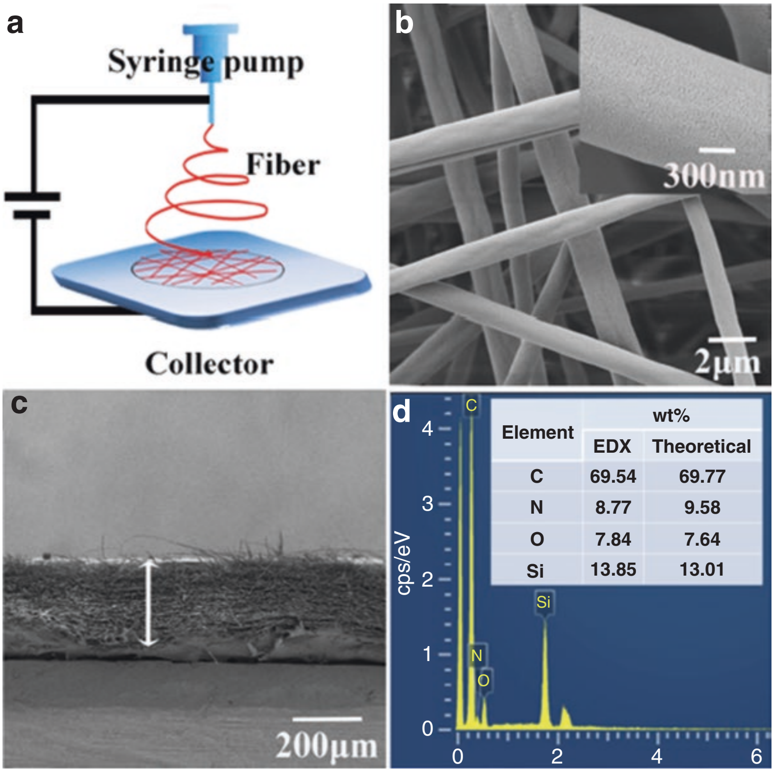

Element	wt%	
	EDX	Theoretical
C	69.54	69.77
N	8.77	9.58
O	7.84	7.64
Si	13.85	13.01

Fig. 1.7 (**a**) Schematic illustration of the electrospinning process. (**b**) Representative SEM image of pH-responsive polymer (PDMS-*b*-P4VP: poly(dimethylsiloxane)-*block*-poly(4-vinylpyridine)) fibers (inset is the zoomed-in image of the surface of a single fiber). (**c**) Cross-sectional morphology and (**d**) EDX spectrum of the polymer fibrous mat (inset table shows the element content obtained using EDX and theoretical calculations). (Reproduced with permission from (Li et al. 2016a), Copyright 2016 The American Chemical Society)

For example, a thermally-responsive poly(*N*-isopropylacrylamide) (PNiPAM) surface was reported by Sun et al. by growing polymers from flat and rough Si substrates using SI-ATRP (Sun et al. 2004). As shown in Fig. 1.8, the authors have fabricated poly(2-(dimethylamino)ethyl methacrylate) (PDMAEMA) polymer brush on a large-scale aluminum substrate (30 × 10 cm^2) in air by using a modified SI-ATRP, so-called SI-“Paint on”-ATRP. This surface shows switchable underwater oleophobicity depending on the solution pH (Dunderdale et al. 2014).

A very serious limitation of conventional SI-ATRP is that it typically requires high concentrations of monomer, and catalyst, use of organic solvents, elevated reaction temperatures, and the reaction solution to be rigorously purged of oxygen (Barbey et al. 2009). Such stringent conditions make it difficult to prepare smart stimuli-responsive surfaces and interfaces outside of laboratory conditions, and due to practical difficulties associated with the reaction setup, impractical for large area (∼1 m^2) functionalization. To overcome these shortcomings, modified ATRP proto-

Fig. 1.8 Functionalization of large real life substrates. (Top) 1.3 L glass jar functionalized by low-chemical content SI-ATRP. Jars contain water adjusted to either pH 2 or pH 10 and *n*-hexane containing blue dye. At pH 2 the surface of the jar was superoleophobic, whereas at pH 10 oil drops adhered to the surface. (Bottom) Aluminum sheet functionalized using SI-"Paint on"-ATRP. (Reproduced with permission from (Dunderdale et al. 2014), Copyright 2014 The American Chemical Society)

cols, called Activators (Re)Generated by Electron Transfer (A(R)GET)-ATRP, water-accelerated ATRP, and SI-"Paint on"-ATRP, have been developed and proposed as solutions to these limitations (Dunderdale et al. 2014; Simakova et al. 2012; Jones and Huck 2001).

LBL deposition is also commonly used to control surface wetting/dewetting properties, which uses self assembly of polyelectrolytes or nanoparticles (NPs) with opposing charges to form smart responsive surfaces and interfaces.

For example, Yang et al. (2011a) prepared polyelectrolyte multilayer (PDDA: poly(diallyldimethylammonium chloride)/PSS: poly(sodium 4-styrene sulfonate), covered cotton fabrics by using LBL deposition. As shown in Fig. 1.9, the resulting surfaces showed switchable wettability between non-wetting (CAs of water and *n*-hexadecane were about 151°and 140°, respectively) and fully wetted state for both water and *n*-hexadecane drops. The stimuli-responsive behavior took advantage of counterion exchange between Cl^- and sodium perfluorooctanoate (PFO) anions to produce these changes in wettability. Lu et al. (2013) also prepared LBL hydrogel (amphiplilic polymers)-covered microstructured Si surfaces which showed controllable wettability through pH-induced reversible collapse/solubilization transitions in solution.

LBL deposition enables the inclusion of various polymers and different-sized NPs within the resulting multilayer thin film, which can be used to increase surface roughness or porosity (Lu et al. 2013; Li et al. 2014a). Other advantages of this technique are that the film structure and chemical composition can be easily controlled, and it can be applicable to large-area substrates of arbitrarily shape,

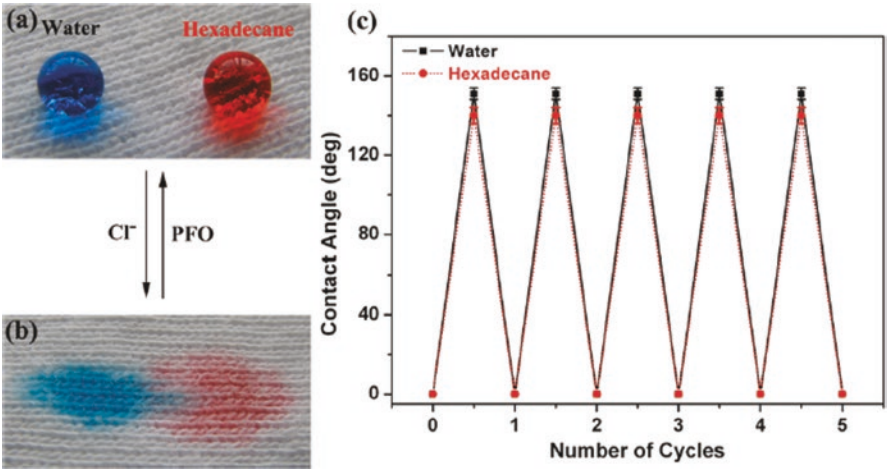

Fig. 1.9 (**a** and **b**) Water and *n*-hexadecane droplets on the polyelectrolyte-deposited cotton fabric surfaces coordinated with PFO anions and Cl⁻, respectively. (**c**) Switchable superhydrophobicity and superoleophobicity of the polyelectrolyte-deposited fabric surfaces with water and *n*-hexadecane *via* consecutive counterion exchange. (Reproduced with permission from (Yang et al. 2011a), Copyright 2011 The American Chemical Society)

porosity, and chemistry (Decher 1997). In conflicting roles, the intermolecular binding between polymers, which ensures stability of LBL films, becomes a major obstacle to the formation of smart responsive surfaces and interfaces capable of switching their surface wetting properties (Guo and Guo 2016).

Other methods, such as self-assembly (Liu et al. 2013; Jin et al. 2011), spray-deposition (Yang et al. 2011b; Zhang et al. 2012), spin-coating (Li et al. 2009), electrodeposition (Xu et al. 2014), LB method (Feng et al. 2001), electrochemical deposition (Wang and Guo 2013) and so on (Wu et al. 2013; Byun et al. 2012; Wang and Zhang 2012), have also been reported to fabricate smart stimuli-responsive surfaces and interfaces. In spite of these methods offering attractive advantages, there are requirements for further improvement of the stability of the smart-responsive surfaces/interfaces prepared by these approaches before widespread use becomes practical.

1.4 Typical Stimuli-Responsive Smart Surfaces and Interfaces

1.4.1 Mechanical (Stress/Stretch) Response

As mentioned above, surface wettability/dewettability are governed by surface structures and chemical compositions. Thus, if either of these factors is reversibly manipulated, surface wettability/dewettability is also reversibly controlled. In most of the reported stimuli-responsive behavior, it is the chemical composition, which is

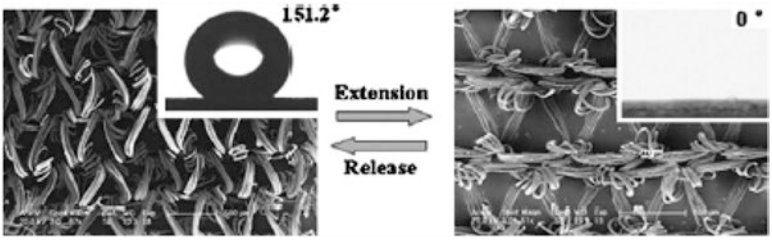

Fig. 1.10 Reversible change in surface structure and wettability of the triangular polyamide film with and without extension. (Reproduced with permission from (Xia et al. 2009), Copyright 2005 The Royal Society of Chemistry)

reversibly changed, however, changes in surface structures also cause changes in wettability/dewettability. There have been a few reports on stress-responsive smart surfaces and interfaces, which rely on this fact (Zhang et al. 2004, 2005; Lin and Yang 2009; Chung et al. 2007; Huang et al. 2015).

Zhang et al. (2004) reported a reversible wettability transition from hydrophobic to superhydrophobic of elastic poly(tetrafluoroethylene) (PTFE) films by stress stimulation. With an increase in the axial extension from 0 to 190%, water CAs increased from 108° to 165° because of the change in the density of the PTFE crystals during the axial extension. Zhang et al. (2005) also reported similar reversible wettability transitions in elastic polyamide films. When the film was bi-axially extended to more than 120%, the water droplet completely spread across the surface showing superhydrophilicity (Fig. 1.10, **right**), while after unloading, the surface returned to superhydrophobic again because of the recovery of surface microstructures (Fig. 1.10, **left**).

Similarly, PDMS films which have a wrinkled topography have shown to change their wettability when stretched. When not under mechanical strain the topography is highly wrinkled meaning that water drops sit on top of the surface in the Cassie-Baxter state, and can slide across the surface at an angle of ~15°. However, when mechanical strain is applied to this surface the wrinkled topography becomes less pronounced and it is harder for the drops to slide. On the same surface the sliding angle increased to ~50° when a mechanical strain of 40% was applied (Lin and Yang 2009). Chung et al. observed that CA's of water drops had only a single value when a PDMS film was smooth, but when compressed to form wrinkles had two different CA's depending on whether the orientation of the wrinkles was parallel or perpendicular to the observer. In this case the CA measured perpendicular to the wrinkles increased from ~65° to ~110° as the film was compressed to form wrinkles (Chung et al. 2007).

1.4.2 pH Response

pH-responsive materials have been widely applied to various fields, such as drug delivery, enzyme-immobilization, oil/water separation, chemo-mechanical system, chemical valves, and sensors (Xia et al. 2009).

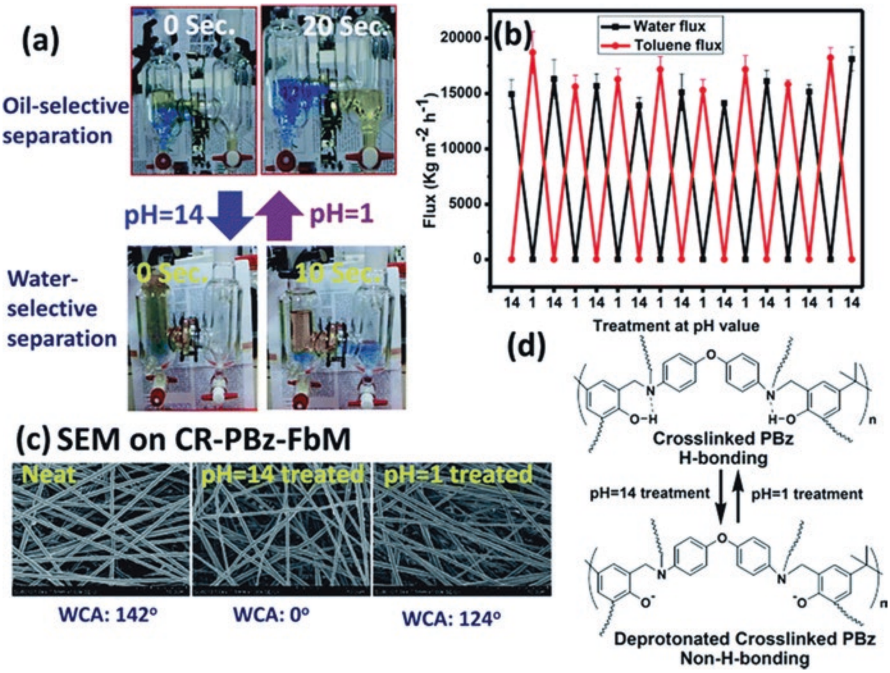

Fig. 1.11 (**a**) pH-induced switching of oil- and water-selectivity of the CR-PBz-FbM membrane in oil/water separation. (**b**) The membrane permeation fluxes in cycled treatment of the membrane with solutions of different pH values (pH 14 and pH 1). The changes in membrane selectivity are almost completely reversible without sacrificing the permeation fluxes. (**c**) SEM micrographs of the CR-PBz-FbM membrane treated with solutions of different pH values (pH 14 for 5 min and pH 1 for 1 min). (**d**) A scheme illustrating the changes in the chemical structure and hydrogen-bonding of CR-PBz-FbM being treated with solutions of different pH values (pH 14 and pH 1). Deprotonation of the crosslinked PBz structure results in loss of hydrogen bonding so as to turn the membrane from oleophilic to hydrophilic. (Reproduced with permission from (Liu and Liu 2016), Copyright 2016 The Royal Society of Chemistry)

For example, Liu and Liu (2016) prepared pH-responsive surfaces by electrospinning. Polybenzoxazine (PBz) was electrospun, and the collected PBz fiber mat then dried at 60 °C under vacuum, and finally cured thermally at 200 °C for 1 h and 240 °C for 3 h. The resulting cross-linked electrospun PBz fiber mat (CR-PBz-FbM) showed a hydrophobic nature. These mats were tested as potential pH-switchable oil/water separation meshes, as shown in Fig. 1.11. It was found that for solutions of pH 14, the mat showed oil-selective behavior, and at pH 1 it showed the opposite behavior being water-selective.

Huang et al. (2015) recently reported smart surfaces of hydrogels containing silanized glass particles showing reversible wettability from superhydrophobicity to superhydrophilicity under the different types of stimuli such as pH, temperature,

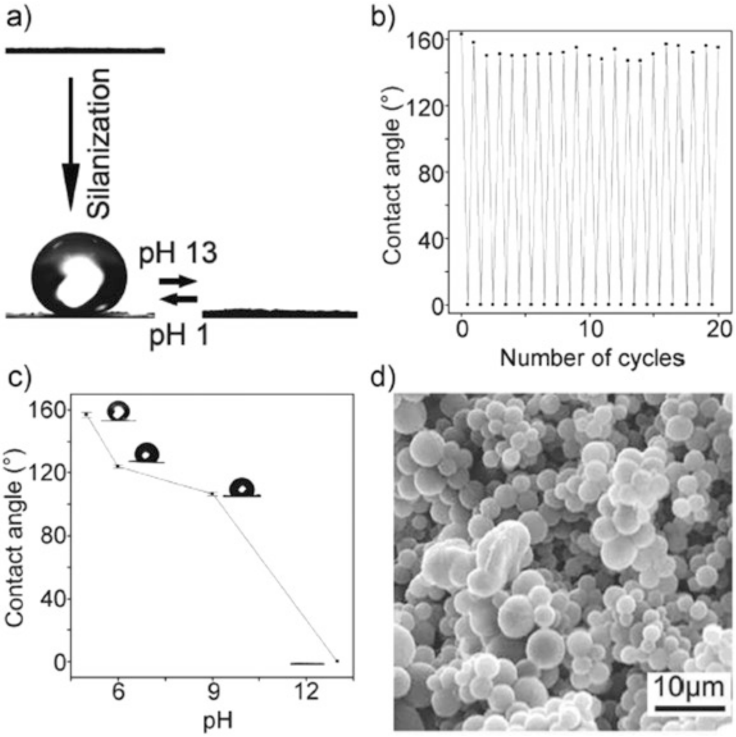

Fig. 1.12 Controlling the wettability of the pH-responsive composite material. (**a**) When the glass particles were not silanized, the water CA on the surface was 0°. After silanization, the surface became superhydrophobic (water CA was more than 150°). When the material was expanded by a solution of pH 13, the surface became superhydrophilic. (**b**) The switch from superhydrophobicity to superhydrophilicity was reversible as demonstrated by expanding and contracting the material in solutions of pH 13 and pH 1, respectively, for 20 times. (**c**) The water CA could be tuned by immersing the material in solutions of different pH. (**d**) An SEM image of the glass particles on the surface of the material (Reproduced with permission from (Huang et al. 2015), Copyright 2015 Wiley-VCH Verlag GmbH & Co. KGaA, Weinheim)

and stress. pH-responsive hydrogels were prepared by mixing acrylic acid, 2-hydroxyethyl methacrylate, ethylene glycol dimethacrylate (cross-linker), 2,2-dimethoxy-2-phenylacetophenone (photoinitiator), and deionized water. The mixture was then poured into the glass container covered with the layers of glass particles, and cured for a certain time. As shown in Fig. 1.12, after silanization using methyltrichlorosilane, the static water CA on the pH-responsive hydrogel surface was more than 150°. When the gel was immersed in a basic solution (pH 13), it expanded and became superhydrophilic, whereas by immersing it in an acidic solution (pH 1), it contracted and became superhydrophobic again, showing excellent tunable and reversible wettability.

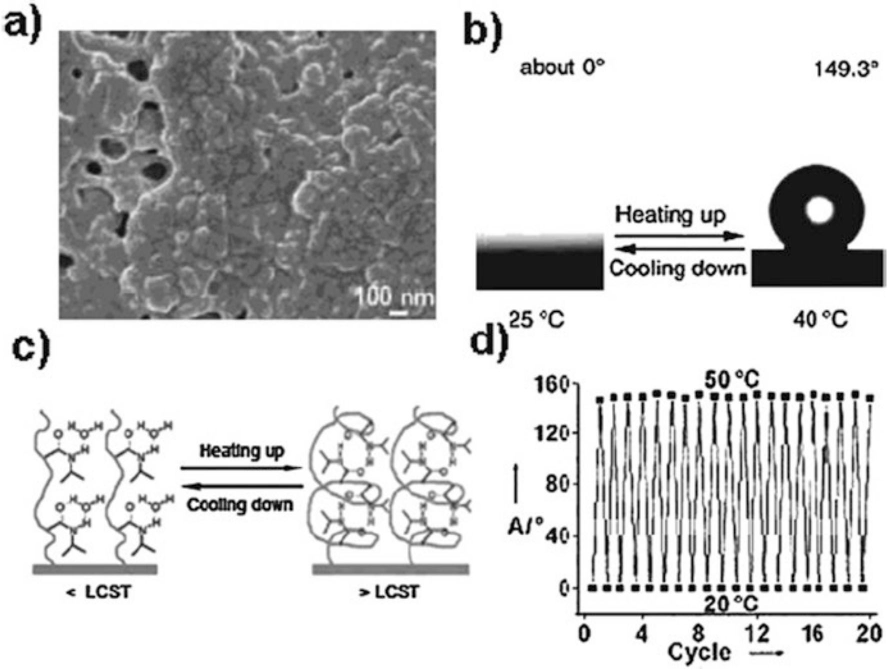

Fig. 1.13 (**a**) SEM image of the nanostructures on rough substrate modified with PNiPAAm. (**b**) Water drop profile for responsive surface at 25 °C and 40 °C. (**c**) Diagram of reversible formation of intermolecular hydrogen bonding between PNiPAAm chains and water molecules (left) and intramolecular hydrogen bonding between C=O and N–H groups in PNiPAAm chains (right) below and above the LCST, which is considered to be the molecular mechanism of the temperature-responsive wettability of a PNiPAAm thin film. (**d**) CAs at two different temperatures 20 °C and 40 °C for PNiPAAm-modified rough substrate. (Reproduced with permission from (Xia et al. 2009), Copyright 2009 The Royal Society of Chemistry)

1.4.3 Temperature Response

There have been numerous reports of materials which change their wettability in response to changes in temperature. Polymeric materials, which show a Lower Critical Solution Temperature (LCST), have been extensively used in this research field. For example, PNiPAAm is a typical temperature-responsive polymer that has a lower LCST of about 32–33 °C (Feng and Jiang 2006; Xia et al. 2009; Sun et al. 2004).

For example, Jiang's group (Xia et al. 2009; Sun et al. 2004) reported a smooth PNiPAAm surface exhibiting a controllable range of water CAs from 63.5° to 93.2°, *i.e.*, changing from slightly hydrophilic to slightly hydrophobic, as the temperature passed through the LCST. This is the result of the competition between intra- and intermolecular hydrogen bonding (Fig. 1.13c). On the other hand, when the PNiPAAm was deposited on a rough surface (Si microconvexes), the wettability could be changed from 0° to 149.3° when the temperature was elevated from 25 °C to 40 °C, indicating reversible switching between superhydrophobicity and superhydrophilicity (Fig. 1.13b, d).

PNiPAAm-based polymers have been commonly used for the preparation of temperature-responsive surfaces (Li et al. 2016b; Wang et al. 2015; Sun et al. 2004; Koenig et al. 2014; Chen et al. 2010; Liu et al. 2015), along with other types of temperature-responsive materials as will be described below.

Yang et al. (2011b) prepared a superhydrophobic carbon nanotube (CNT) film by a simple spray-coating method without any further chemical modification. The surface wettability of the CNT film could be reversibly changed between superhydrophobic and superhydrophilic by alternating between a hot environment and ambient temperature due to the change of surface charges on the CNT film. Facile one-step spray-deposition process for the fabrication of superhydrophobic and superoleophilic SiO_2-NP (SiO_2-NPs were chemically modified with trimethylchlorosilane) films showing a quick temperature-responsive wettability transition was also reported by Zhang et al. (2012). When the as-prepared film was kept in a freezer until the surface temperature dropped down to −15 °C, it switched from superhydrophobic (water CA was about 168°) to hydrophilic (water CA was about 71°), and immediately returned to superhydrophobic by leaving the sample at room temperature for only 3 min. This process could be repeated several times, and good reversibility of the surface wettability was confirmed. This temperature-responsive transition was considered to be related to water vapor condensation on the surface.

1.4.4 Light Response

Several types of photo-sensitive materials have been used to prepare light-responsive smart surfaces and interfaces. Inorganic oxides, such as TiO_2 (Feng et al. 2005; Zhang et al. 2007; Sun et al. 2001), ZnO (Sun et al. 2001; Feng et al. 2004), SnO_2 (Zhu et al. 2006), WO_3 (Wang et al. 2006), and so on are well known to show reversibly switchable wettability.

Among them, TiO_2 particles have been widely used to prepare light-sensitive smart surfaces and interfaces. The main role of the particulate morphology is to provide surface roughness and so increase CAs (Gondal et al. 2014). Whereas the choice of particle material (TiO_2) gives photocatalytic decomposition of organic contaminants. Wang et al. (2016b) prepared a smart surface consisting of TiO_2-NPs doped polyvinylidene fluoride (PVDF) nanofibers by electrospinning, which formed beads-on-string structures with hierarchical roughness. These nanofiber membranes where used in separation of oil/water mixtures and showed switching behavior when UV (or sunlight) irradiated (water CA of 0°) or heat treated (water CA of ~152°) by selectively allowing water or oil to pass, respectively. In addition, these nanofiber membranes exhibited anti-fouling and self-cleaning properties because of the photocatalytic property of TiO_2, as shown in Fig. 1.14. Such properties may enable their reusability for practical applications.

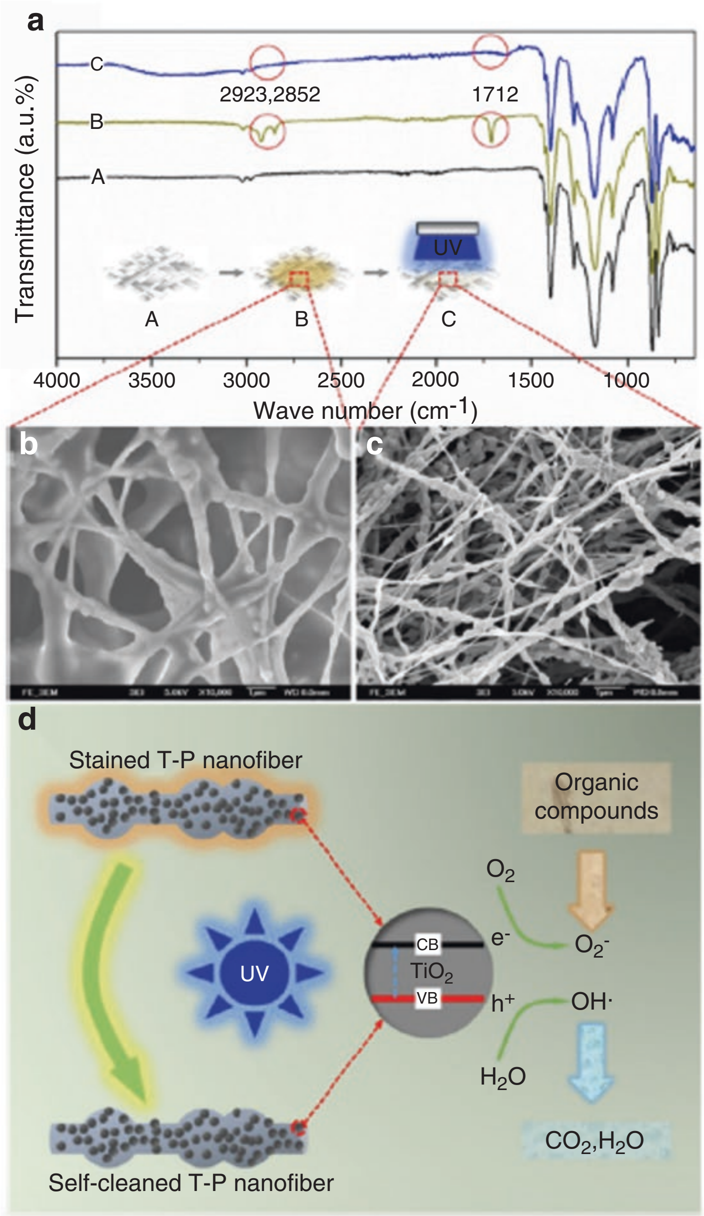

Fig. 1.14 Anti-fouling and self-cleaning behavior of the TiO_2-PVDF nanofibrous membrane. (**a**) FTIR spectrum showing the chemical component difference among the TiO_2-PVDF membrane before and after being stained by oleic acid and the stained TiO_2-PVDF membrane treated by UV-irradiation. FE-SEM images show the top surface of the stained TiO_2-PVDF membrane before (**b**) and after (**c**) UV-irradiation. (**d**) Illustration of the self-cleaning behavior of the TiO_2-PVDF nanofibers and the photocatalytic mechanism of TiO_2-NPs. (Reproduced with permission from (Wang et al. 2016b), Copyright 2016 The American Chemical Society)

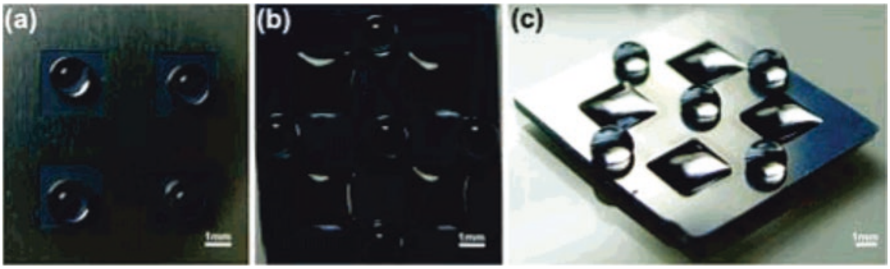

Fig. 1.15 Photographs of substrates with patterned extreme wetting properties. (**a**) Photomask and water droplet profiles on the as-prepared substrate. (**b**) Top and (**c**) angled views of water droplet profiles on the patterned substrate as a result of site-selective UV irradiation. (Reproduced with permission from (Lim et al. 2006), Copyright 2006 The American Chemical Society)

Besides inorganic oxides, some organic materials containing photochromic functional groups (azobenzene (Delorme et al. 2005), spiropyran (Rosario et al. 2002), dipyridylethylene (Cooper et al. 2004), and stilbene (Driscoll et al. 2007)) have an ability to change a reversible conformation through UV/visible irradiation, resulting in changes in their wetting properties. Among these photo-sensitive materials, azobenzene and its derivatives are particularly promising.

For example, Lim et al. (2006) first reported superhydrophobic and superhydrophilic transitions of organic molecules under UV/visible irradiation. Using 7-[(trifluoromethoxyphenylazo) phenoxy]pentanoic acid (CF_3AZO, photo switchable agent), they prepared organic-inorganic hybrid multilayer films by LBL deposition using poly(allylamine hydrochloride) (PAH) and SiO_2-NPs as the polycation and polyanion, respectively. With increases in the number of PAH/SiO_2-NPs bilayers ((PAH/SiO_2-NPs)$_n$), the water CA gradually increased from 76° (flat, $n = 0$) to 152° ($n = 9$) in the absence of UV light (*trans* isomer). When the samples were irradiated with UV light (*cis* isomer), the water CA slowly decreased from 71° (flat, $n = 0$) to 5° ($n = 9$). In this fashion, the surfaces showed reversible switching between superhydrophobicity and superhydrophilicity upon alternating between UV and visible light irradiation. They have also successfully prepared erasable and rewritable micropatterns of extreme wetting properties based on a site-selective UV irradiation (Fig. 1.15).

Although these photo-sensitive organic materials are particularly promising because of their easy chemical modification and reaction diversity, their photo, thermal, and chemical stabilities are inferior, compared to inorganic materials.

1.4.5 Electric Response

Changes in surface wettability of electro-responsive surfaces and interfaces are driven by the re-arrangement of charges and dipoles when an electric potential is applied between a liquid and a solid, resulting in a reduction in the interfacial energy

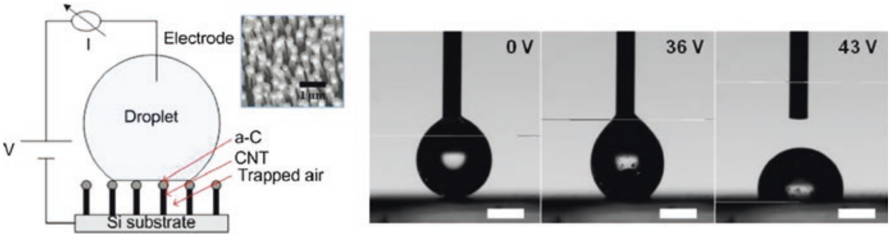

Fig. 1.16 The schematic diagram for electrowetting setup (left). The droplet is in contact with the a-C-NPs and air is trapped between neighboring CNTs in the Cassie state. The inset shows the microstructure of a-C/CNT nanocomposites. The electrowetting images for water at different potentials. The scale bar is 1 mm for all images (right). (Reproduced with permission from (Han et al. 2009), Copyright 2009 The American Chemical Society)

(increase in surface wettability). The advantages of using electrical potentials are the ability to control surface wettability without any changes in the surface composition and morphology. Thus, it is considered a simple, versatile, and effective external stimulus to switch surface wetting behavior (Xu et al. 2014; Mugele and Baret 2005; Kakade et al. 2008; Bodre and Pauporte 2009; Krupenkin et al. 2007; Han et al. 2009).

For instance, Krupenkin et al. (2007) successfully demonstrated fully reversible switching between the superhydrophobic Cassie-Baxter state and the hydrophilic Wenzel state on nanostructured surfaces by the application of an electrical voltage and current. Without an applied voltage, a water droplet on the nanograss substrate was unstable and highly mobile. When 35 V was applied, the water droplet underwent a sharp transition to the immobile state. After a short pulse of electrical current was transmitted through the nanograss substrate, the droplet returned to the original unstable state. Han et al. (2009) also reported an effective control of surface wettability of a nanostructured surface consisting of arrays of amorphous carbon (a-C)-NPs capped on CNTs using an electrowetting technique (Fig. 1.16 **left**). By applying a potential from 0 to 36 V between the water droplet and the solid surface, water CAs slowly reduced from 160° to 142°. When the CAs approached the threshold value (-142°), a transition from the "slippy" Cassie state to the "sticky" Wenzel state (final water CA was 104° at 43 V) was observed (Fig. 1.16 **right**).

1.4.6 Magnetic Response

Smart surfaces and interfaces which can respond to magnetic fields have been reported by Grigoryev et al. (2012) and Cheng et al. (2012c). As shown in Fig. 1.17, Grigoryev et al. (2012) fabricated Ni-wire arrays (micronails) with a high aspect ratio whose top was capped with μm-scale (between 4 and 8 μm) hemispherical

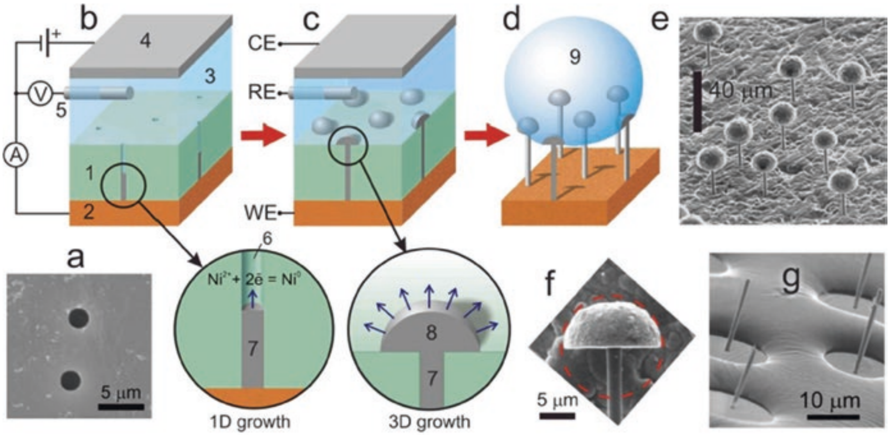

Fig. 1.17 Fabrication and characterization of Ni-micronails. (**a**) SEM micrograph of a PC template. (**b**) Three-electrode electrodeposition setup consisting of a track-etch template (*1*), a metal working electrode (WE) deposited on one side of the PC template (*2*), a Ni-electroplating bath (*3*), a Ni-counter electrode (CE) (*4*), and a reference electrode (RE) (*5*), the enlarged schematic shows the pore-confined 1D growth of Ni inside of the template pore (6), formation of a Ni wire leg (*7*). (**c**) Ni wires reach the top of the PC template and continue to grow. The enlarged schematic shows the unrestricted 3D growth of Ni on the template surface, resulting in the formation of a hemispherical cap (*8*). (**d**) The structure of a bed of Ni micronails after removal of the PC template, and supports the Cassie-Baxter regime (*9*). (**e**) SEM image of a cluster of electrodeposited Ni-micronails. (**f**) Magnification of SEM image of a single Ni-micronail. (**g**) SEM image showing the Cassie-Baxter state for an epoxy resin droplet sitting on a bed of Ni-micronails. The Ni-micronails were separated from the metal substrate to visualize the reverse side of the droplet. (Reproduced with permission from (Grigoryev et al. 2012), Copyright 2012 The American Chemical Society)

caps based on an area-selective electrodeposition using a polycarbonate (PC) membrane possessing uniform cylindrical pores. They demonstrated a wettability transition from superomniphobicity to omniphilicity by applying an external magnetic field. Ni-micronail surface covered with a self-assembled monolayer (SAM) of 1*H*,1*H*,2*H*,2*H*-perfluorodecanethiol showed superomniphobicity without a magnetic field, however, when an external magnetic field (50 mT) was applied and Ni-micronails were bent with an angle of 23° with the surface normal, the transition from the anti-wetting Cassie-Baxter state (water CA was 159° and *n*-hexadecane CA was 153°) to the wetting Wenzel state was observed. Cheng et al. (2012c) also demonstrated reversible wetting/dewetting transitions of microdroplets containing superparamagnetic Fe_3O_4-nanoparticles (NPs) on a highly hydrophobic microstructured Si surface. They successfully controlled the switching between the Cassie state (water CA of 145°) and the Wenzel state (water CA of 135°) by the intensity of the magnetic field and the concentration of Fe_3O_4-NPs in the microdroplet (Fig. 1.18).

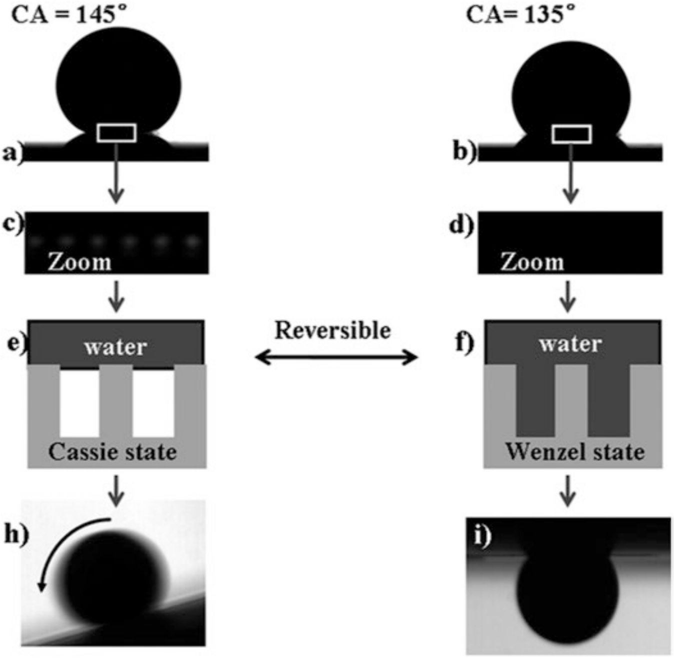

Fig. 1.18 Reversible transition between the Cassie state and the Wenzel state by application of the magnetic fields. (**a** and **b**) The superparamagnetic microdroplet resides in the Cassie state (CA of 145°) and the Wenzel state (CA of 135°), respectively. (**c** and **d**) Higher magnification photos of the interface between the liquid and the substrate with and without air, respectively. (**e** and **f**) Schematic illustration of the two wetting states. (**h** and **i**) In the Cassie state, a microdroplet can roll across the surface, while in the Wenzel state, it is pinned to the surface. (Reproduced with permission from (Cheng et al. 2012c), Copyright 2012 The American Chemical Society)

1.4.7 Gas Response

Zhu et al. reported ammonia-gas responsive surfaces showing switchable wettability on micro/nanostructured indium hydroxide ($In(OH)_3$) films (Zhu et al. 2008) and polyaniline-coated fabrics (Zhu et al. 2007). In the former case, the films were superhydrophobic in air with a water CA of 150.4°, while their surfaces turned to superhydrophilic with a water CA of 0° after exposure to an ammonia vapor. Li et al. (2014b) reported CO_2-gas responsive surface covered with a SAM of *N*-(2-aminoethyl)-5-(1,2-dithiolan-3-yl) pentanamide amidine (NADPA) on Au substrates *via* molecular self-assembly technique. The surface wettability of the NADPA-SAM showed reversible switching because of reversion of the amidine conjugation systems, which was caused by reversible protonation/deprotonation in the presence/absence of CO_2 gas (Fig. 1.19).

Che et al. (2015) also reported CO_2-gas responsive nanofibrous membranes (average diameter of about 700 nm), which are capable of oil/water separation applications. They prepared polymeric membranes using poly(methyl methacrylate)-

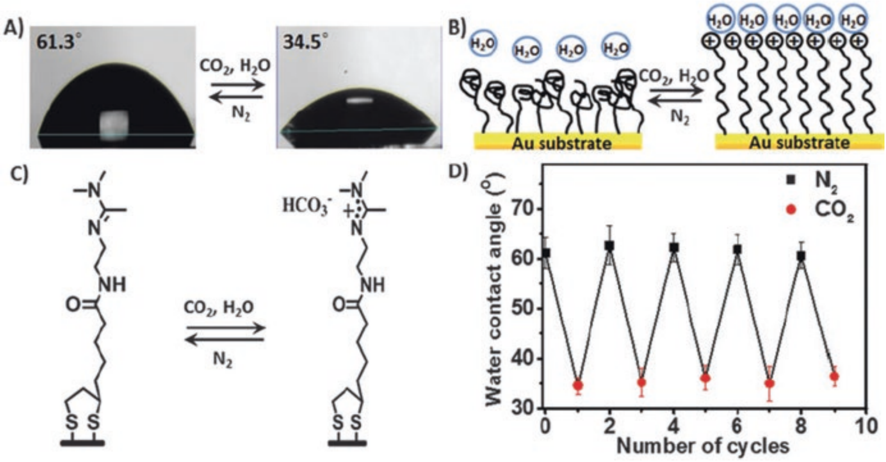

Fig. 1.19 CO_2-responsive switching of the NADPA-SAM. (**a**) A photographic image of the water droplet on a NADPA modified surface before (left) and after (right) the stimuli of CO_2. (**b**) A schematic diagram stimuli-induced transition of surface wettability. (**c**) Changes in the chemical structure of amidine. (**d**) Reversible switching of water CAs. (Reproduced with permission from (Li et al. 2014b), Copyright 2014 The Royal Society of Chemistry)

co-poly(*N*,*N*-diethylaminoethyl methacrylate) (PMMA-*co*-PDEAEMA) by electrospinning, and then tested for water and oil wettability. They successfully demonstrated selective switching for an oil/water separation system using CO_2 or N_2 gas flow. As shown in Fig. 1.20, when an oil/water mixture was introduced to the membrane, oil could pass easily, while water remained on the membrane surface because the membrane surface showed hydrophobic and oleophilic properties. In contrast, when the membranes were submerged in water with CO_2 gas bubbling through the liquid for a few minutes, the separation results dramatically changed. In that case, water could be separated and oil remained on the membrane surface.

1.4.8 Solvent Response

Solvent-responsive smart surfaces and interfaces are influenced by the surrounding media, and their switchable wettability is governed by change in interfacial free energy, which is driven by conversion or rearrangement of polymer chains, induced by solvents (Minko et al. 2003; Motornov et al. 2003; Liu et al. 2005; Song et al. 2007; Wang et al. 2009).

Minko et al. (2003) reported the control of surface wettability by exposing the polymer films to different solvents (toluene, 1,4-dioxane and acidic water). They attached polymer chains of PSF-COOH (PSF: pentafluorostyrene) and PVP-COOH (PVP: poly(*N*-vinylpyrrolidone)) to flat and plasma-etched needle-like PTFE sub-

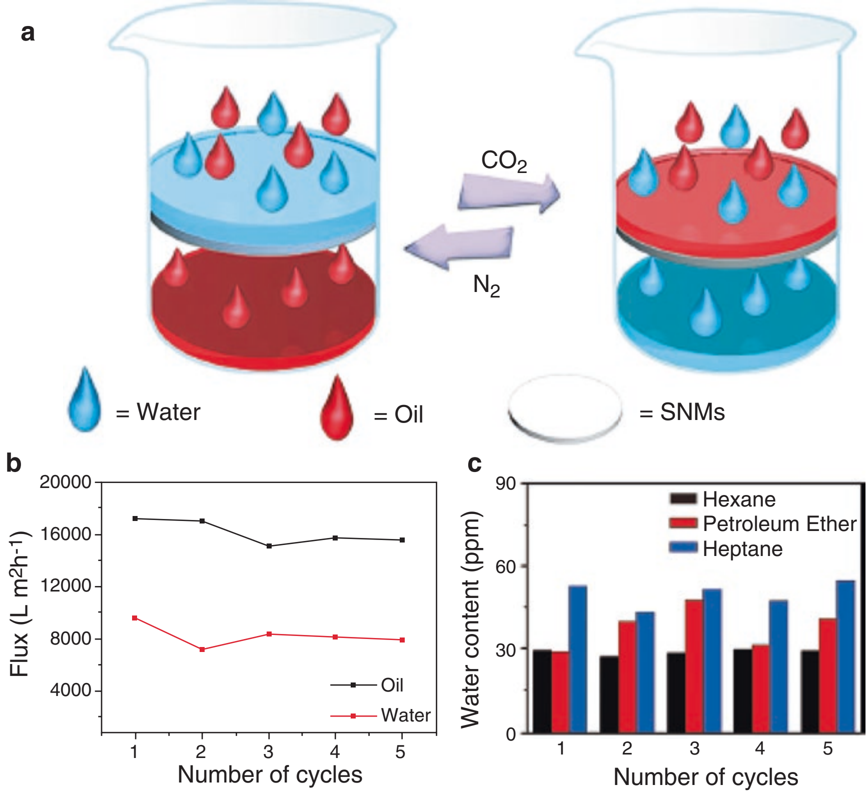

Fig. 1.20 (**a**) Representation of the CO_2 switchable oil/water on-off switch. (**b**) Variations in the flux of oil and water in the absence and presence of CO_2, respectively. (**c**) Water content in oil in the filtrate after permeating oil/water mixtures through the smart nanostructured membranes. (Reproduced with permission from (Che et al. 2015), Copyright 2015 Wiley-VCH Verlag GmbH & Co. KGaA, Weinheim)

strates terminated with hydroxyl and amino groups, which were introduced by the plasma treatment. In the case of selective solvents, upon exposure to toluene, the top of the film surface was predominantly occupied by the PSF component, while upon exposure to acidic water (pH 3), the PSF formed round domains and was buried in the PVP matrix. On the other hand, in the case of non-selective solvents, both polymer components were present on the surface (Fig. 1.21). As a result, after exposure to toluene, acidic water (pH 3), and 1,4-dioxane, the advancing CA (θ_A) of water on the flat substrate was measured to be 118°, 25°, and 75°, respectively. This switching behavior was amplified by the surface roughness. After exposure to toluene, the θ_A of water was increased to 160° and a water droplet rolled easily on the surface, showing low CA hysteresis.

Wang et al. (2009) reported an unusual solvent-responsive smart surface prepared from double amino acid (aspartic acid (AA) and cysteine (Cy)) units grafted

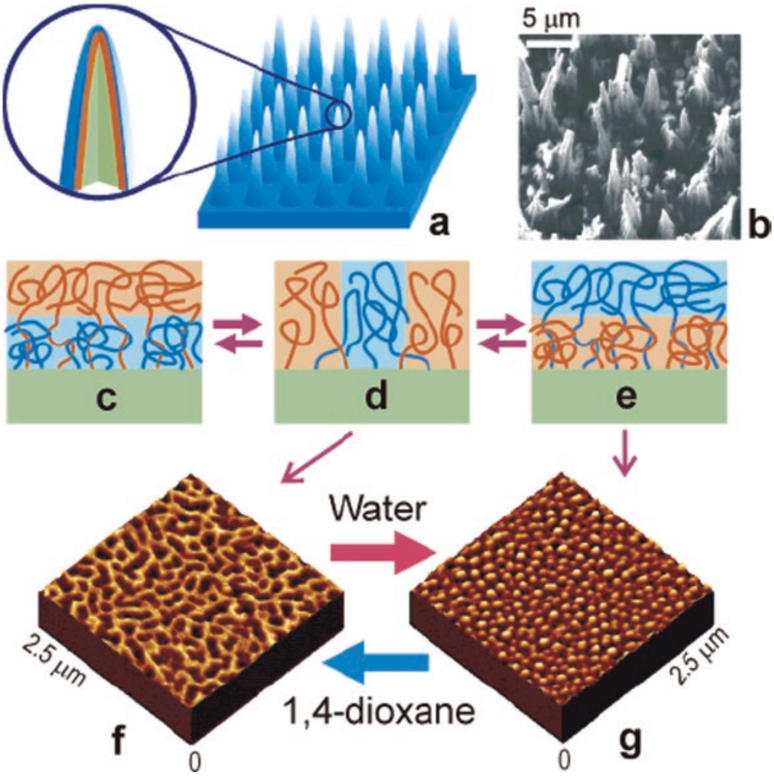

Fig. 1.21 Two-level structure of self-adaptive surfaces (SAS). (**a**) Schematic representation of needle-like surface morphology of the PTFE surface (first level). (**b**) SEM image of the PTFE film after 600 s of plasma etching. (**c**–**e**) Each needle is covered by a covalently grafted mixed brush that consists of hydrophobic and hydrophilic polymers (second level). Its morphology results from an interplay between lateral and vertical phase segregation of the polymers, which switches the morphology and surface properties upon exposure to different solvents. (**c** and **e**) In selective solvents, the preferred polymer preferentially occupies the top of the surface. (**d**) In non-selective solvents, both polymers are present in the top layer. (**f** and **g**) AFM images (model smooth substrate) of the different morphologies after exposure to different solvents. (Reproduced with permission from (Minko et al. 2003), Copyright 2003 The American Chemical Society)

PNiPAAm copolymer film (PNiPAAm-*co*-Cy&AA)). The changes in water CA in response to the solvents (water and methanol) on a flat Si substrate were only 11° (water CAs after water and methanol treatments were about 86° and 75°, respectively). When a structured Si substrate consisting of well-aligned square micro-pillars (side length of about 10 μm and separation of about 12 μm) with nanofibrous structures on the top of each pillar was used, water treatment induced a dramatic increase of hydrophobicity, changing from slightly hydrophilic (water CA of about 72°) to superhydrophobic (water CA was about 156°). However, the reversibility of the wettability switching again was poor. The authors then replaced pure methanol with the mixture of methanol and alkali. They confirmed the

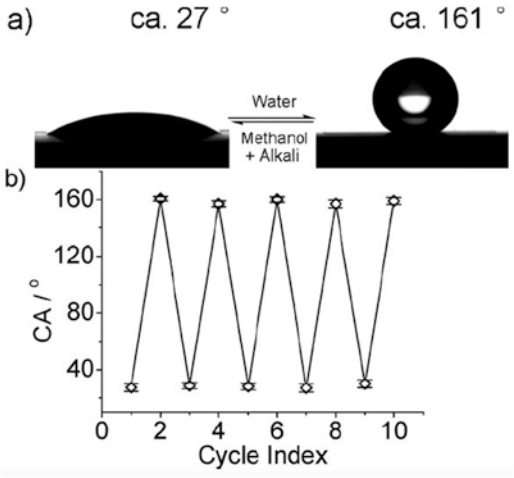

Fig. 1.22 Reversible wettability switching between high hydrophilicity and superhydrophobicity for a PNiPAAm-co-Cy&AA film on a structured substrate when treated with water and methanol-alkali solution alternately: (**a**) water drop profiles, (**b**) cycling experiment. (Reproduced with permission from (Wang et al. 2009), Copyright 2009 The Royal Society of Chemistry)

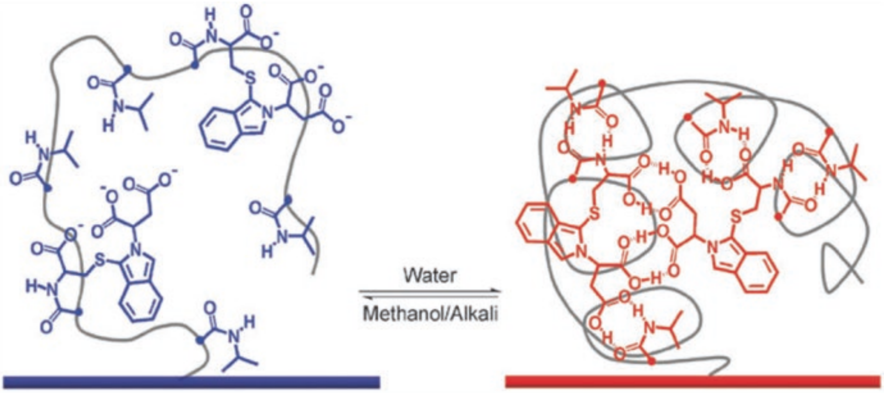

Fig. 1.23 Schematic diagram for the possible mechanism of the solvent-responsive wettability on PNiPAAm-*co*-Cy&AA copolymer film. In this mechanism, methanol-alkali or water treatments influence both the formation or cleavage of the intramolecular hydrogen-bonding, and the aggregation or dispersion of the anions inside the polymer film, which results in a change of the loose or wound conformations of polymer, and the wettability change of the film. (Reproduced with permission from (Wang et al. 2009), Copyright 2009 The Royal Society of Chemistry)

remarkable changes in water CA (water CAs after water and methanol-alkali treatments were about 161° and 27°, respectively) and good reversibility (Fig. 1.22). The methanol treatment weakens both the hydrophobic and hydrogen bonding interactions, and addition of alkali, leads to highly charged carboxyl groups and a highly hydrophilic surface (Fig. 1.23, **left**). In contrast, once the polymer surface contacted water, due to the solvophobic effect and the dielectric properties of water media, the polymer switched back to the bound state, leading to the hydrophobic surface (Fig. 1.23, **right**).

1.5 Summary

This chapter briefly summarizes the basic theories of surface wetting/dewetting properties of flat and rough solid surfaces, such as static/dynamic contact angles (CAs), CA hysteresis, Young's, Wenzel's, and Cassie-Baxter's equations. Although static CA (θ_S) measurements are a conventional way to characterize the surface properties and understand liquid-solid interactions, it has been recently recognized that static dewetting properties of solid surfaces (conventional θ_S values) alone do not closely reflect actual wetting/dewetting properties. Thus, instead of relying on the magnitude of θ_S values, the measurement of dynamic wettability, including the advancing (θ_A) and receding (θ_R) CAs, CA hysteresis, and tilt angles (θ_T) are required to accurately characterize the wetting/dewetting properties of a solid surface. Therefore, besides θ_S values, these factors are now taken into account in the latest definition of super-liquid-repellent (SLR) surfaces and interfaces.

This chapter also introduced an overview of the typical examples of smart surfaces and interfaces possessing controllable wetting/dewetting properties by different external stimuli, such as pH, temperature, light, solvent, mechanical stress, and electric/magnetic fields and so on. In this chapter, we focused on the surfaces/interfaces showing a response to only one of the external stimuli mentioned above. However, such simple responses of the functional surfaces limit their practical applications under complicated conditions. Thus, further development of dual and multiple responsive smart surfaces/interfaces is also necessary. Although these stimuli-responsive surfaces/interfaces, which take advantage of the SLR properties are promising, they are in their infancy and still very challenging. We hope that this book will enhance interest for researchers and engineers in this new research field.

References

Agarwal S, Greiner A, Wendorff JH (2013) Functional materials by electrospinning of polymers. Prog Polym Sci 38:963–991

Alayande SO, Dare EO, Msagati TAM, Akinlabi AK, Aiyedun PO (2016) Superhydrophobic and superoleophillic surface of porous beaded electrospun polystrene and polysytrene-zeolite fiber for crude oil-water separation. Phys Chem Earth 92:7–13

Arslan O, Aytac Z, Uyar T (2016) Superhydrophobic, hybrid, electrospun cellulose acetate nanofibrous mats for oil/water separation by tailored surface modification. ACS Appl Mater Interfaces 8:19747–19754

Barbey R, Lavanant L, Paripovic D, Schüwer N, Sugnaux C, Tugulu S, Klok HA (2009) Polymer brushes via surface-initiated controlled radical polymerization: synthesis, characterization, properties, and applications. Chem Rev 109:5437–5527

Bhardwaj N, Kundu SC (2010) Electrospinning: a fascinating fiber fabrication technique. Biotechnol Adv 28:325–347

Bhushan B, Jung YC (2011) Natural and biomimetic artificial surfaces for superhydrophobicity, self-cleaning, low adhesion, and drag reduction. Prog Mater Sci 56:1–108

Bodre C, Pauporte T (2009) Nanostructured ZnO-based surface with reversible electrochemically adjustable wettability. Adv Mater 21:697–701

Brown PS, Bhushan B (2016) Durable, superoleophobic polymer–nanoparticle composite surfaces with re-entrant geometry via solvent-induced phase transformation. Sci Rep 6:21048

Byun J, Shin J, Kwon S, Jang S, Kim JK (2012) Fast and reversibly switchable wettability induced by a photothermal effect. Chem Commun 48:9278–9280

Cassie ABD, Baxter S (1944) Wettability of porous surfaces. Trans Faraday Soc 40:546–551

Che H, Huo M, Peng L, Fang T, Liu N, Feng L, Wei Y, Yuan J (2015) Co2-responsive nanofibrous membranes with switchable oil/water wettability. Angew Chem Int Ed 54:8934–8938

Chen W, Fadeev AY, Hsieh MC, Öner D, Youngblood J, McCarthy TJ (1999) Ultrahydrophobic and ultralyophobic surfaces: some comments and examples. Langmuir 15:3395–3399

Chen L, Liu MJ, Lin L, Zhang T, Ma J, Song YL, Jiang L (2010) Thermal-responsive hydrogel surface: tunable wettability and adhesion to oil at the water/solid interface. Soft Matter 6:2708–2712

Cheng DF, Urata C, Yagihashi M, Hozumi A (2012a) A statically oleophilic but dynamically oleophobic smooth nonperfluorinated surface. Angew Chem Int Ed 51:2956–2959

Cheng DF, Urata C, Masheder B, Hozumi A (2012b) A physical approach to specifically improve the mobility of alkane liquid drops. J Am Chem Soc 134:10191–10199

Cheng Z, Lai H, Zhang NQ, Sun KN, Jiang L (2012c) Magnetically induced reversible transition between cassie and wenzel states of superparamagnetic microdroplets on highly hydrophobic silicon surface. J Phys Chem C 116:18796–18802

Chung JY, Youngblood JP, Stafford CM (2007) Anisotropic wetting on tunable micro-wrinkled surface. Soft Matter 3:1163–1169

Cooper CGF, MacDonald JC, Soto E, McGimpsey WG (2004) Non-covalent assembly of a photoswitchable surface. J Am Chem Soc 126:1032–1033

Crevoisier GD, Fabre P, Corpart JM, Leibler L (1999) Switchable tackiness and wettability of a liquid crystalline polymer. Science 285:1246–1249

Decher G (1997) Fuzzy nanoassemblies: toward layered polymeric multicomposites. Science 277:1232–1237

Delorme N, Bardeau JF, Bulou A, Poncin-Epaillard F (2005) Azobenzene-containing monolayer with photoswitchable wettability. Langmuir 21:12278–12282

Deng X, Mammen L, Butt HJ, Vollmer D (2012) Candle soot as a template for a transparent robust superamphiphobic coating. Science 335:67–70

Ding B, Wang M, Wang X, Yu J, Sun G (2010) Electrospun nanomaterials for ultrasensitive sensors. Mater Today 13:16–27

Doshi J, Reneker DH (1995) Electrospinning process and applications of electrospun fibers. J Electrost 35:151–160

Driscoll PF, Purohit N, Wanichacheva N, Lambert CR, McGimpsey WG (2007) Reversible photoswitchable wettability in noncovalently assembled multilayered films. Langmuir 23:13181–13187

Dunderdale GJ, Urata C, Miranda DF, Hozumi A (2014) Large-scale and environmentally friendly synthesis of pH-responsive oil-repellent polymer brush surfaces under ambient conditions. ACS Appl Mater Interfaces 6:11864–11868

Dunderdale GJ, Urata C, Sato T, England MW, Hozumi A (2015) Continuous, high-speed, and efficient oil/water separation using meshes with antagonistic wetting properties. ACS Appl Mater Interfaces 7:18915–18919

Fang W, Liu L, Li T, Dang Z, Qiao C, Xu J, Wang Y (2016) Electrospun N-substituted polyurethane membranes with self-healing ability for self-cleaning and oil/water separation. Chem-Eur J 22:878–883

Feng X, Jiang L (2006) Design and creation of superwetting/antiwetting surfaces. Adv Mater 18:3063–3078

Feng C, Zhang Y, Jin J, Song Y, Xie L, Qu G, Jiang L, Zhu D (2001) Reversible wettability of photoresponsive fluorine-containing azobenzene polymer in Langmuir-Blodgett films. Langmuir 17:4593–4597

Feng XJ, Feng L, Jin MH, Zhai J, Jiang L, Zhu DB (2004) Reversible super-hydrophobicity to super-hydrophilicity transition of aligned ZnO nanorod films. J Am Chem Soc 126:62–63

Feng XJ, Zhai J, Jiang L (2005) The fabrication and switchable superhydrophobicity of TiO_2 nanorod films. Angew Chem Int Ed 44:5115–5118

Forsberg PSH, Priest C, Brinkmann M, Sedev R, Ralston J (2010) Contact line pinning on micro-structured surfaces for liquids in the Wenzel state. Langmuir 26:860–865

Fu Q, Rao GVR, Basame SB, Keller DJ, Artyushkova K, Fulghum JE, López GP (2004) Reversible control of free energy and topography of nanostructured surfaces. J Am Chem Soc 126:8904–8905

Furmidge CGL (1962) Studies at phase interfaces. I. The sliding of liquid drops on solid surfaces and a theory for spray retention. J Colloid Sci 17:309–324

Gao L, McCarthy TJ (2006a) The "lotus effect" explained: two reasons why two length scales of topography are important. Langmuir 22:2966–2967

Gao L, McCarthy TJ (2006b) Contact angle hysteresis explained. Langmuir 22:6234–6237

Gao L, McCarthy TJ (2009) Wetting 101°. Langmuir 25:14105–14115

Gondal MA, Sadullah MS, Dastageer MA, McKinley GH, Panchanathan D, Varanasi KK (2014) Study of factors governing oil-water separation process using TiO_2 films prepared by spray deposition of nanoparticle dispersions. ACS Appl Mater Interfaces 6:13422–13429

Grigoryev A, Tokarev I, Kornev KG, Luzinov I, Minko S (2012) Superomniphobic magnetic microtextures with remote wetting control. J Am Chem Soc 134:12916–12919

Guo F, Guo Z (2016) Inspired smart materials with external stimuli responsive wettability: a review. RSC Adv 6:36623–36641

Han ZJ, Tay B, Tan C, Shakerzadeh M, Ostrikov K (2009) Electrowetting control of cassie-to-wenzel transitions in superhydrophobic carbon nanotube-based nanocomposites. ACS Nano 3:3031–3036

Hozumi A, Takai O (1997) Preparation of ultra water-repellent films by microwave plasma-enhanced CVD. Thin Solid Film 303:222–225

Huang ZM, Zhang YZ, Kotaki M, Ramakrishna S (2003) Compos Sci Technol 63:2223–2253

Huang M, Si Y, Tang X, Zhu Z, Ding B, Liu L, Zheng G, Luo W, Yu J (2013) Gravity driven separation of emulsified oil-water mixtures utilizing *in situ* polymerized superhydrophobic and superoleophilic nanofibrous membranes. J Mater Chem A 1:14071–14074

Huang X, Sun YJ, Soh S (2015) Stimuli-responsive surfaces for tunable and reversible control of wettability. Adv Mater 27:4062–4068

Huber DL, Manginell RP, Samara MA, Kim BI, Bunker BC (2003) Programmed adsorption and release of proteins in a microfluidic device. Science 301:352–354

Jain P, Baker GL, Bruening ML (2009) Applications of polymer brushes in protein analysis and purification. Annu Rev Anal Chem 2:387–408

Jin M, Feng X, Feng L, Sun T, Zhai J, Li T, Jiang L (2005) Superhydrophobic aligned polystyrene nanotube films with high adhesive force. Adv Mater 17:1977–1981

Jin CF, Yan RS, Huang JG (2011) Cellulose substance with reversible photo-responsive wettability by surface modification. J Mater Chem 21:17519–17525

Jones DM, Huck WTS (2001) Controlled surface-initiated polymerizations in aqueous media. Adv Mater 13:1256–1259

Kakade B, Mehta R, Durge A, Kulkarni S, Pillai V (2008) Electric field induced, superhydrophobic to superhydrophilic switching in multiwalled carbon nanotube papers. Nano Lett 8:2693–2696

Kawasaki K (1960) Study of wettability of polymers by sliding of water drop. J Colloid Sci 15:402–407

Kim YJ, Ebara M, Aoyagi T (2012) A smart nanofiber web that captures and releases cells. Angew Chem Int Ed 51:10537–10541

Kim YJ, Ebara M, Aoyagi T (2013) A smart hyperthermia nanofiber with switchable drug release for inducing cancer apoptosis. Adv Funct Mater 23:5753–5761

Koenig M, Magerl D, Philipp M, Eichhorn KJ, Müller M, Müller Buschaum P, Stamm M, Uhlmann P (2014) Nanocomposite coatings with stimuli-responsive catalytic activity. RSC Adv 4:17579–17586

Kota AK, Kwon G, Choi W, Mabry JM, Tuteja A (2012) Hygro-responsive membranes for effective oil-water separation. Nat Commun 3:1025

Kota AK, Kwon G, Tuteja A (2014) The design and applications of superomniphobic surfaces. NPG Asia Mater 6:e109

Krupenkin TN, Taylor JA, Wang EN, Kolodner P, Hodes M, Salamon TR (2007) Reversible wetting-dewetting transitions on electrically tunable superhydrophobic nanostructured surfaces. Langmuir 23:9128–9133

Lafuma A, Qéré D (2003) Superhydrophobic states. Nat Mater 2:457–460

Lahann J, Mitragotri S, Tran TN, Kaido H, Sundaram J, Choi IS, Hoffer S, Somorjai GA, Langer R (2003) A reversibly switching surface. Science 299:371–374

Lee KH, Kim HY, Khil MS, Ra YM, Lee DR (2003) Characterization of nano-structured poly(ε-caprolactone) nonwoven mats via electrospinning. Polymer 44:1287–1294

Li D, Xia Y (2004) Electrospinning of nanofibers: reinventing the wheel? Adv Mater 16:1151–1170

Li C, Guo RW, Jiang X, Hu SX, Li L, Cao XY, Yang H, Song YL, Ma YM, Jiang L (2009) Reversible switching of water-droplet mobility on a superhydrophobic surface based on a phase transition of a side-chain liquid-crystal polymer. Adv Mater 21:4254–4258

Li X, Hu D, Huang K, Yang C (2014a) Hierarchical rough surfaces formed by LBL self-assembly for oil-water separation. J Mater Chem A 2:11830–11838

Li N, Thia L, Wang X (2014b) A CO_2-responsive surface with an amidine-terminated self-assembled monolayer for stimuli-induced selective adsorption. Chem Commun 50:4003–4006

Li JJ, Zhou YN, Jiang ZD, Luo ZH (2016a) Electrospun fibrous mat with pH-switchable superwettability that can separate layered oil/water mixtures. Langmuir 32:13358–13366

Li JJ, Zhu LT, Luo ZH (2016b) Electrospun fibrous mat with pH-switchable superwettability that can separate layered oil/water mixtures. Chem Eng J 287:474–481

Lim HS, Han JT, Kwak D, Jin M, Cho K (2006) Photoreversibly switchable superhydrophobic surface with erasable and rewritable pattern. J Am Chem Soc 128:14458–14459

Lin P, Yang S (2009) Mechanically switchable wetting on wrinkled elastomers with dual-scale roughness. Soft Matter 5:1011–1018

Liu CT, Liu YL (2016) pH-induced switches of the oil- and water-selectivity of crosslinked polymeric membranes for gravity-driven oil-water separation. J Mater Chem A 4:13543–13548

Liu Y, Mu L, Liu BH, Kong JL (2005) Controlled switchable surface. Chem-Eur J 11:2622–2631

Liu FM, Pang J, Wang CY, Wang LY (2013) Solvent-responsive wettability of self-assembled monolayers of dithiooctanoic acid derivatives bearing *N*,*N*-disubstituted amide groups. Langmuir 29:13003–13007

Liu H, Zhang X, Wang S, Jiang L (2015) Underwater thermoresponsive surface with switchable oil-wettability between superoleophobicity and superoleophilicity. Small 11:3338–3342

Lu YM, Sarshar MA, Du K, Chou T, Choi CH, Sukhishvili SA (2013) Large-amplitude, reversible, pH-triggered wetting transitions enabled by layer-by-layer films. ACS Appl Mater Interfaces 5:12617–12623

Ma W, Zhang Q, Hua D, Xiong R, Zhao J, Rao W, Huang S, Zhan X, Chen F, Huang C (2016a) Electrospun fibers for oil-water separation. RSC Adv 6:12868–12884

Ma W, Zhang Q, Samal SK, Wang F, Gao B, Pan H, Xu H, Yao J, Zhan X, De Smedt SC, Huang C (2016b) Core-sheath structured electrospun nanofibrous membranes for oil-water separation. RSC Adv 6:41861–41870

Marmur A (2003) Wetting on hydrophobic rough surfaces: to be heterogeneous or not to be? Langmuir 19:8343–8348

Matyjaszewski K, Tsarevsky N (2009) Nanostructured functional materials prepared by atom transfer radical polymerization. Nat Chem 1:276–288

Megelski S, Stephens JS, Bruce Chase D, Rabolt JF (2002) Micro- and nanostructured surface morphology on electrospun polymer fibers. Macromolecules 35:8456–8466

Minko S, Müller M, Motornov M, Nitschke M, Grundke K, Stamm M (2003) Two-level structured self-adaptive surfaces with reversibly tunable properties. J Am Chem Soc 125:3896–3900

Misra M, Singh N, Gupta RK (2017) Enhanced visible-light-driven photocatalytic activity of Au@Ag core-shell bimetallic nanoparticles immobilized on electrospun TiO_2 nanofibers for degradation of organic compounds. Cat Sci Technol 7:570–580

Motornov M, Minko S, Eichhorn KJ, Nitschke M, Simon F, Stamm M (2003) Reversible tuning of wetting behavior of polymer surface with responsive polymer brushes. Langmuir 19:8077–8085

Mugele F, Baret JC (2005) Electrowetting: from basics to applications. J Phys Condens Matter 17:705–774

Ning LQ, Xu NK, Wang R, Liu Y (2015) Fibrous membranes electrospun from the suspension polymerization product of styrene and butyl acrylate for oil-water separation. RSC Adv 5:57101–57113

Nosonovsky M (2007) Multiscale roughness and stability of superhydrophobic biomimetic interfaces. Langmuir 23:3157–3161

Obaid M, Tolba GMK, Motlak M, Fadali OA, Khalil KA, Almajid AA, Kim B, Barakat NAM (2015a) Effective polysulfone-amorphous SiO_2 NPs electrospun nanofiber membrane for high flux oil/water separation. Chem Eng J 279:631–638

Obaid M, Barakat NAM, Fadali OA, Al-Meer S, Elsaid K, Khalil KA (2015b) Stable and effective super-hydrophilic polysulfone nanofiber mats for oil/water separation. Polymer 72:125–133

Onda T, Shibuichi S, Satoh N, Tsujii K (1996) Super-water-repellent fractal surfaces. Langmuir 12:2125–2127

Pan S, Kota AK, Mabry JM, Tuteja A (2013) Superomniphobic surfaces for effective chemical shielding. J Am Chem Soc 135:578–581

Qiu Y, Park K (2001) Environment-sensitive hydrogels for drug delivery. Adv Drug Deliv Rev 53:321–339

Ramakrishna S, Fujihara K, Teo WE, Yong T, Ma Z, Ramaseshan R (2006) Electrospun nanofibers: solving global issues. Mater Today 9:40–50

Rosario R, Gust D, Hayes M, Jahnke F, Springer J, Garcia AA (2002) Photon-modulated wettability changes on spiropyran-coated surfaces. Langmuir 18:8062–8069

Sarbatly R, Krishnaiah D, Kamin Z (2016) A review of polymer nanofibres by electrospinning and their application in oil-water separation for cleaning up marine oil spills. Mar Pollut Bull 106:8–16

Simakova A, Averick SE, Konkolewicz D, Matyjaszewski K (2012) Aqueous ARGET ATRP. Macromolecules 45:6371–6379

Singh N, Mondal K, Misra M, Sharma A, Gupta RK (2016) Quantum dot sensitized electrospun mesoporous titanium dioxide hollow nanofibers for photocatalytic applications. RSC Adv 6:48109–48119

Song XY, Cao MW, Han YC, Wang YL, Kwak JCT (2007) Adsorption of hydrophobically modified poly(acrylamide)-*co*-(acrylic acid) on an amino-functionalized surface and its response to the external solvent environment. Langmuir 23:4279–4285

Sun TL, Qing GY (2011) Biomimetic smart interface materials for biological applications. Adv Mater 23:H57–H77

Sun RD, Nakajima A, Fujishima A, Watanabe T, Hashimoto K (2001) Photoinduced surface wettability conversion of ZnO and TiO_2 thin films. J Phys Chem B 105:1984–1990

Sun T, Wang G, Feng L, Liu B, Ma Y, Jiang L, Zhu D (2004) Reversible switching between superhydrophilicity and superhydrophobicity. Angew Chem Int Ed 43:357–360

Tai MH, Gao P, Tan BYL, Sun DD, Leckie JO (2014) Highly efficient and flexible electrospun carbon-silica nanofibrous membrane for ultrafast gravity-driven oil-water separation. ACS Appl Mater Interfaces 6:9393–9401

Tian Y, Su B, Jiang L (2014) Interfacial material system exhibiting superwettability. Adv Mater 26:6872–6897

Tsujii K, Yamamoto T, Onda T, Shibuichi S (1997) Super oil-repellent surfaces. Angew Chem Int Ed Engl 36:1011–1012

Tuteja A, Choi W, Ma ML, Mabry JM, Mazzella SA, Rutledge GC, McKinley GH, Cohen RE (2007) Designing superoleophobic surfaces. Science 318:1618–1622

Verho T, Bower C, Andrew P, Franssila S, Ikkala O, Ras RHA (2011) Mechanically durable superhydrophobic surface. Adv Mater 23:673–678

Wang Y, Bhushan B (2015) Wear-resistant and antismudge superoleophobic coating on polyethylene terephthalate substrate using SiO_2 nanoparticles. ACS Appl Matter Interface 7:743–755

Wang B, Guo ZG (2013) pH-responsive bidirectional oil-water separation material. Chem Commun 49:9416–9418

Wang GY, Zhang TY (2012) Easy route to the wettability cycling of copper surface between superhydrophobicity and superhydrophilicity. ACS Appl Mater Interfaces 4:273–279

Wang S, Feng X, Yao J, Jiang L (2006) Controlling wettability and photochromism in a dual-responsive tungsten oxide film. Angew Chem Int Ed 45:1264–1267

Wang X, Qing GG, Jiang L, Fuchs H, Sun TL (2009) Smart surface of water-induced superhydrophobicity. Chem Commun:2658–2660

Wang X, Ding B, Li B (2013) Biomimetic electrospun nanofibrous structures for tissue engineering. Mater Today 16:229–241

Wang Y, Lai C, Hu H, Liu Y, Fei B, Xin JH (2015) Temperature-responsive nanofibers for controllable oil/water separation. RSC Adv 5:51078–51085

Wang X, Yu J, Sun G, Ding B (2016a) Electrospun nanofibrous materials: a versatile medium for effective oil/water separation. Mater Today 19:403–414

Wang Y, Lai C, Wang X, Liu Y, Hu H, Guo Y, Ma K, Fei B, Xin JH (2016b) Beads-on-string structured nanofibers for smart and reversible oil/water separation with outstanding antifouling property. ACS Appl Mater Interfaces 8:25612–25620

Wenzel RN (1936) Resistance of solid surfaces to wetting by water. Ind Eng Chem 28:988–994

Wong TS, Sun T, Feng L, Aizenberg J (2013) Interfacial materials with special wettability. MRS Bull 38:366–371

Wu ZL, Wei RB, Buguin A, Taulemesse J, Moigne NL, Bergeret A, Wang XG, Keller P (2013) Stimuli-responsive topological change of microstructured surfaces and the resultant variations of wetting properties. ACS Appl Mater Interfaces 5:7485–7491

Xia F, Zhu Y, Feng L, Jiang L (2009) Smart responsive surfaces switching reversibly between super-hydrophobicity and super-hydrophilicity. Soft Matter 5:275–281

Xin B, Hao J (2010) Reversibly switchable wettability. Chem Soc Rev 39:769–782

Xu LY, Ye Q, Lu XM, Lu QH (2014) Electro-responsively reversible transition of polythiophene films from superhydrophobicity to superhydrophilicity. ACS Appl Mater Interfaces 6:14736–14743

Yang J, Zhang ZZ, Men XH, Xu XH, Zhu XT, Zhou XY (2011a) Counterion exchange to achieve reversibly switchable hydrophobicity and oleophobicity on fabrics. Langmuir 27:7357–7360

Yang J, Zhang ZZ, Men XH, Xu XH, Zhu XT (2011b) Thermo-responsive surface wettability on a pristine carbon nanotube film. Carbon 49:19–23

Zhang JP, Seeger S (2011) Superoleophobic coatings with ultralow sliding angles based on silicone nanofilaments. Angew Chem Int Ed 50:6652–6656

Zhang J, Li J, Han Y (2004) Superhydrophobic PTFE surfaces by extension. Macromol Rapid Commun 25:1105–1108

Zhang JL, Lu XY, Huang WH, Han YC (2005) Reversible superhydrophobicity to superhydrophilicity transition by extending and unloading an elastic polyamide film. Macromol Rapid Commun 26:477–480

Zhang XT, Jin M, Liu ZY, Tryk DA, Nishimoto S, Murakami T, Fujishima A (2007) Superhydrophobic TiO_2 surfaces: preparation, photocatalytic wettability conversion, and superhydrophobic−superhydrophilic patterning. J Phys Chem C 111:14521–14529

Zhang X, Guo Y, Zhang P, Wu Z, Zhang Z (2012) Superhydrophobic and superoleophilic nanoparticle film: synthesis and reversible wettability switching behavior. ACS Appl Mater Interfaces 4:1742–1746

Zhang C, Li P, Cao B (2015) Electrospun microfibrous membranes based on PIM-1/POSS with high oil wettability for separation of oil-water mixtures and cleanup of oil soluble contaminants. Ind Eng Chem Res 54:8772–8781

Zhu W, Feng X, Feng L, Jiang L (2006) UV-manipulated wettability between superhydrophobicity and superhydrophilicity on a transparent and conductive SnO_2 nanorod film. Chem Commun 26:2753–2755

Zhu Y, Li JM, He HY, Wan MX, Jiang L (2007) Reversible wettability switching of polyaniline-coated fabric, triggered by ammonia gas. Macromol Rapid Commun 28:2230–2236

Zhu W, Zhai J, Sun Z, Jiang L (2008) Ammonia responsive surface wettability switched on indium hydroxide films with micro- and nanostructures. J Phys Chem C 112:8338–8342

Part I

Stimuli-Responsive Dewetting/Wetting Smart Surfaces and Interfaces

Chapter 2
Photo-Responsive Superwetting Surface

Dongliang Tian, Yan Li, and Lei Jiang

Abstract Photo-responsive surfaces, especially for the photo-responsive superwetting surface, have aroused great interests in smart control devices for a few years due to their remote control and selectivity. This chapter focuses on the photo-responsive wettability on the superwetting surface and their typical applications, particularly on switchable wettability on photo-responsive surfaces and their applications such as droplet actuation, adhesion control, liquid printing and oil-water separation. Finally, our personal point of the prospects and challenges of the photo-responsive wettability surfaces are presented.

Keywords Photo-responsive surface · Superwetting · Nanomaterials · Liquid actuation · Separation

2.1 Introduction

The phenomenon of liquid wetting is one of the most significant properties for a surface and is usually controlled by chemical components and morphology (Wen et al. 2015; Wang et al. 2015; Choi et al. 2009; Zhang et al. 2008; Fan and Jiang 2008; Liu et al. 2010a; Quéré 2008; Ueda and Levkin 2013). By adjusting the materials component and surface microstructures, the superwetting surface shows extreme wettability, e.g., superhydrophobicity with contact angle (CA) larger than 150° and the superhydrophilicity with CA less than 5°, have been gained

---

D. Tian · Y. Li
Beijing Advanced Innovation Center for Biomedical Engineering, School of Chemistry, Beihang University, Beijing, China

L. Jiang (✉)
Beijing Advanced Innovation Center for Biomedical Engineering, School of Chemistry, Beihang University, Beijing, China

Technical Institute of Physics and Chemistry, Chinese Academy of Sciences, Beijing, China
e-mail: jianglei@iccas.ac.cn

A. Hozumi et al. (eds.), *Stimuli-Responsive Dewetting/Wetting Smart Surfaces and Interfaces*, Biologically-Inspired Systems 11,
https://doi.org/10.1007/978-3-319-92654-4_2

considerable attention owing to their significance in both basic research and unique functional applications (Li et al. 2007; Roach et al. 2008; Xin and Hao 2010; Sun et al. 2011; Zhang and Han 2010; Xia et al. 2012). With the fast advance in interface science, smart responsive surface with switch wettability under the external stimuli have been widely used in the fields of smart transport, printing, microfluidic devices, and so on (Tian et al. 2013a, 2014; Yao et al. 2011; Liu et al. 2010b). Among the different external stimuli, light can be used to reversibly change of the geometric and electronic structures of the photo-responsive molecular materials in solutions, crystals, and gels, which is a very convenient way to non-contact control the surface wettability due to the advantage of selective, precisely controlled, tunable direction, illuminated area, and irradition intensity (Baigl 2012; Wang et al. 2007; Chen et al. 2015). In recent years, a series of photo-responsive interfacial materials with special wettability, e.g., superwetting surfaces, were designed and fabricated, and a great progress of their related applications has been made in this field (Chen et al. 2015; Ichimura et al. 2000; Liu et al. 2010c, 2017; Chaudhury and Whitesides 1992; Kessler et al. 2011; Wooh et al. 2015).

In this chapter, photo-responsive wettability on the superwetting surface and their typical applications were focused on, particularly on switchable wettability on photo-responsive surfaces and their applications. There are four main sections following in this chapter. In Sect. 2.2, we review the switchable wettability on photo-responsive surfaces, including inorganic-oxide, organic-compound and polymer-based photo-responsive surfaces. Section 2.3 introduces the applications including droplet actuation, adhesion control, liquid printing and oil-water separation. Finally, our personal point of the prospects and remaining challenges of the photo-responsive wettability surfaces are presented.

2.2 Switchable Wettability on Photo-Responsive Surfaces

Photo-responsive wettability materials, including the materials from inorganic materials to organic small molecules and polymer materials, make surface wettability intelligently control come true based on the bistable states switch or the surface free energy change with light stimulus.

Inorganic oxides have been widely used in many practical applications and occupy a dominated position owing to their advantages of good stability on chemical and mechanical, low price, and excellent photo/electro-properties. The chemical states change for inorganic oxide materials surface by light driving provide possibility to intelligently control of surface wettability, which shows different mechanism with photocatalysis. The wettability change is consistent with a mechanism of photoproduction exciton, i.e., electrons and holes photogenerated by light irradiation and then absorption of water. The first work was reported by Fujishima et al., the wettability (hydrophilicity and hydrophobicity) of the titanium dioxide (TiO_2) surface could be switched between ultraviolet irradiation and dark storage, and photoinduced amphiphilicity of TiO_2 was realized (Wang et al. 1997; Nakajima et al.

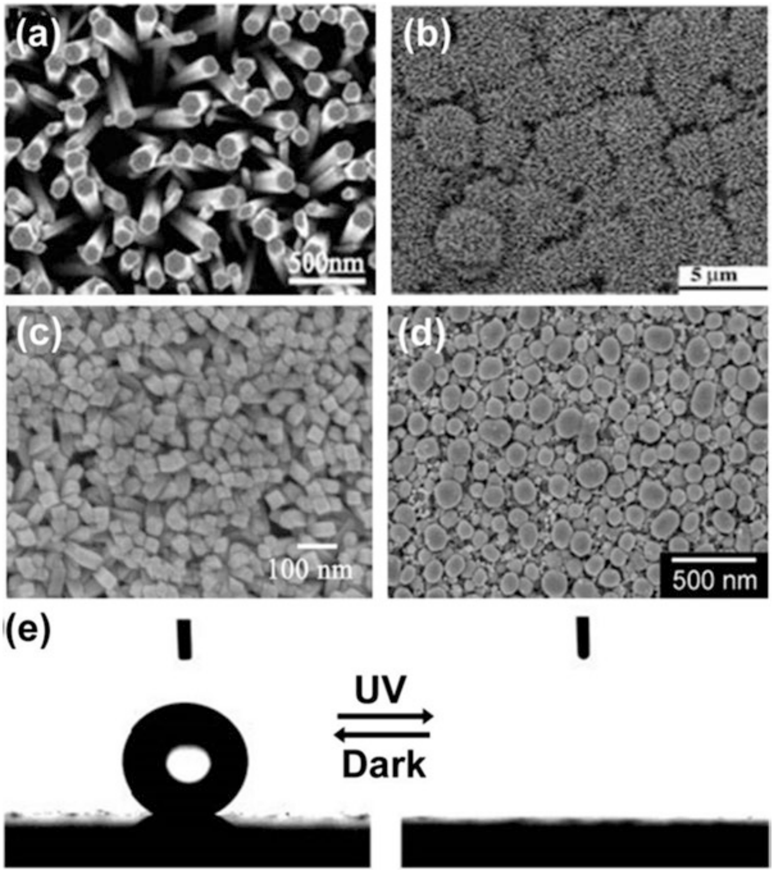

Fig. 2.1 Photo-responsive inorganic materials with switch wettability. (**a**) ZnO (Feng et al. 2004). (**b**) TiO_2 (Feng et al. 2005). (**c**) SnO_2 (Zhu et al. 2006). (**d**) WO_3 (Wang et al. 2006). (**e**) The switch wettability between superhydrophobicity and superhydrophilicity (Feng et al. 2004)

2000). Since then, the study of photo-responsive wettability surface, especially the inorganic substrates with intrinsic photosensitive properties, has attracted widespread interest. Following similar works were observed later with different typical oxide semiconductor such as ZnO, V_2O_5, SnO_2, Ga_2O_3, and WO_3, which have aroused great research attention on the fabrication of light-responsive smart surfaces behaving reversibly wettability switch for a few years (Baigl 2012; Wang et al. 2007; Zhang et al. 2007; Guo et al. 2007; Gao et al. 2007; Yang et al. 2012). Upon UV irradiation (365 nm), the water CAs on the substrates is decreased, while the CAs can slowly be back dark after storage of the substrates in a few days. When the micro- and nanoscale structures were introduced into the materials surface, responsive surface wettability even the switch extreme wettability were realized (Fig. 2.1). For instance, the author's group reported the superhydrophobicity and superhydrophilicity switch of ZnO nanoarray film between dark storage and UV illumination because water and oxygen compete to adsorb to the oxygen vacancies of the surface dissociatively with UV irradiation (Feng et al. 2004). Later, for the similar mechanism, TiO_2 nanorod films were also demonstrated the switch of superhydrophobicity and superhydrophilicity for self-leaning in both extreme states (Feng et al. 2005). For the different functions, such as transparency, superhydrophobic SnO_2 nanorod films were obtained (Zhu et al. 2006). WO_3 is another example of the multifunctional materials with dual-responsive characterization, i.e., wettability switch and photochromism (Wang et al. 2006). These switch wettability materials are promising in applications of microfluidic devices and functional devices. There are also some irreversible wettability transition from superhydrophobicity to superhydrophilicity based on the decomposition of surface small organic molecular for patterning (Tian et al. 2014).

In contrast to inorganic materials, organic-compound/polymer-based photo-responsive wettability surface has been widely developed owing to the advantages of scalable architecture and selectivity of the light control (Pan et al. 2015). The photo-responsive group in the organic responsive surface includes azobenzenes, spiropyrans, diarylethene, cinnamates, etc. (Fig. 2.2). The responsive surface wettability is based on the chemical group changes under photoirradiation, resulting in the surface free energy change and also the surface wettability transition accordingly. The rough structure of the surface can enlarge the responsive range of the special wettability surface based on the photo-responsive change of surface chemical composition, i.e., switching wettability.

One of the typical organic compounds is azobenzene, the molecular structure can be changed between the structure of cis isomer and trans isomer with alternative UV and visible illumination, resulting in the switch wettability between superhydrophobicity to superhydrophilicity. The author's group realized photoinduced wettability switch on an azobenzene monolayer via self-assembly based on electrostatic force (Jiang et al. 2005). The wettability reversible change from superhydrophobicity to hydrophilicity had been obtained corresponding to the trans isomer to cis isomer under UV and Vis irradiation. Similar work was reported by Blasco et al., they prepared light-switchable surface pattern via photoinduced cycloaddition reaction with dipolarophiles based on photo-responsive azobenzene moieties (Blasco et al. 2013). Now the Light induced spiropyran change between nonpolar and polar could also achieve similar wettability switching under visible and UV irradiation based on the rough structures (Rohit et al. 2004). Takase et al. (2016) reported the photo-responsive superhydrophilic surface was achieved on diarylethene microcrystalline films based on the light-induced topographical reversible changes, namely, open ring and close ring, upon the alternative UV light and visible light irradiation.

Photo-responsive polymers with the photo-responsive group like the organic responsive surface are also extensively used in many practical applications based on switch wettability resulting from the molecular structure change.(Abrakhi et al. 2013; Chen et al. 2016; Di et al. 2017; Hersey et al. 2014; Ikbal et al. 2014; Jo et al. 2016; Kessler et al. 2011; Tylkowski et al. 2010; Wagner and Theato 2014; Waugh and Lawrence 2010; Xu et al. 2013)

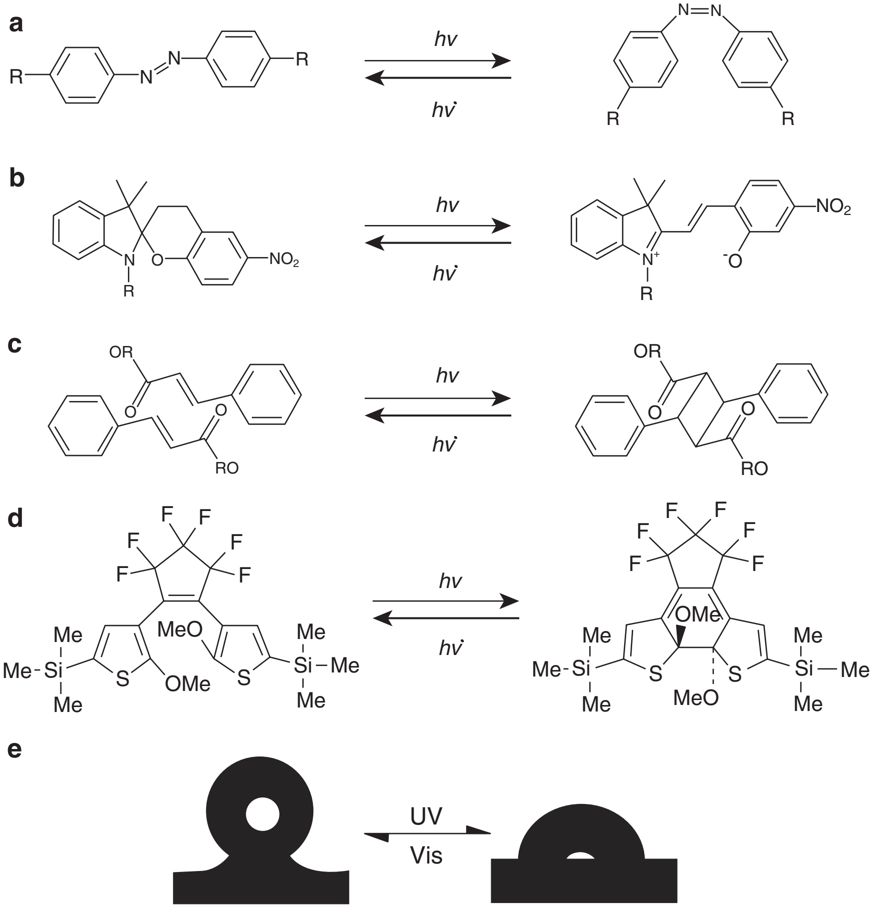

Fig. 2.2 Molecular structures of photo-responsive organic compound materials with switch wettability. (**a**) azobenzenes derivative. (**b**) spiropyrans derivative. (**c**) cinnamates derivative. (**d**) diarylethene derivative. (**e**) Switch wettability based on the photo-responsive surface. The reversible wettability transition is owing to the cis-trans photoisomerization or open ring-closed ring of photo-responsive materials (Wang et al. 2007)

2.3 Applications of the Photo-Responsive Surface Wettability

2.3.1 Photo-Responsive Surface for Droplet Actuation

Liquid moving on surfaces has been extensively investigated owing to the potential applications in drag reduction, micro/nanofluidics, water collection, etc. Photo-responsive surface with switch wettability provide a good chance for liquid moving with gradient illumination. Ichimura et al. (2000) reported that a liquid droplet macroscopic movement on a photo-responsive solid surface by photo-driving. The photo-responsive surface was composed of a photo-responsive monolayer of an azobenzene derivative, O-carboxymethylated calixresorcinarene. Due to the photoisomerizaiton of surface azobenzenes, asymmetrical photoirradiation on the surface could cause a surface free energy gradient and different CA for a liquid droplet with the diameter of several millimeters, on the surface, which would produce a force for directional motion of the liquid droplet. The modified surface under UV irradiation (360 nm) and blue light illumination (436 nm) would result in polar cis-azobenzene groups and cis-to-trans isomerization at the terminal positions, respectively. Accordingly, UV irradiation caused surface free energy increasing for intrinsic hydrophilicity, while blue light irradiation making the surface hydrophobic. With the gradient illumination, an imbalance surface free energy was produced on both droplet edges, and causing the liquid motion from the gradient driving force. Furthermore, the direction and velocity of a liquid droplet motion could be precisely controlled by adjusting the gradient direction and steepness of the light illumination. Such phenomenon was also demonstrated by Yang et al., liquid droplet can be transported by gradient UV and visible light irradiation owing to the gradient in surface tension based on the cis and trans structure change (Fig. 2.3) (Yang et al. 2007). Not limited to the smooth surface, the liquid droplet could also be collected and transported on the fiber surface based on the photoresponsive trans and cis isomers of the polymer with gradient surface roughness (Fig. 2.4) (Feng et al. 2013).

Later, Berná et al. reported similar results (Berná et al. 2005), they realized a liquid droplet macroscopic transfer via photo-responsive rotaxane-based molecular surface. With an external light irradiation trigger, the macrocycle of the rotaxanes was changed from one site to a second position via biased Brownian motion. The biased Brownian motion associated with a configuration transformation, which produced switchable wettability on rotaxane-terminated surface. As light irradiation could achieve biased Brownian motion and a surface energy gradient, which was beneficial to produce force to move a 1 μL diiodomethane droplet up an inclining surface of 12°. Interestingly, Yu et al. (Lv et al. 2016) presented a strategy to drive liquids in a tube independent of both wettability gradients and the Marangoni effect. The driving method was based on capillary force producing from the asymmetric deformation of liquid crystal polymer by light, which could propel simple liquids and complex fluids broad application in chemical engineering and biomedical. Thus it would be promising to be used as micro-pumps in microsystems technology and architecture. Later, Yilmaz et al. realized the liquid motion control through light irradition using temperature-sensitive PNIPAAm-coated plasmonic AuNR arrays (Yilmaz et al. 2015).

On contrast, the light responsive material can be used as liquid media. Recently, Kavokine et al. (2016) demonstrated the light manipulation transport of floating liquid marbles on a water solution containing photosensitive surfactants. When the liquid thickness substrate was enough large, behaving Marangoni regime, photoreversible Marangoni flows generated from irradiation of the solution could transport the liquid marbles to the direction of UV light and opposite to the direction of blue light. While the marbles driven by the free surface deformation move to the opposite surface flow direction below a critical thickness, showing anti-Marangoni regime,

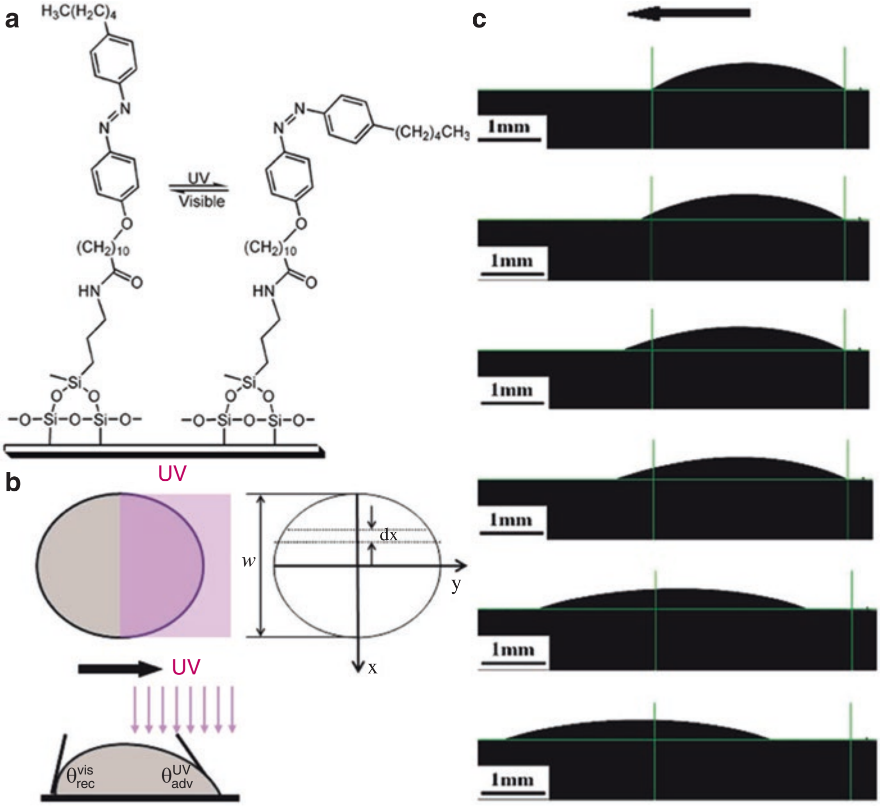

Fig. 2.3 (**a**) Molecular structures of photo-responsive azobenzenes derivative under UV and Vis light illumination, respectively. (**b**) Schematic of different surface tension on the two sides of the droplet induced by gradient UV irradiation. (**c**) UV light driven liquid droplet transport (Yang et al. 2007)

and the speed increased as the liquid thickness decreases. Paven et al. (2016) reported light-driven liquid marbles (LMs) for transport of the materials. LMs could be transferred based on the thermal gradient surface tension generating from the light-heat conversion and released its inner material by illumination of laser or sunlight on the interface of air and water. The LMs could be driven remotely using light for precise position, illumination area, moving direction and velocity.

2.3.2 Photo-Responsive Surface for Adhesion Control

Smart control of surface adhesion is important in many practical applications, such as liquid transfer, controlled release system, and other switch system (Huang et al. 2014). Li et al. (2012a, b) demonstrated a light tunable adhesion switch on a superhydrophobic liquid crystal polymer (LCP) microarray surface containing

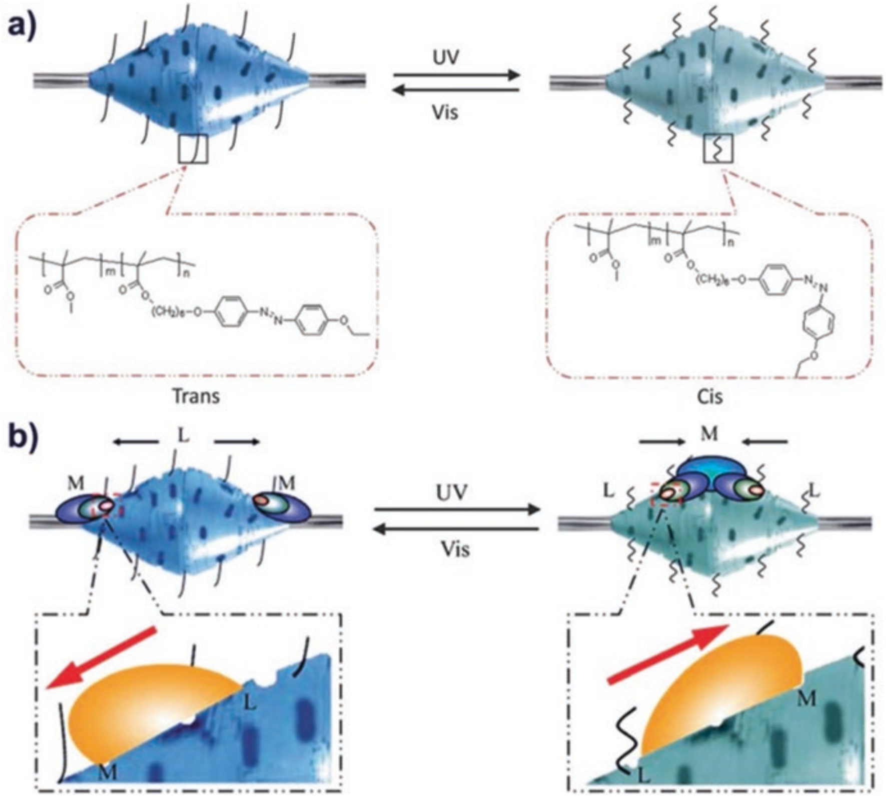

Fig. 2.4 (**a**) Illustration of photoresponsive trans and cis isomers of fiber surface with a roughness gradient. (**b**) Directional droplet gathering on the gradient wettability surface (Feng et al. 2013)

azobenzene group (Fig. 2.5). Based on the photo-isomerization of the azobenzene LCP film with alternative UV/Visible light irradiation, the azobenzene LCP microarray film showed a fast and reversible water adhesion switch on the surface showing superhydrophobic, which could also realize precisely, no contact, local control.

Locklin et al. (Fries et al. 2008) also demonstrated the surface adhesion could be controlled on the photochromic polymer brushes grafted to oxide surfaces. A colorless closed spiropyran (irradiation with visible light) and a colored open merocyanine (irradiation with UV light) form based on the light-induced conformational changes were corresponding to the initial hydrophobicity and hydrophilicity. Li et al. (2014) demonstrated the superhydrophobic carbon nanotube surfaces without any chemical modification could reversibly transform from low adhesion to high adhesion to water by alternative UV/mask irradiation and heat treatment. Recently, the author's group demonstrated a strategy to realize switchable oil adhesion in water on the micro/nano structured ZnO mesh based on the wettability transition owing to the tri-phase contact from the liquid/gas/solid to liquid/liquid/solid (Tian et al. 2013b), which was promising in practical applications of manipulation and

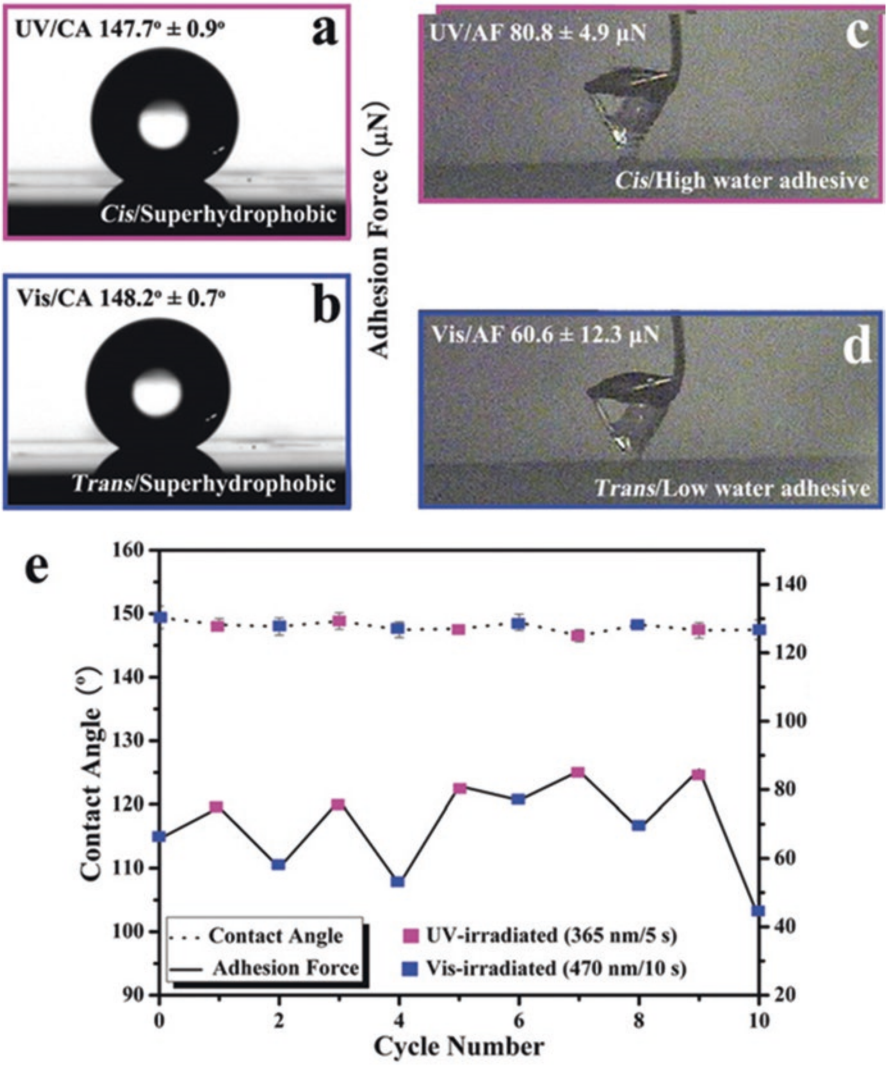

Fig. 2.5 Photo-induced switch adhesion of superhydrophobic azo-polymer coated micro/nanopost array. Water droplet photographs on the nanoarray with UV light illumination (**a**) and visible light illumination (**b**). The maximum water droplet deform on the nanoarray with UV illumination (**c**) and visible light illumination (**d**). (**e**) Water CA and adhesion results change with varying UV and Vis illumination (Li et al. 2012a)

release (Fig. 2.6). Similar work was also demonstrated by Sawai et al. (2013) the photo-induced highly amphiphilic TiO_2 surface showed underwater superoleophobic with low adhesion to oil droplet for the water molecules adsorption on the TiO_2 surface.

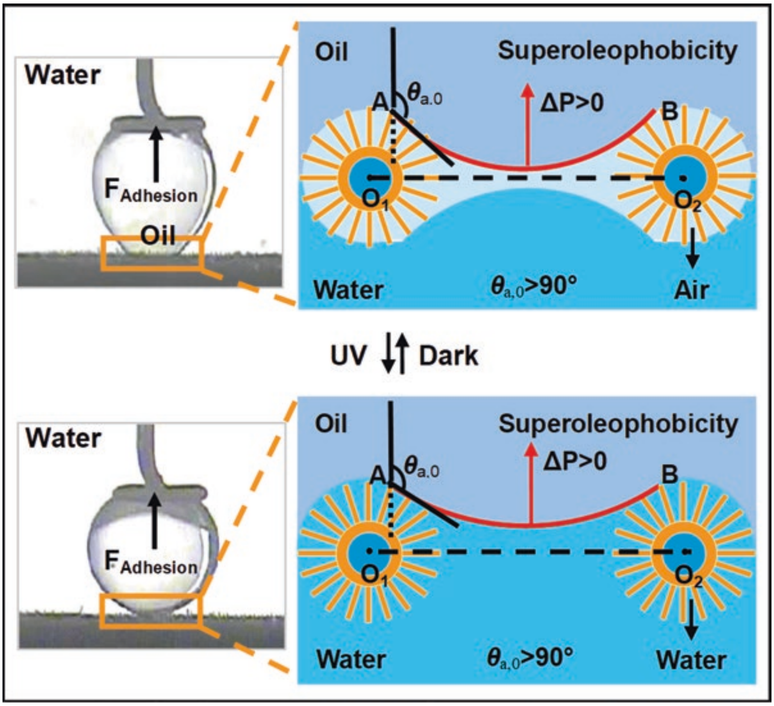

Fig. 2.6 Photoinduced oil adhesion switch in water on the micro/nano structured ZnO mesh (Tian et al. 2013b)

The photo-responsive switchable wettability system can also be used for the biomedical applications. The author's group realized a photoresponsive release system by adjusting the wetting of the mesoporous (MS) nanoparticles surface (Fig. 2.7) (Chen et al. 2014). Upon UV irradiation (365 nm), the surface could be wetted by water based on the spiropyran conformational conversion from "closed" state to "open" state, leading to the release of model cargo molecules, fluorescein disodium, from the pores. This remote stimuli wettability-based smart release system might be promising in the medical applications.

2.3.3 Photo-Responsive Surface for Liquid Printing

The selectivity of light is one of the biggest advantages for the photo-responsive surface, resulting in the wettability change by controlling the light patterns. In order to improve the liquid patterning resolution, the wettability difference between the graphic site and non-graphic areas to liquid, should be improved. Superwetting surface, e.g., superhydrophobicity/superhydrophilicity, is a good way to enhance the wettability contrast of the image site and non-image areas.

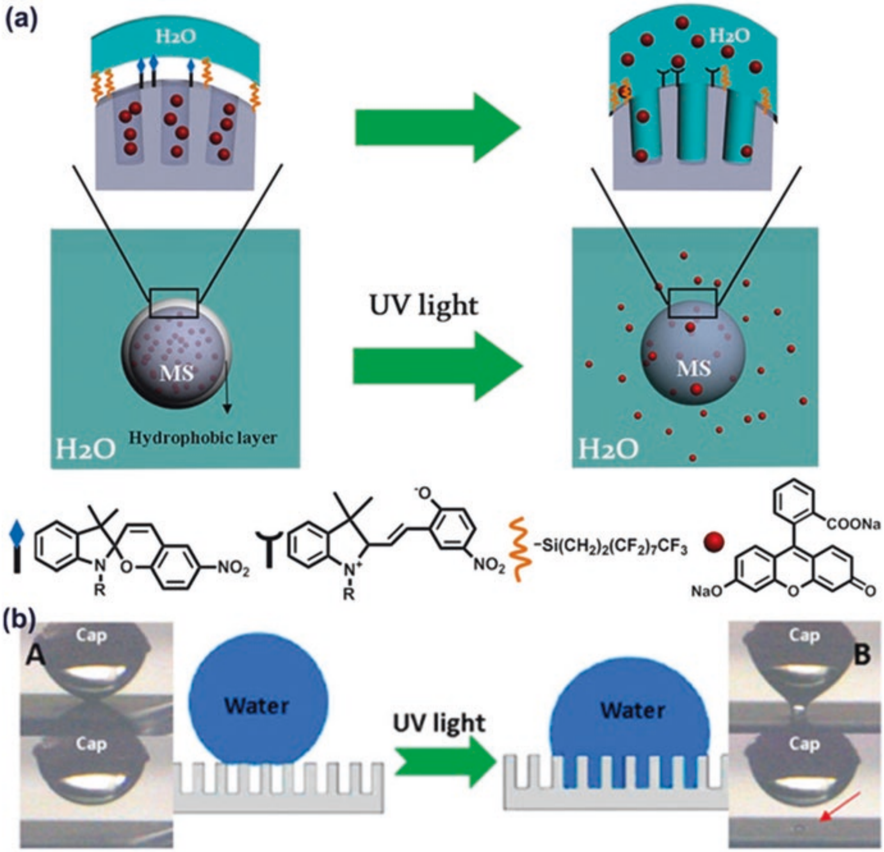

Fig. 2.7 (**a**) The schematic of the light-responsive release system. (**b**) The mechanism illustration of the wetting process of surface (Chen et al. 2014)

Photodecomposition is a common way to achieve the superhydrophobic-superhydrophilic patterns. Tadanaga et al. (2004) prepared the superhydrophobic-superhydrophilic patterns with a large CA difference via photocatalytic cleavage of the fluoroalkyl chain in FAS selectively by the thin TiO_2 layer, which was potential application for printing. Lai et al. (2008) fabricated the micropatterns of superhydrophilicity-superhydrophobicity on the TiO_2 nanoarray film with UV light selectively photocatalytic decomposition of the superhydrophobic monolayer. Serial works were reported by Fujishima et al., (Nishimoto et al. 2009a, b, 2014; Nakata et al. 2009, 2010) TiO_2 based superhydrophilic-superhydrophobic patterns with an extremely high wettability contrast for off-set printing. Fig. 2.8 showing the typical printing process, TiO_2 layer, as a photocatalyst, was coated onto a rough substrate, then hydrophobic SAM was modified to achieve superhydrophobcity, next aqueous UV light-resistant ink was patterned jetting on the substrate and exposed to full-area UV irradiation to achieve area-selection surface superhydro-

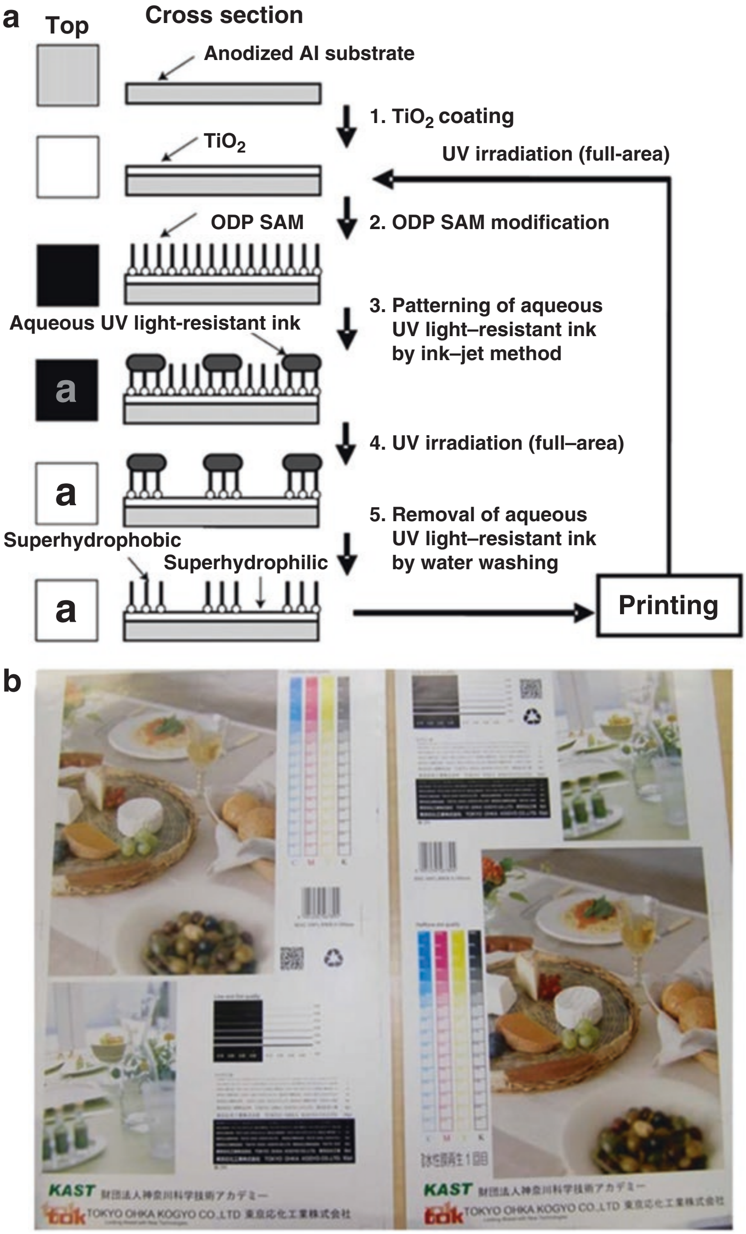

Fig. 2.8 The superhydrophilic-superhydrophobic patterns for off-set printing. (**a**) Schematic of the liquid patterning processes. (**b**) Photographs of the printed plate and reused plate (Nishimoto et al. 2009b)

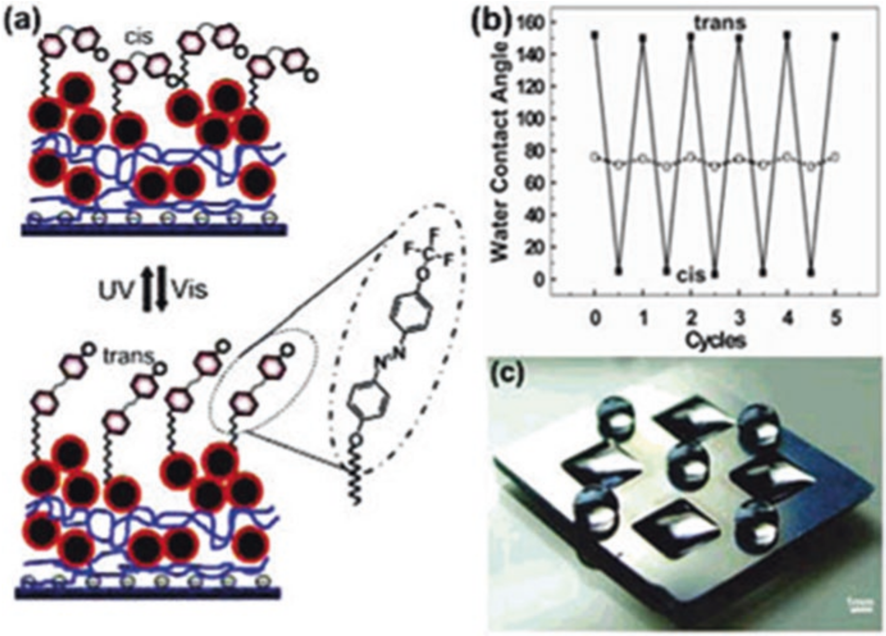

Fig. 2.9 (**a**) Roughness-enhanced photoresponsive surface owing to reversible photoisomerization. (**b**) Wettability reversible transitions on a smooth substrate (□) and a rough multilayer film (■). (**c**) The liquid patterns on the photoresponsive substrate owing to selective UV irradiation (Lim et al. 2006)

philictiy, finally, the patterns of superhydrophilicityd superhydrophobicity were realized on the printing plate after water washing without the use of a photomask. The prepared plate was reusable after photodecomposition of the SAM layer with a resolution of 133 line for color printing (Nishimoto et al. 2009b).

The light-responsive surface with liquid patterning can also be realized on the organic or polymer substrate surface (Zhao 2009; Fries et al. 2008). Lim et al. presented the facile fabrication of a reversibly photoswitchable erasable/rewritable surface pattern with extreme wetting properties of superhydrophobicity/superhydrophilicity, under selective UV/visible illumination (Fig. 2.9) (Lim et al. 2006). The surface was fabricated by combining the self-assembly roughness control and photo-responsive fluorinated azobenzene molecules molecular switching. Ionov et al. (2003) demonstrated stimuli-responsive polymer films chemical patterning is reversibly written and erased with appropriate environment.

2.3.4 Photo-Responsive Surface for Oil-Water Separation

Recently, research on oil/water separation film with special wettability, especially for the on-demand oil/water separation based on the responsive surface wettability, has attracted much attention (Xue et al. 2014; Tao et al. 2014; Gondal et al. 2014; Dong et al. 2016; Korhonen et al. 2011). Based on the photo-responsive switch wettability between superhydrophobicity and superhydrophilicity of the ZnO nanoarray coated mesh, the author's group has realized the photo-responsive water permeation, i.e., water could permeated the mesh under UV illumination, while kept on the mesh after dark storage (Tian et al. 2012). For the underwater oil droplet, the CAs under UV irradiation kept almost the same as those after dark storage. Accordingly, the photo-responsive oil-water separation was demonstrated on the micro/nano structured ZnO mesh, which provided a way to remote control the on-demand separation of the mixture of oil and water (Fig. 2.10). In fact, the photo-responsive oil/water separation mode changed from the type of oil-removing to the type of water-removing. Later, similar work was presented by Yan et al. (2016) an on-demand oil-water separation mesh by light illumination based on the switchable wettability was also demonstrated on the mesh coated by mixtures of ZnO nanoparticles and waterborne polyurethane. The wettability of the coated mesh could reversibly switch from superhydrophobicity/superoleophobicity to superhydrophilicity/underwater superoleophobicity by UV illumination and heat treatment alternately. Gao et al. (2014) reported single-walled carbon nanotube (SWCNT)/TiO_2 nanocomposite ultrathin film was superhydrophilic/underwater superolephobic and could effectively separate both of surfactant-free and surfactant-stabilized oil-in-water emulsions.

Compared to the oil-water separation by filtration, photo-responsive oil/water absorption is another effective strategy for oil-water separation. Zhu et al. (2016) fabricated a robust superhydrophobic sponge with light-responsive spiropyran derivative based on a radical copolymerization process, which showed the photoresponsive oil absorption and desorption. The superhydrophobic MF sponge showed excellent selectivity and high absorption capacity. More importantly, light-controlled oil desorption process could be realized based on the hydrophilictiy of the MF sponge under UV illumination. These findings offered an approach to achieve responsive absorbent material for oil recovery.

2.4 Conclusions and Outlook

In this chapter, recent progress of the photo-responsive wettability on the superwetting surface and their typical applications has been briefly reviewed, particularly on switchable wettability on photo-responsive surfaces and their applications including droplet actuation, adhesion control, liquid printing and oil-water separation. Despite

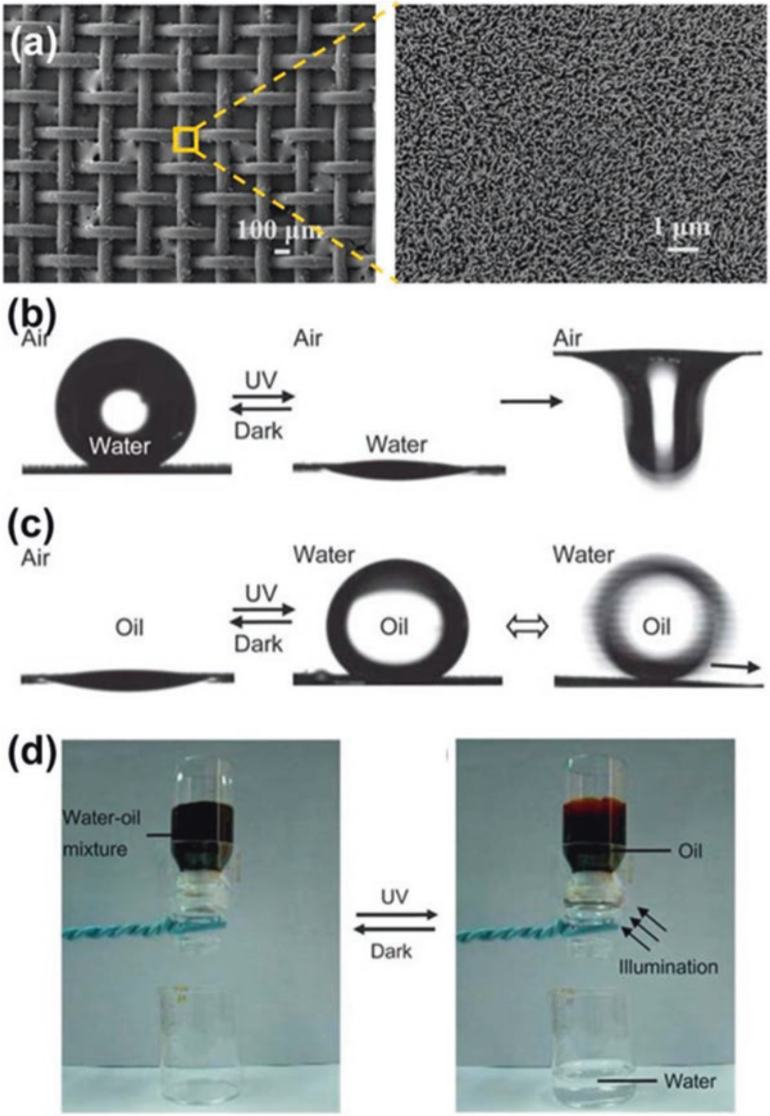

Fig. 2.10 (**a**) SEM the ZnO nanoarray-coated mesh film. (**b**) Photo-induced water permeation on micro/nano structured ZnO mesh films. (**c**) ZnO nanoarrays-coated mesh films surface wettability to oil. (**d**) Photocontrollable water-oil separation (Tian et al. 2012)

much progress in the field of photo-responsive wettability on the superwetting surfaces, there are still numerous challenges remaining in practical applications.

Most of the photo-responsive surfaces are limited to laboratory research and not suitable for practical applications. The sensitivity and stability of the photo-responsive materials should be improved so as to improve the response speed, precision and maneuverability. Photo-responsive actuation in different phase, not limit to liquid, should be developed for different applications. The selectivity of photo-controllable liquid separation should be optimized for high efficient separation. Different external field cooperative control the liquid droplet should be explored for novel application in the microfluidic devices, drug release and intelligent devices.

Acknowledgments The authors are grateful for financial support from the Chinese National Natural Science Foundation (21671012, 21373001, 21601013), Beijing Natural Science Foundation (2172033), the 973 Program (2013CB933004), the Fundamental Research Funds for the Central Universities, and the 111 Project (B14009).

References

Abrakhi S, Péralta S, Fichet O, Teyssié D, Cantin S (2013) Poly(azobenzene acrylate-co-fluorinated acrylate) spin-coated films: influence of the composition on the photo-controlled wettability. Langmuir 29:9499–9509

Baigl D (2012) Photo-actuation of liquids for light-driven microfluidics: state of the art and perspectives. Lab Chip 12:3637–3653

Berná J, Leigh DA, Lubomska M, Mendoza SM, Pérez EM, Rudolf P (2005) Macroscopic transport by synthetic molecular machines. Nat Mater 4:704–710

Blasco E, Piñol M, Oriol L, Schmidt BVKJ, Welle A, Trouillet V (2013) Photochemical generation of light responsive surfaces. Adv Funct Mater 23:4011–4019

Chaudhury MK, Whitesides GM (1992) How to make water run uphill. Science 256:1539–1541

Chen L, Wang W, Su B, Wen Y, Li C, Zhou Y, Li M, Shi X, Du H, Song Y, Jiang L (2014) A light-responsive release platform by controlling the wetting behavior of hydrophobic surface. ACS Nano 8:744–751

Chen K, Zhou S, Yang S, Wu L (2015) Fabrication of all water-based self-repairing superhydrophobic coatings based on UV-responsive microcapsules. Adv Funct Mater 25:1035–1041

Chen L, He C, Huang Y, Huang J, Zhang Y, Gao Y (2016) Poss based fluorinated azobenzene-containing polymers: photo-responsive behavior and evaluation of water repellency. J Appl Polym Sci 133:43540

Choi W, Tuteja A, Chhatre S, Mabry JM, Cohen RE, Mckinley GH (2009) Fabrics with tunable oleophobicity. Adv Mater 21:2190–2195

Di H, Arisaka Y, Masuda K, Yamamoto M, Takeda N (2017) A photoresponsive soft interface reversibly controls wettability and cell adhesion by conformational changes in a spiropyran-conjugated amphiphilic block copolymer. Acta Biomater 51:101–111

Dong T, Cao S, Xu G (2016) Highly porous oil sorbent based on hollow fibers as the interceptor for oil on static and running water. J Hazard Mater 305:1–7

Fan X, Jiang L (2008) Bio-inspired, smart, multiscale interfacial materials. Adv Mater 20:2842–2858

Feng X, Feng L, Jin M, Zhai J, Jiang L, Zhu D (2004) Reversible super-hydrophobicity to super-hydrophilicity transition of aligned ZnO nanorod films. J Am Chem Soc 126:62–63

Feng X, Zhai J, Jiang L (2005) The fabrication and switchable superhydrophobicity of TiO_2 nanorod films. Angew Chem Int Ed 44:5115–5118

Feng SL, Hou YP, Xue Y, Gao LC, Jiang L, Zheng YM (2013) Photo-controlled water gathering on bio-inspired fibers. Soft Matter 9:9294–9297

Fries K, Samanta S, Orski S, Locklin J (2008) Reversible colorimetric ion sensors based on surface initiated polymerization of photochromic polymers. Chem Commun (47):6288–6300

Gao LY, Zheng MJ, Zhong M, Li M, Ma L (2007) Preparation and photoinduced wettability conversion of superhydrophobic β-Ga_2O_3 nanowire film. Appl Phys Lett 91:013101

Gao SJ, Shi Z, Zhang WB, Zhang F, Jin J (2014) Photoinduced superwetting single-walled carbon nanotube/TiO_2 ultrathin network films for ultrafast separation of oil-in-water emulsions. ACS Nano 8:6344–6352

Gondal MA, Sadullah MS, Dastageer MA, Mckinley GH, Panchanathan D, Varanasi KK (2014) Study of factors governing oil-water separation process using TiO_2 films prepared by spray deposition of nanoparticle dispersions. ACS Appl Mater Interfaces 6:13422–13429

Guo M, Peng D, Cai S (2007) Highly hydrophilic and superhydrophobic ZnO nanorod array films. Thin Solid Films 515:7162–7166

Hersey JS, Freedman JD, Grinstaff MW (2014) Photoactive electrospun polymeric meshes: spatiotemporally wetting of textured 3-dimensional structures. J Mater Chem B 2:2974–2977

Huang J, Lai Y, Wang L, Li S, Ge M, Zhang K (2014) Controllable wettability and adhesion on bioinspired multifunctional TiO_2 nanostructure surfaces for liquid manipulation. J Mater Chem A 2:18531–18538

Ichimura K, Oh SK, Nakagawa M (2000) Light-driven motion of liquids on a photoresponsive surface. Science 288:1624–1626

Ikbal M, Banerjee R, Barman S, Atta S, Dhara D, Singh NDP (2014) 1-acetylferroceneoxime-based photoacid generators: application towards sol-gel transformation and development of photoresponsive polymer for controlled wettability and patterned surfaces. J Mater Chem C 2:4622–4630

Ionov L, Minko S, Stamm M, Gohy J, Jérôme R, Scholl A (2003) Reversible chemical patterning on stimuli-responsive polymer film: environment-responsive lithography. J Am Chem Soc 125:8302–8306

Jiang W, Wang G, He Y, Wang X, An Y, Song Y (2005) Photo-switched wettability on an electrostatic self-assembly azobenzene monolayer. Chem Commun (28):3550–3552

Jo H, Haberkorn N, Pan JA, Vakili M, Nielsch K, Theato P (2016) Fabrication of chemically tunable, hierarchically branched polymeric nanostructures by multi-branched anodic aluminum oxide templates. Langmuir 32:6437–6444

Kavokine N, Anyfantakis M, Morel M, Rudiuk S, Bickel T, Baigl D (2016) Light-driven transport of a liquid marble with and against surface flows. Angew Chem Int Ed 55:11183–11187

Kessler D, Jochum FD, Choi J, Char K, Theato P (2011) Reactive surface coatings based on polysilsesquioxanes: universal method toward light-responsive surfaces. ACS Appl Mater Interfaces 3:124–128

Korhonen JT, Kettunen M, Ras RH, Ikkala O (2011) Hydrophobic nanocellulose aerogels as floating, sustainable, reusable, and recyclable oil absorbents. ACS Appl Mater Interfaces 3:1813–1816

Lai Y, Lin C, Wang H, Huang J, Zhuang H, Sun L (2008) Superhydrophilic-superhydrophobic micropattern on TiO_2, nanotube films by photocatalytic lithography. Electrochem Commun 10:387–391

Li XM, Reinhoudt D, Cregocalama M (2007) What do we need for a superhydrophobic surface? A review on the recent progress in the preparation of superhydrophobic surfaces. Chem Soc Rev 36:1350–1368

Li C,Zhang Y,Ju J,Cheng F, Liu M,Jiang L,Yu Y (2012a) In situ fully light-driven switching of superhydrophobic adhesion. Adv Funct Mater 22:760–763

Li C, Cheng F, Lv J, Zhao Y, Liu M, Jiang L, Yu Y (2012b) Light-controlled quick switch of adhesion on a micro-arrayed liquid crystal polymer superhydrophobic film. Soft Matter 8:3730–3733

Li J, Ling J, Yan L, Wang Q, Zha F, Lei Z (2014) UV mask irradiation and heat induced switching on-off water transportation on superhydrophobic carbon nanotube surfaces. Surf Coat Tech 258:142–145

Lim HS, Han JT, Kwak D, Jin M, Cho K (2006) Photoreversibly switchable superhydrophobic surface with erasable and rewritable pattern. J Am Chem Soc 128:14458–14459

Liu KL, Yao X, Jiang L (2010a) Recent developments in bio-inspired special wettability. Chem Soc Rev 39:3240–3255

Liu M, Zheng Y, Zhai J, Jiang L (2010c) Bioinspired super-antiwetting interfaces with special liquid-solid adhesion. Acc Chem Res 43:368–377

Liu Y, Bo X, Sun S, Jia W, Wu L, Yu Y (2017) Humidity and photo-induced mechanical actuation of cross-linked liquid crystal polymers. Adv Mater 29:1604792

Lv JA, Liu Y, Wei J, Chen E, Qin L, Yu Y (2016) Photocontrol of fluid slugs in liquid crystal polymer microactuators. Nature 537:179–184

Nakajima A, Fujishima A, Hashimoto K, Watanabe T (2000) Cheminform abstract: preparation of transparent superhydrophobic boehmite and silica films by sublimation of aluminum acetylacetonate. Adv Mater 31:1365–1368

Nakata K, Nishimoto S, Kubo A, Tryk D, Ochiai T, Murakami T (2009) Fabrication and application of TiO_2-based superhydrophilic-superhydrophobic patterns on titanium substrates for offset printing. Chem Asian J 4:984–988

Nakata K, Nishimoto S, Yuda Y, Ochiai T, Murakami T, Fujishima A (2010) Rewritable superhydrophilic-superhydrophobic patterns on a sintered titanium dioxide substrate. Langmuir 26:11628–11630

Nishimoto S, Sekine H, Zhang X, Liu Z, Nakata K, Murakami T (2009a) Assembly of self-assembled monolayer-coated Al_2O_3 on TiO_2 thin films for the fabrication of renewable superhydrophobic-superhydrophilic structures. Langmuir 25:7226–7228

Nishimoto S, Kubo A, Nohara K, Zhang X, Taneichi N, Okui T, Liu Z, Nakata K, Sakai H, Murakami T, Abe M, Komine T, Fujishima A (2009b) TiO_2-based superhydrophobic–superhydrophilic patterns: Fabrication via an ink-jet technique and application in offset printing. Appl Surf Sci 255:6221–6225

Nishimoto S, Becchaku M, Kameshima Y, Shirosaki Y, Hayakawa S, Osaka A (2014) TiO_2-based superhydrophobic–superhydrophilic pattern with an extremely high wettability contrast. Thin Solid Films 558:221–226

Pan S, Ni M, Mu B, Li Q, Hu X, Lin C (2015) Well defined pillararene-based azobenzene liquid crystalline photoresponsive materials and their thin films with photomodulated surfaces. Adv Funct Mater 25:3571–3580

Paven M, Mayama H, Sekido T, Butt H, Nakamura Y, Fujii S (2016) Liquid marbles: light-driven delivery and release of materials using liquid marbles. Adv Funct Mater 26:3372–3372

Quéré D (2008) Wetting and roughness. Annu Rev Mater Res 38:71–99

Roach P, Shirtcliffe NJ, Newton MI (2008) Progress in superhydrophobic surface development. Soft Matter 4:224–240

Rohit R, Devens GAAG, Mark HJLT, Tclement T (2004) Lotus effect amplifies light-induced contact angle switching. J Phys Chem B 108:12640–12642

Sawai Y, Nishimoto S, Kameshima Y, Fujii E, Miyake M (2013) Photoinduced underwater superoleophobicity of TiO_2 thin films. Langmuir 29:6784–6789

Sun T, Qing G, Su B, Jiang L (2011) Functional biointerface materials inspired from nature. Chem Soc Rev 40:2909–2921

Tadanaga K, Morinaga J, Atsunori Matsuda A, Minami T (2004) Superhydrophobic-superhydrophilic micropatterning on flowerlike alumina coating film by the sol-gel method. Chem Mater 12:590–592

Takase K,Hyodo K,Morimoto M,Kojima Y,Mayama H,Yokojima S,Nakamuraf S, Uchida K (2016) Photoinduced reversible formation of a superhydrophilic surface by crystal growth of diarylethene. Chem Commun 52:6885–6887

Tao M, Xue L, Liu F, Jiang L (2014) An intelligent superwetting PVDF membrane showing switchable transport performance for oil/water separation. Adv Mater 26:2943–2948

Tian D, Zhang X, Tian Y, Wu Y, Wang X, Zhai J (2012) Photo-induced water-oil separation based on switchable superhydrophobicity- superhydrophilicity and underwater superoleophobicity of the aligned ZnO nanorod array-coated mesh films. J Mater Chem 22:19652–19657

Tian DL, Song YL, Jiang L (2013a) Patterning of controllable surface wettability for printing techniques. Chem Soc Rev 42:5184–5209

Tian D, Guo Z, Wang Y, Li W, Zhang X, Jin Z (2013b) Phototunable underwater oil adhesion of micro/nanoscale hierarchical-structured ZnO mesh films with switchable contact mode. Adv Funct Mater 24:536–542

Tian Y, Su B, Jiang L (2014) Interfacial material system exhibiting superwettability. Adv Mater 26:6872–6897

Tylkowski B, Peris S, Giamberini M, Garcia-Valls R, Reina JA, Ronda JC (2010) Light-induced switching of the wettability of novel asymmetrical poly(vinyl-alcohol)-co-ethylene membranes blended with azobenzene polymers. Langmuir 26:14821–14829

Ueda E, Levkin PA (2013) Emerging applications of superhydrophilic-superhydrophobic micropatterns. Adv Mater 25:1234–1247

Wagner N, Theato P (2014) Light-induced wettability changes on polymer surfaces. Polymer 55:3436–3453

Wang R, Hashimoto K, Fujishima A, Chikuni M, Kojima E, Kitamura A (1997) Light-induced amphiphilic surfaces. Nature 388:431–432

Wang S, Feng X, Yao J, Jiang L (2006) Controlling wettability and photochromism in a dual-responsive tungsten oxide film. Angew Chem Int Ed 45:1264–1267

Wang S, Song YL, Jiang L (2007) Photoresponsive surfaces with controllable wettability. J Photochem Photobiol C 8:18–29

Wang S, Liu K, Xi Y, Lei J (2015) Bioinspired surfaces with superwettability: new insight on theory, design and applications. Chem Rev 115:8230–8293

Waugh DG, Lawrence J (2010) On the use of co laser induced surface patterns to modify the wettability of poly(methyl methacrylate) (pmma). Opt Lasers Eng 48:707–715

Wen L, Tian Y, Jiang L (2015) Bioinspired super-wettability from fundamental research to practical applications. Angew Chem Int Ed 54:3387–3399

Wooh S, Koh JH, Lee S, Yoon H, Char K (2015) Trilevel-structured superhydrophobic pillar arrays with tunable optical functions. Adv Funct Mater 24:5550–5556

Xia D, Johnson LM, López GP (2012) Anisotropic wetting surfaces with one-dimensional and directional structures: fabrication approaches, wetting properties and potential applications. Adv Mater 24:1287–1302

Xin B, Hao J (2010) Reversibly switchable wettability. Chem Soc Rev 39:769–782

Xu QF, Liu Y, Lin FJ, Mondal B, Lyons AM (2013) Superhydrophobic TiO_2-polymer nanocomposite surface with UV-induced reversible wettability and self-cleaning properties. ACS Appl Mater Interfaces 5:8915–8924

Xue Z, Cao Y, Liu N, Feng L, Jiang L (2014) Special wettable materials for oil/water separation. J Mater Chem A 2:2445–2460

Yan L, Li J, Li W, Zha F, Feng H, Hu D (2016) A photo-induced ZnO coated mesh for on-demand oil/water separation based on switchable wettability. Mater Lett 163:247–249

Yang D, Piech M, Bell NS, Gust D, Vail S, Garcia AA, Schneider J, Park C-D, Hayes MA, Picraux ST (2007) Photon control of liquid motion on reversibly photoresponsive surfaces. Langmuir 23:10864–10872

Yang P, Wang K, Liang Z, Mai W, Wang CX, Xie W (2012) Enhanced wettability performance of ultrathin ZnO nanotubes by coupling morphology and size effects. Nanoscale 4:5755–5760

Yao X, Song YL, Jiang L (2011) Applications of bio-inspired special wettable surfaces. Adv Mater 23:719–734

Yilmaz M, Kuloglu HB, Erdogan H, Cetin SS, Yavuz MS, Ince GO (2015) Light-driven unidirectional liquid motion on anisotropic gold nanorod arrays. Adv Mater Interfaces 2:1500226

Zhang J, Han Y (2010) Active and responsive polymer surfaces. Chem Soc Rev 39:676–693

Zhang X, Jin M, Liu Z, Tryk DA, Nishimoto S, Murakami T (2007) Superhydrophobic TiO_2 surfaces: preparation, photocatalytic wettability conversion, and superhydrophobic-superhydrophilic patterning. J Phys Chem C 111:14521–14529

Zhang X, Shi F, Niu J, Jiang Y, Wang Z (2008) Superhydrophobic surfaces: from structural control to functional application. J Mater Chem 18:621–633

Zhao Y (2009) Photocontrollable block copolymer micelles: what can we control? J Mater Chem 19:4887–4895

Zhu W, Feng X, Feng L, Jiang L (2006) UV-manipulated wettability between superhydrophobicity and superhydrophilicity on a transparent and conductive SnO_2 nanorod film. Chem Commun (26):2753–2755

Zhu H, Yang S, Chen D, Li N, Xu Q, Li H (2016) A robust absorbent material based on light-responsive superhydrophobic melamine sponge for oil recovery. Adv Mater Interfaces 3:1500683

Chapter 3
pH Responsive Reversibly Tunable Wetting Surfaces

Reeta Pant, Sneha Dattatreya, Jitesh Barman, and Krishnacharya Khare

Abstract Smart surfaces with tunable wetting characteristics have recently gained a lot of attention from scientists and engineers due to the interesting underlying fundamentals as well as tremendous applications in areas including microfluidics, lab-on-a-chip, bio-adhesion, oil-water separation, analytical and medical applications to name a few. Surface wettability can either be tuned by passive methods where different surface energy materials are coated on a surface depending upon the requirement. Alternatively, the surface wettability can be tuned actively where a responsive coating is coated on a surface and the wettability can be tuned with respective external stimulus e.g. light, temperature, pH, electric field, magnetic field, mechanical strain etc. Surfaces with pH responsive wetting behaviour allow control of liquids with high precision which is essentially required in many fluidic devices. Compared to other responsive wetting surfaces, pH responsive wetting surfaces are easy to fabricate and are more stable as well. They also show improved reversible transition between hydrophilic and hydrophobic states with much smaller hysteresis. In this chapter, we discuss various studies involving pH responsive wetting/dewetting system with fundamentals as well as potential applications.

Keywords Wetting · Tunable wetting · Interfacial tension · pH value · Surface engineering

---

R. Pant · S. Dattatreya · J. Barman
Department of Physics, Indian Institute of Technology Kanpur, Kanpur, Uttar Pradesh, India

K. Khare (✉)
Department of Physics, Indian Institute of Technology Kanpur, Kanpur, Uttar Pradesh, India

Center for NanoSciences, Indian Institute of Technology Kanpur,
Kanpur, Uttar Pradesh, India
e-mail: kcharya@iitk.ac.in

A. Hozumi et al. (eds.), *Stimuli-Responsive Dewetting/Wetting Smart Surfaces and Interfaces*, Biologically-Inspired Systems 11,
https://doi.org/10.1007/978-3-319-92654-4_3

3.1 Introduction

Young-Dupré equation (Eq. 3.1) suggests that wettability of a surface can be determined by balancing the three interfacial tensions for a vapor-liquid-solid system in equilibrium (Young 1805).

$$\cos\theta = \frac{\gamma_{SV} - \gamma_{SL}}{\gamma_{LV}} \tag{3.1}$$

where γ's are the interfacial tensions, θ is equilibrium contact angle and S, V, L denote solid, vapor and liquid phases respectively. It is clear from Eq. 3.1 that the contact angle of a liquid on a solid surface can be manipulated by modifying any of the three interfacial tensions. When a liquid comes into contact with a solid surface, resulting wetting morphologies are not only governed by the interfacial properties of only liquid/vapour interface but also by the solid/liquid and solid/vapour interfaces resulting in a certain contact angle of the liquid on the surface. Figure 3.1 shows schematics of wetting of a liquid on a solid surface with different wetting regimes. A liquid is said to wet a solid surface if the liquid spreads over a long distance on it and have a contact angle of 0°. If a liquid remains as a spherical drop once brought into contact with a solid surface, then it is said not to wet the surface and has the contact angle 180°. In between wetting and non wetting regime, there can be a situation when a liquid has a contact angle $0° < \theta < 180°$. This is known as the partial wetting and the liquid has a finite liquid/solid interface. Therefore, the easiest way to modify wettability of a surface is by varying the surface energy of the solid, γ_{SV}, which can be achieved by coating the surface with different materials of different surface energies. In this case, if one would like to change the surface wettability, then the old coating must be replaced by a new appropriate coating to provide desired wettability. So with this method, every time the old coating must be replaced by a new one to manipulate the surface wettability. Often this method is not very convenient or effective. Whereas on heterogeneous or rough surfaces, apparent contact angle of a liquid is obtained by either Wenzel or Cassie-Baxter model, which incorporates surface roughness and/or heterogeneity (Wenzel 1936; Cassie and Baxter 1944). So it is also possible to manipulate surface wettability by

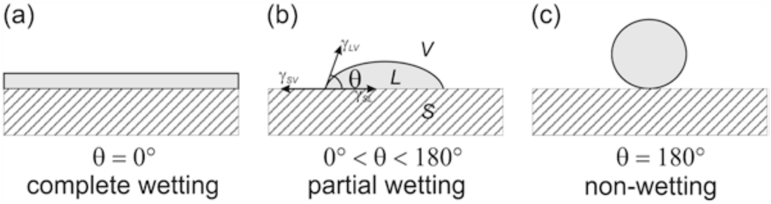

Fig. 3.1 Schematic representation of a droplet on a planar surface. The contact angle θ is determined by a force balance of the three interfacial tensions. (**a**) complete wetting, for $\theta = 0°$, (**b**) partial wetting for $0° < \theta < 180°$ and (**c**) non-wetting for $\theta = 180°$

introducing surface roughness or surface heterogeneity. Alternatively, if we coat a surface with an active material which can change its surface energy in response to an external stimulus i.e. light, temperature, pH, electric field, magnetic field, mechanical strain etc., then the same coating would result in varying wettability depending upon the dose of the stimulus (Xin and Hao 2010; Brinkmann et al. 2007). Many such external stimulus based tunable wetting surfaces have been experimentally studied and analyzed theoretically by various research groups. Each of the techniques has some advantages and disadvantages. For example, light induced tunable wetting surfaces can be prepared on any given surface and it also shows very good response but the drawback of this technique is that it cannot be used in dark places e.g. inside microfluidics or Lab-on-a-Chip devices (Pant et al. 2014). Similarly, electric field induced tunable wetting i.e. electrowetting, is very effective and reversible technique but it requires conducting substrates and conducting liquids (Khare et al. 2007; Barman et al. 2015, 2017). For mechanical strain induced tunable wetting, it is essential to have elastic surface which can be change its topography on application and removal of external mechanical strain. Therefore to obtain reversible tunable wetting for liquids with different pH is also important for various applications. Xin et al. compiled a review article on reversibly switchable wettability which summarizes most of the responsive wetting surfaces (Xin and Hao 2010). As early as in 1987, Klemm et al. performed pH measurements on leaves of *Hedera helix* L. which indicated the amount and strength of acids present on the leaves and the buffering mechanisms (Klemm et al. 1987). To measure the amount and strength of acids on dry leaves the leaf surfaces had to be wetted with water and the pH determined from at least two different wetting thicknesses. Subsequently Holmes-Farley et al. studied the wetting by water of low-density polyethylene film modified at the polymer-water (air) interface and water/polymer contact angles were determined for each of these interfaces; for interfaces containing acidic or basic functional groups as a function of the pH (Holmes-Farley et al. 1988). Jiang et al. demonstrated pH-responsive superhydrophobic/superhydrophilic surfaces using a self-assembled monolayer (SAM) of a dendron thiol as the underlying surface for electrodeposition of gold nanostructures which has also been reported by various research groups (Xin and Hao 2010; Jiang et al. 2005; Yu et al. 2005; Cheng et al. 2014a; Lv et al. 2014; Su et al. 2017; Wang et al. 2007; Xia et al. 2007, 2009; Xiao et al. 2013, 2014; Zhang et al. 2008; Sun et al. 2013; Rios and Smirnov 2011; Lu et al. 2016; Jiang et al. 2008; Geng et al. 2014; Fujii et al. 2011; Cheng et al. 2014b, 2015). Large-scale pH-responsive behavior was obtained by modifying the surface with 2-(11-mercaptoundecanamido) benzoic acid. Magalhães et al. studied wetting of a ferrofluid as a function of the concentration and size of magnetic grains and pH of the solution on Teflon coated glass surfaces (Magalhães et al. 2005). Alexandrova et al. demonstrated effect of pH on liquid/solid and solid/air surface tension and wetting film thickness (Alexandrova et al. 2017). Few superhydrophobic surfaces depict tunable adhesion that is responsive to both temperature and pH (Cheng et al. 2012a). Dental enamel or dental materials also show tunable adhesion which depends on contact time, pH, surface wettability, and isoelectric point (Müller et al. 2010). Bio-inspired special wetting surfaces which responds to external stimuli as temperature and pH (Xu et al. 2012; Tang et al. 2016; San Miguel and Behrens 2011). Smart fabrics with pH tunable wetting behavior is also an important application of pH responsive surfaces (Lee et al. 2012; Pan et al. 2014; Wang et al. 2014; Wu et al. 2015; Yan et al. 2017; Zhang and Guo 2014). Many research have demonstrated application of pH tunability in controlled oil-water separation and filtration (Su et al. 2017; Wu et al. 2015; Cao et al. 2014; Dang et al. 2016; Ju et al. 2014; Li et al. 2016a, b; Wang and Guo 2013; Xiang et al. 2015; Xu et al. 2016; Zhang et al. 2012; Sinha and Purkait 2014). Apart from the mentioned references, there are many other phenomenon and fabrication techniques which exploits various aspects of pH responsive characteristics (Gao et al. 2010; Liu et al. 2012; Ye et al. 2012; Escalé et al. 2013; Lu et al. 2013a; Kulkarni et al. 2014; Tu and Lee 2014; Narkar et al. 2016). In the present chapter, we present detailed discussion on pH responsive reversibly tunable wetting surfaces, related phenomenon and their applications.

3.2 pH Responsive Tunable Wetting Surfaces

As discussed earlier, smart surfaces with reversibly tunable wettability is important for many potential applications. pH responsive tunable wetting surfaces are particularly important where it is required to manipulate different acidic and basic liquids. Bain et al. first demonstrated pH responsive contact angle study of mixtures of molecules of $HS(CH_2)_{10}CO_2H$ and $HS(CH_2)_{10}CH_3$ from solution in ethanol adsorbed on gold substrates (Bain and Whitesides 1989). They observed that monolayers formed by the spontaneous assembly of the binary mixture of organic thiols provide high degree of control over the chemistry and structure of a surface. 200 nm thin film of gold deposited on silicon were used as substrates and were coated by organic thiols by immersing them into thiol solution overnight at room temperature to form monolayers containing mixture of carboxylic acid groups and methyl groups. The two components in the monolayer were not found to be phase separated into macroscopic single component domains, any clusters of carboxylic acids that did form were at most few nanometers across. Fig. 3.2a shows that the contact angles on all the monolayers containing carboxylic acids was constant at low pH and decreased linearly at high pH. It is also observed that the onset of ionization appeared to move to higher values of pH as the proportion of carboxylic acids in the monolayer decreased or the break point in the titration curves moved from pH 6 to pH 9 as the proportion of the components of the monolayer that were terminated by carboxylic acid groups decreased from 100 to 14%. Figure 3.2b shows plots of contact angles of water on three samples immersed in perfluorodecalin: PE-CO_2H (polyethylene carboxylic acid), a pure monolayer of $HS(CH_2)_{10}CO_2H$, and a monolayer adsorbed from a 1:1 mixture of $HS(CH_2)_{10}CO_2H$ and $HS(CH_2)_{10}CH_3$. Here captive drop technique was used rather than sessile drop as perfluorodecalin is denser than water. It is clear from Fig. 3.2b that the initial contact angle of water on PE-CO_2H increased and then decreased slowly. Stable contact angles with acidic or basic drops could be

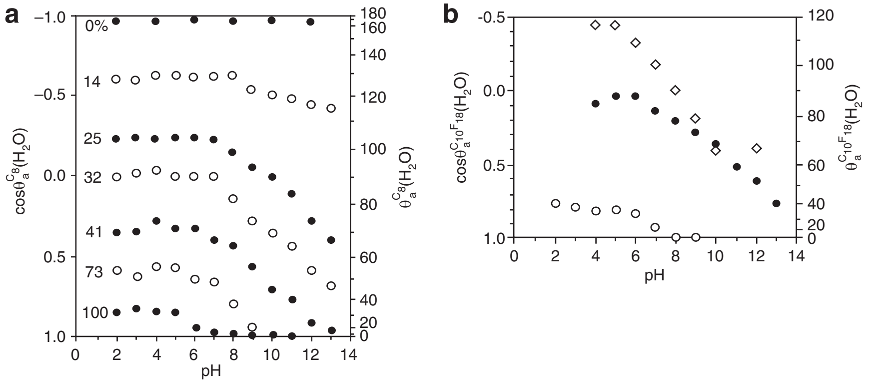

Fig. 3.2 (**a**) advancing contact angles of buffered aqueous solutions measured with sessile drop under cyclooctane on mixed monolayers of $HS(CH_2)_{10}CO_2H$ and $HS(CH_2)_{10}CH_3$ as a function of pH. The curves are labelled by the proportion of the chains in the monolayer that were terminated by a carboxylic acid group. (**b**) Advancing contact angles of buffered aqueous solutions measured with captive drops under perfluorodecalin as a function of pH: PE-CO_2H (diamonds); monolayer of $HS(CH_2)_{10}CO_2H$ (open circles); monolayer adsorbed from a 1:1 mixture of $HS(CH_2)_{10}CO_2H$ and $HS(CH_2)_{10}CH_3$ (solid circles). (Reproduced from Bain and whitesides. Langmuir 1989)

obtained provided that the sample of PE-CO_2H was immersed in the perfluorodecalin for at least 10 min before a drop of water is placed on the surface and a further 10 min was given before the contact angle was measured. So it is clear that monolayers of binary mixtures of molecules of $HS(CH_2)_{10}CO_2H$ and $HS(CH_2)_{10}CH_3$ can be used as pH responsive tunable wetting surfaces.

Xu et al. also showed a novel route to prepare to assemble thin films containing pH-responsive nanostructures of hydrophilic cylindrical domains oriented perpendicular to a silicon substrate (Xu et al. 2006). They prepared amphiphilic block copolymer poly(styrene-*b*-acrylic acid) (PS-*b*-PAA), from the precursor, poly(styrene-*b*-*tert*-butyl acrylate) (PS-*b*-P*t*BA), by an autocatalytic reaction involving surface hydroxyl groups. They performed in-situ AFM to observe the evolution of the nanostructures and the swelling dynamics of PS-*b*-PAA films in aqueous solutions with different pH values. It was found that the films immersed in solution with higher pH swell more rapidly than at the lower pH. Figure 3.3 (2) (k), summarizes the tunable wettability characteristics of PS-*b*-PAA films as a function of pH. For initial PS-*b*-PAA film, water contact angle of 73° is observed which is also obtained about 77° from the Cassie-Baxter equation using an area fraction of 81% PS (19% PAA) at the surface. As pH is increased, the contact angle value decreases abruptly as pH 4.0 is approached and then reaches a constant value of 43° above pH 5.0. The inset shows optical contact angle images of aqueous drops on surfaces with pH > 4.0. The systematic decrease in contact angle is attributed to the conformational rearrangement of PAA chains in response to the high pH environment, resulting in a more hydrophilic surface. The contact angles (~43°) at pH > 4.0 are very similar to the values for grafted PAA brushes (~42°), suggesting that the entire surface is covered by PAA (Janorkar et al. 2004; Li et al. 2005; Treat et al. 2006).

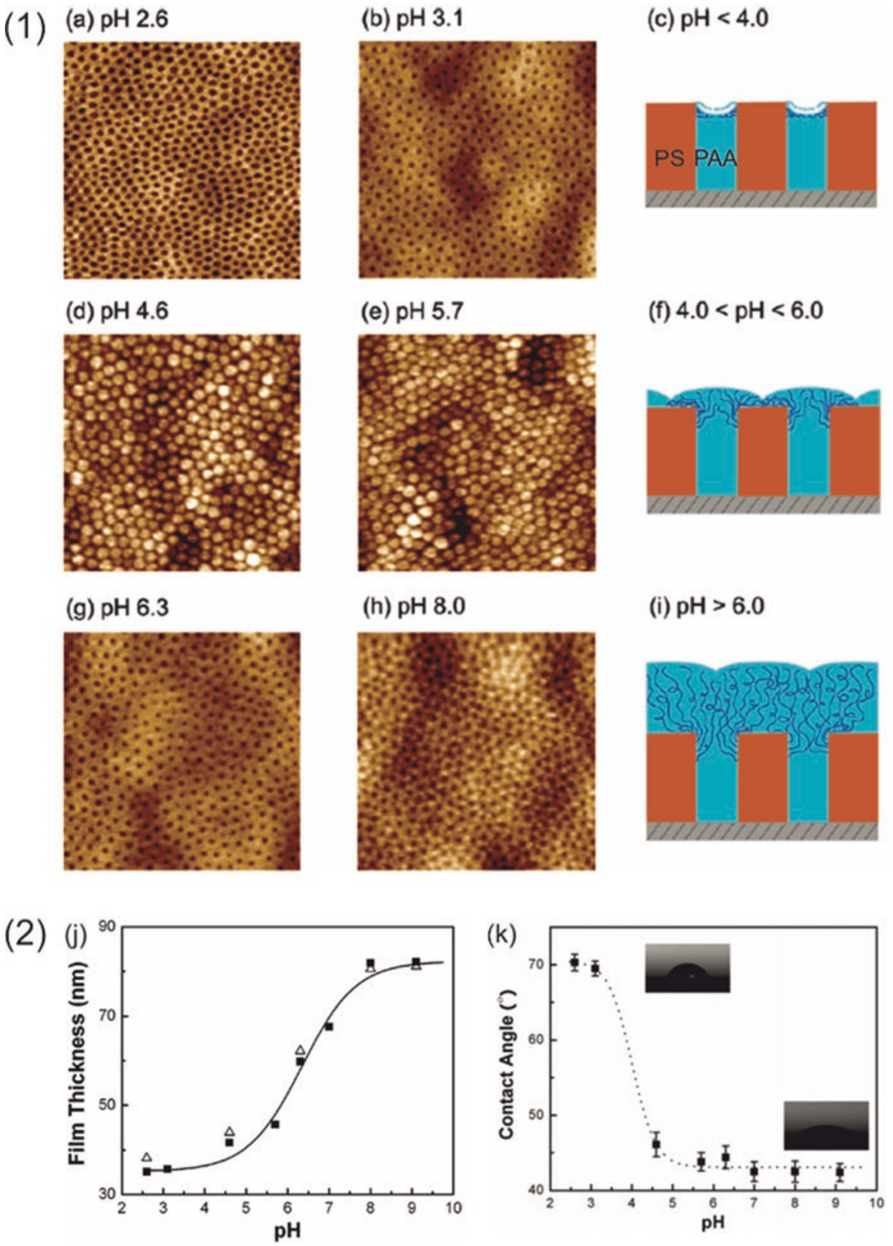

Fig. 3.3 (**1**) AFM images of pH-dependent nanostructures of amphiphilic block copolymer (PS-*b*-PAA) films immersed in buffered solutions with different pH values for 120 min (*a*–*h*). Images are 1 × 1 μm^2 and height scale is 15 nm. Schematic cartoons (*c*–*i*) of cross sections of perpendicularly aligned cylindrical PAA nanodomains embedded in a PS matrix at low, intermediate, and high pH regimes. (**2**) (*j*) Film thickness in aqueous media as a function of pH. Film thickness of different samples after equilibrium swelling (filled squares). Film thickness measured from one sample as pH decreases from 9.1 to 2.6 (open triangles). The solid line is a guide to the eye. Reversible swelling is observed. (*k*) Water contact angles on dried PS-*b*-PAA films after initial immersion at different pH values. The dotted line is a guide to the eye. Inset represents a typical droplet profile at pH < 4.0 and pH > 4.0. The ~30°decrease in contact angle is attributed to surface rearrangement of PAA chains. (Reproduced from Xu et al. Macromolecules 2006)

Uhlmann et al. also demonstrated stimuli responsive binary polymer brushes obtained by “grafting-to” and “grafting-from” methods (Uhlmann et al. 2006). The concept of reversible switching is demonstrated in Fig. 3.4a where a polymer brush made from a hydrophilic polymer (A) and a hydrophobic polymer (B) is treated by a non-selective solvent and selective solvents for both polymers. For good solvents, the inter chain repulsion dominates and the polymer chains form stretched conformation and for a bad solvent the repulsion between polymer and solvent dominates

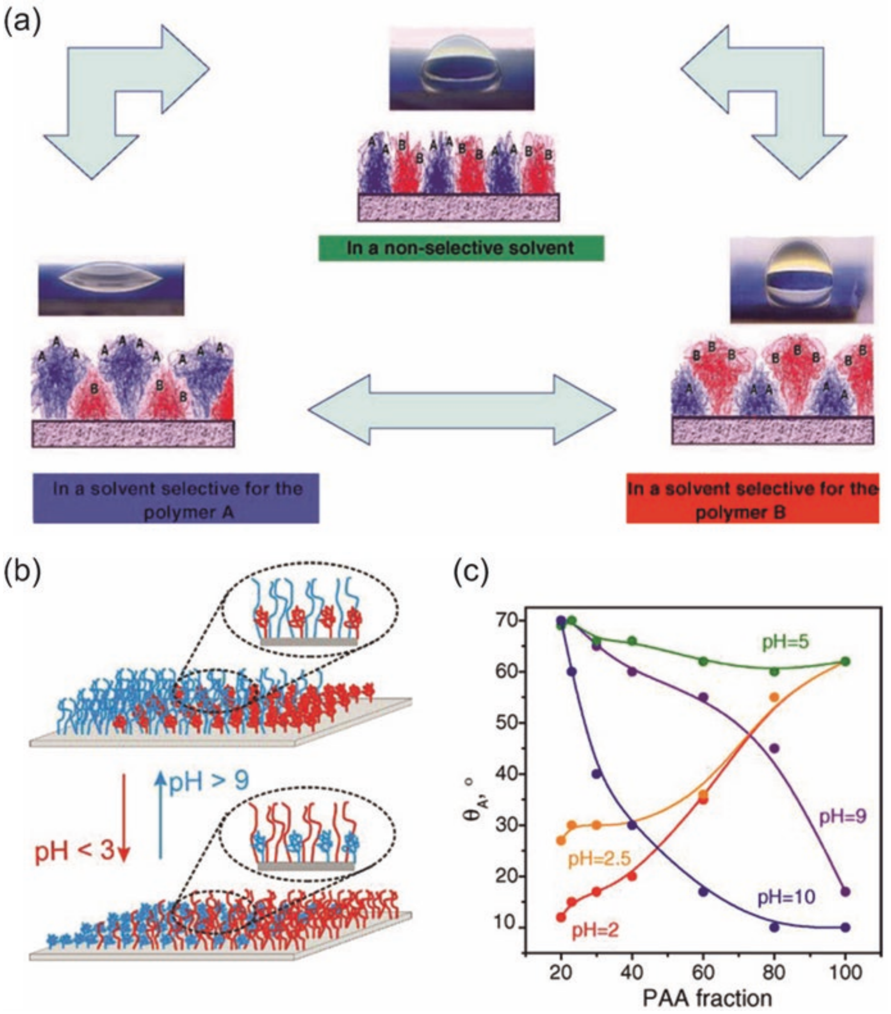

Fig. 3.4 (**a**) Schematic representation of the switching of physico-chemical surface properties of a binary polymer brush in solvents with different properties of the brush components, (**b**) schematic of switching of wettability gradient by pH, and (**c**) advancing contact angle as a function of PAA fraction of the brush and pH. (Reproduced from Uhlmann et al. Progress in Organic Coatings 2006)

causing chain collapse and a coiled polymer conformation. This means that when the brush is treated with a selective solvent for polymer A, it becomes hydrophilic and when it is treated with a selective solvent for component B surface becomes hydrophobic.

For non-selective solvents, both polymers form laterally segregated lamellar-like structures and shows intermediate contact angles. Therefore one may obtain the desired composition of the top layer with respect to A or B polymers as a response to the composition of the environment (liquid or a gaseous phase). Uhlmann et al. also fabricated binary gradient brushes which could gradually change surface wettability as a function of one component as shown in Fig. 3.4b. The gradient brushes were created with polystyrene and with two incompatible polyelectrolytes i.e. poly(acrylic acid) (PAA) and poly(2-vinyl pyridine). The obtained binary gradient brush is able to switch the direction of the wettability gradient by treatment with different pH aqueous solutions. For acidic medium (pH 2), the wettability gradient is along the increase of the poly(2-vinylpyridin) content. Increasing pH to 2.5 decreases the switching amplitude by 10° due to the decrease of the degree of protonation of poly(2-vinylpyridine). For neutral media (pH ~7), the gradient is almost "switched off", whereas it appears again for basic media (pH 9–10), but in the opposite direction, along with the increasing PAA fraction of the brush. Figure 3.4c summarizes the pH dependent wettability gradient as a function of PAA fraction. So this method provides us a tool to tune the direction and the amplitude of the wettability gradient of a binary polyelectrolyte brush by pH.

On the contrary note, Wang et al. demonstrated stable superhydrophobic surfaces of polybenzoxazine over a wide range of pH designed by simple two step casting process (Wang et al. 2006). They prepared superhydrophobic coating on a glass slide by first mixing 2,2-Bis(3,4-dihydro-3-methyl-2H-1,3-benzoxazine) propane (BA-m benzoxazine) with silica nanoparticles (22 nm mean diameter) in tetrahydrofuran and spin coating the mixture on glass followed by modifying the surface with pure BA-m benzoxazine. Figure 3.5 (1) shows surface morphologies of (a) pure BA-mpolybenzoxazine and (b) polybenzoxazine-silica hybrid surface modified with BA-m polybenzoxazine. Figure 3.5 (1) (c) shows zoomed-in magnified image of (b). Figure 3.5 (2) water contact angles measurement on various samples. Pure BA-m benzoxazine film had rms roughness about 0.2 nm resulting in water contact angle of about 108° indicating hydrophobic nature of BA-m benzoxazine as shown in Fig. 3.5 (2) (a). The polybenzoxazine-silica hybrid surface had rms surface roughness of about 191 nm which resulted in water contact angle of about 135° as shown in Fig. 3.5 (2) (b). Upon further coating the polybenzoxazine-silica hybrid surface with pure BA-m polybenzoxazine, the samples showed superhydrophobic behavior with water contact angle as large as 168° as shown in Fig. 3.5 (2) (c and d). These samples also showed very low contact angle hysteresis (Δθ ~ 1°) and very low sliding angle (~3°). The superhydrophobic polybenzoxazine surface consists both micro- and nanoscale roughness due to microislands (300–700 nm) on the polybenzoxazine surface decorated with nanoparticles (from 20 to 60 nm). Figure 3.5 (3) summarizes pH independent superhydrophobic behavior of a superhydrophobic polybenzoxazine film with pH values between 1 and 14. The graph

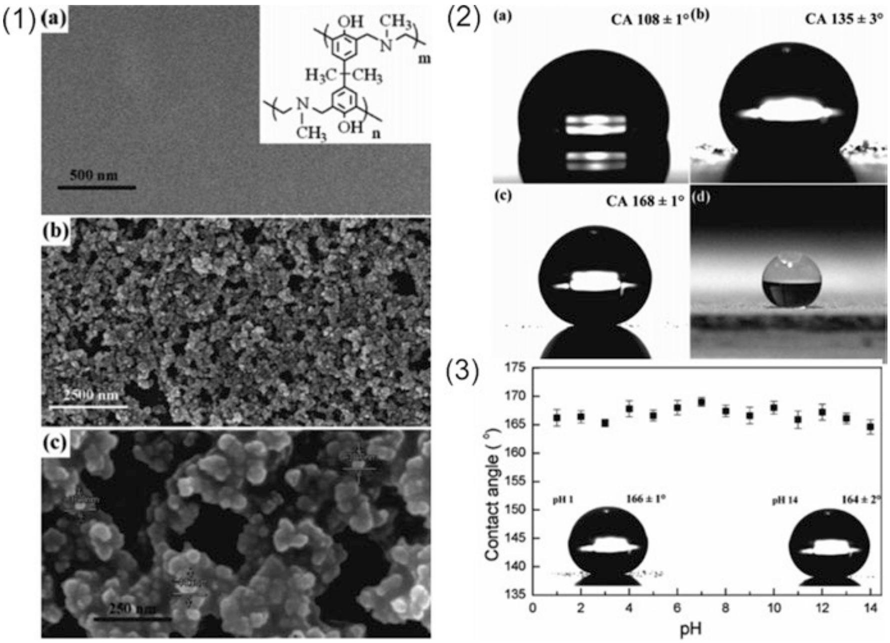

Fig. 3.5 (**1**) SEM images of different polymer surfaces: (*a*) pure BA-mpolybenzoxazine, (*b*) polybenzoxazine-silica hybrid surface modified with BA-m polybenzoxazine, and (*c*) zoomed-in image of (*b*). (**2**) Optical images of water drops on (*a*) smooth cross-linked polybenzoxazine surface, (*b*) polybenzoxazine-silica hybrid surface, (*c*) as-prepared superhydrophobic surface and (*d*) polybenzoxazine-silica hybrid surface modified with BA-m polybenzoxazine. (**3**) Water contact angles on the superhydrophobic surfaces of polybenzoxazine as a function of pH. (Reproduced from Wang et al. Langmuir 2006)

clearly shows that the water contact angle remains between 164° and 168° irrespective of the pH value. Also the contact angle hysteresis and sliding angle was also found to be independent of the pH value. The study confirms that the superhydrophobic polybenzoxazine surfaces can be used in a wide pH range of corrosive water. Such surfaces were also found very robust against high temperature up to 180 °C which is the glass transition temperature of BA-m polybenzoxazine. Such samples also showed robust stability against exposure to various organic solvents and oil (tetrahydrofuran, dichloromethane, acetone, water, ethanol, diesel oil).

Not only aqueous drops, but foams can also show pH responsive behavior. Binks et al. demonstrated pH-Responsive aqueous foams stabilized by polystyrene latex particles coated with pH responsive polymer (Binks et al. 2007).

To prepare foams, they used 2.6 wt % aqueous dispersion of Poly(acrylic acid) (PAA) stabilized polystyrene (PS) latex particles from a 0.1 M NaCl aqueous solution. Natural pH of these dispersions was 4.2 and the pH could be adjusted by adding either HCl or NaOH. The aqueous particle dispersion was shaken using a shaker which spontaneously generated foam which stored and analyzed subsequently. The foams were characterized using optical microscopy and scanning electron microscopy with varying value of pH. Figure 3.6a shows the zeta potentials and the volume weighted average diameters of the PS latex particles with the pH of the aqueous dispersion. Above pH 5, the apparent diameter of the particles was found constant. Around pH 4.5, the apparent diameter value increased sharply and then became almost constant at and below pH 3.5. The zeta potential values at high salt concentration (filled circles) are negative at high pH owing to ionized carboxyl groups of the PAA stabilizer on the surfaces of the particles. At lower pH, particles become less negatively charged and acquire cationic character, with the isoelectric point being located around pH 3.5. Upon shaking, no stable foam was formed at any pH for aqueous dispersions of PAA-stabilized PS latex particles. However 0.1 M NaCl aqueous dispersion produced reasonable stable foams below a critical pH of the aqueous dispersion. Figure 3.6b & c shows foam heights and optical images for different values of pH of the aqueous dispersion. The height of the foam layer is defined as the distance between the foam/dispersion boundary and the three-phase contact line of air, glass, and foam. Therefore the addition of salt not only increases the foamability of particle dispersions but also enhances the formation and stability of air bubbles in water stabilized by charged silica particles. This is due to the fact

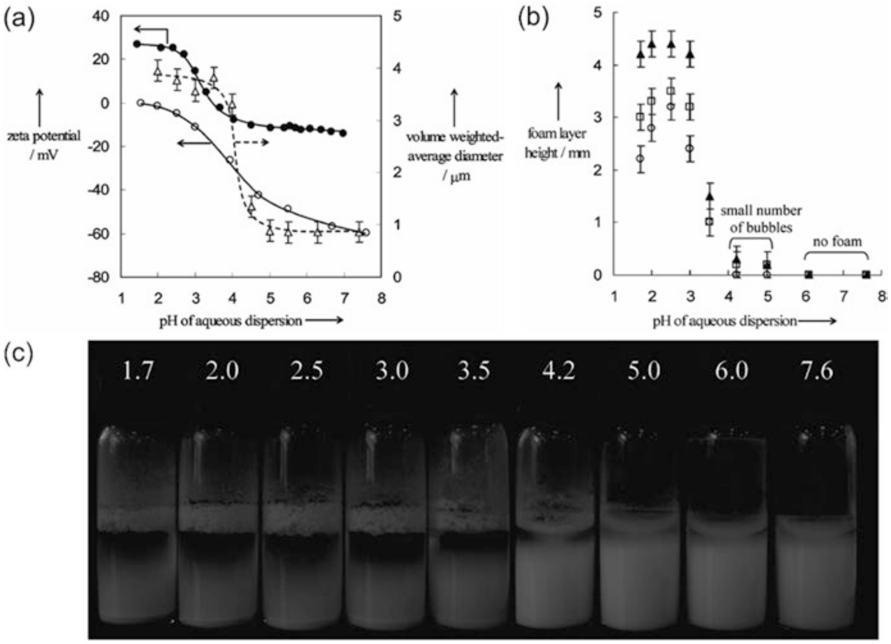

Fig. 3.6 (**a**) Zeta potential (0.1 wt% particles, ●) and volume-weighted average diameter (0.03 wt % particles, Δ) of PAA-stabilized PS latex particles in 0.1 M aqueous NaCl versus pH of the aqueous dispersion. Also shown are the zeta potentials of particles in 0.001 M KCl (o). (**b**) Height of the foam layer versus pH of the aqueous dispersion recorded at different times: immediately after preparation (▲), after 1 week (□), and after 1 month (o). (**c**) Optical photographs of pH-dependent behavior of foams taken 1 week after shaking. (Reproduced from Binks et al. Langmuir 2007)

that the hydrophobicity of the particle surfaces increased with salt concentration, enabling such particles to be well held at the air-water surfaces. At high pH (> 6), no foam can be prepared or they were found very unstable.

Colloidal systems are another important area which, when combined with pH responsive system, can yield very interesting behavior. Motornov et al. reported reversible aggregation and fabrication of superhydrophobic surfaces from stimuli-responsive core-shell nanoparticles using block copolymers covalently bound to silica nanoparticles (Motornov et al. 2007). They used "grafting to" approach to graft amphiphilic block copolymer brushes of poly(styrene-b-2-vinylpyridine-b-ethylene oxide) and poly(styrene-b-4-vinylpyridine) onto two types of silica nanoparticles: colloidal silica (S) of 190 nm diameter and fumed silica (F2) of 15 nm diameter. The stability of particle suspensions in different media suggests that the nanoparticles change and adjust their interfacial energy in the suspensions. Particle's shell provides versatile surface transitions between different core-shell morphologies in selective solvents. Figure 3.7 (1) shows the mechanism of the reversible switching in terms of the PS-2VP-EO brush. In toluene, the outer shell is even less populated by P2VP and PEO than it is in water, while PS is exposed to the exterior of the brush. In water at pH 2, PEO chains and charged P2VP chains are exposed to the particles' exterior whereas in water at pH 5.2, PEO blocks are

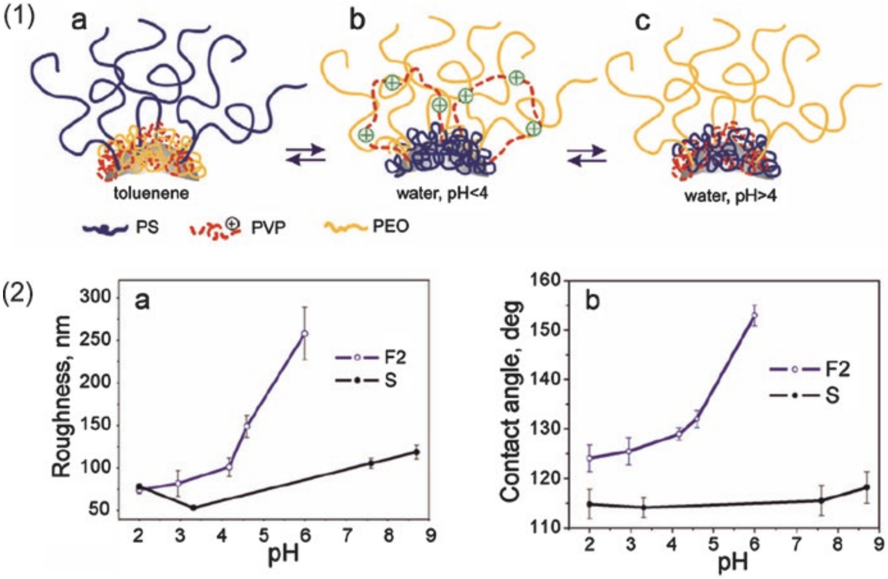

Fig. 3.7 (**1**) Schematics of different morphologies of silica particles (S) prepared from the PS-2VP-EO brushes: (*a*) collapsed P2VP and stretched PS chains in toluene, (*b*) collapsed PS and stretched P2VP, PEO in water at pH < 4 and (*c*) collapsed P2VP, PS, and stretched PEO chains in water at pH > 4. (2) rms roughness (*a*) and contact angles (*b*) of coatings obtained from aqueous suspensions of samples F2 and S on silicon wafers as a function of pH. (Reproduced from Motornov et al. J Coll Inter Sci 2007)

exposed to the shell's exterior, while P2VP is segregated to the inner part of the brush. Subsequently particles S and F2 were coated on intrinsically hydrophilic silicon substrates from 1% aqueous suspensions in the pH range from 2 to 7. The coatings were initially hydrophilic because particle's surface was dominated by the hydrophilic polymer blocks. Heating the surface above the glass transition temperature switched the surface into a hydrophobic one. PS, which is more hydrophobic, is preferentially exposed to the particle shell upon heating. The coating prepared from sample F2 resulted in a superhydrophobic surface with water contact angle of 153° and sliding angle of ~9°. Coating the spheres (S) with grafted triblock copolymer did not produce superhydrophobic surface. In that case, the maximum water contact angle 118° was obtained from the water suspension with pH 7. Figure 3.7 (2) (a) and (b) summarizes the dependence of rms roughness and water contact angle for S and F2 samples as a function of particle suspension pH.

Another noteworthy work on block copolymer grafted "smart surfaces" and pH responsive wetting transition was reported by Zhu et al. in 2007 (Zhu et al. 2007). Block copolymers of Polystyrene–poly(acrylic acid) (PS–PAA) were polymerized by atom transfer radical polymerization and covalently grafted to both smooth and micro-textured surfaces.

PS_{140}–PAA_{40} copolymer grafted surface were found quite inhomogeneous with segmental islands compared to other compositions therefore were used for all experiments. PS_{140}–PAA_{40} copolymer grafted smooth silicon surfaces showed 86° and 76° water contact angle when exposed to toluene and 0.1 M NaOH solutions respectively. Smaller contact angle achieved by the treatment of basic solution can be explained by surface $-COOH$ groups being converted to $-COO^-$ hydrated ions. The electrostatic repulsion overcomes the hydrophobic interaction between alkyl chains. As a result, the PAA chains uncoiled and were exposed at the outermost of the surfaces. When the copolymer surface is exposed to acidic solution, surface shows better hydrophobicity. In this case, the hydrophobic interactions among alkyl chains become the predominant factor, causing the chain to collapse. It induces surface rearrangement, leading to more PS chains covered on the outermost surface instead of PAA chains. This phenomenon is shown schematically in Fig. 3.8a. On smooth surfaces, 86° and 76° water contact angle were obtained when exposed to toluene and 0.1 M NaOH solutions respectively. To enhance the switching amplitude, the copolymer was grafted on rough surface. Hierarchically structured ZnO nanorods were used for the same. On such surfaces, the responsive ranged changed from 153° to 14° when exposed to toluene and 0.1 M NaOH solutions respectively. This was due to the fact that such hierarchically structured ZnO nanorods surface depicts Cassie-Baxter wetting regime due to which the surface became superhydrophobic when exposed to toluene and superhydrophilic when exposed to basic environment. Figure 3.8b shows contact angle images of water drops on smooth and ZnO nanorods based rough surfaces when exposed to toluene and 0.1 M NaOH solutions with 86°, 76° and 153°, 14° contact angles respectively. They also found that the PS–PAA copolymer brushes are not only pH-responsive, but also reversibly switchable. In further intensive study, they repeatedly conducted acid/base exposure treatments to analyze the durability of the samples and found the surface wettabili-

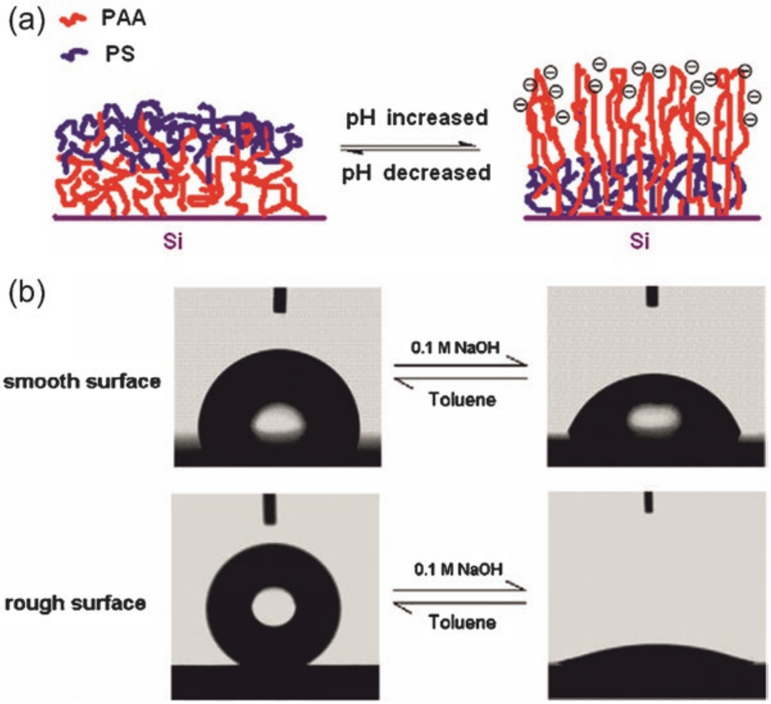

Fig. 3.8 (**a**) Schematics of surface reorganization of PS–PAA copolymer brush covered surface with external acidic and basic inducements and (**b**) contact angle images of water droplets on smooth and rough PS_{140}–PAA_{40} copolymer-grafted surfaces reversibly switched by basic solution and toluene. (Reproduced from Zhu et al. J Coll Inter Sci 2007)

ties could be reversibly switched between a superhydrophobic state and a superhydrophilic state many number of time without losing the characteristics and also with very little variation.

Similar to the above work, Chia et al. demonstrated pH responsive reversibly swellable nanotube arrays of polyelectrolyte multilayers (PEMs) composed of poly(allylamine hydrochloride) (PAH) and poly(acrylic acid) (PAA). This specific PEM system has the ability to undergo pH triggered swelling-deswelling transitions as shown with schematics in Fig. 3.9 (1). PEM assembly was prepared by first immersing a substrate into a polycation solution of PAH and then immersing in a polyanion solution of PAA with controlled parameters. The PEM assembly was etched using track-etched polycarbonate membrane (TEPM) to result into PEM nanotube arrays. Length, diameter and opening structure of nanotube arrays could be controlled using TEPM and other experimental parameters. Fluorescently labeled PAH was used to provide contrast while imaging them with confocal laser scanning microscope.

When PEM nanotubes were immersed in water at pH 5.5, no change in tube dimensions was found similar to that of dry tubes. When immersed in water at

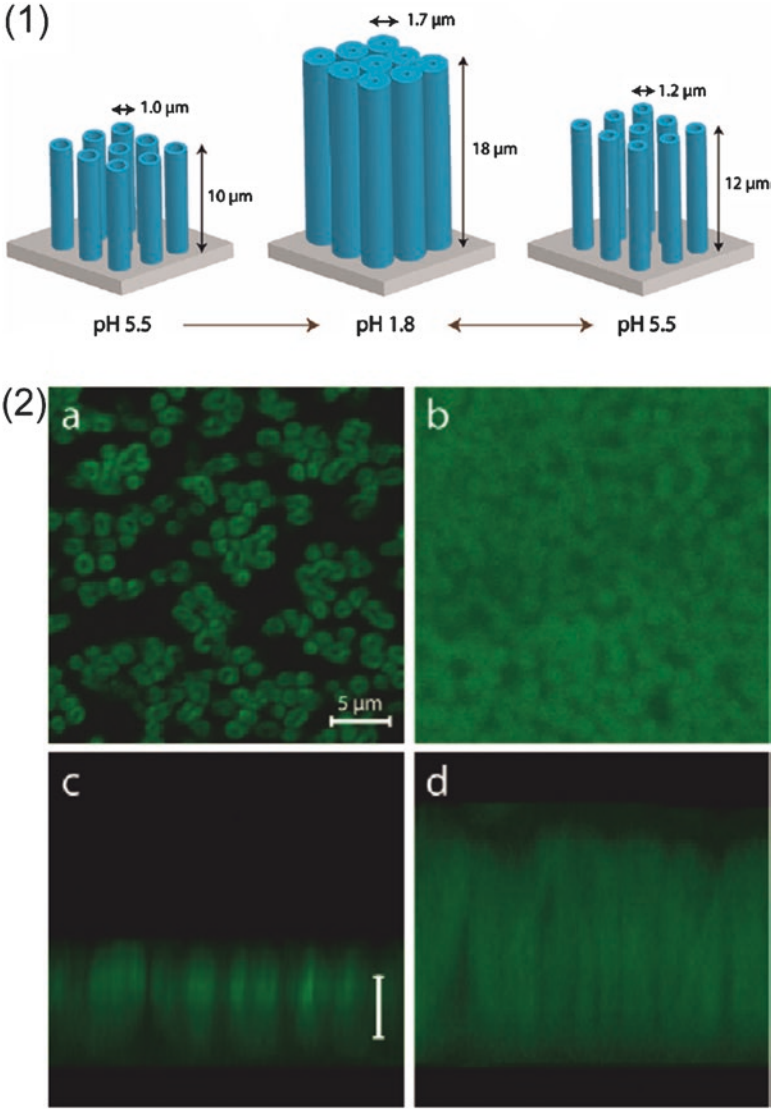

Fig. 3.9 (**1**) Schematic representation of PEM nanotube array illustrating dimensional changes when immersed in solutions with different pH values. (**2**) Top (*a*) and side (*b*) views of confocal images of PEM nanotube arrays immersed in water at pH 5.5 and 1.8, respectively. Both images were scanned at half tube length (not compiled from multiple scans at different heights). Scale bar is 5 µm. (Reproduced from Chia et al. Langmuir 2009)

pH 1.8, the nanotubes swelled substantially in both the vertical and horizontal directions, essentially filling much of the space between tubes. In the highly swollen state, the outer diameter and length of the nanotubes increased from 1.0 to 1.7 µm and 10 to 18 µm, respectively which is shown in Fig. 3.9 (2) a–d. Even in the highly swollen state, however, the tubes remained intact as individual tubes without dissociating completely or merging irreversibly with surrounding tubes. When the pH is increased again to 5.5, the tube dimensions decreased but are found somewhat larger than the original values. This type of swelling-deswelling behavior was also consistently observed in studies of films assembled on planar substrates. Thus, the swelling-deswelling transition of the PEM nanotubes was essentially repeatable for at least a few cycles. The reversible swelling-deswelling transition of the PEM nanotube arrays was also utilized to actuate the simple movement of surface-bound colloidal particles which can potentially be used for example in drug delivery application.

Another important work on ph responsive wettability on cooperative polypeptide surface was reported by Guo et al. in 2010 (Guo et al. 2010). Poly-L-lysine (PLL) was covalently attached to the gold surface modified with an alkanethiol self-assembled monolayer (SAM) via amide bond. Polylysine is an excellent, yet probably simplest, model polypeptide which can adopt different conformations such as random coil, α-helix, or β-sheet dependent on pH and temperature (Wang and Chang 2003). The PLL thin films were fabricated on both smooth and rough substrates. Fig. 3.10 (1) (a) shows SEM images of smooth and rough (silicon pillar) surfaces, (b) shows magnified image of an etched silicon pillar, (c) shows rough substrate that has been modified with a thin film of PLL after gold deposition and (d) shows an etched silicon micropillar after PLL modification which shows that there are many interspaces among the nanowires. Such hierarchical micro/nanostructures of the substrates are useful to enhance surface wettability, either hydrophilicity or hydrophobicity. Contact angle measurements were carried out to evaluate the wettability of the PLL modified surface. Fig. 3.10 (2) (a) shows the optical contact angle images of water droplets on the smooth surface at the different states. The contact angle of

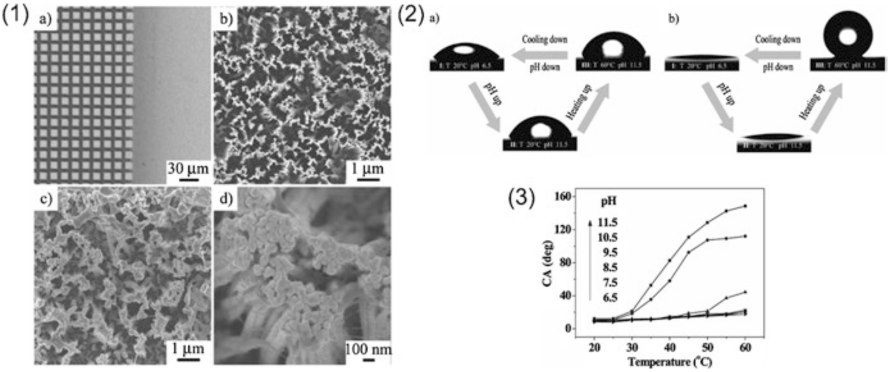

Fig. 3.10 (**1**) (*a*) SEM images of the smooth (right) and rough (left) substrates, (*b*) magnified image of an etched silicon pillar of (*a*), (*c*) etched silicon pillar surface after gold deposition and PLL modification and (*d*) magnified image of the surface in (*c*). (**2**) Optical contact angle images of a water droplet on the smooth (*a*) and rough (*b*) substrates showing the different wettability of state I, II, and III. (**3**) Temperature dependence of water contact angles for PLL thin films on a rough substrate in the range of pH from 6.5 to 11.5. (Reproduced from Guo et al. Langmuir 2010)

a water droplet on the smooth surface in state I (pH 6.5) was 49° and increased to 56° after being immersed in PBS (pH 11.5) for 30 min (state II). Upon increasing the temperature up to 60 °C, the contact angle further increased to 67° (state III). The difference in contact angle between state I and state III was about 17°, and that between state I to state II was about 7°. Compared with the change of contact angles on the smooth substrate (<20°), an extreme change of contact angle (~140°) is identified for the rough substrate. Fig. 3.10 (2) (b) shows the optical contact angle images of a water droplet on the rough surface at different states. The contact angle of a water droplet placed on the freshly prepared rough surface in state I was 8°, corresponding to a superhydrophilic surface.

After increasing the pH from 6.5 to 11.5, the contact angle increased slightly to 12° after 30 min, indicating the surface in state II was also approximately superhydrophilic. However, upon increasing temperature up to 60 °C, the contact angle increased to 148°, indicating a superhydrophobic surface of state III. These results mean that the conformation changes of the polypeptide lead to a macroscopic change in contact angle. The effect of pH and temperature on the apparent contact angle was examined in more detail to further illustrate the switchable wettability. There is no obvious change of contact angle at different temperatures when the pH value was lower than 9.5. The contact angle increases greatly with increasing temperature when the pH value was higher than 10.5. The aggregation of β-sheets via hydrophobic interaction is a temperature favoured process. Therefore, the surface becomes more and more hydrophobic with increased temperature under the high pH value. The pH and temperature stimuli must play in a cooperative way to induce the conformation change of PLL and switch the wettability of the surface.

Liu et al. also demonstrated similar pH responsive reversible wetting transitions on superhydrophobic surfaces with sparsely grafted polymer brushes (Liu et al. 2011). Oxygen plasma hydroxylated anodized alumina substrates were immersed in mixed silane solution including 3-(trichlorosilyl)propyl-2-bromo-2-methyl propanoate (initiator) and 1H,1H,2H,2H-perfluorooctyl trichlorosilane (PFOTS). The mixed monolayers (including covalent bonding initiator and PFOTS) are formed on the anodized alumina substrates. Subsequently typical surface-initiated atom transfer radical polymerization (SIATRP) of (dimethylamino)ethyl methacrylate (DMAEMA) or N-isopropylacrylamide (NIPAm) is performed, therefore sparse polymer brushes (poly(N-isopropylacrylamide), PNIPAm and poly(dimethylamino) ethyl methacrylate, PDMAEMA) are grafted on the positions where initiators originally existed. Then the pressure induced (larger than 250 Pa) wettability changes of the pH responsive polymer (PDMAEMA) modified sample are studied, and acid droplets (pH = 3) and base droplets (pH = 10) were used as probing liquids. For acid drop (pH = 3), the contact angle changed from 145° to 85° after applying the pressure whereas for base drop (pH = 10) the contact angle changed from 157° to 150° after applying the pressure. This was due to the fact that for acid drops, after applying pressure, the drop underwent from Cassie state to Wenzel state causing such large change in the contact angle whereas for base drop, it always stayed in the Cassie state showing little change in the static contact angle.

Cheng et al. used superoleophobic surface to demonstrate under water pH responsive reversible switch of oil adhesion on a nanostructured poly(acrylic acid) (PAA) surface (Cheng et al. 2012b). They prepared a smart nanostructured film by grafting the pH-responsive polymer PAA onto a glass substrate (PAA-G) through a plasma polymerization process. Subsequently a linear PAA chains were grafted on the glass surface. The surface of the PAA-G in solution with a pH value of 2.4 exhibits rough morphology whereas the surface morphology becomes smooth when immersing PAA-G into a solution with a pH value of 8.0. The adhesive forces between the oil droplet and PAA-G surface were quantitatively measured by a high sensitivity micro- electromechanical balance system during a whole approaching, contacting and leaving process. The underwater oil-adhesion on the surface of PAA-G changes with pH values increasing from 1.0 to 12.0 as shown in Fig. 3.11a. At a low pH, the carboxylic groups on neighbouring PAA branched chains form intramolecular hydrogen bonding, which leads to a dehydrated coiled state thus offers a rough surface and lower ratio of water content.

The oil wetting state is typical of a Wenzel state. However for high pH, the carboxylic groups on PAA branched chain form intermolecular hydrogen bonds with surrounding water molecules, which leads to a hydrated stretched state thus provides a surface with low roughness and a high ratio of water content which is a typical Cassie state as shown in Fig. 3.11b. This pH responsive switching in wetting state of a oil drop is responsible to depict reversibly switchable oil adhesion.

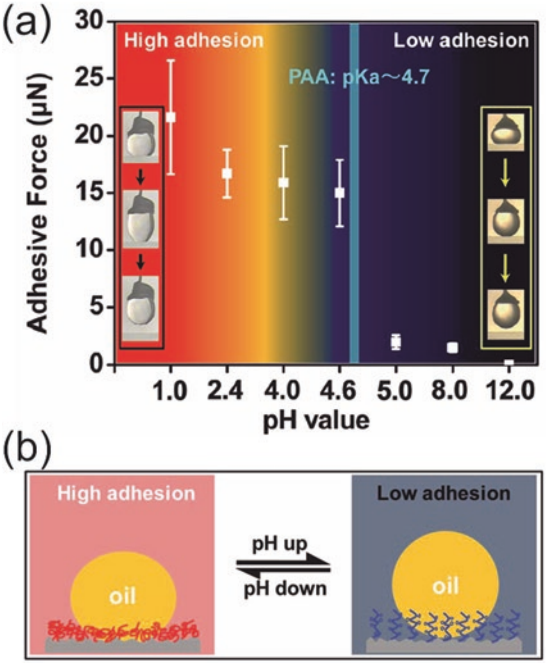

Fig. 3.11 (**a**) Influence of pH values on the adhesive force between the as prepared PAA-G surface and an oil droplet of 1,2-dichloroethane. With the pH values increasing from 1.0 to 12.0, the adhesive force dramatically decreases from 21.6 μN at pH = 1 to zero at pH = 12. The inset photographs are the three-step measuring process, from up to down: the oil droplet is contacting the surface of PAA-G, the oil droplet is leaving the surface and the oil droplet has left the surface. (**b**) Schematics of the proposed mechanism for underwater pH-responsive switchable oil-adhesion. (Reproduced from Cheng et al. Soft Matter 2012a, b)

Lee et al. showed smart electrospun fabrics that undergo reversible superhydrophobic to superhydrophilic transitions as a result of pH changes (Lee et al. 2012). pH tunable amine-based polymer, poly[2-(diisopropylamino) ethylmethacrylate] (PDPAEMA) was used. PDPAEMA was copolymerized with the cross-linkable 3-(trimethoxysilyl) propylmethacrylate (TSPM) to enable the simple, convenient, and stable anchoring of PDPAEMA to arbitrary nanostructures.

The nanoporous structures of the electrospun PS fibers were prepared by phase separation of the polymer-rich and solvent-rich domains during the rapid evaporation of solvent during electrospinning (Megelski et al. 2002). The polymer-rich phases solidified to form a matrix, whereas the solvent-rich phases were eventually transformed into pores. To obtain pH responsive coating, the PS nanoporous fibrous webs were soaked in a 2-methoxyethanol solution containing poly(DPAEMA-*co*-TSPM), so the copolymer infiltrated into the inner porous structures within the PS nanofibers due to capillary action and the low surface tension of 2-methoxyethanol. The TSPM of poly(DPAEMA-co- TSPM) that filled the nanoporous fibrous webs then underwent hydrolysis and self-condensation reactions in the interior and exterior structures of the fibers. Figure 3.12a shows photographs of a water droplet lying on a poly(DPAEMA-co-TSPM)-functionalized fibrous web alternately immersed in solutions of pH 12 and pH 2. The switching from superhydrophilicity to superhydrophobicity could be explained as resulting from the reversible protonation/deprotonation reactions of poly(DPAEMA-co-TSPM). The difference between the wettability properties of the superhydrophobic and superhydrophilic hierarchically structured surfaces was dramatic relative to the difference on flat surfaces. They also evaluated the hysteresis behavior of the water contact angles of the poly(DPAEMA-co-TSPM)-coated fibrous webs under solution pH switching, as shown in Fig. 3.12b.

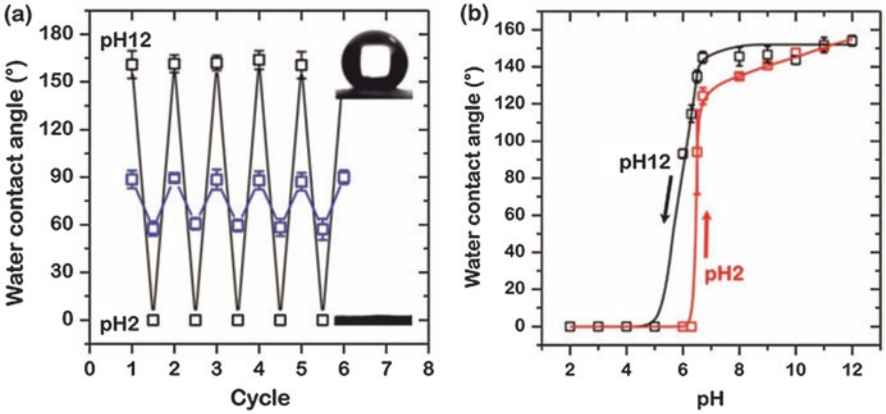

Fig. 3.12 (**a**) Reversible changes in the surface wettability of poly(DPAEMA-*co*-TSPM)-modified fibrous web (black) and smooth substrate (blue) upon immersion in pH 2 and pH 12 solutions. Inset shows the water droplets on the poly(DPAEMA-*co*-TSPM) fibrous web. (**b**) The hysteresis behavior of the water contact angles of the poly(DPAEMA-co-TSPM) fibrous webs upon increasing and decreasing pH cycle. (Reproduced from Lee et al. Soft Matter 2012)

First, the poly(DPAEMA-*co*-TSPM) fibrous webs were immersed in solutions with pH values ranging from pH 11 to pH 2 (black line). Immersion in solutions at pH 11–6.5 did not yield changes in the water contact angle. At pH values below 6.5, the water contact angles dramatically decreased until pH 5 due to the protonation of the PDPAEMAchains, resulting in a superhydrophilic state below pH 5. The pH of the solution was subsequently increased from 2 to 12. The nanofibrous web exhibited a dramatic change in the water contact angle between pH 6.3 and 6.7 (red line), then the water contact angle gradually increased until reaching the superhydrophobic state under basic conditions.

Lu et al. reported the use of layer-by-layer (LbL) hydrogels, composed of amphiphilic polymers that undergo reversible collapsedissolution transition in solutions as a function of pH, to induce sharp, large-amplitude wetting transition at microstructured surfaces (Lu et al. 2013b). To clarify the exact wettability state of the hydrophobic PaAA$_{LbL}$ coated micropillar patterned surfaces, they examined the contact angle hysteresis (Fig. 3.13a), and imaged the behavior of a water droplet on the surface at various pH values using cryo-SEM (Fig. 3.13b–e). At pH < 6, PEAA$_{LbL}$ coated micropillar structured surfaces demonstrated a contact angle hysteresis of >120°, with a receding contact angle close to 0°. In this pH range, the droplet is sticky so that it did not slide down or fall off even when the substrates were turned vertically or upside down (see optical images in Fig. 3.13a). Such stickiness with high contact angle hysteresis is typical for a droplet in a Wenzel state, resulting from the enhanced contact line pinning by the surface structures. Cryo-SEM images (Fig. 3.13b, c) further show that the droplet remains in a complete Wenzel state, with no obvious air bubbles trapped on the micropillared space.

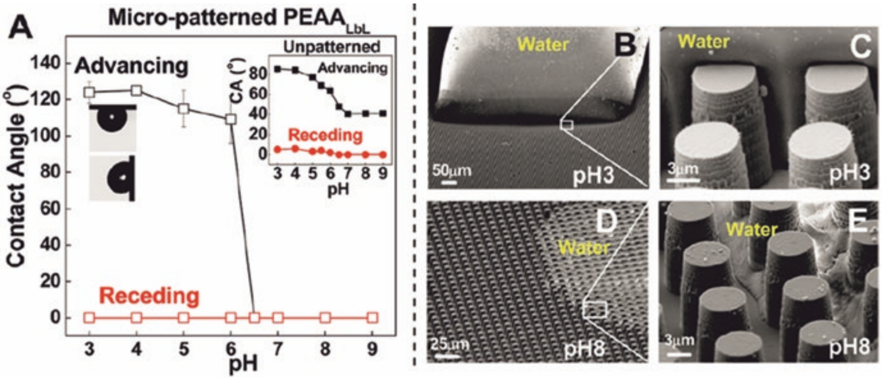

Fig. 3.13 (**a**) Advancing and receding contact angles of PEAA$_{LbL}$ on a micropatterned substrate with a square array of cylindrical pillar structures of ∼15 μm tall, 5 μm in diameter, and 5 μm in interpillar spacing. Optical images show water droplets sticking to the substrate at pH 3, suggesting strong pinning. Inset in the upper right corner represents advancing and receding contact angles of water droplets on unpatterened substrate. (**b**–**e**) Cryo-SEM images of a water droplet on a PEAA$_{LbL}$ coated micropillar patterned substrate at (**b** and **c**) pH 3 and (**d** and **e**) pH 8. (Reproduced from Lu et al. ACS Appl Mater Inter 2013a, b)

This further supports that the sticky behavior of the water droplets at low pH values is because of the enhanced contact line pinning of a droplet boundary by the micropillar structures. Note that although water volume might slightly expand after freezing, they found no difference between the apparent CA of a frozen droplet and that of the initial liquid water droplet. This suggests that the effect of volume change on the wetting state is negligible, if any.

3.3 Summary

In the present chapter, pH responsive reversibly tunable wetting surfaces are discussed in details. pH responsive wetting surfaces are found to be one of the important among external stimulus based responsive wetting surfaces. This is due to the fact that pH responsive coatings can be prepared on any given solid surface which would response to liquids, environments or preparation techniques with different pH values. pH responsive reversible switching between different wetting states on variety of substrates have been demonstrated by various research groups which is summarized in this chapter. pH responsive tunable wetting surfaces have also been used for many applications including effective oil-water separation, superhydrophobic-superhydrophilic transition, drug delivery, smart fabrics, tunable adhesion, bioinspired adhesion to name a few.

Acknowledgement KK acknowledges financial assistance from BRNS (DAE) Young Scientist Research Award and DST, New Delhi through its Unit of Excellence on Soft Nanofabrication at IIT Kanpur.

References

Alexandrova L, Grigorov L, Khristov K, Petkova H (2017) Effects of pH on wetting behavior of 'star-like' block copolymer surfactant solutions. Colloids Surf A Physicochem Eng Asp 519:78–86

Bain CD, Whitesides GM (1989) A study by contact angle of the acid-base behavior of monolayers containing o-mercaptocarboxylic acids adsorbed on gold: an example of reactive spreading. Langmuir 5:1370–1378

Barman J, Swain D, Law BM, Seemann R, Herminghaus S, Khare K (2015) Electrowetting actuated microfluidic transport in surface grooves with triangular cross section. Langmuir 31:1231–1236

Barman J, Pant R, Nagarajan AK, Khare K (2017) Electrowetting on dielectrics on lubricating fluid-infused smooth/rough surfaces with negligible hysteresis. J Adhes Sci Technol 31:159–170

Binks BP, Murakami R, Armes SP, Fujii S, Schmid A (2007) PH-responsive aqueous foams stabilized by ionizable latex particles. Langmuir 23:8691–8694

Brinkmann M, Khare K, Seemann R (2007) Control of liquids by surface energies. In: Hardt S, Schönfrld F (eds) Microfluidic Technologies for Miniaturized Analysis Systems. Springer, Boston, pp 157–202

Cao Y, Liu N, Fu C, Li K, Tao L, Feng L, Wei Y (2014) Thermo and pH dual-responsive materials for controllable oil/water separation. ACS Appl Mater Interfaces 6:2026–2030

Cassie ABD, Baxter S (1944) Wettability of porous surfaces. Trans Faraday Soc 40:546–551

Cheng Z, Lai H, Du M, Zhu S, Zhang N, Sun K (2012a) Super-hydrophobic surface with switchable adhesion responsive to both temperature and pH. Soft Matter 8:9635–9641

Cheng Q, Li M, Yang F, Liu M, Li L, Wang S, Jiang L (2012b) An underwater pH-responsive superoleophobic surface with reversibly switchable oil-adhesion. Soft Matter 8:6740–6743

Cheng M, Liu Q, Ju G, Zhang Y, Jiang L, Shi F (2014a) Bell-shaped superhydrophilic-superhydrophobic-superhydrophilic double transformation on a pH-responsive smart surface. Adv Mater 26:306–310

Cheng Z, Lai H, Du Y, Fu K, Hou R, Li C, Zhang N, Sun K (2014b) PH-induced reversible wetting transition between the underwater superoleophilicity and superoleophobicity. ACS Appl Mater Interf 6:636–641

Cheng Z, Wang J, Lai H, Du Y, Hou R, Li C, Zhang N, Sun K (2015) PH-controllable on-demand oil/water separation on the switchable superhydrophobic/superhydrophilic and underwater low-adhesive superoleophobic copper mesh film. Langmuir 31:1393–1399

Chia KK, Rubner MF, Cohen RE (2009) PH-responsive reversibly swellable nanotube arrays. Langmuir 25(24):14044–14052

Dang Z, Liu L, Li Y, Xiang Y, Guo G (2016) In situ and ex situ pH-responsive coatings with switchable wettability for controllable oil/water separation. ACS Appl Mater Interfaces 8:31281–31288

Escalé P, Van Camp W, Du Prez F, Rubatat L, Billon L, Save M (2013) Highly structured pH-responsive honeycomb films by a combination of a breath figure process and in situ thermolysis of a polystyrene-block-poly(ethoxy ethyl acrylate) precursor. Polym Chem 4:4710–4717

Fujii S, Suzaki M, Armes SP, Dupin D, Hamasaki S, Aono K, Nakamura Y (2011) Liquid marbles prepared from pH-responsive sterically stabilized latex particles. Langmuir 27:8067–8074

Gao Y, Cheng M, Wang B, Feng Z, Shi F (2010) Diving-surfacing cycle within a stimulus-responsive smart device towards developing functionally cooperating systems. Adv Mater 22:5125–5128

Geng Z, Guan S, Jiang HM, Gao LC, Liu ZW, Jiang L (2014) PH-sensitive wettability induced by topological and chemical transition on the self assembled surface of block copolymer. Chin J Polym Sci (English Edition) 32:92–97

Guo Y, Xia F, Xu L, Li J, Yang W, Jiang L (2010) Switchable wettability on cooperative dual-responsive poly-L-lysine surface. Langmuir 26:1024–1028

Holmes-Farley RS, Bain CD, Whitesides GM (1988) Wetting of functionalized polyethylene film having ionizable organic acids and bases at the polymer-water interface: relations between functional group polarity, extent of ionization, and contact angle with water. Langmuir 4:921–937

Janorkar AV, Metters AT, Hirt DE (2004) Modification of poly(lactic acid) films: enhanced wettability from surface-confined photografting and increased degradation rate due to an artifact of the photografting process. Macromolecules 37:9151–9159

Jiang Y, Wang Z, Yu X, Shi F, Xu H, Zhang X, Smet M, Dehaen W (2005) Self-assembled monolayers of dendron thiols for electrodeposition of gold nanostructures: toward fabrication of superhydrophobic/superhydrophilic surfaces and pH-responsive surfaces. Langmuir 21:1986–1990

Jiang Y, Wan P, Smet M, Wang Z, Zhang X (2008) Self-assembled monolayers of a malachite green derivative: surfaces with pH- and UV-responsive wetting properties. Adv Mater 20:1972–1977

Ju G, Cheng M, Shi F (2014) A pH-responsive smart surface for the continuous separation of oil/water/oil ternary mixtures. NPG Asia Mater 6:e111

Khare K, Brinkmann M, Law BM, Herminghaus S, Seemann R (2007) Switching wetting morphologies in triangular grooves. Eur Phys J Spec Top 166:151

Klemm O, Riederer M, Frevert T (1987) pH-response on leaves and isolated cuticles of Hedera helix L. after wetting with artificial rainwater. Environ Exp Bot 27:349–355

Kulkarni SA, Lyles VD, Serem WK, Lu L, Kumar R, Garno JC (2014) Solvent-responsive properties of octadecyltrichlorosiloxane nanostructures investigated using atomic force microscopy in liquid. Langmuir 30:5466–5473

Lee CH, Kang SK, Lim JA, Lim HS, Cho JH (2012) Electrospun smart fabrics that display pH-responsive tunable wettability. Soft Matter 8:10238–10240

Li J, Chen XR, Chang YC (2005) Preparation of end-grafted polymer brushes by nitroxide-mediated free radical polymerization of vaporized vinyl monomers. Langmuir 21:9562–9567

Li JJ, Zhou YN, Jiang ZD, Luo ZH (2016a) Electrospun fibrous mat with pH-switchable superwettability that can separate layered oil/water mixtures. Langmuir 32:13358–13366

Li T, Shen J, Zhang Z, Wang S, Wei D (2016b) A poly(2-(dimethylamino)ethyl methacrylate-co-methacrylic acid) complex induced route to fabricate a super-hydrophilic hydrogel and its controllable oil/water separation. RSC Adv 6:40656–40663

Liu X, Ye Q, Song X, Zhu Y, Cao X, Liang Y, Zhou F (2011) Responsive wetting transition on superhydrophobic surfaces with sparsely grafted polymer brushes. Soft Matter 7:515–523

Liu M, Xue Z, Liu H, Jiang L (2012) Surface wetting in liquid-liquid-solid triphase systems: solid-phase-independent transition at the liquid-liquid interface by lewis acid-base interactions. Angew Chem Int Ed 51:8348–8351

Lu Y, Zhuk A, Xu L, Liang X, Kharlampieva E, Sukhishvili SA (2013a) Tunable pH and temperature response of weak polyelectrolyte brushes: role of hydrogen bonding and monomer hydrophobicity. Soft Matter 9:5464–5472

Lu Y, Sarshar MA, Du K, Chou T, Choi CH, Sukhishvili SA (2013b) Large-amplitude, reversible, pH-triggered wetting transitions enabled by layer-by-layer films. ACS Appl Mater Interf 5:12617–12623

Lu Z, Peng S, Zhang X, Liu Q (2016) Microwetting of pH-sensitive surface and anisotropic MoS_2 surfaces revealed by femtoliter sessile droplets. Langmuir 32:11273–11279

Lv Y, Cao Y, Svec F, Tan T (2014) Porous polymer-based monolithic layers enabling pH triggered switching between superhydrophobic and superhydrophilic properties. Chem Commun 50:13809–13812

Magalhães M, Neto AMF, Bee A, Talbot D, Bourdon A (2005) Wetting of glass surface covered with Teflon by ferrofluid as a function of concentration and size of grains, and pH of the solution. J Magn Magn Mater 289:385–388

Megelski S, Stephens JS, Chase DB, Rabolt JF (2002) Micro- and nanostructured surface morphology on electrospun polymer fibers. Macromolecules 35:8456–8466

Motornov M, Sheparovych R, Lupitskyy R, MacWilliams E, Minko S (2007) Responsive colloidal systems: reversible aggregation and fabrication of superhydrophobic surfaces. J Colloid Interface Sci 310:481–488

Müller C, Lüders Z, Hoth-Hannig W, Hannig M, Ziegler C (2010) Initial bioadhesion on dental materials as a function of contact time, pH, surface wettability, and isoelectric point. Langmuir 26:4136–4141

Narkar AR, Barker B, Clisch M, Jiang J, Lee BP (2016) PH responsive and oxidation resistant wet adhesive based on reversible catechol-boronate complexation. Chem Mater 28:5432–5439

Pan S, Guo R, Xu W (2014) Durable superoleophobic fabric surfaces with counterintuitive superwettability for polar solvents. AICHE J 60:2752–2756

Pant R, Singha S, Bandyopadhyay A, Khare K (2014) Investigation of static and dynamic wetting transitions of UV responsive tunable wetting surfaces. Appl Surf Sci 292:777–781

Rios F, Smirnov SN (2011) PH valve based on hydrophobicity switching. Chem Mater 23:3601–3605

San Miguel A, Behrens SH (2011) Permeability control in stimulus-responsive colloidosomes. Soft Matter 7:1948–1956

Sinha MK, Purkait MK (2014) Preparation and characterization of novel pegylated hydrophilic pH responsive polysulfone ultrafiltration membrane. J Membr Sci 464:20–32

Su X, Li H, Lai X, Zhang L, Liang T, Feng Y, Zeng X (2017) Polydimethylsiloxane-based superhydrophobic surfaces on steel substrate: fabrication, reversibly extreme wettability and oil-water separation. ACS Appl Mater Interfaces 9:3131–3141

Sun W, Zhou S, You B, Wu L (2013) Polymer brush-functionalized surfaces with unique reversible double-stimulus responsive wettability. J Mater Chem A 1:10646–10654

Tang J, Berry RM, Tam KC (2016) Stimuli-responsive cellulose nanocrystals for surfactant-free oil harvesting. Biomacromolecules 17:1748–1756

Treat ND, Ayres N, Boyes SG, Brittain WJ (2006) A facile route to poly(acrylic acid) brushes using atom transfer radical polymerization. Macromolecules 39:26–29

Tu F, Lee D (2014) Shape-changing and amphiphilicity-reversing Janus particles with pH-responsive surfactant properties. J Am Chem Soc 136:9999–10006

Uhlmann P, Ionov L, Houbenov N, Nitschke M, Grundke K, Motornov M, Minko S, Stamm M (2006) Surface functionalization by smart coatings: stimuli-responsive binary polymer brushes. Prog Org Coat 55:168–174

Wang Y, Chang YC (2003) Synthesis and conformational transition of surface-tethered polypeptide: poly(L-lysine). Macromolecules 36:6511–6518

Wang B, Guo Z (2013) PH-responsive bidirectional oil-water separation material. Chem Commun 49:9416–9418

Wang CF, Wang YT, Tung PH, Kuo SW, Lin CH, Sheen YC, Chang FC (2006) Stable superhydrophobic polybenzoxazine surfaces over a wide pH range. Langmuir 22:8289–8292

Wang S, Liu H, Liu D, Ma X, Fang X, Jiang L (2007) Enthalpy-driven three-state switching of a superhydrophilic/superhydrophobic surface. Angew Chem Int Ed 46:3915–3917

Wang B, Guo Z, Liu W (2014) PH-responsive smart fabrics with controllable wettability in different surroundings. RSC Adv 4:14684–14690

Wenzel RN (1936) Resistance of solid surfaces to wetting by water. Ind Eng Chem 28:988–994

Wu J, Jiang Y, Jiang D, He J, Cai G, Wang J (2015) The fabrication of pH-responsive polymeric layer with switchable surface wettability on cotton fabric for oil/water separation. Mater Lett 160:384–387

Xia F, Ge H, Hou Y, Sun T, Chen L, Zhang G, Jiang L (2007) Multiresponsive surfaces change between superhydrophilicity and superhydrophobicity. Adv Mater 19:2520–2524

Xia F, Zhu Y, Feng L, Jiang L (2009) Smart responsive surfaces switching reversibly between super-hydrophobicity and super-hydrophilicity. Soft Matter 5:275–281

Xiang Y, Shen J, Wang Y, Liu F, Xue L (2015) A pH-responsive PVDF membrane with superwetting properties for the separation of oil and water. RSC Adv 5:23530–23539

Xiao M, Cheng M, Zhang Y, Shi F (2013) Combining the Marangoni effect and the pH-responsive superhydrophobicity-superhydrophilicity transition to biomimic the locomotion process of the beetles of genus Stenus. Small 9:2509–2514

Xiao M, Guo X, Cheng M, Ju G, Zhang Y, Shi F (2014) PH-responsive on-off motion of a superhydrophobic boat: towards the design of a minirobot. Small 10:859–865

Xin B, Hao J (2010) Reversibly switchable wettability. Chem Soc Rev 39:769–782

Xu C, Wayland BB, Fryd M, Winey KI, Composto RJ (2006) pH-responsive nanostructures assembled from amphiphilic block copolymers. Macromolecules 39:6063–6070

Xu J, Shuai Y, Zhou L, Kesong L, Lei L (2012) Bio-inspired special wetting surfaces via self-assembly. Sci China: Chem 55:2327–2333

Xu Z, Zhao Y, Wang H, Zhou H, Qin C, Wang X, Lin T (2016) Fluorine-free superhydrophobic coatings with pH-induced wettability transition for controllable oil-water separation. ACS Appl Mater Interf 8:5661–5667

Yan X, Li J, Yi L (2017) Fabrication of pH-responsive hydrophilic/hydrophobic Janus cotton fabric via plasma-induced graft polymerization. Mater Lett 208:46–49

Ye Y, Mao Y, Wang H, Ren Z (2012) Hybrid structure of pH-responsive hydrogel and carbon nanotube array with superwettability. J Mater Chem 22:2449–2455

Young T (1805) An essay on the cohesion of fluids. Phil Trans R Soc Lond 95:65–87

Yu X, Wang Z, Jiang Y, Shi F, Zhang X (2005) Reversible pH-responsive surface: from superhydrophobicity to superhydrophilicity. Adv Mater 17:1289–1293

Zhang Y, Guo Z (2014) PH-responsive wettable fabrics with hierarchical structures. Chem Lett 43:553–555

Zhang Q, Xia F, Sun T, Song W, Zhao T, Liu M, Jiang L (2008) Wettability switching between high hydrophilicity at low pH and high hydrophobicity at high pH on surface based on pH-responsive polymer. Chem Commun:1199–1201

Zhang L, Zhang Z, Wang P (2012) Smart surfaces with switchable superoleophilicity and superoleophobicity in aqueous media: toward controllable oil/water separation. NPG Asia Mater 4:e8

Zhu Y, Shi M, Wu X, Yang S (2007) Amphiphilic copolymer grafted "smart surface" enhanced by surface roughness. J Colloid Interf Sci 315:580–587

Chapter 4
Thermal-Responsive Superwetting Surface

Dongliang Tian, Linlin He, and Lei Jiang

Abstract Thermal-responsive surfaces are commonly existing in the living system and widely used in the practical applications. Recently, thermal-responsive superwetting surfaces have aroused worldwide interest and made big progress in fundamental research and practical applications in smart controllable fluid devices. This chapter focuses on the thermal-responsive superwetting surfaces and their applications, particularly on the switchable wettability on different thermal-responsive surfaces, the superwetting surfaces at high and low temperatures, the cooperation of temperature and other stimulus-responsive superwetting surfaces and the applications of thermal-responsive superwetting surfaces including the movement of liquid droplet, switchable surfaces adhesion and oil/water separation by temperature driving. Finally, we will briefly address personal points of the future development and remaining challenges of the thermal-responsive superwetting surfaces.

Keywords Thermal-responsive surface · Superwetting · Liquid driving · Adhesion control · Separation

4.1 Introduction

Wettability is one of the most important interface properties for a solid surface, which is mainly decided by chemistry composition and geometric structure (Wen et al. 2015; Su et al. 2015; Zhu et al. 2014), has gained tremendous interest in the past 10 years. Special wettability surfaces with superwettability, i.e., the contact

---

D. Tian · L. He
Beijing Advanced Innovation Center for Biomedical Engineering, School of Chemistry,
Beihang University, Beijing, China

L. Jiang (✉)
Beijing Advanced Innovation Center for Biomedical Engineering, School of Chemistry,
Beihang University, Beijing, China

Technical Institute of Physics and Chemistry, Chinese Academy of Sciences, Beijing, China
e-mail: jianglei@iccas.ac.cn

A. Hozumi et al. (eds.), *Stimuli-Responsive Dewetting/Wetting Smart Surfaces and Interfaces*, Biologically-Inspired Systems 11,
https://doi.org/10.1007/978-3-319-92654-4_4

angle (CA) of the surface to water, oil or gas more than 150° or less than 5°, for the related researches in application are being intensively explored and accelerated by discoveries of unique wetting phenomena in both nature and experimental research (Sun et al. 2005; Feng and Jiang 2006; Liu et al. 2010a; Quéré 2008; Huebsch and Mooney 2009; Nishimoto and Bhushan 2013). Especially for the surfaces with reversibly responsive wettability change under different stimuli (Wang et al. 1997, 2007; Tian et al. 2012, 2013a; Lim et al. 2007; Irie et al. 2005; Uchida et al. 2006; Prins et al. 2001; Chen and Bonaccurso 2014; Hayes and Feenstra 2003; Powell et al. 2011; Wheeler 2008; Nagappan and Ha 2015; Yu et al. 2005; Xia et al. 2007; Crevoisier et al. 1999; Yao et al. 2013; Tian et al. 2013b; Liu et al. 2010b; Yan et al. 2009) have been widely investigated due to the great demand for micro-fluidic control, micro-device technology, etc. (Xia and Jiang 2008; Stuart et al. 2010; Chen et al. 2010a). Among them, temperature change is a widely used environmental stimulus for responsive materials to control the wettability, and the related materials are widely used in the application fields of thermally responsive textiles (Jiang et al. 2014; Yang et al. 2012; Hu et al. 2012), controllable drug release, (Yoshida et al. 2017; Zhou et al. 2009) biomedical usages (Yao et al. 2016; Raczkowska et al. 2016; Ju et al. 2013), temperature-controlled microfluidic switches (Saitoh et al. 2005), antifouling applications (Manabe et al. 2016; Gu et al. 2016) and thermally responsive filters for oil/water separation (Wang et al. 2015a). Recently, thermal-responsive wettability on the superwetting surface has a big progress both in the fundamental research and the practical applications.

In this chapter, we focus on the research progress and applications of the thermal-responsive superwetting surfaces such as superhydrophilicity and superhydrophobicity. The major content of this chapter includes six sections. In Sect. 4.2, we review the switchable wettability on different thermal-responsive surfaces. Section 4.3 presents an overview on the superwetting surfaces at high and low temperatures. The cooperation of temperature and other stimulus-responsive superwetting surfaces are addressed in Sect. 4.4. And Sect. 4.5 introduces the applications of thermal-responsive superwetting surfaces including the movement of liquid droplet, switchable surfaces adhesion and oil/water separation by temperature driving. Finally, we will give personal points of the future development and remaining challenges of the thermal-responsive superwetting surfaces.

4.2 Switchable Wettability on Thermal-Responsive Surfaces

4.2.1 Polymer-Based Thermal-Responsive Surfaces

4.2.1.1 LCST Polymer Surfaces

Temperature-responsive polymers often exhibit a flexible conformation of polymer chains change in response to the change of temperature, which have been widely used to prepare thermal-responsive surfaces. Poly-isopropylacrylamide (PNIPAAm) molecules, as a sensitively thermal-responsive polymer, show diverse molecular

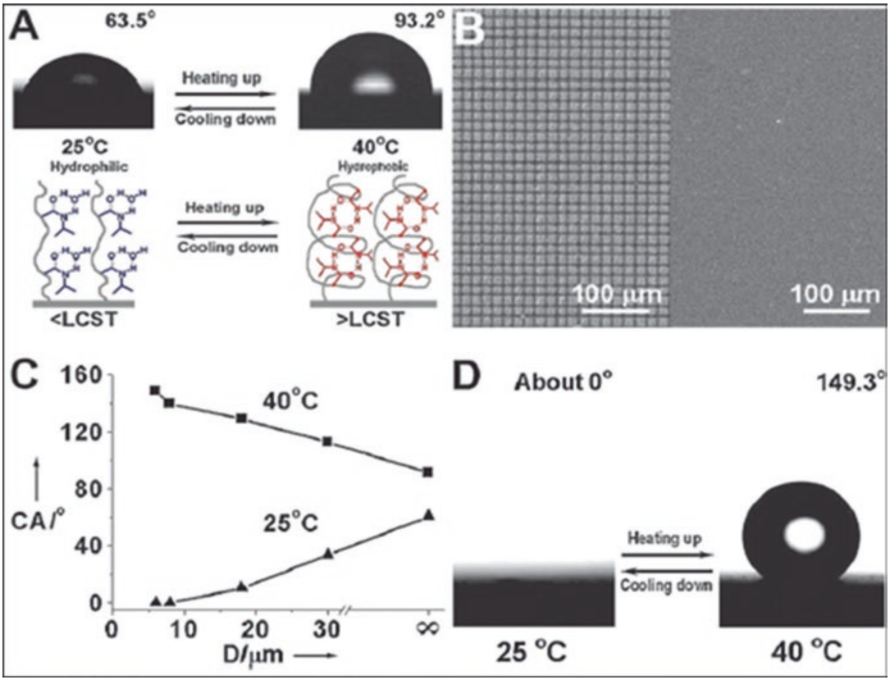

Fig. 4.1 Thermally responsive wettability of the PNIPAAm-modified surface. (**a**) Temperature-responsive switchable wettability on smooth surface. (**b**) The morphology images for rough (left) and smooth substrate (right). (**c**) Water CAs change with groove spacing (**d**) at different temperatures. (**d**) Temperature-responsive switching between superhydrophilicity and superhydrophobicity on rough structured substrate (Sun et al. 2004b)

conformation corresponding to the temperature lower and higher than their lower critical solution temperature (LCST). Below LCST, the PNIPAAm molecular chains showed curved types loosely due to the predominant intermolecular hydrogen bonding of amino groups and carbonyl groups as well as water molecules, indicating hydrophilic. While the PNIPAAm molecular shows hydrophobic above LCST because these PNIPAAm chains transformed to a close-packed conformation, resulting in intramolecular hydrogen bonding excluding the water molecules. On the smooth surface, the wettability change is very limited. By introducing the rough structure, the thermally responsive wettability of the PNIPAM-modified surfaces could be enhanced (Song et al. 2007; Konosu et al. 2011; Gao et al. 2010; Chang and Kuo 2010). The technique of surface-initiated atom-transfer radical polymerization (SIATRP) was employed to fabricate thermal-responsive PNIPAAm layers on rough structures such as carbon nanotubes (Sun et al. 2004a) and silicon nanostructure substrate (Sun et al. 2004b).

The author’s group constructed a micro/nanostructure-enhanced thermal-responsive wettability on a surface modified by PNIPAAm using SIATRP (Fig. 4.1). For a smooth substrate, PNIPAAm thin film showed thermal-responsive wettability transition between hydrophilicity and hydrophobicity with a water CA change of ~

30° from 25 °C to 40 °C. Reversible superwetting switch, i.e., superhydrophilicity and superhydrophobicity, had been realized in temperature change of ~10 °C on the PNIPAAm modified rough substrates, which was contributed to the synergistic effect of the surface micro/nanostructures and chemical component (Sun et al. 2004b). Leon al. fabricated a temperature responsive coating by polymerizing PNIPAM via ATRP on a thin cellulose acetate film with lotus-leaf surface morphology, replicated using solvent assisted micromolding (SAMIM), which could switch reversibly from superhydrophobicity to superhydrophilicity (De and Advincula 2014).

However, owing to the amorphous PNIPAM homopolymer at a wetted surface, it is unsuitable for coating applications. Lots of strategies have been investigated to achieve a thermal-responsive surface with switch wettability by grafting PNIPAM polymers onto different structured substrate surfaces (Li et al. 2014a; Zhou et al. 2014; Zhao et al. 2010, 2012; Nykänen et al. 2014). For instance, the micro/nanostructured composite polymer films containing PNIPAAM with temperature controllable wettability and morphology have been prepared by electrospinning (Wang et al. 2014; Zeng et al. 2010; Gu et al. 2010; Muthiah et al. 2011; Wang et al. 2008). Lyutakov et al. prepared the poly-L-lactide (PLLA) nanofibers by electrospinning based on the thermal-responsive poly(N-isopropylacrylamide) (PNIPAM) nanospheres doped by crystal violet (CV) (Elashnikov et al. 2017). The thermal-responsive wettability and CV release were achieved by changing of the environmental temperature across the LCST of PNIPAM. Song et al. fabricated Poly(N-isopropylmethacrylamide) -block-poly(N-isopropylacrylamide) (PNIPMAM-b-PNIPAm) brush by SIATRP on microstructure enhanced silicon substrate, and multi-stage thermal-responsive wettability could be observed on the roughness enhanced substrate (Song et al. 2014). Three relative stable wettable stages were exhibited at different temperature regions. Below 32 °C, the polymer surface was hydrophilic with the CA of 20.9 ± 2.8° owing to the loose-coiled conformation of the PNIPMAM-b-PNIPAm chains. In the temperature between 32 °C and 44 °C, the surface changed to weak hydrophobic with the CA of 85.2 ± 2.7° and the PNIPAm occurred phase changes firstly because its LCST is about 32 °C. Above 44 °C, the surface became more hydrophobic with the CA of 108.6 ± 2.1° and the conformation changes of PNIPMAM would take place and the polymers chains would further collapse. Jiang et al. fabricated the thermal-responsive PHFBMA-b-(PGMA-g-PNIPAM) block-graft copolymer by controlled free radical polymerization (Jiang and Pang 2016). A wettability tunable cotton fabric was fabricated by dip-coating in the thermal-responsive micelle. The dried cotton fabric, showing smooth and high content of fluorine, was hydrophobic after processed in micelle solution at low temperature, while the dried fabric was hydrophilic with rough and low fluorine content after treated in micelle at high temperature. Liu et al. grafted mixed brushes, i.e., heptadecafluorodecyltrimethoxysilane (HFMS) and poly(N-isopropylacrylamide) (PNIPAM) as oleophilic component and thermal-responsive component via silane coupling chemistry and SIATRP, respectively (Liu et al. 2015). Based on the cooperation effect of PNIPAM and HFMS, the surface showed a temperature-responsive wettability switch between underwater superoleophobicity and superoleophilicity. Li et al. constructed a thermal-responsive wettability surface between hydrophilicity and hydrophobicity based on poly(methyl methacrylate)-block-poly(N-isopropyl-acrylamide) (PMMA-b-PNIPAM) block copolymers (Li et al. 2014b).

4.2.1.2 Shape Memory Polymer Surfaces

Shape memory polymers (SMPs) are a type of materials capable of responsive recovering to their initiating shapes by external stimuli, thus manipulating the wettability from the recovered state to the deformed state. Chen et al. fabricated pillars of SMPs showing different wettability of the tilted state and recovered state (Chen and Yang 2014). The tilted pillars could be recovered by heating higher than the temperature of glass transition for SMPs. The water droplet was fully pinned and unable to roll off the deformed SMP pillars because of the Wenzel wetting state at large spacing ($s = 20$ and 30 μm). While the droplet could slide the straight pillars (both original and recovered) surface with a finite sliding angle owing to a Cassie-Baxter wetting state. Huete et al. also demonstrated the switchable wettability of the micropillars based crosslinked PCO polymeric surface, prepared by laser ablation, due to the thermally induced shape memory effect (García-Huete et al. 2015). The deformed micropillars with lower CA for low roughness, whereas the surface could restore to initiating structure with original hydrophobicity by thermal actuation.

4.2.1.3 Other Polymer Surfaces

In the past decades, many other types of temperature responsive polymers were used to construct thermal-responsive surfaces of superhydrophobicity/superhydrophilicity (Niu et al. 2016; Zhang et al. 2011a; Yokota et al. 2007; Wang et al. 2011). Zareie et al. presented a reversible surface wettability switch on oligo(ethylene glycol)-tethered monolayers self-assembled on gold substrates, which showed temperature-dependent affinity binding and provided a nonspecific adsorption-resistant feature (Fig. 4.2) (Zareie et al. 2008). Hu et al. prepared a poly(ε-caprolactone) coated rough substrate surface with reversibly wettability switch between superhydrophobic and superhydrophilic under temperature stimuli (Hu et al. 2008), which was based on the crystalline/amorphous phase transition of polymer chain. Gao et al. fabricated a thermal-responsive smart wood surfaces with the silica/PCL_{10000} composite film (Gao et al. 2015). The surface wettability could be switched between superhydrophobicity and hydrophilicity under 25 °C and 60 °C, respectively. The reversible surface wettability was based on the cooperation of the surface micro/nano structure and the crystallinity convertibility of the PCL_{10000} polymer with varying temperatures.

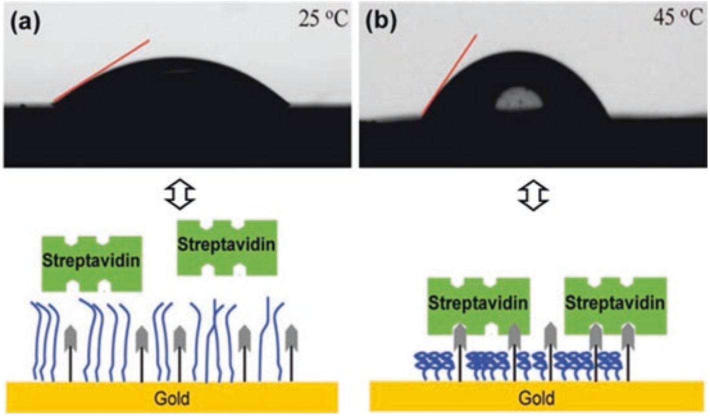

Fig. 4.2 Water CA and schematic mechanism of a PEG12 assembled Au (111) surface at 25 °C (**a**) and 45 °C (**b**), respectively (Zareie et al. 2008)

4.2.2 *Inorganic-Oxide-Based Thermal-Responsive Surfaces*

Most of the thermal-responsive surfaces are fabricated using polymers showing thermal-responsive reversible wettability (González and Frey 2017; Seeber et al. 2011; Shi et al. 2013). It can be accomplished to switch wettability reversibly by thermal-responsive inorganic surfaces (Zhang et al. 2015; Yang et al. 2011). Zhang et al. fabricated transparent thermal-responsive nanoparticle film by spray deposition process with fast reversible wetting transition between superhydrophobicity and hydrophilicity (Zhang et al. 2012). The film could selectively adsorb oil from water surface with antifouling performance to organic solvents.

4.3 Superwetting Surfaces at Diverse Temperatures

4.3.1 *High Temperature*

The phenomena of liquid wetting on the heating solid surfaces are commonly existed in daily lives and practical industrial activities. Recently, lots of studies have showed that the droplets wetting behaviors on hot and ambient-temperature structured surfaces were different owing to the vapor pressure induced by evaporation, which is known as film-boiling or Leidenfrost phenomena (Leidenfrost 1756; Biance et al. 2003).

Mudawar et al. reported surface morphology and chemical composition had the influence on the Leidenfrost phenomena (Bernardin and Mudawar 1999). The author’s group reported the liquid wetting behavior of surfaces with different structures and chemical components from 20 °C to 200 °C (Zhang et al. 2011b). The results indicated that surface structure and wettability had important effects on the

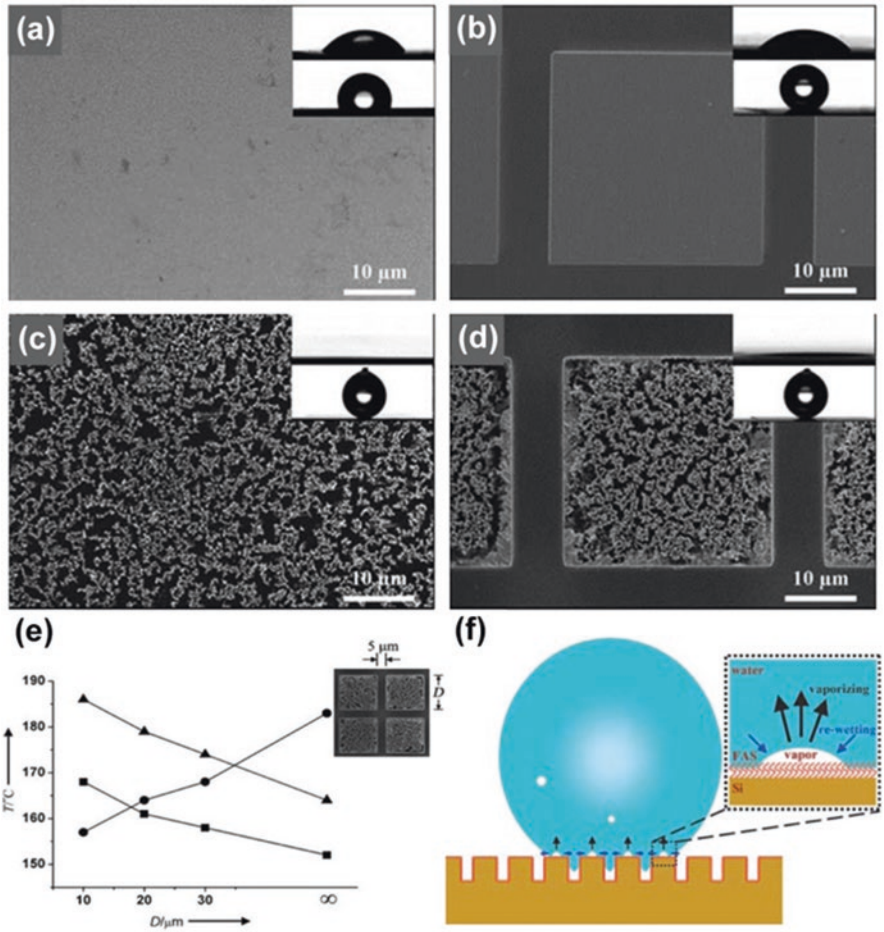

Fig. 4.3 SEM images of silicon wafer with (**a**) flat surface, (**b**) micropillars, (**c**) nanowire arrays, (**d**) the composition of nanowire micropillars. (**e**) The bouncing temperature (Tb) change with different micropillar side lengths D. (**f**) High temperature Cassie wetting state, air bubbles generated and stick on the hydrophobic surface (Zhang et al. 2011b)

wetting transition process. The water droplets spreading and bouncing behavior of on surfaces above 100 °C could be found on superhydrophilic surface and hydrophilic surface as well as hydrophobic surfaces. Leidenfrost point (LFP) decreased at the superhydrophilic surfaces and hydrophobic surfaces with decrease in micropilla length, while it increased for hydrophilic surfaces (Fig. 4.3). More importantly, the Leidenfrost transition disappeared on superhydrophobic surfaces due to the gas lubricating layer. Similarly, Kim et al. revealed that nanoporosity was crucial in increasing the LFP by initiating bubbles nucleation, results in the vapor film disruption (Kim et al. 2011). Subsequently, Vakarelski et al. showed the way of vapor film collapse could be suppressed on superhydrophobic surfaces (Vakarelski et al. 2012).

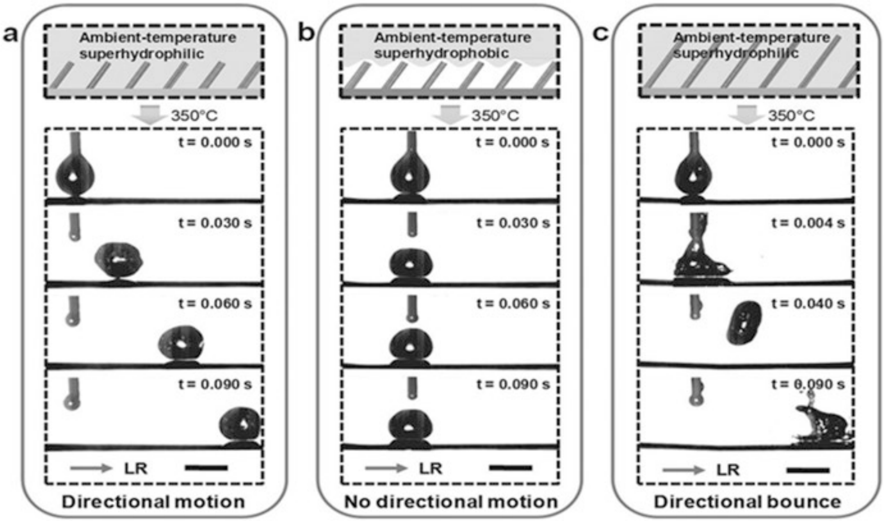

Fig. 4.4 The wetting behavior of droplets on short TSNWs surfaces at high temperature. (**a**) Directional motion of droplet on tilted surface with 60°. (**b**) The droplet showed no directional motion on superhydrophic surface. (**c**) Directional bounce of droplet on long TSNWs surfaces (Liu et al. 2014a)

Toprak et al. constructed ordered 3D nanostructured porous metallic surface via dynamic gas bubble templates based on the relationship between bubbles and solid wettability, which was beneficial for the bubble generation applications in nucleate boiling (Li et al. 2010).

Recently, the author's group investigated the asymmetric structured surface wetting performance at high-temperature (Fig. 4.4) (Liu et al. 2014a). The results indicated that directional droplet transport on tilted silicon nanowires (TSNWs) surface was dependent on its anisotropic wetting performance at high temperature. For the superhydrophilic surface with moderate length at high temperature, the droplet spread asymmetrically and moved directionally owing to the unbalanced forces. For the superhydrophilic TSNWs surface with long TNSWs at high temperature, the droplets showed anisotropic wetting performance and bounce directionally without vapor film formed below. While for the TSNWs surfaces with weak hydrophilicity or short length, no anisotropic wetting performance and directional droplet motion were observed on these surfaces.

4.3.2 *Low Temperature*

Dropwise condensation commonly exists when vapor meet supercooled surface. Biological surfaces with special structures can capture atmospheric water and transport the condensated water directionally. For example, Stenocara beetles from the

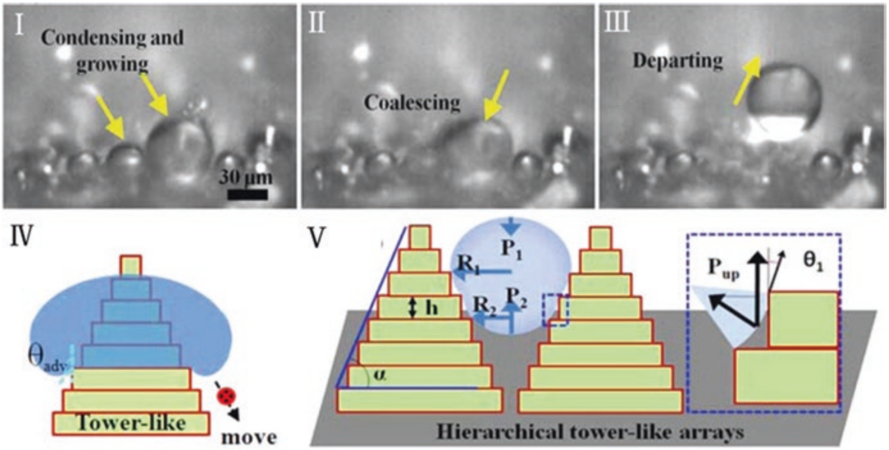

Fig. 4.5 (I–III) Photographs of the coalescing and jumping condensates on the tower-like surface. (IV) Illustration of a droplet on the sidewall of a tower. (V) Scheme of a condensed droplet on the tower-like surface (He et al. 2016)

Namib Desert harvest microdroplets in fog owing to their backs patterns of hydrophilicity and hydrophobicity (Parker and Lawrence 2001). Droplets condensed and removed from hydrophilic regions to hydrophobic domains. Inspired by this phenomenon, a serial of smart surfaces with droplet collecting characteristics from humid environment are fabricated (Zhai et al. 2015; Garrod et al. 2007; Dorrer and Rühe 2008; Varanasi et al. 2009; Thickett et al. 2011).

Chaudhury et al. investigated the fast motion of droplets on a gradient wettability surface from low to high surface energy area (Daniel et al. 2001). The moving speed of the droplets with the size of several hundred micron thousands times as that in Marangoni flows. Boreyko et al. reported that condensate drops could be autonomously removed on a superhydrophobic surface consisting of silicon micropillars and carbon nanotubes no need of any external forces, which had the potential application in enhancing condensation heat transfer (Boreyko and Chen 2009). He et al. investigated the spontaneous uphill movement and removal of condensates on superhydrophobic tower-like arrayed surfaces (Fig. 4.5) (He et al. 2016). The sharp tip of tower-like arrays produced discontinuous and unstable three-phase contact line and decreased the adhesion and promotes fast self-removal of condensates, which was beneficial to understand the spontaneous uphill movement of entrapped condensates.

Based on synergistically principles derived from Namib Desert beetles and cacti as well as pitcher plants, Park et al. presented a strategy to rationally design of surface structures to achieve high growth rate and a greater water collected volume compared to other surfaces (Park et al. 2015). The author's group investigated the condensed fog droplets directionally transport on the wings of Morpho deidamia butterflies (Liu et al. 2014b). On the static wings with micro/nano ratchet-like

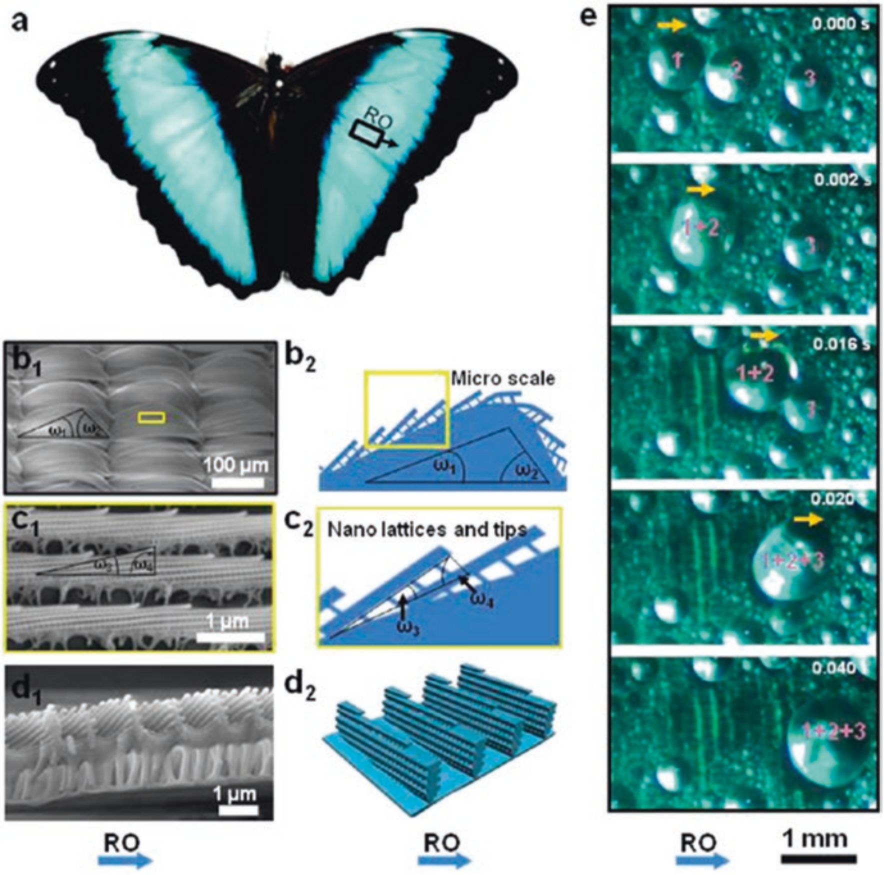

Fig. 4.6 (**a**) Photo of a Morpho deidamia butterfly. (**b$_1$**) The morphology of the overlapped scales on butterfly wings in (**a**). (**c$_1$-d$_1$**) The morphology of the ridges on the scale in (**b$_1$**). (**b$_2$-d$_2$**) Schematic micro/nanoratchet-like structure of butterfly wings. (**e**) Directional fog drops transport on a static butterfly wing (Liu et al. 2014b)

structure, fog droplets randomly condensed, then coalesced and moved directionally (Fig. 4.6).

4.4 Cooperation of Temperature and Other Stimulus-Responsive Superwetting Surfaces

By introducing the surface roughness to thermal-responsive materials surface, switchable surface wettability, especially switch between superhydrophilicity and superhydrophobicity, have been realized successfully. However, single external stimulus limits the applications in complex practical conditions. Two or more external stimulus cooperative driving of the droplet shows more effective to control the liquid wetting behavior. Recently, dual and multiple-responsive surfaces have been developed to meet the requirements of basic research and practical applications (Tonhauser et al. 2012; Xia et al. 2011).

4.4.1 Dual- Responsive Surfaces

Smart responsive surfaces to both temperature and pH have attracted great interests (Li et al. 2014c; Stetsyshyn et al. 2012, 2013; Gao et al. 2016). The author's group explored a temperature and pH dual responsive wettability surface with tunable, by fabricating a copolymer, poly(N-isopropylacrylamide-co-acrylic acid) [P(NIPAAm-co-AAc)], thin film on micro/nano-structured silicon wafers (Xia et al. 2006). Reversible wettability switch between superhydrophilicity and superhydrophobicity was realized on a temperature range of 10 °C and wide pH range of 10. The film showed hydrophilic and hydrophobic at low and high temperature, respectively, and was similar to single thermal-responsive films. Very differently, the film was strongly dependent on the pH change, which showed hydrophobic at low pH value while hydrophilic with the enhanced pH value. The reversible alternation of intermolecular and intramolecular hydrogen bonding of two functional components, NIPAAm and AAc, and water yields their wettability change. Guo et al. reported dual-responsive polypeptide surfaces with wettability change from superhydrophilic states to superhydrophobic states (Fig. 4.7) (Guo et al. 2010). The unfolding/aggregation behaviors of PLL driven by pH and temperature endowed the surface with switch wettability. The PLL molecules showed loose conformations in low pH value, resulting in superhydrophilicity, while showing R-helix conformation in high pH value with hydrophilic state.

Lin et al. fabricated poly(NIPAAm-co-AAc) random copolymer with thermal- and pH-dual responsive behavior (Lin et al. 2014). The PNIPAAm homopolymer LCST could be adjusted approximately from 37 °C to 32 °C by controlling the hydrophilic AAc content. The electrospun poly(NIPAAm-co-AAc) and PU nanofibers exhibited a reversible switch of hydrophilicity and hydrophobicity.

Photo-/thermo- dual-responsive surfaces with superwetting property are also potential for some applications (Joseph et al. 2010; Yuan et al. 2006). Nakata et al. fabricated TiO_2-poly (dimethylsiloxane) (PDMS) composite films that responded to both thermal and UV stimuli by a sol-gel method, i.e., photoinduced superhydrophilicity and thermally stimulated switchable wettability. After treatment by hot water, the film transformed to transparent of visible light and showed photoinduced superhydrophilicity owing to the presence of anatase TiO_2 (Nakata et al. 2010). The composite films could recover their initial wettability due to the conformational change in the molecular bonding around Ti atoms and hydroxyl groups replaced by oxygen. Lyons et al. fabricated superhydrophobic TiO_2-HDPE nanocomposite films using a template lamination method, which responded to both thermal and UV stimuli (Fig. 4.8) (Xu et al. 2013). The nanocomposite surface pre-

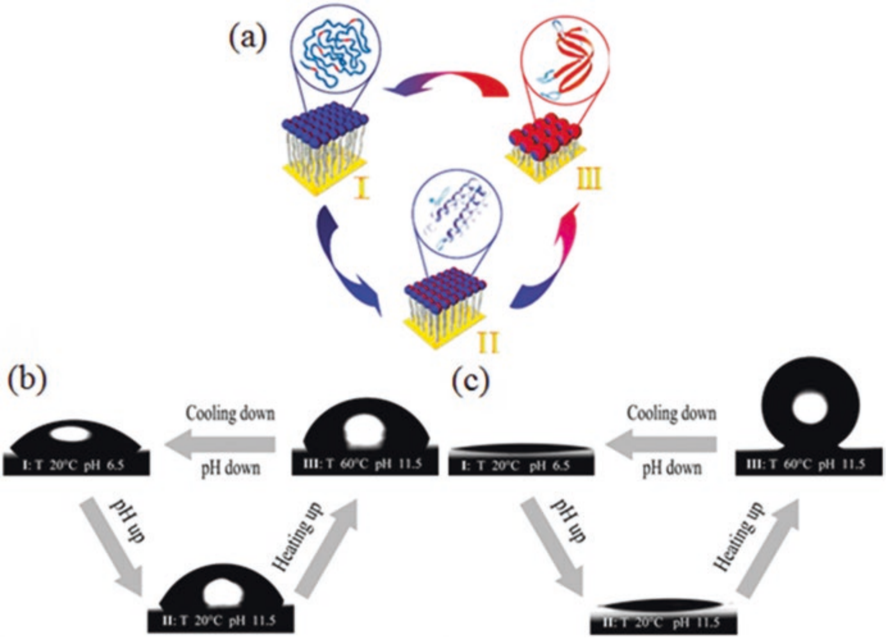

Fig. 4.7 (**a**) Reversible surface wettability switch based on poly-L-lysine (PLL). (**b**, **c**) Water droplet photographs on the smooth (**b**) and rough (**c**) substrates with different state of I, II, and III (Guo et al. 2010)

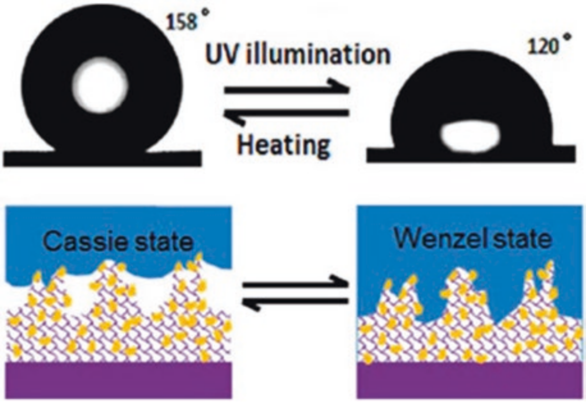

Fig. 4.8 Reversible wettability changes of the TiO_2-polymer nanocomposite surface during alternation of UV Illumination and heating (Xu et al. 2013)

sented a UV-thermal induced reversible wettability change between superhydrophobicity and hydrophilicity owing to the hydrolysis of the TiO_2 nanoparticle surface upon UV irradiation, which could be accelerated in water. The heat treatment would change the Ti-O-H bonds to hydrophobic Ti-O bonds, showing the primary superhydrophobic state.

4.4.2 Multi-Responsive Surfaces

Multi-responsive surfaces are also widely studied for different applications. The author's group developed a multi-responsive surface by incorporating temperature responsive PNIPAAm into pH- and glucose responsive poly(acrylamido phenylboronic acid) (PPBA) (Xia et al. 2007), which was prepared via a SIATRP technique, showing wettability switch of superhydrophilicity and superhydrophobicity (Fig. 4.9). Compared to the dual responsive surfaces with former work (Xia et al. 2006), the surfaces showed wettability changed when varying glucose concentration when fixing the pH and temperature.

Sun et al. also fabricated the smart multi-responsive surfaces (thermo, light and pH responsive) with reversible wettability by simply casting the mixture of poly (styrene-n-butyl acrylate-acrylic acid) (P(S-BA-AA)) and TiO_2 nanoparticles (Sun et al. 2013). The prepared nanocomposite films showed fast responses and excellent reversibility to UV irradiation (Fig. 4.10).

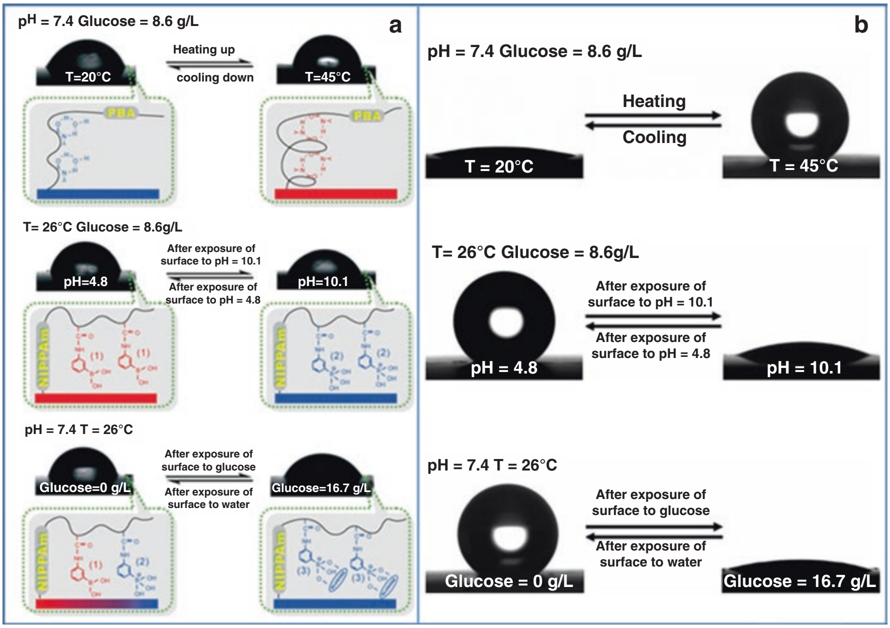

Fig. 4.9 (**a**) Water CA photographs on the flat substrate with the corresponding reversible change of inter- and intramolecular hydrogen bonding. (**b**) Photographs of water CAs on the rough substrate (Xia et al. 2007)

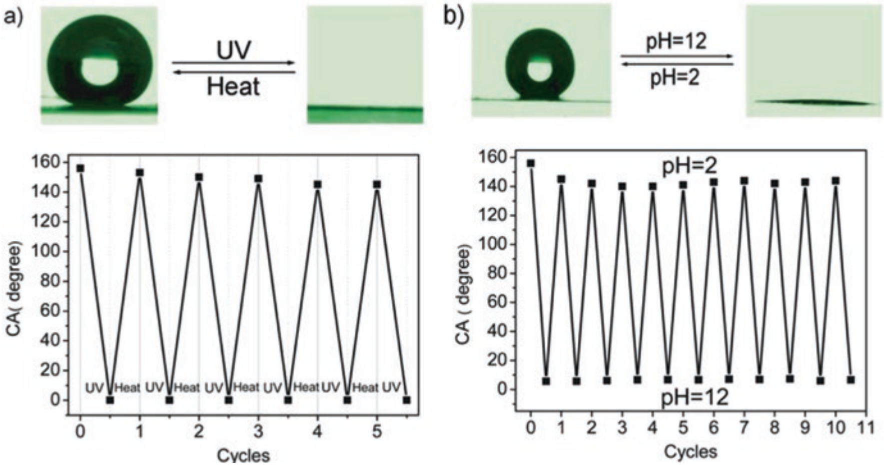

Fig. 4.10 Reversible wettability transition of superhydrophobicity/superhydrophilicity on the nanocomposite films (**a**) alternative UV irradiation and 150 °C treatment and (**b**) alternative treatment with pH = 12 and pH = 2 (Sun et al. 2013)

4.5 Applications of Thermal-Responsive Superwetting Surfaces

4.5.1 Thermal-Driven Movement of a Liquid Droplet

Asymmetric microstructures are of great significance owing to their unique physical properties, e.g., anisotropic wetting or adhesion, and directional transport. Owing to the ability of liquid motion on the asymmetric microstructures with anisotropic wettability, a number of the microstructures combined with responsive materials have been successfully fabricated and studied (Kim et al. 2013). Wang et al. fabricated a thermal-responsive PNIPAM/MHA Janus silicon micropillar array surface to smartly manipulate flow motion of water (Fig. 4.11) (Wang et al. 2015b). The thermal-responsive Janus arrays showed anisotropic wetting and isotropic wetting above or below the LCST of PNIPAM molecule, which could serve as a smart thermovalve in microfluidic channel. Yu et al. demonstrated fluid motion in chips on morphology-patterned thermal-responsive PNIPAAm polymer modified Si stripes (Yu et al. 2017). When the system temperature changed above and below the LCST of PNIPAAm, the surface wettability transition between strong anisotropy and weak anisotropy, resulting in anisotropic and isotropic liquid flow in microchannels.

Controlling the liquids transport on surfaces with a thermal-responsive wettability gradient have attracted a lot of attention (Chakraborty et al. 2015). Hou et al. fabricated a temperature-responsive fiber with spindle-knots using the N-isopropylacrylamide (NIPAAm) polymer (Hou et al. 2013a). The gradient wettability could be manipulated on a spindle-knot by controlling the thermal-responsive conformational change of NIPAAm polymer (Fig. 4.12). Thus the thermal-

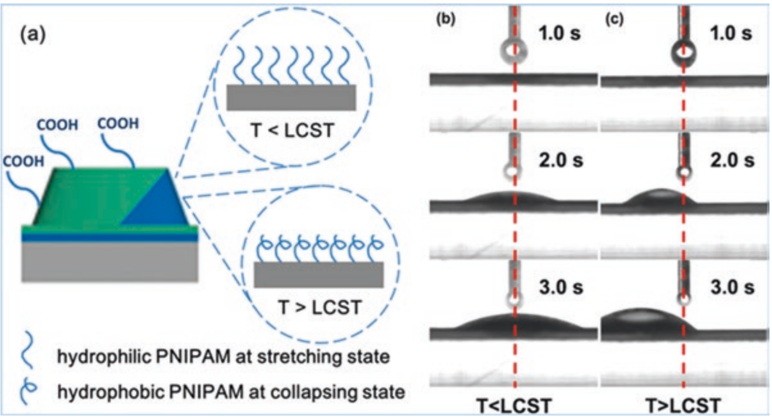

Fig. 4.11 (**a**) Schematic mechanism of the PNIPAM/MHA Janus pillar surface with different temperatures. (**b**, **c**) Water droplet photographs of the PNIPAM/MHA Janus array surface at temperature below and above the PNIPAM brush LCST (Wang et al. 2015b)

responsive water droplets motion could be adjusted reversibly toward the spindle-knots or away from it in humidity (Hou et al. 2013b).

To manipulate liquid flow using the reversible thermal-responsive surfaces has been an increasing important research topic and practical application in microfluidic systems. Chunder et al. realized the smartly regulation of fluid by thermally switchable superhydrophobic/hydrophilic valves (Londe et al. 2008). The valves comprised two different valve surfaces, one was a superhydrophobic polymer surface prepared by the technique of layer-by-layer (LBL) deposition, and the other one was a thermal-responsive switchable polymer PNIPAAm surface. The passive valve, showing superhydrophobic polymer surface, could selectively inhibit the water-based reagents flow and pass through the aqueous solutions with surfactants. While for the thermal-responsive valve, the polymer surface changed hydrophobic and inhibits the water flow at temperature higher than 65 °C, and allowing the water flow on the hydrophilic surface at room temperature. Thus the fabricated microfluidic valve could selectively regulate the test samples flow. Saitoh et al. explored the thermal-responsive PNIPAAm-modified surface to control flow in microfluidics (Saitoh et al. 2002). Reversible wettability change was potential application of liquid flow control in narrow channels (<200 μm).

4.5.2 *Thermal-Driven Switchable Surfaces Adhesion*

Temperature responsive materials can also be used to control the adhesion of water droplets (Wu et al. 2014; Liu et al. 2010c; Song 2014), oil droplets (Chen et al. 2010b) and cell (Yang et al. 2014; Tsuda et al. 2004; Nakayama et al. 2012; Cui et al. 2017; Liu and Wang 2014) on the superwetting surfaces. The author's group

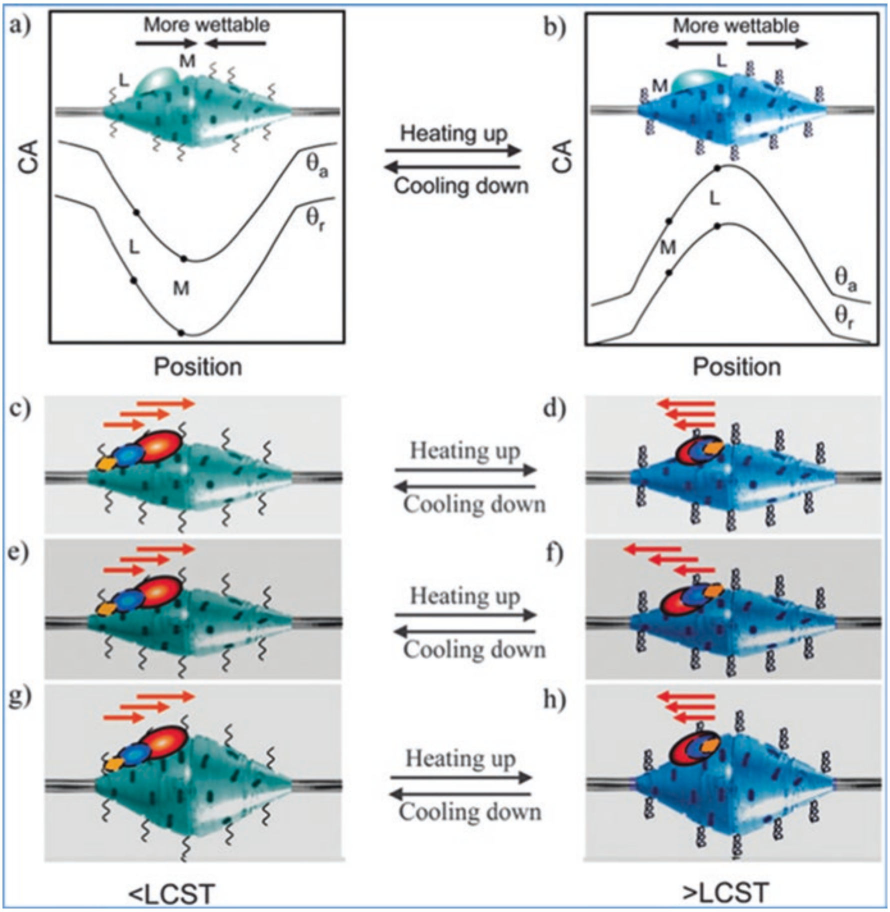

Fig. 4.12 Water droplet motion behavior under different conditions. (**a**) Below LCST, F_W (wettability gradient force) and F_L (Laplace force) can drive the droplet in the same direction. (**b**) Above LCST, F_W and F_L drive the droplet in the opposite direction. (**c**, **e** and **g**) Below LCST, the droplets move towards the spindle-knot completely. (**d**, **f** and **h**) Above LCST, for the spindle-knot with small apex-angle, the droplet moves from the spindle-knot partly away at low RH (relative humidity) (**d**); the droplet moves completely away from the spindle-knot at high RH (**f**); the droplet always moves away from the spindle-knot partly for the larger apex-angle of the spindle knot (**h**) (Hou et al. 2013a)

had done a lot of work in the fields of thermal-driven switchable surfaces adhesion. A versatile strategy was reported that the mobility of spherical water microdroplets could be reversibly controlled in situ on a sidechain liquid-crystal polymer (SCLCP), PDMS-4OCB, surface from rollable (SA ≤ 90°) to pinned (water droplet does not move at any tilt angle, even when the substrate was turned upside down) by temperature (Fig. 4.13) (Li et al. 2009). The wettability switch was attributed to the liquid crystal undergoing a phase transition from the smectic A phase to the

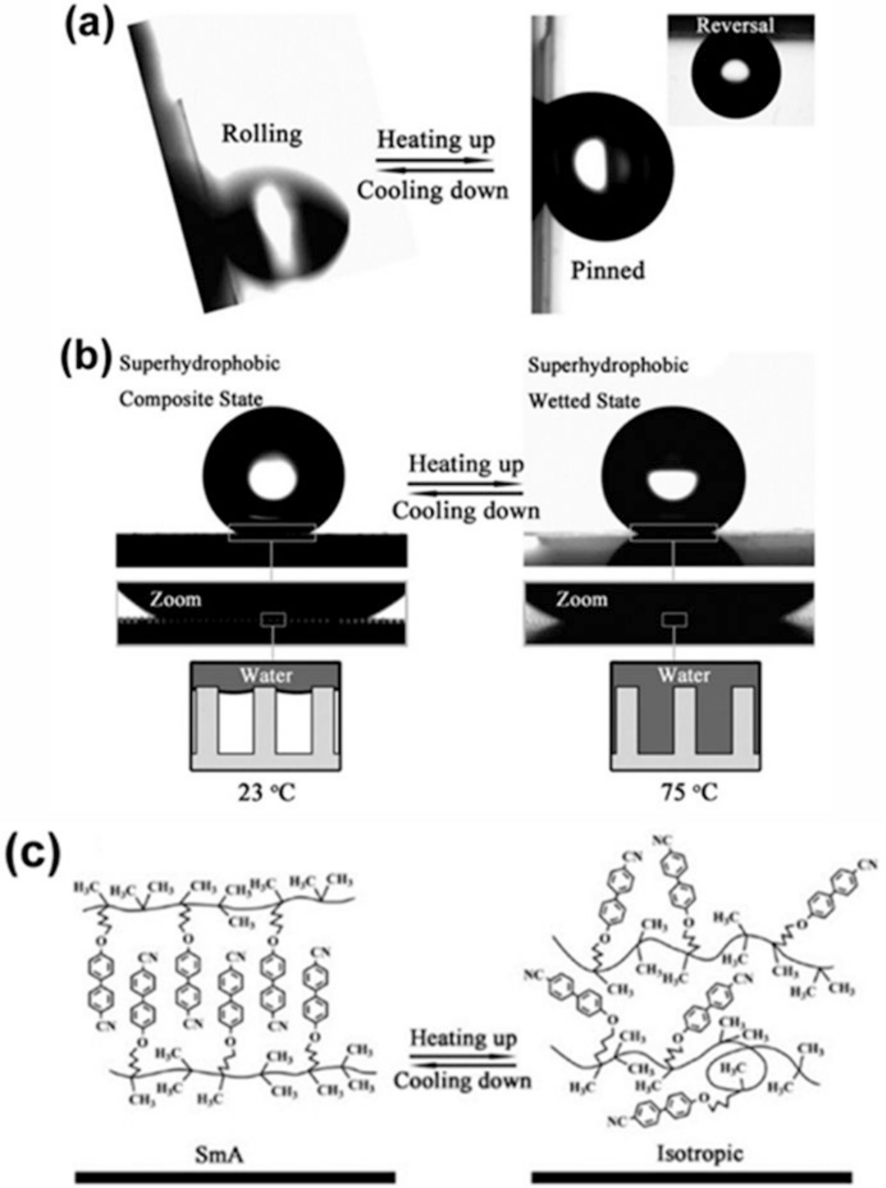

Fig. 4.13 (**a**) Reversible mobility switch of water droplet between rolling state to pinning state. (**b**) Water droplet shows superhydrophobic composite state and wetted state at 23 °C and 75 °C, respectively. (**c**) Schematic conformation rearrangement during the phase transition (Li et al. 2009)

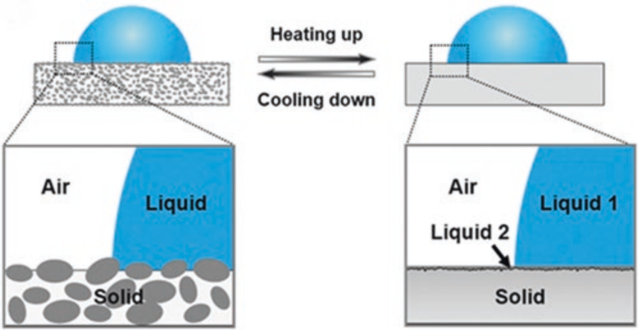

Fig. 4.14 Schematic water adhesion switch on organogel surface below and above T_m (Yao et al. 2014)

isotropic phase. The mobility of a water droplet on the superhydrophobic surface could be thermally controlled from rolling to pinning state. The droplet changed from Cassie's state at 23 °C to Wenzel's state at 75 °C, indicating that the temperature induced wetting state transition led to the switching of adhesion to water droplets.

Recently, we reported a water adhesion switch on thermal-responsive n-paraffin-swollen organogel by thermally activating the transition of air/L_1/L_2/solid system (ALLS) and air/liquid/solid (ALS) system (Yao et al. 2014). The water adhesion switch occurred at the melting temperature (T_m) of n-paraffin. At $T > T_m$, the cross-linked PDMS was wetted by liquefied paraffin, an ALLS system was generated with water drop (L_1) in slippery state with low-adhesion; while at $T < T_m$, solidified paraffin leads to ALS system showing Wenzel state, i.e., high-adhesion to water drops (Fig. 4.14).

Compared to the adhesion control on the thermal-responsive surface in air, the adhesion of underwater oil and cell adhesion were also investigated. A thermal-responsive PNIPAM could be used to control the wettability and adhesion to oil at the water/solid interface reversibly (Chen et al. 2010b). Below LCST (32 °C), the hydrogel surface was underwater superoleophobic with low oil adhesion, while it became high adhesive state with oleophobicity above its LCST. Ordered surface microstructures could further tune the responsive property. Oil droplet could easily roll off of the hydrogel surface at low temperature, while the oil droplet could adhere firmly on the hydrogel surface even if upside down at 40 °C. The thermal-responsive adhesion of platelets were investigated on PNIPAAm-modified smooth substrates (Si-PNIPAAm) and silicon-nanowire arrays (SiNWA-PNIPAAm) in vitro (Chen et al. 2009). The nanoscale topography greatly reduced platelet adhesion in vitro at both temperature below and above LCST of PNIPAAm, while a smooth surface only showed antiadhesion of platelets below the LCST, indicating that the topography effect on oil droplet adhesion was consistent with that of platelets.

4.5.3 Thermal-Driven Oil-Water Separation

Recently, thermal-responsive surfaces have received increasing research interests in on demand treatment of oily waste water (Lei et al. 2017). Based on light initiated free radical polymerization, thermo and pH dual-responsive dimethylamino ethyl methacrylate (DMAEMA) materials have been successfully fabricated (Cao et al. 2014). At a certain pH and temperature, the prepared PDMAEMA hydrogel coated mesh could selective permeation of water and oil and achieve the goal of oil-water separation. Ou et al. fabricated a robust, thermal-responsive PNIPAM/polyurethane (TPU) microfiber web membrane (Ou et al. 2015). At temperatures below LCST, the stretching PNIPAM chains were wrapped by the water molecules, showing hydrophilicity; while at temperatures above LCST, the collapsed PNIPAM chains were wrapped by isopropyl groups, showing hydrophobicity. Nevertheless, the synergism of integrating TPU microfibers and PNIPAM amplifies these properties to superhydrophilicity and superhydrophobicity owing to the rough hierarchical structure. The composite membrane could be used to efficiently separate emulsion of 1 wt% oil-in-water or water-in-oil at 25 °C and 45 °C, respectively. Li et al. constructed a PMMA-b-PNIPAAm membrane with temperature-responsive oil/water wettability via electrospinning technology (Li et al. 2016). The prepared superhydrophilic membranes prewetted by water could be used to separate oil and water by adjusting the temperature (Fig. 4.15). For instance, when heating the polymer membranes above LCST, oil gradually permeated through the membranes owing to the hydrophobicity and oleophilicity. Xue et al. constructed a thermal-responsive mesh membrane by solution casting, i.e., a solution of block copolymer (BCP) with PNIPAAm, which could realize temperature controlled water/oil wettability switch

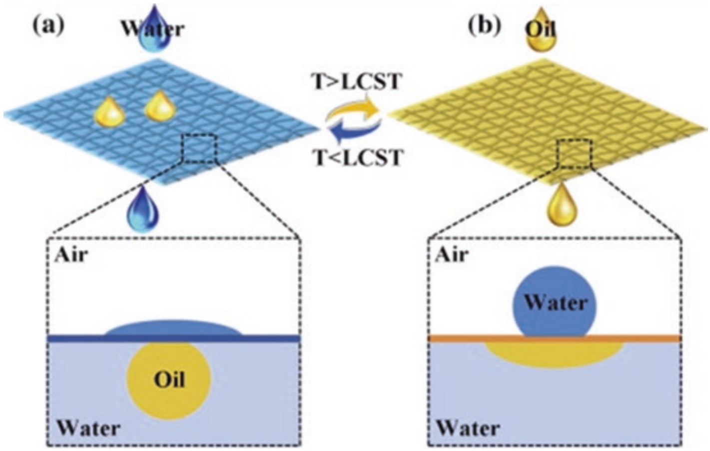

Fig. 4.15 Thermal-responsive oil/water separation. (**a**) water-removal separation. (**b**) oil-removal separation (Li et al. 2016)

(Xue et al. 2013). Below the LCST, water selectively permeated through the mesh, while oil permeation above the LCST.

4.6 Conclusions and Outlook

The recent research progress of temperature responsive superwetting surfaces and their applications has been summarized. The main topics of this chapter include switchable wettability on different thermal-responsive surfaces, the superwetting on various thermal-responsive surfaces at diverse temperatures, and the applications of thermal-responsive superwetting surfaces including the liquid droplet movement, the switchable surfaces adhesion and the oil/water separation under thermal-stimuli. Despite much progress in thermal-responsive materials, there still exist some challenges in practical applications. For instance, the switching extent and reversibility, particular on superwetting surface, are usually needed to be improved in practical applications.

The cooperation of two or multi-field control interface might be a trend to control the wetting and moving behavior of microdroplet or other microscale objects such as cell and particle. Although some recent works were summarized based on thermal-responsive wettability, we would rather regard this is only an opening remark rather than draw conclusions, because thermal-responsive surface research is very attractive and promising in many practical applications in different domains.

Acknowledgments The authors are grateful for financial support from the Chinese National Natural Science Foundation (21671012, 21373001, 21601013), Beijing Natural Science Foundation (2172033), the 973 Program (2013CB933004), the Fundamental Research Funds for the Central Universities, and the 111 Project (B14009).

References

Bernardin JD, Mudawar I (1999) The leidenfrost point: experimental study and assessment of existing models. J Heat Transf 121:894–903

Biance AL, Clanet C, Quéré D (2003) Leidenfrost drops. Phys Fluids 15:1632–1637

Boreyko JB, Chen CH (2009) Self-propelled dropwise condensate on superhydrophobic surfaces. Phys Rev Lett 103(1–4):184501

Cao YZ, Liu N, Fu CK, Li K, Tao L, Feng L, Wei Y (2014) Thermo and PH dual-responsive materials for controllable oil/water separation. ACS Appl Mater Interfaces 6:2026–2030

Chakraborty M, Ghosh UU, Chakraborty S, Dasgupta S (2015) Thermally enhanced self-propelled droplet motion on gradient surfaces. RSC Adv 5:45266–45275

Chang CJ, Kuo EH (2010) Roughness-enhanced thermal-responsive surfaces by surface-initiated polymerization of polymer on ordered ZnO pore-array films. Thin Solid Films 519:1755–1760

Chen L, Bonaccurso E (2014) Electrowetting-from statics to dynamics. Adv Colloid Interface Sci 210:2–12

Chen CM, Yang S (2014) Directed water shedding on high-aspect-ratio shape memory polymer micropillar arrays. Adv Mater 26:1283–1288

Chen L, Liu MJ, Bai H, Chen PP, Xia F, Han D, Jiang L (2009) Antiplatelet and thermally responsive poly (N-isopropylacrylamide) surface with nanoscale topography. J Am Chem Soc 131:10467–10472

Chen T, Ferris R, Zhang JM, Ducker R, Zauscher S (2010a) Stimulus-responsive polymer brushes on surfaces: transduction mechanisms and applications. Prog Polym Sci 35:94–112

Chen L, Liu MJ, Lin L, Zhang T, Ma J, Song YL, Jiang L (2010b) Thermal-responsive hydrogel surface: tunable wettability and adhesion to oil at the water/solid interface. Soft Matter 6:2708–2712

Crevoisier GD, Fabre P, Corpart JM, Leibler L (1999) Switchable tackiness and wettability of a liquid crystalline polymer. Science 285:1246–1249

Cui HJ, Zhang PC, Wang WS, Li GN, Hao YW, Wang LY, Wang ST (2017) Near-infrared (NIR) controlled reversible cell adhesion on a responsive nano-biointerface. Nano Res 10:1345–1355

Daniel S, Chaudhury MK, Chen JC (2001) Fast drop movements resulting from the phase change on a gradient surface. Science 291:633–666

De LA, Advincula RC (2014) Reversible superhydrophilicity and superhydrophobicity on a lotus-leaf pattern. ACS Appl Mater Interfaces 6:22666–22672

Dorrer C, Rühe J (2008) Mimicking the stenocara beetle-dewetting of drops from a patterned superhydrophobic surface. Langmuir 24:6154–6158

Elashnikov R, Slepička P, Rimpelova S, Ulbrich P, Švorčík V, Lyutakov O (2017) Temperature-responsive PLLA/PNIPAM nanofibers for switchable release. Mater Sci Eng C 72:293–300

Feng XJ, Jiang L (2006) Design and creation of superwetting/antiwetting surfaces. Adv Mater 18:3063–3078

Gao J, Liu YL, Xu HP, Wang ZQ, Zhang X (2010) Biostructure-like surfaces with thermally responsive wettability prepared by temperature-induced phase separation micromolding. Langmuir 26:9673–9676

Gao ZX, Zhai XL, Wang CY (2015) Facile transformation of superhydrophobicity to hydrophilicity by silica/poly (epsilon-caprolactone) composite film. Appl Surf Sci 359:209–214

Gao L, Kong TF, Huo YP (2016) Dual thermoresponsive and PH-responsive poly (vinyl alcohol) derivatives: synthesis, phase transition study, and functional applications. Macromolecules 49:7478–7489

García-Huete N, Cuevas JM, Laza JM, Vilas JL, León LM (2015) Polymeric shape-memory micro-patterned surface for switching wettability with temperature. Polymers 7:1674–1688

Garrod RP, Harris LG, Schofield WCE, McGettrick J, Ward LJ, Teare DOH, Badyal JPS (2007) Mimicking a Stenocara Beetle's back for microcondensation using plasmachemical patterned superhydrophobic−superhydrophilic surfaces. Langmuir 23:689–693

González E, Frey MW (2017) Synthesis, characterization and electrospinning of poly (vinyl caprolactam-co-hydroxymethyl acrylamide) to create stimuli-responsive nanofibers. Polymer 108:154–162

Gu SY, Wang ZM, Li JB, Ren J (2010) Switchable wettability of thermos-responsive biocompatible nanofibrous films created by electrospinning. Macromol Mater Eng 295:32–36

Gu YJ, Zhou SX, Luo HL, Wu LM, Gao W, Yang J (2016) Temperature-dependent phase-segregation behavior and antifouling performance of UV-curable methacrylated PDMS/PEG coatings. J Polym Sci Polym Phys 54:1612–1162

Guo Y, Xia F, Xu L, Li J, Yang WS, Jiang L (2010) Switchable wettability on cooperative dual-responsive poly-l-lysine surface. Langmuir 26:1024–1028

Hayes RA, Feenstra BJ (2003) Video-speed electronic paper based on electrowetting. Nature 425:383–385

He M, Ding Y, Chen J, Song YL (2016) Spontaneous uphill movement and self-removal of condensates on hierarchical tower-like arrays. ACS Nano 10:9456–9462

Hou YP, Gao LC, Feng SL, Chen Y, Xue Y, Jiang L, Zheng YM (2013a) Temperature-triggered directional motion of tiny water droplets on bioinspired fibers in humidity. Chem Commun 49:5253–5255

Hou YP, Xue BL, Guan S, Feng SL, Geng Z, Sui X, Lu JH, Cao LC, Jiang L (2013b) Temperature-controlled directional spreading of water on a surface with high hysteresis. Comput Method Appl Mech 5:162–168

Hu SX, Cao XY, Song YL, Li C, Xie P, Jiang L (2008) New responsive property of poly (epsilon-caprolactone) as the thermal switch from superhydrophobic to superhydrophilic. Chem Commun 112:2025–2027

Hu JL, Meng HP, Li GQ, Ibekwe SI (2012) A review of stimuli-responsive polymers for smart textile applications. Smart Mater Struct 21:53001–53023

Huebsch N, Mooney DJ (2009) Inspiration and application in the evolution of biomaterials. Nature 462:426–432

Irie H, Ping TS, Shibata T, Hashimoto K (2005) Reversible control of wettability of a TiO_2 surface by introducing surface roughness. Electrochem Solid-State Lett 8:D23–D25

Jiang BY, Pang H (2016) Synthesis and self-assembly of thermoresponsive block-graft fluoropolymer as well as its tunable wettability surface. J Polym Sci Polym Chem 54:992–1002

Jiang BY, Zhang L, Liao B, Pang H (2014) Self-assembly of well-defined thermo-responsive fluoropolymer and its application in tunable wettability surface. Polymer 55:5350–5357

Joseph G, Pichardo J, Chen GF (2010) Reversible photo−/thermoresponsive structured polymer surfaces modified with a spirobenzopyran-containing copolymer for tunable wettability. Analyst 135:2303–2308

Ju GN, Cheng MJ, Xiao M, Xu JM, Pan K, Wang X, Zhang YJ, Shi F (2013) Smart transportation between three phases through a stimulus-responsive functionally cooperating device. Adv Mater 25:2915–2919

Kim H, Truong B, Buongiorno J, Hu LW (2011) On the effect of surface roughness height, wettability, and nanoporosity on leidenfrost phenomena. Appl Phys Lett 98:083121

Kim SM, Kang DH, Koh JH, Suh HS, Yoon H, Suh KY, Char K (2013) Thermoresponsive switching of liquid flow direction on a two-face prism array. Soft Matter 9:4145–4149

Konosu Y, Matsumoto H, Tsuboi K, Minagawa M, Tanioka A (2011) Enhancing the effect of the nanofiber network structure on thermosresponsive wettability switching. Langmuir 27:14716–14720

Lei ZW, Zhang GZ, Deng YH, Wang CY (2017) Thermo-responsive melamine sponges with switchable wettability by interface-initiated atom transfer radical polymerization for oil/water separation. ACS Appl Mater Interfaces 9:8967–8974

Leidenfrost JG (1756) De Aquae Communis Nonullis Qualitatibus Tractatus. Ovenius, Duisburg on Rhine

Li C, Guo RW, Jiang X, Hu SX, Li L, Cao XY, Yang H, Song YL, Ma YM, Jiang L (2009) Reversible switching of water-droplet mobility on a superhydrophobic surface based on a phase transition of a side-chain liquid-crystal polymer. Adv Mater 21:4254–4258

Li SH, Richard F, Toprak MS, Björn P, Mamoun M (2010) Nature-inspired boiling enhancement by novel nanostructured macroporous surfaces. Adv Funct Mater 18:2215–2220

Li JJ, Zhou YN, Luo ZH (2014a) Thermo-responsive brush copolymers with structure-tunable LCST and switchable surface wettability. Polymer 55:6552–6560

Li JJ, Zhou YN, Luo ZH (2014b) Thermal-responsive block copolymers for surface with reversible switchable wettability. Ind Eng Chem Res 53:18112–18120

Li BL, Lu XL, Ma YH, Chen Z (2014c) Thermo- and PH-responsive behaviors of aqueous poly (acrylic acid)/poly (4-vinylpyridine) complex material characterized by ATR-FTIR and UV-VIS spectroscopy. Eur Polym J 60:255–261

Li JJ, Zhu LT, Luo ZH (2016) Electrospun fibrous membrane with enhanced swithchable oil/water wettability for oily water separation. Chem Eng J 287:474–481

Lim HS, Kwak D, Lee DY, Lee SG, Cho K (2007) UV-driven reversible switching of a roselike vanadium oxide film between superhydrophobicity and superhydrophilicity. J Am Chem Soc 129:4128–4129

Lin XL, Tang DY, Yu ZQ, Feng Q (2014) Stimuli-responsive electrospun nanofibers from poly (N-isopropylacrylamide)-co-poly (acrylic acid) copolymer and polyurethane. J Mater Chem B 2:651–658

Liu HL, Wang ST (2014) Poly (N-isopropylacrylamide)-based thermo-responsive surfaces with controllable cell adhesion. Sci China Chem 57:552–557

Liu KS, Yao X, Jiang L (2010a) Recent developments in bio-inspired special wettability. Chem Soc Rev 39:3240–3255

Liu MJ, Zheng YM, Zhai J, Jiang L (2010b) Bioinspired super-antiwetting interfaces with special liquid-solid adhesion. Acc Chem Res 43:368–377

Liu XJ, Ye QA, Yu B, Liang YM, Liu WM, Zhou F (2010c) Switching water droplet adhesion using responsive polymer brushes. Langmuir 26:12377–12382

Liu CC, Ju J, Ma J, Zheng YM, Jiang L (2014a) Directional drop transport achieved on high-temperature anisotropic wetting surfaces. Adv Mater 26:6086–6091

Liu CC, Ju J, Zheng YM, Jiang L (2014b) Asymmetric ratchet effect for directional transport of fog drops on static and dynamic butterfly wings. ACS Nano 8:1321–1329

Liu HL, Zhang XQ, Wang ST, Jiang L (2015) Underwater thermoresponsive surface with switchable oil-wettability between superoleophobicity and superoleophilicity. Small 11:3338–3342

Londe G, Chunder A, Wesser A, Zhai L, Cho HJ (2008) Microfluidic valves based on superhydrophobic nanostructures and switchable thermosensitive surface for lab-on-a-chip (LOC) systems. Sensor Actuat B-Chem 132:431–438

Manabe K, Matsubayashi T, Tenjimbayashi M, Moriya T, Tsuge Y, Kyung KH, Shiratori S (2016) Controllable broadband optical transparency and wettability switching of temperature-activated solid/liquid-infused nanofibrous membranes. ACS Nano 10:9387–9396

Muthiah P, Hoppe SM, Boyle TJ, Sigmund W (2011) Thermally tunable surface wettability of electrospun fiber mats: polystyrene/poly(N-isopropylacrylamide) blended versus cross-linked poly[(N-isopropylacrylamide)-co-(methacrylic acid)]. Macromol Rapid Commun 32:1716–1721

Nagappan S, Ha CS (2015) Emerging trends in superhydrophobic surface based magnetic materials: fabrications and their potential applications. J Mater Chem A 3:3224–3251

Nakata K, Kimura H, Sakai M, Ochiai T, Sakai H, Murakami T, Abe M, Fujishima A (2010) UV/thermally driven rewritable wettability patterns on TiO_2-PDMS composite films. ACS Appl Mater Interfaces 2:2485–2488

Nakayama M, Yamada N, Kumashiro Y, Kanazawa H, Yamato M, Okano T (2012) Thermoresponsive poly (N-isopropylacrylamide)-based block copolymer coating for optimizing cell sheet fabrication. Macromol Biosci 12:751–760

Nishimoto S, Bhushan B (2013) Bioinspired self-cleaning surfaces with superhydrophobicity, superoleophobicity, and superhydrophilicity. RSC Adv 3:671–690

Niu XQ, Ran F, Chen LM, Lu GJE, Hu PG, Deming CP, Peng Y, Rojas-Andrade MD, Chen SW (2016) Thermo-switchable Janus gold nanoparticles with stimuli-responsive hydrophilic polymer brushes. Langmuir 32:4297–4304

Nykänen A, Hirvonen SP, Tenhu H, Mezzenga R, Ruokolainen J (2014) Wetting behaviour and direct observation of thermally responsive polystyrene-block-poly(N-isopropylacrylamide)-block-polystyrene electrospun fibres in aqueous environment. Polym Int 63:37–43

Ou RW, Wei J, Jiang L, Simon GP, Wang HT (2015) Robust thermoresponsive polymer composite membrane with switchable superhydrophilicity and superhydrophobicity for efficient oil-water separation. Environ Sci Technol 50:906–914

Park KC, Kim P, Grinthal A, He N, Fox D, Weaver JC, Aizenberg J (2015) Condensation on slippery asymmetric bumps. Nature 531:78–82

Parker AR, Lawrence CR (2001) Water capture by a desert beetle. Nature 414:33–34

Powell MR, Cleary L, Davenport M, Shea KJ, Siwy ZS (2011) Electric-field-induced wetting and dewetting in single hydrophobic nanopores. Nature Nanotechnol 6:798–802

Prins MWJ, Welters WJJ, Weekamp JW (2001) Fluid control in multichannel structures by electrocapillary pressure. Science 291:277–280

Quéré D (2008) Wetting and roughness. Annu Rev Mater Res 38:71–99

Raczkowska J, Stetsyshyn Y, Awsiuk K, Zemla J, Kostruba A, Harhay K, Marzec M, Bernasik A, Lishchynskyi O, Ohar H, Budkowski A (2016) Temperature-responsive properties of poly(4-

vinylpyridine) coatings: influence of temperature on the wettability, morphology, and protein adsorption. RSC Adv 6:87469–87477

Saitoh T, Suzuki Y, Hiraide M (2002) Preparation of poly (N-isopropylacrylamide)-modified glass surface for flow control in microfluidics. Anal Sci 18:203–205

Saitoh T, Sekino A, Hiraide M (2005) Manipulate fluid in microchannels with thermo-responsive film. Anal Chim Acta 536:179–182

Seeber M, Zdyrko B, Burtovvy R, Andrukh T, Tsai CC, Owens JR, Kornev KG, Luzinov I (2011) Surface grafting of thermoresponsive microgel nanoparticles. Soft Matter 7:9962–9971

Shi XJ, Chen GJ, Wang YW, Yuan L, Zhang Q, Haddleton DM, Chen H (2013) Control the wettability of poly (N-isopropylacrylamide-co-1-adamantan-1-ylmethyl acrylate) modified surfaces: the more ADA, the bigger impact? Langmuir 29:14188–14195

Song WL (2014) Adhesion switch on a gecko-foot inspired smart nanocupule surface. Nanoscale 6:13435–13439

Song WL, Xia F, Bai YB, Liu FQ, Sun TL, Jiang L (2007) Controllable water permeation on a poly(N-isopropylacrylamide)-modified nanostructured copper mesh film. Langmuir 23:327–331

Song WL, Li H, Wang CM, Yang B (2014) Design of multi-stage thermal responsive wettable surface. Adv Mater Interfaces 1:1400009

Stetsyshyn Y, Zemla J, Zolobko O, Fornal K, Budkowski A, Kostruba A, Donchak V, Harhay K, Awsiuk K, Rysz J, Bernasik A, Voronov S (2012) Temperature and pH dual-responsive coatings of oligoperoxide-graft-poly (N-isopropylacrylamide): wettability, morphology, and protein adsorption. J Colloid Interf Sci 387:95–105

Stetsyshyn Y, Fornal K, Raczkowska J, Zemla J, Kostruba A, Ohar H, Ohar M, Donchak V, Harhay K, Awsiuk K, Rysz J, Bernasik A, Budkowski A (2013) Temperature and pH dual-responsive POEGMA-based coatings for protein adsorption. J Colloid Interf Sci 411:247–256

Stuart MAC, Huck WTS, Genzer J, Muller M, Ober C, Stamm M, Sukhorukov GB, Szleifer I, Tsukruk VV, Urban M, Winnik F, Zauscher S, Luzinov I, Minko S (2010) Emerging applications of stimuli-responsive polymer materials. Nat Mater 9:101–113

Su B, Guo W, Jiang L (2015) Learning from nature: binary cooperative complementary nanomaterials. Small 11:1072–1096

Sun TL, Liu H, Song WL, Wang X, Jiang L, Li L, Zhu DB (2004a) Responsive aligned carbon nanotubes. Angew Chem Int Ed 43:4663–4666

Sun TL, Wang GJ, Feng L, Liu BQ, Ma YM, Jiang L, Zhu DB (2004b) Reversible switching between superhydrophilicity and superhydrophobicity. Angew Chem Int Ed 43:357–360

Sun TL, Feng L, Gao XF, Jiang L (2005) Bioinspired surfaces with special wettability. Acc Chem Res 38:644–652

Sun W, Zhou SX, You B, Wu LM, Mater J (2013) A facile method for the fabrication of superhydrophobic films with multiresponsive and reversibly tunable wettability. J Mater Chem A 1:3146–3154

Thickett SC, Neto C, Harris AT (2011) Biomimetic surface coatings for atmospheric water capture prepared by dewetting of polymer films. Adv Mater 23:3718–3722

Tian DL, Zhang XF, Tian Y, Wu Y, Wang X, Zhai J, Jiang L (2012) Photo-induced water-oil separation based on switchable superhydrophobicity-superhydrophilicity and underwater superoleophobicity of the aligned ZnO nanorod array-coated mesh films. J Mater Chem 22:19652–19657

Tian DL, Guo ZY, Wang YL, Li WX, Zhang XF, Zhai J, Jiang L (2013a) Phototunable underwater oil adhesion of micro/nanoscale hierarchical-structured ZnO mesh films with switchable contact mode. Adv Funct Mater 24:536–542

Tian DL, Song YL, Jiang L (2013b) Patterning of controllable surface wettability for printing techniques. Chem Soc Rev 42:5184–5209

Tonhauser C, Golriz AA, Moers C, Klein R, Butt HJ, Frey H (2012) Stimuli-responsive y-shaped polymer brushes based on junction-point-reactive block copolymers. Adv Mater 24:5559–5563

Tsuda Y, Kikuchi A, Yamato M, Sakurai Y, Umezu M, Okano T (2004) Control of cell adhesion and detachment using temperature and thermoresponsive copolymer grafted culture surfaces. J Biomed Mater Res A 69:70–78

Uchida K, Izumi N, Sukata S, Kojima Y, Nakamura S, Irie M (2006) Photoinduced reversible formation of microfibrils on a photochromic diarylethene microcrystalline surface. Angew Chem Int Ed 45:6470–6473

Vakarelski IU, Patankar NA, Marston JO, Chan DY, Thoroddsen ST (2012) Stabilization of leidenfrost vapour layer by textured superhydrophobic surfaces. Nature 489:274–277

Varanasi KK, Hsu M, Bhate N, Yang WS, Deng T (2009) Spatial control in the heterogeneous nucleation of water. Appl Phys Lett 95:144101

Wang R, Hashimoto K, Fujishima A, Chikuni M, Kojima E, Kitamura A, Shimohigoshi M, Watanabe T (1997) Light-induced amphiphilic surfaces. Nature 388:431–432

Wang ST, Song YL, Jiang L (2007) Photoresponsive surfaces with controllable wettability. J Photochem Photobiol C 8:18–29

Wang N, Zhao Y, Jiang L (2008) Low-cost, thermoresponsive wettability of surfaces: poly(N-isopropylacrylamide)/polystyrene composite films prepared by electrospinning. Macromol Rapid Commun 29:485–489

Wang CF, Liao CS, Kuo SW, Lin HC (2011) Tunable wettability of carbon nanotube/poly (ε-caprolactone) hybrid films. Appl Surf Sci 257:9152–9157

Wang N, Guo FY, Wu J, Zhao Y, Jiang L (2014) Variable responsive wettability films via electrospinning induced by solvents. J Nanomater 9:1–7

Wang Y, Lai C, Hu H, Liu Y, Fei B, Xin JH (2015a) Temperature-responsive nanofibers for controllable oil/water separation. RSC Adv 5:51078–51085

Wang TQ, Chen HX, Liu K, Wang SL, Xue PH, Yu Y, Ge P, Zhang JH, Yang B (2015b) Janus Si micropillar arrays with thermal-responsive anisotropic wettability for manipulation of microfluid motions. ACS Appl Mater Interfaces 7:376–382

Wen LP, Tian Y, Jiang L (2015) Bioinspired super-wettability from fundamental research to practical applications. Angew Chem Int Ed 54:3387–3399

Wheeler AR (2008) Chemistry putting electrowetting to work. Science 322:539–540

Wu Y, Xue YH, Pei XW, Cai MR, Duan HL, Huck WTS, Zhou F, Xue QJ (2014) Adhesion-regulated switchable fluid slippage on superhydrophobic surfaces. J Phys Chem C 118:2564–2569

Xia F, Jiang L (2008) Bio-inspired, smart, multiscale interfacial materials. Adv Mater 20:2842–2858

Xia F, Feng L, Wang ST, Sun TL, Song WL, Jiang WH, Jiang L (2006) Dual-responsive surfaces that switch between superhydrophilicity and superhydrophobicity. Adv Mater 18:432–436

Xia F, Ge H, Hou Y, Sun TL, Chen L, Zhang GZ, Jiang L (2007) Multiresponsive surfaces change between superhydrophilicity and superhydrophobicity. Adv Mater 19:2520–2524

Xia HW, Xia F, Tang YC, Guo W, Hou X, Chen L, Hou Y, Zhang GZ, Jiang L (2011) Tuning surface wettability through supramolecular interactions. Soft Matter 7:1638–1640

Xu QF, Liu Y, Lin FJ, Mondal B, Lyons AM (2013) Superhydrophobic TiO_2-polymer nanocomposite surface with UV-induced reversible wettability and self-cleaning properties. ACS Appl Mater Interfaces 5:8915–8924

Xue BL, Gao LC, Hou YP, Liu ZW, Jiang L (2013) Temperature controlled water/oil wettability of a surface fabricated by a block copolymer: application as a dual water/oil on-off switch. Adv Mater 25:273–277

Yan RX, Gargas D, Yang PD (2009) Nanowire photonics. Nat Photonics 3:569–576

Yang J, Zhang ZZ, Men XH, Xu XH, Zhu XH (2011) Thermo-responsive surface wettability on a pristine carbon nanotube film. Carbon 49:19–23

Yang HR, Esteves ACC, Zhu HJ, Wang DJ, Xin JH (2012) In-situ study of the structure and dynamics of thermo-responsive pnipaam grafted on a cotton fabric. Polymer 53:3577–3586

Yang WK, Tang ZC, Luan YF, Liu W, Li D, Chen H (2014) Thermoresponsive copolymer decorated surface enables controlling the adsorption of a target protein in plasma. ACS Appl Mater Interfaces 6:10146–10152

Yao X, Hu Y, Grinthal A, Wong TS, Mahadevan L, Aizenberg J (2013) Adaptive fluid-infused porous films with tunable transparency and wettability. Nat Mater 12:529–534

Yao X, Ju J, Yang S, Wang JJ, Jiang L (2014) Temperature-driven switching of water adhesion on organogel surface. Adv Mater 26:1895–1900

Yao H, Wei DX, Che XM, Cai LW, Tao L, Liu L, Wu LP, Chen GQ (2016) Comb-like temperature-responsive polyhydroxyalkanoate-graft-poly(2-dimethylamino-ethylmethacrylate) for controllable protein adsorption. Polym Chem 7:5957–5965

Yokota S, Matsuyama K, Kitaoka T, Wariishi H (2007) Thermally responsive wettability of self-assembled methylcellulose nanolayers. Appl Surf Sci 253:5149–5154

Yoshida Y, Kawahara K, Inamoto K, Mitsumune S, Ichikawa S, Kuzuya A, Ohya Y (2017) Biodegradable injectable polymer systems exhibiting temperature-responsive irreversible sol-to-gel transition by covalent bond formation. ACS Biomater Sci Eng 3:56–67

Yu X, Wang Z, Jiang Y, Shi F, Zhang X (2005) Reversible PH-responsive surface: from superhydrophobicity to superhydrophilicity. Adv Mater 17:1289–1293

Yu NZ, Wang SL, Liu YS, Xue PH, Ge P, Nan JJ, Ye SS, Liu WD, Zhang JH, Yang B (2017) Thermal-responsive anisotropic wetting microstructures for manipulation of fluids in microfluidics. Langmuir 33:494–502

Yuan WF, Jiang GY, Wang JX, Wang GJ, Song YL, Jiang L (2006) Temperature/light dual-responsive surface with tunable wettability created by modification with an azobenzene-containing copolymer. Macromolecules 39:1300–1303

Zareie HM, Boyer C, Bulmus V, Nateghi E, Davis TP (2008) Temperature-responsive self-assembled monolayers of oligo (ethylene glycol): control of biomolecular recognition. ACS Nano 2:757–765

Zeng PT, Kuo CC, Lin ST, Chiu YC, Chen WC (2010) New thermoresponsive luminescent electrospun nanofibers prepared from poly[2,7-(9,9-dihexylfluorene)]-block-poly(N-isopropylacrylamide)/PMMA blends. Macromol Chem Phys 211:1408–1416

Zhai L, Berg MC, Cebeci FC, Kim Y, Milwid JM, Rubner MF, Cohen RE (2015) Patterned superhydrophobic surfaces: toward a synthetic mimic of the namib desert beetle. Appl Phys Lett 6:1213–1217

Zhang SJ, Zhan L, Bucknall DG, He LH, Hong KL, Mays JW, Allen MG (2011a) Thermally switchable thin films of an ABC, triblock copolymer of poly (N-butyl methacrylate)-poly (methyl methacrylate)-poly (2-fluoroethyl methacrylate). Appl Surf Sci 257:9673–9677

Zhang T, Wang JM, Chen L, Zhai J, Song YL, Jiang L (2011b) High-temperature wetting transition on micro- and nanostructured surfaces. Angew Chem Int Ed 50:5311–5314

Zhang X, Guo YG, Zhang PY, Wu ZS, Zhang ZJ (2012) Superhydrophobic and superoleophilic nanoparticle film: synthesis and reversible wettability switching behavior. ACS Appl Mater Interfaces 4:1742–1746

Zhang M, Yao G, Cheng YL, Xu YY, Yang L, Lv JG, Shi SW, Jiang XS, He G, Wang PH, Song XP, Sun ZQ (2015) Temperature-dependent differences in wettability and photocatalysis of TiO_2 nanotube arrays thin films. Appl Surf Sci 356:546–552

Zhao TY, Nie FQ, Jiang L (2010) Precise control of wettability from LCST tunable surface. J Mater Chem 20:2176–2181

Zhao X, Liu Y, Lu J, Zhou JH, Li JH (2012) Temperature-responsive polymer/carbon nanotube hybrids: smart conductive nanocomposite films for modulating the bioelectrocatalysis of NADH. Chem-Eur J 18:3687–3694

Zhou MY, Xie R, Yu YL, Chen G, Ju XJ, Yang LH, Liang B, Chu LY (2009) Effects of surface wettability and roughness of microchannel on flow behaviors of thermo-responsive microspheres therein during the phase transition. J Colloid Interface Sci 336:162–170

Zhou Q, Li JH, Yan BF, Wu D, Zhang QQ (2014) Thermo-responsive and antifouling PVDF nanocomposited membranes based on PNIPAAm modified TiO_2 nanoparticles. Chinese J Polym Sci 7:892–905

Zhu Y, Wang D, Jiang L, Jin J (2014) Recent progress in developing advanced membranes for emulsified oil/water separation. NPG Asia Mater 6:e101

Chapter 5
Electric-Responsive Superwetting Surface

Dongliang Tian, Linlin He, and Lei Jiang

Abstract Intelligent control of superwetting surface by external electric field and multi-field synergy has aroused many research interests owing to their importance in practical research and applications. This chapter summarizes the recent research progress of the electrical field responsive superwetting surface, particularly on switchable wettability on electric-responsive surface and the typical applications such as liquid actuation, adhesion control, optical devices, liquid separation, particles manipulation and patterning. Finally, our personal points of the future research development on this research are addressed.

Keywords Electric-responsive surface · Photoelectric cooperation · Superwetting · Liquid actuation · Patterning

5.1 Introduction

Control of special surface wettability has been an effect way to solve many challenging interface science problems in energy, environmental science, biological engineering, chemical manufacturing, etc. (Liu et al. 2017; Tian et al. 2014a; Wang et al. 2015; Wen et al. 2015; Li et al. 2007; Xin and Hao 2010; Sun et al. 2005). Recently, responsive materials have been widely investigated and used to construct smart interface, as their surface properties are responsive to external stimuli (Feng and Jiang 2006; Xia and Jiang 2008; Zhang et al. 2008; Liu et al. 2014; Tian et al. 2014b;

D. Tian · L. He
Beijing Advanced Innovation Center for Biomedical Engineering, School of Chemistry,
Beihang University, Beijing, China

L. Jiang (✉)
Beijing Advanced Innovation Center for Biomedical Engineering, School of Chemistry,
Beihang University, Beijing, China

Technical Institute of Physics and Chemistry, Chinese Academy of Sciences, Beijing, China
e-mail: jianglei@iccas.ac.cn

A. Hozumi et al. (eds.), *Stimuli-Responsive Dewetting/Wetting Smart Surfaces and Interfaces*, Biologically-Inspired Systems 11,
https://doi.org/10.1007/978-3-319-92654-4_5

Nagappan and Ha 2015; Yu et al. 2005; Xia et al. 2007; Crevoisier et al. 1999; Yao et al. 2013). Electric field and the multi-fields synergy were considered as the effective way to control the surface wettability, and have been paid more and more attention due to their advantages of in situ control, fast response and low energy consumption in both basic research and applications (Prins et al. 2001; Hayes and Feenstra 2003; Powell et al. 2011; Wheeler 2008). During the past 20 years, especially the past 10 years, combined with superwetting surfaces, (Tian et al. 2013; Liu et al. 2010a; Yan et al. 2009; Su et al. 2015; Zhang and Han 2010; Quéré 2008; Xia et al. 2012; Roach et al. 2008; Tawfick et al. 2012; Yao et al. 2011) electric-responsive surfaces have made rapid advancement to meet the needs of practical applications with the development in micro/nano- fabrication, and there also remains some challenges in this field.

This chapter will focus on the recent research progress of electic-responsive surface wettability, special for the fast responsive superwetting surface, such as superhydrophilicity and superhydrophobicity, with the control of electrical field and photoelectric cooperation. There are four main sections in this chapter. In Sect. 5.2, we summarize the switchable wettability on electric-responsive surface such as the irreversible and reversible electrowetting on rough surface. Section 5.3 presents a review on the typical applications of electric-responsive surface such as liquid actuation, adhesion control, optical devices, liquid separation, particles manipulation and patterning. Finally, personal perspectives on the development of this research are briefly addressed.

5.2 Switchable Wettability on Electric-Responsive Surface

Since Lippmann found the electrocapillary phenomenon in 1875, (Lippmann 1875) traditional electrowetting was gradually began to study (Nakamura et al. 1973). However, water electrolysis exists in the voltage of a few hundred millivolts, which obstacles the related applied research. Untill 1993, a thin insulating layer was introduced, to avoide the electrolysis of water, between conductive liquid and electrodes in the electrowetting device by Berge et al., the development of electrowetting is accelerated (Berge 1993). Electrowetting is that a conducting droplet contact angle (CA)decreases under an electric field between the droplet and the counter electrode (Fig. 5.1). In the electrowetting process, an electrical potential modifies the interfacial tension and reduces liquid CA on the solid surface without the composition change. To describe the relationship of the CA change and the applied voltage, Berge proposed the electrowetting equation through energy minimization method (Berge 1993). When no trapped charge is existed, the equation can be given as:

$$\cos\theta\left(V\right)=\cos\theta\left(0\right)+\frac{1}{2}\frac{1}{\gamma_{LV}}\frac{\varepsilon_0\varepsilon_r}{d}V^2 \tag{5.1}$$

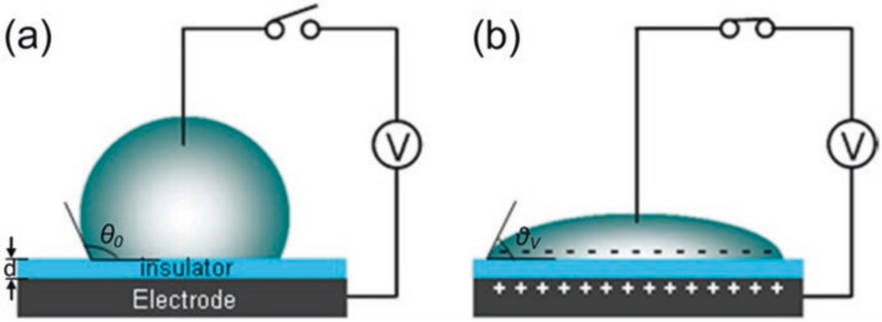

Fig. 5.1 Schematic electrowetting of a droplet at V=0 (**a**) and V>0 (**b**)

where ε_0 is the dielectric constant of vacuum, ε_r is the relative constant of the insulation layer, d is the dielectric film thickness, γ_{LV} is the mercury-vapor surface tension, θ_0 is the CA without an electric field, and θ_v is the CA at a certain voltage V.

However, if the trapped charges exist, a quantity V_T for the trapped charges should be introduced in the above equation and the equation can be adjusted as (Verheijen and Prins 1999):

$$\cos\theta(V) = \cos\theta(0) + \frac{1}{2}\frac{1}{\gamma_{LV}}\frac{\varepsilon_0\varepsilon_r}{d}(V - V_T)^2 \tag{5.2}$$

where V_T is the voltage to compensate the trapped charges effect.

According to the electrowetting equation, the CA continuously decreases with the applied voltage increase until the CA of ~ 0°. For a given electrowetting device, the initial liquid CA is critical to achieve a wider angle tuning range (Berge 1993; Verheijen and Prins 1999). However, in the practical process, reversible electrowetting can only be realized with low voltage change range due to the CA saturation phenomenon (Verheijen and Prins 1999; Girault 2006). Electrowetting can effectively control the motion of fluid in microscale, and has been widely used in microfluidics due to its fast response and low energy consumption (Mugele and Baret 2005; Brown et al. 2009; Xue et al. 2014; Hagedon et al. 2012; Heikenfeld et al. 2009; Moon et al. 2013; Krupenkin and Taylor 2011).

5.2.1 *Irreversible Electrowetting on Rough Surface*

Inspired from nature, surface with special micro/nanostructure can achieve a large initial CA, i.e., superhydrophobic. On the contrary, electrowetting decreases the liquid CA with increasing voltage. Combined superhydrophobicity with electrowetting results, the CA change scope can be effectively enhanced (Fig. 5.2a).

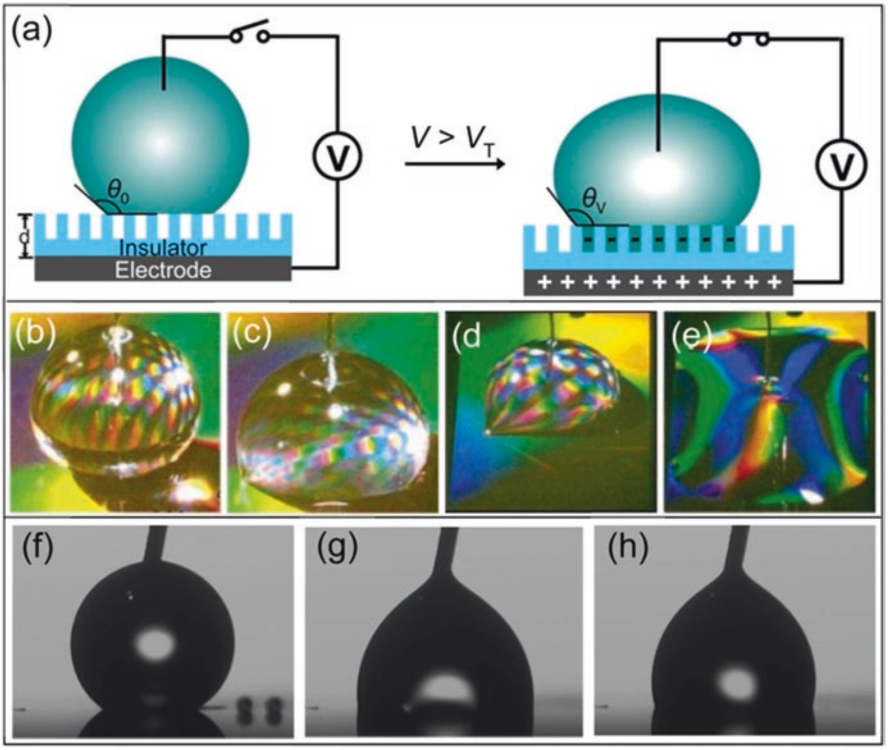

Fig. 5.2 (**a**) Schematic electrowetting on the rough surface. (**b–h**) Electrowetting on the nanopost array substrates (**b–e**) (Krupenkin et al. 2004). (**b–c**) A water droplet CA underwent a sharp transition, with the wetting behavior changed from rolling to the immobile drople. (**d–e**) A cyclopentanol droplet CA dramatically decreased at 50 V. Superhydrophobic SU-8 patterned surfaces for electrowetting (**f–h**) (Herbertson et al. 2006). A initial water droplet (**f**) CA decrease with voltage of 130 V (**g**), and the droplet contact remained when voltage is removed (**h**)

Electrowetting on the surface with micro/nano structures has been paid more and more attention in both theoretical study and application (McHale et al. 2013; Han et al. 2009; Bormashenko et al. 2013; Kakade 2013; Lee et al. 2013; Kwon et al. 2012). The first work was reported by Krupenkin et al., dynamic electrowetting behavior of liquids on nanostructured surfaces was investigated (Fig. 5.2b–e) (Krupenkin et al. 2004). The results indicate that the droplet on the nanostructured surface could transit from superhydrophobicity to complete wetting under 22 V. Later, they realized electrically tunable superlyophobic surfaces from the superlyophobic state to almost complete wetting on a nanonail-covered substrate (Ahuja et al. 2008). Herberston et al. demonstrated the drop wetting state could be converted from Cassie-Baxter to Wenzel regime and fluid penetrated into the micropatterned layers of SU-8 photoresist with an amorphous Teflon® coating (Fig. 5.2f–h) (Herbertson et al. 2006). According to the cosine of the CA is proportional to the square of the applied voltage for increasing bias, electrowetting could be used to estimate the surface roughness factor. Zhu et al. reported that the CA saturation of electrowetting on the aligned carbon nanotube (CNT) films could be effectively reduced from 98° to 50° when NaCl was added to the deionized water (Zhu et al. 2006). Electrowetting phenomenon of water on the superhydrophobic aligned multiwalled nanotube membranes was strongly dependent on polarity for dc bias, which was demonstrated by Wang et al (2007). For a negative bias, the voltage required is 2 orders of magnitude higher bias for the transition. Zhao et al. demonstrated adhesive force could be adjusted by DC bias on the superhydrophobic MnO_2 nanotube membrane, which was also strongly polarity-dependent (Zhao et al. 2011). Similar result was also demonstrated by Kilaru et al., bistable electrowetting was demonstrated owing to a decreased CA retained at 0 V, but CA would increase by a reverse voltage (Kilaru et al. 2007).

5.2.2 Reversible Electrowetting on Rough Surface

Although lots of works on electrowetting induced wettability change from superhydrophobic to hydrophilic on rough structures have been reported, it still suffered a problem of irreversible transition. During the electrowetting process, it consumes considerable energy when the liquid front expands to the nanostructure layer, resulting that the system lacks the energy to be back to the initial state after removal of voltage. To achieve reversible electrowetting, engineering nanostructured surfaces with minimize energy consumption and providing additional energy are two important strategies (Krupenkin et al. 2005, 2007; Bahadur and Garimella 2009; Barberoglou et al. 2010; Laird et al. 2013; Lapierre et al. 2009).

5.2.2.1 Reversible Electrowetting on the Nanostructures in Air

Back pressure of located gas or vapor next to the surface can provide additional energy to realize the reversible electrowetting. With this pressure, the liquid droplet wetting in the nanostructures can be expelled from the nanostructured layer to the initial superhydrophobic state. One of the cases is the gas from the trapped air, e.g., the closed cell structures. Bahadur et al. demonstrated the closed structured surfaces could confine the air under the droplet and prevent the droplet wettability transition from Cassie to the Wenzel state (Bahadur and Garimella 2009). The other case is owing to the vapor produced at the interface for temperature increase. Krupenkin et al. reported the wettability transition from the superhydrophobic state to the hydrophilic state by electrowetting, the liquid penetrated to the nanostructured layer (Krupenkin et al. 2004, 2005, 2007). Under a short pulse of electrical current transmitted through the nanostructured substrate, the vapor pressure pushed the droplet and caused the droplet to disconnect from the substrate surface and to be back to the superhydrophobic state, and reversible electrowetting transition can be realized (Fig. 5.3a).

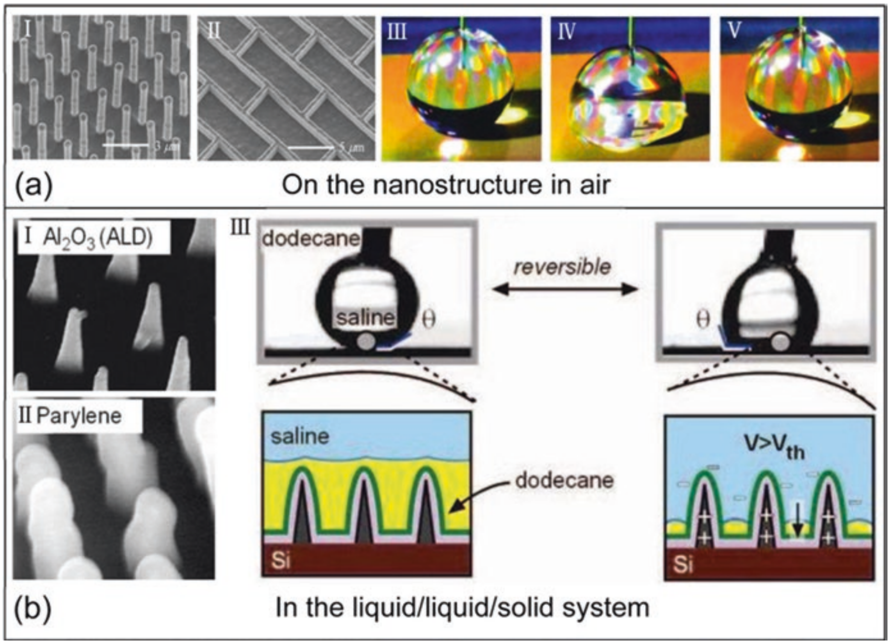

Fig. 5.3 (**a**) Reversible electrowetting on a nanostructure substrate in air (Krupenkin et al. 2007). (**b**) Reversible electrowetting on vertically aligned carbon nanofibers in saline/dodecane system (Dhindsa et al. 2006)

5.2.2.2 Reversible Electrowetting in the Liquid/Liquid/Solid

Using liquid medium instead of air to form a liquid/liquid/solid triphase system, is another way to achieve additional energy for reversible electrowetting. The conductive liquid droplet recovery accompanying with CA increase owing to the aid of buoyancy from the immiscible liquid medium, and realize the reversibility of electrowetting process. Dhindsa et al. demonstrated the reversible electrowetting behaviour of the superhydrophobic vertical carbon nanofibers array in oil phase while not in air (Fig. 5.3b) (Dhindsa et al. 2006). The results indicated that electrowetting could induce a CA reduction from 160° to 100°, the droplets could not spontaneously reverse from hydrophilic to superhydrophobic state in air when the voltage was removed. While for the same substrate in dodecane, the droplets could spontaneously shift from hydrophilic state towards the direction of the superhydrophobic with the competition of the immiscible dodecane and saline into the nanostructure layer after voltage was removed, so the electrowetting could be reversibly change. Similar result was also demonstrated on two kinds of textile fabric for the reversible electrowetting by Bhat et al (2007). The results indicated that water CA could irreversible change from 120° to 70°in air, while it was fully reversible in oil/water medium. Verplanck et al. investigated the reversible electrowetting of liquid droplets on superhydrophobic silicon nanowire both in air and in oil (Verplanck et al. 2007). The results indicated that the CA change range of a saline solution droplet in reversible electrowetting in air or oil environments are 23° and 58°, respectively. The results showed that in the oil phase was much easier to achieve reversible electrowetting than that in air.

5.2.2.3 Reversible Electrowetting of Liquid Marble in Air

In contrast to the increased initial CA of a liquid droplet on the solid surface through increased surface roughness, another effective method to achieve superhydrophobicity is to construct the rough structure on the liquid surface. A liquid marble can be viewed as a liquid droplet resting on a superhydrophobic surface but with the surface structure providing the superhydrophobicity conformal to the liquid surface rather than the underlying solid substrate. Liquid marbles, fabricated by rolling a small droplet around in a hydrophobic powder to spontaneously coat the drop, have aroused interest in recent years (Aussillous and Quere 2001; McHale and Newton 2011). Liquid marbles are highly mobile and can be actuated by electrostatic and magnetic field. The irreversibility of electrowetting is expected to be overcome by a liquid marble, Newton et al. prepared liquid marbles by water coated with hydrophobic lycopodium grains and achieved the completely reversible electrowetting. When electrowetting of marbles was performed, contact area increased with the CA change from 174° to 147° under a 100 V dc bias (Newton et al. 2007; McHale et al. 2007, 2009). Compared with liquid droplet electrowetting, no threshold voltage needed for a droplet deformation was owing to the structure surface conforming to the liquid surface rather than the substrate surface. More hydrophobic grains contacted with the substrate as increasing voltage while not for water within the marble.

5.2.2.4 Reversible Electrowetting on the Liquid Infused Film

To obtain the reversible electrowetting, a liquid lubricant phase can be used to reduce the surface hysteresis to minimize undesirable energy consumption. Hao et al. demonstrated electrowetting on a liquid infused film (EWOLF), which can realize complete reversibility (Hao et al. 2014). The results indicated that the lubricant liquid phase in porous membrane could enhance the viscous energy dissipation efficiently and suppress the droplet oscillation, which led fast response without sacrificing reversibility of the electrowetting. Later, Bormashenko et al. reported a low-voltage EWOLF with lubricated honeycomb polymer surface, owing to the low CA hysteresis inherent for liquid/liquid interfaces (Bormashenko et al. 2015).

Recently, electrowetting-based switch and the reverse electrowetting for electrical power generation and smart device were demonstrated base on special electrode design (Chen et al. 2007). For instance, Lifton et al. reported reserve battery design and structure based on nanostructured superhydrophobic materials, (Lifton et al. 2005, 2008) The superhydrophobic electrodes could be used to separate the liquid electrolyte effectively from the active electrode materials and the “smart” electrochemical energy storage cells could be activated on demand by combining these membranes and microfabricated Zn/MnO_2 electrodes, which provided the possibility of long shelf life.

5.3 Applications of Electric-Responsive Superwetting Surface

Electrowetting can effectively control the liquid droplet CA, and correspondingly to manipulate the movement of fluid in microscale for creating, cutting, merging and transporting of liquid droplet. Due to the advantage of fast response and low energy consumption, electrowetting has attracted more and more attention from the researchers. At present, by combining with the superwetting surface, electrowetting has been investigated and applied in many fields for broad application prospect including liquid droplet actuation, optical switch, liquid lens, display, separation and patterning, etc.

5.3.1 *Electric-Responsive Liquid Actuation*

The unbalanced force on a droplet edge resulting from asymmetric droplet CA is the dominant force for handling and actuation of liquid droplet in microscale. Chung et al. demonstrated a strategy to propel water-floating objects by a quasisteady "streaming" flow generated from ac electrowetting, which was potential application to propel and maneuver various mini/microrobots and boats on water (Fig. 5.4a) (Chung et al. 2009). Manakasettharn et al. fabricated the microflowers by changing

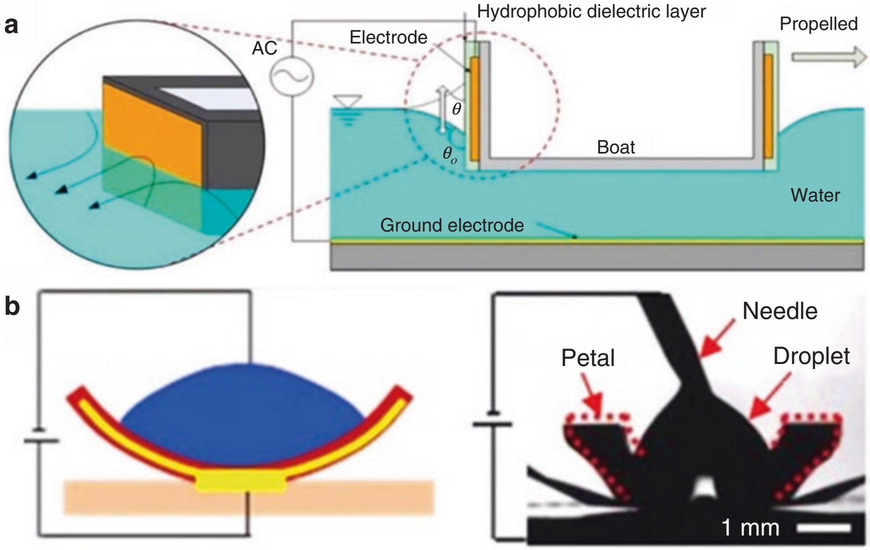

Fig. 5.4 (**a**) Propulsion principle of water-floating objects by ac electrowetting (Chung et al. 2009). (**b**) Electrowetting actuation of a microflower (Manakasettharn et al. 2011)

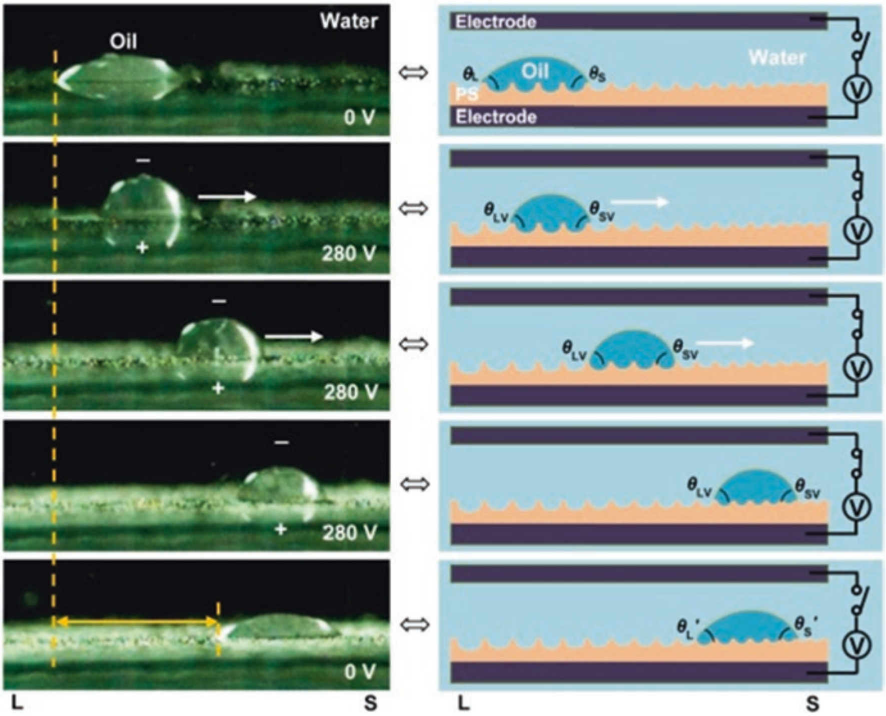

Fig. 5.5 Electric field and gradient microstructure cooperatively drive underwater oil droplet for directional motion (Tian et al. 2016)

its CA on the petals using the electrowetting process, accompanying with the dynamical change of reflective color and iridescence (Fig. 5.4b) (Manakasettharn et al. 2011). Combining with the effects of surface tension and elastic force as well as Coulomb force, Wang et al. demonstrated the flexible thin film could be electrically manipulated to encapsulate and release liquid droplet in a controllable and reversible manner. An ac electric field was applied to actuate vibration of the droplet and film, e.g., dancing following a melody (Wang et al. 2012).

Recently, the author's group realized electric field induced directional underwater oil droplets motion on a gradient porous PS film (Tian et al. 2016). When an underwater oil droplet stayed on the gradient porous PS film surface, an unbalanced pressure exists on both ends of the droplet, giving it an asymmetrical shape (Fig. 5.5). An increasing voltage could efficiently decrease the contact area of oil droplet and gradient-structured surface, so as to overcome the viscous drag on the porous PS film surface. Once the threshold voltage was exceeded, the underwater oil droplet could move directionally and continuously from the large pore area to the small pore site. This work provided a route for driving and controlling directional motion of underwater oil droplets continuously for further application in electrofluidic displays and other microfluidic devices.

5.3.2 Electric-Responsive Adhesion Control

The surface liquid droplet adhesion can be also be controlled based on the wettability transition by electrowetting. Krupenkin et al. realized a droplet wetting behavior change from rolling superhydrophobic behavior to pinning state under the electric field (Krupenkin et al. 2004). Zhao et al. reported electrically adjustable adhesion of a water droplet was strongly polarity-dependent on a superhydrophobic MnO_2 nanotube arrays membrane by application of a small DC bias, i.e., the adhesion was much larger when a negative voltage was applied than the corresponding positive bias, which could be used in the controllable liquid transport (Zhao et al. 2011). Kumari et al. realized the dewetting behavior of superhydrophobic surfaces, i.e., Wenzel-to-Cassie transition, by electrowetting (Kumari and Garimella 2011).

Recently, the author's group demonstrated electrochemical potentials induced an underwater oil droplet motion (Fig. 5.6) (Liu et al. 2010b). Oil droplet adhered to the polypyrrole surface with positive voltage, while the oil droplet CA increased with decreasing adhesive force and rolled down under gravity on the reduced polypyrrole film. A positive voltage on the film could stop the oil droplet again.

5.3.3 Electric-Responsive Surface for Optical Devices

Based on electrowetting, the CA of the droplet change, which is promising in the application of optical devices. One of the important applications based on the CA change is optical lens (Kuiper and Hendriks 2004; Pellat 1895). the focal length varies as the change of the droplet CA. The first maturational microsystem of liquid lenses based on electrowetting at the industrial level was brought by Berge and Peseux (2000). The device is composed of two phases system, i.e., a small oil drop in a closed cell filled with water. The oil drop shape, i.e., the radius of curvature, may be adjusted with the CA change of sessile droplets under a certain electric field within several milliseconds. Accordingly, the pictures of objects can be obtained by adjusting the focal length in a wide range of distances. Following work based on the reduction of the tension to operate the lens, Heikenfeld et al. developed an optical prism by achieving a drop flat meniscuses between two substrates (Smith et al. 2006). The orientation of the prism varied by applying a specific tension to each substrate. Yang et al. used a tunable microlens to control light and the fixed optical properties could be achieved by introduction of a photopolymerizable component (Yang et al. 2003). Owing to the advantage of miniaturization, lower sensitivity to mechanical faults, high optical quality and the durability, the applications of variable lenses were being widely developed such as minuscule digital cameras used in mobile phones and industrial and medical facilities.

Electrowetting-based liquid displays is another important application for optical devices, which operates in modes of transflective, transmissive, and reflective displays, is a good alternative to liquid-crystal displays (LCDs) and electrophoretic

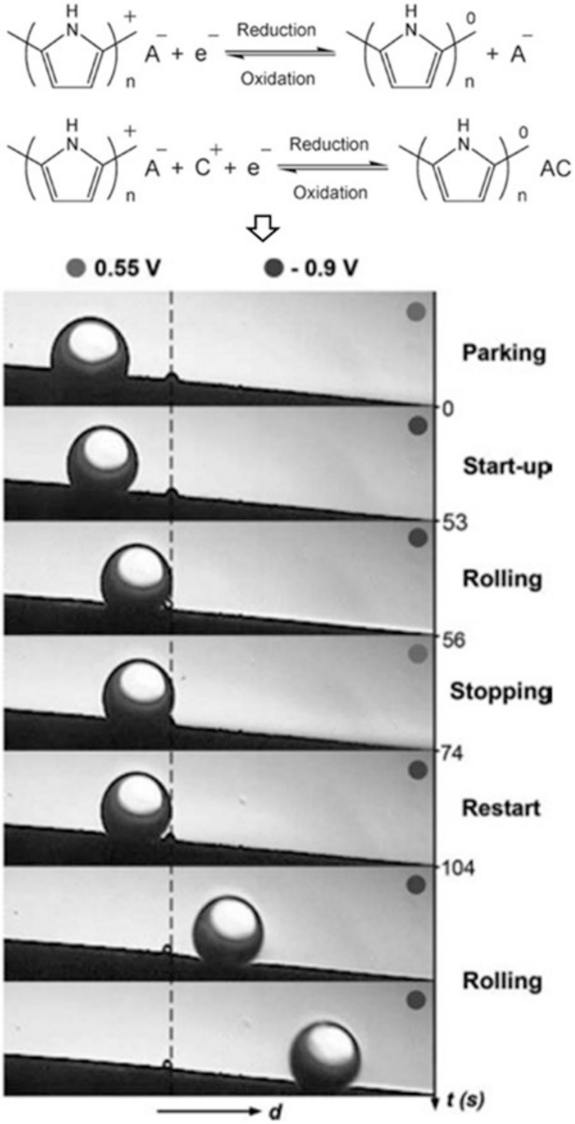

Fig. 5.6 Electrochemical potentials induced underwater oil droplet motion on a PPy surface (Liu et al. 2010b)

displays. Hayes et al. reported an electrowetting-based reflective display, which could be used as an electronic paper (Fig. 5.7a, b) (Hayes and Feenstra 2003). In the display process, an dyed oil droplet wet the hydrophobic insulator and formed a continuous layer without voltage. The incoming light could be strongly absorbed. When a voltage was applied, the oil layer contracted into the pixel corner increased in reflectivity from 2.5 to 35% under a voltage of 20 V. A color display concept was also demonstrated based on each pixel being splitted into three subpixels. However, the white pixels reflectance was much lower than in practical owing to incomplete

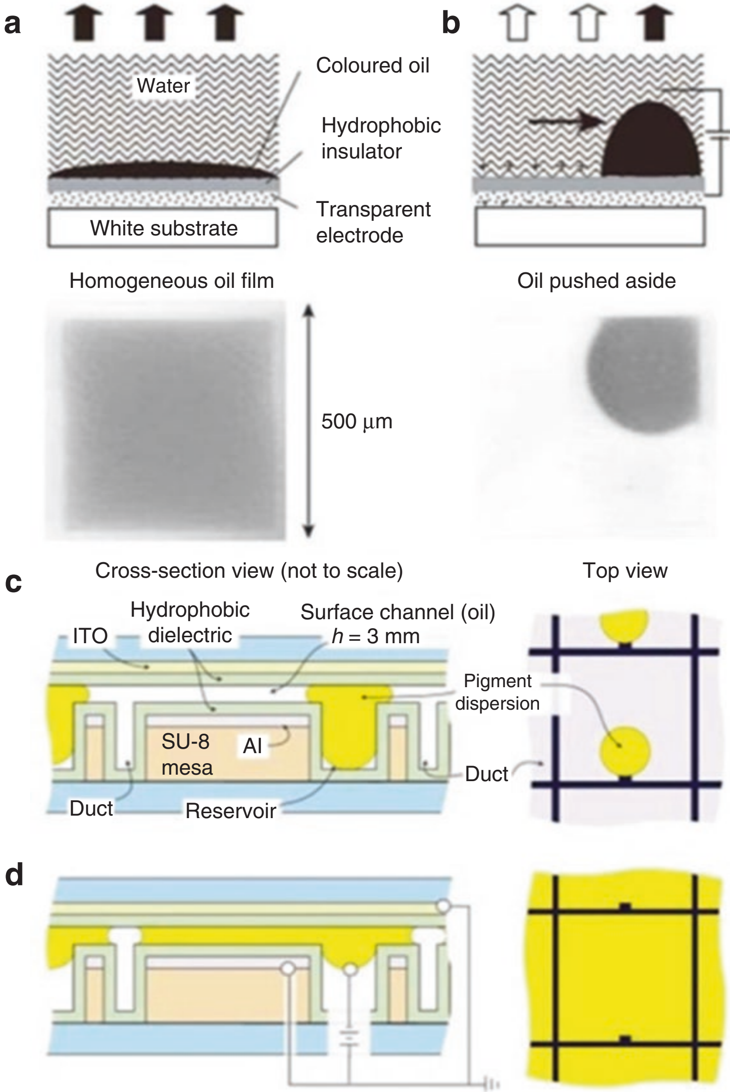

Fig. 5.7 Electrowetting display principle. (**a**) A colored oil film is present without voltage. (**b**) The oil film was caused to contract with applied voltage (Hayes and Feenstra 2003). In the pixels images, the pigment was hidden without voltage (**c**) and the pigment dispersion to the channel with an sufficient voltage (**d**) (Heikenfeld et al. 2009)

removal of the colored oil. Heikenfeld et al. presented a three-dimensional display device by direct view of pigment dispersions (Fig. 5.7c–d) (Heikenfeld et al. 2009). The aqueous dispersion could be pulled from a small reservoir with viewable area of <10% into a channel with viewable area of >90% under external electric field, while it retracted into the reservoir with no voltage, exhibiting ~ 55% white reflectance of preliminary prototypes. Later, they developed an electronic paper by transforming colored ink to front or back of a white microfluidic film with reflective area of >90%, which reduced the colored oil in visible area dramatically without increased operating voltage (Hagedon et al. 2012). Giraldo et al. demonstrated the active-matrix full-color transmissive electrowetting displays including its main technical and system aspects (Giraldo et al. 2010). High oil contraction opened up the transmissive area for high transmittance of the pixel because of no light-absorbing layers in the optical path. Kim et al. developed a liquid field-effect transistor based on electrowetting between competitive insulating/conducting fluids (Kim and Steckl 2007).

5.3.4 Electric-Responsive Liquid Separation

Electrowetting can effectively reduce the CA of conductive liquid, such as water, while it is almost no effect on the non-conductive oil droplet in air and even oil CA increase in water (Tian et al. 2016). Therefore, the opposite wettability change under electric field provides the possibility of smart oil-water separation. Recently, electric-responsive materials have been successfully fabricated for controllable oil/water separation. Tuteja et al. demonstrated on-demand separation of oil-water mixtures on a 50 wt% fluorodecyl POSS + x-PDMS filtration film with an electric field (Kwon et al. 2012). The electrowetting behavior of the as-prepared substrate to water and hexadecane was quite different. The water CA decreased from 115° to 56° when the voltage increasing from 0 to 1.5 kV, while hexadecane CA was independent of voltage. Oil/water separation had been demonstrated with the advantages of controllable and remote operation. Feng et al. demonstrated the electrical switchable wettability to water between superhydrophobicity and superhydrophilicity and controllable water permeation based on a (N-dodecyltrimethoxysilane)-modified 3D copper foam (Lin et al. 2015). Recently, the author's group achieved the electric field induced oil/water separation based on water selectively permeation on the root-like polyaniline nanofibers coated stainless steel mesh (Fig. 5.8) (Zheng et al. 2016). The electric field induced oil/water separation could be realized as long as the electric capillary pressure (*ECP*) larger than the hydrostatic pressure of the membrane to water, *i.e.*, the wettability to water transition from Cassie state to Wenzel state. These works would be promising to gear up the application of smart oil/water separation and related microfluidic devices.

5.3.5 Photoelectric-Responsive Particles Manipulation

Combining the electrowetting with light illumination, photoelectric cooperativewetting has been demonstrated, (Chiou et al. 2003, 2004) which is realized by integrating a photoconductive material layer underneath the electrowetting electrodes or

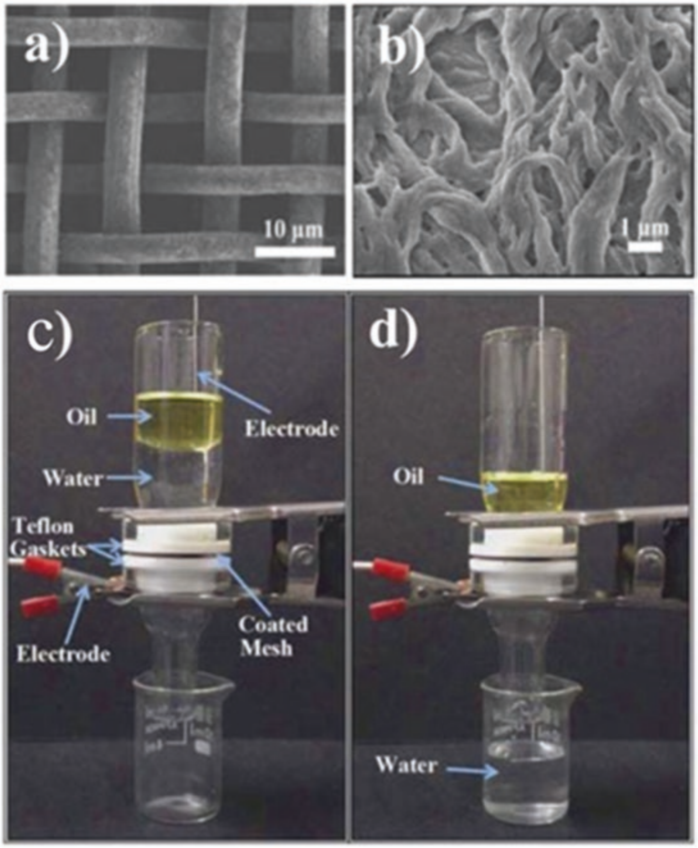

Fig. 5.8 (**a** and **b**) The prepared root-like polyaniline nanofibers coated stainless steel mesh. (**c** and **d**) Electric-responsive oil/water separation (Zheng et al. 2016)

between the dielectric layer and the electrodes in an electrowetting device. The surface tension between the solid-liquid is modified by external electric field under light illumination, which reduces the liquid droplet CA on the solid surface at the illumination area. This process can be regarded as the decease of the thickness of the insulator in electrowetting device, as described in Eqs. 5.1 and 5.2. Light actuation enables complex microfluidic functions to be performed on a single chip, and completely eliminates the wiring bottleneck of conventional electrowetting schemes. It is worth noting that, by designing the form of light, the different state of the liquid droplets can be successfully obtained, such as transport, separate, combine and mix liquid droplets (Hwang and Park 2011; Park et al. 2010; Yu et al. 2013; Gaudet and Arscott 2012; Chuang et al. 2008; Pei et al. 2015). Following the theoretically study of the relationship of the droplet CA and the position of light has also been conducted (Inui 2007).

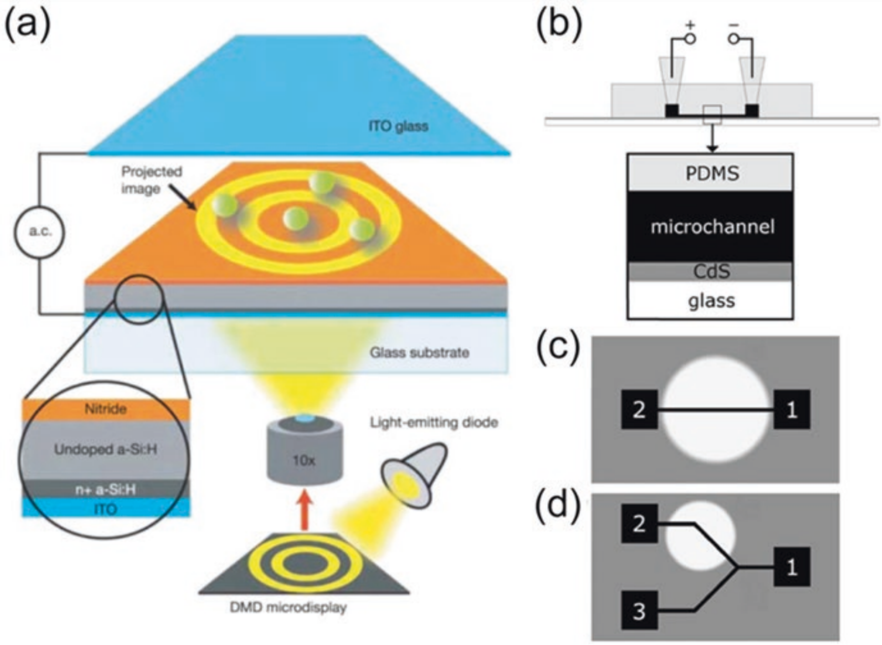

Fig. 5.9 (**a**) Schematic device structure of the optoelectronic tweezers (Chiou et al. 2005). (**b–d**) Schematic optical control of electro-osmosis (Oroszi et al. 2006)

Based on the photoelectric cooperation control mechanism, Chiou et al. demonstrated an optoelectronic tweezers (OET) for single particles manipulation with high-resolution (Fig. 5.9a), (Chiou et al. 2005). When light illuminates the photoconductive layer, its electrical conductivity increased several orders of magnitude and the illuminated areas generate dynamic virtual electrodes configurations, depending on the illumination intensity.

OET can freely catch and transport micro/nanoscale objects, the related applications are far beyond the manipulation in biology and colloidal science (Wu 2011). One of the attractive applications is to assembly nanowires or nanoparticles into arrays with controllable size and density (Jamshidi et al. 2008; Rogers 2008). OET is also promising in the application of biosciences, e.g., quantitative assessment of embryos (Valley et al. 2010). Some other effects of electrokinetic and hydrodynamic were also presented in OET. Light driving fluidic flow based on a.c. electro-osmosis and electrothermal effects may also occur. Oroszi et al. demonstrated electro-osmosis controlled by light, which could be used for effectively modulation of fluid flow by light (Fig. 5.9b–d) (Oroszi et al. 2006).

5.3.6 *Photoelectric-Responsive Patterning*

5.3.6.1 Self-Assemble Patterning

Micro/nanoscale materials patterns are usually prepared through the assembly of colloidal particles with patterned electrodes or micro-moulds. Hayward et al. created ordered patterns of micrometre-sized colloidal particles using patterned ultraviolet (UV) light illuminated on the ITO film electrode surface (Fig. 5.10) (Hayward et al. 2000). The PS beads aggregated in dense packed assembles on the patterned UV irradiation area of the ITO surface under an applied DC field. Following Gong et al. developed rapid crystal formation by the use of AC signal biased ITO electrodes and laser (532 nm) scanned patterns (Gong and Marr 2004). The results showed the existence of polycrystallinity in the assembled structures, and that not only could nucleation be directed with control over crystal annealing and melting.

For biological applications, the potential damage to cell and proteins by UV-light absorption must be avoided. Ozkan et al. reported a strategy to localize polymer beads on an non-patterned semiconductor surface (Ozkan et al. 2002). A photosensitive polymer layer was used to improve the patterning efficiency and resolution. Lee et al. reported optically induced dielectrophoretic forces were used to manipulation and patterning of carbon nanotubes, (Lee et al. 2010) which paved a way to real-time manipulation and miscellaneous patterning of CNTs, and also sorting and separation of bundled and dispersed CNTs. In addition, an electrothermal microfluidic vortex to manipulate the micro/nanoparticles on a parallel plate electrode surface was demonstrated by Williams et al. The particles aggregation is localized to the region of illumination from an infrared (1064 nm) laser without the need of photoconductive materials or complex microfabrication procedures (Williams et al. 2008, 2009; Kumar et al. 2010). Thus nanoscale and molecular-scale particles or objects could be concentrated and patterned by light-controlled fluidic flow.

5.3.6.2 Liquid Patterning for Printing

Liquid patterns are one of the important form for printing, which are promising to gear up the scientific investigation in the fields of biological and health sciences and broadened their applications (Perelaer et al. 2010; Gonzalez-Macia et al. 2010; Weng et al. 2010; Krebs 2009; Kaufmann and Ravoo 2010; Zhang and Yang 2010; Derby 2010; Hart and Wring 1997). The author's group has done some work about photoelectic cooperative wetting for liquid reprography by introducing the anisotropic micro/nanostructures (nanorod, nanopore, and nanotube array) into the different materials (organic, inorganic, polymer) (Fig. 5.11). The opening work of the photoelectric cooperative printing was reported in 2009, (Tian et al. 2009) the precise controllable patterned wettability transition was addressed on the superhydrophobic aligned ZnO photoconductive nanorod array surface via a photoelectric cooperative wetting process. Patterned wetting could be realized only at the patterned illumination site under a bias lower than the electrowetting threshold voltage (Morita et al.

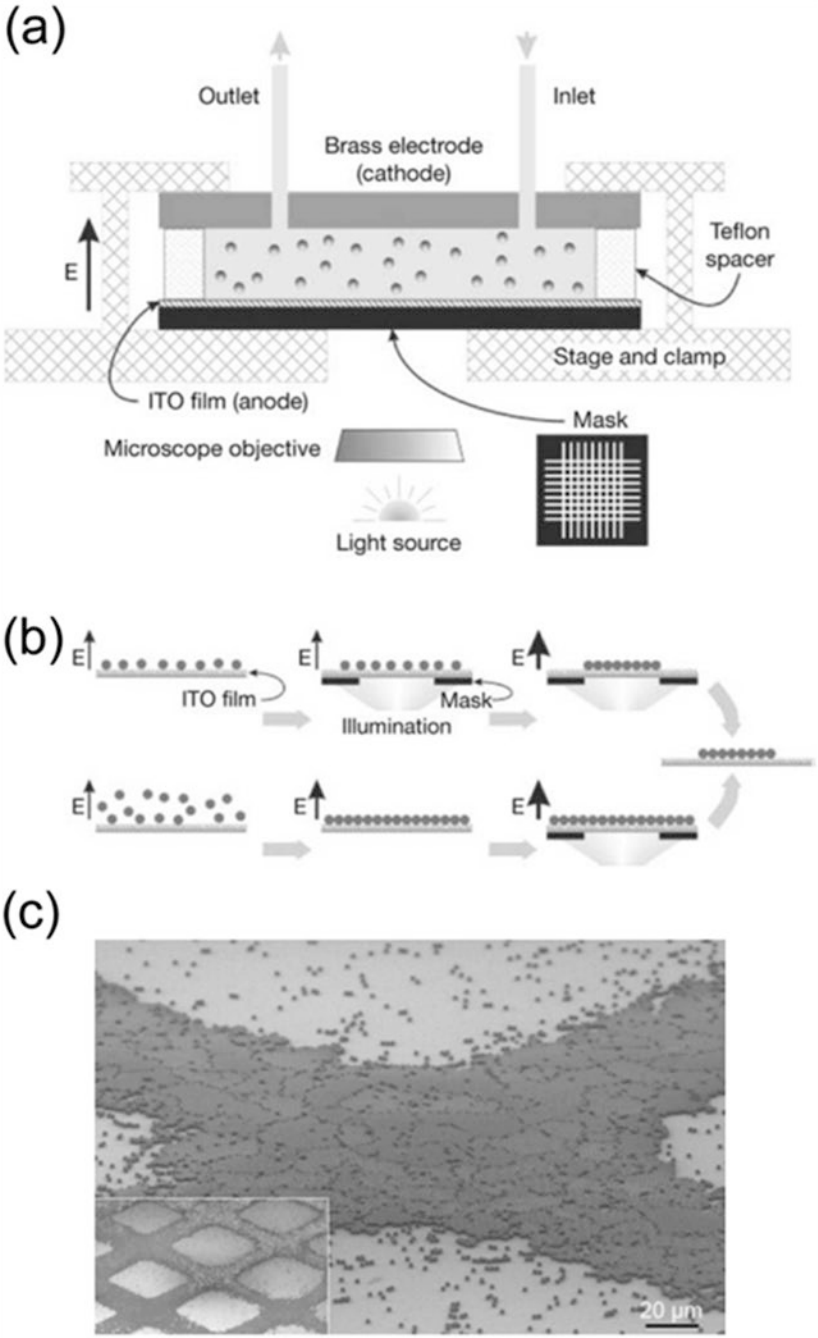

Fig. 5.10 (**a**) Schematic of the apparatus for particle assembly and pattern formation. (**b**) Pattern formation Process. UV light is used to selectively assemble and affix (method A; above) or affix (method B; below) polystyrene particles on the ITO electrode. (**c**) SEM image of a pattern produced by method B (Hayward et al. 2000)

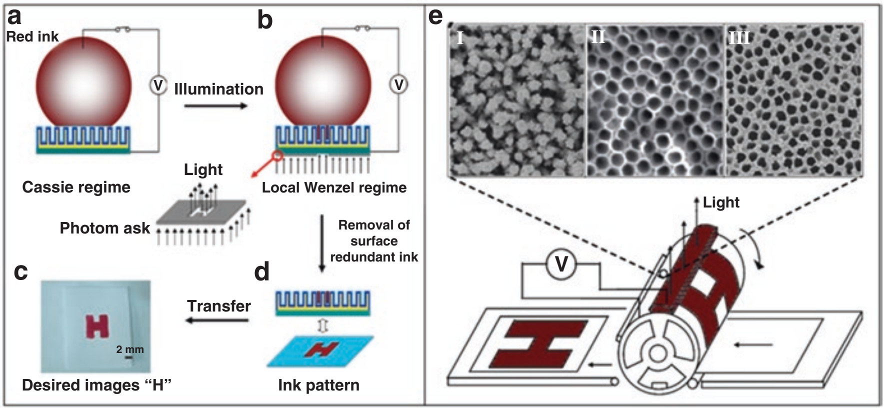

Fig. 5.11 (**a**–**d**) Schematic of the photoelectric cooperative reprography (**a**–**d**) (Tian et al. 2013). (**e**) The as-prepared aligned nanorod (I), (Tian et al. 2009) nanotube (II), (Fan et al. 2012) and nanopore (III) (Tian et al. 2011) array film used in the reprography process

2005; Öner and McCarthy 2000; Snaith and Schmidt-Mende 2007; Kalyanasundaram and Grätzel 1998; Schlettwein et al. 2000; Anantharaju et al. 2009). Liquid reprography was achieved through the patterned wettability transition. Later, similar work was also realizedon the superhydrophobic TiO_2 nanotube arrays photosensitized by CdS quantum dots (Fan et al. 2012). Moreover, TiO_2-coated nanoporous AAO film was also used to achieve robust photoelectric cooperative wetting process with high mechanical strength due to the well-knit and uniform aligned nanopore array (Tian et al. 2011). Not limited to the inorganic materials, other organic or polymer materials with special wetting structure, e.g., a hydrophobic ordered polymeric honeycomb structure, could also realize the similar results (Heng et al. 2014).

Photoelectric cooperative printing can also be realized on the micro-structured mesh substrate. The author's group had carried out some related research work, external field controllable water permeation and related applications were demonstrated on the micro/nanoscale hierarchical structure materials coated mesh substrate (Fig. 5.12). For instance, photoelectric cooperative induced liquid permeation was demonstrated on the anodizing Ti mesh (Guo et al. 2014a). Liquid permeation could be controlled by patterned light illumination under the voltage lower than electrowetting induced permeation threshold voltage, which was promising in the research and application of liquid printing. Later, we realized the patterning of liquid permeation on the micro/nano hierarchical structured ZnO mesh film by photoelectric cooperation (Guo et al. 2014b). Compared to the TiO_2/AAO nanopore array film, the ZnO mesh was beneficial to control microscale liquid with lower threshold voltage and lower adhesion due to the discontinuous triphase contact line. Thus the related work was potential application in smart micro/nanofluidic system and micro/nanoelectronic technology.

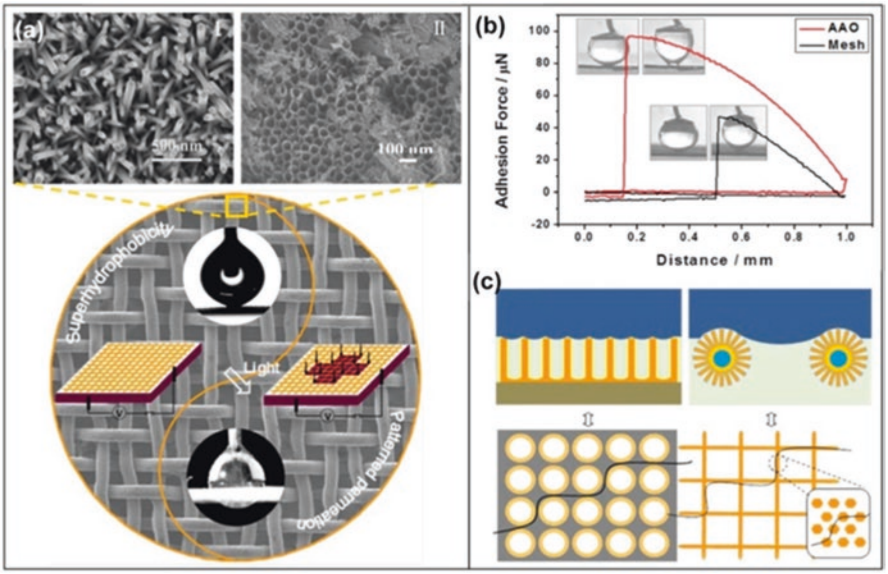

Fig. 5.12 (**a**) Photoelectric cooperative liquid patterning permeation based on the superhydrophobic mesh coated with nanorod array (I) and nanotube array (II). (**b**–**c**) The adhesion force of the ZnO mesh film and TiO_2/AAO nanopore array and schematic adhesion mechanism (Guo et al. 2014a, b)

5.4 Conclusions and Outlook

In this chapter, the recent research and applications of the external field responsive surface wettability and the related applications have been briefly summarized. The topics mainly include electric-responsive surface for irreversible and reversible electrowetting on the rough surface and the related applications such as liquid actuation, adhesion control, optical devices, liquid separation, particles manipulation and patterning. Despite much progress in these fields, there are many challenges in this field to improve the reversible responsive performances and extend their practical applications.

Reversible electrowetting is the pursue in many applications, stable superhydrophobic surface with low adhesion is one of the good candidates for reversible electrowetting, which can be improved by minimization of the undesirable energy consumption based on optimizing the design and modification of the micro/nanostructure layer. Multiphase system, e.g., liquid/liquid/solid tri-phase system, is another way expected to develop a low hysteresis surface for the reversible electrowetting and related applications.

The stability of the surface structure and functionality against external field damage including mechanical stress and chemical contamination should be considered for electrowetting and photoelectric cooperative wetting-based related research and application.

Multi-field cooperation control interface might be developed a trend to control the wetting and moving behavior of microscale objects such as microdroplet, cell and particle, and would also play more important role in optical devices, biomedical facilities, and other related applications in the future.

Acknowledgments The authors are grateful for financial support from the Chinese National Natural Science Foundation (21671012, 21373001, 21601013), Beijing Natural Science Foundation (2172033), the 973 Program (2013CB933004), the Fundamental Research Funds for the Central Universities, and the 111 Project (B14009).

References

Ahuja A, Taylor JA, Lifton V, Sidorenko AA, Salamon TR, Lobaton EJ, Kolodner P, Krupenkin TN (2008) Nanonails: a simple geometrical approach to electrically tunable superlyophobic surfaces. Langmuir 24:9–14

Anantharaju N, Panchagnula MV, Vedantam S (2009) Asymmetric wetting of patterned surfaces composed of intrinsically hysteretic materials. Langmuir 25:7410–7415

Aussillous P, Quere D (2001) Liquid marbles. Nature 411:924–927

Bahadur V, Garimella SV (2009) Preventing the Cassie-Wenzel transition using surfaces with non-communicating roughness elements. Langmuir 25:4815–4820

Barberoglou M, Zorba V, Pagozidis A, Fotakis C, Stratakis E (2010) Electrowetting properties of micro/nanostructured black silicon. Langmuir 26:13007–13014

Berge B (1993) Electrocapilarity and wetting of insulator film by water. C R Acad Sci II 317:157–163

Berge B, Peseux J (2000) Variable focal lens controlled by an external voltage: an application of electrowetting. Eur Phys J E 3:159–163

Bhat K, Heikenfeld J, Agarwal M, Lvov Y, Varahramyan K (2007) Nonwoven electrowetting textiles. Appl Phys Lett 91:024103

Bormashenko E, Pogreb R, Balter S, Aurbach D (2013) Electrically controlled membranes exploiting Cassie-Wenzel wetting transitions. Sci Rep 3:UNSP3028

Bormashenko E, Pogreb R, Bormashenko Y, Aharoni H, Shulzinger E, Grinev R (2015) Progress in low voltage reversible electrowetting with lubricated polymer honeycomb substrates. RSC Adv 5:32491–32496

Brown CV, Wells GG, Newton MI, McHale G (2009) Voltage-programmable liquid optical interface. Nat Photon 3:403–405

Chen TH, Chuang YJ, Chieng CC, Tseng FGJ (2007) A wettability switchable surface by microscale surface morphology change. Micromech Microeng 17:489–495

Chiou PY, Moon H, Toshiyoshi H, Kim CJ, Wu MC (2003) Light actuation of liquid by optoelectrowetting. Sens Actuators A 104:222–228

Chiou PY, Ohta AT, Wu MC (2004) Toward all optical lab-on-a-chip system: optical manipulation of both microfluid and microscopic particles. Proc of SPIE 5514:73–81

Chiou PY, Ohta AT, Wu MC (2005) Massively parallel manipulation of single cells and microparticles using optical images. Nature 436:370–372

Chuang HS, Kumar A, Wereley ST (2008) Open optoelectrowetting droplet actuation. Appl Phys Lett 93:064104

Chung SK, Ryu K, Cho SK (2009) Electrowetting propulsion of water-floating objects. Appl Phys Lett 95:014107

Crevoisier GD, Fabre P, Corpart JM, Leibler L (1999) Switchable tackiness and wettability of a liquid crystalline polymer. Science 285:1246–1249

Derby B (2010) Inkjet printing of functional and structural materials: fluid property requirements, feature stability, and resolution. Annu Rev Mater Res 40:395–414

Dhindsa MS, Smith NR, Heikenfeld J, Rack PD, Fowlkes JD, Doktycz MJ, Melechko AV, Simpson ML (2006) Reversible electrowetting of vertically aligned superhydrophobic carbon nanofibers. Langmuir 22:9030–9034

Fan X, Li X, Tian DL, Zhai J, Jiang L (2012) Optoelectrowettability conversion on superhydrophobic CdS QDs sensitized TiO_2 nanotubes. J Colloid Interface Sci 366:1–7

Feng XJ, Jiang L (2006) Design and creation of superwetting/antiwetting surfaces. Adv Mater 18:3063–3078

Gaudet M, Arscott S (2012) Optical actuation of microelectromechanical systems using photoelectrowetting. Appl Phys Lett 100:224103

Giraldo A, Aubert J, Bergeron N, Derckx E, Feenstra BJ, Massard R, Mans J, Slack A, Vermeulen P (2010) Transmissive electrowetting-based displays for portable multimedia devices. J Soc Inf Display 18:317–325

Girault HH (2006) Electrowetting: shake, rattle and roll. Nat Mater 5:851–852

Gong TY, Marr DWM (2004) Photon-directed colloidal crystallization. Appl Phys Lett 85:3760–3762

Gonzalez-Macia L, Morrin A, Smyth MR, Killard AJ (2010) Advanced printing and deposition methodologies for the fabrication of biosensors and biodevices. Analyst 135:845–867

Guo ZY, Zhang XF, Zheng X, Liu ZY, Cai JH, Tian DL, Li WX, Zhai J, Song YL, Jiang L (2014a) Patterned liquid permeation through the TiO_2 nanotube array coated Ti mesh by photoelectric cooperation for liquid printing. J Mater Chem A 2:2498–2503

Guo ZY, Zheng X, Tian DL, Song YL, Zhai J, Zhang XF, Li WX, Wang XL, Dou SX, Jiang L (2014b) Photoelectric cooperative patterning of liquid permeation on the micro/nano hierarchically structured mesh film with low adhesion. Nanoscale 6:12822–12827

Hagedon M, Yang S, Russell A, Heikenfeld J (2012) Bright e-paper by transport of ink through a white electrofluidic imaging film. Nat Commun 3:1173

Han ZJ, Tay B, Tan CM, Shakerzadeh M, Ostrikov K (2009) Electrowetting control of Cassie-to-Wenzel transitions in superhydrophobic carbon nanotube-based nanocomposites. ACS Nano 3:3031–3036

Hao C, Liu Y, Chen X, He Y, Li Q, Li KY (2014) Electrowetting on liquid-infused film (ewolf): complete reversibility and controlled droplet oscillation suppression for fast optical imaging. Sci Rep 4:6846

Hart JP, Wring SA (1997) Recent developments in the design and application of screen-printed electrochemical sensors for biomedical, environmental and industrial analyses. Trac-Trend Anal Chem 16:89–103

Hayes RA, Feenstra BJ (2003) Video-speed electronic paper based on electrowetting. Nature 425:383–385

Hayward RC, Saville DA, Aksay IA (2000) Electrophoretic assembly of colloidal crystals with optically tunable micropatterns. Nature 404:56–59

Heikenfeld J, Zhou K, Kreit E, Raj B, Yang S, Sun B, Milarcik A, Clapp L, Schwartz R (2009) Electrofluidic displays using Young-Laplace transposition of brilliant pigment dispersions. Nat Photon 3:292–296

Heng LP, Li J, Li MC, Tian DL, Fan LZ, Jiang L, Tang BZ (2014) Ordered honeycomb structure surface generated by breath figures for liquid reprography. Adv Funct Mater 24:7241–7248

Herbertson DL, Evans CR, Shirtcliffe NJ, McHale G, Newton MI (2006) Electrowetting on superhydrophobic SU-8 patterned surfaces. Sensor Actuat A-Phys 130:189–193

Hwang H, Park JK (2011) Optoelectrofluidic platforms for chemistry and biology. Lab Chip 11:33–47

Inui N (2007) Relationship between contact angle of liquid droplet and light beam position in optoelectrowetting. Sens Actuators A 140:123–130

Jamshidi A, Pauzauskie PJ, Schuck PJ, Ohta AT, Chiou PY, Chou J, Yang PD, Wu MC (2008) Dynamic manipulation and separation of individual semiconducting and metallic nanowires. Nat Photon 2:85–86

Kakade BA (2013) Chemical control of superhydrophobicity of carbon nanotube surfaces: droplet pinning and electrowetting behavior. Nanoscale 5:7011–7016

Kalyanasundaram K, Grätzel M (1998) ChemInform abstract: applications of functionalized transition metal complexes in photonic and optoelectronic devices. Coord Chem Rev 177:347–414

Kaufmann T, Ravoo BJ (2010) Stamps, inks and substrates: polymers in microcontact printing. Polym Chem 1:371–378

Kilaru MK, Heikenfeld J, Lin G, Mark JE (2007) Strong charge trapping and bistable electrowetting on nanocomposite fluoropolymer: $BaTiO_3$ dielectrics. Appl Phys Lett 90:212906

Kim DY, Steckl AJ (2007) Liquid-state field-effect transistors using electrowetting. Appl Phys Lett 90:043507

Krebs FC (2009) Polymer solar cell modules prepared using roll-to-roll methods: knife-over-edge coating, slot-die coating and screen printing. Sol Energy Mater Sol Cells 93:465–475

Krupenkin T, Taylor JA (2011) Reverse electrowetting as a new approach to high-power energy harvesting. Nat Commun 2:448

Krupenkin TN, Taylor JA, Schneider TM, Yang S (2004) From rolling ball to complete wetting: the dynamic tuning of liquids on nanostructured surfaces. Langmuir 20:3824–3827

Krupenkin T, Taylor JA, Kolodner P, Hodes M (2005) Electrically tunable superhydrophobic nanostructured surfaces. Bell Labs Tech J 10:161–170

Krupenkin TN, Taylor JA, Wang EN, Kolodner P, Hodes M, Salamon TR (2007) Reversible wetting-dewetting transitions on electrically tunable superhydrophobic nanostructured surfaces. Langmuir 23:9128–9133

Kuiper S, Hendriks BHW (2004) Variable-focus liquid lens for miniature cameras. Appl Phys Lett 85:1128–1130

Kumar A, Kwon JS, Williams SJ, Green NG, Yip NK, Wereley ST (2010) Optically modulated electrokinetic manipulation and concentration of colloidal particles near an electrode surface. Langmuir 26:5262–5272

Kumari N, Garimella SV (2011) Electrowetting-induced dewetting transitions on superhydrophobic surfaces. Langmuir 27:10342–10346

Kwon G, Kota AK, Li YX, Sohani A, Mabry JM, Tuteja A (2012a) On-demand separation of oil-water mixtures. Adv Mater 24:3666–3671

Laird ED, Bose RK, Qi H, Lau KKS, Li CY (2013) Electric field-induced, reversible lotus-to-rose transition in nanohybrid Shish Kebab paper with hierarchical roughness. ACS Appl Mater Interfaces 5:12089–12098

Lapierre F, Thomy V, Coffinier Y, Blossey R, Boukherroub R (2009) Reversible electrowetting on superhydrophobic double-nanotextured surfaces. Langmuir 25:6551–6558

Lee MW, Lin YH, Lee GB (2010) Manipulation and patterning of carbon nanotubes utilizing optically induced dielectrophoretic forces. Microfluid Nanofluid 8:609–617

Lee MW, Latthe SS, Yarin AL, Yoon SS (2013) Dynamic electrowetting-on-dielectric (DEWOD) on unstretched and stretched teflon. Langmuir 29:7758–7767

Li XM, Reinhoudt D, Crego-Calama M (2007) What do we need for a superhydrophobic surface? A review on the recent progress in the preparation of superhydrophobic surfaces. Chem Soc Rev 36:1350–1368

Lifton VA, Simon S, Frahm RE (2005) Reserve battery architecture based on superhydrophobic nanostructured surfaces. Bell Labs Tech J 10:81–85

Lifton VA, Taylor JA, Vyas B, Kolodner P, Cirelli R, Basavanhally N, Papazian A, Frahm R, Simon S, Krupenkin T (2008) Superhydrophobic membranes with electrically controllable permeability and their application to "smart" microbatteries. Appl Phys Lett 93:043112

Lin X, Lu F, Chen YN, Liu N, Cao YZ, Xu LX, Zhang WF, Feng L (2015) Electricity-induced switchable wettability and controllable water permeation based on 3D copper foam. Chem Commun 51:16237–16240

Lippmann G (1875) Relations entre les phenomenes electriques et capillaries. Ann Chim Phys 5:494

Liu MJ, Zheng YM, Zhai J, Jiang L (2010a) Bioinspired super-antiwetting interfaces with special liquid-solid adhesion. Acc Chem Res 43:368–377

Liu MJ, Nie FQ, Wei ZX, Song YL, Jiang L (2010b) In situ electrochemical switching of wetting state of oil droplet on conducting polymer films. Langmuir 26:3993–3997

Liu KS, Cao MY, Fujishima A, Jiang L (2014) Bio-inspired titanium dioxide materials with special wettability and their applications. Chem Rev 114:10044–10094

Liu MJ, Wang ST, Jiang L (2017) Nature-inspired superwettability systems. Nat Rev Mater 2:17036

Manakasettharn S, Taylor JA, Krupenkin TN (2011) Bio-inspired artificial iridophores based on capillary origami: fabrication and device characterization. Appl Phys Lett 99:852–411

McHale G, Newton MI (2011) Liquid marbles: principles and applications. Soft Matter 7:5473–5481

McHale G, Herbertson DL, Elliott SJ, Shirtcliffe NJ, Newton MI (2007) Electrowetting of nonwetting liquids and liquid marbles. Langmuir 23:918–924

McHale G, Elliott SJ, Newton MI, Herbertson DL, Esmer K (2009) Levitation-free vibrated droplets: resonant oscillations of liquid marbles. Langmuir 25:529–533

McHale G, Brown CV, Sampara N (2013) Voltage-induced spreading and superspreading of liquids. Nat Commun 4:1605

Moon JK, Jeong J, Lee D, Pak HK (2013) Electrical power generation by mechanically modulating electrical double layers. Nat Commun 4:1487

Morita M, Koga T, Otsuka H, Takahara A (2005) Macroscopic-wetting anisotropy on the line-patterned surface of fluoroalkylsilane monolayers. Langmuir 21:911–918

Mugele F, Baret JC (2005) Electrowetting: from basics to applications. J Phys Condens Matter 17:R705–R774

Nagappan S, Ha CS (2015) Emerging trends in superhydrophobic surface based magnetic materials: fabrications and their potential applications. J Mater Chem A 3:3224–3251

Nakamura Y, Kamada K, Katoha Y, Watanabe A (1973) Studies on secondary electrocapillary effects. i. The confirmation of young-duprè equation. J Colloid Interface Sci 44:517–524

Newton MI, Herbertson DL, Elliott SJ, Shirtcliffe NJ, McHale G (2007) Electrowetting of liquid marbles. J Phys D Appl Phys 40:20–24

Öner D, McCarthy TJ (2000) Ultrahydrophobic surfaces. Effects of topography length scales on wettability. Langmuir 16:7777–7782

Oroszi L, Dér A, Kirei H, Ormos P, Rakovics V (2006) Control of electro-osmostic flow by light. Appl Phys Lett 89:263508

Ozkan M, Bhatia S, Esener SC (2002) Optical addressing of polymer beads in microdevices. Sens Mater 14:189–197

Park SY, Teitell MA, Chiou EPY (2010) Single-sided continuous optoelectrowetting (SCOEW) for droplet manipulation with light patterns. Lab Chip 10:1655–1661

Pei SN, Valley JK, Wang YL, Wu MC (2015) Distributed circuit model for multi-color light-actuated opto-electrowetting microfluidic device. J Lightwave Technol 33:3486–3493

Pellat H (1895) Mesure de la force agissant sur les die'lectriques liquids non e'lectrise's place's dans un champ e'litrique. C R Acad Sci Paris 119:691–694

Perelaer J, Smith PJ, Mager D, Soltman D, Volkman SK, Subramanian V, Korvinkdf JG, Schubert US (2010) Printed electronics: the challenges involved in printing devices, interconnects, and contacts based on inorganic materials. J Mater Chem 20:8446–8453

Powell MR, Cleary L, Davenport M, Shea KJ, Siwy ZS (2011) Electric-field-induced wetting and dewetting in single hydrophobic nanopores. Nat Nanotechnol 6:798–802

Prins MWJ, Welters WJJ, Weekamp JW (2001) Fluid control in multichannel structures by electrocapillary pressure. Science 291:277–280

Quéré D (2008) Wetting and roughness. Annu Rev Mater Res 38:71–99

Roach P, Shirtcliffe NJ, Newton MI (2008) Progess in superhydrophobic surface development. Soft Matter 4:224–240

Rogers JA (2008) Optoelectronic tweezers-organizing nanowires. Nat Photon 2:69–70

Schlettwein D, Oekermann T, Yoshida T, Tochimoto M, Minoura H (2000) Photoelectrochemical sensitisation of ZnO–tetrasulfophthalocyaninatozinc composites prepared by electrochemical self-assembly. J Electroanal Chem 481:42–51

Smith NR, Abeysinghe DC, Haus JW, Heikenfeld J (2006) Agile wide-angle beam steering with electrowetting microprisms. Opt Express 14:6557–6563

Snaith HJ, Schmidt-Mende L (2007) Advances in liquid-electrolyte and solid-state dye-sensitized solar cells. Adv Mater 19:3187–3200

Su B, Guo W, Jiang L (2015) Learning from nature: binary cooperative complementary nanomaterials. Small 11:1072–1096

Sun TL, Feng L, Gao XF, Jiang L (2005) Bioinspired surfaces with special wettability. Acc Chem Res 38:644–652

Tawfick S, De Volder M, Copic D, Park SJ, Oliver CR, Polsen ES, Roberts MJ, Hart AJ (2012) Engineering of micro- and nanostructured surfaces with anisotropic geometries and properties. Adv Mater 24:1628–1674

Tian DL, Chen QW, Nie FQ, Xu JJ, Song YL, Jiang L (2009) Patterned wettability transition by photoelectric cooperative and anisotropic wetting for liquid reprography. Adv Mater 21:3744–3749

Tian DL, Zhai J, Song YL, Jiang L (2011) Photoelectric cooperative induced wetting on aligned-nanopore arrays for liquid reprography. Adv Funct Mater 21:4519–4526

Tian DL, Song YL, Jiang L (2013) Patterning of controllable surface wettability for printing techniques. Chem Soc Rev 42:5184–5209

Tian Y, Su B, Jiang L (2014a) Interfacial material system exhibiting superwettability. Adv Mater 26:6872–6897

Tian DL, Guo ZY, Wang YL, Li WX, Zhang XF, Zhai J, Jiang L (2014b) Phototunable underwater oil adhesion of micro/nanoscale hierarchical-structured ZnO mesh films with switchable contact mode. Adv Funct Mater 24:536–542

Tian DL, He LL, Zhang N, Zheng X, Dou YH, Zhang XF, Guo ZY, Jiang L (2016) Electric field and gradient microstructure for cooperative driving of directional motion of underwater oil droplets. Adv Funct Mater 26:7986–7992

Valley JK, Swinton P, Boscardin WJ, Lue TF, Rinaudo PF, Wu MC, Garcia MM (2010) Preimplantation mouse embryo selection guided by light-induced dielectrophoresis. PLoS One 5:e10160

Verheijen HJJ, Prins MWJ (1999) Reversible electrowetting and trapping of charge: model and experiments. Langmuir 15:6616–6620

Verplanck N, Galopin E, Camart JC, Thomy V, Coffinier Y, Boukherrou (2007) Reversible electrowetting on superhydrophobic silicon nanowires. Nano Lett 7:813–817

Wang Z, Ci L, Chen L, Nayak S, Ajayan PM, Koratkar N (2007) Polarity-dependent electrochemically controlled transport of water through carbon nanotube membranes. Nano Lett 7:697–702

Wang ZQ, Wang FC, Zhao YP (2012) Tap dance of a water droplet. Proc R Soc A 468:2485–2495

Wang ST, Liu KS, Yao X, Jiang L (2015) Bioinspired surfaces with superwettability: new insight on theory, design, and applications. Chem Rev 115:8230–8293

Wen L, Tian Y, Jiang L (2015) Bioinspired super-wettability from fundamental research to practical applications. Angew Chem Int Ed 54:3387–3399

Weng B, Shepherd RL, Crowley K, Killard AJ, Wallace GG (2010) Printing conducting polymers. Analyst 135:2779–2789

Wheeler AR (2008) Chemistry-putting electrowetting to work. Science 322:539–540

Williams SJ, Kumar A, Wereley ST (2008) Electrokinetic patterning of colloidal particles with optical landscapes. Lab Chip 8:1879–1882

Williams SJ, Kumar A, Green NG, Wereley ST (2009) A simple, optically induced electrokinetic method to concentrate and pattern nanoparticles. Nanoscale 1:133–137

Wu MC (2011) Optoelectronic tweezers. Nat Photon 5:322–324

Xia F, Jiang L (2008) Bio-inspired, smart, multiscale interfacial materials. Adv Mater 20:2842–2858

Xia F, Ge H, Hou Y, Sun TL, Chen L, Zhang GZ, Jiang L (2007) Multiresponsive surfaces change between superhydrophilicity and superhydrophobicity. Adv Mater 19:2520–2524

Xia DY, Johnson LM, López GP (2012) Anisotropic wetting surfaces with one-dimesional and directional structures: fabrication approaches, wetting properties and potential applications. Adv Mater 24:1287–1302

Xin BW, Hao JC (2010) Reversibly switchable wettability. Chem Soc Rev 39:769–782

Xue Y, Markmann J, Duan H, Weissmueller J, Huber P (2014) Switchable imbibition in nanoporous gold. Nat Commun 5:4237

Yan RX, Gargas D, Yang PD (2009) Nanowire photonics. Nat Photon 3:569–576

Yang S, Krupenkin TN, Mach P, Chandross EA (2003) Tunable and latchable liquid microlens with photopolymerizable components. Adv Mater 15:940–943

Yao X, Song YL, Jiang L (2011) Applications of bio-inspired special wettable surfaces. Adv Mater 23:719–734

Yao X, Hu Y, Grinthal A, Wong TS, Mahadevan L, Aizenberg J (2013) Adaptive fluid-infused porous films with tunable transparency and wettability. Nat Mater 12:529–534

Yu X, Wang ZQ, Jiang YG, Shi F, Zhang X (2005) Reversible pH-responsive surface: from superhydrophobicity to superhydrophilicity. Adv Mater 17:1289–1293

Yu TM, Yang SM, Fu CY, Liu MH, Hsu L, Chang HY, Liu CH (2013) Integration of organic opto-electrowetting and poly(ethylene) glycol diacrylate (PEGDA) microfluidics for droplets manipulation. Sensors Actuators B Chem 180:35–42

Zhang JL, Han YC (2010) Active and responsive polymer surfaces. Chem Soc Rev 39:676–693

Zhang JH, Yang B (2010) Patterning colloidal crystals and nanostructure arrays by soft lithography. Adv Funct Mater 20:3411–3424

Zhang X, Shi F, Niu J, Jiang YG, Wang ZQ (2008) Superhydrophobic surfaces: from structural control to functional application. J Mater Chem 18:621–633

Zhao XD, Fan HM, Luo J, Ding J, Liu XY, Zou BS, Feng YP (2011) Electrically adjustable, super adhesive force of a superhydrophobic aligned MnO_2 nanotube membrane. Adv Funct Mater 21:184–190

Zheng X, Guo ZY, Tian DL, Zhang XF, Jiang L (2016) Electric field induced switchable wettability to water on the polyaniline membrane and oil/water separation. Adv Mater Interfaces 3:1600461

Zhu L, Xu J, Xiu Y, Sun Y, Hess DW, Wong CP (2006) Electrowetting of aligned carbon nanotube films. J Phys Chem B 110:15945–15950

Chapter 6
Liquids on Shape-Tunable Wrinkles

Takuya Ohzono

Abstract It is well known that the microstructures of solid surfaces greatly affect the states of liquids in contact. Here, as a simple model system of the microstructures, we focus on buckling-based self-organized wrinkle structures and show the various phenomena and states of liquids on the wrinkles. Since the typical wrinkles have a shallow sinusoidal shape as the cross section, they are not suitable to induce the super-hydrophobicity and super-hydrophilicity, which are usually based on structures with a high-aspect ratio, for example, needles. Although most of such highly structured surfaces are not transformable, our wrinkles are shape-tunable, in which the wrinkle groove depth or orientation can be altered by simply adjusting the applied strain to the sample. Using this shape-tunability, the capillary phenomena of liquids on wrinkle grooves can be controlled. The basic physics of this phenomenon is discussed in terms of the balance between interfacial energies related to the stability of the liquid shapes. Thus, a general condition for the capillary action on sinusoidal grooves has been obtained and supported by experiments, in which the effects of depth of the grooves and contact angles are evaluated. As examples of further application based on this phenomenon, micro-patterning methods are shown such as directed polymer phase separation on grooves, gold nano-ribbon formation on liquid filaments, and novel periodic pattern formations in liquid crystals confined in the grooves.

Keywords Capillary phenomena · Wrinkles · Liquid patterning · Liquid crystals · Gold nano-ribbons · Phase separated polymer patterns

---

T. Ohzono (✉)
Electronics and Photonics Research Institute, National Institute of Advanced Industrial Science and Technology (AIST), Tsukuba, Japan
e-mail: ohzono-takuya@aist.go.jp

A. Hozumi et al. (eds.), *Stimuli-Responsive Dewetting/Wetting Smart Surfaces and Interfaces*, Biologically-Inspired Systems 11,
https://doi.org/10.1007/978-3-319-92654-4_6

6.1 Introduction

Ordered patterns, such as stripes and dots, are ubiquitous in nature (Ball 2001). Especially on the biological surface, their patterns have various functions. For example, stripe patterns of colors found on zebrafish may work as a camouflage cloth or send an alert to predators. More interestingly, their topological patterns/structures exhibit functions relating to the physical contacts to the other objects including solids, air, and liquids (Fig. 6.1). The microstructure of our fingerprints is important for tactile sensing and grips in contact with solid objects (Scheibert et al. 2009). The special corrugated topography found at the wings of dragonflies has superb aerodynamic performance for low Reynolds number flight (Hu and Tamai 2008). The self-cleaning properties known as the lotus effect is based on the superhydrophobicity (Barthlott and Neinhuis 1997) as exhibited by some plant leaves, where the liquid droplets easily fall down owing to the high contact angle; dewetting state. By leaning from these biological functions, the surface technology has also developed, which is recognized as the biomimetic approach. Especially owing to the developments of the observation methods, for example, scanning electron microscopy, atomic force microscopy, and super-resolution optical microscopies, the correlations between the microstructrues/microtextures and the functions have been revealed. Once we know the relationships between the structure and the functions and the mechanism behind them, it is easy to optimize the system for specific

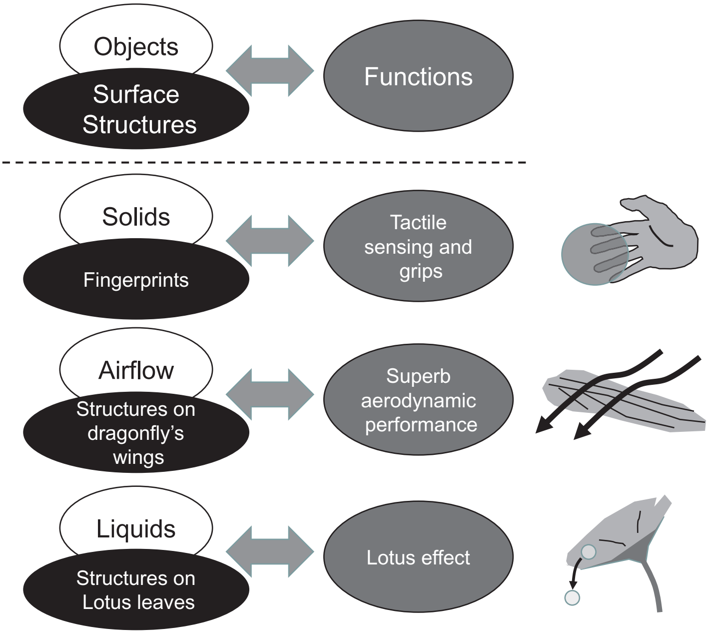

Fig. 6.1 Schematic for relationship between surface structures and functions relating to the physical contacts to the other objects including solids, air, and liquids

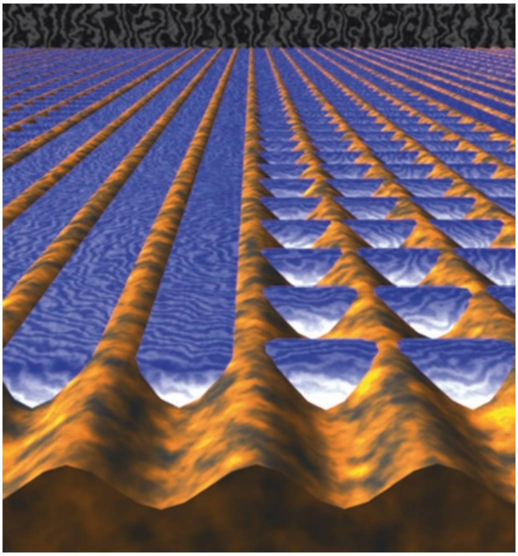

Fig. 6.2 Schematic for liquids on open microgrooves stabilized by capillary force

purposes and to extend the system beyond the biological one. One of such trends may introduce/improve the tunability of the states of functions, for example, the switching ability between wetting and dewetting states, which is the central topic of this monograph, the stimuli-responsive wetting/dewetting properties.

In the present chapter, the attempts to tune the wetting state by changing the microstructures owing to the mechanical stimuli applied on the surface are shown. Especially, we focus on the capillary phenomena on open microgrooves (Fig. 6.2). Using shape-tunable microgrooves, which are based on the self-organized wrinkles, the capillary phenomena on the open microgrooves can be studied in detail. Moreover, as examples of applications based on this capillary phenomenon, micropatterning methods are shown such as directed polymer phase separation on grooves, gold nano-ribbon formation on liquid filaments, and novel periodic pattern formations in liquid crystals confined in the grooves.

6.2 Shape-Tunable Wrinkles

In this section, the basic properties of the wrinkles are reviewed. We here use the term, wrinkles, as a surface with periodic undulations formed through mechanical instability, such as Euler's buckling. Euler's buckling is a phenomenon that occurs during the bending of a plate or a beam under lateral compressive strain. The simplest form of a free plate after buckling under lateral uniaxial stress is approximately half a sine wave with a spatial wavelength double that of the total length of the plate in the stress direction. When the plate is supported by a compliant elastic

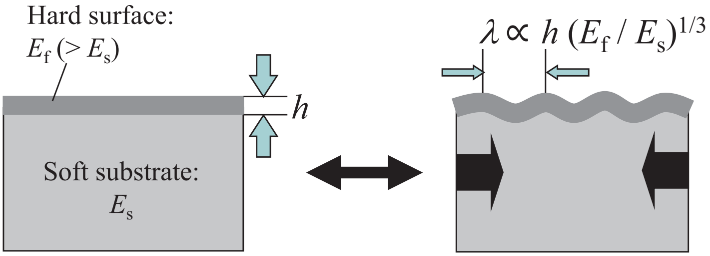

Fig. 6.3 Schematics for the wrinkle system. The structure required for wrinkle formation. The hard surface layer is supported by a soft elastic substrate. Wrinkles form on this structure under lateral compressive strain

or viscoelastic substrate, the resultant spatial wavelength (periodicity) of the wrinkles is reduced and depends on the relative modulus of the plate and soft substrate (Fig. 6.3). This is expressed as $\lambda \propto h\,(E_f/E_s)^{1/3}$, where λ is the wavelength, h is the thickness of the plate, E_f and E_s are the Young's modulus of the plate and the soft substrate (which is thicker than the plate), respectively (Allen 1969; Huang et al. 2004, 2005; Bowden et al. 1998, 1999; Chua et al. 2000; Huck et al. 2000; Moldovan and Golubovic 1999; Sridhar et al. 2001; Huang and Suo 2002; Yoo and Lee 2003; Yoo et al. 2004; Stafford et al. 2004; Harrison et al. 2004; Uchida 2005; Scherf and List 2002; Genzer and Groenewold 2006; Khang et al. 2006; Sun et al. 2006; Watanabe et al. 2002; Okayasu et al. 2004; Edmondson et al. 2006; Nolte et al. 2005; Lin and Yang 2007; Yang et al. 2010; Holmes and Crosby 2010; Hobbie et al. 2010; Hyun et al. 2011; Brau et al. 2011; Vendeparre et al. 2007; Uchida and Ohzono 2010).

The wrinkles with various length scales can be found in nature. The wrinkles on the surface of an animal's body are a familiar example; the relatively hard skin supported by the soft inner tissue can wrinkle under compressive stress. The surface of a paved road may wrinkle because of the expansion of the top hard surface as it heats up in strong sunlight. A similar phenomenon occurs in oil paintings; environmental damage causes the hard surface to expand or the base to shrink. Wrinkle formation is sometimes an irreversible process, such as plastic deformation of a hard skin layer and delamination of a hard layer from a soft substrate. Although irreversible processes are important in practice, in this study we will consider a simple system, where they are minimal.

Microwrinkle systems have been extensively studied in recent years (Huang et al. 2004, 2005; Bowden et al. 1998, 1999; Chua et al. 2000; Huck et al. 2000; Moldovan and Golubovic 1999; Sridhar et al. 2001; Huang and Suo 2002; Yoo and Lee 2003; Yoo et al. 2004; Stafford et al. 2004; Harrison et al. 2004; Uchida 2005; Scherf and List 2002; Genzer and Groenewold 2006; Khang et al. 2006; Sun et al. 2006; Watanabe et al. 2002; Okayasu et al. 2004; Edmondson et al. 2006; Nolte et al. 2005; Lin and Yang 2007; Yang et al. 2010; Holmes and Crosby 2010; Hobbie et al. 2010; Hyun et al. 2011; Brau et al. 2011; Vendeparre et al. 2007; Uchida and Ohzono 2010). Wrinkles with macroscopic wavelengths may not be technologically

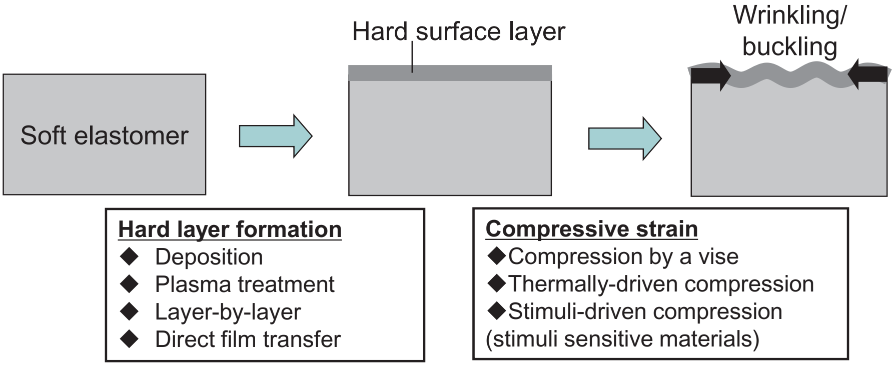

Fig. 6.4 Several methods for preparing microwrinkles

useful; however, microwrinkles with wavelengths in the nanometer to micrometer order have potential utility in various fields of technology. These surface microstructures are spontaneously formed through a mechanical self-organization process without conventional lithographic techniques, and have many potential practical applications in optical devices, microfluidic devices, cell culture substrates, thin film devices such as flexible electronics, and tribological surface materials.

Microwrinkles are fabricated using a thin film, typically several tens (or hundreds) of nanometers thick, which is supported by a relatively soft substrate. The wavelength of the wrinkles is determined by the thickness of the hard film and the mechanical properties of the hard film and the soft substrate. Therefore, in principle microwrinkle structures can be produced in various kinds of technologically important materials (Fig. 6.4). There are four main methods for film fabrication. (1) Direct deposition of metals, such as Au and Pt on to a soft elastic substrate is the most common method. Dip-coating, spin coating, and various plating methods can also be used for the deposition of inorganic and organic materials. (2) A hard skin layer which acts as the thin film can be produced by surface modification of silicone rubber by mild oxygen plasma treatment. Active oxygen species generated by the plasma treatment transform the soft silicone surface into a hard, silica-like skin through chemical degradation. (3) The layer-by-layer method can be used to form a thin film of ionic polymers (Sharp and Jones 2002). (4) Self-supporting thin organic and inorganic films, which are prepared separately (Vendamme et al. 2006), can be transferred onto a soft substrate to form hetero-structures. All these methods allow the film thickness to be controlled on the nanometer scale, and thus the wavelength of the microwrinkles is easily controlled; the typical range is between a few hundred nanometers and hundred micrometers. The wrinkles are formed by the exertion of lateral compressive strain or stress (Figs. 6.3 and 6.4).

In the experiments presented in this chapter, the poly(dimethylsiloxane) (PDMS) elastomers were mainly used as the soft substrate. For experiments of liquid manipulation and liquid crystal alignment using the shape-tunability of microwrinkles, the polyimide layer was mainly used as the top hard layer, which was prepared through

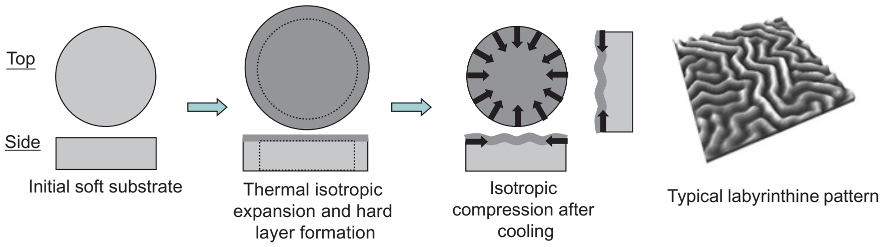

(a) Labyrinthine-like isotropic stripe pattern

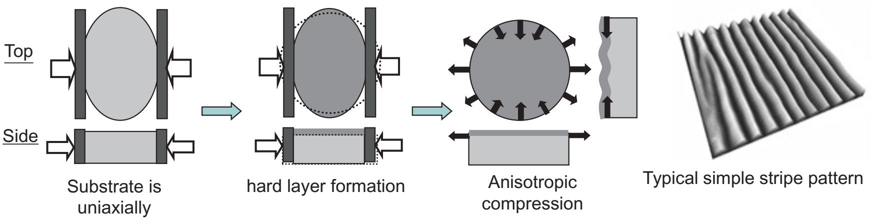

(b) Simple anisotropic stripe pattern

Fig. 6.5 Strain-anisotropy-dependent stripe patterns of wrinkles (**a**) Labyrinthine-like isotropic stripe pattern (**b**) Simple anisotropic stripe pattern

spin-coating the solution. For uniaxial compression of the samples, a small vise was used. For details of the present experiments, refer to their original reports cited at each description.

As mentioned above, the wavelength is determined by the mechanical properties of the hard film and the soft substrate, and by the thickness of the hard film. On the other hand, the pattern of the wrinkles depends on the two-dimensional compressive strain or stress state. Uniaxial strain creates simple patterns of stripes composed of straight crest/groove lines, whereas isotropic strain produces complex labyrinthine or herringbone patterns (Fig. 6.5). Therefore, in principle it is possible to change the orientation of the wrinkles by altering the externally applied strain; the small topographic structures are reversibly changed by the addition of a certain type of strain (Ohzono and Shimomura 2004, 2005a, b, 2006a, b Ohzono et al. 2005, 2007; Watanabe et al. 2007; Vendamme et al. 2007; Ohzono 2008, 2009). If we can reversibly control the surface microstructure, this dynamic system could be applied to optical devices, microfluidic devices, cell culture devices, and thin film devices. In this chapter, we mainly focus on the anisotropic wrinkles (Fig. 6.5b), on which the straight grooves work as the open capillary channels with the tunable groove depth.

In summary, we have reviewed the control of shape-tunable microwrinkles using applied strain. By changing the anisotropy and the absolute value of the applied strain, various transformations of the microwrinkle stripe patterns are possible. Other characteristic features of the transformation are that the wavelength remains almost constant that the process is reversible with small hysteresis. The amplitude, A, of the microwrinkles, which is proportional to the height difference between the crest and the groove bottom, also can be controlled by the strain, s, according to the relation A

$\propto s^{1/2}$ beyond the critical buckling strain. In the next section, the application of shape-tunable microwrinkles to the manipulation of liquid on small scales (de Genne et al. 2003) and various applications toward micropatterning will be described.

6.3 Tunability of the Wetting States and Applications

6.3.1 Tunable Capillary Phenomena Via Change in Groove Depth

Methods of controlling the shape and position of liquids on small scales are important for various applications based on microfluidics (Squires and Quake 2005) and micropatterning (Xia and Whitesides 1998), such as biosensors (van den Heuvel et al. 2006), printable electronics (Sekitani et al. 2009), and photonic materials. Many of these methods rely on the patterning and manipulation of liquids on solids on or below the micrometer scale. Generally, a non-spreading liquid forms a line of contact on a solid, and the triple line has a specific contact angle because of balanced surface tensions in the equilibrium state. The mean curvature of the liquid-air interface is constant and proportional to the Laplace pressure. Thus, the distribution of the contact angle or the Laplace pressure (mean curvature), which can be produced externally or internally, can induce droplet motion (Brzoska et al. 1993; Ichimura et al. 2000; Tersoff et al. 2009; Sumino et al. 2005) or shape deformation (Baret et al. 2005; Khare et al. 2007). Moreover, the dewetting of liquid films (Reiter 1992; Herminghaus et al. 1998; Leopoldes and Damman 2006; Jackman et al. 1998; Gau et al. 1999; Higgins and Jones 2000; Xia et al. 2001; Kargupta and Sharma 2002) and the fingering instability of the receding triple line (Karthaus et al. 1999; Yabu and Shimomura 2005) have been reported as methods for transporting, shaping and patterning liquids on small scales.

Open capillary phenomena have been studied extensively (Wenzel 1936; Cassie and Baxter 1944; Shuttleworth and Bailey 1948; Johnson and Dettre 1964; Lafuma and Quéré 2003; Feng and Jiang 2006; Chung et al. 2007). This type of capillary motion, especially in open microchannels (Khare et al. 2007), is likely to be useful for patterning and shaping liquids into long liquid filaments (LFs), particularly on a small scale. However, there was little published in the literature on this technique because the methods and materials for the *in-situ* control of capillary action were limited. Electrowetting, where the contact angle of a dielectric liquid is modified by applying an electric field, is one such method (Jackman et al. 1998; Gau et al. 1999).

Microwrinkles are suitable for use as an array of open microchannel capillaries because their microtopography is tunable, and therefore allows in situ control of capillary action. In addition, microwrinkles can be easily fabricated over a large area. Based on this idea, we have developed a simple and general method for shaping and patterning various liquids on a micrometer scale (Ohzono et al. 2009).

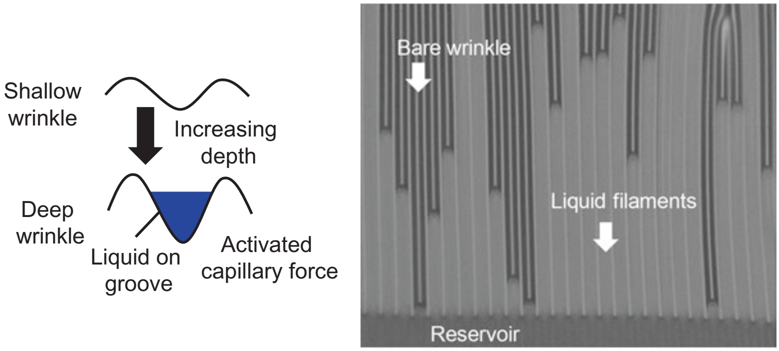

Fig. 6.6 Schematic for the concept of the tunable open capillary using shape-tunable microwrinkles (left) and image of the LFs that fill wrinkle grooves only; crests are left exposed to the air (right)

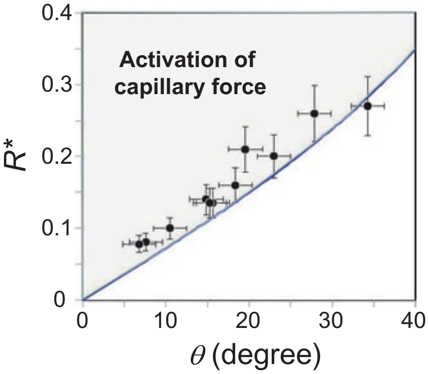

Fig. 6.7 Diagram for capillary-force-induced liquid filaments (LFs) formation with respect to equilibrium contact angle, θ, and the critical aspect ratio, R^*, from theoretical calculations. (Adapted with permission from (Soft Matter, 5 (2009) 4658). Copyright (2009) Royal Society of Chemistry)

Initially, the critical conditions for capillary action were determined (refer to ref. (Ohzono et al. 2009) for experimental details). The capillary action of a large liquid droplet placed on a microwrinkle surface was observed as the groove depth was gradually increased. At a critical point, the liquid started to flow into the wrinkle grooves; the wrinkle crests were still exposed to the air (Fig. 6.6). We have found that the capillary phenomena is generally governed by two key parameters: the equilibrium contact angle, θ, of the liquid on a smooth surface; and the aspect ratio, R, of the microwrinkle groove, which is defined as $R = A/\lambda$. R can be changed by applying compressive strain s perpendicular to the groove direction according to the relation $A \propto s^{1/2}$. The critical aspect ratios of the groove for capillary action, R^*, were determined at each fixed value of θ, which is shown in Fig. 6.7 with theoretical results. To vary θ various combinations of liquids and the chemistries of the wrinkled surface were investigated (Ohzono et al. 2009). In the range of the experimental limits of R (0.08–0.30), R^* for systems with θ in the range of 7–34° were determined, showing monotonic increase with θ. These results suggest that various liquids can be shaped into LFs by adjusting θ through proper surface treatments.

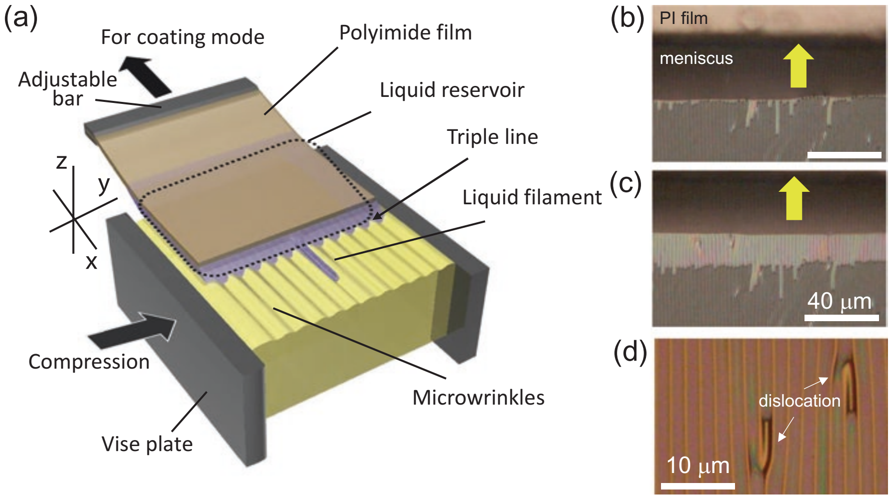

Fig. 6.8 Preparation of a LF array using a simple bar-coating method for large area patterning. (**a**) Schematic of the method. (**b–d**) Optical microscopy images of LF array. Where there are topological defects in the stripe pattern, the grooves are shallow, which leads to unfilled sections of the array. (Adapted with permission from (Soft Matter, 5 (2009) 4658). Copyright (2009) Royal Society of Chemistry)

The obtained critical condition for activation of the capillary force on the sinusoidal groove shown in Fig. 6.7 may be expressed by the function $R^*(\theta) \propto \theta^{\chi}$ was obtained, where χ is a positive constant more than unity. The general condition for capillary phenomena on microwrinkle grooves is important because it also indicates the stability of the liquid filament (LF) on the microwrinkles. Through choosing the parameters (R, θ) we can selectively fill the grooves with liquid to obtain a centimeter-scale LF array, using a simple method, such as bar-coating (Fig. 6.8), in which we do not have to depend on the capillary action of the liquid from a preserver.

Next, we discuss a theoretical model for the present capillary phenomenon on the open channel with sinusoidal grooves. We performed a calculation of the energy variation dE due to the infinitesimal LF growth dx in the x (groove) direction by considering the sinusoidal grooves. The variation is written as $\mathrm{d}E = [\gamma\, l_{\mathrm{lv}} - (\gamma_{\mathrm{sv}} - \gamma_{\mathrm{sl}})\, l_{\mathrm{sl}}]\bullet dx$, where γ is the surface tension of the liquid, $l_{\alpha\beta}$ is the cross-sectional length of the interface specified by the indices (Fig. 6.9), $\gamma_{\alpha\beta}$ is the interfacial tension between phases specified by the indices, and the indices of l, s and v indicate liquid, solid and vapor phases, respectively. Using Young's relation, $\gamma_{\mathrm{sv}} - \gamma_{\mathrm{sl}} = \gamma\cos\theta$, this is rewritten as $\mathrm{d}E = \gamma\,(l_{\mathrm{lv}} - l_{\mathrm{sl}}\cos\theta)\bullet dx = \gamma D\bullet dx$. Since $\gamma > 0$, the sign of D determines the stability of the LF growth. This can be calculated for the sinusoidal grooves as follows.

The wrinkled surface profile is expressed as $z(y,A,\lambda) = \frac{1}{2}A(1\text{-}\cos[2\pi y/\lambda])$ (Fig. 6.9). Since $R = A/\lambda$, the profile can be rewritten as $z(y,R,\lambda) = \frac{1}{2}\lambda R(1\text{-}\cos[2\pi y/\lambda])$. The positive parameter a ($<\lambda/2$) is defined as the y-position of the triple line of the LF along the groove (Fig. 6.9); this determines the width $2a$ of the LF projected on the x-y plane. The liquid is expected to have an equilibrium con-

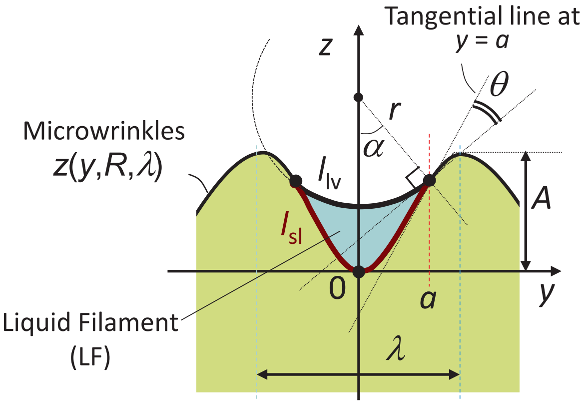

Fig. 6.9 Schematic of the cross section of the wrinkle with a liquid filament. The definitions of the variables for the theoretical model are also shown. (Adapted with permission from (Soft Matter, 5 (2009) 4658). Copyright (2009) Royal Society of Chemistry)

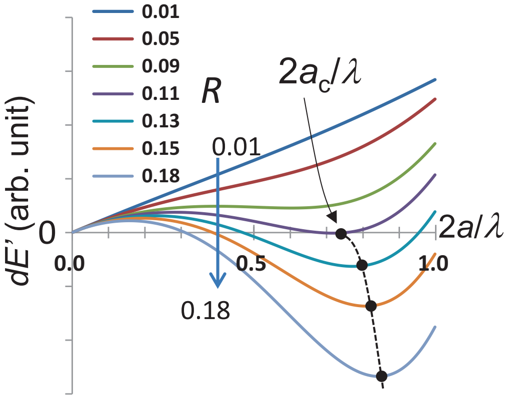

Fig. 6.10 Curves for energy variation due to LF growth dE' vs. $2a/\lambda$ for different values of R with $\theta = 15°$. Local minima with negative dE' indicated by dashed line should be observed for the case of (R,θ). (Adapted with permission from (Soft Matter, 5 (2009) 4658). Copyright (2009) Royal Society of Chemistry)

tact angle θ with respect to the tangential plane of the wrinkle surface. Here, the curvature of the LF in the x-z plane is assumed to be zero. Then, the curvature in the y-z plane is the only other curvature considered, which is expected to have a constant value of $1/r$ and is a function of R, θ, λ and a. Thus, the shape of the cross section including l_{lv} and l_{sl} of the LF is fully specified, provided the geometrical parameters of R, θ, λ and a (Ohzono et al. 2009). Consequently, $dE(R,\theta, a, \lambda)$ (= $\gamma\lambda D(R,\theta, a)\bullet dx$) can be calculated.

In Fig. 6.10, plots of normalised energy variation $dE'(R,\theta, a)$ against the relative width $2a/\lambda$ are shown for different values of R with a fixed θ of 15°, which corresponds to the process along the dashed arrow in Fig. 6.10. As R increases, a local minimum of dE' appears, and it becomes negative at $R \sim 0.11$ and $2a/\lambda \sim 0.72$. This is the theoretical critical aspect ratio R_c for the case of $\theta = 15°$. Although the actual shape of the LF tip is not considered here, the negative dE' implies that the Laplace pressure on the LF becomes negative; the mean curvature becomes negative. The width of the growing LF at the critical point can be determined from the value of $2a$ at the minimum. The theoretical R_c was calculated for various values of θ, which is shown as a solid line in Fig. 6.7. The experimental and theoretical R_c agree with each other. The small deviation of the experimental R_c at larger values is likely due to the experimental difficulty of determining the onset of the LF formation. The force that drives LF growth is proportional to dE' that can be very small near the critical point. Thus, it is difficult to observe the true LF formation near the critical point since it can be too slow to detect on the experimental time scale.

As R further increases, the minimum of $\mathrm{d}E'$ shifts to the larger $2a/\lambda$, which is indicated by the dashed curve in Fig. 6.10. Since the LF is connected to the reservoir with a Laplace pressure of zero, the curvature of the LF, $1/r$, should approach zero. This corresponds to the state at the minimum of $\mathrm{d}E'$. Thus, LFs having a width that gives the minimum energy grow at $R > R_c$. The existence of such a minimum point is a significant feature of the present sinusoidal grooves; for V-shaped grooves, the width of the most stable LF is identical to that of the groove (Khare et al. 2007), where the groove is fully filled with the liquid.

6.3.2 Light-Induced Capillary Phenomena on Wrinkles

The microgrooves of microwrinkles can act as open microchannel capillaries, where only grooves are filled with a liquid. The liquid stabilized in a straight groove is called a liquid filament (LF). For the formation of LFs, the groove morphology and the surface wettability are critical parameters (Fig. 6.7). By changing the morphology, the LF formation can be controlled via capillary. Although the wettability of the liquid is also important for the capillary action, so far the parameter has not been used to change the shape of a liquid on the microwrinkles. For example, if the wettability is enhanced in response to an external stimulus, the capillary action is triggered without changing the morphology of microgrooves.

One way to switch the surface wettability is to exploit the reversible photoisomerization of azobenzene moieties (Seki et al. 1998; Akiyama et al. 2006; Oh et al. 1999, 2001; Jiang et al. 2005; Lim et al. 2006; Yang et al. 2007; Wan et al. 2008; Han et al. 2010). Azobenzene moieties have been paid much attention due to their ease of chemical modifications and their photo-induced structural change between the trans and cis forms. The transformation can change the interfacial properties, and thus, the wetting properties. As a result, manipulation of liquid droplets has been explored on flat solid surfaces possessing azobenzene chromophores (Akiyama et al. 2006; Oh et al. 1999; Yang et al. 2007), where the macroscopic motion of liquids was induced by ultra-violet (UV) and visible (Vis) light irradiation. Thus, this photo-induced switching of the wettability could be used to trigger the capillary action of liquids into microwrinkle grooves. Especially, the precise spatial control of the capillary action is expected by patterned light irradiation (Kikuchi et al. 2009; Glückstad 2004; Liu et al. 2006; Baroud et al. 2007).

Here, we review a technique for preparing micrometer-scale liquid filaments using photoresponsive microwrinkles (Monobe and Ohzono 2012). The wetting characteristics of a microwrinkle surface are switched by light-induced photoisomerization of an azobenzene incorporated in a polymer. The capillary action of

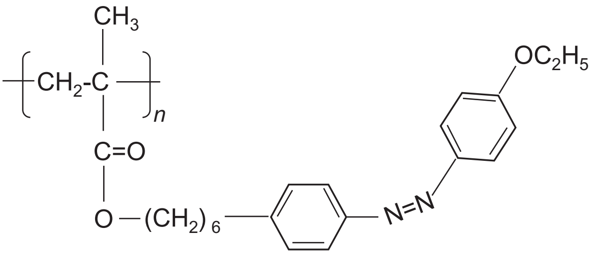

Fig. 6.11 Schematic of a photoresponsive polymer with azobenzene units, Poly{6-[4-(4-ethoxyphenylazo)phenoxy] hexylmethacrylate]}

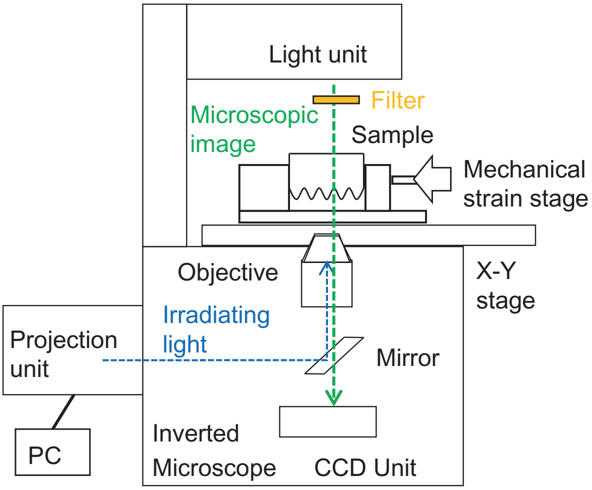

Fig. 6.12 Schematic representation of an inverted optical microscope with a patterned light irradiation apparatus

a liquid into the microgrooves is triggered by the lowered contact angle due to the photoisomerization. Using a micropattern-light-projection apparatus (Kikuchi et al. 2009), liquid filaments (LFs) are formed at desired positions. This point shows a sharp contrast to the previous method, where the spatial control of the liquid filament formation has been difficult because the local control of the exerted strain is technically difficult.

LFs on microgrooves of microwrinkles, which were coated with a photoresponsive polymer (Fig. 6.11), were manipulated at the micrometer-scale by patterned photo irradiation. The wetting characteristics of the microwrinkle grooves were switched by the photoisomerization of azobenzene units incorporated in the polymer. The use of light as an external stimulus is advantageous for fine spatial and sequential controls of the LF formation. For this purpose, a micropattern-light-projection apparatus was used (Fig. 6.12).

First, we examined contact angles of three liquids on a flat surface at room temperature (Table 6.1). The contact angles of propylene carbonate (PC), oleic acid, and 4-cyano-4′-pentylbiphenyl (5CB) on polyimide (PI) with and without the azobenzene polymer layer were measured before (trans-rich) and after (cis-rich) UV

Table 6.1 Contact angles of various liquids on a photoresponsive polymer with azobenzene units and polyimide (PI) surfaces

	trans-Rich	*cis*-Rich	PI
Propylene carbonate (PC)	43°	11°[a]	19°
Oleic acid	23°	5°	17°
5 CB	28°	15°	15°

The values are within an experimental error of ±2°, except for PC on *cis*-rich 2Az6

[a] Contact angle value is within an experimental error of +8°/−4°

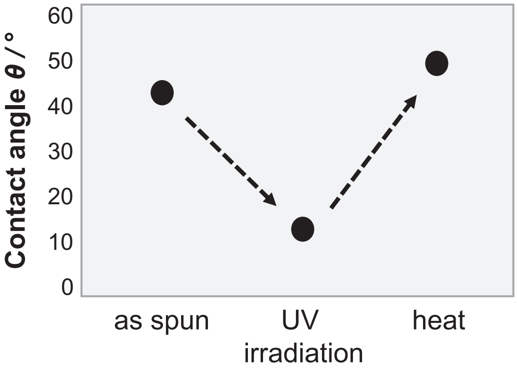

Fig. 6.13 Contact angles of propylene carbonate on a flat surface coated with the azobenzene polymer. The contact angle decreases after UV irradiation and then increased after thermal annealing

light irradiation. After UV irradiation, the contact angles under cis isomer decreases due to an increase in their dipole moments; the surface wettability on the azobenzene polymer layer was changed with UV irradiation.

Figure 6.13 shows the contact angles of PC on a flat surface coated with the azobenzene polymer layer. After UV irradiation, the contact angle decreases from 43° to 11°. The sample was followed by annealing at room temperature for 1 week, resulting the increase in the contact angle back to 49°. With this small change of the contact angle, the formation of LFs on microwrinkles can be controlled by photoirradiation because the contact angle is changed across the critical line (from right to the left) that divides states of LF growth and dewetting, which is shown in Fig. 6.7.

It was demonstrated that the LFs were precisely pullout from a liquid reservoir (Fig. 6.14) (Monobe and Ohzono 2012). A connection between two liquid reservoirs can also be created by the spatially controlled formation of LFs. The processes provide basic procedures for precise micromanipulation of liquids based on the microwrinkle technology. Since no external pumping system is needed for this technique, a new design of microfluidic channels without pumps and valves may be possible. Although the light-driven receding process of LFs instead of the formation is not shown here, a photoresponsive microwrinkle and a liquid with the lower contact angle hysteresis will be suitable. In principle, the present open microfluidic system can be applied to any liquid. However, a chamber will be required for the liquids with high vapor pressures to suppress drying, especially at small scales.

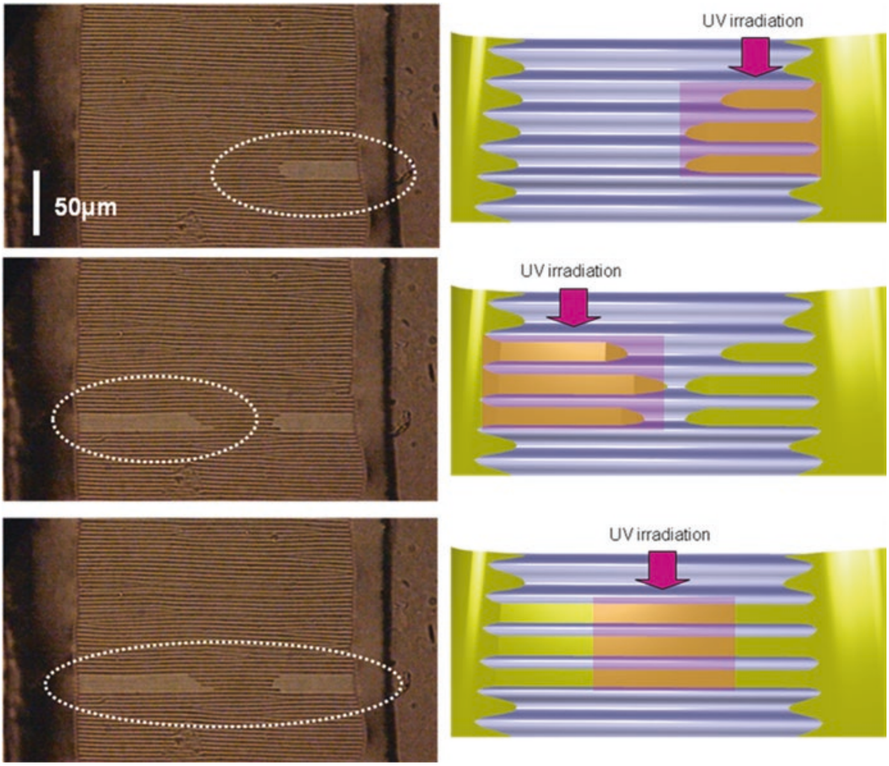

Fig. 6.14 Optical microphotographs of sequential LF photo-manipulation on photoresponsive microwrinkles with 15 µm width. Schematic birds-eye-view images of irradiation of patterned UV light (right). LFs formation after UV light irradiation of each step in the white dotted circle, respectively. (Adapted with permission from (ACS Appl. Mater. Interface 4 (2012) 2212.). Copyright (2012) American Chemical Society)

Nevertheless, the open microfluidic system is advantageous to apply local stimuli to the liquids because we can address liquids directly; for example, we could deposit chemicals or colloids from the top. Thus, the present light-induced LFs formation on microwrinkles will open the way for application in the field of microfluidics, for example, lab-on-a-chip technology, nano-synthesis, or micro-patterning.

6.3.3 Patterned Liquids as Templates for Au Nano-Ribbons

Because the LF array is a line-and-space pattern of a liquid and a solid, the pattern can be used as a unique template for further patterning. Here we introduce a method to fabricate novel nanoribbons based on the thermal evaporation of gold (Fig. 6.15) (Ohzono et al. 2011). On the liquid part of the substrate, rough gold ribbons form

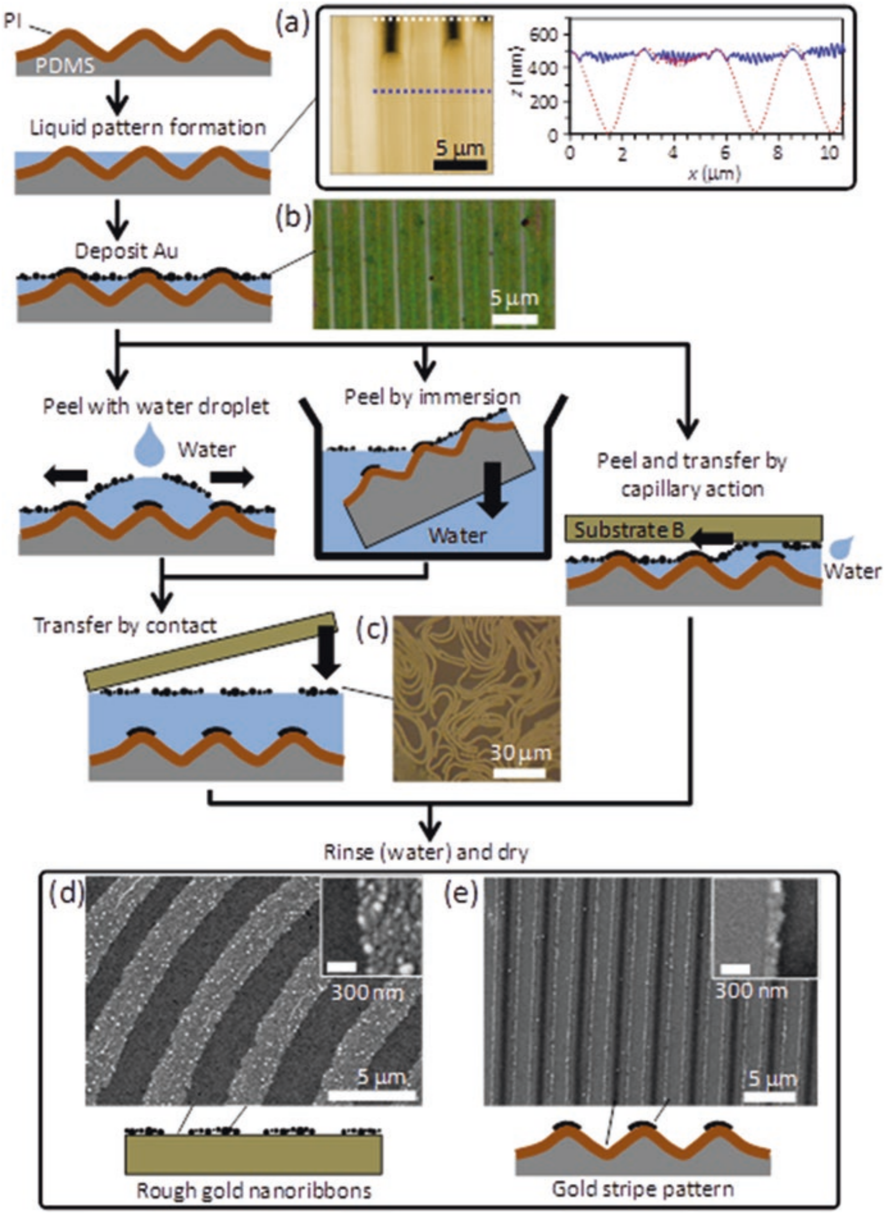

Fig. 6.15 Process flow for fabrication of peelable rough gold nanoribbons and gold stripe pattern with corresponding microscopy images. (**a**) AFM image of liquid micropattern with cross sections taken along white and blue dotted lines in the image, shown as blue and red solid lines in the right-hand graph, respectively. On the liquid part, operation of the AFM-tip becomes unstable, and thus, false oscillating signals appear. (**b**) OM image of gold-deposited liquid micropattern. (**c**) OM image of rough gold nanoribbons floating on water. (**d**) SEM image of rough gold nanoribbons on gold-deposited flat substrate. (**e**) SEM image of striped gold pattern. (Adapted with permission from (Small 7 (2011) 506–513). Copyright (2011) John Wiley and Sons)

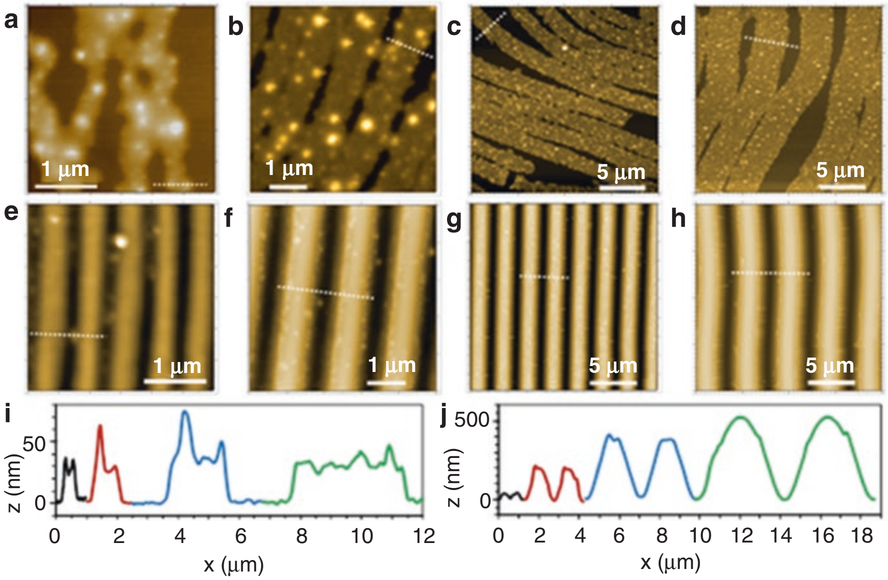

Fig. 6.16 Effect of wavelength λ of microwrinkles on morphology of gold nanoribbons and remaining patterns. (**a**–**d**, **i**) AFM images of rough gold nanoribbons transferred onto flat PDMS surface. (**e**–**h**, **j**) AFM images of gold stripe pattern on microwrinkles. $\lambda \approx 0.6$ (**a**, **e**), 1.4 (**b**, **f**), 2.7 (**c**, **g**), and 4.4 µm (**d**, **h**). AFM profiles indicated by white dotted lines on images are plotted on the same scale in black ($\lambda \approx 0.6$), red ($\lambda \approx 1.4$), blue ($\lambda \approx 2.7$), and green ($\lambda \approx 4.4$) in (**i**, **j**). (Adapted with permission from (Small 7 (2011) 506–513). Copyright (2011) John Wiley and Sons)

because the deposited gold atoms can diffuse, grow, and aggregate in proximity to the liquid-air interface; in contrast, flat gold films form on the solid part of the substrate. Thus, the liquid-air interface with a pattern provides a unique platform for fabrication of the film with a controlled roughness and shape. Here, the ionic liquid is used as a liquid filling the microwrinkle grooves to prevent evaporation of the liquid during the vapor deposition of gold in a high vacuum. The rough gold nanoribbons, which are supported by the liquid, can be peeled away by contact with water, because of the surface tension, and transferred to other substrates (Fig. 6.16, with different widths of ribbons). Even when we use different stripe patterns of microwrinkles, e.g., with a labyrinthine pattern, instead of anisotropic pattern, the identical procedure can be used to fabricate the nanoribbons with the original stripe pattern (Fig. 6.17). The extinction spectrum of the rough gold nanoribbons suggests a characteristic surface plasmon absorption. It may be possible to exploit the control over the shape of these rough gold nanoribbons for use in plasmonic technology. The novelty of this method for obtaining micropatterns is that the process is simple and does not require conventional lithography. We expect that there will be other suitable applications for this LF array.

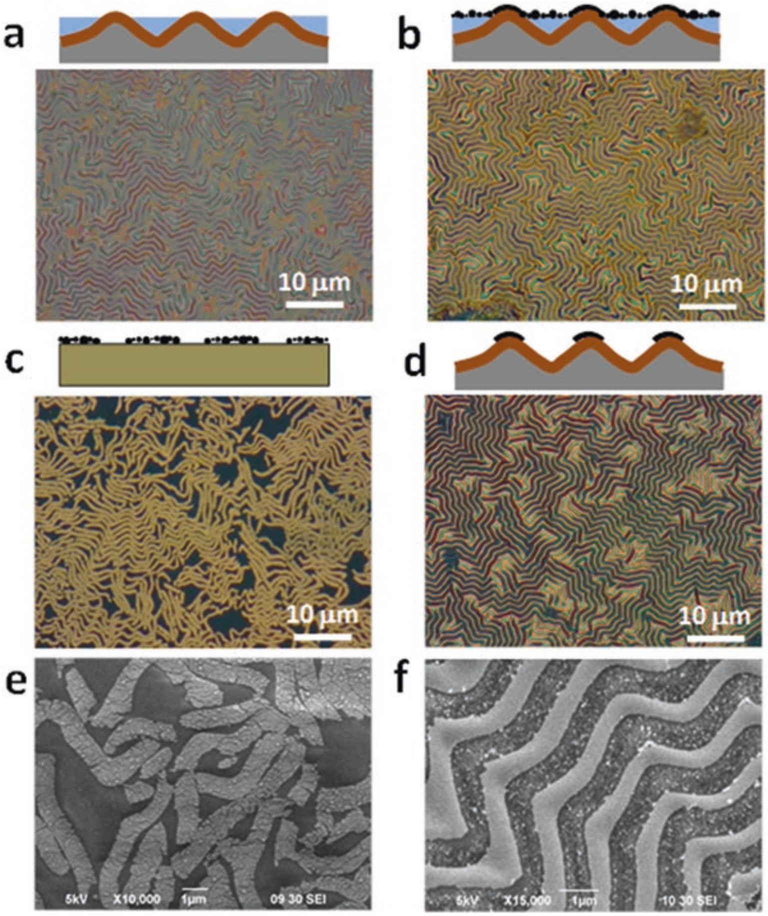

Fig. 6.17 Microscopy images taken during fabrication process of periodic gold pattern with roughness contrast using isotropic microwrinkles with labyrinthine pattern instead of anisotropic pattern. (**a**) Optical microscopy (OM) image of liquid micropattern on isotropic microwrinkles with corresponding schematic. (**b**) OM image of liquid micropattern after gold deposition with nominal thickness of 10 nm, exhibiting enhanced reflection properties, with corresponding schematic. (**c**) OM image of rough gold nanoribbons transferred onto flat PDMS substrate with corresponding schematic and (**e**) SEM image. (**d**) OM image of gold stripe pattern on microwrinkles with corresponding schematic and (**f**) SEM image. (Adapted with permission from (Small 7 (2011) 506–513). Copyright (2011) John Wiley and Sons)

6.3.4 Further Shaping of Liquids Via Transformation of Groove Directions

Since we can change the groove direction (Ohzono and Shimomura 2005a, b), it is interesting to investigate the response of the LF formed on the grooves to changes in the groove direction. This may provide a novel method to further shape the LFs

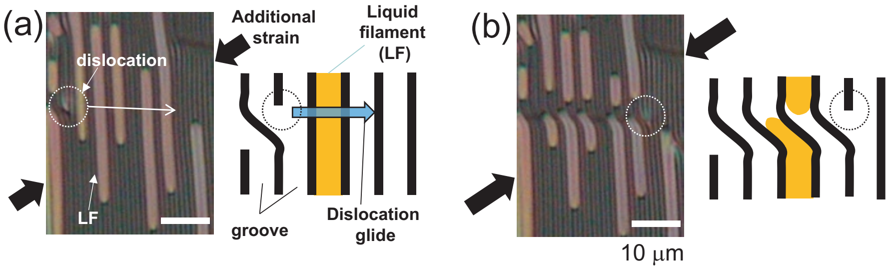

Fig. 6.18 Sequential optical micrographs with schematic representations of the stripe pattern of microwrinkles with LFs under additional compression in the direction indicated by black bold arrows. LFs break up when topographical dislocation glides across them. (Adapted with permission from (Soft Matter, 5 (2009) 4658). Copyright (2009) Royal Society of Chemistry)

by a simple process, e.g., change in the applied anisotropic strain (Ohzono et al. 2009; Ohzono and Monobe 2010).

First, we demonstrate a method of dividing an LF. The additional compressive strain in a direction different from that of the principal compression causes the formation of a pair of topological dislocations and their glide motions (Ohzono and Shimomura 2005b). When the dislocation passes an LF, the local R decreases to a value much less than R_c shown in Fig. 6.7. Thus, the LF becomes partially unstable and breaks up into shorter LFs (Fig. 6.18).

We further investigated the liquid-transformation using the more ordered LF array (Fig. 6.19). In this case, depending on the wettability at the original crest parts, the LFs were rearranged to LFs with new alignment perpendicular to the original one or divided into small droplets with a specific size (or volume) (Fig. 6.19). Since the stability of the LF shape depends on the groove shape, the LF becomes unstable when the groove direction changes. The shape of the droplets was controlled by tuning the contact angle of the liquid at the original crest parts (Fig. 6.19, see (Ohzono et al. 2011) for experimental details). At lower contact angles, the droplets spread in the direction of the newly formed groove, although at higher contact angles the spreading was suppressed. Since $\lambda \approx 2.2$ μm in Fig. 6.20, the droplet volume is less than 1 fL (volume $\approx (R\lambda^3)/2 \approx 0.75 \times 10^{-18}$ m^3 ≈ 0.75 fL, where $R \approx 0.15$). This method for preparing microdroplets with a specific volume is very efficient because of the simplicity of applying strain to the sample macroscopically.

We believe that these liquid transformations on a nanometer or /micrometer scale will find applications in switchable light diffraction gratings and lab-on-a-chip systems, in addition to simple liquid micropatterning. This technique may also be used to investigate the properties of liquids in a confined small space, which are thought to be very different from the bulk properties, such as fluctuation of the liquid surface and liquid crystal alignment.

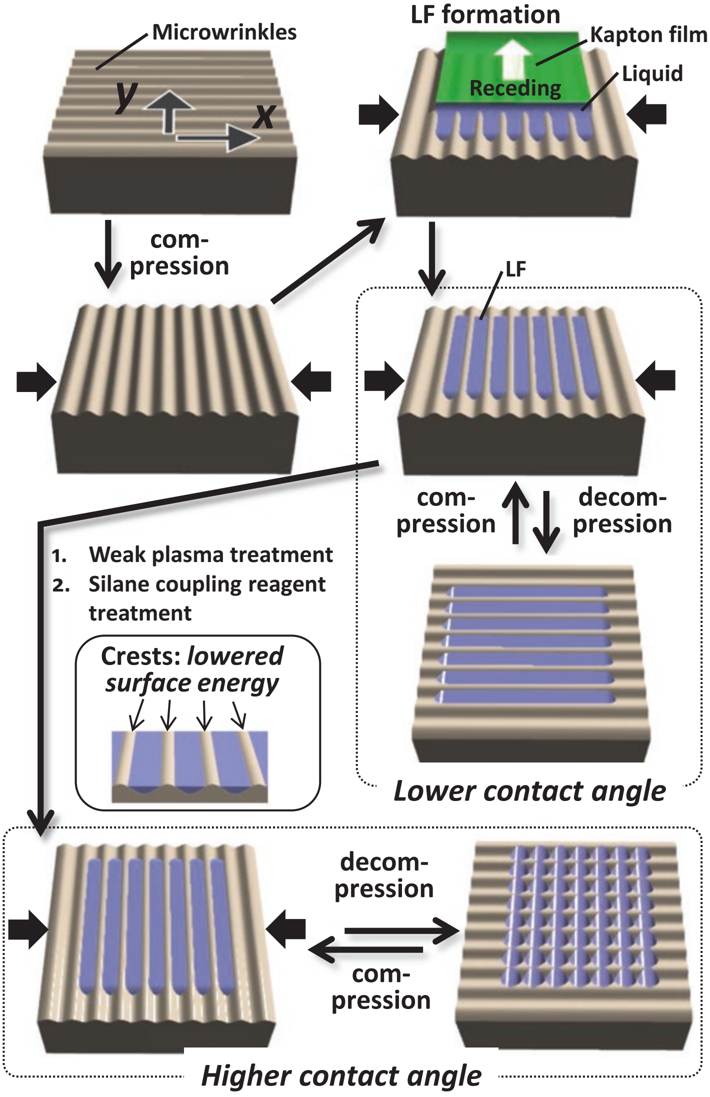

Fig. 6.19 Schematic of liquid filament (LF) array formation and subsequent transformation of the liquid micro-pattern triggered by structural change of the microwrinkles. (Adapted with permission from (Langmuir 26 (2010) 6127). Copyright (2010) American Chemical Society)

6.3.5 Guided Phase Separation of Polymers on Wrinkle Grooves

In general, the topographical patterns on surfaces are key elements in methods of micropatterning. For example, the photoresist patterns on a substrate work as barriers for the following etching process. Another application of the surface

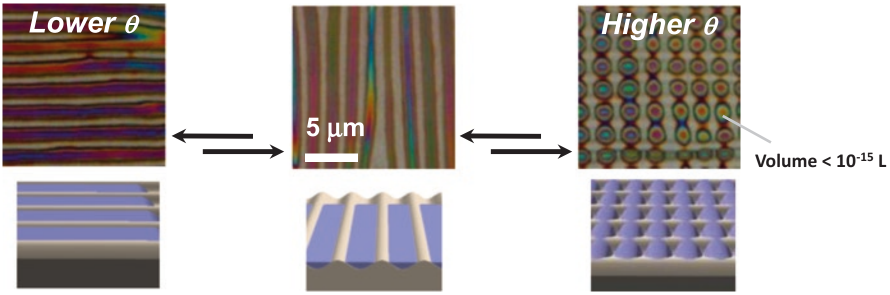

Fig. 6.20 Using the dynamical and non-linear micro-topological change of microwrinkles, we demonstrate that the morphology of an array of liquid filaments formed on microwrinkle grooves are dramatically and reversibly transformed into LFs with a different orientation (left) or a regular array of micro-droplets, "dots" (right), depending on the predefined contact angle. The wavelength of microwrinkles is ~2 µm. (Adapted with permission from (Langmuir 26 (2010) 6127). Copyright (2010) American Chemical Society)

topographical patterns is the heterogeneous coating on them using polymer solutions or colloidal dispersions. The microgrooves of microwrinkles have also shown potential use in the low-cost fabrication of micropatterns as templates for colloidal assembly (Efimenko et al. 2005; Lu et al. 2007), polymer patterning (Hyun et al. 2010), and selective colloidal coating (Yang et al. 2010). Here we focus on the method to pattern polymers from their solutions via wet-coating methods. A key factor for making use of the topographic pattern is the interaction between the surface undulation and the liquid that contains a solute. We have already mentioned that the contact angle and the aspect ratio of the undulation are the critical parameters for sinusoidal grooves to allow the introduction of liquids into only the microwrinkle grooves under quasi-static conditions (Fig. 6.7). In contrast, during a nonequilibrium process, such as solvent evaporation or a chemical reaction, the general conditions are difficult to determine for patterning the liquid in the grooves. For example, during fast solvent evaporation after spin coating a binary polymer solution onto the microgrooves, the relaxation toward equilibrium, including the phase separation process, is hindered by kinetic barriers in the quenched states. Nonetheless, nonequilibrium processes have often been used in engineering (Shimizu et al. 1999) and sometimes result in a variety of patterns through self-organization under nonequilibrium conditions (Nicolis and Prigogine 1977; Yamaguchi et al. 2005).

Here, we review the results obtained by examining the phase-separated morphology of binary polymers on microwrinkle grooves, which are formed during fast solvent evaporation after spin coating (Walheim et al. 1997). To focus on the effect of the substrate topography, the well-studied polystyrene (PS) and poly(2-vinylpyridine) (PVP) system was used, which shows clear phase separation (demixing) after solvent evaporation from a 1:1 (w/w) solution mixture (Boltau et al. 1998). For this binary system, it has been reported that chemical patterns fabricated on a flat substrate by conventional lithography can guide the phase-separated morphology (Boltau et al. 1998). However, little was known about the guiding effect of surface topographic patterns (Wei et al. 2006). We here review the investigation of the effect of polymer concentration on the phase-separated morphology in sinusoidal grooves (Ohzono and Kitahata 2012).

First, the patterns obtained by spin coating a solution of each single polymer component were evaluated. Spin coating a tetrahydrofuran (THF) solution containing a single PS component did not produce a uniform pattern lacking dewetted hole defects. On the other hand, PVP uniformly coated the surface. The results indicate that the affinity of concentrated PVP solutions was higher than that of PS for the polyimide (PI) microwrinkle surface. Because the PVP pyridine substituent is more polar than the PS benzyl substituent, this may explain the higher affinity between PVP and the PI surface, which also has polar imide groups.

Next, results obtained using the binary polymer solution of PS and PVP are shown. Figure 6.21 shows phase-separated patterns on microwrinkles for the PS/PVP blend system. At lower PS concentrations, the PS islands were surrounded by a sea of PVP that only appeared in the grooves. The PS islands joined together as the concentration increased, which was similar to the behavior observed for single PS coating. However, the fused PS islands filled the grooves without creating dewetted holes; uniform PS ribbons were formed over a PVP layer in the grooves. A schematic for the cross-sectional profile is shown in Fig. 6.21h, which was constructed using the AFM images of the samples after selective rinsing (Fig. 6.21i–k). Some PS ribbons peeled away from the grooves after rinsing with ethanol, which selectively removes PVP (Fig. 6.21m–p). The thickness of the PS ribbon was 110 ± 20 nm for the sample coated with the 1.5 wt % binary polymer solution. Casting the ethanol dispersion of the peeled PS ribbons onto a glass substrate confirmed that the PS ribbons were transferred onto the surface after solvent evaporation (Fig. 6.21n).

In summary, tuning the polymer concentration with an appropriate solvent and substrate topography makes this method of spin coating onto microwrinkles a simple, low cost method for fabricating various topography-guided polymer morphologies. PS ribbons, which were not obtained from the sequential process, could be formed. This process is a good example of a microfabrication method using an easily prepared self-organized structure and a highly nonequilibrium process. Although the precise mechanism is difficult to clarify, the concept of using nonequilibrium processes for creating a new structure is likely to be important in future nano-microfabrication, because these strategies are often found in biological systems.

6.3.6 Unique Boundary Condition for Nematic Liquid Crystal Alignment

Since the diagram for capillary-force-induced liquid filaments (LFs) formation with respect to equilibrium contact angle, θ, and the critical aspect ratio, R^*, is universal, we can obtain LFs of liquid crystals (de Gennes and Prost 1993). The critical

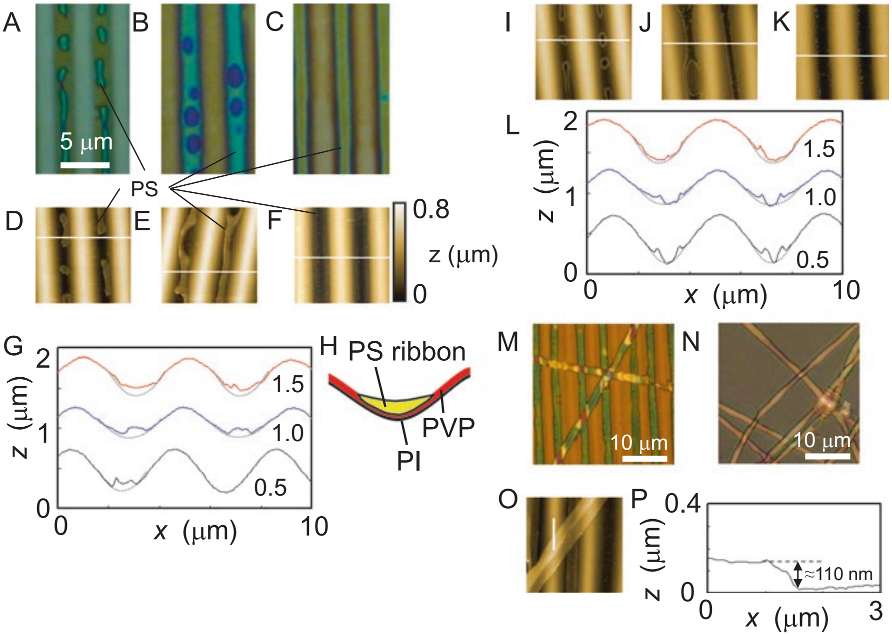

Fig. 6.21 Morphologies of phase-separated polymers spin coated from binary solution on microwrinkles. Optical images of PS/PVP-coated samples with (**a**) 0.5, (**b**) 1.0, and (**c**) 1.5 wt % THF solution. (**d**)-(**f**) Corresponding AFM images (10^2 μm^2). (**g**) Corresponding cross sectional profiles, indicated by white lines in (**d**)-(**f**). The profiles of the bare groove surface are a visual guide. (**h**) A schematic for the cross section of the state with PS ribbons on the PVP underlayer shown in (**c**) and (**f**). (**i**)-(**k**) Corresponding AFM images (102 μm^2) of the samples after a selective rinse using cyclohexane that removes PS parts. (**l**) Corresponding cross sectional profiles of samples with PS removed, indicated by white lines in (**i**)-(**k**). (**m**) Optical images of the sample shown in (**c**) and (**f**) after a selective rinse using ethanol, and (**n**) the peeled PS ribbons transferred onto a slide glass. (**o**) An AFM image and (**p**) the profile corresponding to the sample shown in (**m**). The vertical white line in (**o**) indicates the position of the profile shown in (**p**). (Adapted with permission from (RSC Adv. 2 (2012) 2395). Copyright (2012) Royal Society of Chemistry)

difference between isotropic liquids and liquid crystals is the existence of the internal molecular order for the latter (Fig. 6.22). The internal structures of liquid crystals depends on the phases, e.g., nematic, cholesteric, smectic, discotic, etc.. Moreover, the boundary conditions, which are physical boundary shapes and determine how the molecules align at the boundary, also greatly affect the internal structure of liquid crystals. Thus, various interesting microstructures with topological defects are expected to appear in liquid crystals under special boundary conditions and many studies on the liquid crystalline structures under special boundary conditions have been conducted (Ohzono and Kitahata 2012; de Gennes and Prost 1993; Lavrentovich and Pergamenshchik 1995; Manyuhina et al. 2010; Link et al. 2001; Palffy-Muhoray et al. 1994; Lavrentovich 1994; Carbone et al. 2009; Meyer 1973;

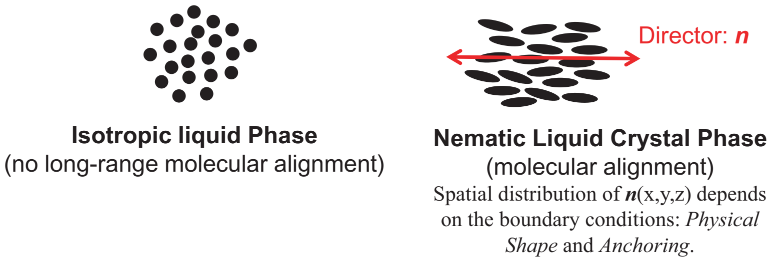

Fig. 6.22 Difference in the molecular orders between isotropic liquids and liquid crystals. Only the case of a nematic phase is shown in the right

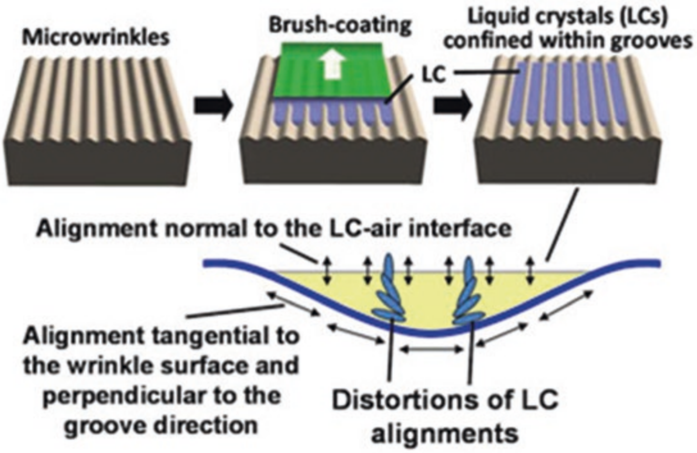

Fig. 6.23 Experimental procedure for confining a liquid crystal within microwrinkle grooves (top) and orientations of the liquid crystal molecules at the interfaces (bottom)

Mihailovic and Oswald 1988; Oswald and Pieranski 2005; Lavrentovich 1998; Yamamoto and Tanaka 2001; Fukuda and Žumer 2011; Fernández-Nieves et al. 2007; Lee and Clark 2001; Kim et al. 2002; Ferjani et al. 2010; Nelson 2002; Tkalec et al. 2011). Here in the following sections, we review the studies of liquid crystalline LFs on microwrinkle grooves, which have induced various new self-organized structures in the liquid crystal alignment. Firstly, the case of a nematic liquid crystal, which is the simplest liquid crystalline phase, is presented in this section (Ohzono and Fukuda 2012a, b; Ohzono et al. 2012a, 2014, 2016).

First, a hard-thin film of polyimide was formed on the surface of silicone rubber and unidirectionally compressed. Microwrinkles with grooves unidirectionally oriented and spaced at several to several tens of micrometers (the spacing could be controlled by changing the thickness of the polyimide film) form spontaneously over the surface of the thin film. The microwrinkles were then brush-coated with a nematic liquid crystal (Fig. 6.23, top center). When the contact angle of the liquid crystal on the polyimide surface was reduced to a certain value, the liquid crystal was confined within the grooves. It was already found that the liquid crystal molecules orient tangential to the surface and perpendicular to the groove direction on the microwrinkle surface (i.e. the polyimide surface). At the liquid crystal-air interface, the orientation of the molecules was perpendicular to the interface. Because of the orientations of the liquid crystal at the interfaces and the curved structure of the microwrinkle groove, the confined liquid crystal could not have a uniform orientational structure (Fig. 6.23, bottom) and was presumed to be substantially distorted inside.

Figure 6.24a, b are polarized microscope images of the liquid crystal confined within a microwrinkle groove. The liquid crystal confined within the wrinkle groove shows a periodic pattern despite the absence of periodicity in the microwrinkles along the groove direction, indicating the spontaneous emergence of the periodic order. A polarized microscope image obtained with a sensitive color plate shows that the liquid crystal has a periodic structure, in which the liquid crystal orientation deviates alternately from the direction perpendicular to the groove (Fig. 6.24c). It is also found that a zigzag line defect along the groove is formed, along with the periodic structure. The periodic structure is a general one independent of the size of the groove. The structure is formed in many grooves of microwrinkles simultaneously, making it easy to form a large-area periodic structure.

Inside the periodic structure, the liquid crystal molecules at the bottom surface of the grooves are oriented tangential to the surface and perpendicular to the groove direction. From the bottom surface towards the air-liquid crystal interface at the top, the orientation of the molecules gradually changes towards a direction perpendicular to the interface and gradually twists away from a direction perpendicular to the grooves (Fig. 6.24d). The directions of the twists are found in Fig. 6.24b. The sense of the twist determines the local orientation of the liquid crystal. Theoretical considerations with the aid of numerical calculations reveal that the twist elastic constant smaller than other elastic constants (which holds for many nematic liquid crystals) is responsible for the periodic structure accompanied by twist deformations. In other words, the smaller twist elastic constant reduces the energy required for deformation required for the above-mentioned distortions in the liquid crystal. The twist deformations drive the line defect away from the groove center. Because the groove width is finite, the line defect would reach the wall of the groove unless the line zigzags periodically. As a result, the clockwise and counterclockwise twists shown in Fig. 6.24 appear alternately by self-organization. [For details of the theoretical arguments conducted by J. Fukuda, see ref. (Ohzono and Fukuda 2012a).]

Next, silica micro-particles (about 500 nm in diameter) are deposited into the nematic liquid crystal confined within microwrinkles. As in the case without the particles, a periodic orientational structure is formed. However, it is found that isolated silica particles are trapped at the kinks of the zigzag line defect (Fig. 6.25). Liquid crystal distortions are concentrated at the kinks of the line defect. The replacement of the regions with large distortions by silica particles reduces the total energy of the system, thus stabilizing it. This is the reason why particles are trapped. The periodicity of the kinks results in the periodic arrangement of particles. In other

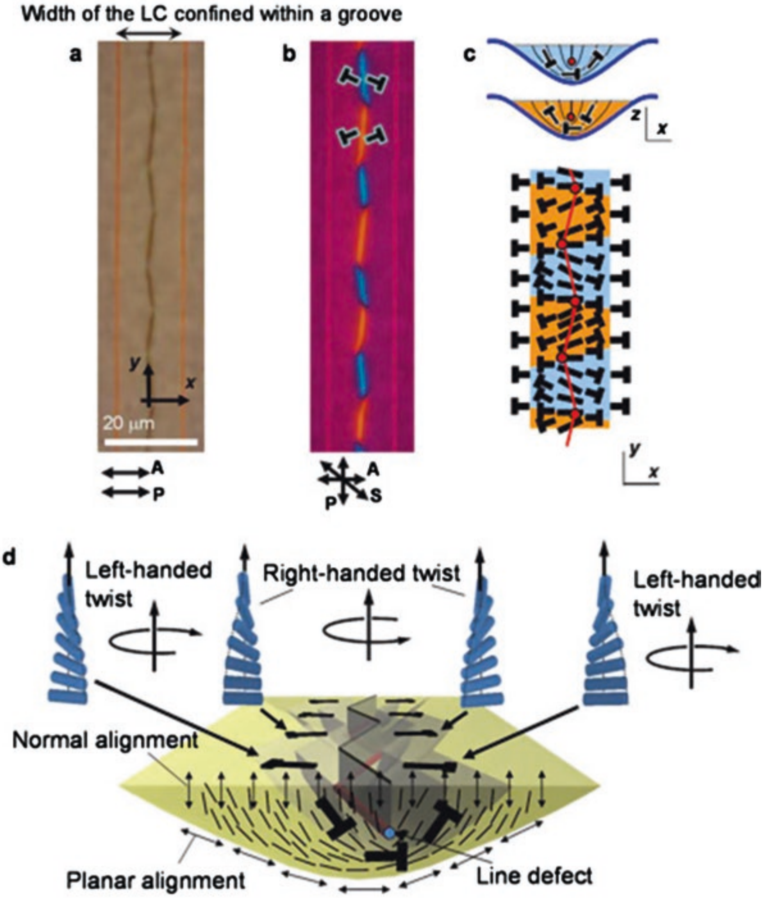

Fig. 6.24 Transmission polarized microscope images and illustration of the periodic orientational structure of the liquid crystal. (**a**) and (**b**) are images of the same region observed with different sets of polarizing plates. P and A show the orientations of the polarizer and the analyzer, respectively. S shows the orientation of the sensitive color plate. The orientation of the liquid crystal can be determined from the color. (**c**) shows the orientation distribution in different planes. In the illustration in the xy plane at the bottom, the deviations of the orientation away from the direction perpendicular to the groove are shown in an exaggerated manner. (**d**) is a three-dimensional illustration. The nail symbols (T) indicate the projection of the molecules inside the groove on the plane on which the symbol is located and the head of the nail comes out of the plane

words, the periodic orientational structure of the liquid crystal serves as a template for the periodic arrangement of particles. Moreover, it has also been demonstrated that low-molecular-weight molecules localize at the zigzag line defects by fluorescence microscopy (Ohzono et al. 2016)

When the nematic liquid crystal was transformed to an isotropic liquid by raising the temperature, the periodic orientational structure disappears and, at the same

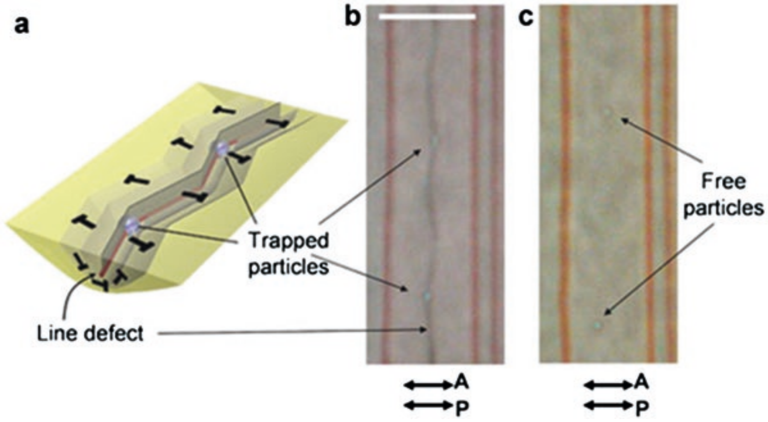

Fig. 6.25 Silica micro-particles trapped in the zigzag line defect in the periodic orientational structure of the liquid crystal. (**a**) is a three-dimensional illustration of how the silica particles are trapped in the line defect. (**b**) is an optical microscope image of the particles and the liquid crystal. (**c**) shows the particles released from the trapped state when the liquid crystal is transformed to an isotropic phase and the line defect disappears

time, the trapped particles are released and move freely (Fig. 6.25c). This indicates that the orientational structure of the liquid crystal indeed traps the particles.

To seek applications of the present zigzag defect structures other than the template for patterning of the micro objects, the effect of chiral dopants on the structural changes were investigated. As a result, the present zigzag defect structures were found to respond very sensitively to the dissolved chiral molecules, inducing a visually detectable change (Fig. 6.26). Thus, we further conducted feasibility study of the present system toward chirality sensing.

Precise analytical methods including artificial gas sensors mimicking biological olfactory systems and chromatography have already been developed for the analysis of the chirality of gas samples. However, these methods require in advance the preparation of a complementary chiral environment that interacts selectively with one of the enantiomers of the molecules to be analyzed. Molecular design, synthesis, and stabilization of such environments for the detection of various molecules are not easy. Moreover, the disadvantage of these methods is that they require complex and expensive apparatuses such as quartz resonators, semiconductor devices, light-reflecting devices, and mass spectrometers. Thus, the simpler methods are anticipated. In this respect, the visual response from the present liquid crystalline system was useful.

The developed method utilized a spontaneously-formed periodic structure of a nematic liquid crystal confined in the microwrinkle grooves (Figs. 6.24 and 6.26) as a chirality sensor. Regions with left-handed and right-handed local twist distortions alternate in this periodic structure of the liquid crystal. Initially, the length of a region with left-handed twist was approximately the same as that with right-handed twist. When chiral molecules in the gas sample dissolve into the liquid crystal after

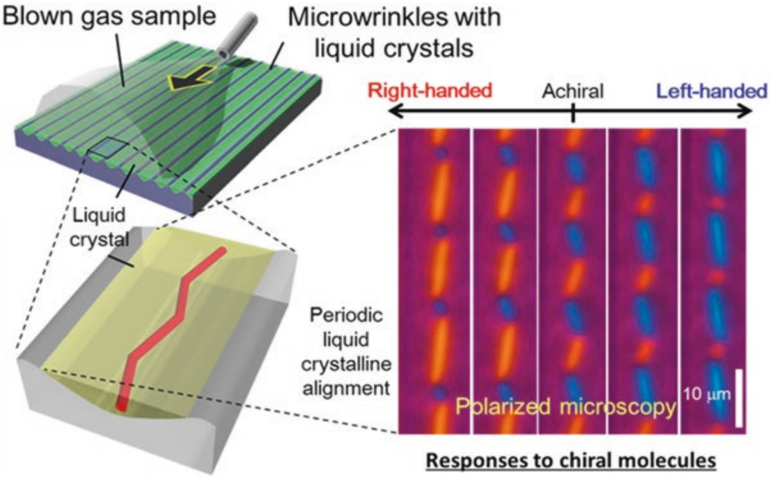

Fig. 6.26 Sensing of chiral gas molecules by the change of the periodic orientational structures of a liquid crystal in microwrinkle grooves

blown onto it, one region with specific twist handedness is energetically more favorable than the other. Thus, the length of the former becomes larger than that of the latter [see ref. (Ohzono et al. 2014) for detail mechanism]. This phenomenon can be utilized for visual detection of the existence of chiral molecules and their chiral handedness. Typical response time is as small as a few seconds, owing to rapid diffusion and homogenization of the gas molecules dissolved from the vapor into the liquid crystal whose effective thickness is as small as 1 μm. It is important to note that this method enables direct analysis of gas samples, and does not require condensation or dissolution of the samples in advance.

In summary, when a liquid crystal is confined within microwrinkle grooves, a liquid crystal structure is formed that is periodic along the direction of the wrinkle grooves. It has been shown that both the effect of confinement and the anisotropic elasticity of the liquid crystal are important in the formation of this structure. This orientational structure of the liquid crystal contains a zigzag line defect and can trap single silica micro-particles at the kink points where the line defect changes direction. This structure, based on the self-organization of liquid crystals, can be applied to optical devices and to easy patterning and capturing of micro-objects such as colloidal particles and small molecules. Moreover, the present zigzag structure can be used as a simple and economical chirality sensor for gas samples that allows its outdoor use. This method makes use of a novel response of a topological defect of a liquid crystal, and can be regarded as an example of an ingenious application of soft materials that respond sensitively to external stimuli. All these new findings have been discovered being based on the method to fabricate LFs on microwrinkle grooves.

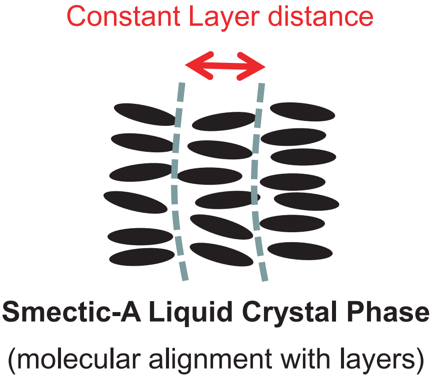

Fig. 6.27 The arrangement of molecules in a smectic-A liquid crystal

6.3.7 *Unique Boundary Condition for Smectic-A Liquid Crystal Alignment*

Finally, the case of another liquid crystalline phase, a smectic-A (SmA) phase, confined within the microwrinkle grooves as liquid filaments (LFs) is briefly shown (Ohzono et al. 2012b). A SmA phase, well known as the second simplest liquid crystalline phase to the nematics, is characterized by the presence of one-dimensional positional order as well as orientational order as in a nematic phase. In a SmA phase molecules in parallel molecular layers tend to be aligned along the layer normal (Fig. 6.27). In confined samples the bulk SmA structure is deformed depending on the elastic properties and the boundary conditions, such as boundary shapes and surface anchoring.

As a representative defect structures of a smectic liquid crystal, focal conic domains (FCDs) (Friedel 1922; Bidaux et al. 1973; Fournier et al. 1990; Blanc and Kleman 2000; Kleman and Lavrentovich 2000, 2009; Ruan et al. 2003; Kleman et al. 2004; Nastishin et al. 2008; Alexander et al. 2010) have been extensively studied. FCDs are a broad class of curvature defects in a layered system with a constraint of constant layer spacing. In themotropic SmA liquid crystal s, the layers of FCDs often show a negative Gaussian curvature, and are wrapped around singular lines that form conic sections. In general, an ellipse, with the eccentricity (e) between 0 and 1, and a hyperbola orient in perpendicular planes. They pass through each other's focal point. The layers take the shape of Dupin cyclides. With $e = 0$, the FCD is called a toric FCD, which consists of a circle with a straight line passing through its centre (Kleman and Lavrentovich 2000; Ruan et al. 2003). With $e = 1$, the FCD is called a parabolic FCD, which consists of two parabolic defect lines with their lying plane perpendicular to each other (Rosenblatt et al. 1977; Stewart 1993; Chatterjee and Anna 2012).

FCDs can self-organize into two-dimensionally packed lattices when the LCs are confined between parallel surfaces with a gap of a few to tens of microns. When the FCDs are further confined in a rectangular microchannel, the size and the regular packing structures are affected by the channel size and the anchoring condition at the walls and the bottom surface (Choi et al. 2004; Shojaei-Zadeh and Anna 2006; Yoon et al. 2007; Bramble et al. 2007; Kim et al. 2009). Patterned surfaces have been also used for controlling the arrangement of FCDs (Guo et al. 2008). For example, a surface with periodic micropillars was shown to accommodate toric FCDs (Honglawan et al. 2011). These spatial controls of FCDs lead to the development of novel applications exploiting spontaneously formed and regularly modulated LC alignments, for example, colloidal assembly (Yoon et al. 2007; Coursault et al. 2012), pattern imprinting (Kim et al. 2010a) and optical patterning (Kim et al. 2010b). These works suggest that a spatially confined LC is a promising system to engineer topological defects for more practical applications, including electro-optic devices and templates for bio-mineralization. Although the structural controls and the energetical consideration of toric FCDs seem successful (Kim et al. 2009), for typical FCDs with $0 < e < 1$, little is known about the relationship between their arrangements and boundary conditions because of the complex internal layer structures (Zappone et al. 2012).

Here, a study of FCDs of a SmA phase confined within a curved open microchannel capillary of microwrinkles is briefly mentioned (Ohzono et al. 2012b). The main differences between rectangular and sinusoidal channels filled with a liquid are (1) the number of singular points of the cross-sectional shape of a confined liquid; the former has four corners and the latter has only two at the three-phase (liquid/solid/air) points and, (2) the curvatures of the solid boundary; the former is composed of only flat surfaces and the latter possesses a curved boundary. These effects on the FCD structure and the arrangement are nontrivial. The present main objective is to explore the internal layer structure of FCDs, how the FCDs pack, and how the characteristic size of the FCD arrays depends on the characteristic periodicity λ of microgrooves accommodating a SmA LC. We use shallow microgrooves with λ varying in the range of 2–20 μm with a fixed aspect ratio. The surface of the groove imposes a planar anchoring with the easy direction perpendicular to the groove direction. The top air/LC interface imposes normal alignment.

As a result, a regular characteristic FCD array forms when λ is above a critical value of approximately 4 μm (Fig. 6.28). From optical observations, a detailed FCD structure that is composed of an ellipse and a hyperbola is proposed (Ohzono et al. 2012b), which is schematically shown in Fig. 6.28. A FCD contains an elliptic line defect, with its eccentricity e being approximately 0.75, lying on wrinkle surface, and a hyperbora lying on the xz plane. The periodicity of the FCDs monotonically increases with increasing the wrinkle wavelength. Quantitative mechanisms for the formation of arrays of FCDs and the effect of boundary curvature on the layer structure are still unclear. They may be explored by changing the aspect ratio of the grooves and anchoring conditions in future studies. Nevertheless, the spontaneous periodic structures prepared without using conventional lithography may be applicable to pattern imprinting (Kim et al. 2010a) and optical patterning (Kim et al. 2010b), electro-optic devices, and templates for colloidal assembly (Yoon et al. 2007; Coursault et al. 2012) and bio-mineralization.

Fig. 6.28 A self-organized regular array of focal conic domains in a smectic-A liquid crystal confined in a curved groove of microwrinkles with a hybrid alignment condition. A schematic for the present array of FCDs in a microwrinkle groove, where cross sections of the layers at the bottom surface projected onto the *xy* plane are shown. Basic ellipses can be recognized

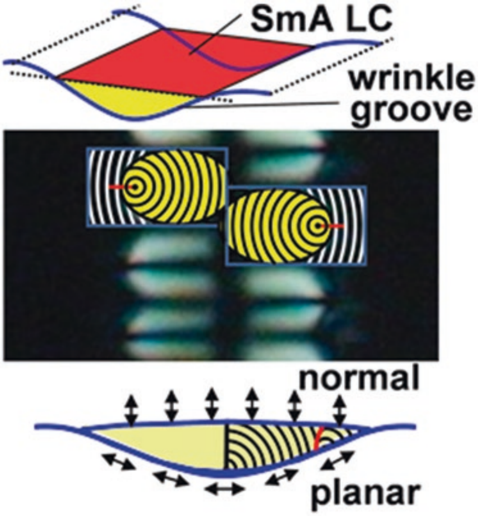

6.4 Summary

In the present chapter, basic capillary phenomena of the liquid on sinusoidal grooves formed on shape-tunable microwrinkles are described. The capillary force on the grooves become active when groove depth becomes larger or contact angle becomes lower than their critical values. It was demonstrated that, as the stimuli, mechanical strain and light can be used. The general conditions for the capillary phenomenon on the sinusoidal grooves are derived computationally, which agree well with the experimental results. Various micro-patterning methods based on this capillary phenomenon are shown, such as directed polymer phase separation on grooves, gold nano-ribbon formation on liquid filaments, and self-organized periodic pattern formations in liquid crystals confined in the grooves. It is expected that the present system may be applied to many other research fields of the interface science. For example, the microwrinkle surface may contribute to understanding in challenging areas where the physical or chemical properties are sensitive to the microscopic boundary shape, such as fluid dynamics at the interface that is important for lubrication problems and liquid crystalline dynamics that is critical for the display technology. As the steps toward such targets, so far in the present results, the shape-tunability was shown to be applicable to micromanipulation of a liquid including liquid crystals, providing new basic understandings of their interfacial behaviors. Moreover, because the formation of microwrinkles is based on the simple mechanical instability of elastic materials, various surface materials with special photonic, biological and chemical functions can be used. Thus, we expect that new applications of easy-to-make shape-tunable microwrinkles, especially regarding the liquids, can be achieved using functional materials with this technology soon.

Acknowledgements This work was partly supported by the New Energy and Industrial Technology Development Organization (NEDO) of Japan under the Industrial Technology Research Grant Program in 2008. The author thanks H. Monobe, Y. Shimizu, H. Yokoyama, M. Yoneya, J. Fukuda, N. Fukuda, M. Fujiwara, Y. Takenaka, H. Kitahata, K. Suzuki, M. Fujiwara, R. Yamaguchi, and T. Yamaguchi for their helpful comments, theoretical and experimental support.

References

Akiyama H, Mallia VA, Tamaoki N (2006) Novel photoresponsive oligomeric mesogens: synthesis, liquid crystalline properties and photo optical studies as a dopant in a chiral glassy liquid crystal. Adv Funct Mater 16:477–484

Alexander GP, Chen BG, Matsumoto EA, Kamien R (2010) Power of the Poincaré group: elucidating the hidden symmetries in focal conic domains. Phys Rev Lett 104:257802

Allen HG (1969) Analysis and design of structural sandwich pannels. Pergamon, New York

Ball P (2001) The self-made tapestry. Oxford University Press, New York

Baret JC, Decre M, Herminghaus S, Seemann R (2005) Electroactuation of fluid using topographical wetting transitions. Langmuir 21:12218–12221

Baroud CN, Delville JP, Gallaire F, Wunenburger R (2007) Hermocapillary valve for droplet production and sorting. Phys Rev E 75:046302

Barthlott W, Neinhuis C (1997) Purity of the sacred lotus, or escape from contamination in biological surfaces. Planta 202:1–8

Bidaux R et al (1973) Statistical properties of focal conic textures in smectic liquid crystals. J Phys (Paris) 34:661–672

Blanc C, Kleman M (2000) Tiling the plane with noncongruent toric focal conic domains. Phys Rev E 62:6739–6748

Boltau M et al (1998) Surface-induced structure formation of polymer blends on patterned substrates. Nature 391:877–879

Bowden N et al (1998) Spontaneous formation of ordered structures in thin films of metals supported on an elastomeric polymer. Nature 393:146–149

Bowden N et al (1999) The controlled formation of ordered, sinusoidal structures by plasma oxidation of an elastomeric polymer. Appl Phys Lett 75:2557

Bramble JP et al (2007) Observations of focal conic domains in smectic liquid crystals aligned on patterned self-assembled monolayers. Liq Cryst 34:1137–1143

Brau F et al (2011) Multiple-length-scale elastic instability mimics parametric resonance of nonlinear oscillators. Nat Phys 7:56–60

Brzoska JB, Brochard-Wyart F, Rondelez F (1993) Motions of droplets on hydrophobic model surfaces induced by thermal gradients. Langmuir 9:2220–2224

Carbone G et al (2009) Mechanically induced biaxial transition in a nanoconfined nematic liquid crystal with a topological defect. Phys Rev Lett 103:167801

Cassie ABD, Baxter S (1944) Wettability of porous surfaces. Trans Faraday Soc 40:546–551

Chatterjee S, Anna SL (2012) Formation and ordering of topological defect arrays produced by dilatational strain and shear flow in smectic-A liquid crystals. Phys Rev E 85:011701

Choi MC et al (2004) Ordered patterns of liquid crystal toroidal defects by microchannel confinement. Proc Natl Acad Sci U S A 101:17340–17344

Chua DBH, Ng HT, Li SFY (2000) Spontaneous formation of complex and ordered structures on oxygen-plasma-treated elastomeric polydimethylsiloxane. Appl Phys Lett 76:721–723

Chung JY, Youngblood JP, Stafford CM (2007) Anisotropic wetting on tunable micro-wrinkled surfaces. Soft Matter 3:1163–1169

Coursault D et al (2012) Linear self-assembly of nanoparticles within liquid crystal defect arrays. Adv Mater 24:1461–1465

de Genne PG, Brochard-Wyart F, Quere D (2003) Capillarity and wetting phenomena: drops, bubbles, pearls, waves. Springer, New York

de Gennes PG, Prost J (1993) The physics of liquid crystals, 2nd edn. Oxford University, New York

Edmondson S, Frieda K, Comrie JE, Onck PR, Huck WTS (2006) Buckling in quasi-2D polymers. Adv Mater 18:724–728

Efimenko K et al (2005) Nested self-similar wrinkling patterns in skins. Nat Mater 4:293–297

Feng X, Jiang L (2006) Design and creation of superwetting/antiwetting surfaces. Adv Mater 18:3063–3078

Ferjani S et al (2010) Mechanically generated surface chirality at the nanoscale. Phys Rev Lett 104:257801

Fernández-Nieves A et al (2007) Novel defect structures in nematic liquid crystal shells. Phys Rev Lett 99:157801

Fournier JB, Dozov I, Durand G (1990) Surface frustration and texture instability in smectic-A liquid crystals. Phys Rev A 41:2252–2255

Friedel G (1922) Les états mésomorphes de la matière. Ann Phys 18:273–274

Fukuda J, Žumer S (2011) Quasi-two-dimensional Skyrmion lattices in a chiral nematic liquid crystal. Nat Commun 2:246

Gau H, Herminghaus S, Lenz P, Lipowsky R (1999) Liquid morphologies on structured surfaces: from microchannels to microchips. Science 283:46–49

Genzer J, Groenewold J (2006) Soft matter with hard skin: from skin wrinkles to templating and material characterization. Soft Matter 2:310–323

Glückstad J (2004) Microfluidics: sorting particles with light. Nat Mater 3:9–10

Guo W, Herminghaus S, Bahr C (2008) Controlling smectic focal conic domains by substrate patterning. Langmuir 24:8174–8180

Han M, Ishikawa D, Honda T, Ito E, Hara M (2010) Light-driven molecular switches in azobenzene self-assembled monolayers: effect of molecular structure on reversible photoisomerization and stable cis state. Chem Commun 46:3598–3600

Harrison C, Stafford CM, Zhang WH, Karim A (2004) Sinusoidal phase grating created by a tunably buckled surface. Appl Phys Lett 85:4016–4018

Herminghaus S et al (1998) Spinodal dewetting in liquid crystal and liquid metal films. Science 282:916–919

Higgins AM, Jones RAL (2000) Anisotropic spinodal dewetting as a route to self-assembly of patterned surfaces. Nature 404:476–478

Hobbie EK et al (2010) Wrinkling and strain softening in single-wall carbon nanotube membranes. Phys Rev Lett 104:125505

Holmes DP, Crosby AJ (2010) Draping films: a wrinkle to fold transition. Phys Rev Lett 105:038303

Honglawan A et al (2011) Pillar-assisted epitaxial assembly of toric focal conic domains of smectic-a liquid crystals. Adv Mater 23:5519–5523

Hu H, Tamai M (2008) Bioinspired corrugated airfoil at low Reynolds numbers. J Aircraft 45:2068–2077

Huang R, Suo Z (2002) Wrinkling of a compressed elastic film on a viscous layer. J Appl Phys 91:1135–1142

Huang Z, Hong W, Suo Z (2004) Evolution of wrinkles in hard films on soft substrates. Phys Rev E 30601(R):70

Huang ZY, Hong W, Suo Z (2005) Nonlinear analyses of wrinkles in a film bonded to a compliant substrate. J Mech Phys Sol 53:2101–2118

Huck WTS et al (2000) Ordering of spontaneously formed buckles on planar surfaces. Langmuir 16:3497–3501

Hyun DC et al (2010) Buckling- assisted patterning of multiple polymers. Adv Mater 22:2642–2646

Hyun DC et al (2011) Strain-controlled release of molecules from arrayed microcapsules supported on an elastomer substrate. Angew Chem Int Ed 50:724–727

Ichimura K, Oh SK, Nakagawa M (2000) Light-driven motion of liquids on a photoresponsive surface. Science 288:1624–1626

Jackman RJ et al (1998) Fabricating large arrays of microwells with arbitrary dimensions and filling them using discontinuous dewetting. Anal Chem 70:2280–2287

Jiang W et al (2005) Photo-switched wettability on an electrostatic self-assembly azobenzene monolayer. Chem Commun 28:3550–3552

Johnson RE, Dettre RH (1964) Study of an idealized heterogenous surface. J Phys Chem 68:1744–1750

Kargupta K, Sharma A (2002) Dewetting of thin films on periodic physically and chemically patterned surfaces. Langmuir 18:1893–1903

Karthaus O et al (1999) Formation of ordered mesoscopic polymer arrays by dewetting. Chaos 9:308–314

Khang DY, Jiang H, Huang Y, Rogers JA (2006) A stretchable form of single-crystal silicon for high-performance electronics on rubber substrates. Science 311:208–212

Khare K et al (2007) Switching liquid morphologies on linear grooves. Langmuir 23:12997–13006

Kikuchi K et al (2009) Stepwise assembly of micropatterned co-cultures using photoresponsive culture surfaces and its application to hepatic tissue arrays. Biotechnol Bioeng 103:552–561

Kim JH, Yoneya M, Yokoyama H (2002) Tristable nematic liquid-crystal device using micropatterned surface alignment. Nature 420:159–162

Kim YH et al (2009) Confined self-assembly of toric focal conic domains (the effects of confined geometry on the efature size of toric focal conic domains). Langmuir 25:1685–1691

Kim YH, Yoon DK, Jeong HS, Jung HT (2010a) Self-assembled periodic liquid crystal defects array for soft lithographic template. Soft Matter 6:1426–1431

Kim YH et al (2010b) Optically selective microlens photomasks using self-assembled smectic liquid crystal defect arrays. Adv Mater 22:2416–2420

Kleman M, Lavrentovich OD (2000) Grain boundariers and the law of corresponding cones in smectics. Euro Phys J E 2:47–57

Kleman M, Lavrentovich OD (2009) Liquids with conics. Liq Cryst 36:1085–1099

Kleman M, Lavrentovich OD, Nastishin YA (2004) Dislocations in solids. Elsevier, Amsterdam

Lafuma A, Quéré D (2003) Superhydrophobic states. Nat Mater 2:457–460

Lavrentovich OD (1994) Geometrical anchoring at an inclined surface of a liquid crystal. Phys Rev A 46(R):722–725

Lavrentovich OD (1998) Topological defects in dispersed words and worlds around liquid crystals, or liquid crystal drops. Liq Cryst 16:117–124

Lavrentovich OD, Pergamenshchik VM (1995) Patterns in thin liquid crystal films and the divergence (surfacelike) elasticity. Int J Mod Phys B 9:2389–2437

Lee B, Clark NA (2001) Alignment of liquid crystals with patterned isotropic surfaces. Science 291:2576–2580

Leopoldes J, Damman P (2006) From a two-dimensional chemical pattern to a three-dimensional topology through selective inversion of a liquid-liquid bilayer. Nat Mater 5:957–961

Lim HS et al (2006) Photoreversibly switchable superhydrophobic surface with erasable and rewritable pattern. J Am Chem Soc 128:14458–14459

Lin PC, Yang S (2007) Spontaneous formation of one-dimensional ripples in transit to highly ordered two-dimensional herringbone structures through sequential and unequal biaxial mechanical stretching. Appl Phys Lett 90:241903

Link DR, Nakata M, Takanishi Y, Ishikawa K, Takezoe H (2001) Patterns in hybrid nematic liquid-crystal films: topography and topology. Phys Rev Lett 87:195507

Liu GL, Kim J, Lu Y, Lee LP (2006) Optofluidic control using photothermal nanoparticles. Nat Mater 5:27–32

Lu C, Möhwald H, Fery A (2007) A lithography-free method for directed colloidal crystal assembly based on wrinkling. Soft Matter 3:1530–1536

Manyuhina OV, Cazabat AM, Ben Amar M (2010) Instability patterns in ultrathin nematic films: comparison between theory and experiment. Europhys Lett 92:16005

Meyer RB (1973) On the existence of even indexed disclinations in nematic liquid crystals. Philos Mag 27:405–424

Mihailovic M, Oswald P (1988) Zigzag disclination in uniaxial nematic phases: study in capillary tubes. J Phys France 49:1467–1475

Moldovan D, Golubovic L (1999) Buckling dynamics of compressed thin sheets (membranes). Phys Rev Lett 82:2884–2887

Monobe H, Ohzono T (2012) Manipulation of liquid filaments on photoresponsive microwrinkles. ACS Appl Mater Interfaces 4:2212–2217

Nastishin YA, Mayer C, Kleman M (2008) Imperfect focal conic domains in a smectics: a textural analysis. Liq Cryst 35:609–624

Nelson DR (2002) Toward a tetravalent chemistry of colloids. Nano Lett 2:1125–1129

Nicolis G, Prigogine I (1977) Self-organization in nonequilibrium systems. Wiley, New York

Nolte AJ, Rubner MF, Cohen RE (2005) Determining the Young's modulus of polyelectrolyte multilayer films via stress-induced mechanical buckling instabilities. Macromolecules 38:5367–5370

Oh SK, Nakagawa M, Ichimura KJ (1999) Self-assembled monolayers derived from calix[4]resorcinarenes exhibiting excellent desorption resistance and their applicability to surface energy photocontrol. Chem Lett 28:349–350

Oh SK, Nakagawa M, Ichimura KJ (2001) Relationship between the ability to control liquid crystal alignment and wetting properties of calix[4]resorcinarene monolayers. J Mater Chem 11:1563–1569

Ohzono T (2008) Hysteresis in coupled arrays of bistable microwrinkles. Appl Phys Express 1:065002

Ohzono T (2009) Control of cooperative switching of microwrinkle orientations by nanopatterns. Chaos 19:033104

Ohzono T, Fukuda J (2012a) Zigzag line defects and manipulation of colloids in a nematic liquid crystal in microwrinkle grooves. Nat Commun 3:701

Ohzono T, Fukuda J (2012b) Transition of frustrated nematic order and fluctuation of topological defects in microwrinkle groove. Soft Matter 8:11552–11556

Ohzono T, Kitahata H (2012) Phase-separated binary polymers spin coated onto microwrinkles. RSC Adv 2:2395–2398

Ohzono T, Monobe H (2010) Morphological transformation of a liquid micropattern on dynamically tunable microwrinkles. Langmuir 26:6127–6132

Ohzono T, Shimomura M (2004) Ordering of microwrinkle patterns by compressive strain. Phys Rev B 69:132202

Ohzono T, Shimomura M (2005a) Geometry-dependent stripe rearrangement processes induced by strain on preordered microwrinkle patterns. Langmuir 21:7230–7237

Ohzono T, Shimomura M (2005b) Effect of thermal annealing and compression on the stability of microwrinkle patterns. Phys Rev E 72:25203

Ohzono T, Shimomura M (2006a) Simple fabrication of ring-like microwrinkle patterns. Colloids Surf A Physicochem Eng Asp 505:284–285

Ohzono T, Shimomura M (2006b) Defect-mediated stripe reordering in wrinkles upon gradual changes in compression direction. Phys Rev E 73:40601

Ohzono T, Matsushita SI, Shimomura M (2005) Coupling of wrinkle patterns to microsphere-array lithographic patterns. Soft Matter 1:227–230

Ohzono T et al (2007) Spatial forcing of self-organized microwrinkles by periodic nanopatterns. Adv Mater 19:3229–3232

Ohzono T, Monobe H, Shiokawa K, Fujiwara M, Shimizu Y (2009) Shaping liquid on a micrometre scale using microwrinkles as deformable open channel capillaries. Soft Matter 5:4658–4664

Ohzono T, Monobe H, Fukuda N, Fujiwara M, Shimizu Y (2011) Formation of peelable rough gold patterns on an ionic liquid template. Small 7:506–513

Ohzono T, Fukuda J, Suzuki K, Yamaguchi T (2012a) ±1/2 wedge disclinations stabilized by a sinusoidal boundary in a thin hybrid nematic liquid-crystal film. Phys Rev E 86:030701

Ohzono T, Takenaka Y, Fukuda J (2012b) Focal conics in a smectic-a liquid crystal in microwrinkle grooves. Soft Matter 8:6438–6444

Ohzono T, Yamamoto T, Fukuda J (2014) A liquid crystalline chirality balance for vapours. Nat Commun 5:3735

Ohzono T, Katoh K, Fukuda J (2016) Fluorescence microscopy reveals molecular localisation at line defects in nematic liquid crystals. Sci Rep 6:36477

Okayasu T, Zhang HL, Bucknall DG, Briggs GAD (2004) Spontaneous formation of ordered lateral patterns in polymer thin-film structures. Adv Funct Mater 14:1081–1088

Oswald P, Pieranski P (2005) Nematic and cholesteric liquid crystals. Taylor & Francis, New York

Palffy-Muhoray P, Gartland EC, Kelly JR (1994) A new configurational transition in inhomogeneous nematics. Liq Cryst 16:713–718

Reiter G (1992) Dewetting of thin polymer films. Phys Rev Lett 68:75–78

Rosenblatt CS, Pindak R, Clark NA, Meyer RB (1977) The parabolic focal conic – a new smectic a defect. J Phys (Paris) 38:1105–1115

Ruan IZ, Sambles JR, Stewart IW (2003) Self-organized periodic photonic structure in a nonchiral liquid crystal. Phys Rev Lett 91:033901

Scheibert J, Leurent S, Prevost A, Debrégeas G (2009) The role of fingerprints in the coding of tactile information probed with a biomimetic sensor. Science 323:1503–1506

Scherf U, List EJW (2002) Semiconducting polyfluorenes—towards reliable structure–property relationships. Adv Mater 14:477–487

Seki T, Sekizawa H, Morino S, Ichimura K (1998) Inherent and cooperative photomechanical motions in monolayers of an azobenzene containing polymer at the air−water interface. J Phys Chem B 102:5313–5321

Sekitani T et al (2009) Stretchable active-matrix organic light-emitting diode display using printable elastic conductors. Nat Mater 8:494–499

Sharp JS, Jones RAL (2002) Micro-buckling as a route towards surface patterning. Adv Mater 14:799–802

Shimizu H, Horiuchi S, Kitano T (1999) An appearance of heterogeneous structure in a single-phase state of the miscible PVME/PS blends. Macromolecules 32:537–540

Shojaei-Zadeh S, Anna SL (2006) Role of surface anchoring and geometric confinement on focal conic textures in smectic-A liquid crystals. Langmuir 22:9886–9893

Shuttleworth R, Bailey GLJ (1948) The spreading of a liquid over a rough solid. Discuss Faraday Soc 3:16–22

Squires TM, Quake SR (2005) Microfluidics: fluid physics at the nanoliter scale. Rev Mod Phys 77:977–1026

Sridhar N, Srolovitz DJ, Suo Z (2001) Kinetics of buckling of a compressed film on a viscous substrate. Appl Phys Lett 78:2482–2484

Stafford CM et al (2004) A buckling-based metrology for measuring the elastic moduli of polymeric thin films. Nat Mater 3:545–550

Stewart IW (1993) On the parabolic cyclide focal-conic defect in smectic liquid crystals. Liq Cryst 15:859–869

Sumino Y, Magome N, Hamada T, Yoshikawa K (2005) Self-running droplet: emergence of regular motion from nonequilibrium noise. Phys Rev Lett 94:068301

Sun Y, Kumar V, Adesida I, Rogers JA (2006) Buckled and wavy ribbons of GaAs for high-performance electronics on elastomeric substrates. Adv Mater 18:2857–2862

Tersoff J, Jesson DE, Tang WX (2009) Running droplets of gallium from evaporation of gallium arsenide. Science 324:236–238

Tkalec U et al (2011) Reconfigurable knots and links in chiral nematic colloids. Science 333:62–65

Uchida N (2005) Orientational order in buckling elastic membranes. Physica D 205:267–274

Uchida N, Ohzono T (2010) Orientational ordering of buckling-induced microwrinkles on soft substrates. Soft Matter 6:5729–5735

van den Heuvel MGL, de Graaff MP, Dekker C (2006) Molecular sorting by electrical steering of microtubules in kinesin-coated channels. Science 312:910–914

Vendamme R, Onoue S, Nakao A, Kunitake T (2006) Robust free-standing nanomembranes of organic/inorganic interpenetrating networks. Nat Mater 5:494–501

Vendamme R et al (2007) Synthesis and micromechanical properties of flexible, self-supporting polymer-SiO_2 nanofilms. Langmuir 23:2792–2799

Vendeparre H et al (2007) Slippery or sticky boundary conditions: control of wrinkling in metal-capped thin polymer films by selective adhesion to substrates. Phys Rev Lett 99:188302

Walheim S et al (1997) Structure formation via polymer demixing in spin-cast films. Macromolecules 30:4995–5003

Wan P et al (2008) Tuning surface wettability through photocontrolled reversible molecular shuttle. Chem Commun 30:5710–5712

Watanabe M, Shirai H, Hirai T (2002) Wrinkled polypyrrole electrode for electroactive polymer actuators. J Appl Phys 92:4631–4637

Watanabe H, Ohzono T, Kunitake T (2007) Fabrication of large, robust nanomembranes from diverse, cross-linked polymeric materials. Maclomolecules 40:1369–1371

Wei JH, Coffery DC, Ginger DS (2006) Nucleating pattern formation in spin-coated polymer blend films with nanoscale surface templates. J Phys B 110:24324–24330

Wenzel N (1936) Resistance of solid surface to wetting by water. Ind Eng Chem 28:988–994

Xia Y, Whitesides GM (1998) Soft lithography. Angew Chem Int Ed 37:550–575

Xia Y, Qin D, Yin Y (2001) Surface patterning and its application in wetting/dewetting studies. Curr Opin Colloid Interface Sci 6:54–64

Yabu H, Shimomura M (2005) Preparation of self-organized mesoscale polymer patterns on a solid substrate: continuous pattern formation from a receding meniscus. Adv Funct Mater 15:575–581

Yamaguchi T, Epstein IR, Shimomura M, Kunitake T (2005) Introduction: engineering of self-organized nanostructures. Chaos 15:047501

Yamamoto J, Tanaka H (2001) Transparent nematic phase in a liquid-crystal-based microemulsion. Nature 409:321–325

Yang D et al (2007) Photon control of liquid motion on reversibly photoresponsive surfaces. Langmuir 23:10864–11087

Yang S, Khare K, Lin PC (2010) Harnessing surface wrinkle patterns in soft matter. Adv Funct Mater 20:2550–2564

Yoo PJ, Lee HH (2003) Evolution of a stress-driven pattern in thin bilayer films: Spinodal wrinkling. Phys Rev Lett 91:154502

Yoo PJ, Suh KY, Kang H, Lee HH (2004) Polymer elasticity-driven wrinkling and coarsening in high temperature buckling of metal-capped polymer thin films. Phys Rev Lett 93:034301–034304

Yoon DK et al (2007) Internal structure visualization and lithographic use of periodic toroidal holes in liquid crystals. Nat Mater 6:866–870

Zappone B, Meyer C, Bruno L, Lacaze E (2012) Periodic lattices of frustrated focal conic defect domains in smectic liquid crystal films. Soft Matter 8:4318–4326

Chapter 7
Solvent Response

Motoyasu Kobayashi

Abstract Solvent-responsive surfaces prepared by various polymer brushes are described. The motivation and attractive feature of polymer brushes for the design of stimuli- responsive surface was also explained. Polymer brushes, in general, form a relatively stretched conformation in a good or theta solvent due to high osmotic pressure, but collapse in a poor solvent. Therefore, swollen thickness and morphology of brush can be changeable by a selective solvent. AB-type diblock copolymer brushes or binary mixed brushes treated with a selective solvent gave characteristic nano-patterned morphologies attributed to self-assemble behavior which induced large roughness on the surface to result in the wettability change. Swollen thickness and interfacial structures of polyelectrolyte brushes in aqueous solution are strongly affected with pH, added salt concentration, ion species, and temperature. pH-Responsive surface prepared by binary components mixed polyelectrolyte brushes was mentioned. Thermo-sensitive poly(*N*-isopropyl acrylamide) (PNiPAAm) brushes was used as a cell culture surface to achieve the smooth detachment of contiguous cell sheets under reduced temperature by using hydration behavior of PNiPAAm below lower critical solution temperature. Super hydrophilic poly(sulfobetine) brush was fabricated on super hydrophobic poly(vinylidene fluoride) (PVDF) membranes. The resulting membranes successfully separated oil and water from their dispersed mixture by filtration of water with suction and to remain oil portion on the membranes. This is a typical smart application of the characteristic oleophobic behavior underwater of poly(sulfobetine) brush. Various applications of super hydrophilic polyelectrolyte brushes can be expected in the future.

Keywords Polymer brushes · Surface-initiated polymerization · Surface grafting · Polyelectrolyte · Selective solvent · Antifouling

---

M. Kobayashi (✉)
Department of Applied Chemistry, Advanced School of Engineering, Kogakuin University, Tokyo, Japan
e-mail: motokoba@cc.kogakuin.ac.jp

A. Hozumi et al. (eds.), *Stimuli-Responsive Dewetting/Wetting Smart Surfaces and Interfaces*, Biologically-Inspired Systems 11,
https://doi.org/10.1007/978-3-319-92654-4_7

7.1 Introduction

Surface grafting of polymer is one of the promising methods of surface modification. The “surface graft” means here the immobilization of polymers chemically or physically on the surface of different materials. Usually, one chain end of the polymers is covalently bonded to the solid substrate surface to form a teeth brush like structure, and to cover the surface by thin grafting layer like a carpet. Therefore, the surface-grafted polymers are called “polymer brushes” (Rühe 2004). If the water-soluble polymer were immobilized on the material surface, hydrophilic surface would be obtained maintaining the bulk properties of substrates. Similarly, when the hydrophobic fluoropolymer is grafted on the surface, water-repulsive surface is formed. In addition, the surface-grafted polymers do not release from the surface even in a solvent or solution because the polymers are immobilized by covalent bond with the surface. The surface modification effect can remain stable for a long period. This is much different point from the conventional casting film.

Furthermore, if stimuli-responsive functional polymers were grafted on the substrate surface, they would perform stimuli-responsive surface of which wettability, control of adsorption, adhesion, elasticity, morphology, and frictional properties are switchable response to environment condition, such as, temperature, solvent quality, pH, salt species, and ionic strength of a solution. Therefore, the surface properties can be designed by choosing an appropriate surface-grafted polymer with desired chemical properties. This is why the polymer brushes are frequently used for the fabrication of stimuli-responsive surface. In this chapter, various stimuli-responsive surfaces fabricated by polymer brushes are mainly introduced.

7.2 Polymer Brushes

Several procedures to prepare the polymer brushes via “grafting-from” and “grafting-to” approaches have been developed. The “grafting-to” method prepare the brushes by the absorption of end-functionalized polymers or block copolymers having the functional groups or segment which chemically or physically bond with the substrate surface. In general, it is hard to increase the graft density, which is the number of polymer chains onto the surface per unit area, because of the steric hindrance between the absorbed polymers with large free radius of gyration (See Fig. 7.1a). On the other hand, A “grafting-from” method is the polymerization of monomers from the initiator immobilized on the substrate surface. The later method takes a lot of process and more complex than the former one, because the “grafting-from” method includes two steps consisting of initiator immobilization on the surface and chain growth reaction from the surface-tethered initiating cites. However, the surface-initiated chain growth reaction using monomers with relatively smaller hydrodynamic volume could produce a brush with considerably high graft density (Fig. 7.1b).

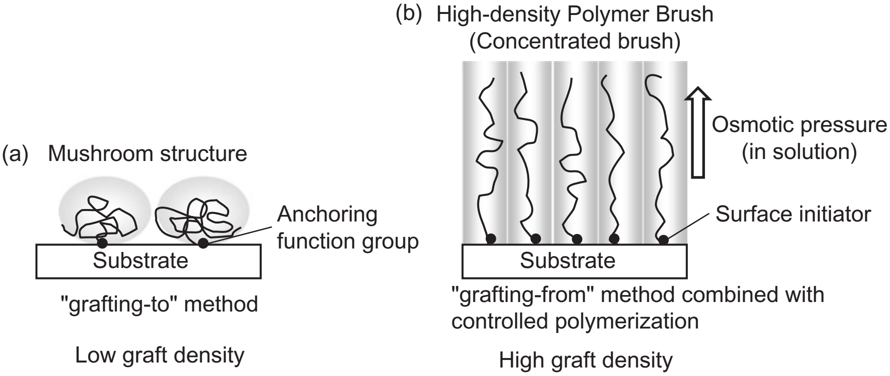

Fig. 7.1 Chain structure images of the surface-grafted polymers with (**a**) low graft density prepared by "grafting-to" method and (**b**) high graft density prepared by "grafting-from" method combined with controlled polymerization

Surface-tethered polymers with a high graft density exhibit various unique properties compared with the low density brush, in particular, in a solution. When the polymer brushes were immersed to a good solvent, the polymer brushes form a swollen structure and increase the thickness of brush layer due to high osmotic pressure and chain stretching direction normal to the substrate surface, whereas the brushes collapse in a poor solvent to form a shrunk structure. The structure change results in a variety of morphologies including a smooth and rough surface. Therefore, the swollen thickness and the surface morphology of the brush vary with solvent quality, such as a good solvent, poor solvent, and theta solvent. These switchable brush structures could be regard as solvent response surfaces.

To induce the surface morphology change by solvent treatment, block copolymer brushes or mixed brushes are required. A block copolymer brush consists of several different component blocks which are sequentially connected in one tethered chain. A mixed brush is assemble of chemically different polymers tethered on a surface individually. Both are prepared by surface-initiated controlled/ living polymerization technique which enable to produce the well-defined polymer brushes having a predictable molecular weight, narrow molecular weight distribution (MWD), controlled block sequence, and graft density. In particular, controlled radical polymerization, such as nitroxide-mediated living free radical polymerization (NMRP), atom transfer radical polymerization (ATRP), and reversible addition fragmentation chain transfer (RAFT) polymerization, were widely used to prepare the polymer brushes, nowadays, because of abundance of monomer species and convenient process. Figure 7.2 shows a typical procedure for polymer brush synthesis by surface-initiated ATRP (SI-ATRP) using a copper bromide catalyst. The following sections describe several reports related with the solvent response surfaces designed by well-defined functional polymer brushes.

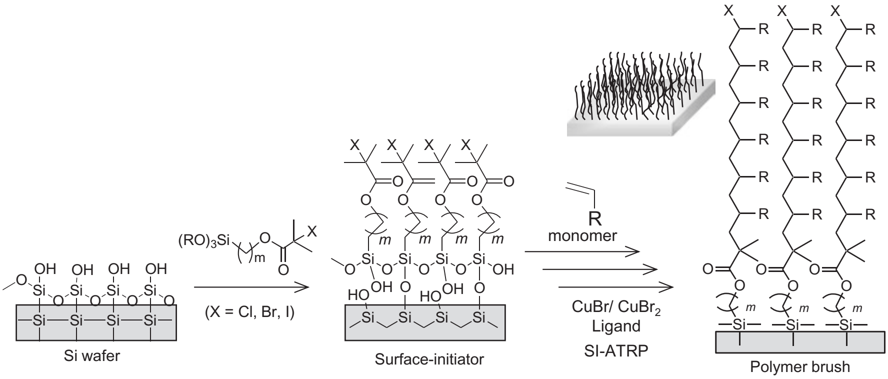

Fig. 7.2 Typical procedure example for polymer brush synthesis by surface-initiated atom transfer radical polymerization of vinyl monomer from the surface-immobilized alkyl halide (initiator) on silicon wafer

7.3 Organic Solvent Response Surfaces

The morphology of the surface-tethered AB diblock copolymer brush on a substrate has been well studied due to its unique structure appeared in selective solvents which are a good solvent or a theta solvent for one block but a poor solvent for another block. In the selective solvents, less soluble block form a self-assemble core, and more soluble blocks form a shell around the core. Eventually, the block copolymer brushes produce an ordered array structure. For example, Brritain et al. prepared polystyrene -*block*- poly(methyl methacrylate) (PS-*b*-PMMA) brush and PS-*block*- poly(methyl acrylate) (PS-*b*-PMA) brush on a flat substrates (Zhao et al. 2000). PS block was connected with substrate surface, and PMMA and PMA blocks were located at the outermost free surface side. These diblock brushes afforded smooth surface after treatment with dichloromethane (CH_2Cl_2), but relatively rough surface by treatment with cyclohexane (cHex) which favor PS rather than PMMA and PMA. In mixture solvent of CH_2Cl_2 and cHex, increasing with the cHex content, the surface morphology of these diblock brushes changed from the featureless smooth surface to very rough surface consisting of self-assemble array, as shown in Fig. 7.3. Advancing water contact angle on (PS-*b*-PMMA) brush surface also increased from 99 deg. to 120 deg. after the treatment with cHex.

Amphiphilic block copolymer brush also induces the surface rearrangement by solvent. Iyoda et al. prepared PMMA-*block*-poly(acrylamide) (PMMA-*b*-PAAm) brush on silicon wafer by surface-initiated sequential ATRP of MMA as the first monomer and of AAm as the second monomer (Kong et al. 2001). After treatment with water, hydrophilic PAAm block stretched to cover the PMMA block surface in water, whereas PMMA block were shrunk near the substrate. Treatment of brush

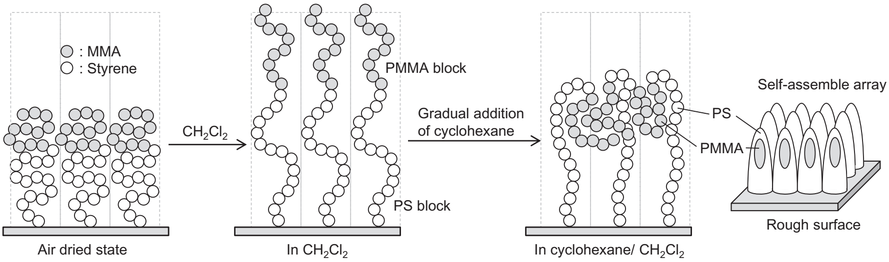

Fig. 7.3 Schematic illustration of self-assemble array of PS-*b*-PMMA copolymer brush in cyclohexane/ CH_2Cl_2 mixture. White and gray circles stand for styrene and MMA units of polymer chains, respectively

substrate with toluene resulted in a swollen structure of PMMA block and segregation of PAAm block near the interface of toluene, leading to phase separation.

A binary mixed polymer brushes exhibits drastic lateral and vertical reorganization by treatment with selective solvents. Zhao et al. synthesized Y-shape binary initiator having a nitroxy moiety and an alkyl bromide group to immobilize on the silicon wafer, and carried out ATRP of MMA and successive NMRP of styrene to prepare PS/PMMA mixed brush (Zhao et al. 2004), as shown in Fig. 7.4a. Both brushes were homogeneously stretched chain structure in chloroform, however, the treatment of glacial acetic acid induce the rough surface due to the formation of micelle like aggregation structure consisting of shrunk PS core shielded by PMMA shell. Feng et al. carried out surface-initiated UV photo polymerization of styrene from azo-type radical initiator immobilized on gold surface, and subsequent polymerization of MMA from the same substrates using unreacted azo initiator to give the mixed brushes with a random distribution of PS and PMMA (Feng et al. 2004a). Because the radical initiation efficiency of azo compound is not quantitative, some unreacted initiator still remained on the surface even after the first polymerization of styrene, and could initiate the 2nd polymerization of MMA to give the binary mixed brush (Fig. 7.4b).

PS/ PMMA mixed brush formed swollen structure of both polymers in THF to show smooth surface. Non polar cHex solvent yielded a surface enriched in PS due to the collapse of PMMA brush, whereas treatment with a polar isobutanol afforded a surface enriched in PMMA due to the collapse of PS brush. Similar morphological change behavior induced by selective solvents have been also reported on other mixed brush surfaces, such as poly(acrylic acid)/ poly(butyl acrylate) brushes in water/ toluene or chloroform/ methanol solvents (Ye et al. 2011), poly(styrene-*co*-2,3,4,5,6-pentafluorostyrene)/ PMA brushes in toluene/ acetone solvents (Lemieux et al. 2003), and PMMA/ poly(ethyleneglycol methacrylate) brushes in THF/ toluene/ethanol solvents (Feng et al. 2009) (Fig. 7.5).

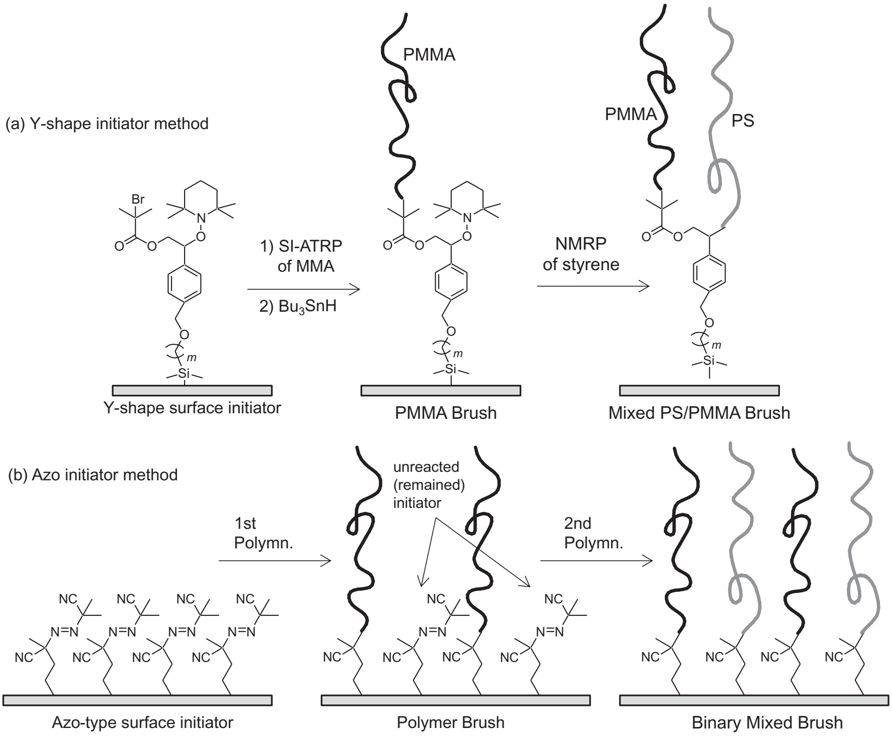

Fig. 7.4 Binary mixed brush preparation by surface-initiated radical polymerization using (**a**) Y-shape bi-functional initiator and (**b**) azo group containing initiator

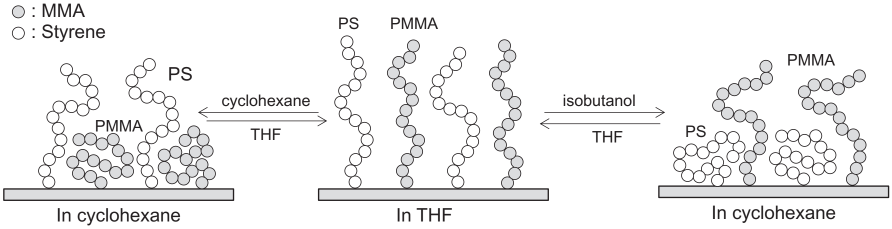

Fig. 7.5 Surface morphology switching of PS/ PMMA mixed brush by treatment with selective solvent using cyclohexane and isobutanol. White and gray circles stand for styrene and MMA units of polymer chains, respectively

7.4 Aqueous Solution Response Surface

In general, the chain conformation of ion-containing polymer brushes in aqueous solution are very difficult to understand completely, because too many factors, such as pH, ionic strength, ion species, short-range excluded volume interactions, long

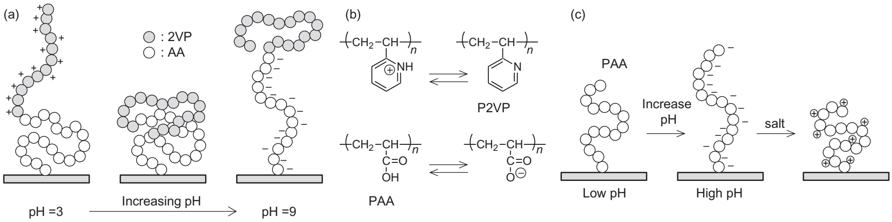

Fig. 7.6 (**a**) Conformational change in P2VP-*b*-PAA brush in a low and high pH solution, (**b**) chemical structure of protonated P2VP in a low pH condition and negatively charged PAA in basic aqueous solution, and (**c**) conformational change in PAA brush by pH and added salt. White and gray circles stand for acrylic acid and 2-vinyl pyridine units of polymer chains, respectively

range electrostatic interactions, and translational entropies of the counter-ions (Zhulina and Rubinstein 2012), should be carefully considered. However, the polyelectrolyte brushes represent excellent water wettability based on super hydrophilicity, attractive underwater antifouling, and water lubrication. Therefore, various types of stimuli-response polyelectrolytes brushes have been developed until now.

Minko et al. prepared gradient mixed brush of PAA and poly(2-vinyl pyridine) (P2VP) by “grafting-to” method (Ionov et al. 2004a). After the treatment with lower pH aqueous solution, water contact angle of PAA brush surface was higher than 60 deg., whereas the water contact angle was lower than 20 deg. by the treatment with high pH solution, due to the negatively charged PAA (Fig. 7.6). In the case of mixed brush with P2VP/PAA =8/2, water contact angle was lower than 20 deg. after the acidic treatment, because the P2VP chains were highly protonated and stretched away from the surface (Fig. 7.6). The change of pH affected the change of charge distribution of mixed brushes. The water contact angle switching assisted by different pH solution was also observed on PS/ 2VP mixed brush surface by treatment with HCl and toluene/ THF (Sidorenko et al. 1999; Ionov et al. 2004b).

The conformational behavior of polyelectrolyte brushes in aqueous solution depends on the type of polyelectrolyte. The polyelectrolyte chains, which possess either positive or negative charges in their molecules, in a salt-free solution form relatively stretched chain structures because of strong intramolecular repulsive interactions between the charged groups on the polymer chains, whereas they collapse with increasing salt concentration because of the electrostatic screening effect of the added salts as shown in Fig. 7.6c (Rühe et al. 2004; Pincus 1991; Biesalski et al. 2004). The resulting polyelectrolytes behave like electrically neutral polymers in aqueous salt solutions with high ionic strength (Takahashi et al. 1970; Nagasawa and Eguchi 1976). Positively or negatively charged polyelectrolyte brushes also collapse with increasing content of organic solvent because the low dielectric constant of solvent (Albright and Gosting 1946) induce the electrostatic attractions between the charged groups (Wang et al. 2012; Liu et al. 2013; Long et al. 2013). The types of salt and counter ion also affect the chain conformation of polyelectrolytes in aqueous solution (Azzaroni et al. 2005; Xu and Liu 2014). The effect of counter cation on negatively charged polyelectrolyte brushes have been well studied by Liu

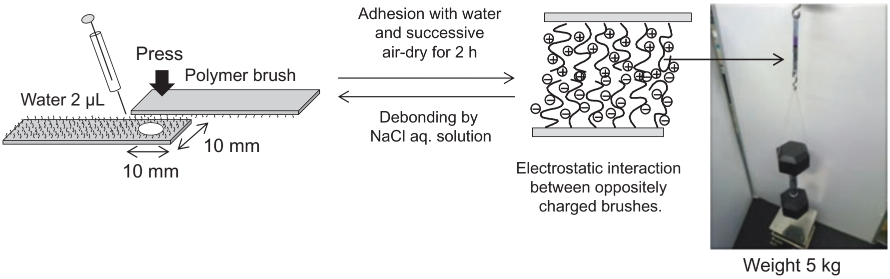

Fig. 7.7 Repeatable adhesion achieved by oppositely charged polyelectrolyte brushes

et al. (Hou et al. 2011; Pozar et al. 2011; Wang et al. 2014) Murdoch et al. investigated the influence of mobile anion hydrophilicity, poorly hydrated thiocyanate and strongly hydrate acetate, on the conformation of weak cationic poly(2-diisopropylaminoethyl methacrylate) brush in aqueous solution by neutron reflectively (NR) measurement to observe swollen brush structure in acetate ion solution and collapsed conformation in thiocyanate solution (Murdoch et al. 2016).

The effect of pH on polyelectrolyte brush can be observed in adhesion property. LaSpina et al. found out that the interaction between poly(*N,N*-dimethylaminoethyl methacrylate) (PDMAEMA) brush and poly(methacrylic acid) gel were switchable by pH condition (LaSpina et al. 2007). The adhesive interaction must be originated in the electrostatic interaction between opposite charges as well as hydrogen bonding between amine and carboxyl groups. Both interaction depends on pH. Sudre et al. also measured adhesive interaction between pH-responsible PAA brush and PDMAEMA gel surface in various pH solution by contact mechanism method (Sudre et al. 2012). Switchable adhesion strength by pH value inspired the reversible adhesion system using polyelectrolyte brushes. Kobayashi et al. achieved repeatable adhesion based on electrostatic interaction between oppositely charged polymer brushes. Two substrates with oppositely charged polyelectrolyte brushes bonded strongly to each other, and smoothly debonded in aqueous NaCl solution, as shown in Fig. 7.7 (Kobayashi et al. 2011; Yoshioka et al. 2017).

Polyzwitterions, so-called polybetaines, which have oppositely charged groups in the same monomer units, also show characteristic solution behavior depending on the ionic strength of the aqueous solution (Kudaibergenov 2002). Polyzwitterions forms rather shrunken chain structures in salt-free water compared to those in an aqueous salt solution because of strong inter- or intra-molecular attractive interactions between ion groups in the polymer chains. For example, a typical sulfobetaine polymer, poly[3-(*N*-2-methacryloyloxyethyl-*N,N*-dimethyl)-ammonatopropanesulfonate] (PMAPS) (Fig. 7.8), is not soluble in a salt free water below room temperature, because of strong attractive interactions between the sulfobetaines, but is soluble in aqueous salt solutions (Kikuchi et al. 2015). Increase in swollen thickness of PMAPS brush with increase in salt concentration was characterized by neutron reflectively (NR) measurement (Kobayashi et al. 2013a; Higaki et al. 2017). In contrast, poly(2-methacryloyloxyethyl phosphorylcholine) (PMPC) is known as an

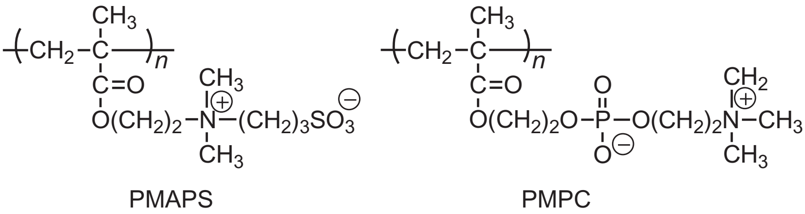

Fig. 7.8 Chemical structure of PMAPS and PMPC

exceptional polyzwitterion because no conformational change occurs in PMPC brush even in a salt solution. Light scattering study proved that hydrodynamic radius and intermolecular interaction of PMPC are independent of salt concentration (Matsuda et al. 2008a). The reason for the curious independence of ionic strength on PMPC conformation in aqueous media is unclear. The phosphorylcholine group might have some specific hydration mechanism or interaction with water molecules (Kitano et al. 2003). Although the PMPC in aqueous solution is hardly affected by salt ion and temperature, PMPC has very rare property, cononsolvency, in water/ ethanol mixture (Matsuda et al. 2008b). PMPC is soluble in pure water as well as pure ethanol, but insoluble in the mixture in which ethanol content is 35 ~ 80 vol%. Drastic change from swollen PMPC brush in deuterium oxide (D_2O) to collapse in the mixture of ethanol-d4/ D_2O was clearly observed by NR measurement (Kobayashi et al. 2014). These results indicate that PMPC is also a solvent responsive polymer.

PMAPS exhibit continuous phase separation in water at the upper critical solution temperature (UCST) (Schulz et al. 1986; Chen et al. 2000). NR measurement showed the PMAPS brush chain extended and defused into the direction of water interface, as the solution temperature elevated (Kobayashi and Takahara 2013). Kobayashi et al. applied the thermo-sensitive nature of the dipole-dipole interaction between PMAPS brushes to the repeatable adhesion (Kobayashi and Takahara 2013).

Poly(*N*-isopropyl acrylamide) (PNiPAAm) is well-known as a temperature-triggered stimuli-response polymer having the lower critical solution temperature (LCST) in aqueous solution. PIPAAm is soluble with a hydrated, extended chain conformation in aqueous solution below 32 °C and becomes insoluble due to chain dehydration and aggregation above this temperature. Okano and his co-workers prepared PNiPAAm brushes with appropriate thickness on poly(4-vinylbenzyl chloride)-coated polystyrene surfaces using surface- initiated ATRP, and cultured endothelia cells on PNiPAAm brush surface at 37 °C. Confluent cell monolayers spontaneously detached as contiguous cell sheets from PNiPAAm brush surface at reduced temperature (20 °C), as shown in Fig. 7.9. Effect of brush thickness and preparation method on the cell detachment behavior was also studied (Kumashiro et al. 2013). This useful application of stimuli-response hydrophilic polymer brush is expected to contribution to cell- sheet engineering and chromatography (Nagase et al. 2010).

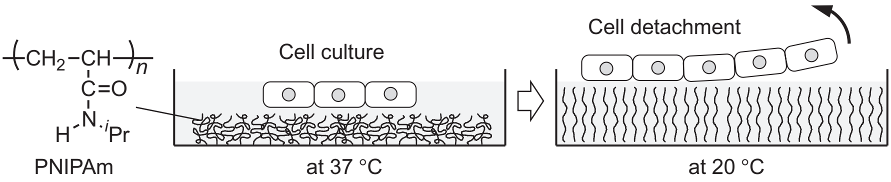

Fig. 7.9 Cell adhesion and detachment controlled by thermo-responsive PNiPAAm brush surfaces

PMPC was developed polyzwitterion by Ishihara in 1990 as a biocompatible polymer inspired by chemical structure of phosphatidylcholine molecule in phospholipid membrane of living cell (Ishihara et al. 1990). PMPC brush shows extremely low water contact angle below 3 deg. in air (Kobayashi et al. 2012). Air bubble and oil droplet in contact with PMPC brush surface in water formed sphere like shapes, indicating the super hydrophilic surface. The surface free energy of PMPC brush was estimated to be 74.5 mN/m by Owens-Wendt method, and the work of adhesion between dichloroethane oil and brush in water was as low as 0.04 mN/m (Kobayashi et al. 2013b). Such a low work of adhesion induces the detachment of oil droplets from the PMPC brush surface in aqueous media, which is expected to many applications, such as self-cleaning and antifouling systems (Higaki et al. 2015, 2016).

Super hydrophilicity of polyzwitterion brushes can be applied to oil/ water separation. Zhu et al. carried out surface-initiated ATRP of MAPS from the surface of pre-treated poly(vinylidene fluoride) (PVDF) membrane with 0.22 μm pore to prepare the PMAPS-*graft*-PVDF membrane (Zhu et al. 2013), of which surface exhibits very low water contact angle (11 deg.) in air and high contact angle of oil (1,2-dichloroethane) (158 deg.) in water, indicating a super hydrophilic and underwater super oleophobic properties. They prepare dispersed oil/ water mixture (oil 20 v/v%) including isooctane/water, hexane/water, diesel/water, petroleum ether/ water, and soybean oil/water by sonication. These milky oil/ water mixtures were filtrated with suction by the PMAPS-*graft*-PVDF membrane, then water passed through the membrane and oily portion remained on the membrane (Fig. 7.10). The oil contents after separation was all less than 10 ppm and the isooctane content was as low as 0.2 ppm. This is a smart application using a unique oleophobic property underwater of PMAPS brush.

Those oil/ water separation system using a super hydrophilic coat on hydrophobic mesh film have been already reported, such as PAA-*graft*-PVDF (Yang et al. 2015), and combination of poly(styrene-*co*-maleic anhydride) with aqueous cationic fluorosurfactant (Brown et al. 2014) Although the polymer brush was not used, the combination of super hydrophobic and super oleophilic materials has been also proposed to separate the oil and water using a polytetrafluoroethylene (PTFE) coated stainless steel mesh (Feng et al. 2004b), carbon nanotube sponges (Gui et al. 2010),

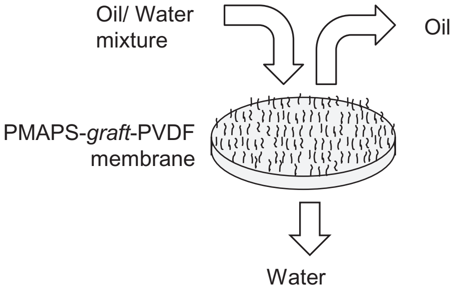

Fig. 7.10 Oil/ water separation using a super hydrophilic PMAPS-grafted PVDF membrane

polydimethylsiloxane (PDMS) coated nanowire membrane (Yuan et al. 2008), hydrophobic aerogels (Standeker et al. 2007), cross-linked oil absorbing polymer gel (Ono et al. 2007), and cross-linked poly(orthocarbonate)s (Sonmez and Wudl 2005).

7.5 Summary

In this chapter, recent works on solvent-responsive surfaces assisted by polymer brushes were described. Surface morphology change takes places by self-assemble behavior of block copolymer brushes or binary mixed brushes in a selective solvent, to results in a roughness enhanced surface and wettability switching. Water soluble polymer brushes, polyelectrolyte brush in particular, are sensitive to pH, added salt ion concentration, and temperature of aqueous solution. Thermo-sensitive brushes, such as PNiPAAm and PMAPS, and super hydrophilic PMPC brushes have become the attractive key players to design the new bio interface materials, nowadays. Antifouling and oil/ water separation system are expected technology for many years to come in the future. It is expected that the fundamental researches and applications of super hydrophilic coating or brushes spread in the various fields.

References

Albright PS, Gosting LJ (1946) Dielectric constants of the methanol-water system from 5 to 55°. J Am Chem Soc 68:1061–1063

Azzaroni O, Moya S, Farhan T, Brown AA, Huck WTS (2005) Switching the properties of polyelectrolyte brushes via “hydrophobic collapse”. Macromolecules 38:10192–10199

Biesalski M, Johannsmann D, Rühe J (2004) Electrolyte-induced collapse of a polyelectrolyte brush. J Chem Phys 120:8807–8814

Brown PS, Atkinson ODLA, Badyal JPS (2014) Ultrafast oleophobic hydrophilic switching surfaces for antifogging, self-cleaning, and oil-water separation. ACS Appl Mater Interfaces 6:7504–7511

Chen L, Honma Y, Mizutani T, Liaw DJ, Gong JP, Osada Y (2000) Effects of polyelectrolyte complexation on the UCST of zwitterionic polymer. Polymer 41:141–147

Feng J, Haasch RT, Dyer DJ (2004a) Photoinitiated synthesis of mixed polymer brushes of polystyrene and poly(methyl methacrylate). Macromolecules 37:9525–9537

Feng L, Zhang Z, Mai Z, Ma Y, Liu B, Jiang L, Zhu D (2004b) A super-hydrophobic and super-oleophilic coating mesh film for the separation of oil and water. Angew Chem Int Ed 43:2012–2014

Feng L, Wang Y, Wang S (2009) Mixed poly(methyl methacrylate)/poly(ethylene glycol) brushes: study of switching behavior in selective solvent. J Appl Polym Sci 112:2112–2119

Gui X, Wei J, Wang K, Cao A, Zhu H, Jia Y, Shu Q, Wu D (2010) Carbon nanotube sponges. Adv Mater 22:617–621

Higaki Y, Nishida J, Takenaka A, Yoshimatsu R, Kobayashi M Takahara A (2015) Versatile inhibition of marine organism settlement by zwitterionic polymer brushes. Polym J 47:811–818

Higaki Y, Kobayashi M, Murakami D, Takahara A (2016) Anti-fouling behavior of polymer brush immobilized surfaces. Polym J 48:325–331

Higaki Y, Inutsuka Y, Sakamaki T, Terayama Y, Takenaka A, Higaki K, Yamada NL, Moriwaki T, Ikemoto Y, Takahara A (2017) Effect of charged group spacer length on hydration state in zwitterionic poly(sulfobetaine) brushes. Langmuir 33:8404–8412

Hou Y, Liu GM, Wu Y, Zhang GZ (2011) Reentrant behavior of grafted poly(sodium styrenesulfonate) chains investigated with a quartz crystal microbalance. Phys Chem Chem Phys 13:2880–2886

Ionov L, Houbenov N, Sidorenko A, Stamm M, Luzinov I, Minko S (2004a) Inverse and reversible switching gradient surfaces from mixed polyelectrolyte brushes. Langmuir 20:9916–9919

Ionov L, Stamm M, Minko S, Hoffmann F, Wolff T (2004b) Switching and structure of binary reactive polymer brush layer. Macromol Symp 210:229–235

Ishihara K, Ueda T, Nakabayashi N (1990) Preparation of phospholipid polymers and their properties as polymer hydrogel membranes. Polym J 22:355–360

Kikuchi M, Terayama Y, Ishikawa T, Hoshino T, Kobayashi M, Ohta N, Jinnai H, Takahara A (2015) Salt dependence of the chain stiffness and excluded-volume strength for the polymethacrylate-type sulfopropylbetaine in aqueous NaCl solutions. Macromolecules 48:7194–7204

Kitano H, Imai M, Mori T, Gemmei-Ide M, Yokoyama Y, Ishihara K (2003) Structure of water in the vicinity of phospholipid analogue copolymers as studied by vibrational spectroscopy. Langmuir 19:10260–10266

Kobayashi M, Takahara A (2013) Environmentally friendly repeatable adhesion using a sulfobetaine-type polyzwitterion brush. Polym Chem 4:4987–4992

Kobayashi M, Terada M, Takahara A (2011) Reversible adhesive-free nanoscale adhesion utilizing oppositely charged polyelectrolyte brushes. Soft Matter 7:5717–5722

Kobayashi M, Terayama Y, Yamaguchi H, Terada M, Murakami D, Ishihara K, Takahara A (2012) Wettability and antifouling behavior on the surfaces of superhydrophilic polymer brushes. Langmuir 28:7212–7222

Kobayashi M, Terayama Y, Kikuchi M, Takahara A (2013a) Chain dimensions and surface characterization of superhydrophilic polymer brushes with zwitterion side groups. Soft Matter 9:5138–5148

Kobayashi M, Matsugi T, Saito J, Imuta J, Kashiwa N Takahara A (2013b) Direct modification of polyolefin films by surface-initiated polymerization of a phosphobetaine monomer. Polym Chem 4:731–739

Kobayashi M, Ishihara K, Takahara A (2014) Neutron reflectivity study of the swollen structure of polyzwitterion and polyelectrolyte brushes in aqueous solution. J Biomater Sci Polym Ed 25:1673–1686

Kong X, Kawai T, Abe J, Iyoda T (2001) Amphiphilic polymer brushes grown from the silicon surface by atom transfer radical polymerization. Macromolecules 34:1837–1844

Kudaibergenov S (2002) Polyampholytes. Kluwer Academic/Plenum Publishers, New York, pp 137–146

Kumashiro Y, Fukumori K, Takahashi H, Nakayama M, Akiyama Y, Yamato M, Okano T (2013) Modulation of cell adhesion and detachment on thermo-responsive polymeric surfaces through the observation of surface dynamics. Colloids Surf B Biointerfaces 106:198–207

LaSpina R, Tomlinson MR, Ruiz-Pérez L, Chiche A, Langridge S, Geoghegan M (2007) Controlling network-brush interactions to achieve switchable adhesion. Angew Chem Int Ed 46:6460–6463

Lemieux M, Usov D, Minko S, Stamm M, Shulha H, Tsukruk VV (2003) Reorganization of binary polymer brushes: reversible switching of, surface microstructures and nanomechanical properties. Macromolecules 36:7244–7255

Liu LD, Wang T, Liu C, Lin K, Ding YW, Liu GM, Zhang GZ (2013) Mechanistic insights into amplification of specific ion effect in water-nonaqueous solvent mixtures. J Phys Chem B 117:2535–2544

Long YC, Wang T, Liu LD, Liu GM, Zhang GZ (2013) Ion specificity at a low salt concentration in water-methanol mixtures exemplified by a growth of polyelectrolyte multilayer. Langmuir 29:3645–3653

Matsuda Y, Kobayashi M, Annaka M, Ishihara K, Takahara A (2008a) Dimensions of a free linear polymer and polymer immobilized on silica nanoparticles of a zwitterionic polymer in aqueous solutions with various ionic strengths. Langmuir 24:8772–8778

Matsuda Y, Kobayshi M, Annaka M, Ishihara K, Takahara A (2008b) UCST-type cononsolvency behavior of poly(2-methacryloxyethyl phosphorylcholine) in the mixture of water and ethanol. Polym J 40:479–483

Murdoch TJ, Willott JD, de Vos WM, Nelson A, Prescott SW, Wanless EJ, Webber GB (2016) Influence of anion hydrophilicity on the conformation of a hydrophobic weak polyelectrolyte brush. Macromolecules 49:9605–9617

Nagasawa M, Eguchi Y (1976) The charge effect in sedimentation I. Polyelectrolyte. J Phys Chem 71:880–888

Nagase K, Kumazaki M, Kanazawa H, Kobayashi J, Kikuci A, Akiyama Y, Annaka M, Okano T (2010) Thermoresponsive polymer brush surfaces with hydrophobic groups for all-aqueous chromatography. ACS Appl Mater Int 2:1247–1253

Ono T, Sugimoto T, Shinkai S, Sada K (2007) Lipophilic polyelectrolyte gels as super-absorbent polymers for nonpolar organic solvents. Nauret Mater 6:429–433

Pincus P (1991) Colloid stabilization with grafted polyelectrolytes. Macromolecules 24:2912–2919

Pozar J, Bohinc K, Vlachy V, Kovacevic D (2011) Ion-specific and charge effects in counterion binding to poly(Styrenesulfonate) anions. Phys Chem Chem Phys 13:15610–15618

Rühe J (2004) Polymer brushes on the way to tailor-made surfaces. In: Advincula RC, Brittain WJ, Caster KC, Rühe J (eds) Polymer brushes: synthesis, characterization, applications. Wiley VCH, Weinheim, pp 1–31

Rühe J, Ballauff M, Biesalski M, Dziezok P, Gröhn F, Johannsmann D, Houbenov N, Hugenberg N, Konradi R, Minko S, Motornov M, Netz RR, Schmidt M, Seidel C, Stamm M, Stephan T, Usov D, Zhang H (2004) Polyelectrolyte brushes. Adv Polym Sci 165:79–150

Schulz DN, Peiffer DG, Agarwal PK, Larabee J, Kaladas JJ, Soni L, Handwerker B, Garner RT (1986) Phase behaviour and solution properties of sulphobetaine polymers. Polymer 27:1734–1742

Sidorenko A, Minko S, Meuser KS, Duschner H, Stamm M (1999) Switching of polymer brushes. Langmuir 15:8349–8355

Sonmez HB, Wudl F (2005) Cross-linked poly(orthocarbonate)s as organic solvent sorbents. Macromolecules 38:1623–1626

Standeker S, Novak Z, Knez Z (2007) Adsorption of toxic organic compounds from water with hydrophobic silica aerogels. J Colloid Interface Sci 31:362–368

Sudre G, Olanier L, Tran Y, Hourdet D, Creton C (2012) Reversivle adhesion between a hydrogel and a polymer brush. Soft Matter 8:8184–8193

Takahashi A, Kato N, Nagasawa M (1970) The osmotic pressure of polyelectrolyte in neutral salt solutions. J Phys Chem 74:944–946

Wang T, Liu GM, Zhang GZ, Craig VSJ (2012) Insights into ion specificity in water-methanol mixtures via the reentrant behavior of polymer. Langmuir 28:1893–1899

Wang T, Long Y, Liu L, Wang X, Craig VSJ, Zhang G, Liu G (2014) Cation-specific conformational behavior of polyelectrolyte brushes: from aqueous to nonaqueous solvent. Langmuir 30:12850–12859

Xu Y, Liu G (2014) Amplification of Hofmeister effect by alcohols. J Phys Chem B 118:7450–7456

Yang R, Moni P, Gleason KK (2015) Ultrathin zwitterionic coatings for roughness-independent underwater superoleophobicity and gravity-driven oil-water separation. Adv Mater Interfaces 2(2): 1400489

Ye P, Dong H, Zhong M, Matyjaszewski K (2011) Synthesis of binary polymer brushes via two-step reverse atom transfer radical polymerization. Macromolecules 44:2253–2260

Yoshioka H, Izumi C, Shida M, Yamaguchi K, Kobayashi M (2017) Repeatable adhesion by proton donor-acceptor interaction of polymer brushes. Polymer 119:167–175

Yuan J, Liu X, Akubulut O, Xu J, Suib SL, Kong J, Stellacci F (2008) Superwetting nanowire membranes for selective absorption. Nature Nanotechnol 3:332–336

Zhao B, Brittain WJ, Zhou W, Cheng SZD (2000) AFM study of tethered polystyrene-b-poly(methyl methacrylate) and polystyrene-b-poly(methyl acrylate) brushes on flat silicate substrates. Macromolecules 33:8821–8827

Zhao B, Haasch RT, MacLaren S (2004) Solvent-induced self-assembly of mixed poly(methyl methacrylate)/polystyrene brushes on planar silica substrates: molecular weight effect. J Am Chem Soc 126:6124–6134

Zhu Y, Zhang F, Wang D, Pei XF, Zhang W, Jin J (2013) A novel zwitterionic polyelectrolyte grafted PVDF membrane for thoroughly separating oil from water with ultrahigh efficiency. J Mater Chem A 1:5758–5765

Zhulina EB, Rubinstein M (2012) Ionic strength dependence of polyelectrolyte brush thickness. Soft Matter 8:9376–9383

Chapter 8
Magnetic-Responsive Superwetting Surface

Dongliang Tian, Na Zhang, Yan Li, and Lei Jiang

Abstract Magnetic-responsive materials surfaces, especially for the magnetic-responsive superwetting surface, has attracted more and more attention in basic research and practical applications in intelligent fluid-controllable devices, owing to their advantages of in situ control, fast response, remote control and low energy consumption. This chapter focuses on the magnetic-responsive wettability on the superwetting surface and their typical applications, particularly on switchable wettability on magnetic-responsive surfaces and their applications such as tunable adhesion surface, microstructure fabrication, droplet actuation, and smart separation. Finally, our personal points of the future research prospect of this research are discussed.

Keywords Magnetic-responsive surface · Superwetting · Tunable adhesion · Liquid actuation · Separation

8.1 Introduction

Surface wettability is a very important surface property of solid or liquid, which is dominated by the chemical component and micro/nanostructures of surface (Tian et al. 2014a; Sun et al. 2011; Xia et al. 2012; Zhang and Han 2010; Quéré 2008; Tian et al. 2013; Li et al. 2007; Xin and Hao 2010). For a surface with fixed composition, micro/nanostructures are the main contribution to obtain a superwetting

---

D. Tian · N. Zhang · Y. Li
Beijing Advanced Innovation Center for Biomedical Engineering, School of Chemistry, Beihang University, Beijing, China

L. Jiang (✉)
Beijing Advanced Innovation Center for Biomedical Engineering, School of Chemistry, Beihang University, Beijing, China

Technical Institute of Physics and Chemistry, Chinese Academy of Sciences, Beijing, China
e-mail: jianglei@iccas.ac.cn

A. Hozumi et al. (eds.), *Stimuli-Responsive Dewetting/Wetting Smart Surfaces and Interfaces*, Biologically-Inspired Systems 11,
https://doi.org/10.1007/978-3-319-92654-4_8

surface such as superhydrophobic and superhydrophilic surface (Sun et al. 2005; Wen et al. 2015; Zhang et al. 2008; Xia and Jiang 2008; Su et al. 2015; Yao et al. 2011; Feng and Jiang 2006). Accompanying with the rapid advancement of micro/nanofabrication technology, the superwetting surfaces, as a research hot topic, have made great progress and gear up the development of the related applications area (Wang et al. 2015a; Liu et al. 2010a, b, 2014;). Under the rapid development of the interface science in special wettability, smart responsive materials surface with switch extreme wettability have been widely explored and used in the fields of smart driving, chemical manufacturing, environmental science, and microfluidic devices, and so on (Wang et al. 1997, 2007; Tian et al. 2014b; Xia et al. 2007; Crevoisier et al. 1999; Yao et al. 2013). Recently, magnetic field responsive surface have been broadly investigated and applied due to the advantages of in situ control, fast response, remote control and low energy consumption (Liu et al. 2010a, 2014). Combined with the magnetic-responsive surfaces with super-wetting surfaces, many phenomena arose and the important research results have been demonstrated, developed and used to solve the challenging problems in the world.

This chapter will focus on the recent progress of the magnetic-responsive superwetting surface and their typical applications, particularly on switchable wettability of magnetic-responsive surfaces and the related applications. There are four main sections in this chapter. In Sect. 8.2, we summarize the switchable wettability on magnetic-responsive surfaces. Section 8.3 reviews on the applications including tunable surface adhesion, microstructure fabrication, droplet actuation, and smart separation. Finally, our personal point of the prospects and challenges of the magnetic-responsive wettability surfaces are addressed.

8.2 Switchable Wettability on Magnetic-Responsive Surfaces

Magnetic responsive materials can fast response to magnetic field accompanying with the structure or morphology of the surface change, resulting in the surface wettability change. Recently, the magnetic responsive wettability switch has attracted increasing interest for the fast response and remote control property. Magnetic responsive surface structure is one of the important ways to realize the wettability switch. Grigoryev et al. demonstrated the wetting behavior of microstructured reentrant surfaces could be switched from a liquid-repellent (superomniphobic) state to a wetting state by increasing the reentrant angle of the overhang structures from 0° to 23° using an external magnetic field (Fig. 8.1a–j) (Grigoryev et al. 2012). The nonwetting-to-wetting transition due to magnetically induced bending of micronails to change the local geometric angle (reentrant angle), i.e., reconstruction of the reentrant curvature. Lee et al. demonstrated the surface morphology of the magnetorheological elastomer (MRE) films, fabricated by polydimethylsiloxane (PDMS) and various concentrations of fluorinated carbonyl iron particles, changed owing to the alignment of the iron particles along the magnetic field lines (Fig. 8.1k–l) (Lee et al. 2015). At low concentrations of iron particles and low magnetic field

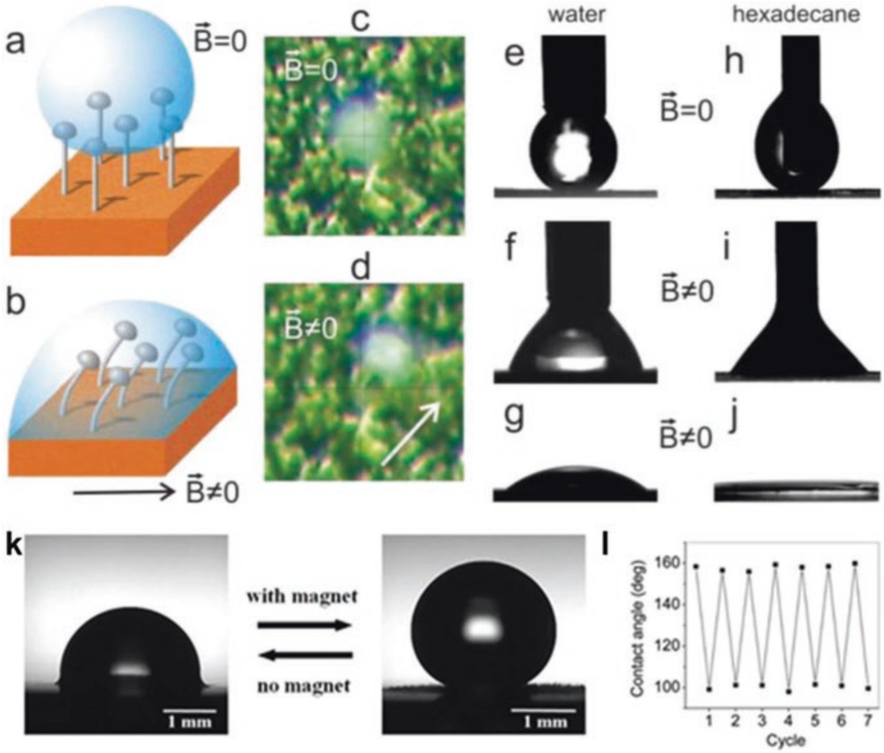

Fig. 8.1 Magnetic-responsive transition of nonwetting-to-wetting. (**a**) A liquid droplet on the vertical micronails showing Cassie-Baxter state. (**b**) The droplet on the bending micronail caps to the wetting Wenzel state under external magnetic field. (**c, d**). Photographs showing the upright and bending of Ni micronail under no field (**c**) and in an external magnetic field (**d**), respectively. (**e–j**) Photographs showing different stages of the CAs of water (**e–g**) and hecadecane on a Ni micronails bed (**h–j**) (Grigoryev et al. 2012). (**k–l**) Reversible switching characteristics of the water CA on the magnetorheological elastomer films by alternating the magnetic field strength (Lee et al. 2015)

intensities, needle-like microstructures predominated, while more mountain-like microstructures were formed with the increasing concentration of iron particles or magnetic field intensity. Accordingly, the surface roughness reversibly increased the water contact angle (CA) from 100° to 160° and decreased the sliding angle from 180° to 10° upon application of a magnetic field. Zhou et al. reported magnetic responsive wettability to water on a nanostructured surface, prepared by polymeric tubes with embedded superparamagnetic magnetite (Fe_3O_4) nanoparticles (Zhou et al. 2011). The water CA on the nanostructured film decreased linearly with the increasing applied magnetic field in terms of magnetically induced conformation changes in the film nanostructure.

Ferrofluid drops, prepared by dispersing the magnetic particles into the dispersing agent, are also used to realize the wettability transition. Duvivier et al. investigated the aqueous ferrofluid drops impact on superhydrophobic surface (Duvivier et al. 2012). The result showed that the higher the drop diameter, the more difficult to get rebound, and the apparent gravitational acceleration had no effect on this parameter because the drop height was smaller than the corresponding capillary length. Poesio et al. investigated the electromagnetic stimulation induced ferrofluid droplets wetting transitions on superhydrophobic surfaces (Poesio and Wang 2014). A small liquid droplet (1–10 μl) could be transformed from Cassie to Wenzel close to the resonant frequency even magnetic forces were small due to the Laplace pressure increase resulting from the large deformation. Conversely, wettabilty transition could not happen under inertia forces.

8.3 Applications of the Magnetic-Responsive Superwetting Surface

8.3.1 Magnetic-Responsive Surface Adhesion

Magnetic field is a very effective way for fast, in situ and remote dynamic control of the liquid wetting behavior. Based on the magnetic responsive wettability transition between Cassie state to Wenzel state, accompanying with the adhesion changed from high adhesion to low adhesion. The author's group has done a lot work in this field, we realized the reversibly directional transport of superparamagnetic droplets without loss under magnetic fields on the superhydrophobic surface (Fig. 8.2) (Hong et al. 2007). During the transport process, an aligned polystyrene (PS) nanotube surface with high adhesion was used to catch and release the superparamagnetic microdroplet under external magnetic field as a "mechanical hand". The no-loss of droplet transport would be promising in the application of microfluidic devices.

Later, we developed a switchable adhesive surface with superhydrophobicity under different magnetic field intensity (Cheng et al. 2008). For a superparamagnetic microdroplet, the low adhesive rolling state and high adhesive pinning state could be tuned by magnetizing and demagnetizing the surface (Fig. 8.3). When the surface was magnetized, inducing the magnetization of Fe_3O_4 nanoparticles, the trapped air pockets could be propelled out for magnetic interaction between the microdroplet and the surface. Recently, we also demonstrated that a superparamagnetic microdroplet could be transit from Cassie to Wenzel state reversibly on a microstructured silicon surface with high hydrophobicity under magnetic field (Cheng et al. 2012). The magnetic field intensity and the superparamagnetic Fe_3O_4 nanoparticles content in the microdroplet are critical to the wettability transition. The anisotropic wetting behavior of superparamagnetic microdroplet on superhydrophobic microscale ratchet structure surface with nanoparticles, was also realized by alternative external magnetic field (Zhang et al. 2009). Recently, Timonen et al. measured kinetic energy dissipation of water-based magnetic droplets on superhydrophobic surfaces based on the transverse oscillating motion (Timonen et al. 2013a).

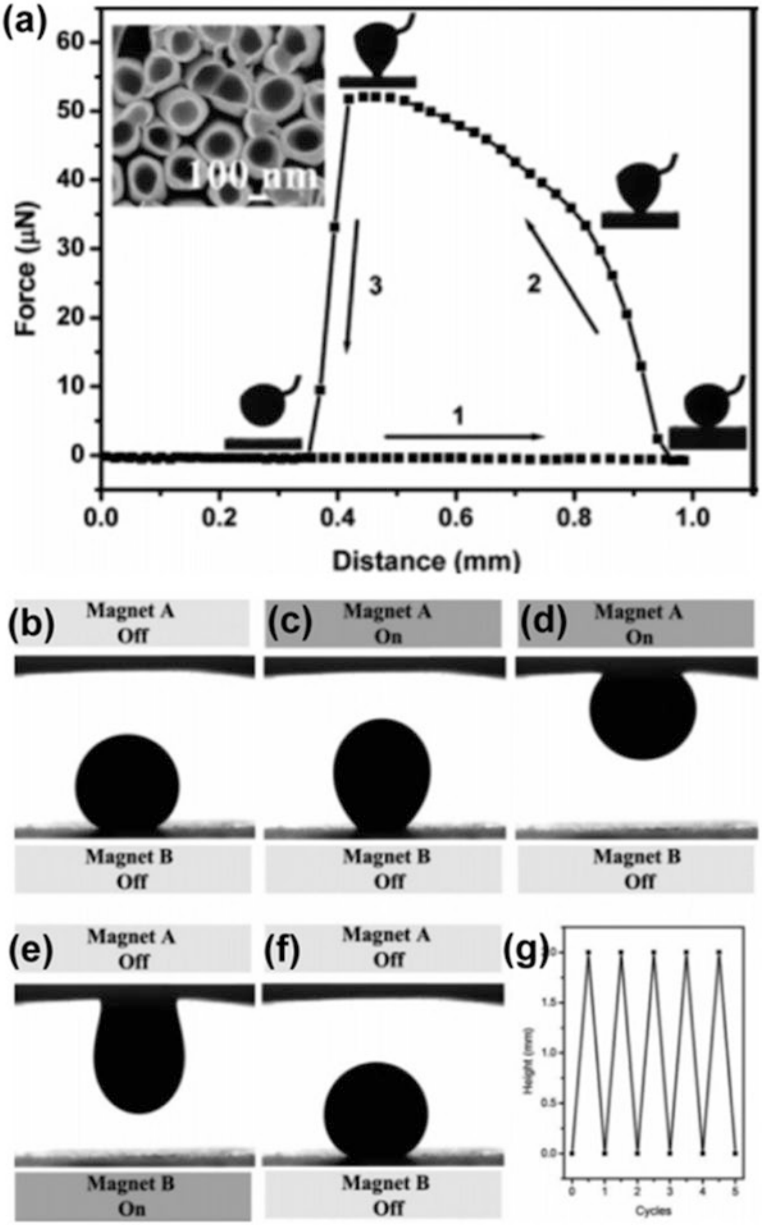

Fig. 8.2 (**a**) Adhesion testing results of the superparamagnetic microdroplet on the PS nanotube surface. (**b–f**) Magnetic responsive no loss transport of superparamagnetic microdroplet by. (**g**) Superparamagnetic microdroplet was reversiby transported upward and downward with varying magnetic fields (Hong et al. 2007)

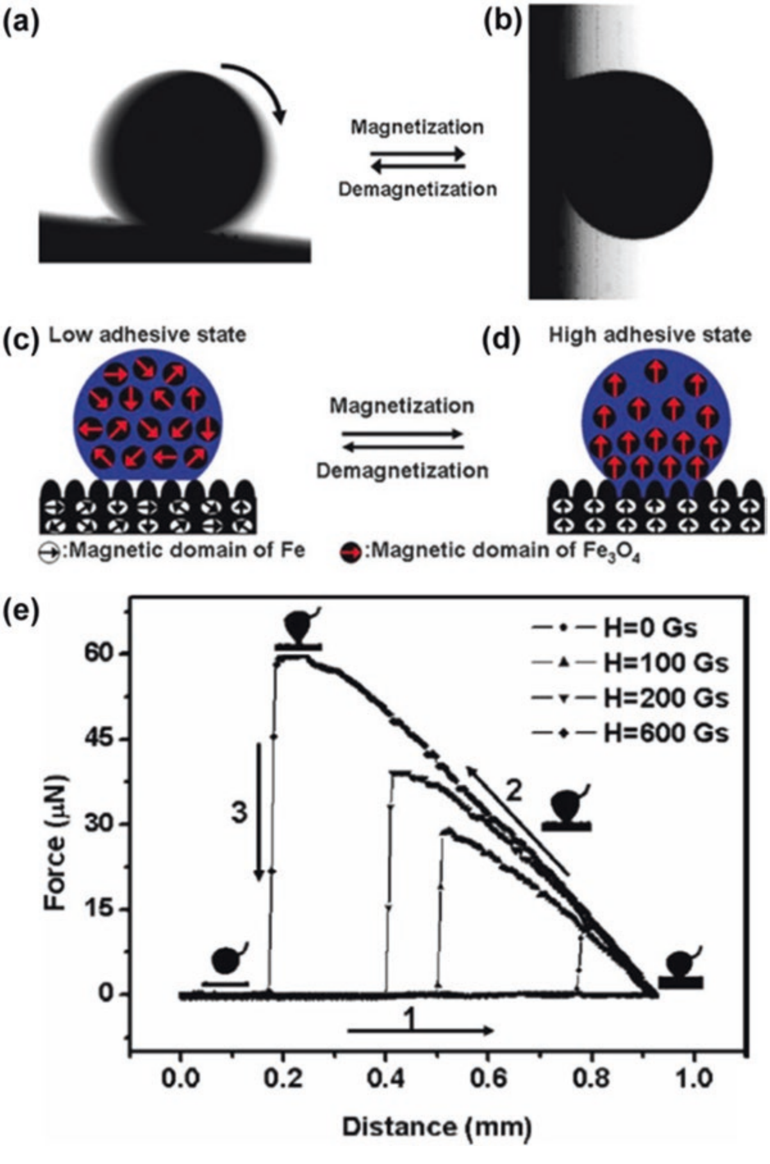

Fig. 8.3 Before and after magnetization of the superhydrophobic iron surface, a superparamagnetic microdroplet with (**a**) rolling state, and (**b**) pinning state, respectively. (**c, d**) A superparamagnetic microdroplet wetting state on the superhydrophobic iron surface. (**e**) Adhesion force of the superparamagnetic microdroplet on the as-prepared iron surface (Cheng et al. 2008)

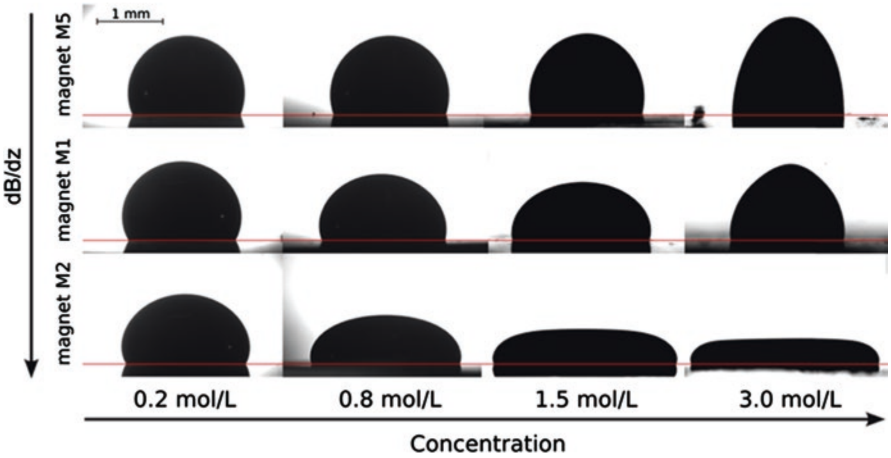

Fig. 8.4 Ferrofluid drops shape with various concentrations and gradient magnetic field (Rigoni et al. 2016)

8.3.2 *Magnetic Field Assisted Microstructure Fabrication*

Based on the magnetic-responsive surface wettability, the shape of liquid droplet containing magnetic micro/nanomaterial can be adjusted using an external magnetic field, which is beneficial for the microstructure assembly and fabrication. Egatz-Gómez et al. demonstrated that the micro-droplets containing paramagnetic particles could be induced motion on superhydrophobic surfaces by magnetic field (Egatz-Gómez et al. 2007). Paramagnetic microparticles chains could be formed and moved under a magnetic field, producing the CA difference of the droplet, which could be used to move, coalesce, and split drops of water as well as drops of biological fluids. Zhu et al. reported the deformation of a ferrofluid droplet on a superhydrophobic surface under the effect of a uniform magnetic field (Zhu et al. 2011). The results showed that an increasing flux density would increase the droplet width and decrease the droplet height. Rigoni et al. reported the wetting properties of water-based ferrofluid with various concentrations on flat substrates were dependent on the permanent magnets of different sizes and strengths (Rigoni et al. 2016). The shape of the droplet changed from flattened drops to drops extended normally to the substrate with the magnetic attraction (Fig. 8.4).

Magnetic field induced the deformation of liquid marble was also studied. Nguyen et al. investigated the magnetic field responsive deformation of ferrofluid

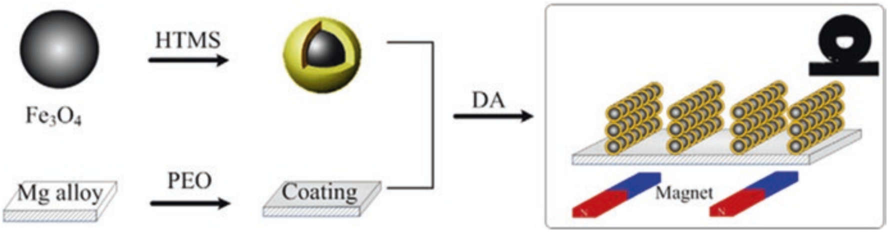

Fig. 8.5 Schematic preparation procedure of superhydrophobic surface based on the magnet-induced assembly deposition process (Qiu et al. 2016)

marbles (Nguyen 2013). The marble was deformed with a larger contact area under anincreasing magnetic field intensity. Hu et al. demonstrated the magnetic responsive liquid marble was highly compressible with rapid self-recovering ability (Hu et al. 2014). Timonen et al. reported that the magnetic droplets could self-assemble to complicated dynamic dissipative structures on superhydrophobic surfaces under external magnetic field (Timonen et al. 2013b). Based on the magnetic tunable dynamic dewetting properties of droplets on surfaces, ferrofluid-molding method (Lee et al. 2014), i.e., ferrofluid as the mother mold, had been used to fabricate polymer microarrays.

Based on the magnetic-responsive liquid morphology, some special structure could be constructed under the magnetic field. Huang et al. prepared cone microstructure with certain inclination angle through controlling the magnetic field direction, followed by UV-curable (Huang et al. 2015). The inclination of the cone-shaped microstructures, showing anisotropic wettability to water and direction selective manner. The author's group provided a way to precisely print three-dimensional (3D) microstructures with controllable base angle, diameter and height through two-dimensional (2D) interface manipulation (Wang et al. 2015b). To develop functional materials, ink was important to achieve 3D materials with desired microstructures and elaborate properties. Qiu et al. constructed a superhydrophobic array structure surface with a water CA of 157° based on the magnet-induced assembly deposition process (Fig. 8.5) (Qiu et al. 2016). The hydrophobic magnetic nanoparticles could be anchored easily onto substrates under an external magnetic field.

8.3.3 Magnetic-Responsive Liquid Transport

Dynamically tunable surface structure is promising in liquid droplets manipulation and transport, cell manipulation, and tuning optical applications. Inspired by liquid or cell transport ability of hair and motile cilia, Zhu et al. fabricated dynamically magnetic-responsive micropillar arrays with a large tuning tilt angles ranging from 0° to 57°, which could be used for precise and continuous control of fluid spreading direction on demand and fluid drag (Fig. 8.6) (Zhu et al. 2014). Drotlef et al. demonstrated magnetic-responsive microparticles transport based on the reversible

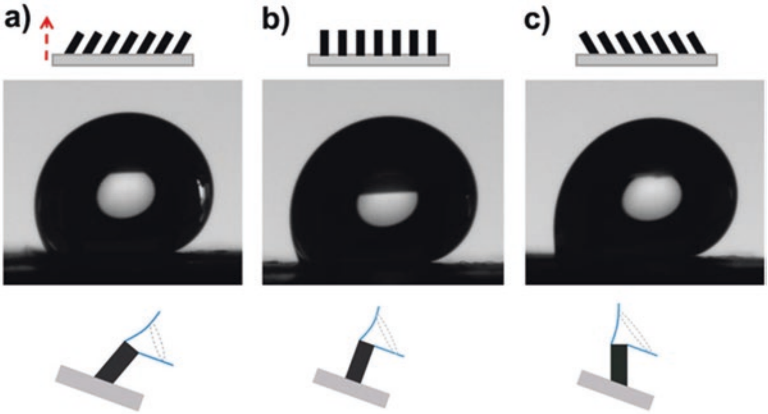

Fig. 8.6 Magnetic-responsive microstructures with the tuning tilt angle (Drotlef et al. 2014)

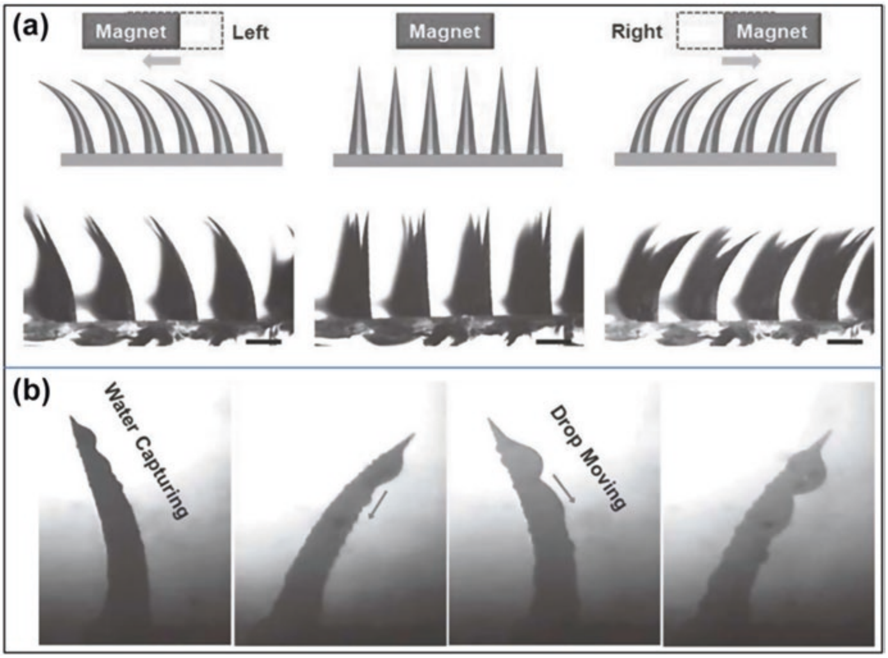

Fig. 8.7 (**a**) The magnetic-responsive cactus-inspired array. (**b**) Magnetic field assisted fog water capture and transport to on flexible cone (Peng et al. 2015)

topography change of magnetic micropillars via gradient external magnetic field (Drotlef et al. 2014).

Peng et al. demonstrated magnetically induced fog harvesting through magnetically responsive flexible conical arrays with cactus-inspired spine structures (Fig. 8.7) (Peng et al. 2015). Static fog water could be spontaneously captured and

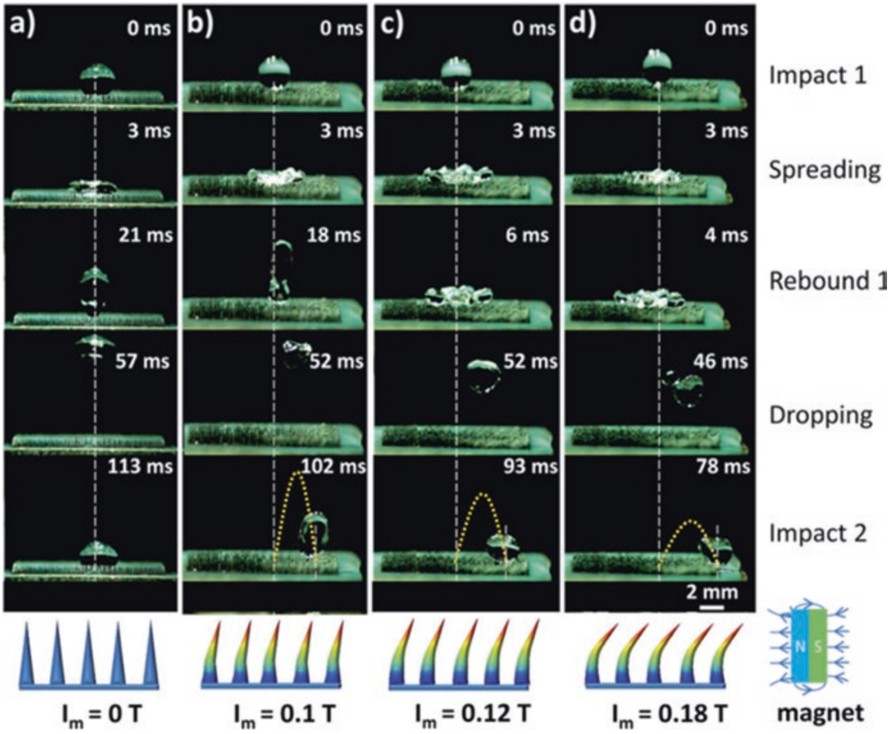

Fig. 8.8 Potographs of droplet impact motion under different magnetic fields. (**a**) At 0 T the droplet impacts and rebounds vertically. (**b–d**) Under the effect of a magnetic field (0.1 T, 0.12 T, 0.18 T), after the first impact, the drop shows asymmetric shapes and rebounds with a rebound angle. The rebound height decreases and the horizontal deviation distance increases gradually with an increase of the magnetic field strength (Wang et al. 2016a)

directionally transported from the tip to the base of the spine continuously through periodic vibration of the flexible conical spine and the Laplace pressure difference arising from the conical shape of the spine.

Wang et al. fabricated a magnetic field responsive superhydrophobic flexible needle surface with tunable tilt angles of the needle, via soft-lithography and crystal growth (Fig. 8.8) (Wang et al. 2016a). The droplet motion, rebound angle, height and horizontal deviation distance could be controlled by the magnetic strength and responsive structure. In addition, based on the different pinning forces on both sides of the droplet, the fast spin behavior of a droplet after detaching from the surface had been observed.

Seo et al. developed a superhydrophobic magnetic elastomer for fast control and transport of droplet (Seo et al. 2013). The droplet movement was easily controlled by magnetic actuation induced local deformation of the elastomer surface, with tunable direction and speed by varying magnetic field. Damodara et al. realized the manipulation of aqueous droplets by creating local deformation on a superhydro-

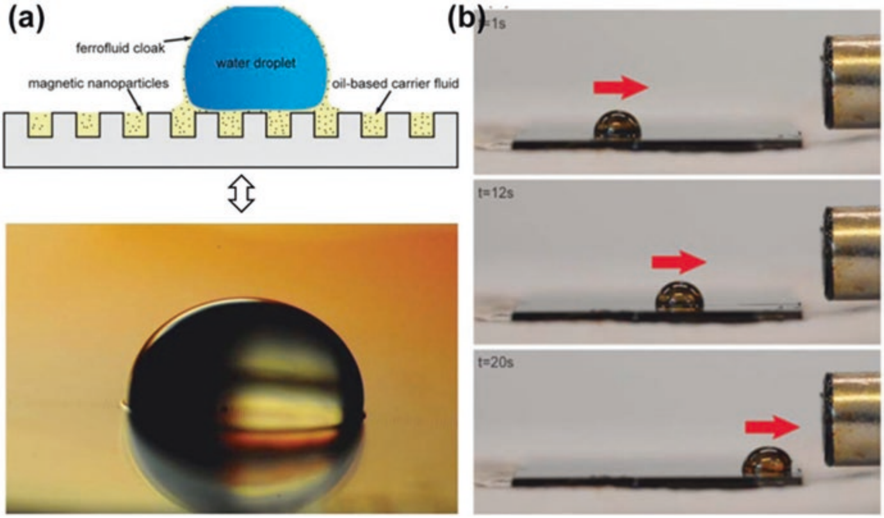

Fig. 8.9 Ferrofluid-impregnated textured surface for liquid driving. (**a**) Water droplet on the composite surface. (**b**) Droplet mobility towards the magnet (Khalil et al. 2014)

phobic surface, comprising iron microparticles embedded in PDMS, under the magnetic field (Damodara and Sen 2017). The superhydrophobic surface offered CA higher than 175° and lower roll off angle less than 7° to facilitate controlled transport of droplets.

When oil is introduced into the micro/nano-structures, the friction and hysteresis of the surface will be decreased. Khalil et al. presented a lubricant-impregnated surface, i.e., a textured solid was impregnated with a ferrofluid, which could manipulate a variety of different liquids including diamagnetic, viscous, electrically conductive and even solid particles utilizing a spatially non-uniform magnetic field (Fig. 8.9) (Khalil et al. 2014). Chen et al. fabricated transparent slippery surfaces based on nanoporous films (Chen et al. 2014). These slippery surfaces with small CA hysteresis and low adhesion of water, ionic liquids, and organic liquids (e.g., glycerol), which was beneficial for the 3D manipulation of drops using external magnetic forces. Recently, the author's group proposed a strategy to achieve a fast responsive smart interface for controllable liquid transport by integrating magnetic fluid into the nanoarray via modulation of an external magnetic field (Tian et al. 2016). A water droplet could follow the motion of the gradient composite interface structure as it responded to the gradient magnetic field motion. Mats et al. showed that droplets with sufficient concentrations of paramagnetic salt could be controlled on a superhydrophobic surface by magnetic field, which was more facile control droplet movement compared to systems of containing ferrofluids or superparamagnetic particles (Mats et al. 2016).

Liquid marble is also an important form for driving the liquid droplet (Zhao et al. 2012). Bormashenko et al. fabricated ferrofluidic marbles by polyvinylidene fluoride and γFe_2O_3 nanopowder (Bormashenko et al. 2008). Ferrofluidic marbles could slide on the superhydrophobic surfaces with a velocity of 25 cm/s by a magnetic field with low-friction. Zhang et al. prepared magnetic responsive liquid marbles through core–shell magnetic nanoparticles modified by a block copolymer (poly(2-vinylpyridine-bdimethylsiloxane) (Zhang et al. 2012a). The liquid marbles kept stable based on the hydrophobic property of the particles, and the marbles could be remotely controlled by magnet. Lin et al. prepared superhydrophobic and superparamagnetic cellulose-based microspheres, containing cellulose and magnetic Fe_3O_4, for transporting and manipulating liquid droplets via the form of liquid marbles (Lin et al. 2016). Mats et al. reported the magnetic actuation of aqueous droplets movement on superhydrophobic fluorinated silica nanoparticles (FSNPs) surface with relatively low magnetic particles concentrations (Mats et al. 2015).

8.3.4 Magnetic-Responsive Liquid Separation

Magnetic materials with special wettability, such as superhydrophobic and superoleophilic, can also be used to control the immiscible liquid droplets or other objects on the water surface. Moreover, they can be used to treat the oily water and further separate the oil from water by magnetic field with the advantages of easy recovery of the adsorbent without filtration or centrifugation (Wu et al. 2014).

8.3.4.1 Magnetic-Responsive Separation Based on Micro/Nanoparticles

Magnetic nanoparticles, e.g., Fe_3O_4, have attracted much attention in many application fields (Chen et al. 2013; Dudchenko et al. 2015; Pavía-Sanders et al. 2013; Yu et al. 2015). Wang et al. reported that liquid marble prepared by the 1H, 1H, 2H, 2H-perfluorodecanethiol modified the hybrid Fe_3O_4@PDA@Ag nanoparticles could be used for inner liquid droplet manipulation with high resolution and oil/water separation as well as antibacterial purpose (Wang et al. 2015c). Pan et al. reported magnetic responsive superhydrophobic and superoleophilic core-shell Fe_2O_3@C nanoparticles could selectively absorb oil in water, which was reusable by ultrasonic treatment (Fig. 8.10) (Zhu et al. 2010).

Recently, by mimicking the mussels' surface, the superhydrophobic and superoleophilic magnetic nanoparticles were synthesized using core material of carbonyl iron particles. When the nanoparticles spread on oil spilled water surface, the particles showed oil marble properties and could be used to removal of oil without loss of magnetic nanoparticles (Zhang et al. 2012b). Zhang et al. prepared the superhydrophobic and superoleophilic polydopamine (PDA)/Fe_3O_4 microparticles by mimicing the lotus leaf structure (Zhang et al. 2016). The magnetic PDA/Fe_3O_4 microparticles could be used for oil transportation and oil/water separation. Yang et al. prepared the superhydrophobic and superparamagnetic Fe_3O_4@polydopamine (Fe_3O_4@PDA) composite microspheres for oil/water separation (Yang et al. 2014).

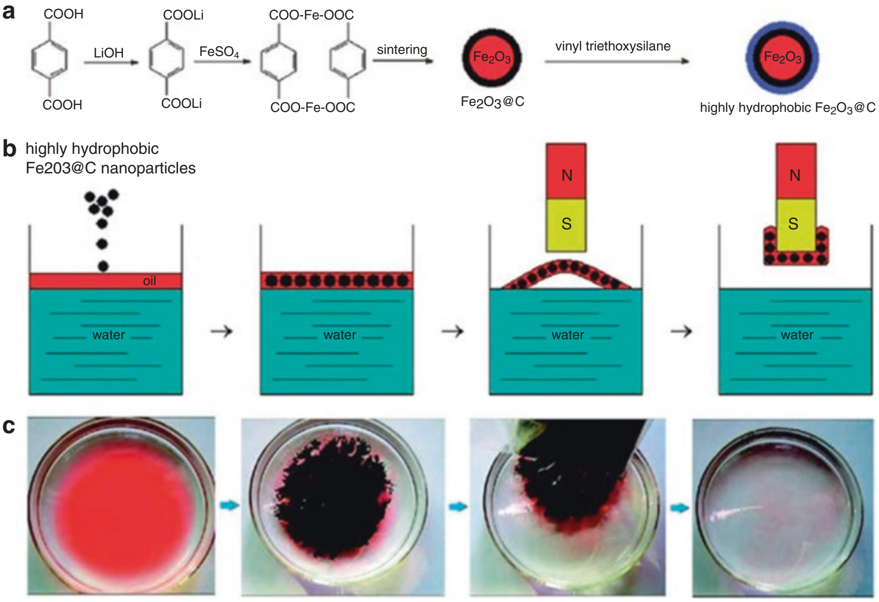

Fig. 8.10 (**a**) Illustrations for preparation of Fe_2O_3@C nanoparticles. (**b–c**) Magnetic responsive oil removal from water surface by superhydrophobic and superoleophilic Fe_2O_3@C nanoparticles (Zhu et al. 2010)

8.3.4.2 Magnetic-Responsive Separation Based on Sponge

Superhydrophobic sponge could be constructed by the microparticles modification for oil-water separation with high absorption capability. Usually, the oil absorbed foams in the separation process could be restored to original state of absorption capacity and hydrophobicity after squeezing and washing process (Yu et al. 2016a). Calcagnile et al. fabricated the superhydrophobic and superoleophilic foam materials by coating submicrometer PTFE particles to PU foam/iron oxide nanoparticle composites (Calcagnile et al. 2012), which could absorb and remove oil on water by applying an external magnetic field. Pan et al. presented magnetically controllable oil absorption by superhydrophobic and superoleophilic 3D macroporous Fe/C nanocomposites without any modification (Chu and Pan 2012). Recently, the author's group fabricated smart magnetically driven fibrous films (Wu et al. 2015a), Fe_3O_4@PVDF/F fibrous films with superhydrophobic/superoleophilic propeties, by electrospun, which were the ideal material for remote oil removal (Xue et al. 2014; Nagappan and Ha 2015). Gui et al. fabricated a magnetic-responsive CNT sponge with water CA of >145°, showing highly stable at strong acidic and basic pH conditions (Fig. 8.11) (Gui et al. 2013). The magnetic-responsive hydrophobic sponges

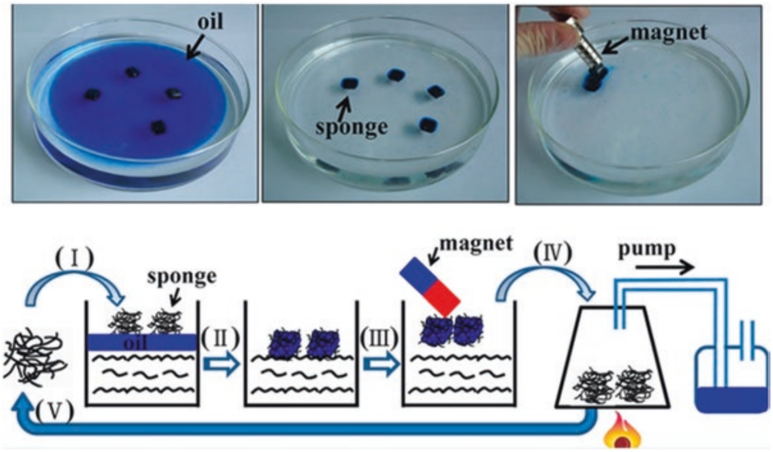

Fig. 8.11 The recycling of spilled oil sorption by Me-CNT sponges. (I) Oil on the surface; (II) the sponge adsorbs spilled oil; (III) the sponge is collected by magnet; (IV) regeneration process; (V) reuse in the oil/water separation (Gui et al. 2013)

were widely used for oil absorption, and can be recycled for sorption of oils from water and be used for larger scale oil absorption.

Li et al. fabricated a nanoparticle-loaded (FeO, CoO, NiO, CuO and Ag) superhydrophobic sponge for oil-water separation (Li et al. 2012). The magnetic-responsive superhydrophobic sponge was increasing dramatically for oils absorption and separation from water, easy removal by external magnet, and recyclable, which indicated the potential application in practical applications. Recently, ultralight weight magnetic foams of Fe_2O_3/C, Co/C and Ni/C foams with superhydrophobic and superoleophilic properties were prepared (Chen and Pan 2013), which could separate larger amount of oils due to the ultralight weight and then collected by magnetic field. Wu et al. constructed magnetic-responsive superhydrophobic PU sponges, which could selectively absorb both light oils and heavy oils in water, and were reusable and durable (Wu et al. 2015b). Li et al. prepared a magnetic-responsive, superhydrophobic silicone sponges by polymerization of organosilanes with silica coated Fe_3O_4 nanoparticles (Fe_3O_4@silica NPs). The sponges showed fast and high efficient oil/water separation (Li et al. 2014). The magnetic nanoparticles could provide magnetic-responsiveness and surface roughness (Liu et al. 2015a). Turco et al. fabricated a magnetic responsive porous PDMS sponges integrating with multi-walled CNTs (PDMS–MWNTs) (Turco et al. 2015). The superhydrophobic and superoleophilic sponges showed high and fast absorption for various organic liquids and also behaved high mechanical and thermal stability. Inspired from the bioadhesion of marine mussels, Zhu et al. reported a method to anchor nanoparticles onto macroscopic porous substrates with dopamine (Fig. 8.12) (Zhu and Pan 2014). The achieved superhydrophobic polyurethane (PU) sponge substrates by adding n-dodecanethiol were suitable for oil/water separation with high selectivity and recyclability.

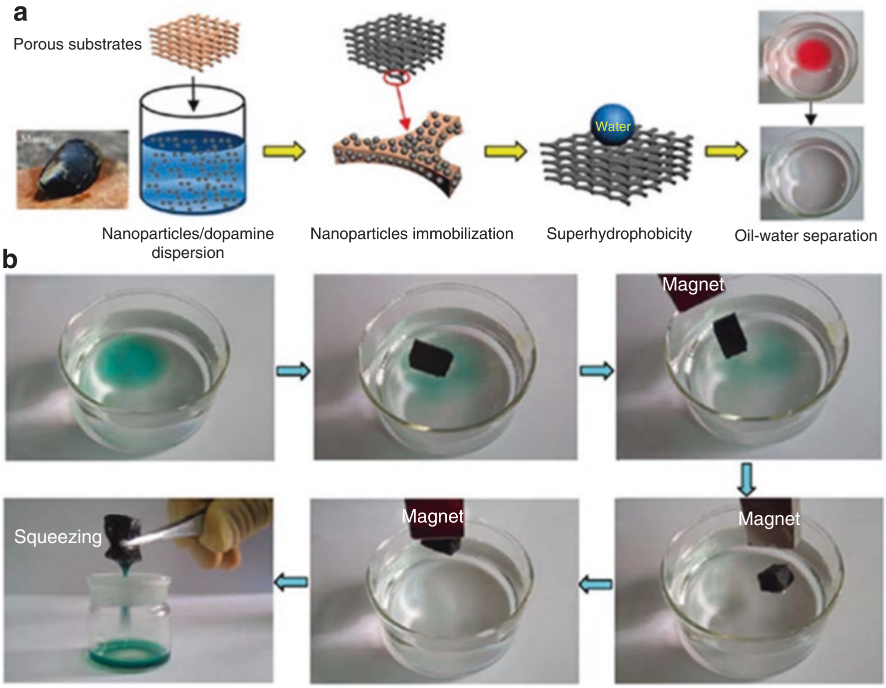

Fig. 8.12 (**a**) Schematic porous substrate preparation and oil-water separation. (**b**) Magnetic responsive superhydrophobic sponge for oil collection from water surface (Zhu and Pan 2014)

Bay et al. fabricated a superhydrophobic and oleophilic ultra-thin porous graphite sponge (Bay et al. 2016). The prepared sponge could be applied for magnetic controllable targeted sorption and collection of different oils. Liu et al. fabricated magnetic-responsive polymer-based graphene foam (MPG), showing superhydrophobic and superoleophilic, to separate oil and water by oil absorption (Liu et al. 2015b). In the polymer-based graphene foam, graphene sheets were used to improve the adhesion of the polyurethane (PU) sponge franmework. The MPG could separate a broad of oil–water mixtures by magnetic manipulation with high absorption capacity and selectivity. Ge et al. fabricated magnetic superhydrophobic foam by dipping method (Ge et al. 2015). After compressing test even 200 cycles, the superhydrophobic foams could effectively separate oils from water surface by magnetic actuation, which might provide a new way for the solution of the oil fouling. Yu et al. developed durable magnetic polystyrene foam (DMMPF), by introducing Fe_3O_4 particles coated by oleic acid and PS microspheres (Yu et al. 2016b). The prepared DMMPF could continuously separate of various oils and organic solvents from the water surface, showing high efficiency and selectivity. The absorbed oils were 40.1 times as its own weight, which could be collected by extrusion.

Chen et al. fabricated nickel foams functionalized by coating hydrogel (Chen et al. 2015). The prepared nickel foams systems could be applied to selectively remove little water from oil by magnetic field and also separate the surfactant-stabilized W/O emulsions. Duan et al. reported the prepared the superhydrophobic/superoleophilic iron particles could be used to separate oil/water mixtures and O/W emulsions, as well as even surfactant-stabilized W/O emulsions, with a high separation efficiency (Duan et al. 2015). The work was promising in application of wastewater treatment, and the emulsions and dispersions separation. Peng et al. constructed superhydrophobic magnetic cellulose sponge (SMCE) by coating Fe_3O_4 on cellulose sponge surface via codeposition method and modified with hexadecyltrimethoxysilane, which could separate oil from water even surfactant-stabilized W/O emulsions (Peng et al. 2016).

Du et al. constructed 0D/2D hybrid microstructures coated commercial melamine foams (MF) (Du et al. 2016a). The surface roughness could be dramatically enhanced by these hybrid-dimensional microstructures so as to remote control of water/oil selectivity to achieve excellent oil/water separation efficiency >99%. They also fabricated a quartz fiber based 3D monolithic materials with ultrahigh thermostability and mechanical flexibility, which exhibited great potential in water remediation for large oil absorption capacity (50- to 172-fold weight gain) (Du et al. 2016b). Wang et al. prepared magnetically superhydrophobic kapok fiber for oil sorption-based separation (Wang et al. 2016b). Magnetic-responsive Fe_3O_4 nanoparticles were used to improve the hydrophobicity and oleophilicity of the kapok fiber surfaces and to drive the fiber to contaminated water region with a magnet for further absorbing floating oils on water surface. By mixing of PTFE with MWCNT and Fe_3O_4 nanoparticles in 30 ml chloroform at 60 °C, Ge et al. prepared the magnetic-responsive superhydrophobic bulk material, which was stable in strong acidic and basic pH values, and also higher temperatures (Ge et al. 2013). The superhydrophobic matrix can absorb lots of oils from spilled water surface and remove easily with a magnet. The bulk material could be restored by burning the absorbed oil. Flores et al. constructed magnetic-responsive hybrid networks by conjugation of PAA-b-PS SCK nanoparticles to amine-functionalized IONs with similarly size, which could be applied in the remediation of water contaminated with complex pollutants such as crude oil (Flores et al. 2015). The graphene/metal oxide hydrogels and aerogels with 3D interconnected networks and porous microstructures also exhibited excellent capability for removal of heavy metal ions and oils from water, and was promising in the application of adsorbents for water purification or other applications (Cong et al. 2012).

Magnetic fluid can also be used for liquid transport and separation. Rashin et al. demonstrated that magnetite-coconut oil nanofluid could be used to remove oil spill from water with efficiency of 91% (Rashin et al. 2014). In the separation process, the superhydrophobic and superoleophilic nanofluids collected contaminant oil through London dispersive forces while were completely repelling the water molecules. Recently, we also demonstrated the underwater oil droplets manipulation and free transfer by magnetic fluid on a stable oil/water/solid tri-phase surface (Feng et al. 2016).

8.4 Conclusions and Outlook

The magnetic-responsive wettability on the superwetting surface and their typical applications has been briefly reviewed, particularly on switchable wettability on magnetic-responsive surfaces and their applications including tunable surface adhesion, microstructure fabrication, droplet actuation, and smart separation. Although there are great progresses in magnetic-responsive wettability on the superwetting surfaces, there are still some problems and chances in practical applications.

Special surface wettability based on the suitable materials and micro/nanostructure is critical for the responsive interface control. The multiphase system, e.g., liquid/liquid/solid system, is expected to obtain the reversible behaviour of the interface. Moreover, responsive materials surface wettability control with external field, especially for the multi-field cooperation control interface might be developed a trend to control the wetting and moving behavior of microdroplet or other microscale objects such as cell and particle, and will play more important role in biofluidic chips, microfluidic devices, drug release and other intelligent devices.

Acknowledgments The authors are grateful for financial support from the Chinese National Natural Science Foundation (21671012, 21373001, 21601013), Beijing Natural Science Foundation (2172033), the 973 Program (2013CB933004), the Fundamental Research Funds for the Central Universities, and the 111 Project (B14009).

References

Bay HH, Patino D, Mutlu Z, Romero P, Ozkan M, Ozkan CS (2016) Scalable multifunctional ultra-thin graphite sponge: free-standing, superporous, superhydrophobic, oleophilic architecture with ferromagnetic properties for environmental cleaning. Sci Rep 6:21858

Bormashenko E, Pogreb R, Bormashenko Y, Musin A, Stein T (2008) New investigations on ferrofluidics: ferrofluidic marbles and magnetic-field-driven drops on superhydrophobic surfaces. Langmuir 24:12119–12122

Calcagnile P, Fragouli D, Bayer IS, Anyfantis GC, Martiradonna L, Cozzoli PD, Cingolani R, Athanassiou A (2012) Magnetically driven floating foams for the removal of oil contaminants from water. ACS Nano 6:5413–5419

Chen N, Pan Q (2013) Versatile fabrication of ultralight magnetic foams and application for oil-water separation. ACS Nano 7:6875–6883

Chen M, Jiang W, Wang F, Shen P, Ma P, Gu J, Mao J, Li F (2013) Synthesis of highly hydrophobic floating magnetic polymer nanocomposites for the removal of oils from water surface. Appl Surf Sci 286:249–256

Chen L, Geissler A, Bonaccurso E, Zhang K (2014) Transparent slippery surfaces made with sustainable porous cellulose lauroyl ester films. ACS Appl Mater Interfaces 6:6969–6976

Chen BY, Ju GN, Sakai E, Qiu JN (2015) Underwater low adhesive hydrogel-coated functionally integrated device by a one-step solution-immersion method for oil–water separation. RSC Adv 5:87055–87060

Cheng ZJ, Feng L, Jiang L (2008) Tunable adhesive superhydrophobic surfaces for superparamagnetic microdroplets. Adv Funct Mater 18:3219–3225

Cheng ZJ, Lai H, Zhang NQ, Sun KN, Jiang L (2012) Magnetically induced reversible transition between cassie and wenzel states of superparamagnetic microdroplets on highly hydrophobic silicon surface. J Phys Chem C 116:18796–18802

Chu Y, Pan QM (2012) Three-dimensionally macroporous Fe/C nanocomposites as highly selective oil-absorption materials. ACS Appl Mater Interfaces 4:2420–2425

Cong H-P, Ren X-C, Wang P, Yu S-H (2012) Macroscopic multifunctional graphene-based hydrogels and aerogels by a metal ion induced self-assembly process. ACS Nano 6:2693–2703

Crevoisier GD, Fabre P, Corpart JM, Leibler L (1999) Switchable tackiness and wettability of a liquid crystalline polymer. Science 285:1246–1249

Damodara S, Sen AK (2017) Magnetic field assisted droplet manipulation on a soot-wax coated superhydrophobic surface of a PDMS-iron particle composite substrate. Sensors Actuat B Chem 239:816–823

Drotlef D-M, Blümler P, Papadopoulos P, Del Campo A (2014) Magnetically actuated micropatterns for switchable wettability. ACS Appl Mater Interfaces 6:8702–8707

Du R, Feng Q, Ren H, Zhao Q, Gao X, Zhang J (2016a) Hybrid-dimensional magnetic microstructure based 3D substrates for remote controllable and ultrafast water remediation. J Mater Chem A 4:938–943

Du R, Zhao Q, Li P, Ren H, Gao X, Zhang J (2016b) Ultrathermostable, magnetic-driven, and superhydrophobic quartz fibers for water remediation. ACS Appl Mater Interfaces 8:1025–1032

Duan C, Zhu T, Guo J, Wang Z, Liu X (2015) Smart enrichment and facile separation of oil from emulsions and mixtures by superhydrophobic/superoleophilic particles. ACS Appl Mater Interfaces 7:10475–10481

Dudchenko AV, Rolf J, Shi L, Olivas L, Duan W, Jassby D (2015) Coupling underwater superoleophobic membranes with magnetic pickering emulsions for fouling-free separation of crude oil/water mixtures: an experimental and theoretical study. ACS Nano 9:9930–9941

Duvivier D, Rioboo R, Voué M, Coninck JD (2012) Drop impact on superhydrophobic surfaces–varying gravitational effects. Atomization Spray 22:409–429

Egatz-Gómez A, Schneider J, Aella P, Yang D, Domínguez-García P, Lindsay S, Picraux ST, Rubio MA, Melle S, Marquez M, García AA (2007) Silicon nanowire and polyethylene superhydrophobic surfaces for discrete magnetic microfluidics. Appl Surf Sci 254:330–334

Feng XJ, Jiang L (2006) Design and creation of superwetting/antiwetting surfaces. Adv Mater 18:3063–3078

Feng H, Xu X, Hao W, Du Y, Tian D, Jiang L (2016) Magnetic field actuated manipulation and transfer of oil droplets on a stable underwater superoleophobic surface. Phys Chem Chem Phys 18:16202–16207

Flores JA, Pavía-Sanders A, Chen Y, Pochan DJ, Wooley KL (2015) Recyclable hybrid inorganic/organic magnetically active networks for the sequestration of crude oil from aqueous environments. Chem Mater 27:3775–3782

Ge B, Zhang ZZ, Zhu XT, Ren G, Men XH, Zhou XY (2013) A magnetically superhydrophobic bulk material for oil removal. Colloids Surf A Physicochem Eng Asp 429:129–133

Ge B, Zhu X, Li Y, Men X, Li P, Zhang Z (2015) Versatile fabrication of magnetic superhydrophobic foams and application for oil–water separation. Colloids Surf A Physicochem Eng Asp 482:687–692

Grigoryev A, Tokarey T, Kornev KG, Luzinov I, Minko S (2012) Superomniphobic magnetic microtextures with remote wetting control. J Am Chem Soc 134:12916–12919

Gui X, Zeng Z, Lin Z, Gan Q, Xiang R, Zhu Y, Cao A, Tang Z (2013) Magnetic and highly recyclable macroporous carbon nanotubes for spilled oil sorption and separation. ACS Appl Mater Interfaces 5:5845–5855

Hong X, Gao XF, Jiang L (2007) Application of superhydrophobic surface with high adhesive force in no lost transport of superparamagnetic microdroplet. J Am Chem Soc 129:1478–1479

Hu YJ, Jiang H, Liu J, Li YF, Hou XY, Li CZ (2014) Highly compressible magnetic liquid marbles assembled from hydrophobic magnetic chain-like nanoparticles. RSC Adv 4:3162–3164

Huang C-Y, Lai M-F, Liu W-L, Wei Z-H (2015) Anisotropic wettability of biomimetic micro/nano dual-scale inclined cones fabricated by ferrofluid-molding method. Adv Funct Mater 25:2670–2676

Khalil KS, Mahmoudi SR, Abu-dheir N, Varanasi KK (2014) Active surfaces: ferrofluid-impregnated surfaces for active manipulation of droplets. Appl Phys Lett 105:041604

Lee CP, Chen YH, Lai MF (2014) Ferrofluid-molding method for polymeric microlens arrays fabrication. Microfluid Nanofluid 16:179–186

Lee S, Yim C, Kim W, Jeon S (2015) Magnetorheological elastomer films with tunable wetting and adhesion properties. ACS Appl Mater Inter 7:19853–19856

Li XM, Reinhoudt D, Crego-Calama M (2007) What do me need for a superhydrophobic surface? A review on the recent progress in the preparation of superhydrophobic surfaces. Chem Soc Rev 36:1350–1368

Li J, Shi L, Chen Y, Zhang YB, Guo ZG, Su BL, Liu WM (2012) Stable superhydrophobic coatings from thiol-ligand nanocrystals and their application in oil/water separation. J Mater Chem 22:9774–9781

Li L, Li B, Wu L, Zhao X, Zhang J (2014) Magnetic, superhydrophobic and durable silicone sponges and their applications in removal of organic pollutants from water. Chem Commun 50:7831–7833

Lin X, Ma W, Wu H, Cao S, Huang L, Chen L, Takahara A (2016) Superhydrophobic magnetic poly (DOPAm-co-PFOEA)/Fe_3O_4/cellulose microspheres for stable liquid marbles. Chem Commun 52:1895–1898

Liu MJ, Zheng YM, Zhai J, Jiang L (2010a) Bioinspired super-antiwetting interfaces with special liquid-solid adhesion. Acc Chem Res 43:368–377

Liu KS, Yao X, Jiang L (2010b) Recent developments in bio-inspired special wettability. Chem Soc Rev 39:3240–3255

Liu KS, Cao MY, Fujishima A, Jiang L (2014) Bio-inspired titanium dioxide materials with special wettability and their applications. Chem Rev 114:10044–10094

Liu S, Xu Q, Latthe SS, Gurav AB, Xing R (2015a) Superhydrophobic/superoleophilic magnetic polyurethane sponge for oil/water separation. RSC Adv 5:68293–68298

Liu C, Yang J, Tang Y, Yin L, Tang H, Li C (2015b) Versatile fabrication of the magnetic polymer-based graphene foam and applications for oil–water separation. Colloids Surf A Physicochem Eng Asp 468:10–16

Mats L, Young R, Gibson GTT, Oleschuk RD (2015) Magnetic droplet actuation on natural (colocasia leaf) and fluorinated silica nanoparticle superhydrophobic surfaces. Sensor Actuat B Chem 220:5–12

Mats L, Logue F, Oleschuk RD (2016) "Particle-free" magnetic actuation of droplets on superhydrophobic surfaces using dissolved paramagnetic salts. Anal Chem 88:9486–9494

Nagappan S, Ha CS (2015) Emerging trends in superhydrophobic surface based magnetic materials: fabrications and their potential applications. J Mater Chem A 3:3224–3251

Nguyen NT (2013) Deformation of ferrofluid marbles in the presence of a permanent magnet. Langmuir 29:13982–13989

Pavía-Sanders A, Zhang S, Flores JA, Sanders JE, Raymond JE, Wooley KL (2013) Robust magnetic/polymer hybrid nanoparticles designed for crude oil entrapment and recovery in aqueous environments. ACS Nano 7:7552–7561

Peng Y, He YX, Yang S, Ben S, Cao MY, Li K, Liu KS, Jiang L (2015) Magnetically induced fog harvesting via flexible conical arrays. Adv Funct Mater 25:5967–5971

Peng H, Wang H, Wu J, Meng G, Wang Y (2016) Preparation of superhydrophobic magnetic cellulose sponge for removing oil from water. Ind Eng Chem Res 55:832–838

Poesio P, Wang EN (2014) Resonance induced wetting state transition of a ferrofluid droplet on superhydrophobic surfaces. Exp Thermal Fluid Sci 57:353–357

Qiu Z, Sun J, Wang R, Zhang Y, Wu X (2016) Magnet-induced fabrication of a superhydrophobic surface on ZK60 magnesium alloy. Surf Coat Tech 286:246–250

Quéré D (2008) Wetting and roughness. Annu Rev Mater Res 38:71–99

Rashin MN, Kutty RG, Hemalatha J (2014) Novel coconut oil based magnetite nanofluid as eco-friendly oil spill remover. Ind Eng Chem Res 53:15725–15730

Rigoni C, Pierno M, Mistura G, Delphine T, René M, Bacri CR, Hassan AA (2016) Static magnetowetting of ferrofluid drops. Langmuir 32:7639–7646

Seo KS, Wi R, Im SG, Kim DH (2013) A superhydrophobic magnetic elastomer actuator for droplet motion control. Polym Adv Technol 24:1075–1080

Su B, Guo W, Jiang L (2015) Learning from nature: binary cooperative complementary nanomaterials. Small 11:1072–1096

Sun TL, Feng L, Gao XF, Jiang L (2005) Bioinspired surfaces with special wettability. Acc Chem Res 38:644–652

Sun TL, Qing GY, Su BL, Jiang L (2011) Functional biointerface materials inspired from nature. Chem Soc Rev 40:2909–2921

Tian DL, Song YL, Jiang L (2013) Patterning of controllable surface wettability for printing techniques. Chem Soc Rev 42:5184–5209

Tian Y, Su B, Jiang L (2014a) Interfacial material system exhibiting superwettability. Adv Mater 26:6872–6897

Tian DL, Guo ZY, Wang YL, Li WX, Zhang XF, Zhai J, Jiang L (2014b) Phototunable underwater oil adhesion of micro/nanoscale hierarchical-structured ZnO mesh films with switchable contact mode. Adv Funct Mater 24:536–542

Tian DL, Zhang N, Zheng X, Hou GL, Tian Y, Du Y, Jiang L, Dou SX (2016) Fast responsive and controllable liquid transport on a magnetic fluid/nanoarray composite interface. ACS Nano 10:6220–6226

Timonen JVI, Latikka M, Ikkala O, Ras RHA (2013a) Free-decay and resonant methods for investigating the fundamental limit of superhydrophobicity. Nat Commun 4:2398

Timonen JVI, Latikka M, Leibler L, Ras RHA, Ikkala O (2013b) Switchable static and dynamic self-assembly of magnetic droplets on superhydrophobic surfaces. Science 341:253–257

Turco A, Malitesta C, Barillaro G, Greco A, Maffezzoli A, Mazzotta E (2015) A magnetic and highly reusable macroporous superhydrophobic/superoleophilic PDMS/MWNT nanocomposite for oil sorption from water. J Mater Chem A 3:17685–17696

Wang R, Hashimoto K, Fujishima A, Chikuni M, Kojima E, Kitamura A, Shimohigoshi M, Watanabe T (1997) Light-induced amphiphilic surfaces. Nature 388:431–432

Wang ST, Song YL, Jiang L (2007) Photoresponsive surfaces with controllable wettability. J Photochem Photobiol C 8:18–29

Wang ST, Liu KS, Yao X, Jiang L (2015a) Bioinspired surfaces with superwettability: new insight on theory, design, and applications. Chem Rev 115:8230–8293

Wang LB, Li FY, Kuang MN, Gao M, Wang JX, Huang Y, Jiang L, Song YL (2015b) Interface manipulation for printing three-dimensional microstructures under magnetic guiding. Small 11:1900–1904

Wang B, Liu Y, Zhang YB, Guo ZG, Zhang H, Xin JH, Zhang L (2015c) Bioinspired superhydrophobic Fe_3O_4@Polydopamine@Ag hybrid nanoparticles for liquid marble and oil spill. Adv Mater Interfaces 2:1500234

Wang L, Gao C, Hou Y, Zheng Y, Jiang L (2016a) Magnetic field-guided directional rebound of a droplet on a superhydrophobic flexible needle surface. J Mater Chem A 4:18289–18293

Wang J, Geng G, Liu X, Han F, Xu J (2016b) Magnetically superhydrophobic kapok fiber for selective sorption and continuous separation of oil from water. Chem Eng Res Des 115:122–130

Wen L, Tian Y, Jiang L (2015) Bioinspired super-wettability from fundamental research to practical applications. Angew Chem Int Ed 54:3387–3399

Wu L, Zhang JP, Li B, Wang A (2014) Magnetically driven super durable superhydrophobic polyester materials for oil/water separation. Polym Chem 5:2382–2390

Wu J, Wang N, Zhao Y, Jiang L (2015a) Simple synthesis of smart magnetically driven fibrous films for remote controllable oil removal. Nanoscale 7:2625–2632

Wu L, Li L, Li B, Zhang J, Wang A (2015b) Magnetic, durable and superhydrophobic polyurethane@Fe_3O_4@SiO_2@fluoropolymer sponges for selective oil absorption and oil/water separation. ACS Appl Mater Interfaces 7:4936–4946

Xia F, Jiang L (2008) Bio-inspired, smart, multiscale interfacial materials. Adv Mater 20:2842–2858

Xia F, Ge H, Hou Y, Sun TL, Chen L, Zhang GZ, Jiang L (2007) Multiresponsive surfaces change between superhydrophilicity and superhydrophobicity. Adv Mater 19:2520

Xia DY, Johnson LM, López GP (2012) Anisotropic wetting surfaces with one-dimensional and directional structures: fabrication approaches, wetting properties and potential applications. Adv Mater 24:1287–1302

Xin BW, Hao JC (2010) Reversibly switchable wettability. Chem Soc Rev 39:769–782

Xue Z, Cao Y, Liu N, Feng L, Jiang L (2014) Special wettable materials for oil/water separation. J Mater Chem A 2:2445–2460

Yang F, Dong Y, Guo Z (2014) Facile fabrication of core shell Fe_3O_4@ polydopamine microspheres with unique features of magnetic control behavior and special wettability. Colloids Surf A Physicochem Eng Asp 463:101–109

Yao X, Song YL, Jiang L (2011) Applications of bio-inspired special wettable surfaces. Adv Mater 23:719–734

Yao X, Hu Y, Grinthal A, Wong T-S, Mahadevan L, Aizenberg J (2013) Adaptive fluid-infused porous films with tunable transparency and wettability. Nat Mater 12:529–534

Yu L, Hao G, Liang Q, Zhou S, Zhang N (2015) Facile preparation and characterization of modified magnetic silica nanocomposite particles for oil absorption. Appl Surf Sci 357:2297–2305

Yu L, Zhou X, Jiang W (2016a) Low-cost and superhydrophobic magnetic foam as an absorbent for oil and organic solvent removal. Ind Eng Chem Res 55:9498–9506

Yu L, Hao G, Zhou S, Jiang W (2016b) Durable and modified foam for cleanup of oil contamination and separation of oil–water mixtures. RSC Adv 6:24773–24779

Zhang JL, Han YC (2010) Active and responsive polymer surfaces. Chem Soc Rev 39:676–693

Zhang X, Shi F, Niu J, Jiang YG, Wang ZQ (2008) Superhydrophobic surfaces: from structural control to functional application. J Mater Chem 18:621–633

Zhang JH, Cheng ZJ, Zheng YM, Jiang L (2009) Ratchet-induced anisotropic behavior of superparamagnetic microdrople. Appl Phys Lett 94:144104

Zhang L, Cha D, Wang P (2012a) Remotely controllable liquid marbles. Adv Mater 24:4756–4760

Zhang L, Wu J, Wang Y, Long Y, Zhao N, Xu J (2012b) Combination of bioinspiration: a general route to superhydrophobic particles. J Am Chem Soc 134:9879–9881

Zhang L, Li L, Dang Z (2016) Bio-inspired durable, superhydrophobic magnetic particles for oil/water separation. J Colloid Interface Sci 463:266–271

Zhao Y, Xu Z, Parhizkar M, Fang J, Wang X, Lin T (2012) Magnetic liquid marbles, their manipulation and application in optical probing. Microfluid Nanofluid 13:555–564

Zhou Q, Ristenpart WD, Stroeve P (2011) Magnetically induced decrease in droplet contact angle on nanostructured surfaces. Langmuir 27:11747–11751

Zhu Q, Pan Q (2014) Mussel-inspired direct immobilization of nanoparticles and application for oil–water separation. ACS Nano 8:1402–1409

Zhu Q, Tao F, Pan Q (2010) Fast and selective removal of oils from water surface via highly hydrophobic core-shell Fe_2O_3@C nanoparticles under magnetic field. ACS Appl Mater Interfaces 2:3141–3146

Zhu GP, Nguyen NT, Ramanujan RV, Huang XY (2011) Nonlinear deformation of a ferrofluid droplet in a uniform magnetic field. Langmuir 27:14834–14841

Zhu Y, Antao DS, Xiao R, Wang EN (2014) Real-time manipulation with magnetically tunable structures. Adv Mater 26:6442–6446

Part II
Practical Applications

Chapter 9
Stimuli-Responsive Smart Surfaces for Oil/Water Separation Applications

Jai Prakash, Narendra Singh, Rashika Mittal, and Raju Kumar Gupta

Abstract The emerging field of developing nanomaterials with stimuli responsive smart surfaces allows one to tune the surface properties for various useful applications such as self-cleaning surfaces, energy, oil/water separation, tunable optical lenses, microfluidics, and sensors etc. Such materials with smart surfaces having reversible switching properties between superhydrophilicity and superhydrophobicity, have shown strong capability for oil/water separation and been investigated extensively in the last decade. The oil/water separation is a field of high significance as it has direct practical implementation to resolve the problems of industrial oily wastewater and other oil/water pollutions. Various factors affecting the stimuli response of these smart surfaces such as light, pH, temperature, gas, electric and magnetic field etc. have been summarized to evaluate the enhanced surface properties for oil/water separation. Beside this, dual responsive smart surfaces have also been summarized for oil/water separations. This chapter highlights the recent accomplishments carried out in the development of such smart nanomaterials surfaces for oil/water separation.

Keywords Stimuli-responsive surfaces · Smart surfaces · Switchable wettability · Superhydrophobicity · Superhydrophilicity · Oil/water separation

---

J. Prakash
Department of Chemical Engineering, Indian Institute of Technology Kanpur,
Kanpur, Uttar Pradesh, India

N. Singh · R. K. Gupta (✉)
Department of Chemical Engineering, Indian Institute of Technology Kanpur,
Kanpur, Uttar Pradesh, India

Center for Nanosciences and Center for Environmental Science and Engineering,
Indian Institute of Technology Kanpur, Kanpur, Uttar Pradesh, India
e-mail: guptark@iitk.ac.in

R. Mittal
Department of Chemical Engineering, Indian Institute of Technology Kanpur,
Kanpur, Uttar Pradesh, India

Department of Chemical Engineering, Manipal Institute of Technology,
Manipal, Karnataka, India

A. Hozumi et al. (eds.), *Stimuli-Responsive Dewetting/Wetting Smart Surfaces and Interfaces*, Biologically-Inspired Systems 11,
https://doi.org/10.1007/978-3-319-92654-4_9

9.1 Introduction

Stimuli response is an action/reaction that a material or body respond to its environment from the molecular to the macroscopic level and the human body is one of the best example in this respect (Nelson 2008). This natural behavior has given a direction to produce such materials with stimuli responsive properties, which show promising applications in various fields of science and technology (Mendes 2008). The research and development in the field of surface science particularly surfaces with stimuli-responsive properties have been progressed a lot in the past decade because of their multi-applications ranging from energy, environment, tunable optical lenses, microfluidics/nanofluidics, and sensors to biomedical (Mendes 2008; Zhou and Huck 2006; Zhang et al. 2012a, 2013a; Rodríguez-Hermida et al. 2016). Due to their switchable stimuli properties, these surfaces are also called smart surfaces (Mendes 2008; Zhang et al. 2012a; Sun et al. 2004a; Nagappan et al. 2016). These smart surfaces with stimuli-responsive properties are considered as the basic building blocks for the development of the nanofluidic devices because of their ability to change in the wettability (hydrophilic or hydrophobic nature of the surfaces) (Mendes 2008).

The wettability is a unique surface property of solid materials that generally depends on their chemical compositions, and geometrical structure. Specially, nanomaterials with smart surfaces based on stimuli responsive behavior, provide understanding of controlled surface wettability and realization of their surface properties for reversible switching on or off ability. Great research efforts have been carried out to synthesize such smart surfaces and study their role in wettability for oil/water separation (Zhang et al. 2012a, 2013a; Xue et al. 2013, 2014). Functional surfaces with reversibly switching wettability functionality for oil/water separation have been center of extensive research interest with the aim of taking forward this field for fundamental and technological applications in last few years. The oil/water separation is very important research by application point of view in industries for oily wastewater treatment and controlling environmental water pollution. Recently, versatile surfaces for oil contaminated water treatment have generated global interest to minimize the hazardous effects over aquatic, human life. The "oil removal" and "water removal" types of oil/water separation films with built-in unique surface wettability towards oil and water have been extensively used (Xue et al. 2014). Earlier, several kind of surfaces and thin films or substrates with superhydrophobic nature have been synthesized by controlling the physical-chemical properties and roughness etc. (Li et al. 2001; Tadanaga et al. 1997, 2000).

For the first time, Feng et al. (2004a) reported teflon-coated stainless steel mesh with both the surface properties of superhydrophobicity and superoleophilicity, which served as functional surface for oil/water separation. The material surface must have excellent wettability properties with a large water contact angle (CA) and low water sliding angle. In addition, it should also have low oil CA (Feng et al. 2004a). Kota et al. (2012) reported a hygro-responsive membranes surfaces having both nature of superhydrophilicity and superoleophobicity in both air and under water. They showed that these membranes could be used to separate broad concentration range of oil/water mixtures with >99.9% separation efficiency and was only gravity driven technique and high energy efficient. Similarly, Zhang et al. (2013b) developed a superhydrophobic-superoleophilic poly(vinylidene fluoride) (PVDF) membrane that could separate both micrometer and nanometer-size surfactant free and surfactant stabilized water-in-oil emulsions driven by only gravity and having high separation efficiency.

Interestingly, a great deal of research has been carried out in related field specially in last decades and a variety of such smart surfaces with external stimuli response have been reported. The development of stimuli-responsive surfaces has provided directions for controlling the wettability in reverse order and various strategies have been implemented such as light-irradiation, pH, gas, electric field, thermal treatment etc. and extensively studied (Sun et al. 2004b; Guo and Guo 2016). However, reversible switching between superhydrophilicity and superhydrophobicity using smart surfaces has not been explored for oil/water separation too much and it is still an emerging field. The development of stimuli-responsive nanomaterials with controlled oil/water separation capability is challenging for practical applications as also indicated by some of the recent review articles (Guo and Guo 2016; Ma et al. 2016a; Zhu and Guo 2016; Lee et al. 2017). These smart surfaces produced by using advanced functional materials exhibit controlled oil wettability, while in aqueous media or vice-versa and have shown their promising properties even underwater conditions (Xue et al. 2014; Tian et al. 2012). This controlled wettability of water and oil on such smart surfaces with hydrophilicity or hydrophobicity and oleophilicity or oleophobicity nature could be obtained by modifying their outer stimuli response triggered by several effects such as photo-irradiation, pH, temperature, gas, electric/magnetic fields, or as their combined effect (Fig. 9.1). In the present chapter, we highlight on the various stimuli responsive smart surfaces for oil/water separation along with recent developments in this direction.

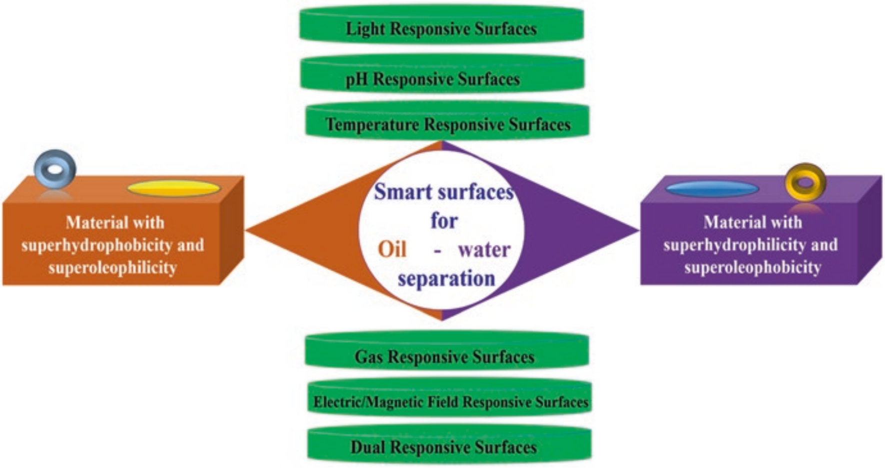

Fig. 9.1 Smart surfaces based on material's properties for oil/water separation and several parameters effects for stimuli response

9.2 Various Stimuli-Responsive Smart Surfaces for Oil/Water Separation

9.2.1 Light Responsive Smart Surfaces

Oil/water separation is a global challenge because of the modern industrialization leading to oily water pollution and oil spill accidents due to the offshore oil production among many others. As discussed above, there have been developed many approaches for the cleaning of this kind of oily pollution in water system (Tian et al. 2011a, 2012; Chen et al. 2015; Zhou et al. 2017; Yong et al. 2015). Interestingly, stimulus responsive surface wettability property leading to switchable superhydrophobicity–superhydrophilicity activity, has been studied and found very effective for oil/water separation (Tian et al. 2012). To observe their wettability response under light irradiation, various solid substrates have been used for interchanging between superhydrophobicity and superhydrophilicity such as ZnO, TiO_2 as observed owing to light sensitivity. Steerable water penetration films have been designed and developed based on such an extreme wettability switch, which has significant implications for comprehending the natural actions and making of modern micro/nanofluidic devices (Tian et al. 2012; Yan et al. 2016; Feng et al. 2004b). It is still a challenge to separate oil and water via photoresponsive smart surfaces even though there has been much progress in this realm. Tian and co-workers (Tian et al. 2011a, 2012) have carried out significant research for developing photoresponsive smart surfaces in order to separate oil and water from oily water. They realized that for photoinduced oil/water separation to occur, the materials with photoresponsive smart surfaces should have special surface structures and developed mesh film kind of micro/nanoscale hierarchical structured ZnO-coated pore array surface (Tian et al. 2011b). It has been reported that semiconductor materials like ZnO has wide band gap, good surface wettability and photoinduced switching behavior between superhydrophilicity and superhydrophobicity (Wang et al. 2007). The aligned ZnO nanorod array coated stainless steel mesh film showed better response to water permeability under irradiation, and opposite behavior i.e. impermeable response to water, while in dark conditions. The switching behavior was attributed to the designed nanostructure and pore size of microscale mesh. In addition, pore structures facilitate the wetting process under the ultraviolet (UV) irradiation because of the capillary effect (Tian et al. 2011b). Later, Tian et al. (2012), developed similar photoresponsive mesh films exhibiting switchable superhydrophobicity–superhydrophilicity, and underwater superoleophobicity behavior at the oil–water–solid three-phase interface (Figs. 9.2 and 9.3).

As prepared ZnO nanorod array based mesh films as shown in Fig. 9.2 were investigated for the surface wettability of oil and water under UV irradiation and dark condition. These films showed superhydrophobic behavior as investigated by CA measurement measured after keeping in the dark, while it showed superhydro-

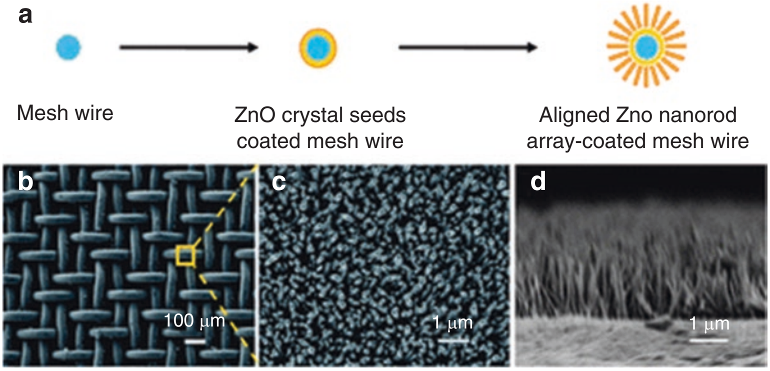

Fig. 9.2 (**a**) Schematic diagrams of the preparation process. The inner circularity represents the stainless steel wire and the outer radial pattern is the corresponding aligned ZnO nanorod array layer. (**b**) SEM (top view) images of the as-prepared aligned ZnO nanorod array-coated stainless steel mesh films. (**c**) local enlarged view of (**b**), and (**d**) is the SEM side view of the aligned ZnO nanorod array-coated stainless steel mesh film. (Reproduced with permission from (Tian et al. 2012), Copyright 2012 The Royal Society of Chemistry)

philic behavior under UV irradiation (Fig. 9.3a). Similarly, when CA measurements were performed with oil, films showed superoleophilicity in air and superoleophobicity underwater and also behave differently under dark and UV irradiation for different oils used in the experiments (Fig. 9.3b–c). Other factors such as pore size also affects the superoleophobicity underwater and it should be smaller than 200 μm. They also studied the oil/water separation in air based on the ZnO mesh film's superhydrophobicity and superoleophilicity after storage in the dark (Tian et al. 2011a). Yan et al. (2016) have recently reported a photo-induced ZnO coated mesh with switchable wettability for oil/water separation with high separation efficiency.

Similarly, TiO_2 based smart surfaces with reversible switchable underwater superoleophobicity–superoleophilicity behavior have been developed for the oil/water separation (Yong et al. 2015). These photoinduced stimuli responsive rough TiO_2 surfaces have been created by femtosecond laser ablation, which act in UV as well as visible light irradiation (Yong et al. 2015). It was found that these smart surfaces are superhydrophobic in air and superoleophilic in water, whereas under UV irradiation surfaces behave as superoleophobic in water along with the probability of recovering underwater superoleophilic state after storing in dark. Besides, the metal oxide nanomaterials, single walled carbon nanotubes (SWCNT) ultrathin network films were also found to be very useful for stimuli responsive separation of oil/water mixture due to its unique nanostructures containing pores of nanosize (Shi et al. 2013). This excellent behavior of SWCNT for oil/water separation was combined with photoresponsive wettability of TiO_2 to develop a different type of nanocomposite mess network with superhydrophilicity and underwater superoleophobicity driven by UV light irradiation, which showed high separation efficiency for oil/water system with or without surfactant (Gao et al. 2014).

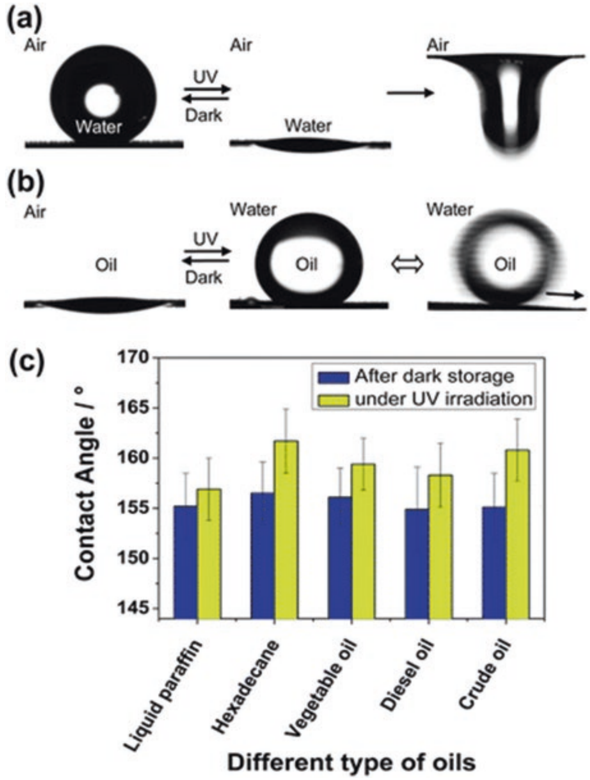

Fig. 9.3 Photo-induced surface wettability of the aligned ZnO nanorod arrays-coated mesh films. (**a**) Photographs of a water droplet on the coated mesh film after dark storage (left) and under UV irradiation (middle) in air with a CA of ~155° and ~0°, respectively. When more water is added, the water droplet will drop (right). (**b**) Photographs of an oil droplet (1,2-dichloroethane) on the mesh film in air (left) and underwater (middle) with a contact angle of ~0° and ~156°, respectively, and sliding angle of ~2.6° (right). (**c**) CA of different oil droplets on the underwater mesh after storage in the dark and under UV irradiation. (Reproduced with permission from (Tian et al. 2012), Copyright 2012 The Royal Society of Chemistry)

Gao et al. (2014) reported superwetting SWCNT and TiO_2 nanocomposite ultrathin mesh films prepared by coating of TiO_2 on SWCNT mesh films. These films showed excellent behavior for the ultrafast separation of oil/water in nanoemulsions induced by photoirradiation because of their superhydrophilic and underwater superoleophobic properties under the influence of UV light irradiation. In addition, these nanocomposite mesh films also show good antifouling properties along with recyclability due to self-cleaning ability of TiO_2 photocatalyst (Fig. 9.4). Kim et al. (2015) prepared nano sponge using hydrophobic hydrocarbon and hydrophilic TiO_2, in which hydrocarbon specifically absorbed the oil from water and released in water under the UV irradiation.

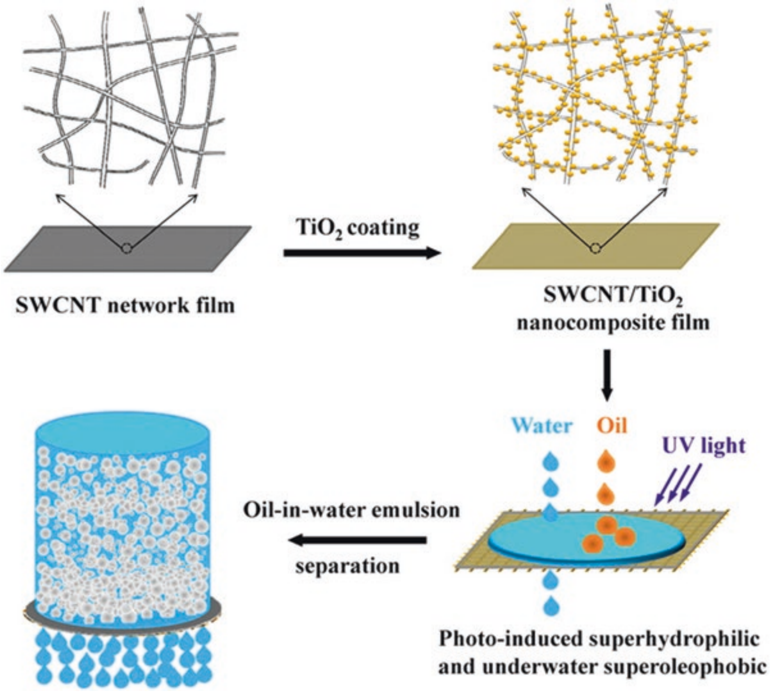

Fig. 9.4 Schematic showing the preparation process of the SWCNT/TiO_2 nanocomposite film and for separation of an oil-in-water emulsion. (Reproduced with permission from (Gao et al. 2014), Copyright 2014 American Chemical Society)

Similarly, a superhydrophobic polybenzoxazine/TiO_2 films with excellent stimuli responsive behavior under UV irradiation were produced with self-cleaning properties (Zhang et al. 2016). These surfaces showed low adhesion superhydrophobic surface property, which switched to greater adhesion while irradiating with UV light and became low adhesive again on heating. Zhu et al. (2016) prepared vinyl modified melamine-formaldehyde sponge and later modified with the light responsive spiropyran derivative via radical copolymerization process. This material showed superhydrophobic nature ~155.5° water CA and high selectivity towards oils and organic compounds with absorption capacity of 74 to 154 times of its weight, while materials changed its nature to hydrophilic and resulted in oil release under UV irradiation.

The photoirradition has also been used to synthesize multifunctional surfaces (Li et al. 2016a; Ye et al. 2016) that work as stimuli responsive smart surfaces as discussed above, for examples: a self-cleaning underwater superoleophobic surfaces (Zhang et al. 2013a; Zhou et al. 2017; Gao et al. 2014; Ye et al. 2016; Gunatilake and Bandara 2017a) and superhydrophobic surfaces (Chen et al. 2015; Zhang et al. 2016) for oil/water separation.

9.2.2 pH Responsive Smart Surfaces

Various pH responsive smart surfaces based on polymer (Zhang et al. 2012a; Li et al. 2015, 2016b; Dang et al. 2016; Liu and Liu 2016; Low et al. 2017; Zhou et al. 2016), graphene (Zhao et al. 2016) and other metallic nanomaterials (Cheng et al. 2015, 2016; Liu et al. 2017; Lü et al. 2017; Guo et al. 2017) have been reported in the last decades with excellent oil/water separation capability. Zhang et al. (2012a) developed the first pH responsive smart surface materials composed of nonwoven textiles and polyurethane (PU) sponges providing switchable behavior between superoleophilicity and superoleophobicity. It contained blocks of pH-responsive poly(2-vinylpyridine) and oleophilic/hydrophobic polydimethylsiloxane (i.e., P2VP-*b*-PDMS). With this, it was realized that the block copolymers containing covalently bonded blocks having changed physical-chemical properties, provided special kind of materials with excellent stimuli behavior for the development of smart materials for oil/water separation. Dunderdale et al. (2014a) developed a pH responsive polymer based brush showing superoleophobic properties and capable of repelling oil from water under ambient conditions.

In recent years, there have been a lot of progress in developing such polymer based smart surfaces with pH stimuli responsive materials. Dang et al. (2016) designed a pH responsive smart surfaces by nonfluorine-containing copolymer and silica on several materials such as fabric, filter papers or PU foams. These materials with coated surface showed good wettability and switchable behavior between superhydrophilicity and superhydrophobicity in order to separate oil/water/oil three phase mixtures, by *in-situ* and *ex-situ* pH change of the solution used. Wu et al. (2015) synthesized poly(methacrylic acid) (PMAA) functionalized cotton fabrics for oil/water separation. As the pH was increased, surface became superhydrophobic to superhydrophilic and underwater superoleophobic, which was highly efficient and selective for oil/water separations.

In another interesting work, cellulose nanocrystals with grafted polymer brushes such as poly(oligoethylene glycol) methacrylate (POEGMA) and PMAA, were used as functional materials with smart surfaces for the oil/water separation (Tang et al. 2016). These composite systems could be used to control the stabilization and destabilization of oil/water nanoemulsion by triggering pH and temperature. The oil droplets could be stabilized at higher pH, whereas at lower pH resulted in oil/water phase separation.

The copper mesh films were also reported as smart surfaces showing superhydrophobic and superhydrophilic for non-alkaline and alkaline water, respectively (Cheng et al. 2015). Using this copper mess film as a membrane and tuning the nanostructures along with the pore sizes as well as the pH of the water system, the film showed superoleophobicity in alkaline water with excellent oil/water separation effect. Similarly, Cheng et al. (2016) developed a nanostructured pH responsive copper mesh films by attaching pH responsive molecules on the surface of the film. Interestingly, it was found that both the nanostructures created on the copper film as well as the attached pH responsive molecules, played important roles for the pH

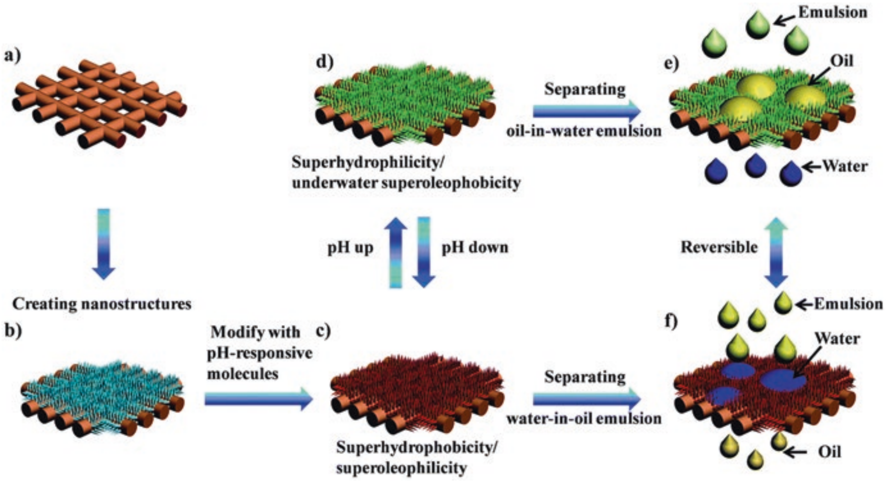

Fig. 9.5 Schematic illustration of the design principle for the pH-responsive separating film: (**a** and **b**) creating nanostructures on the copper mesh substrate to adjust the pore size. (**b** and **c**) Modification of responsive molecules to endow the film with different wettabilities: superhydrophobicity/superoleophilicity for non-basic water (**c**) and applications in separating water-in-oil emulsions (**f**); superhydrophilicity/underwater superoleophobicity (**d**) for basic water and applications in separating oil-in-water emulsions (**e**). A reversible transition between the two wetting states can be realized by alternately changing the water pH, and thus bidirectional separation of different types of emulsions can be realized. (Reproduced with permission from (Cheng et al. 2016), Copyright 2016 The Royal Society of Chemistry)

responsive behavior of the surface, resultant combined effects enhanced the surface wettability and reversibly switchable property between the superhydrophobic/ superoleophilic and the superhydrophilic/underwater superoleophobic states (Fig. 9.5).

Very recently, Liu et al. (2017) developed a bio-inspired copper foam as pH responsive smart device prepared by electroless Ag deposition, which was then modified using a solution of thiols containing carboxylic groups and methyl groups ($HS(CH_2)_{11}CH_3$ and $HS(CH_2)_{10}COOH$) (Fig. 9.6). These copper foam mesh was found to be pH responsive and switchable reversely from superhydrophobicity to hydrophilicity for efficient oil/water separation from their mixture (Fig. 9.7). It was found that at $pH < 7$, the surface showed superhydrophobic, while the water CA was sharply decreased for $pH > 10$ and showed hydrophilic behavior for $pH > 12$.

The cross-linked benzoxazine (CR-PBz) polymers based membranes with ultralow surface energy have shown hydrophobicity and oleophilicity surface properties and used as a pH stimuli surfaces for oil/water separations (Liu and Liu 2016). Liu and Liu (2016) demonstrated that cross-linked electrospun PBz fiber mat (CR-PBz-FbM) with fiber and pore sizes of 1.6 µm and 5.9 µm, respectively, showed a water CA ~142° and exhibited an excellent oil selective behavior. These polymer based fiber membranes were used for oil/water separation as a pH-induced reversible switch as shown in Fig. 9.8. It was found that for pH = 14 of the solution, the

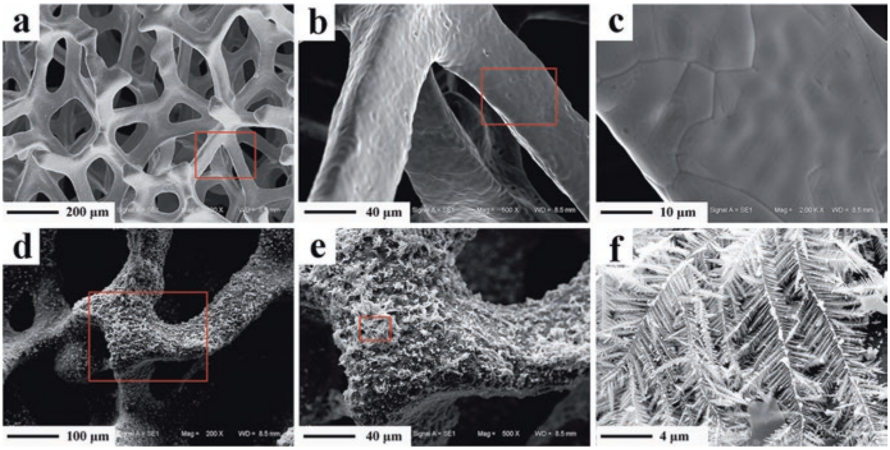

Fig. 9.6 Surface morphology of (**a**–**c**) the untreated copper foam and (**d**–**f**) copper foam after immersion in the solution of $AgNO_3$ solution for 30 s. (Reproduced with permission from (Liu et al. 2017), Copyright 2017 The Royal Society of Chemistry)

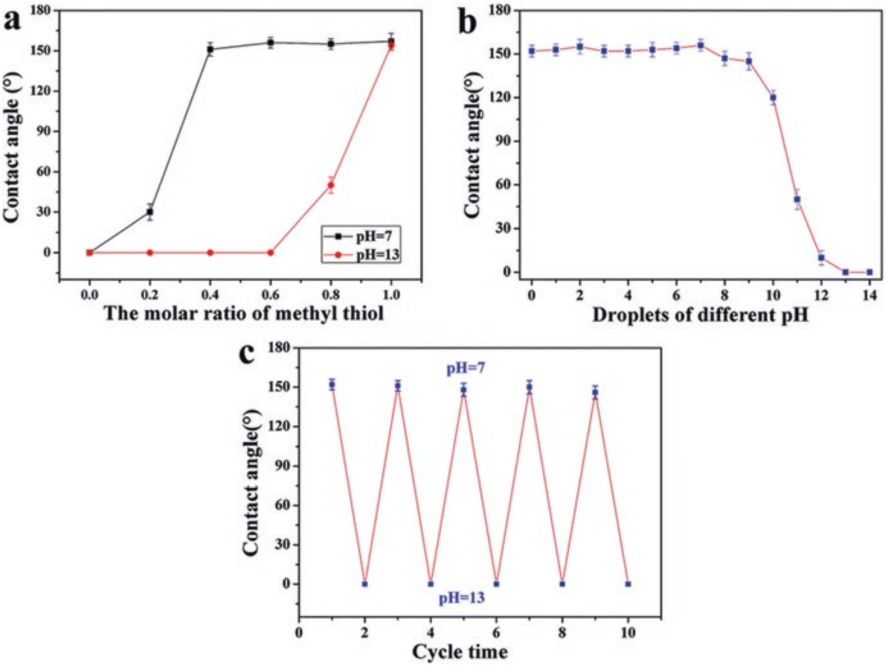

Fig. 9.7 (**a**) CA as a function of the molar ratio of methyl thiol for water (pH = 7) and basic (pH = 13) droplets on the anodized substrate. (**b**) CA as a function of droplets of different pH values on the as-prepared copper foam surfaces that have been modified with 60% $HS(CH_2)_{11}CH_3$ and 40% $HS(CH_2)_{10}COOH$. (**c**) Wetting transition cycles with the water or basic water droplets on the as-prepared copper foam. (Reproduced with permission from (Liu et al. 2017), Copyright 2017 The Royal Society of Chemistry)

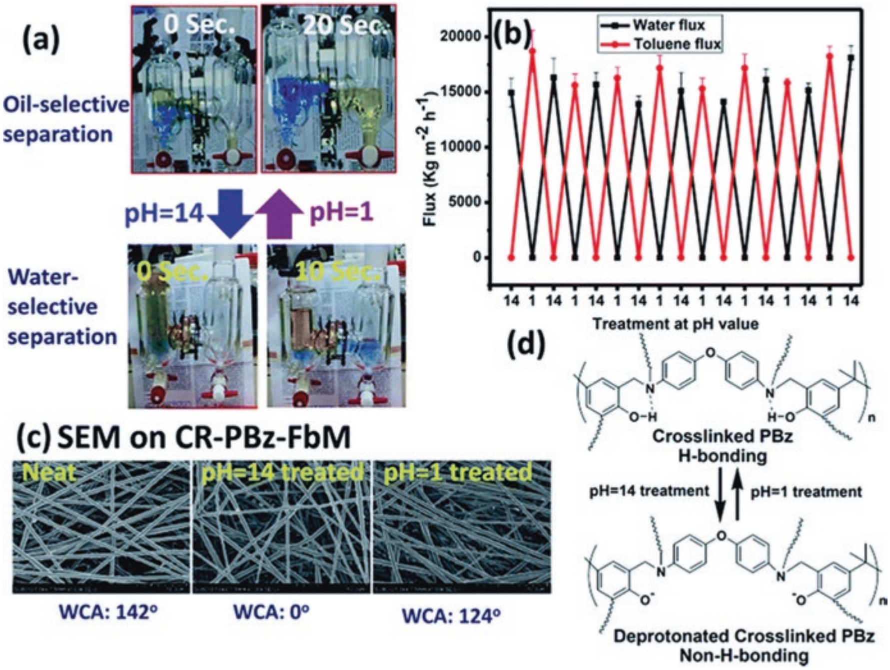

Fig. 9.8 (**a**) pH-Induced switch of the oil- and water-selectivity of the CR-PBz-FbM membrane in oil-water separation; (**b**) the membrane permeation fluxes in cycled treatment of the membrane with solutions of different pH values (pH = 14 and pH = 1). The changes in membrane selectivity are almost completely reversible without sacrificing the permeation fluxes; (**c**) SEM micrographs of the CR-PBz-FbM membrane treated with solutions of different pH values (pH = 14 for 5 min and pH = 1 for 1 min); (**d**) a scheme illustrating the changes in the chemical structure and hydrogen-bonding of CR-PBz-FbM being treated with solutions of different pH values (pH = 14 and pH = 1). Deprotonation of the crosslinked PBz structure results in loss of hydrogen bonding so as to turn the membrane from oleophilic to hydrophilic. (Reproduced with permission from (Liu and Liu 2016), Copyright 2016 The Royal Society of Chemistry)

membrane showed oil to water selective behavior, while at pH = 1, it showed the opposite behavior. It was first of this kind of selectivity shown by these membranes showing complete reversible behavior due to change in pH of the solution as pH-induced switches of surface between hydrophobicity and hydrophilicity for oil and water selectivity, respectively. However, it was realized that the selectivity was not enough to be an excellent smart surface and it could be improved by reducing the pore sizes of the membranes without changing the porosity of the material (Fig. 9.8) (Liu and Liu 2016).

Similarly, Li et al. (2016b, c) developed a polymer poly(dimethylsiloxane)-*block*-poly(4-vinylpyridine) (PDMS-b-P4VP) mat using electrospinning technique (Fig. 9.9), which showed excellent pH switchability for oil/water separation. It was found that at a pH = 7, water droplet showed water CA of 155° on the fibrous mat surface, whereas, at pH = 4 of the solution, water droplet gradually wetted and spread

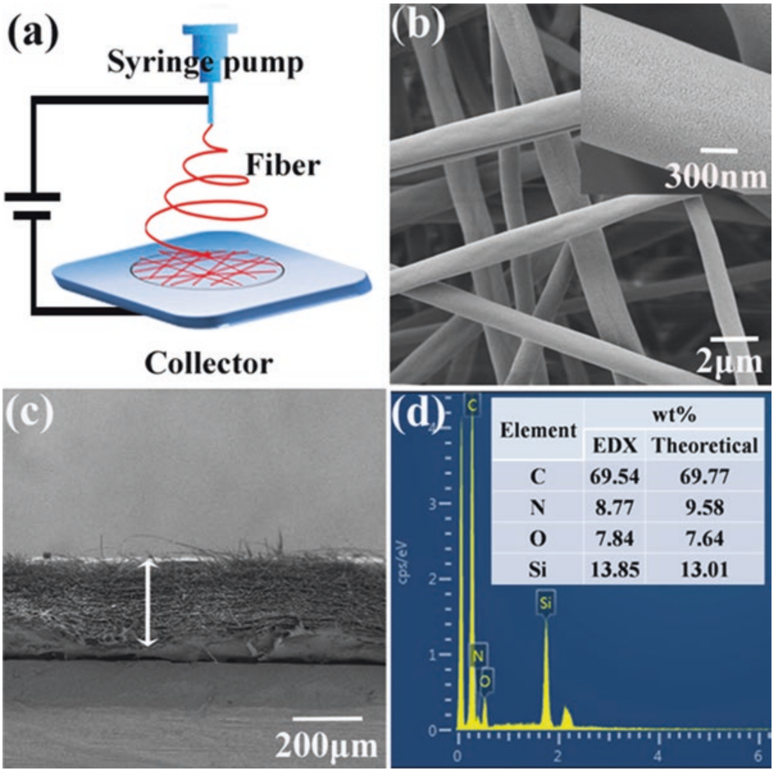

Element	wt%	
	EDX	Theoretical
C	69.54	69.77
N	8.77	9.58
O	7.84	7.64
Si	13.85	13.01

Fig. 9.9 (**a**) Schematic illustrating the electrospinning process. (**b**) Representative SEM image of polymer fibers; inset is the zoomed-in image of the surface of a single fiber. (**c**) Cross-sectional morphology and (**d**) EDX spectrum of the polymer fibrous mat (inset table shows the element content obtained using EDX and theoretical calculations) (Reproduced with permission from (Li et al. 2016c), Copyright 2016 American Chemical Society)

over the surface in 480 s showing superhydrophilic nature of polymer fibers mat (Fig. 9.10). When oil (hexane) drop was placed on the fibrous mat, it was absorbed by mat as shown in Fig. 9.10 (**d**). They demonstrated the effective oil/water separation from the layered mixtures varying with the pH of the solution driven by gravity. The PDMS-b-P4VP fibrous mats showed controlled separations for oil (hexane) and water with high fluxes of ~ 9000 and 27,000 L h^{-1} m^{-2}, respectively. Interestingly, when a composite of these fibrous mats was formed with silica nanoparticulate, these nanocomposites exhibited an improved behavior in respect of the thermal stability of the nanostructures, pH switchability response along with their performance in separating oil/water. An improved high fluxes of ~9000 and 32,000 L h^{-1} m^{-2} for oil and water were recorded, respectively with composite fibrous mats. Interestingly, Zhou et al. (2016) studied the composition effect of copolymer in order to create pH responsive smart surfaces with high wettability and excellent oil/water separation.

Very recently, Lu et al. (2017) developed pH responsive magnetic nanoparticles (Fe_3O_4) using co-precipitation technique for their application in separation of oil

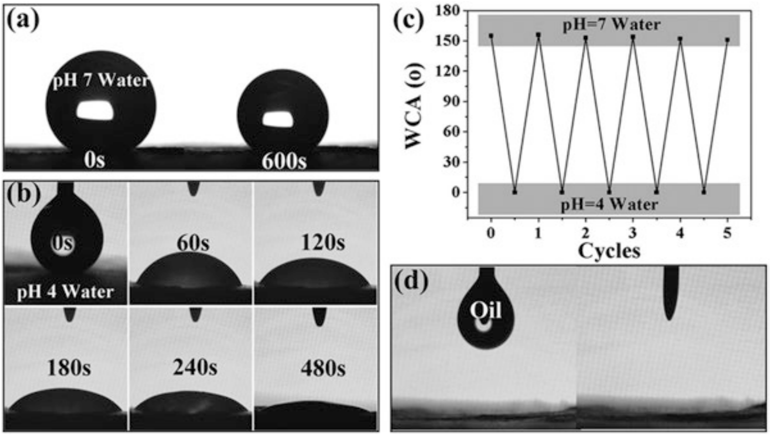

Fig. 9.10 CA measurements of the as-prepared polymer fibrous mat in air. (**a**) Images of a neutral water droplet on the mat surface at 0 s (left) and 600 s (right). (**b**) Dynamic images of a pH 4 water droplet spreading over the mat gradually within 480 s. (**c**) pH-Switchable water wettability of the as-prepared mat between superhydrophobicity and superhydrophilicity. (**d**) Absorption of the hexane droplet as soon as it contacts the surface (Reproduced with permission from (Li et al. 2016c), Copyright 2016 American Chemical Society)

from oil/water system. These nanoparticles were coated with silica followed by functionalization via (3-aminopropyl)triethoxysilane (APTES) molecular layer. It was observed that these nanoparticles exhibited excellent separation ability for oil/water system with neutral and acidic solutions. On the other hand, in the case of alkaline solution, the separation efficiency was low. The observed results were explained by electrostatic interaction and interfacial activity in oil/water system (Fig. 9.11).

9.2.3 Temperature Responsive Smart Surfaces

The separation of organic compounds from water system is a growing environmental problem and number of methods involving new chemistry and new engineering approaches are being implemented. Particularly, the development of a new classes of materials with smart surfaces, which can be used to separate out oil or any other similar organic compounds from water systems at one temperature and separate water from oil system at another temperatures is an another promising pathway in this direction (Janout et al. 2007; Crevoisier et al. 1999). Sun et al. (2004b) reported that thermally responsive wettability on the surfaces could be induced by tuning/modifying the surface roughness. They studied the poly(N-isopropylacrylamide) (PNIPAAm) surfaces and observed the reversible switching between superhydrophilicity and superhydrophobicity at difference of very narrow temperature range (10 °C) attributed to the combined effect of surface roughness and the chemical

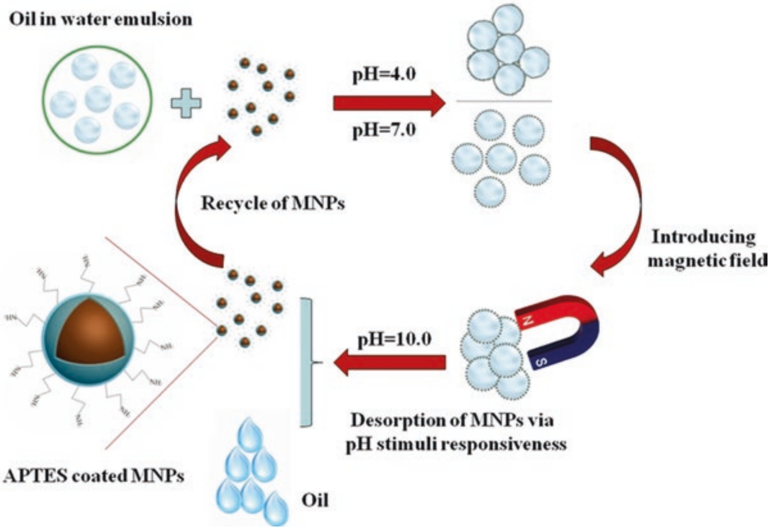

Fig. 9.11 Schematic illustration of the recycle of (3-aminopropyl)triethoxysilane (APTES) coated MNPs via regulating pH values during oil-water separation. (Reproduced with permission from (Lü et al. 2017), Copyright 2017 Elsevier)

changes on the surfaces. A class of thermosensitive materials have been studied for removing emulsified oil droplets from aqueous media or oil/water separation (Lü et al. 2016; Yuan et al. 2017; Gunatilake and Bandara 2017b). Smart thermoresponsive polymeric materials based smart surfaces with switchable oil/water wettability have been also utilized for oil/water separation (Li et al. 2016b; Tang et al. 2016; Yuan et al. 2017; Ou et al. 2016; Luo et al. 2014).

Xiang et al. (2015) developed a thermal responsive PVDF membrane modified with micro-hydrogel consisting of N-isopropylacrylamide (NIPAAm) and N-vinyl pyrrolidone (NVP) with triethoxyvinylsilane (VTES) for efficient separation of oil/water or water/oil microemulsion. The prepared membrane showed the under oil superhydrophobicity and under water superoleophobicity. The PVDF membrane showed excellent separation efficiency, high permeability, etc. and it completely removed the droplets bigger than the diameter of 20 nm and 40 nm by triggering temperature below and above lower critical solution temperature (LCST). Ou et al. (2016) developed a thermoresponsive polymer nanocomposite membrane composed of PU microfiber web and PNIPAM that was switchable between the superhydrophilicity and superhydrophobicity for oil/water separation with high efficiency. It was demonstrated that the nanocomposite, thermoresponsive PU-PNIPAM membrane had switchable property between superhydrophilicity and superhydrophobicity, when temperature changed from 25 °C to 45 °C and these membranes were able to separate 1 wt % oil-in-water emulsion and 1 wt % water-in-oil emulsion at 25 °C and 45 °C, respectively, with a high separation efficiency of ≥99.26% (Fig. 9.12).

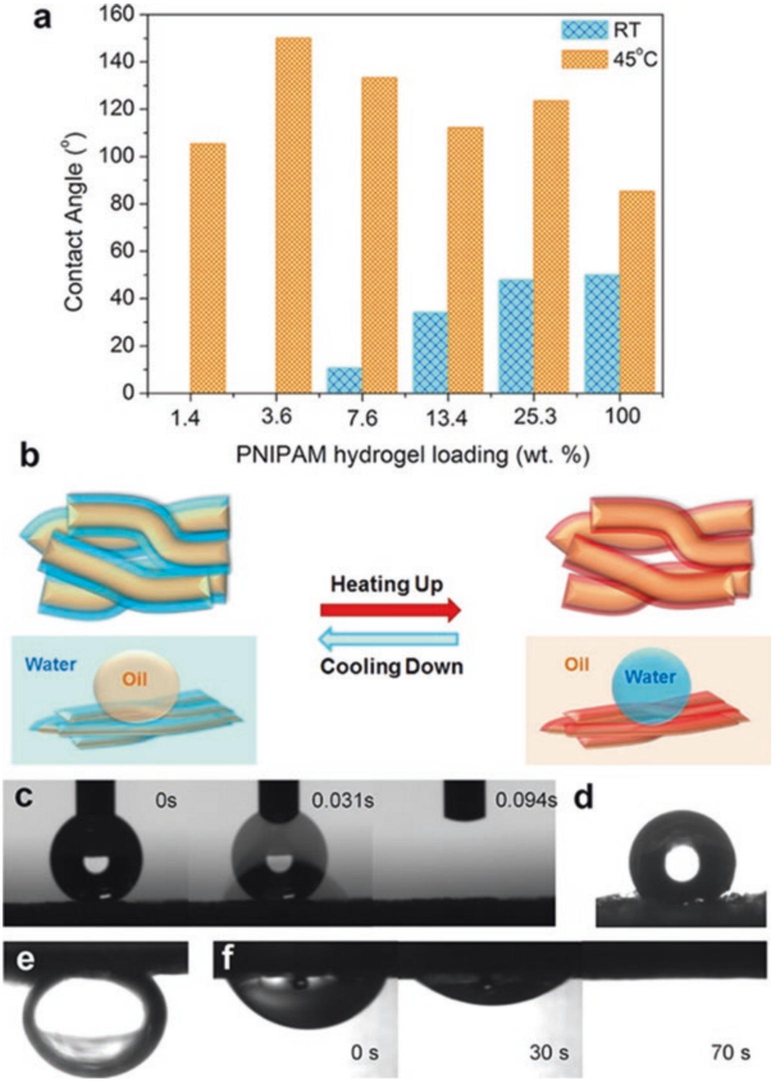

Fig. 9.12 (**a**) Water contact angles of swollen TPU-PNIPAM membranes (1.4, 3.6, 7.6, 13.4, and 25.3 wt %) and the swollen PNIPAM hydrogel (100 wt %) at room temperature (RT) and 45 °C. (**b**) Schematic diagram of switching wettability of TPU-PNIPAM membrane at different temperatures. (**c**) A water droplet (1 μL) spreading on a swollen TPU-PNIPAM-3.6 membrane within 0.094 s at room temperature. (**d**) Water contact angle (150.2°) of swollen TPU-PNIPAM-3.6 membrane at 45 °C. (**e**) Underwater–oil contact angle (141.3°) of swollen TPU-PNIPAM-3.6 membrane at room temperature. (**f**) Underwater–oil contact angle of swollen TPU-PNIPAM-3.6 membrane at 45 °C. Hexadecane was used for testing the underwater–oil contact angle. (Reproduced with permission from (Ou et al. 2016), Copyright 2016 American Chemical Society)

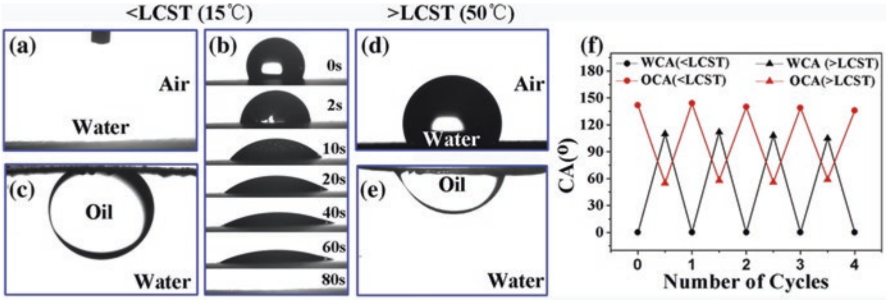

Fig. 9.13 Water and oil wettability of electrospun fibrous membrane at temperature below the LCST (**a**–**c**) and temperature above the LCST (d and e). (**a**) Image of a water droplet on the membrane in air with a WCA of almost 0°. (**b**) Images of the dynamic water droplet spread over the fiber membrane within 12 s. (**c**) Images of an oil droplet (hexane) on the membrane underwater with an OCA of ~153° (left) and sliding angle of ~4° (right). (**d**) Image of a water droplet on the membrane in air with a WCA of ~130°. (**e**) Image of an oil droplet (hexane) on the membrane underwater with an OCA of ~37°. (**f**) Reversible oil/water wettability at different temperatures. (Reproduced with permission from (Li et al. 2016b), Copyright 2016 Elsevier)

Li et al. (2016b) synthesized polymer based thermoresponsive smart membranes using solution casting and electrospinning technology. These membranes were composed of temperature responsive copolymer poly(methyl methacrylate)-*block*-poly(N-isopropylacrylamide) (PMMA-*b*-PNIPAAm) and showed temperature modulable oil/water wettability. Interestingly, electrospun fibrous membranes were found to be better temperature responsive materials for oil/water separation with high efficiency of 98% as compared to the membrane produced by solution casting method. This excellent performance of electrospun fibrous is due to the 3D network, large surface-to-volume ratio, porous and random entangled structures with high flux of about 9400 L h^{-1} m^{-2} and 4200 L h^{-1} m^{-2} for water and oil, respectively. The Li and co-workers actively researched on these thermoresponsive polymers (PMMA-*b*-PNIPAAm) and their switchable behavior between hydrophilicity and hydrophobicity close to their LCST of about 32–33 °C and predicted that these surfaces could be reversibly switched, when temperature fluctuated below or above the LCST (Luo et al. 2014).

The electrospun polymeric fibrous membranes were studied using CA for water separation at various temperatures. It was found that these polymeric surfaces showed superhydrophilic and underwater superoleophobic characteristics below the LCST as shown in Fig. 9.13. On the other hand, the wettability behavior of the membrane switched to hydrophobicity and underwater oleophilicity above LCST. The reversible wetting switching behavior of these membranes can be seen in the Fig. 9.13f. Moreover, a recent review provides more details on the development of designing and synthesizing nanofibers materials mainly effective for oil/water separation (Wang et al. 2016).

9.2.4 Gas Responsive Smart Surfaces

As we studied in above sections, different kind of smart surfaces stimuli responsive towards various external factors such as light, pH, temperature etc. have been progressively investigated. Besides the progress, there are some drawbacks of the way of treating these materials like high energy light bombardment or higher temperature, which can damage the materials and affect the responsive behavior. Similarly, change in pH of the solutions can promote complex formation and slows cyclic process (Che et al. 2015). To overcome these problems, there have been progress carried out using gas as an external factor to study the change in surface wettability and their smart behavior for the separation of oil/water systems.

Some polymer based materials were developed earlier which showed gas responsive behavior containing amine group such as poly(2-dimethylaminoethyl methacrylate) (PDMAEMA), which exhibited hydrophilic or hydrophobic nature due to exposure of some gases like CO_2 or N_2 (Yan et al. 2011, 2013; Yan and Zhao 2013; Zhang et al. 2012b). These results made it possible to develop gas responsive smart surfaces for oil/water wettability in the application of oil/water separation.

Xu et al. (2015) reported such kind of materials with smart surface having superamphiphobic coating, which after exposure to ammonia gas becomes superhydrophilic and superoleophobic and characteristics make it a promising materials for oil/water separation. These materials composed of silica nanoparticles, TiO_2, polyester fabric, and PU sponge etc. exhibited excellent surface properties for water separation from the bulk oil. It was found that for water and oils (1,2-dichloroethane) (DCE) CAs are more than 150°. Interestingly, it was found that after exposure to ammonia vapors, the surface became hydrophilic with CA~0° and oil repellent with oil CA >150°. The various CAs were observed during the exposure of ammonia vapors for different exposure times. After the ammonia vapor treatment, the surface became hydrophilic because the water spread in very short time, while oil droplets were found to be stable on the surface. DCE CA of fabric under the exposure of ammonia during underwater oil wettability was found to be 153°. After examining the surface properties towards the both water and oil, the as synthesized fabric coating was also used to separate oil/water mixture [hexadecane and water (1:1, v/v)] (Xu et al. 2015). Xu et al. (2016) synthesized superamphiphile (D-OA) assembly via electrostatic interaction of Jeffamine D 230 and oleic acid. D-OA formed a highly stable oil/water emulsion, when mixed with paraffin oil. The phase separation occurred after passing CO_2 gas through stable emulsion, while stable emulsion can be obtained upon replacement of CO_2 gas to N_2 gas at 60 °C (Fig. 9.14).

Recently, Fan et al. (2017) developed a superhydrophobic zirconium surfaces with mastoids kind of structures coated on carbon fibers. These fabrics under the influence of ammonia gas, showed hydrophilic and underwater superoleophobic surface properties, which is used for oil/water separation. Che et al. (2015) fabricated electrospun poly(methyl methacrylate)-co-poly(N, N-diethyl amino ethyl methacrylate) polymer based smart membranes, which showed stimuli responsive properties towards oil/water separation triggered by CO_2 gas. The polymeric mem-

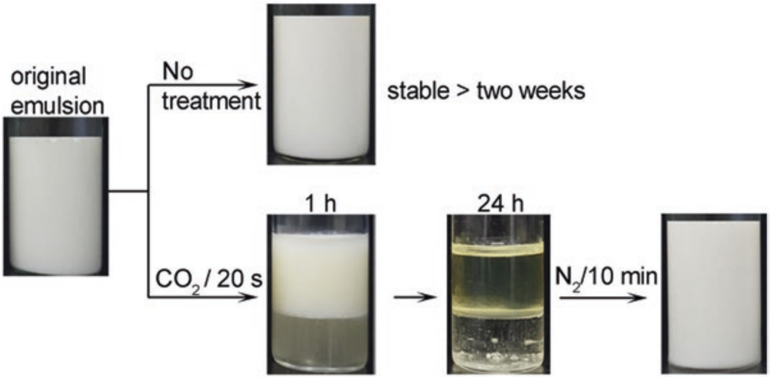

Fig. 9.14 Stability and reversible breaking-reforming of paraffin oil in water emulsions stabilized by D-OA. The original emulsion was prepared with 3 wt% D-OA and 50 wt% water. (Reproduced with permission from (Xu et al. 2016), Copyright 2016 Elsevier)

branes with a high surface roughness, interface to volume area due to electrospinning and nanoporous structures in combination with CO_2 responsive showed excellent oil/water separation ability. These polymeric membranes were tested for water and oil wettability and hence were used for selective switching for the separation of oil/water system using CO_2 or N_2 gas flow. It was found that when oil/water mixture was allowed to pass through the membranes, oil could pass easily, whereas water remained on the surface because it showed hydrophobic and oleophilic behavior as studied separately. Opposite to this, it was observed that when the membranes were kept in water with CO_2 gas flow for few minutes, the separation results were completely reversed. Then, water could be separated through the membranes and oil remained on the surface of the membranes. Again, after removing CO_2 by introducing N_2, it showed the reversible or switching behavior. Using these smart fibers membranes, the water quantity in various oil/water system was investigated. This investigation reveals that low level water content can be estimated. For example, water concentration estimated was 30, 40 and 60 ppm in hexane, petroleum ether and n-heptane, respectively, which showed the higher separation efficiency of these electrospun membranes.

Zhu et al. (2008) prepared the indium oxide film with micro and nanostructures and it showed the excellent switchable properties upon exposure of NH_3 gas as shown in Fig. 9.15.

9.2.5 Electric and Magnetic Field Responsive Smart Surfaces

Functional materials with stimuli responsive smart surfaces towards external environment as mentioned above are very useful for oil/water separation. Moreover, reversible wettability and controlled oil/water separation induced by electricity is

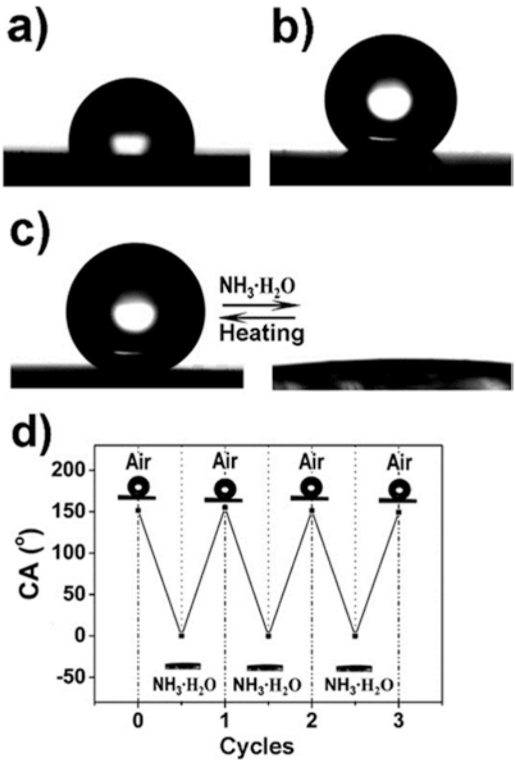

Fig. 9.15 Surface wettability of the $In(OH)_3$ films. Shape of a 2 μL water droplet on the surface of (**a**) $In(OH)_3$ microcube films in the air with the water contact angle of 102.2 ± 3.6°; (**b**) $In(OH)_3$ nanorod film in the air with a water contact angle of 146.2 ± 0.6°; (**c**) $In(OH)_3$ microcube and nanorod multiple film (left) in the air with a water contact angle of 150.4 ± 0.9° and (right) after being exposed to ammonia hydroxide atmosphere for 20 h with a water contact angle of 0°; (**d**) smart surface wettability switched between superhydrophobicity and superhydrophilicity shows excellent reproducibility by the alternate storage in the air and ammonia hydroxide atmosphere. (Reproduced with permission from (Zhu et al. 2008), Copyright 2008 American Chemical Society)

another promising method with additional benefit of *in-situ* and fast response (Lin et al. 2015; Kwon et al. 2012; Zheng et al. 2016). Electric responsive surfaces are useful for changing the wettability of polar liquids (Kwon et al. 2012). Kwon et al. (2012) first demonstrated the separation of oil/water mixture with 99.9% efficiency induced by electric field.

Similarly, Lin et al. (2015) developed a 3D copper foam modified with *N*-dodecyltrimethoxysilane, which could be switched between superhdrophobicity and superdydrophilicity using electric field as a driving source for stimuli response (Fig. 9.16).

The mechanism of electric field induced separation of water from oil/water mixture has been shown schematically in Fig. 9.17. When Cu foam acted as anode, the

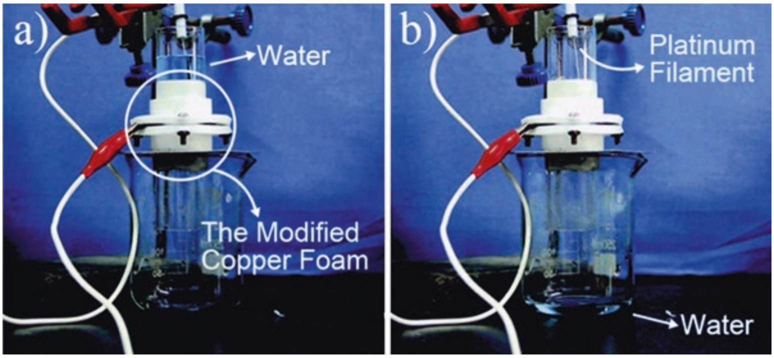

Fig. 9.16 Controllable water permeation conducted by electricity: (**a**) water remains on the modified foam before the voltage is applied; (**b**) water penetrates through the foam after a low voltage added. (Reproduced with permission from (Lin et al. 2015), Copyright 2015 The Royal Society of Chemistry)

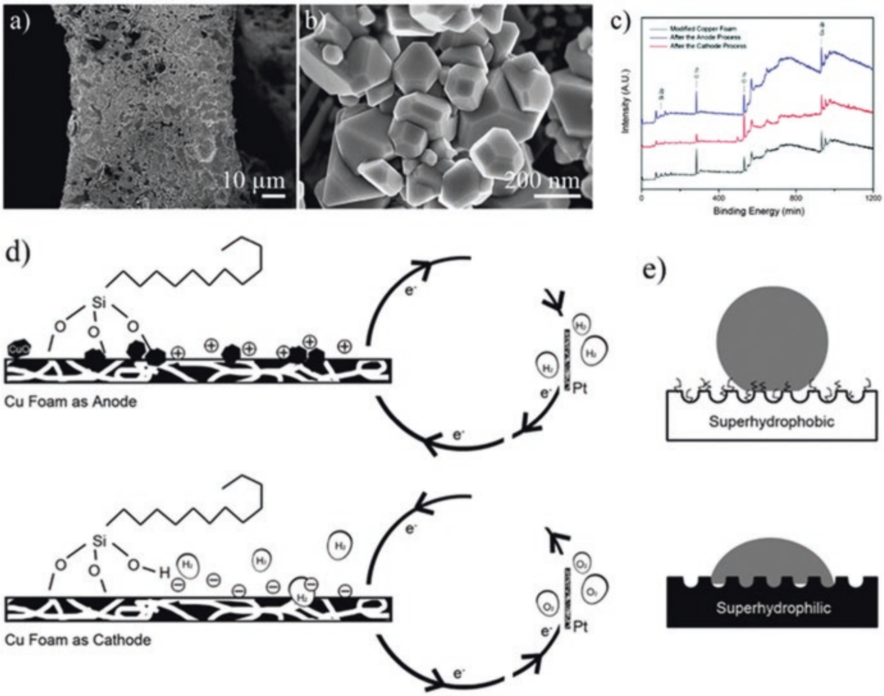

Fig. 9.17 SEM images and the XPS pattern of the modified-copper foam: (**a** and **b**) SEM images after the anode process at different magnifications; (**c**) XPS pattern of the modified foam before the electrode process, after the anode process and after the cathode process. Mechanism of the switchable wettability induced by electricity: (**d**) schematic illustration of the electrolysis process for the anode and the cathode; and (**e**) wetting behaviour model of each special wettability surface. (Reproduced with permission from (Lin et al. 2015), Copyright 2015 The Royal Society of Chemistry)

CuO structure grew up on the surface of Cu foam and surface became rough (Fig. 9.17a, b) resulting it from hydrophobic to superhydrophobic. When Cu foam acted as cathode, the surface became smooth due to loss of modified layer during electrolysis as shown in Fig. 9.17d, e. The composition changes in the copper foam were monitored using XPS spectra (Fig. 9.17c) (Lin et al. 2015).

Recently, Zheng et al. (2016) have reported electric responsive smart surfaces comprising of polyaniline nanofibers mesh, which could be triggered by electric field for their application in separation of oil/water system. These polymeric based smart surfaces were realized to be superhydrophobic as well as underwater superoleophobic. Interestingly, it was found that superhydrophobic property of the mesh could be switched to hydrophilic at applied voltage of 160 V whereas, at 170 V, water could be selectively filtered through the mesh. The mesh showed underwater superoleophobicity, which remained similar or enhanced under the effect of electric field. The oil/water separation through the mesh under the electric field could be observed, when electric capillary pressure was larger as compared to the hydrostatic pressure of surface water on the mesh.

Similarly, there are few studies showing magnetic field stimuli responsive materials for oil/water separation (Chen et al. 2014; Ma et al. 2016b). Chen et al. (2014) synthesized polymer based magnetic composite particles by grafting polymer on Fe_3O_4 for harvesting oil from oil/water mixture using wettable surface properties of these composite particles. These composite materials were found to be working as solid stabilizers for harvesting oil and Fe_3O_4 allowed simple separation of pickering emulsions, when magnetic field was applied. As soon as temperature was increased around 50 °C, the polymer component worked as a destabilizer for emulsion resulting in release of oil. Recent investigation by Ma et al. (2016b) on bifunctional demulsifier consisting of magnetic particles shows that these could be a promising materials for the oil/water separation. They showed that magnetite/reduced graphene oxide composites modified with octadecyltrimethoxysilane (ODTS) demulsified significantly water and oil in oil/water emulsions due to its surface wetting properties under the effect of magnetic field.

9.2.6 Dual Stimuli Responsive Smart Surfaces

So far, we have discussed the materials with smart surfaces, which are stimuli responsive to one of the external factor such as light, pH, temperature, gas, electric/magnetic, etc. There are other materials with smart surfaces responsive on the implication of more than one external environment. This section includes the recent developments of such dual or multiple responsive materials and their applications for the separation of oil/water systems.

9.2.6.1 Photo-Thermal Dual Responsive Smart Surfaces

Hu et al. (2015) introduced photothermal stimuli responsive nanomaterials based on SWCNT membrane, which served as switchable device for the oil/water emulsion separation. These stimuli smart surfaces were composed of Au nanorods/poly(N-isopropylacrylamide-co-acrylamide) cohybrid with SWCNT nanoporous membranes. In this composition, the SWCNT membranes showed hydrophobic and superoleophilic surface wetting properties with pores of nanometer sizes, which made them capable of separating oil from oil/water mixture with a higher flux rate that can be increased under light irradiation (Shi et al. 2013; Hu et al. 2015). In addition, introduction of copolymer and noble metal nanorods provide the thermal responsive behavior providing ultrahigh separation efficiency (>99.99%) along with antifouling as well as reproducibility (Hu et al. 2015). Recently, Yan et al. (2016) have reported a photo-induced ZnO coated mesh synthesized by spraying superhydrophobic ZnO nanoparticles and waterborne PU mixtures on stainless steel mesh that worked as an excellent photo-thermal stimuli responsive surface for oil/water separation. The materials showed the switching behavior between superhydrophobicity and superhydrophilicity/underwater superoleophobicity under UV illumination and heat treatment (Fig. 9.18). These dual stimuli responsive surfaces, when treated under heat and photo irradiation, allowed both water removal and oil removal from oil/water mixture. They achieved separation efficiency up to 99.0% for light oil/water mixture and above 97.0% for heavy oil/water mixture with good repeatability.

9.2.6.2 pH and Temperature Responsive Smart Surfaces

As we discussed in above sections, stimulus-responsive polymer surfaces have been used broadly as a smart surfaces for the oil/water separation and are promising materials for fabricating devices with controlled properties. Cao et al. (2014) fabricated thermo and pH dual controllable oil/water separation materials via photo-initiated free radical polymerization of dimethylamino ethyl methacrylate (DMAEMA). These materials showed superhydrophilicity and underwater superleophobicity at particular temperature and pH values and could be applied for selective separation of water from oil/water systems. It was found that water could go through the polymeric material, when temperature is below 55 °C (and $\text{pH} < 13$) and oil remained on the mesh. On the other hand, oil could go through the mesh as soon as temperature reach above 55 °C or pH ˃ 13 (Cao et al. 2014). Wu et al. (2016) synthesized pH-thermo responsive cotton fabrics grafted by PDMAEMA, which showed highly effective oil/water separations. The dual responsive materials showed switchable superhydrophilic (~0°) and hydrophobic behavior (130°) via regulating pH or temperature condition. Cotton fabric could absorb oil ~ 4 times of its own weight from oil/water system and released completely in acid or cold water.

In another report, Li et al. (2016d) have recently shown that separation efficiency of 98.35% could be achieved even after 15 cycles of uses for oil/water system like

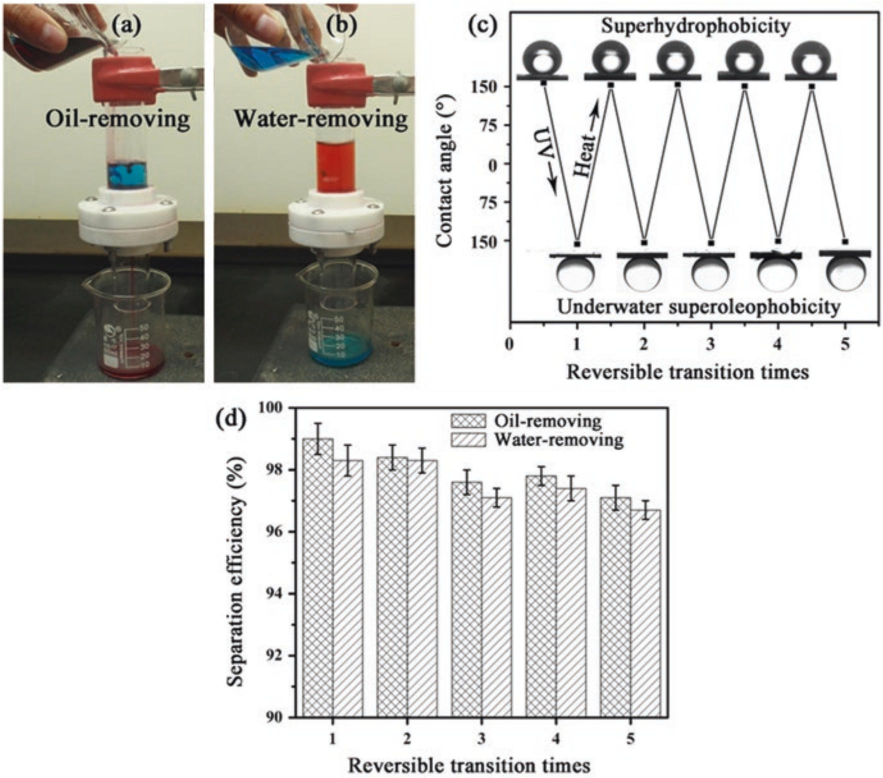

Fig. 9.18 (**a** and **b**) Photograph of photo-thermal induced oil/water separation process; (**c**) water and oil CAs and (**d**) separation efficiency in reversible transition. (Reproduced with permission from (Yan et al. 2016), Copyright 2016 Elsevier)

silicon oil using hydrogel mesh. Hydrogel materials were coated on stainless steel mesh by simply immersing in the hydrogel solution.

As shown in Fig. 9.19, PDMAEMA coated hydrogel meshes were tested for oil/water separation, which showed difference in wettability performance with oil at various temperatures and pH because of its dual responsive nature (pH and thermal). When the oil/water mixture was poured on the mesh, water could simply permeated through the mess, whereas, oil retained on the mesh. It was also found that other parameters/conditions such as composition and temperature around the experimental zone also affected the separation efficiency of these smart hydrogel materials. As compared to the room temperature, oil could be seen in the water sample at higher temperature exhibiting its (hydrogel mesh) ability to separate water from the oil/water mixture at room temperature. In addition, retaining oil could be possible by varying the temperature (Li et al. 2016d). These hydrogel coated mesh were also tested for their pH responsive nature with the oil/water system at various pH values. The difference in color as shown in Fig. 9.20 indicates the difference in pH of the

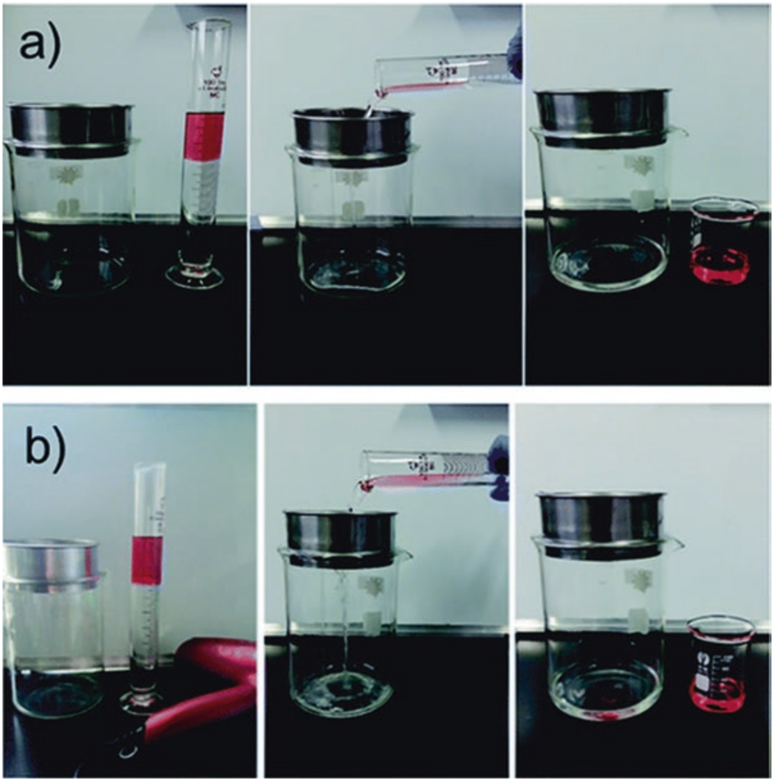

Fig. 9.19 The application performance of the temperature-controllable oil/water separation. (**a** and **b**) The as-coated mesh was placed under a beaker and a mixture of silicone oil and water (25 °C and 55 °C, dyed by oil red) was mixed well. As the mixture was poured into the as-coated mesh, water passed through quickly, but the oil was repelled in the upper mesh. In Fig. **b**, there is visible oil (dyed by oil red) in the water sample at high temperature in contrast to Fig. **a**, when poured into the as-coated mesh. The separations were finished and water samples were collected in the beaker below for further analysis. (Reproduced with permission from (Li et al. 2016d), Copyright 2016 The Royal Society of Chemistry)

solutions. It was observed that at higher pH value, the solution could go through the mess with oil and coated mesh contained 44% water, while earlier it was 0.06% in alkaline conditions. These changes were attributed to the protonation degree of tertiary amine group within the polymeric materials which was decreased, when pH was high (Li et al. 2016d). Similarly, Tang et al. (2016) showed that cellulose nanocrystals with grafted binary polymer brushes could be used to stabilize and destabilize the oil/water emulsion systems through controlling the temperature and pH of the solution.

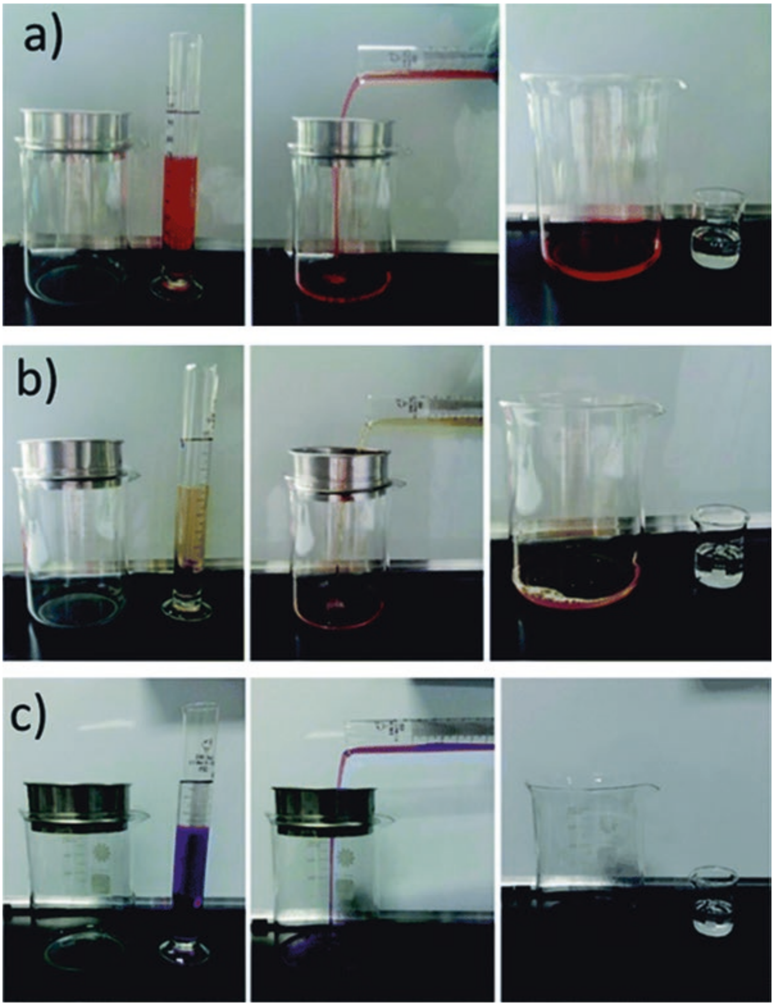

Fig. 9.20 The application performance of the pH-controllable oil/water separation. The as-coated mesh was placed under a beaker and a mixture of silicone oil and water (dyed by cresol red) was mixed well with pH solutions of 1.0, 7.0 and 14.0. (**a** and **b**) As the mixture was poured into the as-coated mesh, water could pass through quickly, but the oil was repelled in the upper mesh. (**c**) The mixture passed through the mesh altogether. (Reproduced with permission from (Li et al. 2016d), Copyright 2016 The Royal Society of Chemistry)

9.2.6.3 Other Dual/Multiple Responsive Smart Surfaces

Su et al. (2017) fabricated polydimethylsiloxane (PDMS) based superhydrophobic surfaces. These PDMS based surfaces were prepared by electroless deposition of $CuSO_4$ and UV light curing of PDMS. It was found that these surfaces exhibited water CA of 160° and sliding angle <5°. It preserved the superhydrophobicity while immersing in various aqueous solutions at different pH. Under UV irradiation, these surfaces were found to exhibit switching behavior from superhydrophobic to superhydrophilic state and again recovered to the hydrophobic state in the dark with water CA 140°. These smart surfaces also showed higher oil/water separation efficiency (96.8% for hexane and 95.8% for chloroform) (Su et al. 2017). Wang et al. (2015) synthesized Fe_3O_4-SiO_2 thin layer- PDMAEMA core-shell-shell nanoparticles, core Fe_3O_4 nanoparticles via solvothermal method followed by thin layer of SiO_2 to get stable nanoparticles and later PDMAEMA shell via radical polymerization. The Fe_3O_4 core is active to separate oil droplets under external magnetic field, while PDMAEMA shell provides pH responsive smart surfaces. Longer PDMAEMA arms were suitable for a broader range of pH, but showed reduced magnetic response. Optimized Fe_3O_4 nanoparticles with PDMAEMA arm showed the efficient separation of diesel droplets from water with a very good reusability without any loss in morphology or separation efficiency. Dunderdale et al. (2014b) fabricated PDMAEMA polymer based smart surfaces by radical polymerization method, which were found to be responsive to multiple external stimuli such as pH, ionic strength, and temperature. These multiple responsive behavior could be achieved by varying several parameters such as thicknesses, structures, composition and degree of hydration etc. Recently, smart materials with dual stimuli responsive by voltage and ion exchange have been reported (Taleb et al. 2016). These materials were prepared by electrochemical copolymerization, which contained fluorinated chains and pyridinium groups responsible for superoleophobic and switching behavior, respectively. The pyridinium groups were found to be mainly responsible for switchable performance due to its counter ion exchange mechanism. Interestingly, it was found that by controlling the composition of the polymer, and voltage/ion exchange parameters, the higher oil CA as compared to that of water CA could be achieved (Taleb et al. 2016).

9.3 Summary

The present chapter describes recent developments in the field of stimuli responsive smart materials due to the external environment such as light, pH, gas, temperature, and electrical/magnetic effects, etc. particularly for their applications in oil/water separation. It also includes dual stimuli responsive materials, which have shown great potential in this field. Materials can be designed for oil/water separations via tuning micro/nanostructures, functionality, pore sizes of materials etc. In last few years, research in oil/water separation has grown with the development of new fabrication techniques and functional materials. It has been realized that the development of functional materials with smart surfaces for highly efficient separation of oil/water systems along with cost effective stimuli is still a challenge. This indicates that extensive investigations will have to be carried out in this direction to make it more environment friendly and industrialized.

Acknowledgment RKG acknowledges financial assistance from Department of Science and Technology (DST), India, through the INSPIRE Faculty Award (Project No. IFA-13 ENG-57) and Grant No. DST/TM/WTI/2 K16/23(G). JP acknowledges DST, India for the prestigious INSPIRE faculty award (INSPIRE/04/2015/002452). DST support to the Center for Nanosciences is acknowledged.

References

Cao Y, Liu N, Fu C, Li K, Tao L, Feng L, Wei Y (2014) Thermo and pH dual-responsive materials for controllable oil/water separation. ACS Appl Mater Interfaces 6:2026–2030

Che H, Huo M, Peng L, Fang T, Liu N, Feng L, Wei Y, Yuan J (2015) CO_2-responsive nanofibrous membranes with switchable oil/water wettability. Angew Chem Int Ed 54:8934–8938

Chen Y, Bai Y, Chen S, Ju J, Li Y, Wang T, Wang Q (2014) Stimuli-responsive composite particles as solid-stabilizers for effective oil harvesting. ACS Appl Mater Interfaces 6:13334–13338

Chen Y, Li F, Cao W, Li T (2015) Preparation of recyclable CdS photocatalytic and superhydrophobic films with photostability by using a screen-printing technique. J Mater Chem A 3:16934–16940

Cheng Z, Wang J, Lai H, Du Y, Hou R, Li C, Zhang N, Sun K (2015) pH-controllable on-demand oil/water separation on the switchable superhydrophobic/superhydrophilic and underwater low-adhesive superoleophobic copper mesh film. Langmuir 31:1393–1399

Cheng Z, Li C, Lai H, Du Y, Liu H, Liu M, Jin L, Zhang C, Zhang N, Sun K (2016) A pH-responsive superwetting nanostructured copper mesh film for separating both water-in-oil and oil-in-water emulsions. RSC Adv 6:72317–72325

Crevoisier G, Fabre P, Corpart J-M, Leibler L (1999) Switchable tackiness and wettability of a liquid crystalline polymer. Science 285:1246–1249

Dang Z, Liu L, Li Y, Xiang Y, Guo G (2016) In situ and ex situ pH-responsive coatings with switchable wettability for controllable oil/water separation. ACS Appl Mater Interfaces 8:31281–31288

Dunderdale GJ, Urata C, Miranda DF, Hozumi A (2014a) Large-scale and environmentally friendly synthesis of pH-responsive oil-repellent polymer brush surfaces under ambient conditions. ACS Appl Mater Interfaces 6:11864–11868

Dunderdale GJ, Urata C, Hozumi A (2014b) An underwater superoleophobic surface that can be activated/deactivated via external triggers. Langmuir 30:13438–13446

Fan Y, He Y, Luo P, Chen X, Yu Z, Li M (2017) Facile way in building superhydrophobic zirconium surface for controllable water-oil separation. Mater Lett 188:115–118

Feng L, Zhang Z, Mai Z, Ma Y, Liu B, Jiang L, Zhu D (2004a) A super-hydrophobic and super-oleophilic coating mesh film for the separation of oil and water. Angew Chem Int Ed 43:2012–2014

Feng X, Feng L, Jin M, Zhai J, Jiang L, Zhu D (2004b) Reversible super-hydrophobicity to super-hydrophilicity transition of aligned ZnO Nanorod films. J Am Chem Soc 126:62–63

Gao SJ, Shi Z, Zhang WB, Zhang F, Jin J (2014) Photoinduced superwetting single-walled carbon nanotube/TiO_2 ultrathin network films for ultrafast separation of oil-in-water emulsions. ACS Nano 8:6344–6352

Gunatilake UB, Bandara J (2017a) Efficient removal of oil from oil contaminated water by super-hydrophilic and underwater superoleophobic nano/micro structured TiO2 nanofibers coated mesh. Chemosphere 171:134–141

Gunatilake UB, Bandara J (2017b) Fabrication of highly hydrophilic filter using natural and hydrothermally treated mica nanoparticles for efficient waste oil-water separation. J Environ Manag 191:96–104

Guo F, Guo Z (2016) Inspired smart materials with external stimuli responsive wettability: a review. RSC Adv 6:36623–36641

Guo S, Li X, Zhou M, Cai Z (2017) The smart surfaces with reversible transformations from superhydrophobicity to superhydrophilicity. Mater Lett 193:13–17

Hu L, Gao S, Ding X, Wang D, Jiang J, Jin J, Jiang L (2015) Photothermal-responsive single-walled carbon nanotube-based ultrathin membranes for on/off switchable separation of oil-in-water nanoemulsions. ACS Nano 9:4835–4842

Janout V, Myers SB, Register RA, Regen SL (2007) Self-cleaning resins. J Am Chem Soc 129:5756–5759

Kim DH, Jung MC, Cho SH, Kim SH, Kim HY, Lee HJ, Oh KH, Moon MW (2015) UV-responsive nano-sponge for oil absorption and desorption. Sci Rep 5:12908

Kota AK, Kwon G, Choi W, Mabry JM, Tuteja A (2012) Hygro-responsive membranes for effective oil–water separation. Nat Commun 3:1025

Kwon G, Kota AK, Li Y, Sohani A, Mabry JM, Tuteja A (2012) On-demand separation of oil-water mixtures. Adv Mater 24:3666–3671

Lee CH, Tiwari B, Zhang D, Yap YK (2017) Water purification: oil-water separation by nanotechnology and environmental concerns. Environ Sci Nano 4:514–525

Li H, Wang X, Song Y, Liu Y, Li Q, Jiang L, Zhu D (2001) Super-"amphiphobic" aligned carbon nanotube films. Angew Chem 113:1793–1796

Li J-J, Zhou Y-N, Luo Z-H (2015) Smart fiber membrane for pH-induced oil/water separation. ACS Appl Mater Interfaces 7:19643–19650

Li G, Fan H, Ren F, Zhou C, Zhang Z, Xu B, Wu S, Hu Y, Zhu W, Li J, Zeng Y, Li X, Chu J, Wu D (2016a) Multifunctional ultrathin aluminum foil: oil/water separation and particle filtration. J Mater Chem A 4:18832–18840

Li J-J, Zhu L-T, Luo Z-H (2016b) Electrospun fibrous membrane with enhanced swithchable oil/water wettability for oily water separation. Chem Eng J 287:474–481

Li J-J, Zhou Y-N, Jiang Z-D, Luo Z-H (2016c) Electrospun fibrous mat with pH-switchable superwettability that can separate layered oil/water mixtures. Langmuir 32:13358–13366

Li T, Shen J, Zhang Z, Wang S, Wei D (2016d) A poly(2-(dimethylamino)ethyl methacrylate-co-methacrylic acid) complex induced route to fabricate a super-hydrophilic hydrogel and its controllable oil/water separation. RSC Adv 6:40656–40663

Lin X, Lu F, Chen Y, Liu N, Cao Y, Xu L, Zhang W, Feng L (2015) Electricity-induced switchable wettability and controllable water permeation based on 3D copper foam. Chem Commun 51:16237–16240

Liu C-T, Liu Y-L (2016) pH-induced switches of the oil- and water-selectivity of crosslinked polymeric membranes for gravity-driven oil-water separation. J Mater Chem A 4:13543–13548

Liu Y, Zhang K, Son Y, Zhang W, Spindler LM, Han Z, Ren L (2017) A smart switchable bioinspired copper foam responding to different pH droplets for reversible oil-water separation. J Mater Chem A 5:2603–2612

Low LE, Tey BT, Ong BH, Chan ES, Tang SY (2017) Palm olein-in-water Pickering emulsion stabilized by Fe3O4-cellulose nanocrystal nanocomposites and their responses to pH. Carbohydr Polym 155:391–399

Lü T, Zhang S, Qi D, Zhang D, Zhao H (2016) Thermosensitive poly(N-isopropylacrylamide)-grafted magnetic nanoparticles for efficient treatment of emulsified oily wastewater. J Alloys Compd 688, Part B:513–520

Lü T, Zhang S, Qi D, Zhang D, Vance GF, Zhao H (2017) Synthesis of pH-sensitive and recyclable magnetic nanoparticles for efficient separation of emulsified oil from aqueous environments. Appl Surf Sci 396:1604–1612

Luo PG, Yang F, Yang S-T, Sonkar SK, Yang L, Broglie JJ, Liua Y, Sun Y-P (2014) Carbon-based quantum dots for fluorescence imaging of cells and tissues. RSC Adv 4:10791–10807

Ma Q, Cheng H, Fane AG, Wang R, Zhang H (2016a) Recent development of advanced materials with special wettability for selective oil/water separation. Small 12:2186–2202

Ma S, Wang Y, Wang X, Li Q, Tong S, Han X (2016b) Bifunctional demulsifier of ODTS modified magnetite/reduced graphene oxide nanocomposites for oil–water separation. ChemistrySelect 1:4742–4746

Mendes PM (2008) Stimuli-responsive surfaces for bio-applications. Chem Soc Rev 37:2512–2529

Nagappan S, Moorthy MCS, Rao KM, Ha C-S (2016) Stimuli-responsive smart polymeric coatings: an overview. In: Hosseini M, Makhlouf ASH (eds) Industrial applications for intelligent polymers and coatings. Springer, Cham, pp 27–49. https://doi.org/10.1007/978-3-319-26893-4_2

Nelson A (2008) Stimuli-responsive polymers: engineering interactions. Nat Mater 7:523–525

Ou R, Wei J, Jiang L, Simon GP, Wang H (2016) Robust thermoresponsive polymer composite membrane with switchable superhydrophilicity and superhydrophobicity for efficient oil–water separation. Environ Sci Technol 50:906–914

Rodríguez-Hermida S, Tsang MY, Vignatti C, Stylianou KC, Guillerm V, Pérez-Carvajal J, Teixidor F, Viñas C, Choquesillo-Lazarte D, Verdugo-Escamilla C, Peral I, Juanhuix J, Verdaguer A, Imaz I, Maspoch D, Giner Planas J (2016) Switchable surface hydrophobicity–hydrophilicity of a metal–organic framework. Angew Chem Int Ed 55:16049–16053

Shi Z, Zhang W, Zhang F, Liu X, Wang D, Jin J, Jiang L (2013) Ultrafast separation of emulsified oil/water mixtures by ultrathin free-standing single-walled carbon nanotube network films. Adv Mater 25:2422–2427

Su X, Li H, Lai X, Zhang L, Liang T, Feng Y, Zeng X (2017) Polydimethylsiloxane-based superhydrophobic surfaces on steel substrate: fabrication, reversibly extreme wettability and oil–water separation. ACS Appl Mater Interfaces 9:3131–3141

Sun T, Wang G, Feng L, Liu B, Ma Y, Jiang L, Zhu D (2004a) Reversible switching between superhydrophilicity and superhydrophobicity. Angew Chem 116:361–364

Sun T, Wang G, Feng L, Liu B, Ma Y, Jiang L, Zhu D (2004b) Reversible switching between superhydrophilicity and superhydrophobicity. Angew Chem Int Ed 43:357–360

Tadanaga K, Katata N, Minami T (1997) Super-water-repellent Al_2O_3 coating films with high transparency. J Am Ceram Soc 80:1040–1042

Tadanaga K, Morinaga J, Matsuda A, Minami T (2000) Superhydrophobic−superhydrophilic micropatterning on flowerlike alumina coating film by the sol−gel method. Chem Mater 12:590–592

Taleb S, Darmanin T, Guittard F (2016) Superoleophobic/superhydrophobic PEDOP conducting copolymers with dual-responsivity by voltage and ion exchange. Mater Today Commun 6:1–8

Tang J, Berry RM, Tam KC (2016) Stimuli-responsive cellulose nanocrystals for surfactant-free oil harvesting. Biomacromolecules 17:1748–1756

Tian D, Zhang X, Wang X, Zhai J, Jiang L (2011a) Micro/nanoscale hierarchical structured ZnO mesh film for separation of water and oil. PCCP 13:14606–14610

Tian D, Zhang X, Zhai J, Jiang L (2011b) Photocontrollable water permeation on the micro/nanoscale hierarchical structured ZnO mesh films. Langmuir 27:4265–4270

Tian D, Zhang X, Tian Y, Wu Y, Wang X, Zhai J, Jiang L (2012) Photo-induced water-oil separation based on switchable superhydrophobicity-superhydrophilicity and underwater superoleophobicity of the aligned ZnO nanorod array-coated mesh films. J Mater Chem 22:19652–19657

Wang S, Song Y, Jiang L (2007) Photoresponsive surfaces with controllable wettability. J Photochem Photobiol C 8:18–29

Wang X, Shi Y, Graff RW, Lee D, Gao H (2015) Developing recyclable pH-responsive magnetic nanoparticles for oil-water separation. Polymer (UK) 72:361–367

Wang X, Yu J, Sun G, Ding B (2016) Electrospun nanofibrous materials: a versatile medium for effective oil/water separation. Mater Today 19:403–414

Wu J, Jiang Y, Jiang D, He J, Cai G, Wang J (2015) The fabrication of pH-responsive polymeric layer with switchable surface wettability on cotton fabric for oil/water separation. Mater Lett 160:384–387

Wu JD, Zhang C, Jiang DJ, Zhao SF, Jiang YL, Cai GQ, Wang JP (2016) Self-cleaning pH/thermo-responsive cotton fabric with smart-control and reusable functions for oil/water separation. RSC Adv 6:24076–24082

Xiang Y, Wang Y, Lin H, Wang Y, Xiong Z, Liu F (2015) Efficient separation of O/W and W/O micro-emulsion by thermally responsive superantiwetting PVDF membrane. React Funct Polym 97:86–95

Xu Z, Zhao Y, Wang H, Wang X, Lin T (2015) A superamphiphobic coating with an ammonia-triggered transition to superhydrophilic and superoleophobic for oil–water separation. Angew Chem Int Ed 54:4527–4530

Xu P, Wang Z, Xu Z, Hao J, Sun D (2016) Highly effective emulsification/demulsification with a CO2-switchable superamphiphile. J Colloid Interface Sci 480:198–204

Xue B, Gao L, Hou Y, Liu Z, Jiang L (2013) Temperature controlled water/oil wettability of a surface fabricated by a block copolymer: application as a dual water/oil on–off switch. Adv Mater 25:273–277

Xue Z, Cao Y, Liu N, Feng L, Jiang L (2014) Special wettable materials for oil/water separation. J Mater Chem A 2:2445–2460

Yan Q, Zhao Y (2013) CO_2-stimulated diversiform deformations of polymer assemblies. J Am Chem Soc 135:16300–16303

Yan Q, Zhou R, Fu C, Zhang H, Yin Y, Yuan J (2011) CO_2-responsive polymeric vesicles that breathe. Angew Chem Int Ed 50:4923–4927

Yan Q, Wang J, Yin Y, Yuan J (2013) Breathing polymersomes: CO_2-tuning membrane permeability for size-selective release, separation, and reaction. Angew Chem Int Ed 52:5070–5073

Yan L, Li J, Li W, Zha F, Feng H, Hu D (2016) A photo-induced ZnO coated mesh for on-demand oil/water separation based on switchable wettability. Mater Lett 163:247–249

Ye S, Cao Q, Wang Q, Wang T, Peng Q (2016) A highly efficient, stable, durable, and recyclable filter fabricated by femtosecond laser drilling of a titanium foil for oil-water separation. Sci Rep 6:37591

Yong J, Chen F, Yang Q, Farooq U, Hou X (2015) Photoinduced switchable underwater superoleophobicity-superoleophilicity on laser modified titanium surfaces. J Mater Chem A 3:10703–10709

Yuan X, Li W, Zhu Z, Han N, Zhang X (2017) Thermo-responsive PVDF/PSMA composite membranes with micro/nanoscale hierarchical structures for oil/water emulsion separation. Colloids Surf A Physicochem Eng Asp 516:305–316

Zhang L, Zhang Z, Wang P (2012a) Smart surfaces with switchable superoleophilicity and superoleophobicity in aqueous media: toward controllable oil/water separation. NPG Asia Mater 4:e8

Zhang J, Han D, Zhang H, Chaker M, Zhao Y, Ma D (2012b) In situ recyclable gold nanoparticles using CO2-switchable polymers for catalytic reduction of 4-nitrophenol. Chem Commun 48:11510–11512

Zhang L, Zhong Y, Cha D, Wang P (2013a) A self-cleaning underwater superoleophobic mesh for oil-water separation. Sci Rep 3:2326

Zhang W, Shi Z, Zhang F, Liu X, Jin J, Jiang L (2013b) Superhydrophobic and superoleophilic PVDF membranes for effective separation of water-in-oil emulsions with high flux. Adv Mater 25:2071–2076

Zhang W, Lu X, Xin Z, Zhou C (2016) Development of a superhydrophobic polybenzoxazine surface with self-cleaning and reversible water adhesion properties. RSC Adv 6:106054–106063

Zhao X, Su Y, Liu Y, Li Y, Jiang Z (2016) Free-standing graphene oxide-palygorskite nanohybrid membrane for oil/water separation. ACS Appl Mater Interfaces 8:8247–8256

Zheng X, Guo Z, Tian D, Zhang X, Jiang L (2016) Electric field induced switchable wettability to water on the polyaniline membrane and oil/water separation. Adv Mater Interfaces 3:1600461-n/a

Zhou F, Huck WTS (2006) Surface grafted polymer brushes as ideal building blocks for "smart" surfaces. PCCP 8:3815–3823

Zhou Y-N, Li J-J, Luo Z-H (2016) Toward efficient water/oil separation material: effect of copolymer composition on pH-responsive wettability and separation performance. AICHE J 62:1758–1771

Zhou C, Cheng J, Hou K, Zhu Z, Zheng Y (2017) Preparation of $CuWO_4@Cu_2O$ film on copper mesh by anodization for oil/water separation and aqueous pollutant degradation. Chem Eng J 307:803–811

Zhu H, Guo Z (2016) Understanding the separations of oil/water mixtures from immiscible to emulsions on super-wettable surfaces. J Bionic Eng 13:1–29

Zhu W, Zhai J, Sun Z, Jiang L (2008) Ammonia responsive surface wettability switched on indium hydroxide films with micro- and nanostructures. J Phys Chem C 112:8338–8342

Zhu H, Yang S, Chen D, Li N, Xu Q, Li H, He J, Lu J (2016) A robust absorbent material based on light-responsive superhydrophobic melamine sponge for oil recovery. Adv Mater Interfaces 3:1500683-n/a

Chapter 10
Anti-(bio)Fouling

Yuji Higaki and Atsushi Takahara

Abstract This chapter reviews the anti-(bio)fouling systems based on polymer brushes. Charged polymer brushes are well-hydrated in aqueous solutions to produce liquid-infused smooth interface. Because of the extremely low interfacial tension in the water-infusion soft interfaces and water, the hydrated charged polymer brushes exhibit outstanding anti-fouling capability in aqueous solutions. We present here anti-(bio)fouling properties of the charged polymer brushes to oils, asphaltenes, and marine fouling organisms including barnacle cypris larvae, mussel larvae, and marine bacteria.

Keywords Charged polymers · Polymer brushes · Liquid-infused surfaces · Wetting · Hydration

10.1 Introduction

Development of versatile anti-(bio)fouling surfaces, that are effective for a variety of foulant, is an important industrial issue because material performances often deteriorate as a result of foulant accumulation on the surfaces (Yebra et al. 2004). The anti-fouling materials are required to be mechanically durable, and effective for a long time under harsh condition. Medical materials are often required to prevent adhesion and denaturalization of bio-macromolecules and cells on the surface. Materials used in marine industries ought to prevent attachment of marine adhesive organisms to keep the performances. To address these issues, the materials have to employ smart interface design.

Y. Higaki
Institute for Materials Chemistry and Engineering, International Institute for Carbon-Neutral Energy Research (WPI-I2CNER), Kyushu University, Fukuoka, Japan
e-mail: y-higaki@cstf.kyushu-u.ac.jp

A. Takahara (✉)
Institute for Materials Chemistry and Engineering, Kyushu University, Fukuoka, Japan
e-mail: takahara@cstf.kyushu-u.ac.jp

A. Hozumi et al. (eds.), *Stimuli-Responsive Dewetting/Wetting Smart Surfaces and Interfaces*, Biologically-Inspired Systems 11,
https://doi.org/10.1007/978-3-319-92654-4_10

Lotus effect is well-known as a typical natural anti-fouling system, and massive researchers have been devoted their efforts for mimicking the lotus system and exploring the anti-fouling mechanisms (Bhushan 2012; Bittoun and Marmur 2012; Barthlott and Neinhuis 1997). The hierarchically fractal micro/nano-structured surface geometry is covered with waxy liquids to readily repel water droplets to remove dirt by rolling up with water droplets. The superhydrophobic character is originated from the mosaic structure that consist of solid and trapped air, so called Cassie-Baxter state. Superamphiphobic surfaces that repel both water and low surface tension liquids have been reported by fabricating several special microstructures (Tuteja et al. 2007). Although the amphiphobic performance has been demonstrated, the special surface geometry often lost the superamphiphobicity by deficiency of the ordered structure to induce the liquid pinning.

In contrast to the topographic surface geometry design, liquid-infused smooth surfaces have been payed attention as another type of liquid-repellent surface (Wong et al. 2011; Ma et al. 2013; Huang et al. 2013; Miranda et al. 2014). Wong et al. reported surfaces with extremely low liquid contact angle hysteresis by infusion of low surface energy liquids into porous/textured solids (Wong et al. 2011). The liquid films of perfluorinated fluids were produced spontaneously by wetting the low surface tension porous/textured solids such as nanopost arrays modified with a low-surface energy fluoroalkyl silane, and a random network of Teflon nanofibers. For the lubricating fluid, a low-surface-tension perfluorinated liquids that are non-volatile and are immiscible with both aqueous and hydrocarbon liquids were applied. This amphiphobic surface design was inspired by the surface of the insect-eating *Nepenthes* pitcher plant (Gaume et al. 2002; Bohn and Federle 2004; Bauer and Federle 2009). The pitcher rim has an anisotropic microstructure of radial ridges. The surface is covered with epidermal cells, and the ridge has steps towards the pitcher inside. Hydrophilic nectar is secreted from the rim edge to spread on the ridge surface, thereby water is incorporated in the nectar to give a fluid film under humid weather conditions. The fluid film is so smooth and repels the adhesive oil at the insect foot tip; thereby the insect slides down along with the anisotropic ridge like water slider to be captured in the bottom. The downward steps in the ridge prevent hanging of insects on the slippery slider. As can be seen in the capture system of the pitcher plant, selective liquid infusion and stable fluid film formation by means of surface geometry and interfacial tension control are key points for the slippery surfaces.

Polymer brushes are defined as polymer films whose polymer chains are bound to the substrates by the attachment of the chain ends (Chen et al. 2017; Zoppe et al. 2017; Kobayashi et al. 2013; Stuart et al. 2010; Milner 1991; Advincula et al. 2004; Huang and Wirth 1997). The interfacial properties of the polymer brushes have been investigated because the surface-bound polymer chains exhibit solvent dependent peculiar interfacial characteristics. Also, we can incorporate functionalities to the films by introducing functional groups to the polymer chains. The polymer brushes act as a platform for the liquid retention, because the polymer chains are solvated with good solvents to produce solvated thin polymer layer. The well-solvated polymer layer works as a fluid film (Klein et al. 1994; Spencer 2014).

Physisorption approaches involving adsorption of binding groups to substrate have been applied for the preparation of polymer brushes. This is a typical "grafting-to" method. Although the polymer chains are not released in the good solvent, the grafting density is quite low because large polymer chains hardly approach to substrate surfaces that are sterically hindered by pre-existing bound chains. Polymer brushes are also produced by polymerization of monomers from surface immobilized initiators. This surface-initiated polymerization technique is preferable for the increase of the graft density. Recent development in controlled radical polymerization enables us to produce high-density polymer brushes as a result of the high initiator efficiency and controlled chain growth. Because of the high osmotic pressure due to the large concentration gradient in the high-density polymer brushes, the polymer brushes are spontaneously solvated to produce fluid films. The surface-tethered polymer chains are supposed to be stretched normal to the substrate in good solvent to avoid overlapping of the neighboring chains competing with the entropic loss by chain extension. Therefore, the liquid infusion capability of the polymer brushes improves with increasing the graft density, and the well-solvated polymer brush layer avoids the foulant penetration to keep the compatible liquids beside the chains, thereby it shows superior anti-fouling performance.

The hydration state and lubrication properties of charged polymer brushes have been reported (Chen et al. 2010; Kitano 2016; Murdoch et al. 2016; Higaki et al. 2017; Murakami et al. 2016; Kobayashi et al. 2014a; Wang et al. 2013; Lee and Spencer 2008). The surfaces of living cells, cartilage, the vitreous body of eyes, and synovial joints are all hydrophilic, and those surfaces consist of polyelectrolytes. The charged polymers are well-hydrated by electrostatic interaction of the charged groups in the polymers and waters. The well-hydrated charged polymer brushes show drastically low coefficient of friction (Kobayashi et al. 2014a; Raviv et al. 2003; Zhang et al. 2016). We have demonstrated the hydrodynamic lubrication in the highly swollen charged polymer brushes by using double spacer layer ultra-thin-film interferometry (Kobayashi et al. 2014a). The charged polymer brushes promote the formation of fluid lubrication layer that separates the rubbing surfaces preventing direct contact of the friction probe, leading to the drastic reduction in the coefficient of friction. The anti-fouling capability of the charged polymer brushes have been demonstrated (Ishihara et al. 1991, 1998; Zhang et al. 2006a, b; Cheng et al. 2007; Jiang and Cao 2010; Sin et al. 2014; Higaki et al. 2015; Kobayashi et al. 2012). Especially, the zwitterionic charged polymers composed of zwitterion pendant groups such as poly(phosphobetaine)s, poly(sulfobetaine)s, and poly(carboxybetaine)s exhibit outstanding anti-fouling capability. Ishihara et al. demonstrated the excellent protein repellency in surfaces modified with poly[2-(methacryloyloxy)ethyl phosphorylcholine (PMPC) (Ishihara et al. 1991, 1998). Jiang et al. have reported the outstanding anti-fouling capability of zwitterionic polymer brushes for a variety of organisms such as barnacle cypris larvae, marine algae, and marine bacteria (Cheng et al. 2007, 2009; Jiang and Cao 2010; Aldred et al. 2010; Zhang et al. 2009). It should be noted that the hydration state is modulated by interaction with ions, thereby the anti-fouling performance associate with

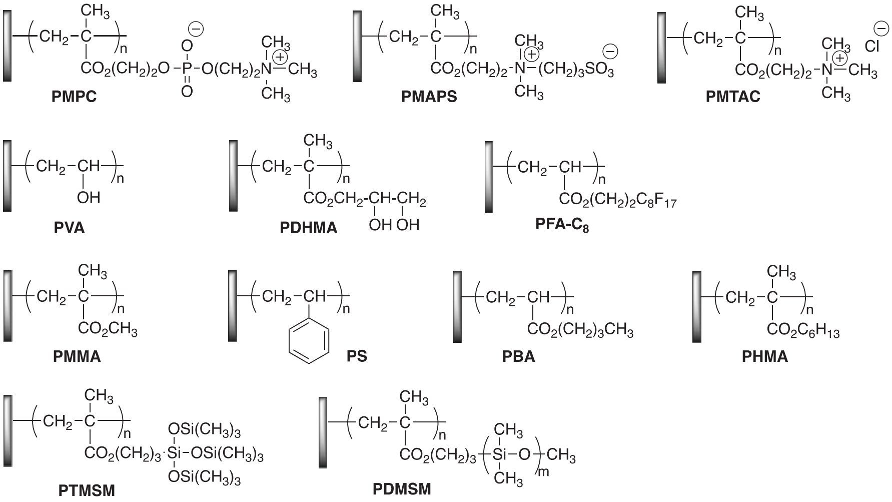

Fig. 10.1 Chemical structure of the polymer brushes appearing in this chapter. Abbreviation: *PMPC* poly[2-(methacryloyloxy)ethyl phosphorylcholine], *PMAPS* poly(3-[dimethyl(2′-methacryloyloxyethyl)ammonio]propanesulfonate), *PMTAC* poly[2-(methacryloyloxy)ethyltrimethylammonium chloride], *PVA* poly(vinyl alcohol), *PDHMA* poly(2,3-dihydroxypropyl methacrylate), *PFA-C$_8$* poly(2-perfluorooctylethyl acrylate), *PMMA* poly(methyl methacrylate), *PS* polystyrene, *PBA* poly(butyl acrylate), *PHMA* poly(hexyl methacrylate), *PTMSM* poly(3-[tris(trimethylsiloxy)silyl]propylmethacrylate), *PDMSM* poly(3-[poly(dimethylsiloxy)silyl] propylmethacrylate)

salt concentration (Higaki et al. 2017; Wang et al. 2013). Therefore, the anti-fouling properties depend on the environment that the surfaces are located.

This review summarizes anti-fouling properties of charged polymer brushes with water-retention capability. The anti-fouling performances to oils, asphaltenes, and marine fouling organisms were highlighted. Chemical structures of the polymer brushes appearing in this chapter are shown in Fig. 10.1.

10.2 Liquid-Infusion Anti-fouling System with Charged Polymer Brushes

10.2.1 Oil Foulants

Charged polymer brushes exhibit outstanding oil droplet repellency in water, whereas the oil droplets spread on the surface in ambient air. The wetting behavior of a wide variety of polymer brushes was reported in detail (Kobayashi et al. 2012). The static and dynamic contact angles of various droplets were recorded with a drop shape analysis system equipped with a video camera at room temperature. The contact angles of an air bubble and a hexadecane droplet in water were measured on the polymer brush substrate facing downward in a transparent glass vessel filled with

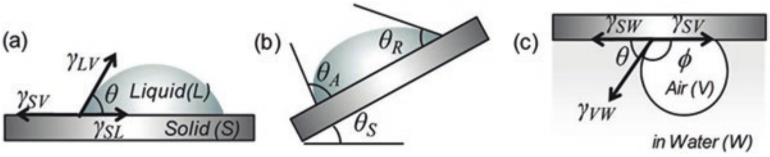

Fig. 10.2 Definitions of (**a**) static (θ), (**b**) advancing (θ_A), receding (θ_R), and sliding (θ_S) contact angles of liquid on a solid surface in air, and (**c**) the contact angle ϕ of an air bubble in water. (Reprinted with permission from Kobayashi et al. (2012). Copyright (2012) American Chemical Society)

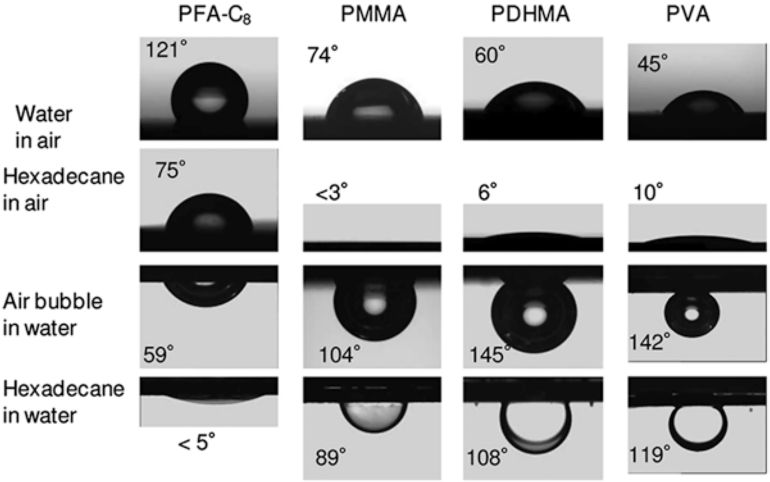

Fig. 10.3 Photographs (side view) of water and hexadecane droplets on nonionic polymer brushes in ambient air, and an air bubble and hexadecane in contact with the polymer brushes in water. (Reproduced with permission from Kobayashi et al. (2012). Copyright (2012) American Chemical Society)

deionized water. The air bubble or hexadecane droplet (10 μL) was released from beneath the brush substrate using a microsyringe. Definitions for the contact angles were illustrated in Fig. 10.2.

Figures 10.3 and 10.4 show side views of water and *n*-hexadecane droplets in ambient air, and side views of air bubbles and *n*-hexadecane droplets in water for the nonionic and charged polymer brushes, respectively. Water droplets exhibited lower contact angles on the charged polymer brushes than those on nonionic hydrophilic polymer brushes. All the examined liquids with low surface tension including *n*-hexadecane spread on the charged polymer brushes in ambient air. The surface free energies of charged polymer brushes were determined by Owens' method to be 70–74 mN/m, which were much higher than those for nonionic hydrophilic polymer brushes. However, once the charged polymer brushes were dipped into water, the *n*-hexadecane liquid films were rolled up followed by detaching from the charged polymer brushes. In the case of non-ionic hydrocarbon polymers including

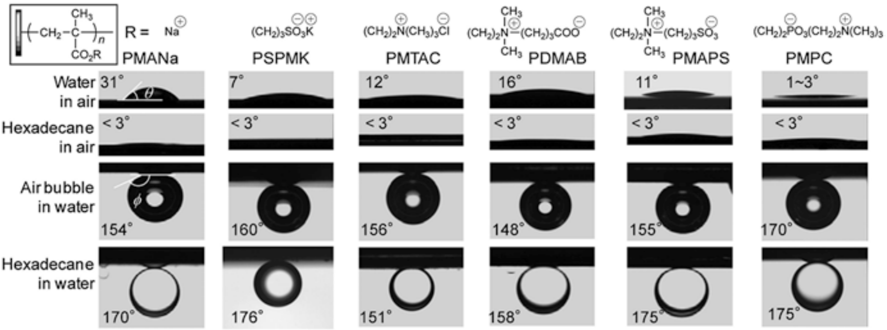

Fig. 10.4 Photographs (side view) of water and hexadecane droplets on charged polymer brushes in ambient air, and air bubbles and hexadecane droplets in contact with the polymer brushes in water. (Reprinted with permission from Kobayashi et al. (2012). Copyright (2012) American Chemical Society)

poly(methyl methacrylate) (PMMA), poly(2,3-dihydroxypropyl methacrylate) (PDHMA), and poly(vinyl alcohol) (PVA), the *n*-hexadecane was rolled up but stayed on the substrate. The poly(perfluorooctylethyl acrylate) (PFA-C_8) brushes exhibit outstanding liquid droplet repellency to repel both water and *n*-hexadecane droplets in air, whereas the droplets spread on the PFA-C_8 brushes in water to reduce the surface free energy. The *n*-hexadecane droplet wetting behavior on fluoropolymer brushes indicates that fluoropolymers are capable of repelling the oils in dry condition, whereas the hydrophobic oils and foulants are supposed to adhere to the surface in aqueous solutions.

The air bubbles in contact with the polymer brushes showed spherical shape, whereas the spherical bubbles were distorted by the buoyancy. The charged polymer brushes repelled both air bubbles and *n*-hexadecane droplets in water. The air bubbles on the brush surface were hardly pinned in water thereby sweeping away. The contact angles of air bubbles and hexadecane droplets in water were constant for at least 20 min. The work of adhesion for oils to polymer brushes in water was determined by Young–Dupré equation. The work of adhesion for silicone oil on the PMPC brush surface was 0.054 mN/m, whereas those for unmodified silicon substrate was 11.2 mN/m.

The oil droplet repellency in the charged polymer brushes is attributed to the affinity with water. The swollen structure of the hydrated charged polymer brushes has been figured out by neutron reflectivity (NR) (Kobayashi et al. 2014b). The scattering length density profile for the hydrated polymer brushes in deuterium oxide solutions were obtained from the curve fitting of the NR profiles. Poly(2-(methacryloyloxy)ethyltrimethylammonium chloride) (PMTAC) brushes are well-swollen in deuterium oxide, and the swollen thickness is over twice of the thickness in dry state. The swollen PMTAC brushes exhibit thick diffusive interface. The zwitterionic polymer brushes including a poly(phosphobetaine) of PMPC brush and a poly(sulfobetaine) of poly(3-[dimethyl(2′-methacryloyloxyethyl)ammonio]propanesulfonate) (PMAPS) brush are also swollen in aqueous solutions. The hydration of the charged polymer brushes was also investigated by quartz crystal microbalance with dissipation monitoring system (QCM-D) (Wang et al. 2013; Azzaroni et al. 2005). Because of the high affinity between the charged polymer brushes and water, spontaneous penetration of water to the oil/charged polymer interface occur by soaking the charged polymer brushes in water, thereby the oil film on the charged polymer brushes are rolled up to reduce the interfacial tension. The extremely low adhesion force of *n*-hexadecane in aqueous solutions leads to anti-fouling of oil foulants as well as hydrophobic substances.

10.2.2 Asphaltenes

Asphaltenes are defined as components of crude oil which insoluble in low-boiling paraffinic solvents but soluble in aromatic solvents (Leontaritis and Mansoori 1988). The components aggregate in crude oil to precipitate in pipelines leading to the blocking. Therefore, the suppression of asphaltene adsorption is required in the petroleum industry. Asphaltenes consist of heterogeneous macromolecules with high degrees of aromaticity and polarity. The strong π-π interaction in the aromatic cores as well as the dipole of the heteroatoms induce the strong aggregation followed by adsorption.

Zeng et al. reported determination of the molecular interactions of an asphaltene model compound in toluene or *n*-heptane by the use of surface force apparatus (SFA) to figure out the mechanisms of asphaltene adsorption in organic solvent (Wang et al. 2012a, b). *N*-(1-hexylheptyl)-*N*′-(5-carboxylicpentyl) perylene-3,4,9,10-tetracarboxylic acid bisimide (C5Pe) was used as a model compound for asphaltenes. The C5Pe consists of a proper molecular weight polyaromotic core with heteroatoms, hydrocarbon chains, and polar carboxylic acid. The C5Pe is soluble in toluene but insoluble in *n*-heptane, and slowly aggregates in mixed solution of toluene and *n*-heptane. These behaviors are consistent with natural asphaltenes, thereby the C5Pe is regarded as a model compound for the surface-active components in asphaltenes. The informations obtained from the asphaltene model compound is viable for understanding the molecular mechanisms of asphaltene aggregation during heavy oil processing. The pre-adsorbed C5Pe films showed no significant adhesion force in toluene, while strong adhesion force was detected in *n*-heptane. Genzer et al. investigated asphaltene adsorption onto self-assembled monolayers (SAMs) of alkyl silane compounds (Turgman-Cohen et al. 2009). They reported that the wettability of the substrates is not a dominant factor for asphaltene adsorption, but the thickness of the SAMs is the important factor. The shielding of interactions between asphaltenes and the underlying polar silicon substrate would be crucial, thereby the longer alkyl chain buffer layer results in the better depression for asphaltene adsorption. Sjöblom et al. monitored asphaltene adsorption onto chemically modified silica particles (Hannisdal et al. 2006). The amount of adsorption was significant for the hydrophilic silica particles, indicating that the strong interaction between the asphaltenes and SiO_2 is responsible for the sludge formation.

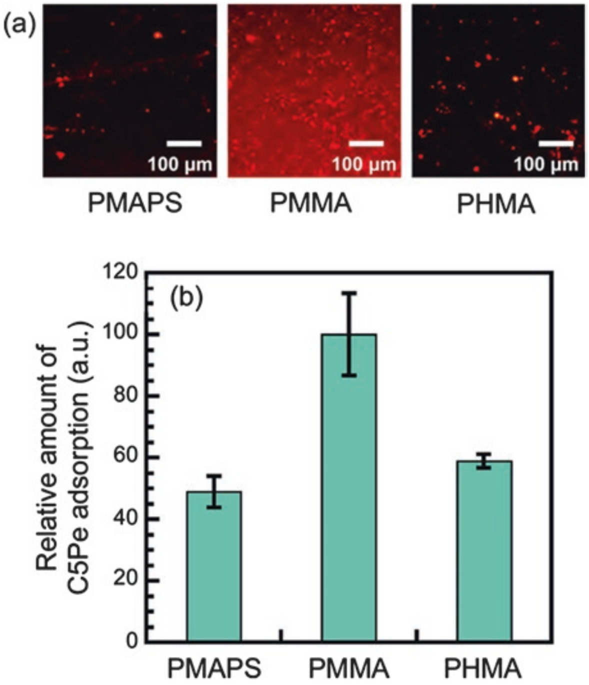

Fig. 10.5 (**a**) Fluorescence microscopy images of the polymer brush surfaces after C5Pe adsorption test. (**b**) Relative amount of C5Pe adsorption onto the polymer brush surfaces. (Reproduced with permission from Higaki et al. (2014). Copyright (2014) American Chemical Society)

The adsorption behavior of the C5Pe in model oil [toluene/*n*-heptane = 1/4 (v/v)] on polymer brushes was examined (Higaki et al. 2014). Polymer brushes were soaked in a 0.2 mg/mL toluene solution of C5Pe for 24 h. The polymer brushes were lifted from the solution and dried. During drying, the polymer brush surface was fixed vertically with respect to the ground. Fluorescence microscopy images of the polymer brushes after the C5Pe adsorption test demonstrated that the zwitterionic PMAPS brush and poly(hexyl methacrylate) (PHMA) brush show less C5Pe adsorption than the PMMA brush (Fig. 10.5).

The detachability of the asphaltene deposited films on polymer brushes was examined. Natural asphaltenes were extracted from a vacuum residual oil according to the IP143 standard method. A 1.0 wt% toluene solution of the extracted natural asphaltenes was deposited on the polymer brushes and dried in air. The asphaltene deposition films strongly attached to the polymer brush surface in dry state. The asphaltene films were soaked in a model oil (toluene/*n*-heptane = 1/4 (vol/vol)) or pure water followed by shaking for 20 min. The asphaltene deposit films on the PHMA brushes detached in the model oil, whereas the asphaltene films remain adhered to the PMAPS and PMMA brushes. Meanwhile, the asphaltene deposit films on the PMAPS brush detached in water, whereas the asphaltene films remain adhered to the PHMA and PMMA brushes (Fig. 10.6).

The adsorption behavior is associated with the interfacial energy between the polymer brushes and asphaltenes or liquids. The interfacial free energies of polymer-brushes/asphaltenes (γ_{SA}), polymer-brushes/toluene (γ_{SO}), and polymer-brushes/

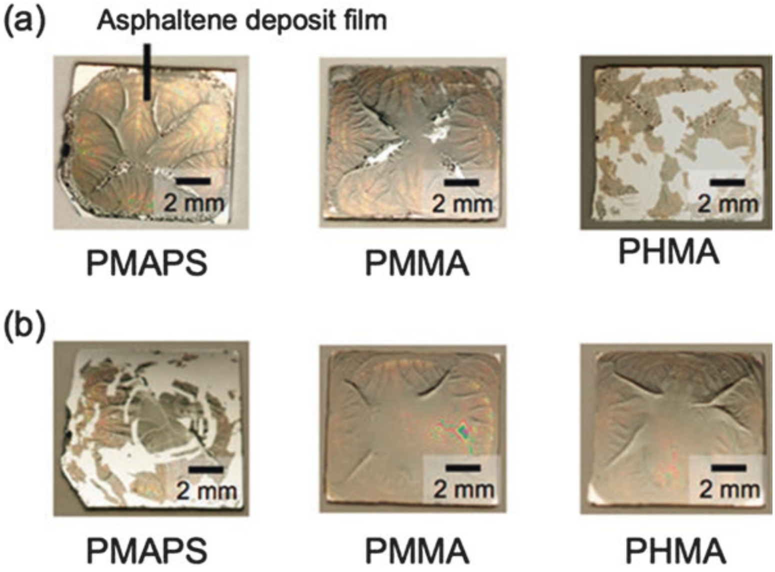

Fig. 10.6 Appearances of asphaltene deposit films on the polymer brushes after shaking in (**a**) a model oil (toluene/*n*-heptane = 1/4 (v/v)) and (**b**) water. (Reprinted with permission from Higaki et al. (2014). Copyright (2014) American Chemical Society)

water (γ_{SW}) were determined by the extended Fowkes equation by the use of static contact angle data for the water and diiodomethane droplets (Fowkes 1963). The PHMA brushes exhibited lower γ_{SA} than PMAPS brushes. Although the substantial amount of C5Pe strongly adsorbed onto the PMMA brushes, the PMMA brushes showed an intermediate value of γ_{SA}. The order of adsorption amount of C5Pe would be associated with contrast in the γ_{SA} and γ_{SO}. For the PHMA brush, the γ_{SO} is relatively low, and is similar magnitude to the γ_{SA}. In this case, the solvent (toluene) wets the PHMA brush, leading to effective suppression of the C5Pe adsorption. For the PMMA brush and PMAPS brushes, the γ_{SO}s are higher than γ_{SA}s, indicating that C5Pe adsorption is preferred over solvent wetting. The surface free energy of the PMAPS brush is significantly higher than that for the other polymer brushes. Strong electrostatic interaction between the charged sulfobetaine groups and C5Pe seems to promote the significant C5Pe adsorption, but the PMAPS brushes inhibited the C5Pe adsorption. The charged PMAPS chains would accumulate tiny amount of water in the toluene to produce hydrated PMAPS interface. The hydrated layer prevents penetration of the adsorbent due to the extremely low interface energy of the PMAPS brushes/water interface.

The detachment of the asphaltene deposit films is associated with the interfacial free energy for the polymer brushes/liquid interfaces. The PHMA brush exhibits low interfacial free energy for the model oil. The model oil is supposed to wet the PHMA brushes spontaneously, the interfacial tension would reduce due to the high mobility and low density of the swollen brush chains leading to the detachment of the asphaltene films. A similar mechanism is applied for the charged PMAPS brushes in water. The interfacial free energies dictate the asphaltene adsorption behavior; meanwhile, the swollen chain dynamics in the polymer brushes would associate with the adsorption of foreign objects in addition to the surface energy.

10.2.3 Marine Fouling Organisms

Marine organism settlement reduces the fuel efficiency and navigation performance of ocean vessels, as well as the heat exchange efficiency of seawater cooling systems in thermal and atomic power plants, which makes it extremely important issue in marine industries (Callow and Callow 2011; Lejars et al. 2012; Flemming et al. 2009). Marine fouling involves diverse organisms, and develops in stages, from the formation of an initial conditioning film of biomolecules followed by biofilm formation and colonizations. Marine environment is much more harsh than physiological environment because of the cascading fouling of diverse organisms, mechanical damage, and sunlight irradiation, so that anti-fouling systems in marine field requires a high level of versatility, mechanical durability, and chemical stability. Because the toxic anti-fouling coatings employing highly toxic and environment retentive biocides were regulated by international marine organization, non-toxic anti-fouling approaches have been investigated. Several alternatives to biocidal coatings have been already developed, such as fouling release coatings, microtopographical surfaces (Schumacher et al. 2007a, b) and self-polishing coatings.

Silicone polymers and/or fluoropolymers have been applied as base resin for fouling release coatings because of their low surface free energy. Weakly attached fouling organisms are released by hydrodynamic shear flow during navigation. Marine organisms often apply the microtopographical surfaces as a defense system against biofouling. Brennan et al. studied the effect of feature size, geometry, and roughness in the microtopographic surface of a polydimethylsiloxane (PDMS) elastomer on the settlement of zoospores of alga (Schumacher et al. 2007a, b). The microtopographies significantly reduced the spore settlement compared to a smooth surface. They applied an engineered dimensionless roughness index (ERI) including the surface fraction and the degree of freedom of spore movement for description of the indirect correlation between spore settlement and surface topography. The anti-fouling capability clearly depends on both the feature size and surface geometry. The wettability, surface fluid dynamics and attachment point reduction have been cited as potential factors contributing to the improved anti-fouling performance. Gong et al. studied settlement, metamorphosis, and long term growth of barnacles on soft substrate of hydrophilic hydrogels and hydrophobic PDMS gels (Ahmed et al. 2011). The initial settlement and metamorphosis of cyprid larvae significantly increased along with the substrate elastic modulus while are independent on the substrate wettability. The growth rate of barnacles on soft substrates is exactly lower than that on the rigid PS substrate.

Anti-biofouling characters of non-charged hydrophilic polymers, such as poly(ethylene glycol), has been elucidated. The steric exclusion effect, surface hydration and neutral net-charge are generally regarded as key factors in the anti-biofouling performance (Jeon et al. 1991; Magin et al. 2011). Anti-biofouling properties of the zwitterionic poly(phosphobetaine)s for biomolecules and cells have been demonstrated (Ishihara et al. 1991, 1998). Jiang et al. studied the antifouling properties of poly(sulfobetaine) and poly(carboxybetaine) brushes for proteins, mammalian cells, and marine fouling organisms including spores of a green alga, diatom cells, and barnacle cypris larvae (Zhang et al. 2006b, 2009; Cheng et al. 2007, 2009; Jiang and Cao 2010; Aldred et al. 2010). The zwitterionic polymer brushes almost completely inhibited settlement of those foulants. Although both poly(sulfobetaine)s and poly(carboxybetaine)s inhibited settlement of barnacle cypris larvae, the surface exploration behavior depended on the zwitterion structures (Callow and Callow 2011). The cypris larvae were actively explored on the poly(sulfobetaine) brushes but unwilling or unable to settle, whereas the cypris larvae spent little time on the poly(carboxybetaine) brushes, and swimming away immediately from the surface. The difference in the exploration behavior indicates that the settlement inhibition mechanism is not identical for the zwitterionic polymers. Because the adhesive proteins and adhesion apparatus are diverse in the organisms, the anti-fouling properties ought to show organism specificity. Anti-biofouling capability of various polymer brushes against marine organisms, a barnacle cypris larva, a mussel larva in its adhesion period and marine bacteria, was investigated by settlement tests and careful observations of the settlement behavior to figure out the fouling organism species specific anti-fouling capability of the polymer brushes (Higaki et al. 2015).

10.2.3.1 Barnacle Cypris Larvae

Cypris larva is the final larval stage of barnacle. The barnacle cypris larvae explore appropriate places for attachment by ‘walking’ on substrates (Aldred and Clare 2009). Adhesive substances are secreted from their cuticular antennule tips to adhere to surfaces. Their repeatable adhesion has been explained by van der Waals interactions during the contact of splitting cuticular villi and capillary adhesion of viscous glycoproteins. The cypris larvae metamorphose into juveniles after the temporary settlement. The firmly attached juvenile subsequently metamorphoses into a calcified adult barnacle.

Two pieces of the same type of polymer brush samples were introduced into a PS container, then soaked in filtered seawater. The PS container was covered with a plankton filtering net to avoid barnacle cypris larvae settlement onto the container wall. Then, 40 artificially grown barnacle cypris larvae were added to the container. Settlement tests were carried out in discrete containers for each polymer brush species, thereby the tests were not ‘choice assays’ in which several types of substrates are introduced into the container. The exploration behavior was carefully observed by optical microscopy. Cypris larvae that actively walked on the substrates by

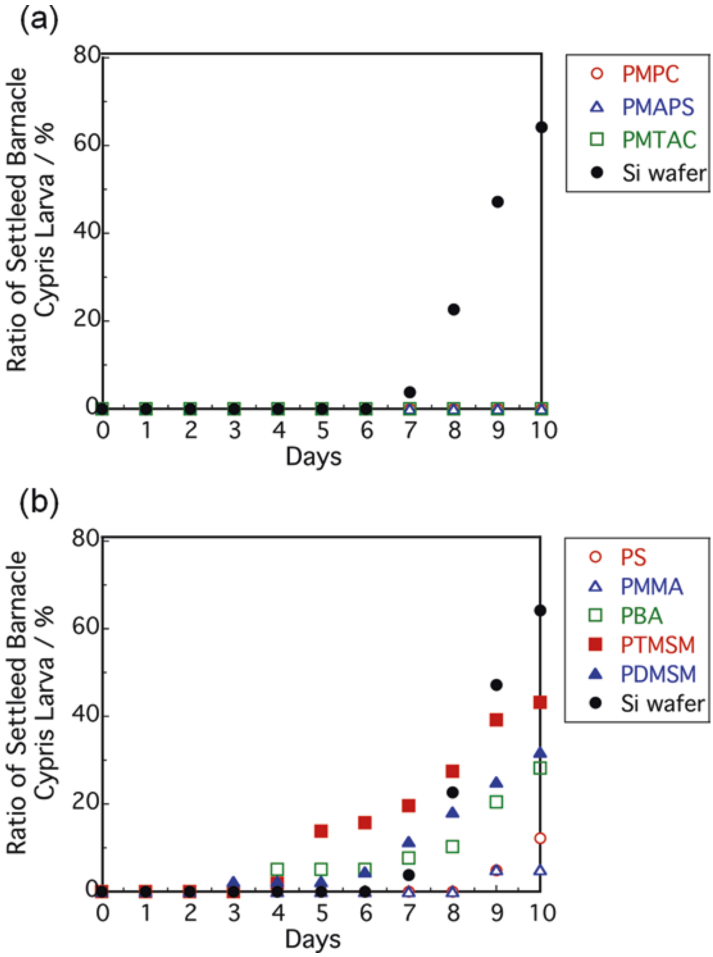

Fig. 10.7 Evolution of the ratio of 'settled' barnacle cypris larva on (**a**) zwitterionic and cationic polyelectrolytes brushes and (**b**) hydrocarbon and silicone-containing polymer brushes during the settlement tests. Abbreviations: see Fig. 10.1. (Reproduced with permission from Higaki et al. (2015). Copyright (2015) Nature Publishing Group)

antennule attachment were termed as 'searching', while those staying on the substrate and metamorphosed into juveniles were termed as 'settled'.

Figure 10.7 shows evolution of the number of settled barnacle cypris larvae during the test period. On the bare Si wafer and hydrophobic polymer brushes includingpolystyrene(PS),PMMA,poly(butylacrylate)(PBA),poly(3-[tris(trimethylsiloxy)silyl]propylmethacrylate) (PTMSM), and poly(3-[poly(dimethylsiloxy)silyl]propylmethacrylate) (PDMSM), the cypris larvae showed active searching. For the bare Si wafer, 63% of the cypris larvae settled after 10 days. The hydrophobic glassy polymer brushes, namely PS and PMMA, exhibited better anti-settlement character, whereas the hydrophobic flexible polymer brushes, namely PBA, PTMSM, and PDMSM, allowed the cypris larvae settlement. The contrast in the hydrophobic polymers may be attributed to the degree of surface free energy, because the PBA, PTMSM, and PDMSM exhibit lower surface free energy than the PS and PMMA. Meanwhile, the cypris larvae exhibited no searching activity on the cationic PMTAC and zwitterionic polymer brushes (PMPC, PMAPS) throughout the test period. The cypris larvae were positioned sideways on the cationic and zwitterionic polymer brushes rather than face-on. The cypris larvae walking with antennule attachment was rarely observed. Because all the cypris larvae showed active exploration at the plankton filtering net, the high settlement ability in the artificially cultured cypris larvae was ensured. The activity of the cypris larvae was further confirmed by introducing bare Si wafers in the test containers after the settlement test period. Most of the remaining unsettled cypris larvae immediately settled on the Si wafers within a day, thereby the activity of the cypris larvae was maintained. The exploration behavior observation indicated that the excellent anti-settlement performance of the charged polymer brushes is originated from the discourage of the 'walking' and 'searching' activities of the barnacle cypris larvae.

10.2.3.2 Mussel Larvae

Mussels inhabit to a wide variety of substrates using adhesive byssus (Lee et al. 2011). The byssus consists of a bundle of collagenous threads tipped with an adhesive plaque. The mussel adhesive plaque proteins have been identified, and are called as mussel foot proteins (m.f.p.). The m.f.p. include large amount of post-translationally modified residues and basic residues. The rapid adhesion and high adhesive strength of the byssus plaque has drawn considerable attention as a model system for adhesives that are effective in wet conditions. The attachment process of the mussel using byssus threads consists of three major steps: (a) exploration and identification of suitable sites for settlement by 'walking' via temporary attachment of the suction pad at the byssus tip, (b) pressing the suction pad to the substrate to remove water in the cavity and (c) secreting m.f.p. into the cavity of the suction pad to adhere the byssus to the substrate.

Settlement test for the mussel larvae was carried out in a similar experiment set up with barnacle cypris larvae settlement test, and evaluated by counting the number of settled mussel larvae after the 6-day test period (Fig. 10.8). The zwitterionic polymer brushes (PMPC and PMAPS) exhibited significant inhibition of mussel larvae settlement, whereas the cationic polyelectrolyte (PMTAC) and the hydrophobic polymers (PS, PMMA, PTMSM and PDMSM) showed negligible effects comparable to a bare Si wafer. The cationic polyelectrolyte brushes permitted settlement of mussel larvae in contrast with barnacle cypris larvae, namely the cationic polyelectrolyte brushes show organism specific antifouling capability. The mussel larvae settled on the hydrophobic polymer brushes to a similar degree as the bare Si wafers, and no significant chemical structure dependence was observed for the number of settled mussel larvae.

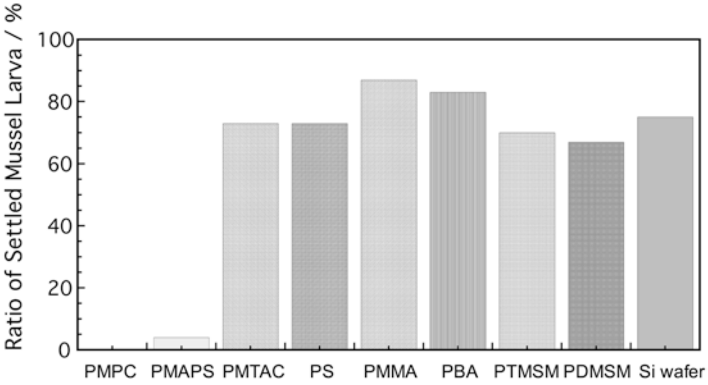

Fig. 10.8 The ratio of 'settled' mussel larva to the initial population of mussel larva. The number of 'settled' mussel larvae on the polymer brushes was counted after a settlement test period of 6 days. Abbreviations: see Fig. 10.1. (Reproduced with permission from Higaki et al. (2015). Copyright (2015) Nature Publishing Group)

The mussel larvae showed active exploration on all of the polymer brushes including the zwitterionic polymer brushes that show settlement inhibition for the mussel larvae. The mussel larvae crept on the polymer brush surfaces by attaching their foot. Although the mussel larva intended to settle on the zwitterionic polyelectrolyte brush surfaces, they flipped on the substrate. The failed attachment indicates the low adhesion force between the plaque and zwitterionic polymer brushes. The charged residues and hydroxylated tyrosine (Dopa, 3,4-dihydroxyphenyl-L-alanine) residues in m.f.p. exhibit weak interaction with the hydrated zwitterionic polymers, probably because of the water retention in the polymer brushes during the vacuum and dewetting processes. The electrostatic interaction greatly diminished in the presence of high dielectric constant media. Therefore, the PMPC and PMAPS brushes, which are strongly hydrated in saline seawater, were able to prevent mussel larvae settlement, whereas the PMTAC, which collapses in a saline environment, allowed m.f.p. adhesion. The hydrated water in the zwitterionic polymer brushes would remain at the cavity of the suction pad, thereby the adhesion efficiency of the m.f.p. plaques reduced. The neutral net-charge is also preferable for the adhesive force reduction of m.f.p. with large fraction of charged residue.

10.2.3.3 Marine Bacteria

Marine bacteria adhesion is critical for inhibiting slime growth and subsequent macro-fouling settlement, because they are a major constituent of bio-films. Generally, bacteria have a negative charge in basic aqueous solutions due to the dissociation of carboxylic acid and phosphate residues. Marine bacteria approach substrates by Brownian motion and adhere to surfaces weakly by van der Waals interaction (Marshall et al. 1971). The extracellular polymeric substances, which

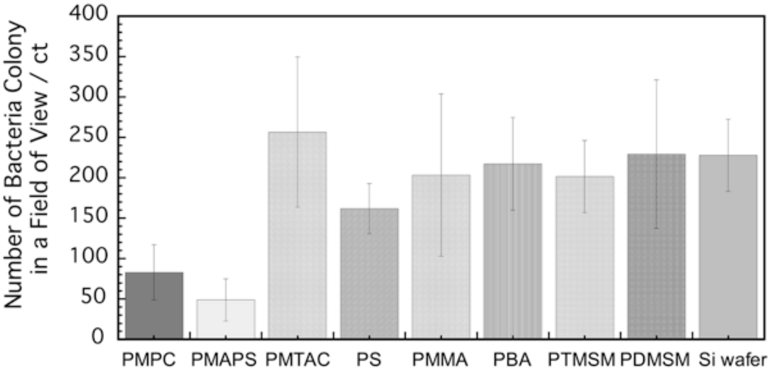

Fig. 10.9 Number of bacteria on the polymer brushes in microscopic fields. The data were averaged from ten observations. Error bars represent the standard deviation. Abbreviations: see Fig. 10.1. (Reproduced with permission from Higaki et al. (2015). Copyright (2015) Nature Publishing Group)

mainly consists of polysaccharides, penetrate an electric bilayer energy barrier to achieve the adhesion (Morisaki et al. 1999). In saline seawater, the electric bilayer gets thinner and the electrostatic repulsive forces are less effective due to the charge screening effect of bound ions to permit non-specific adhesion of marine bacteria to any substrate, regardless of the surface potential.

The anti-bacteria adsorption efficiency of the polymer brushes was examined (Fig. 10.9). The polymer brush test pieces were soaked in natural seawater containing native bacteria for 6 days, then the test pieces were immersed in a filtered and sterilized tris-buffer solution. The bacteria were stained by 4′,6-diamidino-2-phenylindole, and the number of bacteria in the field was counted by fluorescent microscopy observation. The zwitterionic polymer brushes exhibit outstanding anti-fouling performance compared with hydrophobic polymer brushes, unmodified Si wafer and cationic polyelectrolyte brushes. Bacteria colonies would adhere weakly on the net-neutral hydrated zwitterionic polymer brushes, thereby easily detached by water flow. Hydrated water diminishes the electrostatic interactions, and the water flow causes detachment of the bacteria colonies. The bacteria preferably adhered to cationic polymer brushes, probably because of the strong electrostatic interaction as well as poor hydration in saline seawater.

10.3 Conclusion

We have presented here anti-(bio)fouling properties of charged polymer brushes for oil foulants and marine fouling organisms. The overall picture arising from the works reviewed here is that the zwitterionic polymer brushes exhibit versatile anti-fouling capability. The outstanding anti-fouling characteristics are attributed to the hydration states and net-neutral surface charge. The highly-hydrated charged polymer brushes produce water-infused soft interfaces that promote hydrodynamic lubrication state and water flow assisted anti-fouling performance.

The study of high-density polymer brushes has been intensively investigated during the last few decades both in the field of physics in the confined surface-tethered polymer chains and development of stimuli responsive soft interfaces. The hydration states have been explored by various approaches including AFM, (Zhang et al. 2016; Shi et al. 2016) QCM-D, (Wang et al. 2013; Liu et al. 2017) and NR (Murdoch et al. 2016; Kobayashi et al. 2014b; Dunlop et al. 2012; Galvin et al. 2014) so far. Charged polymer brushes are proved to produce well-hydrated water-infused smooth soft interfaces in aqueous solutions. However, the hydration states depend on various factors such as co-existing ions, charged macromolecules (proteins, polysaccharides and so on), and the concentration. How far the interfacial performances associate with the hydration states that is variable depending on the environments is still far from being fully understood.

Another interesting aspect is hydrogen bonding network structure of the waters confined in the charged polymer brushes. It is well-known that the surface tension of ice-water is far different from bulk water, thereby the hydrogen bonding configuration in the hydrated water would associate with the anti-biofouling performances. Therefore, the hydrogen bonding network structure of waters in hydrated charged polymer brushes is of wide interest, and has been explored by various spectroscopic methods including infrared, (Kitano et al. 2003; Murakami et al. 2013) Raman, (Kitano 2016) sum frequency generation (SFG), (Leng et al. 2014; Nagasawa et al. 2015) and X-ray absorption and emission (Yamazoe et al. 2017) spectroscopies, and is still under debate.

Future progress is required in both experimental studies and theories in order to understand the interplay in hydration state and anti-fouling performances. During the next few decades, a drastic progress in this issue is expected by means of advanced experimental procedures utilizing quantum beams and innovative sensing systems, resulting in the development of extreme soft anti-fouling materials.

Acknowledgements This research was financially supported by the Exploratory Research for Advanced Technology (ERATO), Japan Science and Technology Agency (JST). This work was performed under the Cooperative Research Program of "Network Joint Research Center for Materials and Devices".

References

Advincula RC, Brittain WJ, Caster KC, Rühe J (2004) Polymer brushes: synthesis, characterization and applications. Wiley, Weinheim

Ahmed N, Murosaki T, Kakugo A, Kurokawa T, Gong JP, Nogata Y (2011) Long-term in situ observation of barnacle growth on soft substrates with different elasticity and wettability. Soft Matter 7:7281–7290

Aldred N, Clare AS (2009) Chapter 2: Mechanisms and principles underlying temporary adhesion, surface exploration and settlement site selection by barnacle Cyprids: a short review. In: Functional surfaces in biology, vol 2. Springer, Berlin, pp 43–65

Aldred N, Li G, Gao Y, Clare AS, Jiang S (2010) Modulation of barnacle (Balanus amphitrite Darwin) cyprid settlement behavior by sulfobetaine and carboxybetaine methacrylate polymer coatings. Biofouling 26:673–683

Azzaroni O, Moya S, Farhan T, Brown AA, Huck WT (2005) Switching the properties of polyelectrolyte brushes via “hydrophobic collapse”. Macromolecules 38:10192–10199

Barthlott W, Neinhuis C (1997) Purity of the sacred lotus, or escape from contamination in biological surfaces. Planta 202:1–8

Bauer U, Federle W (2009) The insect-trapping rim of Nepenthes pitchers: surface structure and function. Plant Signal Behav 4:1019–1023

Bhushan B (2012) Bioinspired structured surfaces. Langmuir 28:1698–1714

Bittoun E, Marmur A (2012) The role of multiscale roughness in the lotus effect: is it essential for super-hydrophobicity? Langmuir 28:13933–13942

Bohn HF, Federle W (2004) Insect aquaplaning: Nepenthes pitcher plants capture prey with the peristome, a fully wettable water-lubricated anisotropic surface. Proc Natl Acad Sci U S A 101:14138–14143

Callow JA, Callow ME (2011) Trends in the development of environmentally friendly fouling-resistant marine coatings. Nat Commun 2:244–210

Chen S, Li L, Zhao C, Zheng J (2010) Surface hydration: principles and applications toward low-fouling/nonfouling biomaterials. Polymer 51:5283–5293

Chen W-L, Cordero R, Tran H, Ober CK (2017) 50th anniversary perspective: polymer brushes: novel surfaces for future materials. Macromolecules 50:4089–4113

Cheng G, Zhang Z, Chen S, Bryers JD, Jiang S (2007) Inhibition of bacterial adhesion and biofilm formation on zwitterionic surfaces. Biomaterials 28:4192–4199

Cheng G, Li G, Xue H, Chen S, Bryers JD, Jiang S (2009) Zwitterionic carboxybetaine polymer surfaces and their resistance to long-term biofilm formation. Biomaterials 30:5234–5240

Dunlop IE, Thomas RK, Titmus S, Osborne V, Edmondson S, Huck WTS, Klein J (2012) Structure and collapse of a surface-grown strong polyelectrolyte brush on sapphire. Langmuir 28:3187–3193

Flemming HC, Murthy PS, Venkatesan R, Cooksey K (2009) Marine and industrial biofouling, vol 4. Springer, Berlin/Heidelberg

Fowkes FM (1963) Additivity of intermolecular forces at interfaces. i. determination of the contribution to surface and interfacial tensions of dispersion forces in various liquids. J Phys Chem 67:2538–2541

Galvin CJ, Dimitriou MD, Satija SK, Genzer J (2014) Swelling of polyelectrolyte and polyzwitterion brushes by humid vapors. J Am Chem Soc 136:12737–12745

Gaume L, Gorb S, Rowe N (2002) Function of epidermal surfaces in the trapping efficiency of Nepenthes alata pitchers. New Phytol 156:479–489

Hannisdal A, Ese M-H, Hemmingsen PV, Sjöblom J (2006) Particle-stabilized emulsions: effect of heavy crude oil components pre-adsorbed onto stabilizing solids. Colloids Surf A Physicochem Eng Asp 276:45–58

Higaki Y, Hatae K, Ishikawa T, Takanohashi T, Hayashi J-I, Takahara A (2014) Adsorption and desorption behavior of asphaltene on polymer-brush-immobilized surfaces. ACS Appl Mater Interfaces 6:20385–20389

Higaki Y, Nishida J, Takenaka A, Yoshimatsu R, Kobayashi M, Takahara A (2015) Versatile inhibition of marine organism settlement by zwitterionic polymer brushes. Polym J 47:811–818

Higaki Y et al (2017) Effect of charged group spacer length on hydration state in zwitterionic poly(sulfobetaine) brushes. Langmuir 33:8404–8412

Huang X, Wirth MJ (1997) Surface-initiated radical polymerization on porous silica. Anal Chem 69:4577–4580

Huang X, Chrisman JD, Zacharia NS (2013) Omniphobic slippery coatings based on lubricant-infused porous polyelectrolyte multilayers. ACS Macro Lett 2:826–829

Ishihara K, Ziats NP, Tierney BP, Nakabayashi N, Anderson JM (1991) Protein adsorption from human plasma is reduced on phospholipid polymers. J Biomed Mater Res 25:1397–1407

Ishihara K, Nomura H, Mihara T, Kurita K, Iwasaki Y, Nakabayashi N (1998) Why do phospholipid polymers reduce protein adsorption? J Biomed Mater Res 39:323–330

Jeon SI, Lee JH, Andrade JD, Degennes PG (1991) Protein surface interactions in the presence of polyethylene oxide .1. Simplified theory. J Colloid Interface Sci 142:149–158

Jiang S, Cao Z (2010) Ultralow-fouling, functionalizable, and hydrolyzable zwitterionic materials and their derivatives for biological applications. Adv Mater 22:920–932

Kitano H (2016) Characterization of polymer materials based on structure analyses of vicinal water. Polym J 48:15–24

Kitano H, Imai M, Mori T, Gemmei-Ide M, Yokoyama Y, Ishihara K (2003) Structure of water in the vicinity of phospholipid analogue copolymers as studied by vibrational spectroscopy. Langmuir 19:10260–10266

Klein J, Kumacheva E, Mahalu D, Perahia D, Fetters LJ (1994) Reduction of frictional forces between solid surfaces bearing polymer brushes. Nature 370:634–636

Kobayashi M, Terayama Y, Yamaguchi H, Terada M, Murakami D, Ishihara K, Takahara A (2012) Wettability and antifouling behavior on the surfaces of superhydrophilic polymer brushes. Langmuir 28:7212–7222

Kobayashi M, Terayama Y, Kikuchi M, Takahara A (2013) Chain dimensions and surface characterization of superhydrophilic polymer brushes with zwitterion side groups. Soft Matter 9:5138–5148

Kobayashi M, Tanaka H, Minn M, Sugimura J, Takahara A (2014a) Interferometry study of aqueous lubrication on the surface of polyelectrolyte brush. ACS Appl Mater Interfaces 6:20365–20371

Kobayashi M, Ishihara K, Takahara A (2014b) Neutron reflectivity study of the swollen structure of polyzwitterion and polyeletrolyte brushes in aqueous solution. J Biomater Sci Polym Ed 25:1673–1686

Lee S, Spencer ND (2008) Sweet, hairy, soft, and slippery. Science 319:575–576

Lee BP, Messersmith PB, Israelachvili JN, Waite JH (2011) Mussel-inspired adhesives and coatings. Annu Rev Mater Res 41:99–132

Lejars M, Margaillan A, Bressy C (2012) Fouling release coatings: a nontoxic alternative to biocidal antifouling coatings. Chem Rev 112:4347–4390

Leng C, Han X, Shao Q, Zhu Y, Li Y, Jiang S, Chen Z (2014) In situ probing of the surface hydration of zwitterionic polymer brushes: structural and environmental effects. J Phys Chem C 118:15840–15845

Leontaritis KJ, Mansoori GA (1988) Asphaltene deposition: a survey of field experiences and research approaches. J Pet Sci Eng 1:229–239

Liu L, Kou R, Liu G (2017) Ion specificities of artificial macromolecules. Soft Matter 13:68–80

Ma W, Higaki Y, Otsuka H, Takahara A (2013) Perfluoropolyether-infused nano-texture: a versatile approach to omniphobic coatings with low hysteresis and high transparency. Chem Commun 49:597–599

Magin CM, Finlay JA, Clay G, Callow ME, Callow JA, Brennan AB (2011) Antifouling performance of cross-linked hydrogels: refinement of an attachment model. Biomacromolecules 12:915–922

Marshall KC, Stout R, Mitchell R (1971) Mechanism of the initial events in the sorption of marine bacteria to surfaces. J Gen Microbiol 68:337–348

Milner ST (1991) Polymer brushes. Science 251:905–914

Miranda DF, Urata C, Masheder B, Dunderdale GJ, Yagihashi M, Hozumi A (2014) Physically and chemically stable ionic liquid-infused textured surfaces showing excellent dynamic omniphobicity. APL Mater 2:056108

Morisaki H, Nagai S, Ohshima H, Ikemoto E, Kogure K (1999) The effect of motility and cell-surface polymers on bacterial attachment. Microbiology 145:2797–2802

Murakami D, Kobayashi M, Moriwaki T, Ikemoto Y, Jinnai H, Takahara A (2013) Spreading and structuring of water on superhydrophilic polyelectrolyte brush surfaces. Langmuir 29:1148–1151

Murakami D, Kobayashi M, Higaki Y, Jinnai H, Takahara A (2016) Swollen structure and electrostatic interactions of polyelectrolyte brush in aqueous solution. Polymer 98:464–469

Murdoch TJ, Willott JD, de Vos WM, Nelson A, Prescott SW, Wanless EJ, Webber GB (2016) Influence of anion hydrophilicity on the conformation of a hydrophobic weak polyelectrolyte brush. Macromolecules 49:9605–9617

Nagasawa D, Azuma T, Noguchi H, Uosaki K, Takai M (2015) Role of interfacial water in protein adsorption onto polymer brushes as studied by SFG spectroscopy and QCM. J Phys Chem C 119:17193–17201

Raviv U, Giasson S, Kampf N, Gohy J-F, Jérôme R, Klein J (2003) Lubrication by charged polymers. Nature 425:163–165

Schumacher JF et al (2007a) Engineered antifouling microtopographies-effect of feature size, geometry, and roughness on settlement of zoospores of the green alga Ulva. Biofouling 23:55–62

Schumacher JF, Aldred N, Callow ME, Finlay JA, Callow JA, Clare AS, Brennan AB (2007b) Species-specific engineered antifouling topographies: correlations between the settlement of algal zoospores and barnacle cyprids. Biofouling 23:307–317

Shi C, Yan B, Xie L, Zhang L, Wang J, Takahara A, Zeng H (2016) Long-range hydrophilic attraction between water and polyelectrolyte surfaces in oil. Angew Chem Int Ed 55:15017–15021

Sin MC, Chen SH, Chang Y (2014) Hemocompatibility of zwitterionic interfaces and membranes. Polym J 46:436–443

Spencer ND (2014) Aqueous lubrication with poly(ethylene glycol) brushes. Tribol Online 9:143–153

Stuart MAC et al (2010) Emerging applications of stimuli-responsive polymer materials. Nat Mater 9:101–113

Turgman-Cohen S, Fischer DA, Kilpatrick PK, Genzer J (2009) Asphaltene adsorption onto self-assembled monolayers of alkyltrichlorosilanes of varying chain length. ACS Appl Mater Interfaces 1:1347–1357

Tuteja A et al (2007) Designing superoleophobic surfaces. Science 318:1618–1622

Wang J, van der Tuuk Opedal N, Lu Q, Xu Z, Zeng H, Sjöblom J (2012a) Probing molecular interactions of an asphaltene model compound in organic solvents using a surface forces apparatus (SFA). Energy Fuel 26:2591–2599

Wang J, Lu Q, Harbottle D, Sjöblom J, Xu Z, Zeng H (2012b) Molecular interactions of a polyaromatic surfactant C5Pe in aqueous solutions studied by a surface forces apparatus. J Am Chem Soc 116:11187–11196

Wang T, Wang X, Long Y, Liu G, Zhang G (2013) Ion-specific conformational behavior of polyzwitterionic brushes: exploiting it for protein adsorption/desorption control. Langmuir 29:6588–6596

Wong T-S, Kang SH, Tang SKY, Smythe EJ, Hatton BD, Grinthal A, Aizenberg J (2011) Bioinspired self-repairing slippery surfaces with pressure-stable omniphobicity. Nature 477:443–447

Yamazoe K, Higaki Y, Inutsuka Y, Miyawaki J, Cui Y-T, Takahara A, Harada Y (2017) Enhancement of the hydrogen-bonding network of water confined in a polyelectrolyte brush. Langmuir 33:3954–3959

Yebra DM, Kiil S, Dam-Johansen K (2004) Antifouling technology-past, present and future steps towards efficient and environmentally friendly antifouling coatings. Prog Org Coat 50:75–104

Zhang Z, Chao T, Chen S, Jiang S (2006a) Superlow fouling sulfobetaine and carboxybetaine polymers on glass slides. Langmuir 22:10072–10077

Zhang Z, Chen S, Chang Y, Jiang S (2006b) Surface grafted sulfobetaine polymers via atom transfer radical polymerization as superlow fouling coatings. J Phys Chem B 110:10799–10804

Zhang Z, Finlay JA, Wang L, Gao Y, Callow JA, Callow ME, Jiang S (2009) Polysulfobetaine-grafted surfaces as environmentally benign ultralow fouling marine coatings. Langmuir 25:13516–13521

Zhang Z, Moxey M, Alswieleh A, Morse AJ, Lewis AL, Geoghegan M, Leggett GJ (2016) Effect of salt on phosphorylcholine-based zwitterionic polymer brushes. Langmuir 32:5048–5057

Zoppe JO, Ataman NC, Mocny P, Wang J, Moraes J, Klok H-A (2017) Surface-initiated controlled radical polymerization: state-of-the-art, opportunities, and challenges in surface and interface engineering with polymer brushes. Chem Rev 117:1105–1318

Chapter 11
Toward Enviromentally Adaptive Anti-icing Coating

Chihiro Urata

Abstract The formation, adhesion, and accumulation of ice and snow on solid surfaces causes multiple problems such as decreased power generation efficiency, increased energy consumption, and mechanical and/or electrical failure. These problems incur huge economic loss and threaten the safety of electrical appliances. Therefore, much effort has been expended in understanding the mechanism of icing and the relationship between liquids and surfaces at low temperatures. By controlling the characteristics of surface features such as wettability, topography, and lubricity, researchers have developed various anti-icing or icephobic coatings. However, despite the multiple propositions and tested scenarios, most of these coatings are insufficiently ice-repellant under a single atmospheric condition, so their applicability is limited in practice. Icing conditions become complex and variable as the surrounding environment changes, demanding a more adaptable ice-resistant surface. This chapter summarizes the most recent progress on passive anti-icing coatings, particularly stimuli-responsive anti-icing coatings with active surface function, prepared by various types of methods.

Keywords Ice adhesion · Icephobic · Pagophobic · Deicing · Anti-icing · Adaptive coating

11.1 Introduction

Ordered patterns, among various natural phenomena, the formation and accumulation of snow and ice is particularly threatening to industrialization and to modern day dependence on machinery. Ice and snow decreases the functionality of large-scale systems such as aircraft (Marwitz et al. 1997; Gent et al. 2000; Mosher et al.

C. Urata (✉)
Structural Materials Research Institute, National Institute of Advanced Industrial Science and Technology (AIST), Nagoya, Japan
e-mail: chihiro-urata@aist.go.jp

A. Hozumi et al. (eds.), *Stimuli-Responsive Dewetting/Wetting Smart Surfaces and Interfaces*, Biologically-Inspired Systems 11,
https://doi.org/10.1007/978-3-319-92654-4_11

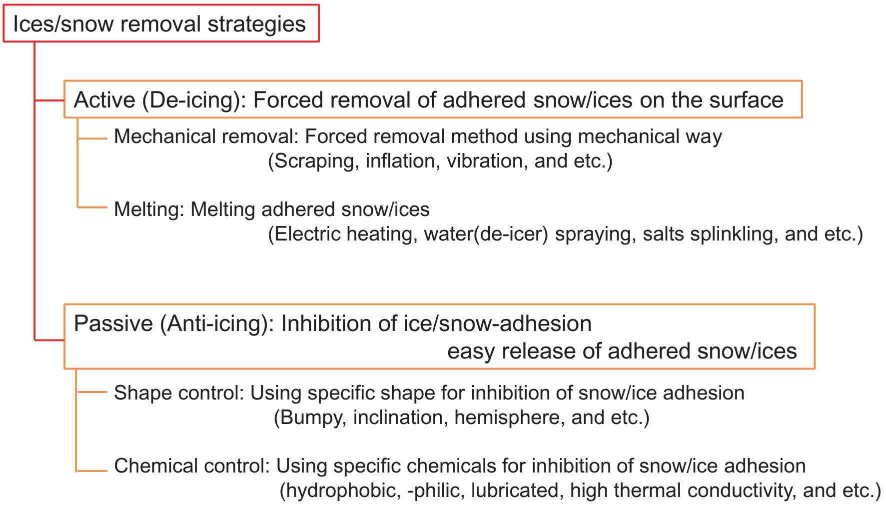

Fig. 11.1 Conventional strategies for ices and snow free surface

2010), power lines (Laforte et al. 1998; Lu et al. 2009), offshore platforms (Makkonen et al. 2001), wind turbines (Dalili et al. 2009; Parent and Ilinca 2011; Botta et al. 1998), ships (Chatterson and Carson Cook 2008), photovoltaic devices (Fillion et al. 2014; Jelle 2013), trains (Kloow 2011), and road (Andrey and Olley 1990; Andersson and Chapman 2011) as well as household appliances such as refrigerators and air conditioners (Emery and Siegel 1990; Huang et al. 2009). This loss of functionality, or even complete breakdown, causes economic loss, and is occasionally fatal. There are two current methods to address the removal of ice and snow (Fig. 11.1); active (de-icing) and passive (anti-icing).

Active removal methods are widely used at present. They include mechanical scraping, thermal treatments, and removal of accumulated ice by de-icing fluids or salts. The crudest method is mechanical de-icing, the physical removal of ice from easily accessible apparatuses such as power networks and overhead transmission lines. The aggregated ice is removed by direct scraping or by the energy imparted from shock waves, vibrations, or twisting conductors. Direct access is essential for mechanical de-icing, but a device with restricted access can be successfully de-iced by helicopters and shotguns. Although effective, the blunt force of mechanical de-icing places additional stress on networks, potentially leading to network or power failure. Therefore, mechanical de-icing is sometimes neither safe nor efficient.

Another approach is applying melting. Electrothermal treatments can effectively remove ice from some systems. These treatments heat and maintain the surface temperature above the freezing point, preventing ice formation or accelerating melting. The most effective de-icing approach in engineering, which has gained worldwide recognition, is the Joule effect for heating line conductors (Farzaneh et al. 2008). For example, conventional traffic lights can produce sufficient heat to melt the ice/snow adhered on their surfaces. When conventional lights are replaced with

LED bulbs to reduce the cost and energy usage, ice and snow adhesion begins anew (Hansen 2011). Thus, the effectiveness–efficiency balance presents a significant challenge to electrothermal de-icing methods. Additionally, this method requires an electric flow, risking electromagnetic disturbances to the apparatus's operation.

The final and most popular active de-icing strategy is the chemical method. Freezing point depressants, such as salts, glycols, alcohols, and other organic liquids with crystallization temperatures lower than water, are applied to windscreens and similar surfaces (Thomas et al. 1996; Gerbino-Bevins 2011). However, these solutions are inefficient and temporary, requiring multiple applications that increase the cost of de-icing and possibly harm the environment. In winter, the snow/ice on roads and sidewalks is often melted by salts such as NaCl, $CaCl_2$, and $MgCl_2$, which are highly soluble and enter the roadside environment via runoff or splashing (75–90% of the applied NaCl is lost in this way). Therefore, although salts can be an efficient, minimal-cleanup solution for melting ice and snow on roads, the salt solution can permeate and contaminate the groundwater (Howard and Haynes 1993; Williams et al. 2000). Residual salt can also affect roadside vegetation, aquatic organisms, steel frames, and cars (Sanzo and Hecnar 2006). Sol-gel technology has reduced the frequency of salt application, but its practical applicability is limited by high cost (Ayres et al. 2007).

Overall, many active ice-removal methods have high energy requirements (which increases their cost) and are difficult to apply in standalone circumstances. More passive anti-icing methods, which proactively prevent ice formation and adhesion on surfaces, are being currently explored. Because an ideal passive anti-icing coating maintains a clear surface with no external input, passive anti-icing methods have drawn much attention in various applications. For example, cold northern districts are ideally situated for photovoltaic (PV) power generation in winter, because the efficiency of a PV panel increases with decreasing surrounding temperature (Fillion et al. 2014; Jelle 2013). In addition, the sunlight is scattered and reflected by snow, although ice and snow accumulation on the PV panel hinder this process and risk collapse of the panel. Thus, understanding the mechanism of ice formation has become a major research focus and the subject of numerous reviews (Lv et al. 2014; Kreder et al. 2016; Liu et al. 2016; Sojoudi et al. 2016; Jha et al. 2016). Despite the success of modern anti-icing coatings, their widespread use in industry is banned by a number of limitations. Many of these coatings cannot adapt to continuously changing surrounding environments, and are effective under certain conditions but unsuccessful or even detrimental in others. For example, superhydrophobic surfaces with micro- and nano-scale roughness can prevent ice accumulation (Cao et al. 2009; Kulinich and Farzaneh 2009a, b; Wang et al. 2010; Antonini et al. 2011; He et al. 2011; Menini et al. 2011; Guo et al. 2012; Ruan et al. 2013; Boinovich and Emelyanenko 2013; Arianpour et al. 2013; Bharathidasan et al. 2014; Davis et al. 2014), but exert detrimental effects in certain environments (Varanasi et al. 2010; Kato et al. 2004; Farhadi et al. 2011; Jung et al. 2011; Kulinich et al. 2011; Chen et al. 2012; Nosonovsky and Hejazi 2012; Oberli et al. 2014; Wang et al. 2012a). At present, no coatings can completely prevent ice or snow accretion over a desired period, although many anti-icing strategies with environmental adaptability and

Fig. 11.2 Key factors that affect anti-icing properties: (**a**) static contact angle, (**b**) dynamic contact angle, (**c**) hardness, (**d**) lubricative property

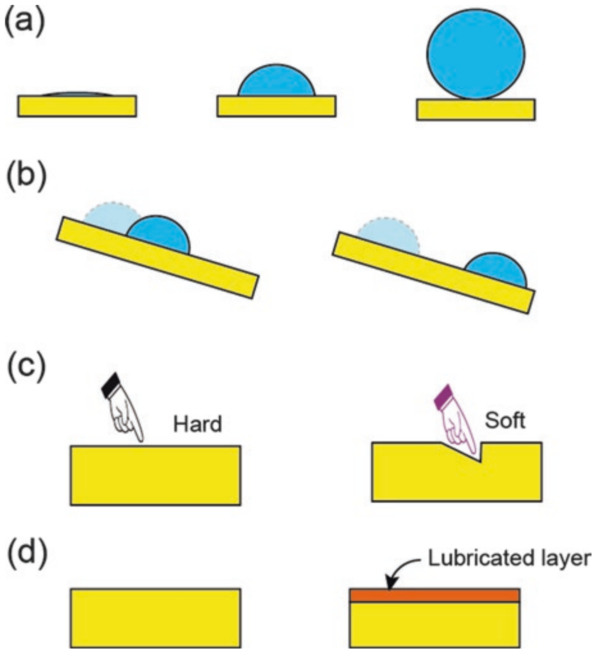

stimuli-responsive properties have been emerging (Stone 2012; Lv et al. 2014; Kreder et al. 2016; Liu et al. 2016; Sojoudi et al. 2016; Jha et al. 2016; Nath et al. 2017). This review will examine current anti-icing coatings that work by controlling the surface properties of the coatings (Fig. 11.2).

11.1.1 Definition of Icing

According to the ISO-12494 standard (Atmospheric icing of structures n.d.), ice accretion is the process by which ice and snow accumulate on the surface of an object exposed to the atmosphere. The physical properties, shape, and appearance of the accreted ice greatly depend on the meteorological and surrounding conditions (e.g., the surface structure of the object, the wind speed, air temperature, liquid water content, droplet size distribution, droplet temperature, and humidity). Various atmospheric icing types are distinguished in Fig. 11.3. Depending on the ice/snow formation processes, atmospheric icing types are generally categorized into three types; precipitation icing, in-cloud icing, and sublimation icing. Precipitation icing is formed by glaze, rain that has become super-cooled and freezes on impact with cold surfaces or wet/dry snow accretions. In-cloud icing occurs when super-cooled liquid water droplets collide with or freeze on an object. For example, ice is known to easily accumulate on aircraft wings when passing through clouds during takeoff, especially in winter (Marwitz et al. 1997; Gent et al. 2000; Mosher et al. 2010). As this

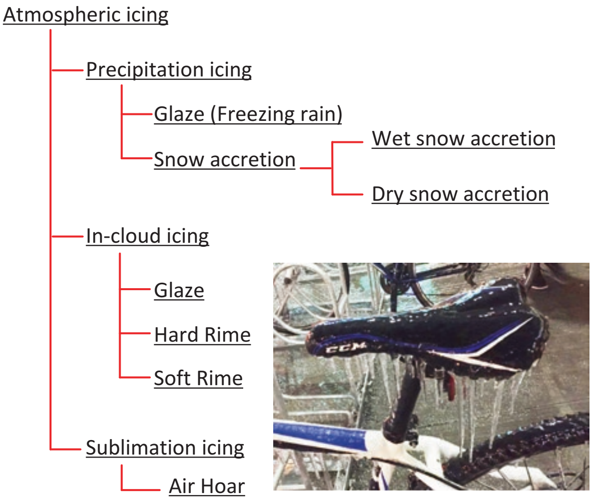

Fig. 11.3 Categories of atmospheric icing (Inset image: icicles formation on a saddle of a bicycle after freezing rain, Toronto)

accumulation lowers the aerodynamic lifting forces, the wings of an aircraft must be sprayed before departure during winter. Finally, sublimation icing refers to the direct formation of frost from water vapor on a solid surface. Frost formation at the boundary between a cold sub-zero surface and a warm surface fits into this category.

In this chapter, icephobicity defines the property that allows surfaces to repel and prevent ice formation. Sojoudi et al. suggested that pagophobicity (derived from the classical Greek word pagos, meaning ice) more appropriately describes the diverse phenomena related to anti-icing properties (Sojoudi et al. 2016). For readability, this review refers to snow/ice-repellant surfaces as anti-icing surfaces.

11.1.2 Evaluation of Anti-icing Property

The complexity ice formation process has hindered the artificial production of particular icing conditions and the establishment of standards for estimating the performances of anti-icing coatings. Nevertheless, three estimation methods (Wang et al. 2012b, 2014a, b; Alizadeh et al. 2012; Boinovich et al. 2013; Chu and Scavuzzo 1991) dominate the literature (Fig. 11.4). First, anti-icing coatings can be evaluated by freezing delay measurements (Fig. 11.4a). Water or super-cooled water droplets are placed on a substrate cooled to below the freezing point at low humidity (to prevent frost formation) or injected on the coatings. This test simulates the ice adhesion to aircraft, transmission lines, towers, and other infrastructures exposed to clouds or freezing rain. The coating is assessed by whether the water droplets bounce from or stick to the surface.

The second method, frosting delay measurement (Fig. 11.4b), is more practical than freezing delay measurement because the frosting is tested in a humid environment, simulating the frosting on a heat exchanger. In this test, the surface or

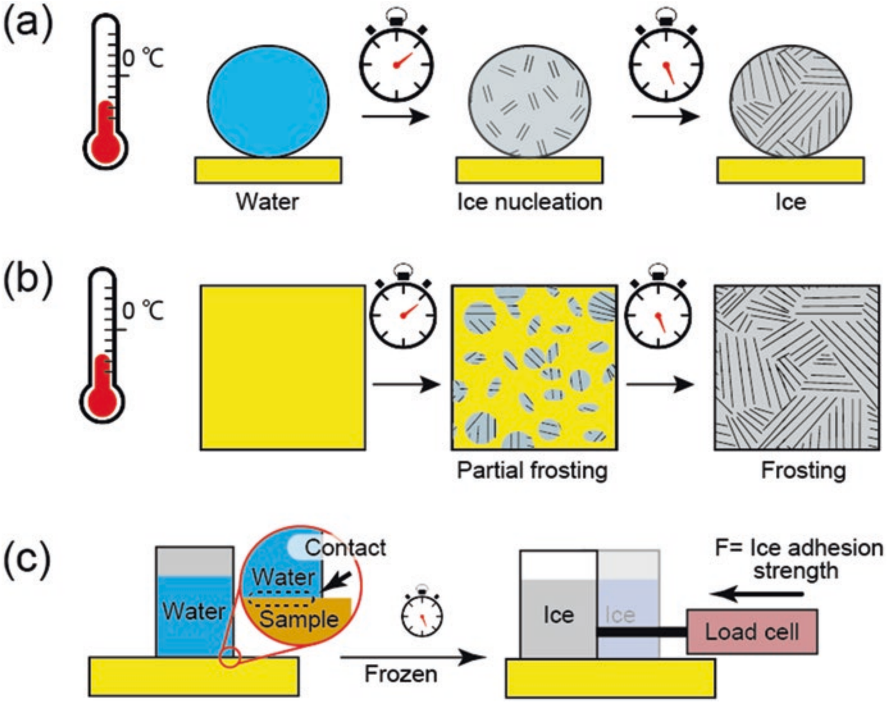

Fig. 11.4 Evaluation methods of anti-icing performances: (**a**) Freezing delay measurement, (**b**) Frosting delay measurement, (**c**) Ice adhesion strength measurement

surrounding temperature of the coatings is generally cooled to below zero degrees Celsius to promote frost formation from atmospheric moisture. The frosting behavior is monitored by a video camera, and preserved for further analysis. The anti-frosting properties are evaluated by the frosting delay (time to full coverage by frost) and coverage behavior (homogeneous or heterogeneous). As frost formation is highly sensitive to the temperature, humidity, and thermal conductivity of the substrate and coatings, the frosting-delay data of different studies are not easily compared.

Finally, anti-icing coatings can be evaluated by measuring the shear force (ice-adhesion strength) between the coating and adhered ice (usually a deliberately prepared ice pillar) (Fig. 11.4c). In general, ice pillars on the test coating are prepared by pouring water on ice molded pipes at the freezing temperature. Once formed, the ice pillars are pushed with load cells and their adhesion strength curves are obtained. This simple method has become the de facto standard for comparing anti-icing properties. In contrast, a common protocol and environmental standards for measuring ice adhesion are currently unrecognized. Recently, Kreder et al. broadly overviewed the ice-adhesion values reported in the literature (Kreder et al. 2016). They noticed that liquid-infused lubricated anti-icing coatings reduce the ice-adhesion strength to ultra-low levels (<10 kPa). This chapter will describe the types of anti-icing coatings in more detail.

11.2 Anti-icing Coatings

Anti-icing properties and surface wettability are believed to be strongly correlated; surfaces with high static-contact angles improve the anti-icing properties by reducing the surface–water contact area (Cao et al. 2009; Kulinich and Farzaneh 2009a, b; Wang et al. 2010; Antonini et al. 2011; He et al. 2011; Menini et al. 2011; Guo et al. 2012; Ruan et al. 2013; Boinovich and Emelyanenko 2013; Arianpour et al. 2013; Bharathidasan et al. 2014; Davis et al. 2014; Varanasi et al. 2010; Saito et al. 1997; Meuler et al. 2010a). However, this correlation has been disputed and new coatings that disregard the wettability are emerging (Fig. 11.5b). In this section, we summarize the history and recent progress for environmental adaptive anti-icing coatings prepared by various strategies; (1) simple wettability control, (2) superhydrophobic modification, (3) lubricating modification, and (4) hybridized methods.

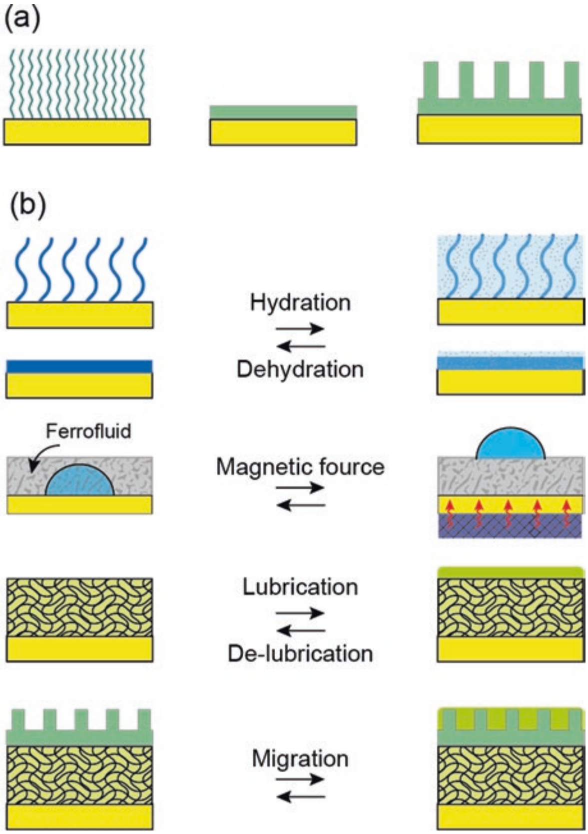

Fig. 11.5 Surface properties of anti-icing coatings: (**a**) conventional wettability control, (**b–e**) emerging anti-icing coatings with environmental adaptability and stimuli-responsive properties: (**b**) hygroscopic coating, (**c**) ferrofluid covered surface, (**d**) thermally responsive lubricating coating, (**e**) hybridization of superhydrophobic surface with deicer infused coating

11.2.1 *Correlation Between Wettability and Icephobic Property of a Solid Surface*

Surface wettability, which is indicated by the static and/or dynamic contact angle of water on the surface, is believed to be highly correlated with the anti-icing properties of the surface (Fig. 11.6) (Alizadeh et al. 2013; Cao et al. 2009; Kulinich and Farzaneh 2009a, b; Wang et al. 2010; Antonini et al. 2011; He et al. 2011; Menini et al. 2011; Guo et al. 2012; Ruan et al. 2013; Boinovich and Emelyanenko 2013; Arianpour et al. 2013; Bharathidasan et al. 2014; Davis et al. 2014; Varanasi et al. 2010; Saito et al. 1997; Meuler et al. 2010a). For example, researchers reported that the ice-adhesion strength lowered with increasing of the static contact angles or decreasing of the contact angle hysteresis (Saito et al. 1997; Meuler et al. 2010a). However, there are conflicting reports on this correlation in the literatures (Varanasi et al. 2010; Kato et al. 2004; Farhadi et al. 2011; Jung et al. 2011; Kulinich et al. 2011; Chen et al. 2012; Nosonovsky and Hejazi 2012; Oberli et al. 2014; Wang et al. 2012a; Yin et al. 2010; Yang et al. 2011; Zou et al. 2011; Li et al. 2012;

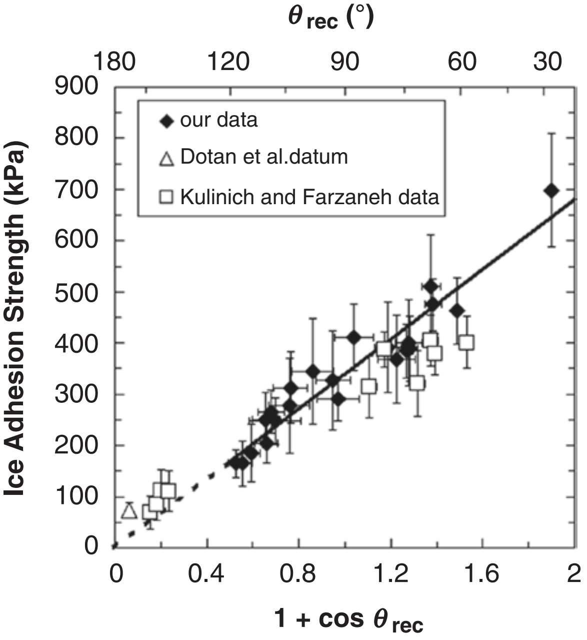

Fig. 11.6 Compilation of average strengths of ice adhesion reported by Meuler et al. (22 nominally smooth test substrates at −10 °C, ◆), by Kulinich and Farzaneh (Langmuir 2009, 25, 8854–8856) (10 textured test substrates at −10 °C, □), and by Dotan et al. (J. Adhes. Sci. Technol. 2009, 23, 1907–1915) (one textured test substrate at −8 °C, Δ). The solid and dashed lines represent the linear best fit to our data. (predicted average strength of ice adhesion = (340 ± 40 kPa)(1 + cos θrec), R2 = 0.92). (Adapted with permission from (*ACS Appl. Mater. Interfaces* 2010, 2, 3100–3110) Copyright © 2010 American Chemical Society)

Kirillova et al. 2016). Zou et al. reported that the negative correlation between ice-adhesion strength and water-contact angle is limited to surfaces with similar roughness (Zou et al. 2011). The surface wettability was uncorrelated with ice formation in a comparative experiment of representative superhydrophilic, hydrophilic, hydrophobic, and superhydrophobic surface samples (Yin et al. 2010). Jung et al. reported unexpectedly long freezing delays on hydrophilic surfaces with nanometer-scale roughness (Jung et al. 2011). The delay was at least one order of magnitude longer than typical superhydrophobic surfaces with larger roughness and low wettability. Li et al. investigated evaporation, condensation, and the subsequent ice formation process in a closed cell (Li et al. 2012). They found that the normalized surface-ice nucleation rate is approximately one order of magnitude lower on a flat hydrophilic surface than on a flat hydrophobic surface. Evidently, the relationship between the wettability and icephobicity property of a surface is highly complex and poorly understood, but might be clarified by common protocols and environmental standards for evaluating the anti-icing properties of surfaces, which are currently lacking.

Meanwhile, Kirillova et al. reported an unique approach to reduce icing adhesion strengthen using a heterogeneously distributed hydrophobic and hydrophilic surface prepared from Janus particles (Fig. 11.7) (Kirillova et al. 2016). These surfaces exhibit special surface “edge” morphologies arising from the structure and orientation of the Janus particles. Their experimental results and Monte Carlo simulations revealed a three-step process of ice formation (Fig. 11.8): (i) water nucleation, determined by the size of the hydrophilic domains formed by the Janus particles; (ii) spontaneous amalgamation and the quick spreading of liquid water on hydrophobic clusters, and (iii) solidification of the liquid clusters. During the last step, large irregular dendrites of ice crystals are formed. The dendrites appear to develop extremely quickly along the hydrophilic clusters by absorbing water droplets that have not yet frozen. The evaporation forms a dry band around single ice crystals, leaving a substantial part of the surface ice-free. The interaction of both effects reduces the ice adhesion. In fact, less ice adheres to layers of Janus particles (*ca.* 56 kPa) than to layers of either hydrophilic (*ca.* 350 kPa) or hydrophobic (*ca.* 70 kPa) particles.

11.2.2 Superhydrophobic Surfaces

Superhydrophobic/omniphobic (Erbil et al. 2003; Ozbay and Erbil 2015) surfaces have shown substantial promise as water repellants, because liquid droplets (<10 μL) contacting such surfaces freely roll off at small tilt angles (<10°). Therefore, it is thought that if water can be bounced or repelled from a superhydrophobic surface before freezing, such surfaces could be exploited as passive anti-icing coatings (Cao et al. 2009; Kulinich and Farzaneh 2009a, b; Wang et al. 2010; Antonini et al. 2011; He et al. 2011; Menini et al. 2011; Guo et al. 2012; Ruan et al. 2013; Boinovich and Emelyanenko 2013; Arianpour et al. 2013; Bharathidasan et al. 2014; Davis et al.

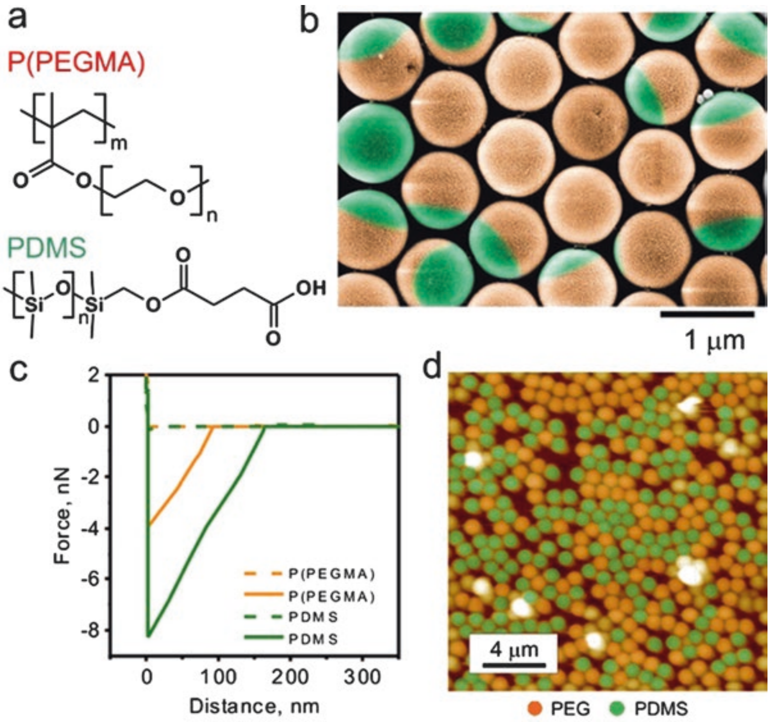

Fig. 11.7 Representative layers prepared with P(PEGMA)/PDMS Janus particles: (**a**) chemical formulas of the polymers; (**b**) false color SEM image (orange side, P(PEGMA); green side, PDMS; the original image can be found in Supporting Information, Figure S2); (**c**) direct force measurements on the P(PEGMA)/PDMS Janus particle layer at 80% relative humidity (dashed line, approaching curve; solid line, retracting curve; the respective force curves measured under water are displayed in Figure S3); (**d**) false color mapping of the Janus particle orientation using AFM direct force measurements (orange, P(PEGMA); green, (PDMS)). Adapted with permission from (*Chem. Mater. 2016, 28, 6995–7005*) Copyright © 2016 American Chemical Society

2014). Superhydrophobic surfaces have been prepared by combining low-surface energy materials, such as alkyl and perfluoroalkyl groups, into the designed surface texture. However, some researchers have pointed out the limited anti-icing success of superhydrophobic surfaces in varying humidity environments (Varanasi et al. 2010; Kato et al. 2004; Farhadi et al. 2011; Jung et al. 2011; Kulinich et al. 2011; Chen et al. 2012; Nosonovsky and Hejazi 2012; Oberli et al. 2014; Wang et al. 2012a; Meuler et al. 2010b; Schutzius et al. 2015). In fact superhydrophobicity is completely lost at high humidity because moisture can condense in the void of the rough structure (Fig. 11.9). If the high-humidity conditions are sustained, the droplets will coalesce into an ice layer. Similar degradation occurs after multiple icing/de-icing cycles, as ice penetrates the surface texture and increases the ice adhesion. The limitations of superhydrophobic surfaces as anti-icing coatings have since been confirmed in multiple studies. Varanasi et al. (2010) reported that frost nucleation occurs on all areas of a superhydrophobic surface texture, eroding the

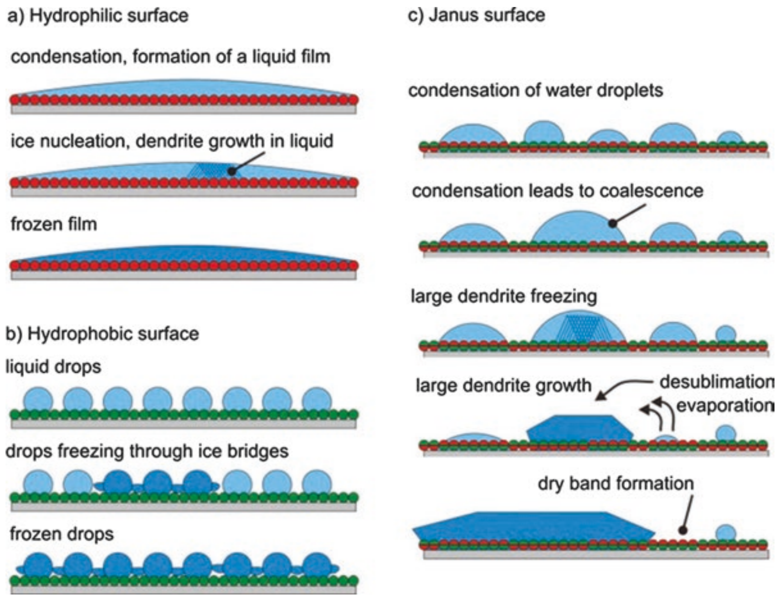

Fig. 11.8 Mechanisms of the ice layer formation on (**a**) rough hydrophilic, (**b**) hydrophobic, and (**c**) Janus surfaces. (Adapted with permission from (*Chem. Mater. 2016, 28, 6995–7005*) Copyright © 2016 American Chemical Society)

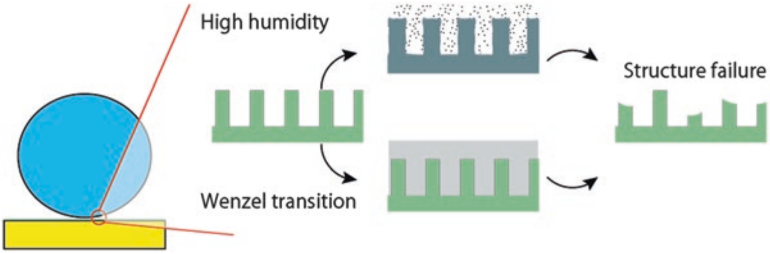

Fig. 11.9 Drawbacks of superhydrophobic surface for anti-icing coating

superhydrophobic properties, and increasing the ice-adhesion strength. Kulinich et al. (2011) demonstrated that when ice eventually accumulates on a superhydrophobic surface, the surface microstructure is gradually damaged by icing and deicing. High humidity exacerbates this phenomena and increases the ice-adhesion strength. Chen et al. (2012) discovered that (i) superhydrophobic surfaces cannot reduce ice adhesion and (ii) the ice-adhesion strength is actually lower on flat hydrophobic and hydrophilic surfaces than on structured superhydrophobic and superhydrophilic surfaces (Fig. 11.10). Finally, Nosonovsky and Hejazi (2012) analyzed why superhydrophobic surfaces are not always icephobic. They found that the force required to detach ice pieces from a surface depends on two factors: the contact angle and the initial size of the interfacial cracks. For example, surfaces with small

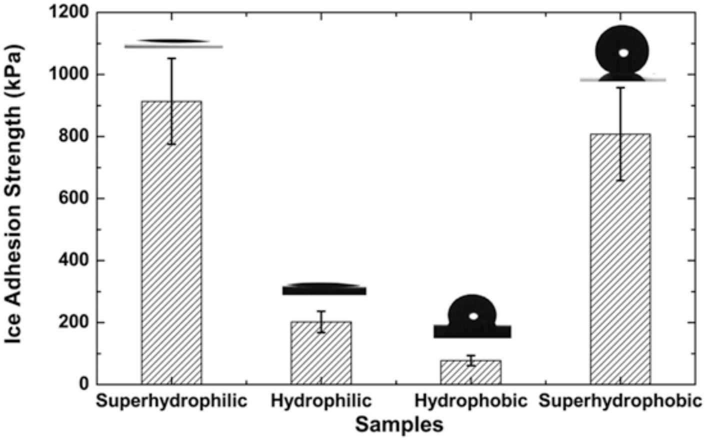

Fig. 11.10 Average ice adhesion strengths on four different silicon wafer surfaces (superhydrophilic to superhydrophobic) measured at −15 °C with a probe speed of 0.5 mm/s. Insets are the profiles of water droplets on the corresponding surfaces. Adapted with permission from (*Appl. Phys. Lett. 2012, 101*) Copyright © 2012 American Institute of Physics

cracks may strongly bind ice even if their receding angle is large. Overall, superhydrophobic surfaces are not yet a practical solution to anti-icing, and other routes need to be explored.

11.2.3 Lubricated Coatings

Wong et al. proposed an innovative idea for anti-icing coatings based on lubricated surfaces (Wong et al. 2011; Irajizad et al. 2016). Their coating, named slippery liquid-infused porous surface (SLIPS), has been embraced and adapted by many researchers, leading to various types of anti-icing coatings infused with lubricating liquids. Anti-icing coatings with extraordinary low ice adhesion strength (<10 kPa, the lowest value is 2 Pa (Irajizad et al. 2016)) were achieved by the SLIPS approach. In general, these coatings are prepared by infusing lubricating oil into a solid backbone. The lubricated coatings are prepared by one of two approaches; post-infusing or pre-infusing (Fig. 11.11). In the post-infusing method, the lubricating liquid is infused into preformed matrices such as sponges, porous materials, or swellable polymers. In the pre-infusing method, the lubricating liquids are mixed with miscible polymer precursors. After the crosslinking of the polymer backbone, the mobile infused lubricating oil migrates over the surface. In both methods, the lubricating surface films provide smooth, defect-free, and slippery properties on the coated substrates. This review introduces five types of lubricated anti-icing coatings.

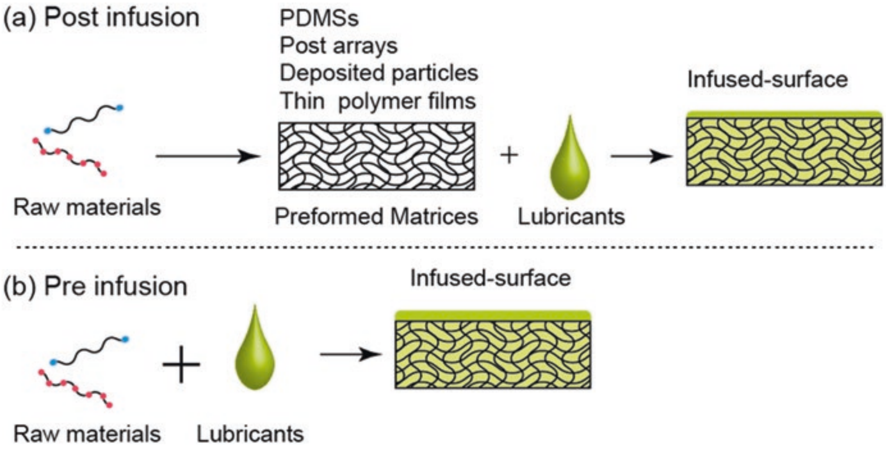

Fig. 11.11 Preparative method of (**a**) post-infused and (**b**) pre-infused anti-icing coatings

11.2.3.1 Anti-icing Property of SLIPS

The SLIPS method of Wong et al. (Stone 2012; Kim et al. 2012, 2013; Wilson et al. 2013; Vogel et al. 2013) was inspired by tropical pitcher plants (Nepenthes spp.). Generally, SLIPS are prepared by the post-infusing method. The SLIPS layer is applied to the surfaces using a portfolio of technologies developed by the Aizenberg group. SLIPS layers can be applied to a wide range of materials and repel various liquids and products, from motor oil to blood and lotions (http://slipstechnologies.com/about-slips/). To form a continuous lubricating layer, a porous polymeric substrate such as Teflon or epoxy resin is infused with a film of perfluorinated lubricating liquid. The lubricant can wet and wick into the porous membrane, and spread over the surface-texture features. Thus, when water is dropped onto a SLIPS layer, a composite solid–lubricant–water interface is formed and the water droplets easily slide off the surface even at small tilt angles. As demonstrated by the Aizenberg group, a SLIPS coating is particularly useful in anti-icing applications as it not only reduces ice accretion, but enables easy removal of accumulated ice and melted water by gravity at low tilt angles (Kim et al. 2012). Using an electrodeposition technique, Wong et al. coated aluminum substrate with a nanostructured coating hydrophobized by fluorosilane, and finally infused the surface with drops of perfluorinated lubricant. The result was a SLIPS-coated aluminum surface with high resistance to ice accumulation and very low ice-adhesion strength (Fig. 11.12). Any condensed water droplets were removed from the SLIPS surface by gravity at low tilt angles, inhibiting ice formation (Kim et al. 2012). The invention of SLIPS has inspired many similar publications (Anand et al. 2012; Smith et al. 2013; Subramanyam et al. 2013; Rykaczewski et al. 2013; Chen et al. 2013, 2014a, b; Liu et al. 2013, 2015; Dou et al. 2014; Chen et al. 2014a; Zhu et al. 2013; Eifert et al. 2014; Yin et al. 2015), and several reviews papers the synthesis and properties of

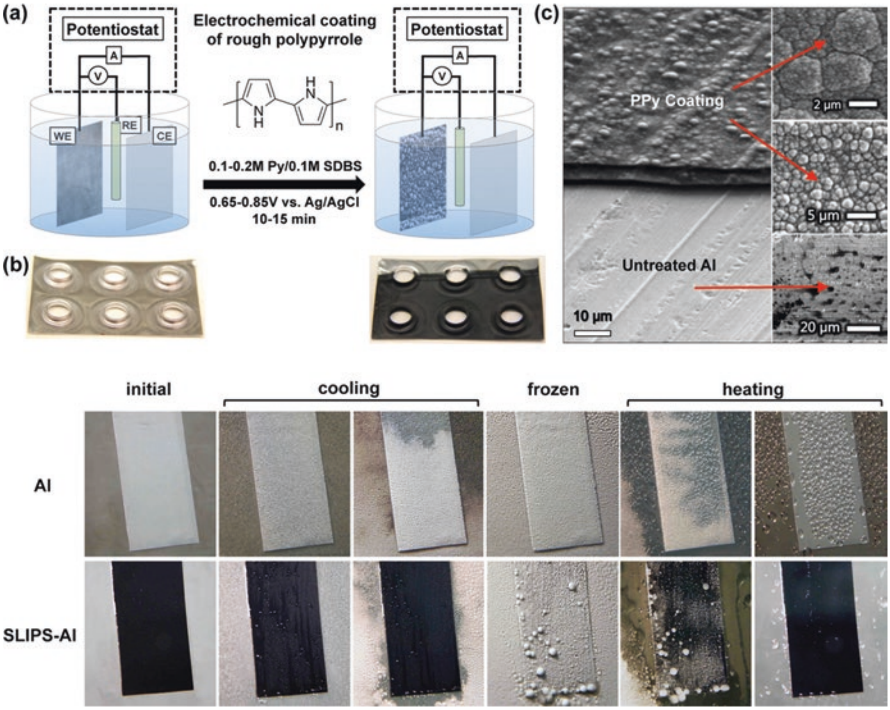

Fig. 11.12 (**a**) Schematics of the procedure for electrochemical coating of nanostructured polypyrrole on aluminum sheet (WE, Al 1100 alloy as working electrode; RE, Ag/AgCl reference electrode; CE, Pt gauze counter electrode). (**b**) Photographs of untreated punch-pressed aluminum sample (left) and partially coated aluminum sample (right). PPy-coated area appears black in the picture. Substrate size = 6 cm × 9 cm. (**c**) SEM images comparing the morphology of untreated area of aluminum with PPy-coated area. Insets show higher magnification SEM images for the two areas. (**d**) Still images extracted from the movies simulating ice formation by deep freezing (−10 °C) in high-humidity condition (60% RH) and subsequent deicing by heating. The morphology of accumulated ice on SLIPS-Al is significantly different from that on bare Al. Condensation/freezing cycle: from room temperature to −10 °C at 5 °C/min. Melting (defrost) cycle: from −10 to 25 °C at ~10 °C/min. Ice still forms mostly around the edges of SLIPS-Al by bridging from the surrounding aluminum substrate, while it forms uniformly all over the aluminum substrate. Fects (tall features above the level of the lubricant layer) on the surface of SLIPS-Al led to the pinning of droplets while they were sliding which eventually led to the formation of large ice crystals on SLIPS-Al. The samples are mounted with 75° tilt angle, and the widths of the substrates are approximately 3 cm. (Adapted with permission from (*ACS Nano* 2012, 6, 6569–6577) Copyright © 2012 American Chemical Society)

SLIPS have been recently published (Stone 2012; Lv et al. 2014; Kreder et al. 2016; Liu et al. 2016; Sojoudi et al. 2016; Jha et al. 2016; Nath et al. 2017).

SLIPS achieves its icephobicity via two routes: the impact of super-cooled water droplets on surfaces at sub-zero temperatures, or direct ice condensation from the vapor phase of super-saturated humid ambient air. The roughness and chemical heterogeneity of a surface are generally determined by the contact-angle hysteresis over a spectrum of contact angles (Erbil 2006, 2014), evaluated by the three-phase contact line of a droplet pinned at a surface defect. Therefore, the icephobicity crucially depends on the contact surface area and the ease of sliding drops on a surface. In anti-icing applications, if the freezing point of the infused liquid is well below the temperature of the application, the SLIPS will minimize the contact-angle hysteresis because the interface between the infused liquid and water minimizes the contact-angle pinning (Wong et al. 2011; Kim et al. 2012).

In a series of experiments, Varanasi and co-workers (Anand et al. 2012; Smith et al. 2013; Subramanyam et al. 2013; Rykaczewski et al. 2013) investigated the relationship between anti-icing and liquid-infused surfaces in matrices of lithographically preformed textured surfaces infused with various liquids. In this method, the physicochemical parameters (such as surface tension of the solid/liquid, topography of the surface texture, and the level of infused liquids) are easily tuned. They reported that lubricants can cloak the water droplets forming on them (Fig. 11.13), thus preventing condensate growth, accelerating the depletion of the impregnated lubricating oil, and contaminating the droplets. As condensed water droplets on perfluorinated fluid lubricated surfaces cannot be evaporated, even under superheated conditions, the water (or ice) will be pinned to the post tops of the lubricant impregnated surfaces (LISs) (Anand et al. 2012). However, further studies by Varanasi's group showed promising anti-icing results for LISs with thick excess lubricant films on the textured solid. Unfortunately, the excess films are unstable and will drain under external forces (such as gravity and drag) to attain thermodynamically stable configurations (Smith et al. 2013).

Varanasi and co-workers also studied frost formation on nano/micro-structured superhydrophobic surfaces with and without the perfluorinated lubricating oil layer (Rykaczewski et al. 2013). The results were mixed, as the anti-icing properties of the surface were lost after a few frosting–defrosting cycles. To prevent this loss, liquid reservoirs that replenish the lubricant are required (Rykaczewski et al. 2013). The Aizenberg group (Vogel et al. 2013) proposed improving the thermodynamic stability of SLIPS by a closed-cell architecture using an inverse colloidal monolayer template, which achieves a transparent, nanoporous SLIPS composite. As the lubricants were locked in the structures, the composite was thermodynamically stable over 9 months of vertical storage; moreover, the surface showed very low ice-adhesion strength (10 ± 7 kPa).

Although effective, SLIPS is not free of limitations. The main problems are longevity, cost of the perfluorinated liquid lubricants, and cloaking of the lubricant-infused surfaces. The first two issues arise from the short retention time of the perfluorinated lubricant in the pores (the lubricant tends to leak or evaporate), and the high cost of the perfluorinated lubricant, which challenges the economic feasibility of this approach.

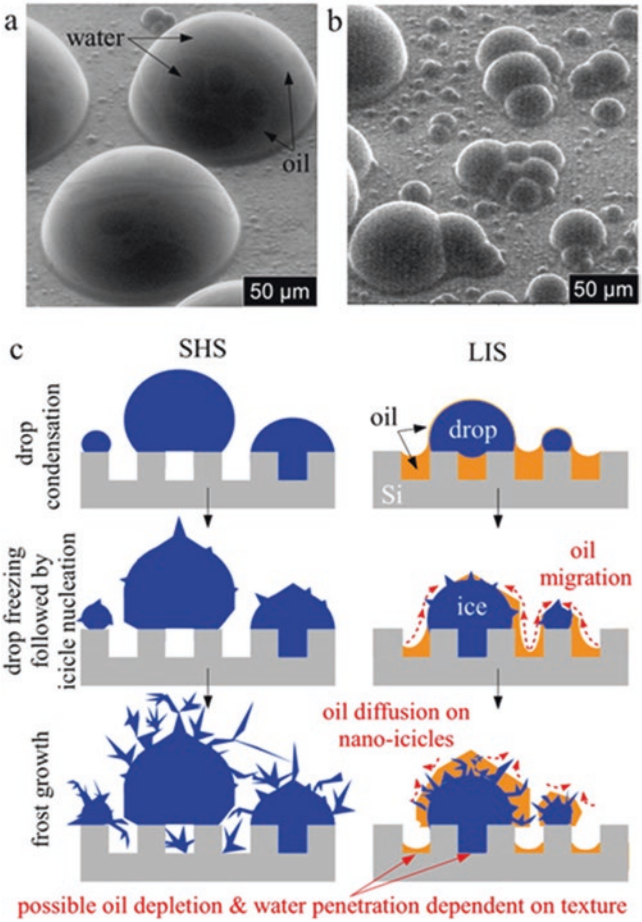

Fig. 11.13 ESEM images of (**a**) oil swirls on top of drops and (**b**) compound drops condensed on NP-LIS and schematic illustrations contrasting with (**c**) the mechanism of frost growth via drop condensation and freezing on SHS and LIS. (The extent of illustrated oil depletion and water penetration into the substrate is dependent on the length scale of the underlying texture.) (Adapted with permission from (*Langmuir 2013, 29, 5230–5238*) Copyright © 2013 American Chemical Society)

11.2.3.2 Slippery Ferrofluid Surfaces

Irajizad et al. proposed new anti-icing surfaces with exceptionally low anti-icing adhesion strength using ferrofluids as slippery lubricant layers (Fig. 11.14) (Irajizad et al. 2016). Such a surface, which enables remote droplet manipulation, is a magnetic slippery surface (MAGSS) that creates a low-energy liquid–liquid interface. MAGSSs constitute a thin ferrofluid/oil film with intrinsically smooth and defect-free properties down to the molecular scale. The use of ferrofluids is inspired by

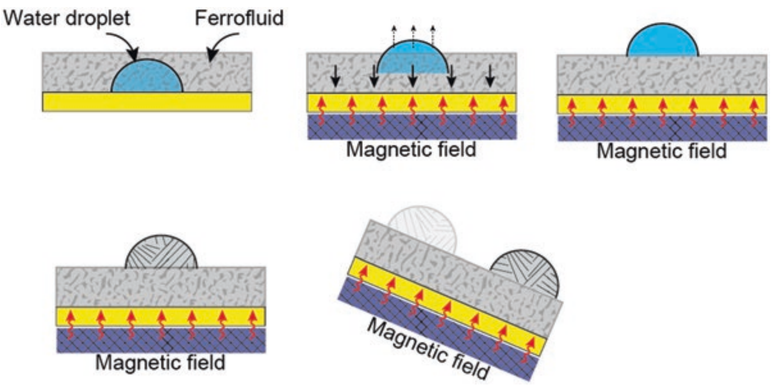

Fig. 11.14 Magnetic slippery surface (MAGSS): (**a**) Principal of anti-icing property using MAGSS, (**b**) Ice adhesion properties of MAGSS

multiple premises; that after single exposure to a magnetic field, the magnetic volumetric force will lock the thin liquid film; that ferrofluids will self-heal in the presence of a magnetic field; that spatial locking of the ferrofluid by the magnetic field increases the durability under high shear stresses; that oil-based ferrofluids evaporate very slowly, improving the longevity of the anti-icing agent; and that ferrofluid thin films enable versatile surfaces without micro/nanofabrication, which reduces the production costs. As the downward volumetric force of an immiscible water droplet on MAGSS is insufficient to penetrate the thin film, a liquid–liquid interface with low friction is formed. These liquid–liquid interfaces provide a low-energy site for heterogeneous ice nucleation (the Gibbs energy barrier approaches the homogenous limit). Consequently, the delay time of ice formation is 2–3 orders of magnitude higher than in superhydrophobic surfaces, the ice-adhesion strength is extremely low, and the shear flows are stable up to a Reynolds number of 10^5. Irajizad and coworkers also demonstrated the effectiveness of their surfaces for manipulating liquid drops and preventing scaling formation on pipes (Irajizad et al. 2017; Masoudi et al. 2017). Because the surface preparations require no micro/macro structuring, MAGSS can be applied on any type of solid surface. However, ferromagnetic slippery surfaces lack transparency and require a magnetic field to obtain their superior properties. Therefore, the effectiveness of MAGSS in future applications requires further investigation.

11.2.3.3 Hygroscopic Surfaces

As explained above, liquid-infused surfaces are prone to depletion of the infused liquid by evaporation or leaking. To solve this problem, Chen et al. proposed a new concept for anti-icing coatings named self-lubricating liquid water layer (SLWL) (Chen et al. 2013, 2014a; Dou et al. 2014; He et al. 2016; Liu et al. 2017). Inspired by ice-skating, the SLWL concept covers solid surfaces with hygroscopic

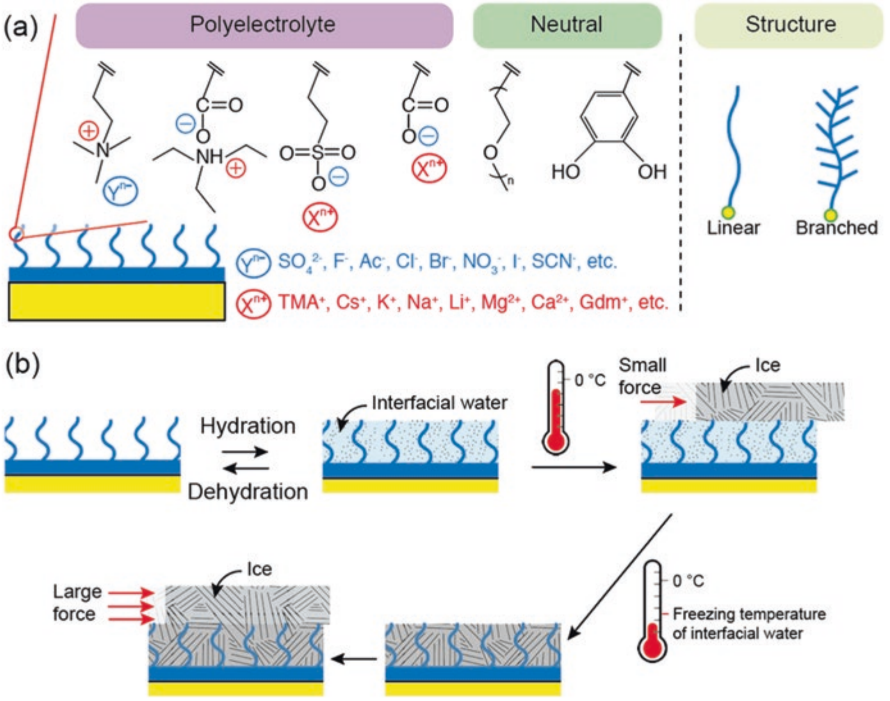

Fig. 11.15 Hygroscopic anti-icing coatings: (**a**) Schematic illustration of the structure of hygroscopic anti-icing coatings, (**b**) principal of anti-icing properties using hygroscopic anti-icing coatings

(hydrophilic) polymer layers, such as cationic, anionic, and non-ionic (Fig. 11.15). When water absorbs or condenses, this hygroscopic polymer network swells and liquefies, forming slippery interfacial water layers on the surface (Chen et al. 2013). Owing to the interfacial water layer, the ice-adhesion strength on this surface falls to below 100 kPa, 1–2 orders of magnitude lower than that of pristine substrates. In both humid and dry conditions, ice or frost placed on the surface will induce the self-lubricating water layer by melting (Chen et al. 2013). Although the structure, thickness, and nature of the interfacial water layer are incompletely understood, the anti-icing properties are known to be affected by several physico-chemical parameters, such as the environmental temperature and ionic species. The temperature effects of ice-adhesion on hygroscopic surfaces have been well researched by several groups. For example, Wang and his coworkers investigated the temperature dependence of ice-adhesion strength on these surfaces, and confirmed the existence of the frozen points of interfacial water layer (Fig. 11.15b). A polyacrylic-coated surface preserved its low ice-adhesion strength (ca. 70 kPa) as the temperature was lowered to −25 °C (Chen et al. 2013). When the temperature was further decreased, the values increased sharply and reached ca. 1100 kPa around −30 °C. Below −30 °C, the adhesion strength remained constant (ca. 1100 kPa) because of frozen of the interfacial water. As also reported by Wang et al., the threshold temperature of the phase transition can be controlled by applying different types of polymer layers. The ice-adhesion strength of crosslinked hyaluronic acid-dopamine polymer layers remained low (ca. 65 kPa) from −15 to −42 °C, rapidly increased between −42 and −50 °C, then remained constant (at 529 kPa) below –50 °C (Chen et al. 2014a). The phase-transition threshold of the polyurethane nanoparticle-based coatings was observed between –53 and –60 °C (Dou et al. 2014).

The effects of polymer structure and ionic species on the ice-adhesion behavior of hygroscopic surfaces have also been investigated. Chernyy et al. compared the ice-adhesion strengths of three types of polyelectrolyte brushes; poly[2-(methacryloyloxy)ethyl]-trimethylammonium chloride], poly(3-sulfopropyl methacrylate), and poly(sodium methacrylate) (Chernyy et al. 2014). Furthermore, the counter-ions of the polyelectrolytes were exchanged with 13 ions (H^+, Li^+, Na^+, K^+, Ag^+, Ca^{2+}, La^{3+}, $C_{16}N^+$, F^-, Cl^-, BF_4^-, SO_4^{2-}, and $C_{12}SO_3^-$). Relative to unmodified glass, the Li^+ ions reduced the ice adhesion by 40% and 70% at −18 °C and −10 °C, respectively, and the Ag^+ ions reduced the ice adhesion by 80% at −10 °C. Also at −10 °C, the superhydrophilic polyelectrolyte brushes exhibited a lower anti-icing property than partially hydrophobic brushes such as poly(methyl methacrylate) and surfactant-exchanged polyelectrolyte brushes. To interpret their data, Chernyy et al. enhanced the quasi-liquid layer in the presence of highly hydrated ions at the interface. Although not fully proven, the chemical nature of the polymer/brushes might influence the structure of the interfacial water layers under this condition, changing the tendency of water to crystallize at the brush–water interface.

Heydari et al. investigated the effect of polymer structure (linear or bottle brush) on the melting points of the interfacial water layer and the resulting ice-adhesion strengths (Heydari et al. 2016). The bottle brush diblock copolymer, poly(ethylene oxide) (PEO)-poly(methacryloxyethyl trimethylammonium chloride) (METAC), substantially reduced the ice-adhesion shear from that of bare silica, by 90% at −5 °C and by over 50% even at −20 °C, these values are lower than liner PEO. This observation qualitatively agrees with differential scanning calorimetry data, which revealed a lower melting point of hydration water in the bottle-brush polymer structure than in the linear architecture.

Using cationic and anionic polymer brushes, Wang et al. also explored the effect of counter-ions on heterogeneous ice nucleation and the effect of hydration on ice formation, but did not test the ice-adhesion strengths. On highly hydrated polymer brush surfaces with hydrophilic counter-ions, the trapped freezable water molecules directionally moved toward the ice growth front, facilitating ice formation. In contrast, the dehydrated polymer brush surfaces with hydrophobic counter-ions inhibited ice propagation by forming a water-depletion region between the water droplets. The ice propagation rates on the two surface types differed by up to five orders of magnitude.

Chen et al. reported an alternative post-infusion method using self-lubricating interfacial water as the anti-icing coating (Chen et al. 2017). To design the self-lubricating icephobic coatings, they pre-infused polydimethylsiloxane (PDMS)-poly(ethylene glycol) (PEG) amphiphilic copolymers into a polymer matrix. The coatings exhibited lower ice-adhesion strengths (50 kPa) than those previously achieved on smooth, hydrophobic solid surfaces. The PEG component of the amphiphilic copolymer formed strong hydrogen bonds with the water molecules. Even when substantially cooled, the hydrogen-bonded water molecules at the surface did not freeze, thereby providing a self-lubricating, interfacial liquid-like layer that reduced the adhesion strength of ice to the surface. Similar result was also reported by Ozbay et al. (2015).

11.2.3.4 Swollen Crosslinked Polymers

Although most lubricated anti-icing coatings are prepared by the post-infusing method, the pre-infusing method is emerging as an attractive alternative with several advantages over the standard approach. First, this one-pot procedure requires no infusing process, so is scalable. Second, the swelling deformation induced by the post-infusing method can be disregarded. Finally, the composition of the infused oils and/or polymer backbone can be tuned, expanding the range of release phenomena of the coatings. In general, pre-infusion mixes the infusion lubricating liquid with a precursor solution of solid matrices. Zhu et al. (2013) developed an economical technique for preparing silicone-oil pre-infused polydimethylsiloxane (PDMS) coatings with different silicone-oil contents. The infusion of 20–40 wt.% of silicone oil into PDMS reduced the ice-adhesion tensile strength on aluminum by 95% (~40 kPa), which values are much lower than that of pure PDMS (290 kPa).

Golovin et al. (2016) and Beemer et al. (2016) reported a pre-infusing method fabricated by a similar synthetic pathway. By tailoring the amount/viscosity of the oils and the crosslinking density of the PDMS backbone, they prepared silicone-oil pre-infused PDMS with low ice-adhesion strength (<5 kPa) and high mechanical durability.

Applying the same pre-infusing concept, our group developed self-lubricating organogels (SLUGs), which spontaneously release lubricating liquids from inner gel matrices to their outer surfaces (Fig. 11.16) (Urata et al. 2015). This process, known as syneresis, is achieved by tuning the affinity between the infusing lubricating oil and the polymer backbone. By exploiting syneresis, a SLUG surface can infuse 600 vol.% of the lubricating oil toward the polymer backbone, dramatically reducing the ice-adhesion strength (to below 1 kPa). The SLUG surface also reduces the adhesion of contaminants (including water) and viscous emulsions (even after solidification) by forming a syneretic liquid layer on the topmost surface. We can also bestow reversible thermal-responsive syneretic properties on SLUGs by finely controlling the affinity between the lubricants and the polymer backbone. In our experiments, lubricants with high and low affinity were mixed to control the oil-release temperature. Depending on the composition of lubricant mixture, the lubricating oil releasing temperature was arbitrarily controlled between −15 and 35 °C. The thermal responsivity of the coatings reduces the unnecessary loss of oils at higher temperatures. Lubricating oil can only be released in an icing environment. When the environment warms, the oil is re-absorbed into the organogel matrix. In addition, the organogel surface can be spontaneously rendered superhy-

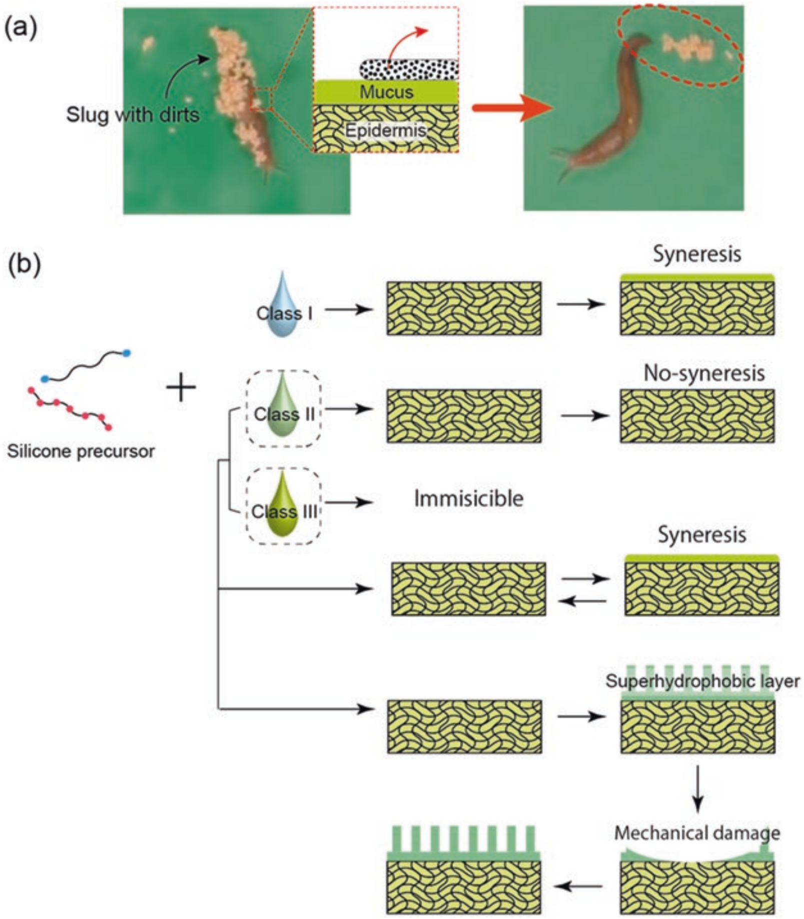

Fig. 11.16 Self-lubricating organogels (SLUGs): (**a**) Appearance of self-cleaning behavior of slug, (**b**) Schematic illustration of the preparation and properties of SLUGs

drophobic by selecting a reactive liquid, such as n-octadecyltrichlorosilane, as the organic phase. Superhydrophobicity is conferred by polycondensation reactions with humid air. The superhydrophobicity on this type of sample was also regenerated on newly formed surfaces after cutting. The controllability of the composition of the coatings is another advantages over the conventional post-infusing method.

11.2.3.5 Integration of Superhydrophobic Surfaces with Other Approach

Inspired by the toxin glands of tropical frogs, Rykaczewski et al. developed a hybrid approach combining superhydrophobic surfaces with a lubricant-infused matrix (Fig. 11.17) (Sun et al. 2015). This semi-passive coating consists of an outer porous superhydrophobic surface and a wick-like underlying dermis infused with

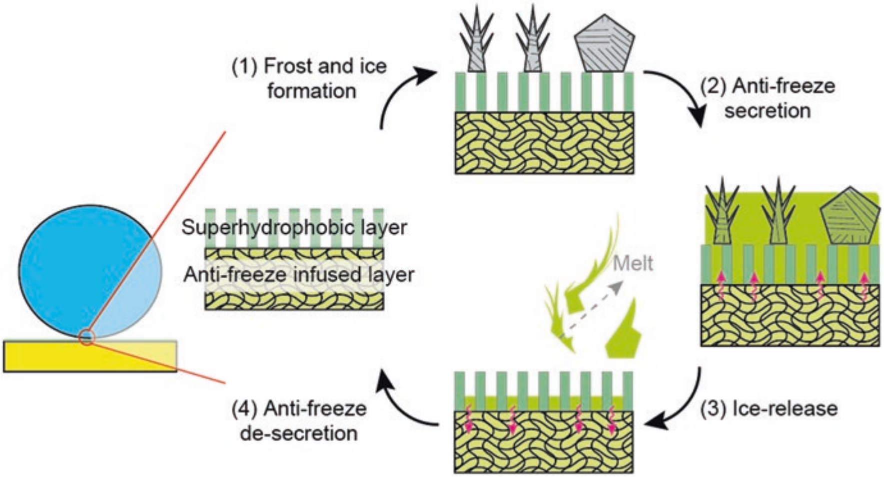

Fig. 11.17 Schematic illustration of anti-icing property inspired by the toxin glands of tropical frogs

antifreeze liquid. The surface superhydrophobic layer can delay and/or prevent glaze formation by repelling large impinging droplets. Consequently, when the surrounding environment is primed for frost and rime growth, the porosity of the bumpy superhydrophobic surface should enable microscale contact between the antifreeze and the penetrating liquid or solid water. This contact triggers the release of functional liquid that melts the ice and eventually removes it from the surface. Under extreme icing conditions, antifreeze release can also facilitate the removal of accumulated ice by creating a thin lubricating melt layer.

Matsubayashi et al. reported a new concept for anti-icing coating that integrates superhydrophobicity with electrothermogenic ability (Matsubayashi et al. 2016). An electrical conductive superhydrophobic coating was prepared from composite nanoparticles of the conductive poly(3,4-ethylenedioxythiophene):poly(styrenesulfonate) embedded in ethyl cyanoacrylate. Because of the combination of water repellency (static contact angle >160°) and efficient heating ability (260.8 °C cm^2/W), obtained coating possess super-repellency of supercooled water droplets and ability to melt formed frost (Fig. 11.18).

11.3 Summary

This chapter summarized a history and the recent progress of anti-icing coatings. Surface wettability, which is indicated by the static and/or dynamic contact angle of water on the surface, is believed to be highly correlated with the anti-icing properties of the surface. Therefore, superhydrophobic surfaces were expected to show excellent anti-icing performance by repelling water droplets before they froze.

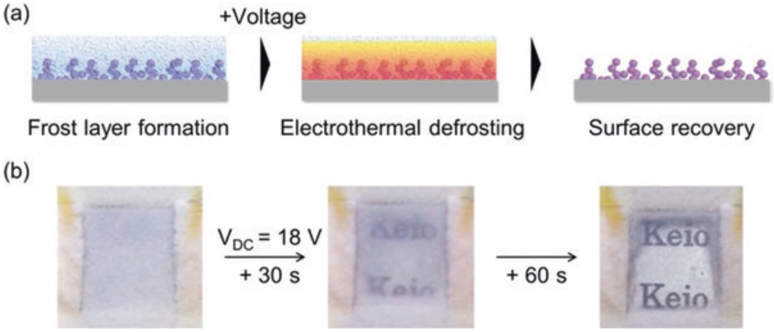

Fig. 11.18 (**a**) Cross-sectional schematic images illustrating the voltage-induced electrothermal defrosting process. (**b**) Defrosting of the conductive superhydrophobic coating performed before and after applying the DC voltage of 18 V. (Adapted with permission from (*ACS Appl. Mater. Interfaces 2016, 8, 24212-24220*) Copyright © 2016 American Chemical Society)

However, researchers realized that the anti-icing property of superhydrophobic surfaces are limited under low humidity conditions and unsuccessful or even detrimental in others.

Recently, anti-icing coatings with environmental adaptability and stimuli-responsivity have been emerging by introducing dynamic properties. Slippery liquid-infused porous surface (SLIPS), have been embraced and adapted by many researchers leading to various types of anti-icing coatings infused with lubricating liquids. Because of the presence of the mobile lubricating liquid layer, anti-icing coatings with extraordinary low ice adhesion strength (<10 kPa) were achieved by the SLIPS approach. The ice adhesion strength was greatly reduced by at least 5–6 orders of magnitude (2 Pa) compared to conventional anti-icing coatings in extreme cases. The surface lubricating layer can be replenished because of the mobility of lubricating liquids. As we reported, a thermoresponsive surface lubricating property was also achieved by a similar method. The drawback of the SLIPS strategy, that liquid-infused surfaces are prone to depletion of the infused liquid by evaporation or leaking, was resolved using hygroscopic materials. Hydrated surfaces with aqueous lubricating layers offer the advantage of simplicity and longevity because the surface lubricant water can be replenished semi permanently by atmospheric moisture. However, ice adhesion strength is not low enough compared to the SLIPS strategy. A semi-passive strategy, which amalgamates active and passive strategies, is another solution for adaptive anti-icing coatings. The combination of a superhydrophobic surface with an underlying antifreeze liquid infused layer overcomes the weakness of the superhydrophobic strategy.

Although passive ice-repellent coatings continue to be improved, each have limitations with regards to icephobicity, processability, cost, longevity, and durability. Understanding the successes and failures of each technology make it possible to design surfaces that incorporate features from multiple strategies to further improve versatility for adapting to changing environments. In addition to the material improvements, it is the lack of the common standard method to evaluate the anti-icing property that hinders the development of this field. Consensus between fundamental and practical researchers will be the best way to solve the problems caused by ice and snow accumulation which can cause huge economic loss and threaten the safety of lives.

Acknowledgements The author thanks A. Hozumi for beneficial discussion for this chapter. The author thanks C. Ottawa for her helpful comments on manuscript and Enago (www.enago.jp) for the English language review. The author thanks T.-E. Fang for kindly providing a picture after the freezing rain.

References

“Atmospheric icing of structures”. https://www.iso.org/standard/72443.html

Alizadeh A, Yamada M, Li R, Shang W, Otta S, Zhong S, Ge L, Dhinojwala A, Conway KR, Bahadur V et al (2012) Dynamics of ice nucleation on water repellent surfaces. Langmuir 28:3180–3186

Alizadeh A, Bahadur V, Kulkarni A, Yamada M, Ruud JA et al (2013) Hydrophobic surfaces for control and enhancement of water phase transitions. MRS Bull 38:407–411

Anand S, Paxson AT, Dhiman R, Smith JD, Varanasi KK et al (2012) Enhanced condensation on lubricant-impregnated nanotextured surfaces. ACS Nano 6:10122–10129

Andersson AK, Chapman L (2011) The impact of climate, change on winter road maintenance and traffic accidents, in west Midlands, UK. Accid Anal Prev 43:284–289

Andrey J, Olley R (1990) The relationship between weather and road safety: past and future research directions. Clim Bull 24:123–136

Antonini C, Innocenti M, Horn T, Marengo M, Amirfazli A et al (2011) Understanding the effect of superhydrophobic coatings on energy reduction in anti-icing systems. Cold Reg Sci Technol 67:58–67

Arianpour F, Farzaneh M, Kulinich SA (2013) Hydrophobic and ice-retarding properties of doped silicone rubber coatings. Appl Surf Sci 265:546–552

Ayres J, Simendinger WH, Balik CM (2007) Characterization of titanium alkoxide sol-gel systems designed for anti-icing coatings: I. Chemistry. J Coat Technol Res 4:463–471

Beemer DL, Wang W, Kota AK (2016) Durable gels with ultra-low adhesion to ice. J Mater Chem A 4:18253–18258

Bharathidasan T, Kumar SV, Bobji MS, Chakradhar RPS, Basu BJ et al (2014) Effect of wettability and surface roughness on ice adhesion strength of hydrophilic, hydrophobic and superhydrophobic surfaces. Appl Surf Sci 314:241–250

Boinovich LB, Emelyanenko AM (2013) Anti-icing potential of superhydrophobic coatings. Mendeleev Commun 23:3–10

Boinovich LB, Emelyanenko AM, Ivanov VK, Pashinin AS et al (2013) Durable icephobic coating for stainless steel. ACS Appl Mater Interfaces 5:2549–2554

Botta G, Cavaliere M, Holttinen H (1998) Ice accretion at aqua spruzza and its effects on wind turbine operation and loss of energy production. In: Proceedings of the international conference, wind energy production in cold climate, BOREAS IV, Hetta, Finland, March 31–April 2

Cao L, Jones AK, Sikka VK, Wu J, Gao D et al (2009) Anti-icing superhydrophobic coatings. Langmuir 25:12444–11244

Chatterson M, Carson Cook J (2008) “The effects of icing on commercial fishing vessels” an interactive qualifying project report for the United States Coast Guard

Chen J, Liu J, He M, Li K, Cui D, Zhang Q, Zeng X, Zhang Y, Wang J, Song Y et al (2012) Superhydrophobic surfaces cannot reduce ice adhesion. Appl Phys Lett 101:111603

Chen J, Dou RM, Cui DP, Zhang QL, Zhang YF, Xu FJ, Zhou X, Wang JJ, Song YL, Jiang L et al (2013) Robust prototypical anti-icing coatings with a self-lubricating liquid water layer between ice and substrate. ACS Appl Mater Interfaces 5:4026–4030

Chen J, Luo ZQ, Fan QR, Lv JY, Wang JJ et al (2014a) Anti-ice coating inspired by ice skating. Small 10:4693–4699

Chen L, Geissler A, Bonaccurso E, Zhang K et al (2014b) Transparent slippery surfaces made with sustainable porous cellulose lauroyl ester films. ACS Appl Mater Interfaces 6:6969–6976

Chen D, Gelenter MD, Hong M, Cohen RE, McKinley GH et al (2017) Icephobic surfaces induced by interfacial nonfrozen water. ACS Appl Mater Interfaces 9:4202–4214

Chernyy S, Jarn M, Shimizu K, Swerin A, Pedersen SU, Daasbjerg K, Makkonen L, Claesson P, Iruthayaraj J et al (2014) Superhydrophilic polyelectrolyte brush layers with imparted anti-icing properties: effect of counter ions. ACS Appl Mater Interfaces 6:6487–6496

Chu M, Scavuzzo R (1991) Adhesive shear strength of impact ice. AIAA J 29:1921–1926

Dalili N, Edrisy A, Carriveau R (2009) A review of surface, engineering issues critical to wind turbine performance. Renew Sust Energ Rev 13:428–438

Davis A, Yeong YH, Steele A, Bayer IS, Loth E et al (2014) Superhydrophobic nanocomposite surface topography and ice adhesion. ACS Appl Mater Interfaces 6:9272–9279

Dou R, Chen J, Zhang Y, Wang X, Cui D, Song Y, Jiang L, Wang J et al (2014) Anti-icing coating with an aqueous lubricating layer. ACS Appl Mater Interfaces 6:6998–7003

Eifert A, Paulssen D, Varanakkottu SN, Baier T, Hardt S et al (2014) Simple fabrication of robust water-repellent surfaces with low contact-angle hysteresis based on impregnation. Adv Mater Interfaces 1:1300138

Emery A, Siegel B (1990) Experimental measurements of the effects of frost formation on heat exchanger performance. Presented at Proceedings of AIAA/ASME thermo physics and heat transfer conference, 18–20 June, Seattle, WA

Erbil HY (2006) Surface chemistry of solid and liquid interfaces. Blackwell Publishing, Oxford

Erbil HY (2014) The debate on the dependence of apparent contact angles on drop contact area or three-phase contact line: a review. Surf Sci Rep 69:325–365

Erbil HY, Demirel AL, Avci Y, Mert O et al (2003) Transformation of a simple plastic into a superhydrophobic surface. Science 299:1377–1380

Farhadi S, Farzaneh M, Kulinich SA (2011) Anti-icing performance of superhydrophobic surfaces. Appl Surf Sci 257:6264–6269

Farzaneh M, Volat C, Leblond A (2008) Anti-icing and de-icing techniques for overhead lines. Springer, Dordrecht, pp 229–268

Fillion RM, Riahi AR, Edrisy A (2014) A review of icing prevention in photovoltaic devices by surface engineering. Renew Sust Energ Rev 32:797–809

Gent RW, Dart NP, Cansdale JT (2000) Aircraft icing. Philos Trans R Soc London, Ser A 358:2873–2911

Gerbino-Bevins BM (2011) Performance rating of de-icing chemicals for winter operations. Civil Engineering Theses, Dissertations, and Student Research 20. http://digitalcommons.unl.edu/civilengdiss/20

Golovin K, Kobaku SP, Lee DH, DiLoreto ET, Mabry JM, Tuteja A et al (2016) Designing durable icephobic surfaces. Sci Adv 2:e1501496

Guo P, Zheng Y, Wen M, Song C, Lin Y, Jiang L et al (2012) Icephobic/anti-icing properties of micro/nanostructured surfaces. Adv Mater 24:2642–2648

Hansen DJA (2011) Combating the effects of snow and ice on LED traffic signals: the city of green bay response. IMSA J 49: 38, 42–43, 45

He M, Wang J, Li H, Song Y et al (2011) Superhydrophobic surfaces to condensed micro-droplets at temperatures below the freezing point retard ice/frost formation. Soft Matter 7:3993–4000

He Z, Xie WJ, Liu Z, Liu G, Wang Z, Gao YQ, Wang J et al (2016) Tuning ice nucleation with counterions on polyelectrolyte brush surfaces. Sci Adv 2:e1600345

Heydari G, Tyrode E, Visnevskij C, Makuska R, Claesson PM et al (2016) Temperature-dependent deicing properties of electrostatically anchored branched brush layers of poly(ethylene oxide). Langmuir 32:4194–4202

Howard KW, Haynes J (1993) Groundwater contamination due to road de-icing chemicals-salt balance implications. Geosci Can 20:1–8

Huang L, Liu Z, Liu Y, Gou Y, Wang J et al (2009) Experimental study on frost release on fin-and-tube heat exchangers by use of a novel anti-frosting paint. Exp Thermal Fluid Sci 33:1049–1054

Irajizad P, Hasnain M, Farokhnia N, Sajadi SM, Ghasemi H et al (2016) Magnetic slippery extreme icephobic surfaces. Nat Commun 7:13395

Irajizad P, Ray S, Farokhnia N, Huasnain M, Baldelli S, Ghasemi H et al (2017) Remote droplet manipulation on self-healing thermally activated magnetic slippery surfaces. Adv Mater Interface 34:1700009

Jelle BP (2013) The challenge of removing snow downfall on photovoltaic solar cell roofs in order to maximize solar energy efficiency-research opportunities for the future. Energ Buildings 67:334–351

Jha KC, Anim-Danso E, Bekele S, Eason G, Tsige M et al (2016) On modulating interfacial structure towards improved anti-icing performances. Coatings 6:3

Jung S, Dorrestijn M, Raps D, Das A, Megaridis CM, Poulikakos D et al (2011) Are superhydrophobic surfaces best for icephobicity? Langmuir 27:3059–3066

Kato T, Nakajima A, Irie H et al (2004) Adhesion and sliding of wet snow on a superhydrophobic surface with hydrophilic channels. J Mater Sci 39:547–555

Kim P, Wong TS, Alvarenga J, Kreder MJ, Adorno-Martinez WE, Aizenberg J et al (2012) Liquid-infused nanostructured surfaces with extreme anti-ice and anti-frost performance. ACS Nano 6:6569–6577

Kim P, Kreder MJ, Alvarenga J, Aizenberg J et al (2013) Hierarchical or not? effect of the length scale and hierarchy of the surface roughness on omniphobicity of lubricant-infused substrates. Nano Lett 13:1793–1799

Kirillova A, Ionov L, Roisman IV, Synytska A et al (2016) Hybrid hairy Janus particles for anti-icing and de-icing surfaces: synergism of properties and effects. Chem Mater 28:6995–7005

Kloow L (2011) “High-speed train operation in winter climate”, ISBN: 978-91-7501-121-9

Kreder MJ, Alvarenga J, Kim P, Aizenberg J et al (2016) Design of anti-icing surfaces: smooth, textured or slippery? Nat Mater Rev 1:1–15

Kulinich SA, Farzaneh M (2009a) Ice adhesion on superhydrophobic surfaces. Appl Surf Sci 255:8153–8157

Kulinich SA, Farzaneh M (2009b) How wetting hysteresis influences ice adhesion strength on superhydrophobic surfaces. Langmuir 25:8854–8856

Kulinich SA, Farhadi S, Nose K, Du XW et al (2011) Superhydrophobic surfaces: are they really ice-repellent? Langmuir 27:25–29

Laforte JL, Allaire MA, Laflamme J (1998) State-of-the-art on power line de-icing. Atmos Res 46:143–158

Li K, Xu S, Shi W, He M, Li H, Li S, Zhou X, Wang J, Song Y et al (2012) Investigating the effects of solid surfaces on ice nucleation. Langmuir 28:10749–10754

Liu H, Zhang P, Liu M, Wang S, Jiang L et al (2013) Organogel-based thin films for self-cleaning on various surfaces. Adv Mater 25:4477–4481

Liu Q, Yang Y, Huang M, Zhou Y, Liu Y, Liang X et al (2015) Durability of a lubricant-infused electrospray silicon rubber surface as an anti-icing coating. Appl Surf Sci 346:68–76

Liu B, Zhang K, Tao C, Zhao Y, Li X, Zhu K, Yuan X (2016) Strategies for anti-icing: low surface energy or liquid-infused? RSC Adv 6:70251–70260

Liu Z, He Z, Lv J, Jin Y, Wu S, Liu G, Zhoud F, Wang J et al (2017) Ion-specific ice propagation behavior on polyelectrolyte brush surfaces. RSC Adv 7:840–844

Lu J, Jiang Z, Zhang H, Lei H, Li B, Fang Z et al (2009) Analysis of human power grid ice disaster accident in 2008. Autom Electr Power Syst 11:005

LV J, Song Y, Jiang L, Wang J (2014) Bio-inspired strategies for anti-icing. ACS Nano 8:3152–3169

Makkonen L, Laakso T, Marjaniemi M, Finstad KJ et al (2001) Modeling and prevention of ice accretion on wind turbines. Wind Eng 25:3–21

Marwitz J, Politovich M, Bernstein B et al (1997) Meteorological conditions associated with the ATR72 aircraft accident near Roselawn, Indiana, on 31 October 1994. Bull Am Meteorol Soc 78:41–52

Masoudi A, Irajizad P, Farokhnia N, Kashyap V, Ghasemi H et al (2017) Anti sliding magnetic slippery surfaces. ACS Appl Mater Interface 9:21025–21033

Matsubayashi T, Tenjimbayashi M, Manabe K et al (2016) Integrated anti-icing property of super-repellency and electrothermogenesis exhibited by PEDOT:PSS/cyanoacrylate composite nanoparticles. ACS Appl Mater Interfaces 8:24212–24220

Menini R, Ghalmi Z, Farzaneh M (2011) Highly resistant icephobic coatings on aluminum alloys. Cold Reg Sci Technol 65:65–69

Meuler AJ, Smith JD, Varanasi KK, Mabry JM, McKinley GH, Cohen RE et al (2010a) Relationships between water wettability and ice adhesion. ACS Appl Mater Interfaces 2:3100–3110

Meuler AJ, McKinley GH, Cohen RE (2010b) Exploiting topographical texture to impart icephobicity. ACS Nano 4:7048–7052

Mosher FR, Schaum D, Herbster C, Guinn T et al (2010) Analysis of causes of icing conditions which contributed to the crash of continental flight 3407. Presented at 14th conference on aviation, range, and aerospace meteorology, Atlanta, GA, 17–21 January, 2010

Nath S, Ahmadi SF, Boreyko JB (2017) A review of condensation frosting. Nanoscale Microscale Thermophys Eng 21:81–101

Nosonovsky M, Hejazi V (2012) Why superhydrophobic surfaces are not always icephobic. ACS Nano 6:8488–8491

Oberli L, Caruso D, Hall C, Fabretto M, Murphy PJ, Evans D et al (2014) Condensation and freezing of droplets on superhydrophobic surfaces. Adv Colloid Interf Sci 210:47–57

Ozbay S, Erbil HY (2015) Superhydrophobic and oleophobic surfaces obtained by graft copolymerization of perfluoroalkyl ethyl acrylate onto SBR rubber. Colloids Surf A Physicochem Eng Asp 481:537–546

Ozbay S, Yuceel C, Erbil HY (2015) Improved icephobic properties on surfaces with a hydrophilic lubricating liquid. ACS Appl Mater Interfaces 7:22067–22077

Parent O, Ilinca A (2011) Anti-icing and de-icing techniques for wind turbines: critical review. Cold Reg Sci Technol 65:88–96

Ruan M, Li W, Wang B, Deng B, Ma F, Yu Z et al (2013) Preparation and anti-icing behavior of superhydrophobic surfaces on aluminum alloy substrates. Langmuir 29:8482–8491

Rykaczewski K, Anand S, Subramanyam SB, Varanasi KK et al (2013) Mechanism of frost formation on lubricant-impregnated surfaces. Langmuir 29:5230–5238

Saito H, Takai K, Yamauchi G (1997) Water and ice-repellent coatings. Surf Coat Int 80:168–171

Sanzo D, Hecnar SJ (2006) Effects of road de-icing salt (NaCl) on larval wood frogs rana sylvatica. Environ Pollut 140:247–256

Schutzius TM, Jung S, Maitra T, Eberle P, Antonini C, Stamatopoulos C, Poulikakos D et al (2015) Physics of icing and rational design of surfaces with extraordinary icephobicity. Langmuir 31:4807–4821

Smith JD, Dhiman R, Anand S, Reza-Garduno E, Cohen RE, McKinley GH, Varanasi KK et al (2013) Droplet mobility on lubricant- impregnated surfaces. Soft Matter 9:1772–1780

Sojoudi H, Wang M, Boscher ND, McKinley GH, Gleason KK et al (2016) Durable and scalable icephobic surfaces: similarities and distinction from superhydrophobic surfaces. Soft Matter 12:1938–1963

Stone HA (2012) Ice-phobic surfaces that are wet. ACS Nano 6:6536–6540

Subramanyam SB, Rykaczewski K, Varanasi KK (2013) Ice adhesion on lubricant-impregnated textured surfaces. Langmuir 29:13414–13418

Sun X, Damel VG, Liu S, Rykaczewski K et al (2015) Bioinspired stimuli-responsive and antifreeze-secreting anti-icing coatings. Adv Mater Interfaces 2:1400479

Thomas SK, Cassoni RP, MacArthur CD (1996) Aircraft anti-icing and de-icing techniques and modeling. J Aircr 33:841–854

Urata C, Dunderdale GJ, England MW, Hozumi A et al (2015) Self-lubricating organogels (SLUGs) with exceptional syneresis-induced anti-sticking properties against viscous emulsions and ices. J Mater Chem A 3:12626–12630

Varanasi KK, Deng T, Smith JD, Hsu M, Bhate N et al (2010) Frost formation and ice adhesion on superhydrophobic surfaces. Appl Phys Lett 97:23410

Vogel N, Belisle RA, Hatton B, Wong TS, Aizenberg J et al (2013) Transparency and damage tolerance of patternable omniphobic lubricated surfaces based on inverse colloidal monolayers. Nat Commun 4:2176–2185

Wang F, Li C, Lv Y, Lv F, Du Y et al (2010) Ice accretion on superhydrophobic aluminum surfaces under low-temperature conditions. Cold Reg Sci Technol 62:29–33

Wang H, He G, Tian Q (2012a) Effects of nano-fluorocarbon coating on icing. Appl Surf Sci 258:7219–7224

Wang D, Tao T, Xu G, Luo A, Kang S et al (2012b) Experimental study on frosting suppression for a finned-tube evaporator using ultrasonic vibration. Exp Thermal Fluid Sci 36:1–11

Wang C, Zhang W, Siva A, Tiea D, Wynne KJ et al (2014a) Laboratory test for ice adhesion strength using commercial instrument. Langmuir 30:540–547

Wang C, Fuller T, Zhang W, Wynne KJ et al (2014b) Thickness dependence of ice removal stress for a polydimethylsiloxane nanocomposites: Sylgard 184. Langmuir 30:12819–12826

Williams DD, Williams NE, Cao Y (2000) Road salt contamination of groundwater in a major metropolitan area and development of a biological index to monitor its impact. Water Res 34:127–138

Wilson PW, Lu W, Xu H, Kim P, Kreder MJ, Alvarenga J, Aizenberg J et al (2013) Inhibition of ice nucleation by slippery liquid-infused porous surfaces (SLIPS). Phys Chem Chem Phys 15:581–585

Wong TS, Kang SH, Tang SKY, Smythe EJ, Hatton BD, Grinthal A, Aizenberg J et al (2011) Bioinspired self-repairing slippery surfaces with pressure-stable omniphobicity. Nature 477:443–447

Yang S, Xia Q, Zhu L, Xue J, Wang Q, Chen Q et al (2011) Research on the icephobic properties of fluoropolymer-based materials. Appl Surf Sci 257:4956–4962

Yin L, Xia Q, Xue J, Yang S, Wang Q, Chen Q et al (2010) In situ investigation of ice formation on surfaces with representative wettability. Appl Surf Sci 256:6764–6769

Yin X, Zhang Y, Wang D, Liu Z, Liu Y, Pei X, Yu B, Zhou F et al (2015) Integration of self-lubrication and near-infrared photothermogenesis for excellent anti-icing/deicing performance. Adv Funct Mater 25:4237–4245

Zhu L, Xue J, Wang Y, Chen Q, Ding J, Wang Q et al (2013) Icephobic coatings based on silicon-oil-infused polydimethylsiloxane. ACS Appl Mater Interfaces 5:4053–4062

Zou M, Beckford S, Wei R, Ellis C, Hatton G, Miller MA et al (2011) Effects of surface roughness and energy on ice adhesion strength. Appl Surf Sci 257:3786–3792

Chapter 12
Stimulus-Responsive Soft Surface/Interface Toward Applications in Adhesion, Sensor and Biomaterial

Syuji Fujii, Erica J. Wanless, Shin-ichi Yusa, Grant B. Webber, and Naoyuki Ishida

Abstract Surfaces/interfaces that respond to external stimulus, such as pH, salt, temperature, photo and electric field, represent one of the most active and emerging scientific research areas and have many unexplored applications. This evolving research field faces lots of exciting challenges regarding the design, fabrication and engineering of the surfaces/interfaces. In this chapter, the scientific progress in the area of stimulus-responsive gas-solid and liquid-solid surfaces/interfaces is highlighted. First, the synthetic methods of stimulus-responsive surfaces/interfaces by polymerization (grafting-from, grafting-to and grafting-through approaches) and adsorption of stimulus-responsive polymeric materials (micelles and microgels) are introduced. Then, the methods for characterization of such surfaces/interfaces,

---

S. Fujii (✉)
Department of Applied Chemistry, Faculty of Engineering, Osaka Institute of Technology, Osaka, Japan

Nanomaterials Microdevices Research Center, Osaka Institute of Technology, Osaka, Japan
e-mail: syuji.fujii@oit.ac.jp

E. J. Wanless
Discipline of Chemistry, University of Newcastle, Callaghan, NSW, Australia

Priority Research Centre for Advanced Particle Processing and Transport, University of Newcastle, Callaghan, NSW, Australia

S. Yusa
Department of Applied Chemistry, Graduate School of Engineering, University of Hyogo, Hyogo, Japan

G. B. Webber
Discipline of Chemical Engineering, University of Newcastle, Callaghan, NSW, Australia

Priority Research Centre for Advanced Particle Processing and Transport, University of Newcastle, Callaghan, NSW, Australia

N. Ishida
Division of Applied Chemistry, Graduate School of Natural Science and Technology, Okayama University, Okayama, Japan

A. Hozumi et al. (eds.), *Stimuli-Responsive Dewetting/Wetting Smart Surfaces and Interfaces*, Biologically-Inspired Systems 11,
https://doi.org/10.1007/978-3-319-92654-4_12

including spectroscopic and radiation methods, are discussed followed by descriptions of their applications in adhesion, lubrication, sensor, actuator, drug delivery and cell culture. Finally, challenges and future trends in this exciting field are also discussed. Tight interdisciplinary research is crucial to continue developing science and engineering of the stimulus-responsive surfaces/interfaces.

Keywords Contact angle · Electrostatic interactions · Polymer grafting · Layer-by-layer · Polyelectrolyte · Self-assembly · Stimuli response

12.1 Introduction

Stimulus-responsive synthetic materials, which are able to respond to external or internal stimulus, represent one of the most exciting and active scientific areas with a wide range of potential applications (Stuart et al. 2010; Yoshida and Lahann 2008). Consequently, stimulus-responsive polymers have received enormous attention in the last decade (Brown et al. 2013; Mendes 2008; Liu and Urban 2010; Chen et al. 2010; Ahn et al. 2008; Pasparakis and Vamvakaki 2011; Urban 2011). Mother Nature is a source of inspiration for the design and development of the stimulus-responsive materials using elegant responsive systems based on polymers. Scientists have been trying to mimic nature in designing and engineering "smart" synthetic materials which can reveal responses, adapting to small amplitude changes in their environment (e.g. pH, temperature, light, ion strength, electric or magnetic field, mechanical force, enzymatic or redox reactions) to exhibit changes in shape and mechanical, wetting or optical properties.

Introduction of stimulus-responsive components to surfaces/interfaces can allow them to controllably alter their properties on demand upon the application of an external stimulus, while the substrate characteristics (e.g. shape and size) are maintained. These surfaces/interfaces are of significant interest of the scientific community due to their wide variety of potential applications, including "lab-on-chip" and microfluidic devices, controlled drug delivery, sensor development, enzyme immobilization, bioseparation, controlled cell adhesion and self-cleaning surfaces.

This chapter highlights the scientific progress in the area of stimulus-responsive gas-solid and liquid-solid surfaces/interfaces. We first introduce the synthetic methods of stimulus-responsive surfaces/interfaces by polymerization and adsorption of stimulus-responsive polymeric materials. Then, the methods for characterization of such surfaces/interfaces are discussed followed by descriptions of applications of these stimulus-responsive surfaces/interfaces.

12.2 Synthesis of Stimulus-Responsive Soft Surfaces/Interfaces

12.2.1 Synthesis Methods

Materials are sometimes surface designed to provide them with suitable properties for desired end-use applications. In this sense, surface modifications via well-defined polymer chains play an important role. Apart from physical adsorption methods, solid surfaces can be modified by three kinds of polymer-based approaches (Fig. 12.1):

1. "Grafting from" method: Polymerization is performed from initiating points immobilized on the surface of the solid (i.e., surface-initiated graft polymerization).
2. "Grafting to" method: Pre-synthesized polymers containing anchoring groups are reacted with the solid surface.
3. "Grafting through" method: Polymerization is performed in the presence of polymerizable groups previously immobilized on the solid surface.

"Grafting through" methods are rarely used as compared to "grafting from" and "grafting to" approaches. In "grafting from" methods, the initiators are immobilized on the solid surface, and the polymer chains are subsequently propagated from the initiating points. It is possible to immobilize well-defined polymer brushes on solid surfaces with high density using controlled/living radical polymerization (CLRP) techniques. On the other hand, in "grafting to" methods, the concentration of polymer on the solid surface increases upon adsorption, creating a barrier to subsequent adsorption. Thus, the possibility that new polymer chains reach the surface against the concentration gradient decreases exponentially. Therefore, the corresponding "grafting to" methods cannot reach beyond certain limits of grafting density.

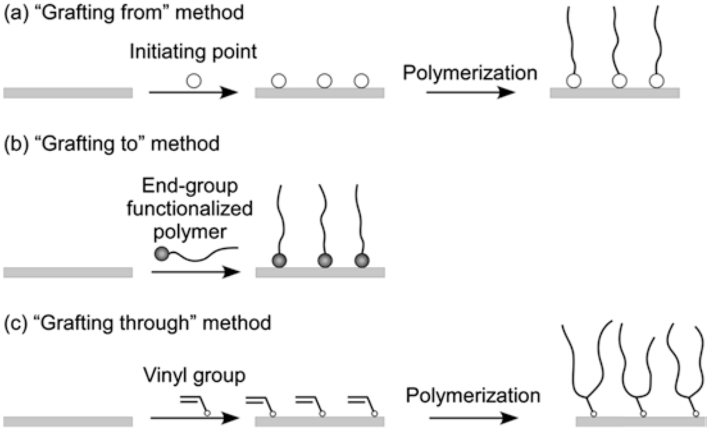

Fig. 12.1 Surface graft polymerization methods

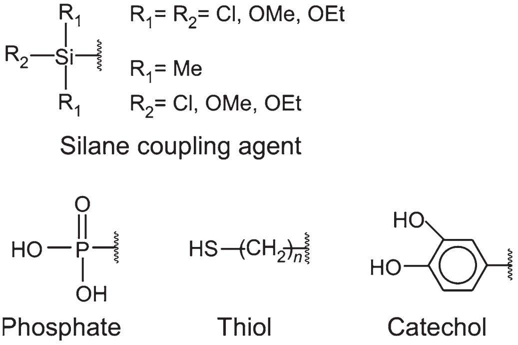

Fig. 12.2 Typical anchoring groups used for graft polymerization

All grafting methods require the presence of "anchoring groups" to bind the polymer to the substrate surface. Figure 12.2 shows typical examples of chemical structures containing anchoring groups. Silane coupling agents can be surface bound to silica, glass, silicon and metal oxide materials, among others. On the other hand, phosphoric acid, thiol and catechol groups can be attached to metal, gold, and other surfaces, respectively. "Grafting to" approaches are carried out by connecting the polymer end (or pendent group) with the substrate surface. In "grafting from" approaches, the initiators are first immobilized to the substrate surface using the anchoring group and polymerization is subsequently initiated from the starting points on the substrate. In "grafting through" approaches, anchoring groups containing polymerizable functional groups are first immobilized on the substrate surface and graft copolymerization is subsequently performed to immobilize the polymer chains.

12.2.1.1 Controlled/Living Radical Polymerization

Controlled/living radical polymerization (CLRP) allows precise control of the primary structure of a polymer chain. CLRP is typically applied to prepare various novel functional polymer materials (Möller and Matyjaszewski 2012; Tsarevski and Sumerlin 2013). As in the case of anionic and cationic polymerizations, CLRP allows control of the molecular weight and molecular weight distribution while also being suitable for the synthesis of block copolymer and functionalization of polymer chain end groups. In addition, CLRP presents a number of advantages such as utilization of various initiator designs and functional monomers, compatibility with a wide range of solvents, and resistance to impurities. CLRP has developed and become widely adopted faster than other living radical polymerization systems because of its simplicity and versatility. CLRP is essentially a radical polymerization method. Therefore, unlike living systems based on ionic polymerization, CLRP involves a termination reaction. The polymerization conditions need to be optimized for achieving the desired controlled polymer design.

Fig. 12.3 Reaction mechanism of the CLRP process

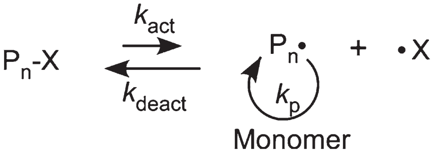

CLRP is conceptually based (Fig. 12.3) on the reversible protection of the propagating radicals (P_n) with protective groups (X). The covalently bonded P_n-X group is called the dormant species. The polymer chain is evenly and gradually grown by repetitive deprotection (i.e., activation of P_n), monomer addition (i.e., chain propagation), and protection (deactivation of P_n) steps.

Several CLRP methods are available using different protective groups. For example, atom transfer radical polymerization uses a halogen as a protective group and a transition metal as a catalyst for performing the activation/deactivation cycles (Matyjaszewski 2012). Reversible addition/fragmentation chain transfer (RAFT) radical polymerization uses a dithioester functionality as a protective group (Hill et al. 2015). Nitroxide radical mediated radial polymerization (NMRP) uses a nitroxyl functionality as a protective group (Husseman et al. 1999). Organotellurium mediated radical polymerization (TERP) uses an organotellurium compound as a protective group (Yamago 2009). Each of these methods has its own characteristics.

Atom Transfer Radical Polymerization (ATRP)

Atom transfer radical polymerization (ATRP) was first reported by Matyjaszewski et al. (Wang and Matyjaszewski 1995; Matyjaszewski and Xia 2001; Coessens et al. 2001) and Sawamoto et al. (Kato et al. 1995; Kamigaito et al. 2004) and is currently used for preparing various polymer architectures such as block copolymers, graft copolymers, star polymers, hyperbranched polymer, etc. ATRP proceeds via a radical polymerization, or "living polymerization", because the carbon–halogen bonds are reversibly activated by a transition metal complex to generate P_n. Recently, an activators continuously regenerated by electron transfer ATRP (ARGET-ATRP) method has been reported to control the radical polymerization process by using small amounts of copper as a catalyst (Jakubowski and Matyjaszewski 2005; Oh et al. 2006). For detailed information on ATRP, refer to the excellent reviews reported by Matyjaszewski and co-workers (Möller and Matyjaszewski 2012; Matyjaszewski 2012; Coessens et al. 2001).

In ATRP, the transition metal (Mt^n) acts on the carbon–halogen bond (P_n-X) of the initiator, and the halogen atom is then temporarily displaced to the transition metal via single electron oxidation of the metal. Propagating radicals (P_n•) are simultaneously generated, thereby allowing polymerization by addition of monomers (Fig. 12.4). Ligands (L) are typically used to increase the solubility of the transition metal. The process of generating P_n• is reversible. The halogen atom returns to P_n• to generate a carbon–halogen bond upon reduction of the high

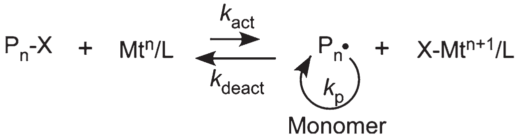

Fig. 12.4 Atom transfer radical polymerization (ATRP) reaction mechanism: P_n-X is the dormant species, Mt^n and Mt^{n+1} are metals with their respective valence, X refers to halogen, L is the ligand, P_n• is the propagating radical, k_{act}, k_{eact}, and k_p are the rate constants of the activation, deactivation, and propagation processes

oxidation state transition metal. P_n• are reversibly generated from species with carbon–halogen covalent bonds (i.e., dormant species). The exchange reaction between the carbon radical species and the dormant species is fast. The bimolecular termination reaction between P_n• is restricted since the equilibrium keeps the concentration of these species low. Therefore, both the molecular weight and the molecular weight distribution can be controlled, and the polymerization proceeds following a "living" mechanism.

In ATRP, the selection of the halogen and the transition metal complex species serving as an initiator and a single electron oxidation catalyst, respectively, is important. Thus, depending on the monomer, it is necessary to use appropriate transition metal complex and halogen-containing initiator species. ATRP allows controlled polymerization of various kinds of monomers such as methacrylate, acrylate, styrene, acrylamide, acrylonitrile, etc. Apart from being applied to a wide range of monomers, ATRP also allows polymerization to progress from initiator species containing carbon–halogen bonds, which are activated by small amounts of a transition metal complex. ATRP is widely used in "grafting from" methods since the introduction of initiating points on the surface can be readily achieved.

Reversible Addition-Fragmentation Chain Transfer Polymerization (RAFT) As revealed by Chiefari et al., narrow molecular weight distribution polymers can be produced by polymerization of styrene and methacrylate monomers in the presence of a chain transfer agent (CTA) having a dithioester structure (Chiefari et al. 1998). This CLRP method is denoted as the RAFT radical polymerization method, and its mechanism can be described as follows. First, the primary radicals originating from the radical initiators are added to the monomer to generate the propagating radicals. The propagating radicals are added to the C=S bond in the CTA to produce the intermediate radicals. Dissociation of the C–S bond takes places with the production of a macro-CTA species containing a terminal thiocarbonylthio group and a new propagating radical. Although the new propagating radical reacts adding monomers to the polymer chain, polymerization proceeds in accordance with a "living mechanism" with the suppression of side reactions since the macro-CTA compound is an inactivated dormant species.

Figure 12.5 shows the detailed reaction mechanism of the RAFT polymerization process. CTAs (**1**) for RAFT radical polymerization contain thiocarbonylthio functionalities (S=C–S) with R and Z as substrate groups. These R and Z substrate groups influence the polymerization rate and control the obtained polymers. The R group is cleaved from CTA to give a radical (R•) which reacts with the monomer to generate propagating radicals (P_n• and P_m•). The structure of the Z group affects the stability of intermediate radicals (**2** and **5**). Various kinds of CTA have been reported. CTA can be classified by the structure of the Z group into dithioester (Z = Ph, CH_2Ph, CH_3, etc.), trithiocarbonate (Z = SCH_3, SC_2H_5, $SC_{12}H_{25}$, etc.), xanthate (Z = OPh, PC_2H_5, etc.), and dithiocarbamate (Z = $N(C_2H_5)_2$, pyrrole, etc.). In order to prepare polymers with well-controlled structure via RAFT radical polymerization, an appropriate combination of monomer and CTA must be selected. Despite the absence of a general rule, the following can be used as a guide; dithioester and trithiocarbonate CTAs can be used to control the polymerization of conjugated monomers such as styrene, methacrylate, acrylate, etc., while xanthate and dithiocarbamate CTAs can be used to control the polymerization of unconjugated monomers such as vinyl acetate, *N*-vinyl pyrrolidone, *N*-vinyl carbazole, etc.

The mechanism of RAFT polymerization (Fig. 12.5) involves five elementary reactions: (a) initiation and propagation; (b) addition to the CTA (pre-equilibrium); (c) reinitiation; (d) chain equilibrium by reversible addition/fragmentation (main equilibrium); and (e) termination. The initiation reaction (Fig. 12.5a) allows the radical polymerization to start via heat- or light-induced cleavage of the initiator to generate primary radicals as well as conventional free-radical polymerization. Other

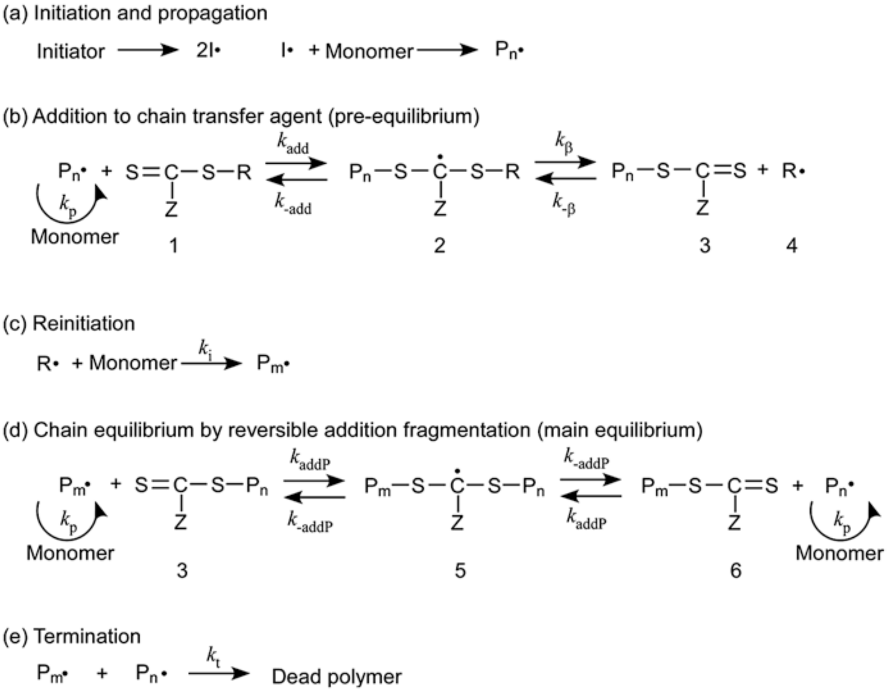

Fig. 12.5 Reaction mechanism of the RAFT radical polymerization process

systems such as redox, UV-light, plasma, γ-ray irradiation can be applied for initiation. The primary and propagating radicals are easily added to the CTA, and the propagation reaction gradually progresses via reversible addition and fragmentation reactions.

In conventional free-radical polymerization, the primary radicals (I•) generated from the initiator are added to the monomer to generate the propagating radicals (P_n• and P_m•). However, in the RAFT process, the propagating radicals are mostly generated from R• (**4**), which is fragmented from the CTA. At the early stage of RAFT polymerization, the propagating radicals are reversibly added to the CTA to give intermediate radicals (**2**). Reversible β-cleavage of the intermediate radicals (**2**) generate R• (**4**) (i.e., chain transfer reaction). In controlled RAFT radical polymerization processes, polymerization is mainly initiated from R• (**4**) since the concentration of the initiator is typically lower than that of the CTA, and the reactivity of the CTA is significantly higher than that of the monomer. Therefore, almost all propagating chains are generated from R• (**4**). When R• (**4**) formation is low at the early polymerization stage or it presents hindered reinitiation (Fig. 12.5c), an induction period is often observed. The process involving consumption of CTA (**1**) and reversible fragmentation of the intermediate radical (**2**) to generate re-initiatable R• (**4**) (Fig. 12.5b) is called pre-equilibrium.

In the pre-equilibrium step, a polymer chain (**3**) containing a thiocarbonylthio group at the chain end is generated as a result of the chain transfer reaction from the propagating radical to the CTA. The polymer chain (**3**) is denoted as dormant because the corresponding propagating radical is capped with the CTA. The polymer chain (**3**) is a macro-CTA. Main equilibrium (Fig. 12.5d) is established by reversible addition and fragmentation reactions between the propagating chains (P_n• and P_m•) and the macro-CTA (**3** and **6**) species. In the main equilibrium step, the propagating radicals are reversibly added either to the monomer (to elongate the chain) or to the macro-CTA dormant species. The intermediate radicals (**2** and **5**) do not react with the propagating radicals and monomers in the pre- and main equilibrium steps because they are stabilized by steric hindrance (Kwak et al. 2002).

In controlled RAFT radical polymerization, the following conditions are satisfied: (a) pre-equilibrium is established fast enough; (b) reinitiation by fragmented R• (**4**) takes place efficiently; (c) the total number of macro-CTA (**3** and **6**) and intermediate radical (**5**) species (dormant species at main equilibrium) is significantly larger than that of the propagating radicals (P_n• and P_m•). Therefore, the possibility of undergoing termination reaction (Fig. 12.5e) via reactions between the propagating radicals is reduced. In fact, the molecular weight of the polymer obtained via RAFT radical polymerization increases linearly with the monomer conversion. The molecular weight distribution of the obtained polymer is narrow. Block copolymers can be obtained under appropriate conditions. These results indicate that the influence of the radical polymerization termination reaction, commonly observed in ordinary radical polymerization processes, is extremely low in this case such that the polymerization proceeds following a "living" mechanism. Most of the polymers obtained via RAFT radical polymerization can be recovered as a macro-CTA species containing a thiocarbonylthio group at the polymer chain end. To perform RAFT radical

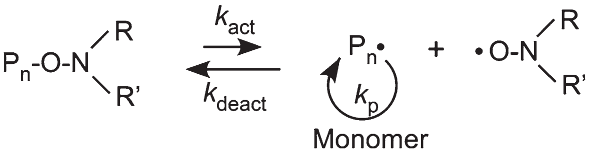

Fig. 12.6 Reaction mechanism of nitroxide-mediated radical polymerization (NMP)

polymerization from the substrate surface, it is necessary to convert this functional group on the surface of the CTA. Monomer should polymerize in the presence of the CTA-immobilized substrate to prepare the polymer brush.

Nitroxide-Mediated Radical Polymerization (NMP)
Nitroxide radicals such as 2,2,6,6-tetramethylpiperidine 1-oxyl (TEMPO) and its derivatives are stable radicals that do not react with oxygen radicals and vinyl monomers. However, these radicals readily react with alkyl radicals to generate alkoxyamines. Conventionally, these stable radicals have been used as spin-trapping agents and polymerization inhibitors.

Polymers with various structures have been recently synthesized via NMP (Hawker et al. 2001; Fischer and Radom 2001). TEMPO derivatives are often used in NMP because of their favorable equilibrium constants and activation reaction rates. An alkoxyamine-type initiator was found to control the polymerization. End group-functionalized polymers were synthesized using alkoxyamines containing hydroxyl, amine, and ester functional groups.

A radical polymerization method using alkoxyamine as an initiator was proposed in the 1980s to prepare oligomers (Rizzardo 1987). The relatively weak C–ON bond in alkoxyamine generates alkyl and nitroxide (X•) radicals via heating-induced homolysis (Fig. 12.6). The alkyl radicals can initiate polymerization to generate propagating radicals (P_n•) in the presence of the monomers, thereby starting the propagating reaction. Competitive binding reaction takes place between the alkyl and nitroxide radicals to generate alkoxyamine (P_n-X). When the P_n-X undergoes reversible cleavage and addition reactions, the degree of polymerization is expected to progress with the conversion such that the obtained polymer has a narrow molecular weight distribution (Johnson et al. 1990). Georges et al. reported that narrow molecular weight distribution polystyrene can be obtained by polymerization of styrene in the presence of benzyl peroxide (BPO) and TEMPO at high temperature (Georges et al. 1990).

12.2.1.2 "Grafting from" Approach

Among the various CLRP methods, surface-initiated ATRP (SI-ATRP) is the most studied technique (Pyun et al. 2003). To achieve activation/deactivation cycles at a frequency sufficiently high to control polymerization, it is effective to add a low molecular-weight dormant compound (i.e., a free initiator) (Ejaz et al. 1998). This method can be applied to various SI-ATRP systems. It was experimentally confirmed that the grafted polymer chains have similar molecular weight and molecular

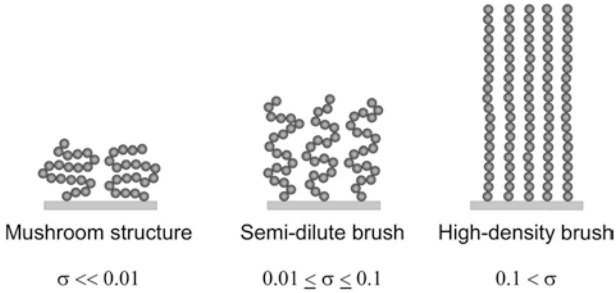

Fig. 12.7 Relationship between the graft density of the polymer brush (σ) and the structure of the polymer chains

weight distribution as compared to the free polymer chains produced from the free initiator in solution (Tsujii et al. 2006). Therefore, the characteristics of the free polymer can be used to characterize the grafted polymer chains.

After immobilization of the initiating groups on the surface of various materials, CLRP can be performed to prepare high-density polymer brushes with a well-defined structure. Polymer brushes can be classified into semi-dilute and high-density brushes depending on their grafting density (σ). High-density polymer brushes can be achieved via CLRP because of the high efficiency of the surface initiation and uniform propagation steps of the polymer chains (Tsujii et al. 2006). Generally, the polymer chains in good solvent form a random coil structure. When one chain end group in the polymer chain is immobilized on the surface of the substrate, the polymer chains form a mushroom-like structure (Fig. 12.7). When the graft chains start to overlap each other with increasing σ, the grafted polymer chains extend in the direction normal to the interface to avoid chain-chain interactions. These polymer chains are called polymer brushes, while polymer brushes with relatively low σ are denoted as semi-dilute brushes.

At $\sigma = 0.7$ chains/nm^2, the thickness of a swollen film formed from poly(methyl methacrylate) (PMMA) brushes reached 80–90% of the fully expanded chain length, and the grafted polymer chains were oriented in the normal direction. Conventional semi-dilute brushes present thicknesses up to 20–30% of the fully expanded polymer chain length. The swelling of polymer brushes results from the balance between the osmotic pressure (derived from mixed entropy changes of the solvent and the polymer) and the extension stress caused by the configuration enthalpic changes produced by chain elongation. Consequently, polymer brushes are antagonized between large osmotic pressure and extension stress (Tsujii et al. 2006).

As an example of surface-initiated graft polymerization via CLRP, graft polymerization of methyl methacrylate (MMA) from the surface of silica gel nanoparticles via ATRP was proposed (Ohno et al. 2010). First, an ATRP initiator containing a triethoxysilyl group was immobilized on the surface of silica gel nanoparticles with a diameter of 15 nm. ATRP of MMA was performed in *N,N*-dimethylformamide

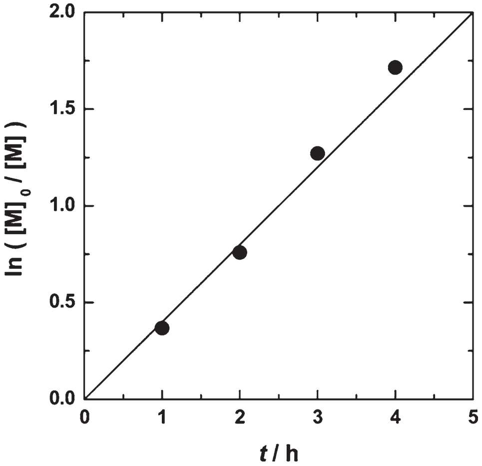

Fig. 12.8 ln([M]$_0$/[M]) vs *t* plot for the solution polymerization of methyl methacrylate (MMA) in *N*,*N*-dimethylformamide (10 wt%) at 70 °C with initiator-fixed silica nanoparticles of an average diameter 15 nm (0.5 wt%): [MMA]$_0$/[ethyl 2-bromoisobutylate]$_0$/[Cu^{I}Cl]$_0$/[4,4′-dinonyl-2,2′-bipyridine]$_0$ = 600/1/2/4. (Copyright 2010, reproduced from Ohno et al. (2010) with permission from the ACS)

(DMF) using a copper complex as a catalyst in the presence of free initiators. The addition of free initiators to the polymerization system allowed adjustment of the concentration of the capping agents (i.e., divalent copper halide in ATRP) via a sustained radical effect (Fischer 1997). The first-order plot of the polymerization of MMA generated a straight line passing through the origin (Fig. 12.8). This observation suggests that the concentration of the propagating radicals in the polymerization system remained constant with the polymerization time. The number-average molecular weight (M_n) of the free polymer (PMMA produced in DMF) was plotted against the conversion (Fig. 12.9). The experimental M_n values increased with the conversion and were close to the theoretical M_n values assuming polymerization following a “living” mechanism. The molecular weight distribution (M_w/M_n) was relatively narrow. After the graft polymerization of MMA, the silica gel nanoparticles were treated with hydrogen fluoride to break the PMMA chains. The M_n values of the cleaved PMMA polymer were plotted against the conversion, and the obtained values were close to those dictated by theory. The M_w/M_n values for the cleaved PMMA polymer were relatively narrow. Thus, the molecular properties of the graft polymer and the free polymer chains are almost identical.

The hydrodynamic diameter (D_h) of PMMA-SiNP in acetone is plotted against the M_n of the PMMA-grafted chains (Fig. 12.10). The D_h value at the most compact core–shell structure can be calculated from the density of bulk PMMA (Ohno et al. 2003). The D_h value at the fully stretched core–shell structure can be calculated based on the fully expanded planar zig-zag PMMA chain. These D_h values are also plotted against the experimental values obtained for PMMA-SiNP. The experimen-

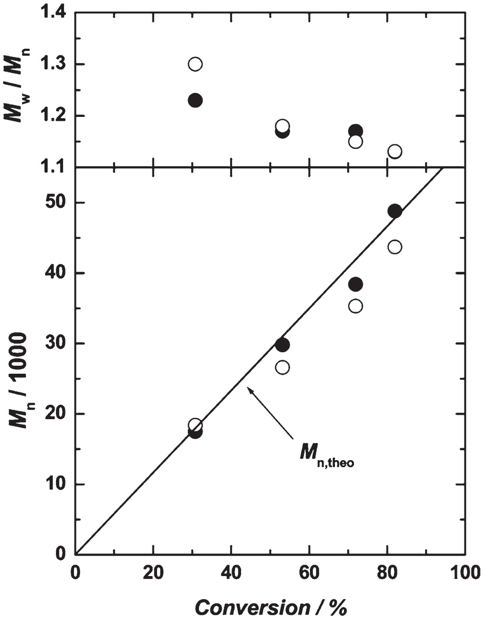

Fig. 12.9 Evolution of the number-average molecular weight (M_n) and the polydispersity index (M_w/M_n) of graft (○) and free (●) polymers as a function of the monomer conversion for a solution polymerization process of methyl methacrylate (MMA) in *N,N*-dimethyl formamide (10 wt%) at 70 °C with initiator-fixed silica nanoparticles of an average diameter of 15 nm (0.5 wt%): $[\text{MMA}]_0$/[ethyl 2-bromoisobutylate]$_0$/$[\text{Cu}^{\text{I}}\text{Cl}]_0$/[4,4′-dinonyl-2,2′-bipyridine]$_0$ = 600/1/2/4 (Copyright 2010, reproduced from Ohno et al. (2010) with permission from the ACS)

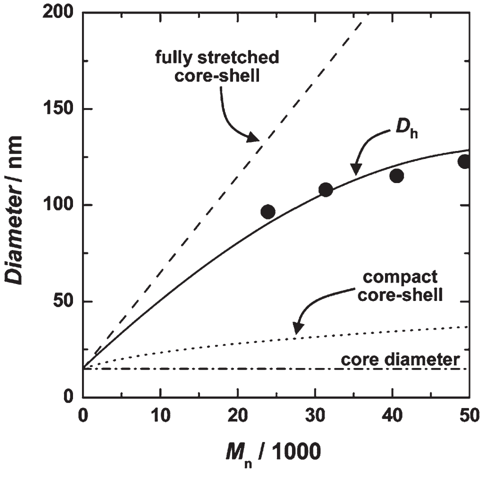

Fig. 12.10 Average hydrodynamic diameter (D_h) of silica nanoparticles (SiNPs) grafted with poly(methyl methacrylate) (PMMA-SiNP) as a function of M_n of the PMMA graft chains. The D_h values were determined by dynamic light scattering in dilute acetone suspension at 30 °C. The diameters of the SiNP cores are 15 nm. The broken and dotted lines represent the diameters of the fully stretched and compact core–shell models, respectively. (Copyright 2010, reproduced from Ohno et al. (2010) with permission from the ACS)

tal D_h values are intermediate between those of the compact core–shell and the fully stretched models.

In plasma graft polymerization, the substrates are treated with plasma, and the monomer is subsequently polymerized from the surface of the substrate to contact the monomer and the surface. Gas is excited either electrically or magnetically to generate low-temperature plasma containing electrons, radical, ions, neutral particles and ultra-violet. Although the plasma treatment of polymers is a combination of multiple effects, the role of each component is unknown. However, low-temperature plasma treatment is widely used on polymers for surface treatments, etching method on microfabrication, and so on (Denes and Manolache 2004; Laroussi and Akan 2007). In plasma graft polymerization, the substrate is first irradiated with plasma to generate radical species. Subsequently, the substrate is contacted with the monomer solution to propagate the polymer chains from the surface. Plasma does not alter the bulk properties of the substrate, since this treatment affects only to the surface of the substrate (Hirotsu and Isayama 1989; Iwata et al. 1991). Therefore, the polymer chains can be grafted to the substrate surface remaining after the plasma treatment.

12.2.1.3 "Grafting to" Approach

Polymers can be covalently attached on the surface of substrates by "grafting from" and "grafting to" methods (Advicula et al. 2004; Zhao and Brittain 2000). In "grafting to" methods, polymer chains with a desired length are first prepared then surface immobilized. The "grafting to" method suffers from low grafting density owing to the excluded volume effect of the polymer brushes. However, the "grafting to" method is convenient to prepare mixed polymer brushes with controlled ratios (Huang et al. 2004). Although the polymer chains prepared by the "grafting to" approach can be fully characterized before grafting, this characterization is more difficult in the case of "grafting from" methods. In solution, the distances separating the surface grafting points are comparable to the polymer chain coil size. Therefore, "mushrooms" with low grafting density are formed on the surface. When the brush height increases linearly with the polymer molecular weight, a "strongly stretched" regime is reached (de Gennes 1980). The "strongly stretched" regime is difficult to achieve using the "grafting to" approach. To increase the graft density of the "grafting to" methods, polymer coils are grafted to the surface under shrunk conditions. Coil shrinking can be achieved via melting in the absence of solvent (Taylor and Jones 2010, 2013) or using less favorable solvents (e.g., θ solvents) (Kingshott et al. 2002). These situations change the scaling low of the polymer chain size and its molecular weight.

Minko et al. (2002) prepared binary brushes on a silicon wafer functionalized with 3-glycidoxypropyl trimethoxysilane. Polystyrene and poly(2-vinylpyridine) with terminal carboxylic acid groups were spin-coated on the substrate. Graft reactions were carried out to increase temperature above the glass transition temperature

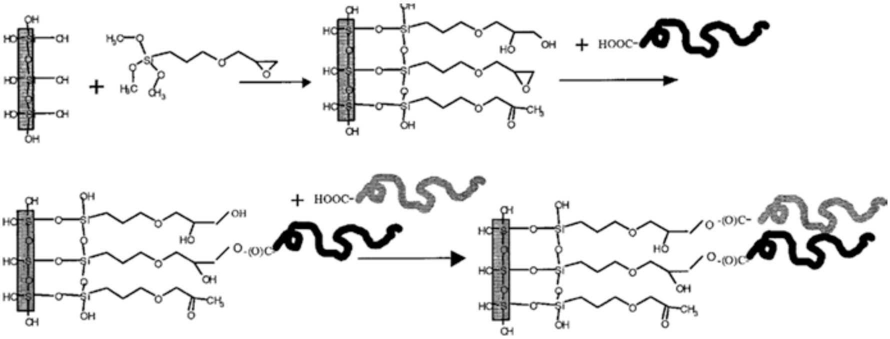

Fig. 12.11 Schematic representation of the synthesis of binary brushes of polystyrene (black) and poly(2-vinylpyridine) (gray) chains on 3-glycidoxypropyl trimethoxysilane immobilized on a silicon surface. (Copyright 2002, reproduced from Minko et al. (2002) with permission from the ACS)

of the polymers to react between the epoxy groups on the substrate and the carboxylic acid groups at the chain end (Fig. 12.11). The composition of the brush chains can be tuned by controlling the time and temperature of the grafting reaction.

In θ solvents, the excluded volume interactions of the polymer coils are suppressed. In the case of polyethylene glycol (PEG), a θ point can be achieved by controlling the temperature and the ionic strength. Hung and Penn (2005) reported polystyrene grafted to an epoxy immobilized surface in cyclohexane that is a poor solvent. Polystyrene brushes with weight-average molecular weight of 14,500 g/mol can be prepared with a grafting density up to 0.08 chains/nm^2. Emilsson et al. (2015) prepared PEG brushes on a gold substrate by "grafting to" of PEG with a terminal thiol group in a 0.9 M Na_2SO_4 solution at room temperature. This method is a "cloud point grafting"-like strategy that does not require an increase in the temperature. High-density PEG brushes with a molecular weight of 10,000 g/mol (0.4 chains/nm^2) can be readily achieved by this method. Murray et al. (Wuelfing et al. 1998) prepared PEG-functionalized gold nanoparticles using a "grafting to" approach. Corbierre et al. (2001, 2004) prepared styrene-functionalized gold nanoparticles containing thiol-terminated polystyrene.

Biocompatible poly(2-oxazoline)s showed a sharp-transition thermo-responsive behavior, and the transition temperature can be readily controlled within a broad temperature range (Hoogenboom 2009). Agrawal et al. (2012) prepared carboxyl-terminated poly(2-isopropyl-2-oxazoline) via ring-opening cationic polymerization (Fig. 12.12). Substrate-grafted poly(2-isopropyl-2-oxazoline) brushes can be used for the surface stabilization of nanoparticles (e.g., gold). Gold nanoparticles are known to have excellent catalytic and optical properties, thereby rendering a wide applicability to this system in a variety of potential areas (e.g., displays, sensors, catalysis, and optical filters).

Copper-catalyzed alkyne-azide click (CuAAC) reaction, the most used "click" reaction, is useful for the "grafting to" approach. CuAAC reactions proceed rapidly with high conversions under mild conditions and without side reactions and byproducts (Kolb et al. 2001). Furthermore, the resulting aromatic triazole ring is stable.

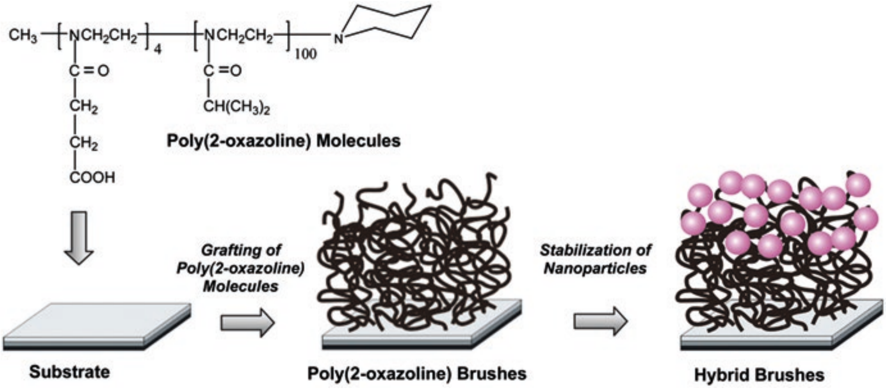

Fig. 12.12 Schematic illustration of the fabrication of poly(2-oxazoline) brushes and the stabilization of gold nanoparticles thereon. (Copyright 2012, reproduced from Agrawal et al. (2012) with permission from the ACS)

Fig. 12.13 Surface modification of a Ge substrate with a partially azidified silane self-assembled monolayer (SAM) followed by click reaction with alkyne-terminated polymers. (Copyright 2012, reproduced from Zhang et al. (2016) with permission from the ACS)

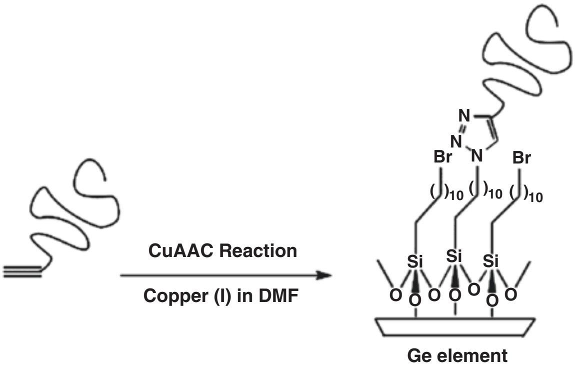

Zhang et al. (2016) prepared alkyne-terminated poly(*n*-butyl methacrylate) and polystyrene via ATRP using an alkyne-functional initiator (Fig. 12.13). The surface of the substrate was first coated with a monolayer of pure bromosilane, and the Ge silanized substrate was subsequently immersed in a saturated sodium azide solution to convert 33% of bromosilane into azide. The alkyne-terminated polymers reacted with the azide-functionalized Ge surface via a CuAAC reaction to prepare polymer brushes.

12.2.1.4 "Grafting Through" Approach

The "grafting through" polymerization technique is used for the copolymerization of free monomers in solution and polymerizable units (mostly vinyl units) attached to the surface of substrates. Free polymer chains are initially formed in solution and subsequently reacted with the surface-attached monomers. Therefore, the polymer chains are covalently bonded to the substrate surface during polymerization. Since the propagating chains are attached to the surface-attached polymerizable units, a polymer graft layer is formed on the substrate surface. The polymerization mechanism was studied by experimental and theoretical methods (Datta and Genzer 2013, 2016). Despite this approach being widely used in industrial applications, the "grafting through" method has not been extensively studied from a scientific point of view and details on the mechanism are not well known. Laible studied the attachment of polymer layers on the surface of solid oxides such as silica and various inorganic pigments through surface-attached monomers (Laible and Hamann 1980). Chaimberg and Cohen (1994) developed a model describing the overall reaction kinetics of the layer formation. Bialk et al. (2002) reported that the integration of more than one surface-bound monomer was not favored.

Sarsabili et al. (2013) prepared polystyrene/MCM-41 nanocomposites by a "grafting through" approach. MCM-41 is composed of mesoporous silica nanoparticles. The polymerization was carried out by RAFT. The MCM-41 was modified with a methacrylate group using 3-methacryloxypropyldimethylchlorosilane. In the "grafting through" approach, broad M_w/M_n is obtained, with cross-linking between the polymer chains. Kalajahi et al. (2011) prepared poly(methyl methacrylate) (PMMA) grafted on multi-walled carbon nanotubes (MWCNTs) by a "grafting through" method. MWCNTs were modified with methacrylate groups by multi-step modification processes. MWCNTs were treated under acid conditions to obtain carboxylated MWCNTs. Subsequently, the carboxyl groups were reacted with 1,4-butanediol to obtain hydroxyl groups-modified MWCNTs. Finally, hydroxyl groups-modified MWCNTs were reacted with 3-methacryloxypropyldimethylchlorosilane to obtain methacrylate-functionalized MWCNTs. Methyl methacrylate was polymerized in the presence of methacrylate-functionalized MWCNTs by a "grafting through" approach to prepare MWCNT/PMMA nanocomposites.

Sobani et al. (2013) prepared aerogel/polystyrene nanocomposites via a RAFT radical polymerization technique. The silica aerogel nanoparticles were modified by 3-methacryloxylpropyldimethylchlorosilane containing vinyl bonds in its structure. A styrene monomer was polymerized in the presence of modified silica aerogel nanoparticles via RAFT (i.e., a "grafting through" approach). The molecular weight increased with the conversion, thereby suggesting that the polymerization followed a "living" mechanism. The molecular weight of the aerogel-grafted polystyrene was lower than that of the free dispersed polystyrene. M_w/M_n of the polymer chains increased upon the addition of silica aerogel nanoparticles. Fazli et al. (2015) prepared PMMA-grafted hydrophilic silica aerogel nanoparticles. The surface of the hydrophilic silica aerogel nanoparticles was modified by 3-(trimethoxysilyl)propyl methacrylate. MMA was polymerized in the presence of modified silica aerogel nanoparticles via ATRP to obtain PMMA-grafted silica aerogel nanoparticles by a "grafting through" approach.

Henze et al. (2014) prepared polystyrene-grafted silica gel using a "grafting through" approach. Methacrylate moieties were immobilized on the surface of the silica gel via a silane coupling group (Fig. 12.14). During the polymerization of styrene in the presence of the modified silica gel in a conventional radical polymer-

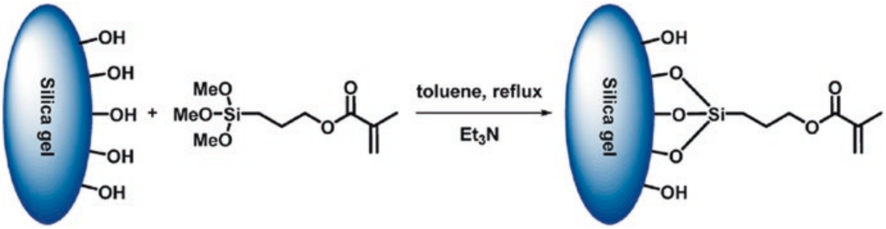

Fig. 12.14 Covalent attachment of silane containing polymerizable moieties to the surface of a silica gel: reaction of 3-methacryloylpropyl trimethoxysilane with the hydroxyl groups of the silica gel. (Copyright 2014, reproduced from Fazli et al. (2015) with permission from the ACS)

ization, free polymer chains were formed in the solution. During chain growth, the surface-attached monomers become integrated in the polymer chains, leading instantaneously to covalent linking of the growing polymer chains on the silica gel surface. The progressive attachment of more polymer chains resulted in the formation of a polymer layer attached on the surface of the silica gel.

12.2.1.5 Adsorption of Polymer Micelle/Microgel

Introduction of stimulus-responsive character to a solid substrate can be attained by adsorption of stimulus-responsive polymer micelle/microgel onto the substrate. Advantages offered by stimulus-responsive micelle/microgel layers adsorbed on the substrates over alternative polymeric molecular coatings include (1) the large volume change, (2) the relative ease of synthesis of stimulus-responsive polymeric micelles and microgels by self-assembly of block copolymers and emulsion or dispersion polymerization, and (3) facile layer preparation by spontaneous deposition from micelle/microgel dispersions. Micelle/microgel layers on the substrates can also offer advantages over layer-by-layer polyelectrolyte films for applications that require control over the lateral morphology or layer thickness. The driving forces for the micelle/microgel to adsorb onto the substrate are electrostatic interactions and van der Waals forces. However this approach faces similar disadvantages as the “grafting to” approach; notably the grafting density is limited due to the adsorption process.

12.2.2 Synthesis Methods of Stimulus-Responsive Surfaces/Interfaces

12.2.2.1 pH-Responsive Surfaces

Poly(acrylic acid) (PAA) shows pH-responsive behavior in water. Under acidic conditions, the pendent carboxyl groups are protonated. Under basic conditions, the pendent carboxyl groups are ionized by deprotonation; the polymer chains then

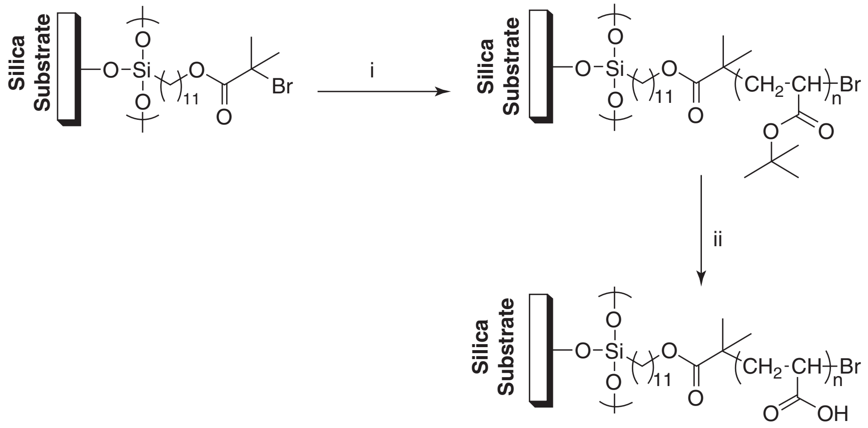

i) tert-Butyl acrylate, acetone, CuBr, PMDETA, 2-bromo-ethylisobutyrate, 60 °C, 4 h.
ii) 190 - 200 °C, 30 min.

Fig. 12.15 Synthetic route for the formation of poly(acrylic acid) (PAA) brushes on a silica substrate. (Copyright 2006, reproduced from Treat et al. (2006) with permission from ACS)

expand due to electrostatic repulsion. pH-responsive polymer brushes are the subject of intense research effort.

Treat et al. (2006) prepared PAA brushes on a flat silica surface via surface-initiated atom transfer radical polymerization (SI-ATRP) of *tert*-butyl acrylate (Fig. 12.15). The pendent *tert*-butyl groups were deprotected using a chemical-free strategy, i.e., heating for only 30 min. Conventional acid hydrolysis of the pendent groups of polymer brushes is difficult because the anchoring group contains an ester group. As the pendent *tert*-butyl groups were deprotected, the thickness of the polymer layer and the surface energy of the polymer film decreased. The PAA-grafted substrate was immersed in water, then the pH was adjusted from acidic to basic. The brush height values were 16 and 26 nm at pH 2 and 9, respectively. Under basic conditions, the pendent carboxylic acid groups become deprotonated, and the brush thickness increased due to Coulombic repulsion forces.

The effects of graft density on the conformational changes of PAA polymer brushes at different pH values have been studied (Wu et al. 2007). The swelling behavior of PAA brushes depends on their graft densities at pH 4 and 5.8. The swelling behavior is independent of the graft density when the pendent carboxyl groups are completely ionized at pH 10. At pH 10, the PAA polymer brushes can act as strong polyelectrolytes.

A pH-responsive polymer has been grafted on the surface of silica particles via surface-initiated reversible addition-fragmentation chain transfer (SI-RAFT) radical polymerization (Fig. 12.16) (Inoue et al. 2011). First, an amino group was immobilized on the surface of silica particles with diameters of 11 μm using 3-aminopropyltriethoxysilane. A chain transfer agent (CTA) containing an activated carboxyl group was reacted with the amino groups to obtain CTA-immobilized silica particles (CTA-SiO_2). 6-(Acrylamido)hexanoic acid (AaH) was polymerized in

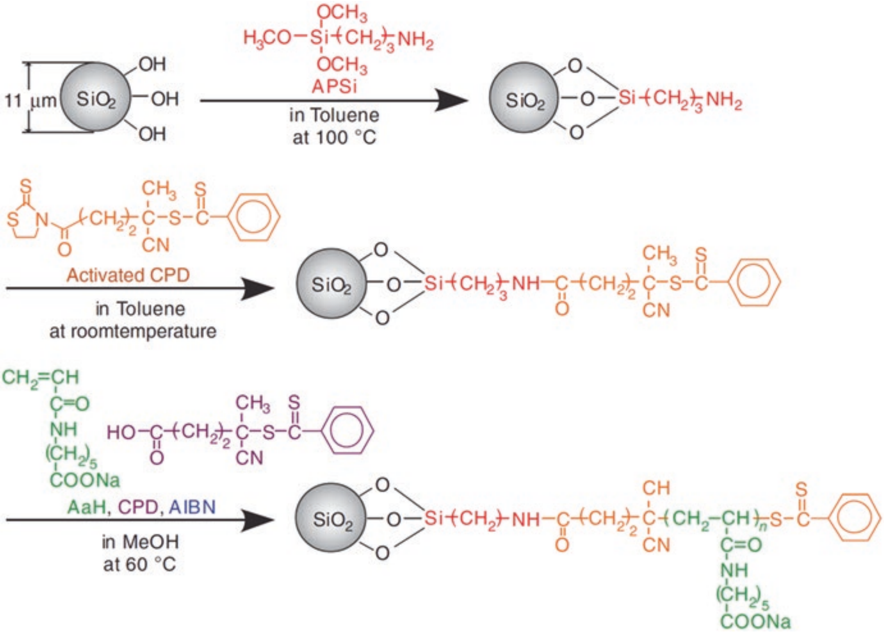

Fig. 12.16 Synthetic route of pH-responsive poly(6-(acrylamido)hexanoate)-grafted silica particles (PAaH-SiO_2) via reversible addition-fragmentation chain transfer (RAFT)-controlled radical polymerization. (Copyright 2011, reproduced from Inoue et al. (2011) with permission from Springer Nature)

the presence of CTA-SiO_2 and free CTA in methanol. After the polymerization, poly(6-(acrylamide)hexanoic acid) (PAaH)-grafted silica particles (PAaH-SiO_2) were isolated from free PAaH. The molecular weight distribution (M_w/M_n) of the free PAaH was narrow (1.07). The graft density of PAaH was 0.28 chains/nm^2, estimated by thermogravimetric analysis (TGA). At pH 3 in water, PAaH-SiO_2 was flocculated due to hydrophobic interactions between the pendent protonated hydrophobic hexanoic acid groups of the grafted PAaH chains. At pH 10, PAaH-SiO_2 was dispersed due to electrostatic repulsion between the pendent ionized hexanoate anions of the grafted PAaH chains.

Basic polymers, such as poly(2-(dimethylamino)ethyl methacrylate) (PDMAEMA), also exhibit pH-responsive behavior. In acidic aqueous solution, the tertiary amine groups are ionized by protonation, while in basic solution (above the effective pK_a) they are unionized due to deprotonation. Therefore, under acidic conditions, the thickness of the protonated PDMAEMA brush layer increases; under basic conditions, the thickness decreases. The pH-responsive behavior of PDMAEMA brushes is opposite to that of PAA brushes. Sanjuan et al. (2007) prepared dense PDMAEMA brushes with a relatively low molecular weight distribution on the surface of a silicon substrate by a “grafting from” approach using SI-ATRP. The pH-dependent swelling behavior of the polymer brushes was studied

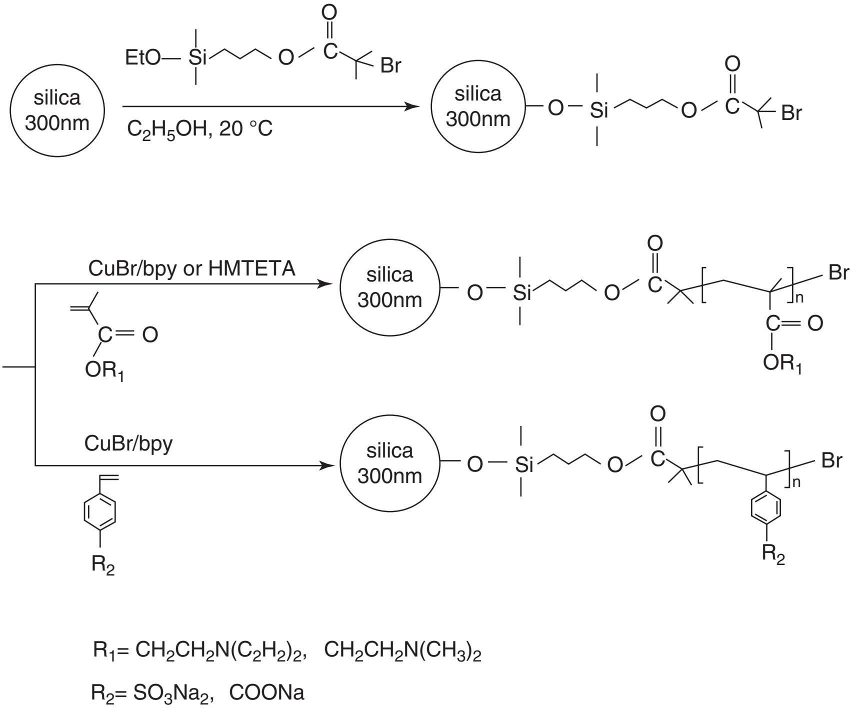

Fig. 12.17 Schematic representation of the synthesis of polyelectrolyte-grafted silica particles via surface-initiated atom transfer radical polymerization (SI-ATRP). (Copyright 2003, reproduced from Chen et al. (2003) with permission from Elsevier)

using neutron reflectivity and ellipsometry. The high-graft-density PDMAEMA brushes swelled at lower pH values. This corresponds to a shift in pK_a with increasing grafting density.

Chen et al. (2003) prepared polyelectrolyte-grafted silica particles using initiator-immobilized monodisperse silica particles 304 nm in diameter by SI-ATRP (Fig. 12.17). Four ionic vinyl monomers, namely sodium 4-styrenesulfonate, sodium 4-vinylbenzoate, DMAEMA, and 2-(diethylamino)ethyl methacrylate (DEAEMA), were used. The TGA results indicated that the polymer contents of the silica particles changed from 0.6 to 6% in weight. Generally, polyelectrolyte brushes on silica particles enhance the colloidal stabilities of the particles against flocculation in water due to the introduction of steric and electrostatic repulsions. When acidic polymer brushes were grafted on the silica particles, the size estimated from dynamic light scattering (DLS) measurements increased due to hydrophobic interactions between the protonated graft polymer chains. In contrast, when basic polymer brushes were grafted on the silica particles, their sizes increased at basic pH values. The sizes of the PDMAEMA-grafted polystyrene latex particles varied with pH (Zhang et al. 2006).

Li et al. (2008a) prepared poly(4-vinylpyridine) (PVP) grafted gold nanoparticles via SI-ATRP. At pH < 3.1, the PVP brushes were positively charged due to the formation of pyridinium ions. Therefore, the polymer chains extended due to electrostatic repulsions, and the resulting highly charged particles were colloidally stable. At pH 3.8–4.4, the pendent pyridinium groups were readily deprotonated; the polymer chains then collapsed onto the gold particles. Therefore, the particle size decreased by approximately 50%. At pH values above 5.5, the gold nanoparticles aggregated. The two-stage red shift of the gold surface plasmon resonance response is attributed to the polymer collapse and to particle agglomeration.

Introduction of pH-responsive character can be also achieved by adsorption of polymer micelles/microgels. Ma et al. have studied adsorption of shell cross-linked polymer micelles consisting of PAA-*b*-poly(methyl acrylate) (PAA-PMA) onto solid substrate (Ma and Wooley 2000). Atomic force microscopy (AFM) studies indicated that the PAA-PMA micelles formed 2D arrays with long-range order, when deposited onto mica substrate from aqueous solution (Ma et al. 2001). This long-range order could be controlled by varying the micelle diameter and the micelle charge density. AFM height-image measurements confirmed that some flattening occurred when these micelles were dried on the substrates.

The group of Armes, Wanless, Webber, Sakai and Biggs synthesized PDMAEMA-poly(2-(diethylamino)ethyl methacrylate) (PDEAEMA) copolymers and selectively quaternized the PDMAEMA block to varying degrees. These copolymers exist as free unimers in aqueous solution at low pH and form micelles, with PDEAEMA core and PDMAEMA corona morphology, at high pH. They conducted a series of studies on adsorption of PDMAEMA-*b*-PDEAEMA micelles onto substrates using atomic force microscope (AFM) and quartz crystal microbalance (Webber et al. 2002, 2004, 2005a, 2006a, b). The AFM studies indicate that the unquaternized PDMAEMA-*b*-PDEAEMA micelles adsorbed in an ordered monolayer, with localized regions exhibiting hexagonal close-packing. Long-range structural order is also evident, and this ordering was resilient to the replacement of the bulk micelle dispersions with pure water. The mean centre-to-centre distance of the micelle increased with the degree of quaternization. While the lightly quaternized PDMAEMA-*b*-PDEAEMA micelle monolayer exhibited some degree of order, the highly quaternized micelles formed much more random surface structures. In all cases, these adsorbed layers were not affected by replacing the bulk micelle dispersions with water at pH 9. Interestingly, different morphological responses were observed from the surface-adsorbed micelles depending on the quaternization degree by changing the pH of the overlying aqueous solution. Unquaternized PDMAEMA-*b*-PDEAEMA micelles open and close their PDEAEMA core at low and high pHs, respectively, and this change was reversible due to the formation of localized polymer brushes (Fig. 12.18). On the other hand, lightly quaternized micelles showed irreversible changes, and highly quaternized micelle monolayers are disrupted by the addition of acid. They rationalized these differences by electrostatic arguments. The difference of pH-responsive behavior was also investigated by quartz crystal microbalance studies, which showed that the adsorbed mass of the micelles decreased with increasing degree of quaternization.

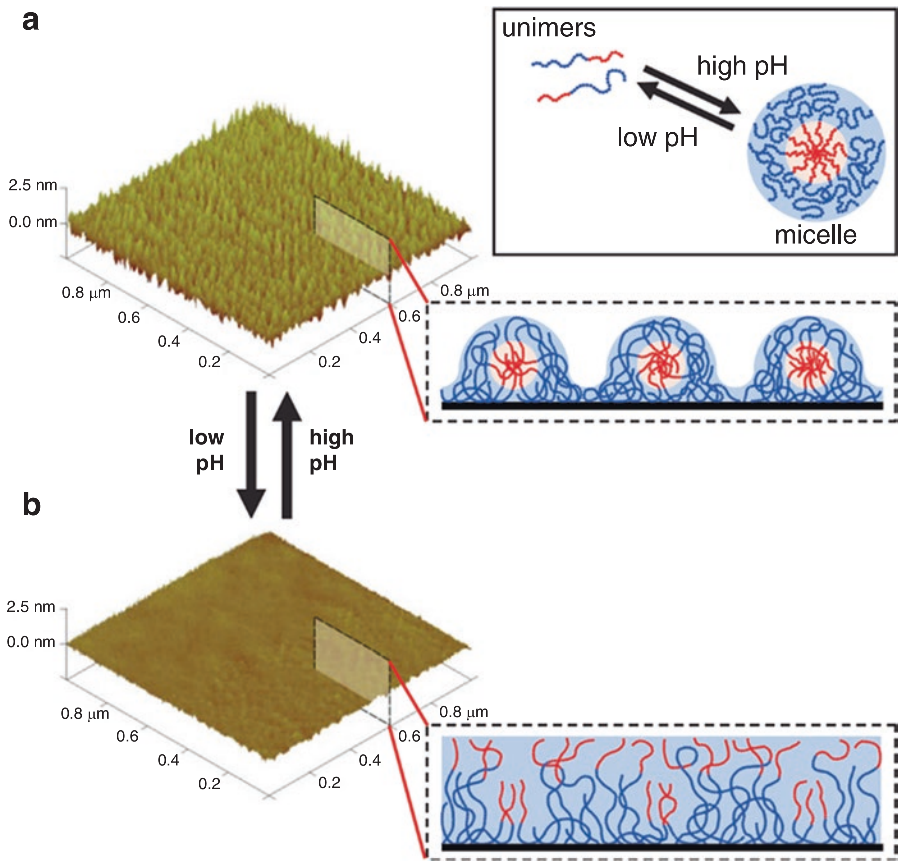

Fig. 12.18 Schematic representation of the pH-responsive behavior of a monolayer of adsorbed PDMAEMA-*b*-PDEAEMA micelles at the mica-aqueous solution interface (A) > pH 7 and (B) < pH 7. The inset shows the analogous behavior of the same diblock copolymer in bulk solution, whereby micellar dissociation occurs at low pH. (Copyright 2004, reproduced from Webber et al. (2004) with permission from Wiley)

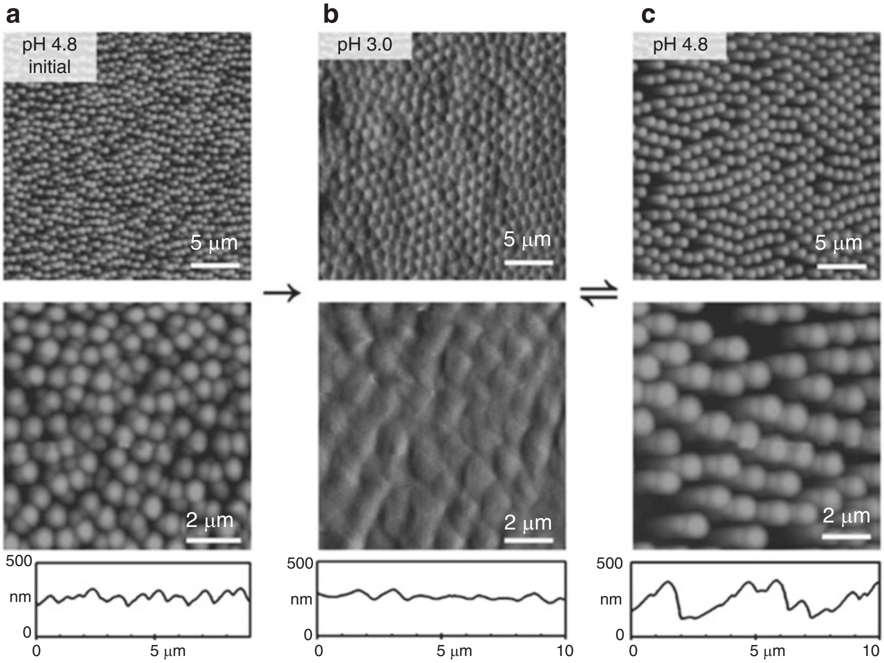

Fig. 12.19 In situ AFM images of P2VP particles on a planar silica surface: (a) initial P2VP latex at pH 4.8 (initial adsorption after rinsing), (b) swollen P2VP microgel at pH 3.0 and (c) deswollen P2VP particles upon returning to pH 4.8. The sample pH was cycled several times between (b) pH 3.0 and (c) pH 4.8, and the morphology was fully reversible (as noted by the equilibrium arrows). (Copyright 2007, reproduced from Fitzgerald et al. (2007) with permission from RSC)

Fitzgerald et al. studied the formation and morphological changes of a pH-responsive microgel layer adsorbed on silica and mica substrates using AFM (Fig. 12.19) (Fitzgerald et al. 2007). First, submicrometer-sized lightly cross-linked poly(2-vinylpyridine) (P2VP) particles were adsorbed in their non-solvated particulate form at pH 4.8 to produce a structurally-disordered monolayer that covers the entire substrate. In situ exposure of this P2VP particle layer on the substrate to acid induced a non-swollen particle-to-microgel transition at pH 3.0. This particle swelling (along with some degree of desorption) produced a uniform, swollen microgel film with localized hexagonal packing. The microgel partially deswelled to form individual oblate spheroidal P2VP latex particles when the solution pH was returned to 4.8, which retained the localized order previously induced by swelling. The swelling and deswelling of this P2VP layer on the substrate was reversible during subsequent pH cycles, and no further desorption was observed. The initial adsorbed amount was less than that predicted by the standard Random Sequential Adsorption model (RSA) for hard particle adsorption, which was explained by the unexpected deformation of these P2VP particles due to their strong electrostatic attraction to the solid–liquid interface.

12.2.2.2 Salt-Responsive Surfaces

Polyelectrolyte brushes respond not only to pH but also to concentrations of various ions in solution. Polyelectrolyte brushes grafted to the surfaces of substrates have been studied both experimentally and theoretically (Gong et al. 2007). The behaviors of strong and weak polyelectrolyte brushes vary with the concentration of added salts. At high salt concentrations, the polyelectrolyte brushes behave like uncharged polymer brushes due to screening effects. This state is called "neutral brush". At lower salt concentrations, the ionic concentrations inside and outside of the polymer brushes change; this results in electrostatic interactions that lead to expansion of the brushes. This state is called "salted brush". When the salt concentration decreases further, the polyelectrolyte brushes achieve the "osmotic brush" state. The thickness of the osmotic brushes is fully expanded to release all counter ions. The screening effects of weak polyelectrolyte brushes are different from those of strong polyelectrolyte brushes. The salt concentrations inside and outside the weak polyelectrolyte brushes are almost identical in the neutral brush and salted brush regions. Namely, the ionization state of a weak polyelectrolyte brush near the substrate surface is the same as that of the bulk polymer chains in aqueous solution. The salt concentration near the substrate surface is higher than that outside the polymer brushes in the osmotic brush region. The experimental thickness values of PAA brush layers at varying salt concentrations agree with theoretical values. Fully deprotonated PAA brushes on the flat silica surface respond to changes in salt concentration (Currie et al. 2000). The brush height decreases from 22 to 17 nm with increasing NaCl concentration. These phenomena agree with the end-to-end distances of the polyelectrolyte chains estimated from molecular dynamics simulations (Stevens and Plimptom 1998).

Huck et al. (Azzaroni et al. 2007) studied the effects of counter ions of pendent quaternary amines on the properties and structures of poly(2-(methacryloyloxy) ethyl-trimethylammonium chloride) (PMETAC) brushes. The properties of wettable polymer brushes are sensitive to the nature of the counter anion. As the original chloride anions were replaced with other anions, the wettability of the polymer brushes increased as follows: $ClO_4^- > SNC^- > I^- > Br^- > Cl^- > PO_4^{3-}$. This order is related to the Hofmeister series.

Higaki et al. (2017) prepared poly(sulfobetaine) brushes via SI-ATRP on a glass substrate surface. The ion-specific modulation of the interfacial interaction potential via densely packed, uniform poly(sulfobetaine) brushes was studied. The obtained results indicated that the interaction of ions with zwitterionic polymer brushes does not correspond to the classical Hofmeister series.

12.2.2.3 Temperature-Responsive Surfaces

Temperature-responsive polymer brushes prepared via surface-initiated controlled/living radical polymerization (SI-CLRP) have been studied for a wide variety of applications, such as catalysis (Li et al. 2008b), cell adhesion control (Matsuda and

Ohya 2005; Xu et al. 2006; Mizutani et al. 2008), and chromatography (Nagase et al. 2007, 2008a, b; Seino et al. 2006). Most of the thermoresponsive polymer brushes studied exhibited lower critical solution temperatures (LCSTs). Below the LCST, the surfaces of the polymer-grafted substrate are hydrophilic due to hydration of the grafted polymer chains. In contrast, above the LCST the surface becomes hydrophobic due to dehydration of the grafted polymer brushes.

Poly(*N*-isopropylacrylamide) (PNIPAM) is one of the most studied thermoresponsive polymers. PNIPAM exhibits a reversible temperature-dependent transition in water at its LCST of approximately 32 °C. The transition temperature range from a clear aqueous solution to a turbid solution is very narrow. In contrast, the LCST of the PNIPAM polymer brushes decreases, and the transition temperature range increases.

Tenhu et al. (Raula et al. 2003) prepared spherical gold clusters coated with PNIPAM via SI-RAFT radical polymerization (Fig. 12.20). The number-average diameter of the gold nanoparticles was 3.2 nm. The M_n of the grafted PNIPAM was 21,000 g/mol. The optical properties of the PNIPAM-grafted gold clusters could be controlled due to the temperature-responsive PNIPAM brushes. As the temperature increased, the surface plasmon decreased and blue shifted.

Thiol groups can be attached to a gold surface. Therefore, polymers containing thiol groups at the ends of the polymer chains can be attached to the surface of gold particles (Fig. 12.21). Thiol-terminated PNIPAM was prepared via RAFT radial polymerization. This PNIPAM containing thiol groups was attached to the surface of gold nanoparticles (Yusa et al. 2007). The thiol-terminated PNIPAM was readily

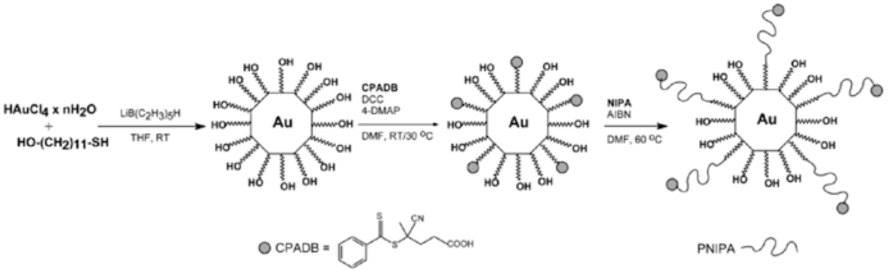

Fig. 12.20 Reaction steps for the preparation of poly(*N*-isopropylacrylamide) (PNIPAM)-coated gold clusters. (Copyright 2003, reproduced from Raula et al. (2003) with permission from ACS)

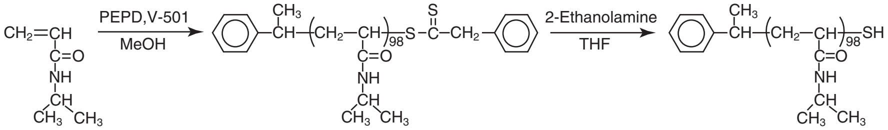

Fig. 12.21 Preparation of thiol-terminated poly(*N*-isopropylacrylamide) (PNIPAM) via reversible addition-fragmentation chain transfer (RAFT) radical polymerization. (Copyright 2007, reproduced from Yusa et al. (2007) with permission from ACS)

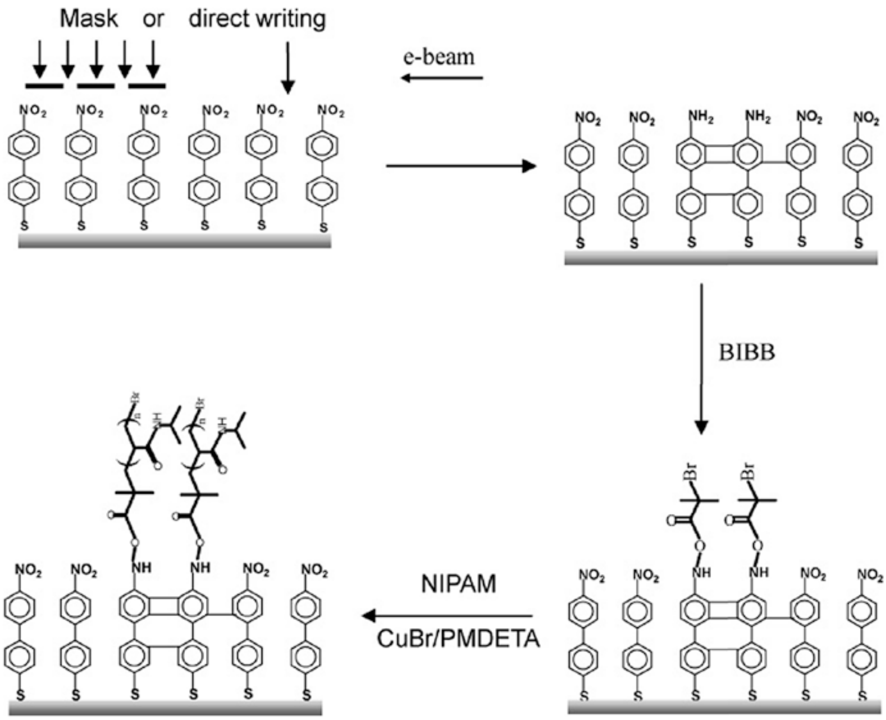

Fig. 12.22 Preparation process of PNIPAM brushes by chemical lithography and surface initiated atom transfer radical polymerization (SI-ATRP) on a gold substrate. The 4′-nitro-1,1′-biphenyl-4-thiol monolayer was irradiated by an electron beam, resulting in intra-layer cross-linking and conversion of the nitro groups to amino groups. The binding of bromoisobutyl bromide to the amino groups provides the surface initiator. SI-ATRP of *N*-isopropylacrylamide (NIPAM) was performed at the regions irradiated by an electron beam. (Copyright 2007, reproduced from He et al. (2007) with permission from ACS)

characterized by NMR spectroscopy and gel-permeation chromatography (GPC). The M_n and M_w/M_n values for thiol-terminated PNPAM were 12,200 g/mol and 1.08, respectively. Heat-induced association and dissociation of the PNIPAM-coated gold nanoparticles was completely reversible in 50 mM NaCl aqueous solution.

He et al. (2007) prepared micro- and nano-patterns of temperature-responsive PNIPAM brushes on a gold substrate using chemical lithography combined with SI-ATRP (Fig. 12.22). Self-assembled monolayers of 4′-nitro-1,1′-biphenyl-4-thiol were constructed by a chemical lithography technique where cross-linked 4′-amino-1,1′-biphenyl-4-thiol was prepared within a nitro-terminated matrix. Bromide groups were introduced to the amino groups in the monolayer to initiate ATRP. This fabrication method enables the generation of spatially defined polymer patterns. Cells can adhere, spread and proliferate on patterned PNIPAM brushes at 37 °C, which is above the LCST. Wei et al. (2008) prepared a gold nanorods/PNIPAM core-shell nanohybrid by SI-ATRP. Gold nanorods can convert absorbed near-infrared radiation (NIR) into localized heat. The nanohybrids showed temperature- and NIR-responsive properties. The temperature responsive range is between 32 and 37 °C. The PNIPAM brushes were loaded with anti-cancer reagents, and NIR-responsive release behavior was confirmed. The phase transition temperature of the PNIPAM brushes decreased as the salt concentration increased (Jhon et al. 2006). This observation can be explained by the tendency of salt ions to affect the structures of water molecules, i.e., the Hofmeister effect. The phase transition temperature of free PNIPAM shows a linear decrease with increasing salt concentration. In contrast, the phase transition temperature of PNIPAM brushes is non-linear. These differences in LCST behavior between free PNIPAM and PNIPAM brushes arise because the PNIPAM brushes exist in a confined space with a high polymer chain density. Li et al. (2005) reported a gas-phase polymerization procedure to generate polymer-grafted silicon oxide-based substrates. Surface initiated vapor deposition polymerization of *N*-isopropylacrylamide (NIPAM) was performed using nitroxide-mediated radical polymerization.

Balamurugan et al. (2003) prepared PNIPAM brushes on a gold substrate using SI-ATRP. The dry thickness of the PNIPAM brushes was about 50 nm, estimated by surface plasmon resonance (SPR) spectroscopy. The hydration transition for the PNIPAM brushes occurred over a broad range of temperatures, from 10 to 40 °C. This result is in agreement with theoretical predictions. The PNIPAM brushes in the outermost region remained highly solvated up to a temperature of 32 °C and were densely packed; meanwhile, fewer solvated chains within the brush layer underwent dehydration and collapse over a broad temperature range. Liu et al. (Wu et al. 2008) prepared hybrid silica nanoparticles with temperature-responsive PNIPAM brushes. The graft density was 0.454 chains/nm^2 based on TGA. A two-stage phase transition with heating over a broad temperature range of 20 to 37 °C was observed. The first phase transition occurred in the temperature range of 20 to 30 °C; this corresponds to the collapse of the inner region of the PNIPAM brushes close to the silica core. The second phase transition occurred above 30 °C and can be ascribed to the low chain density of the outer region.

Yim et al. (2004, 2006) have studied the temperature-responsive behavior of PNIPAM brushes with increasing temperature using neutron reflectivity. The conformational changes of the PNIPAM brushes varied with their molecular weights and surface grafting densities. The most remarkable conformational changes were observed for PNIPAM brushes with high molecular weights and intermediate grafting densities. Plunkett et al. (2006) studied PNIPAM chain collapse as a function of PNIPAM molecular weight and grafting density using surface force and contact angle (CA) measurements. Above the LCST, the advancing water CA increased on PNIPAM brushes with high molecular weights and grafting densities. However, this change was less pronounced in brushes with low molecular weight chains and low densities. Below the LCST, the force-distance profiles suggested nonideal polymer behavior. The PNIPAM brush appeared to adopt a two-layer structure with a compressible outer layer and a dense inner layer. Idota et al. (2006) reported similar findings.

Sun et al. (2004) studied the dependence of the wettability of PNIPAM brushes on the roughness of the substrate. The CAs of PNIPAM brushes prepared on a flat surface were 63.5 and 93.2° at 25 and 40 °C, respectively. The CAs of PNIPAM brushes prepared on substrates with a groove spacing of 6 μm and a depth of 5 μm were 0 and 149° at 25 and 40 °C, respectively. The temperature-responsive water CAs for the PNIPAM brushes on a rough substrate has been studied. The combination of the changes in the surface chemical properties and surface roughness can enhance stimuli-responsive wettability.

Li et al. (2007a) prepared core-shell gold nanoparticle hybrids with PNIPAM and *N,N′*-methylenebisacrylamide (MBAA) using SI-ATRP. The gold nanoparticles were first modified with a disulfide initiator of ATRP. Slight cross-linking polymerization between NIPAM and MBAA occurred on the surface to afford core-shell gold/copolymer nanostructures. These assembled nanostructures were used to encapsulate other nanoparticles, biomolecules, dyes, or drugs by a temperature-responsive breathing process. The influence of the amount of crosslinking agent (MBAA) on the LCST of random copolymer brushes was studied. 0.5 mol% MBAA content did not affect the LCST of the brushes. In contrast, when 1 or 2 mol% contents of MBAA were used, the LCST values increased to 34 and 36 °C, respectively.

Li et al. (2006) performed SI-ATRP of methoxyldi(ethylene glycol) methacrylate (DEGMMA) and methoxytri(ethylene glycol) methacrylate (TEGMMA) in THF at 40 °C in the presence of a free initiator (Fig. 12.23). The cloud points of aqueous solutions of free poly(DEGMMA) and poly(TEGMMA) were 25 and 48 °C, respectively. The thermo-responsive phase transition of the polymer brushes on silica particles began at a lower temperature and continued over a broader range of 4 to 10 °C. The weak transitions of the polymer brushes may be due to interchain interactions in the brush layer.

Polymer brushes exhibiting an upper critical solution temperature (UCST) have also been reported (Azzaroni et al. 2006). Polysulfobetaine methacrylate (PSBMA) was grafted on a gold substrate using SI-ATRP. The temperature dependence of the water CA on the PSBMA brushes was studied. The water CA on the PSBMA

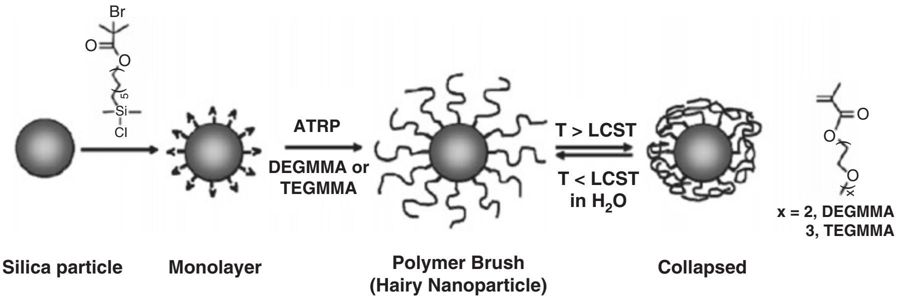

Fig. 12.23 Synthesis of thermosensitive hairy hybrid nanoparticles. (Copyright 2006, reproduced from Li et al. (2006) with permission from ACS)

brushes on the gold substrate at room temperature was 79°, which indicates that the surface is hydrophobic. With increasing temperature the surface became hydrophilic; the water CA decreased to 58°. The UCST of free PSBMA in pure water is 33 °C. In contrast, the UCST of the PSBMA brushes demonstrated a wider temperature region of 40 to 50 °C.

Random copolymerization can also be used to alter the phase transition temperatures of polymer brushes. Jonas et al. (2007) prepared random copolymer brushes (P(MEO_2MA-*co*-OEGMA)) composed of 2-(2-methoxyethoxy)ethyl methacrylate (MEO_2MA) and oligo(ethylene glycol) methacrylate (OEGMA) via SI-ATRP. The LCST of the random polymer brushes could be adjusted from 32 to 40 °C depending on their compositions. These random copolymers were nontoxic and nonimmunogenic; therefore, the polymer brushes can be used for biomedical applications.

In addition to homopolymer and random copolymer brushes, block copolymer brushes have also been prepared. Kizhakkedathua et al. (2004) prepared block copolymer brushes composed of poly(*N,N*-dimethylacrylamide) (PDMAA) and PNIPAM on polystyrene latex via SI-ATRP. The thickness of the polymer brushes changed in a wide temperature range from 20 to 80 °C.

Li et al. (2007b) grafted block copolymers of PNIPAM and poly(methoxy oligo(ethylene glycol) methacrylate) (PMOEGMA) onto gold nanoparticles by SI-ATRP. The core-shell nanoparticles showed two thermo-responsive points near 33 and 55 °C in water, corresponding to thermally induced conformational changes of the inner PNIPAM and outer PMOEGMA layers, respectively.

Introduction of pH-responsive character can be also introduced by adsorption of polymer micelles/microgels. Poly(ε-caprolactone)-*b*-PAA (PCL-PAA) micelles with PCL core/PAA corona morphology on solid substrate showed temperature-induced flattening (Zhang et al. 2000). The flattening could be tuned by changing the temperature due to the semi-crystalline nature of the PCL core (Zhang et al. 2002a). The PCL-PAA micelles have disk-like shapes on the solid substrate below the melting temperature (T_m) of the PCL block due to the rigid crystalline core. An increase of temperature above the T_m led to a reduction in height, which meant spreading on the substrate. In contrast, the PCL-PAA micelles have disk-like shapes when dispersed in aqueous media, and the spherical shape was maintained above the T_m. This difference in morphology at high temperature was due to the molten fluid-like PCL core adapting to the surrounding environment. Interestingly, micelles showed broader structures with decreased height after hydrolysis of PCL core component. The PAA-*b*-polyisoprene (PAA-PI) micelles with PI core/PAA corona morphology showed a similar behavior (Murthy et al. 2003). The PI has a relatively low glass transition temperature (T_g) of −63 °C, and the PAA-PI micelles have hydrophobic fluid-like PI cores at ambient temperature. Therefore, significant deformation occurred after adsorption onto mica at room temperature. After reaction of the PI block with HCl, the T_g of the PI micelle cores significantly increased to 33 °C. Thus, adsorption of these HCl-treated micelles onto the substrate at 22 °C initially resulted in negligible deformation of their spherical morphology due to the glassy nature of these cores. However, once the temperature increased to above the

T_g, significant flattening of the adsorbed micelles occurred. (Note that core cross-linking of polymer micelle can prevent shape deformation, since only spherical morphologies are observed above and below the T_g.)

Poly[(*N*-isopropylacrylamide)-*co*-(acrylic acid)] (P(NIPAM-*co*-AA)) microgel can be adsorbed onto positively-charged glass slides. It was demonstrated that these microgel can work as micro-lenses, which could switch between lensing and non-lensing states by varying temperature (Serpe et al. 2004). Multilayers of P(NIPAM-*co*-AA) microgels and poly(allylamine hydrochloride) (PAH) can be prepared on the glass substrate using spin coating (Serpe et al. 2005) and the layer-by-layer technique (Serpe et al. 2003). It was demonstrated that these microgel-based films could be used to thermally control the uptake and release of doxorubicin (Serpe et al. 2005).

12.2.2.4 Photo-Responsive Surfaces

Spiropyran and azobenzene are suitable materials for the preparation of photo-switchable surfaces because they demonstrate reversible photo-induced isomerization behaviors (Groten et al. 2012; Abrakhi et al. 2013). Each photo-switching compound has advantages and disadvantages. For example, *trans*-*cis* isomerization of azobenzene, which has a simple structure, is not usually quantitative. Although photo-isomerization of spiropyran is almost quantitative, the reaction can be accompanied by decomposition, thermal relaxation, and side reactions, resulting in reduced photo-isomerization (Klajn 2014).

Yuan et al. (2006) synthesized a copolymer containing azobenzene by copolymerization with *N,N*-dimethylacrylamide (DMAA) and photo-responsive 4-phenylazophenyl acrylate (Fig. 12.24). The copolymer demonstrates a light-tunable LCST. A dual stimuli-responsive surface that could change its wettability in response to both temperature and light was prepared using a “grafting to” method involving copolymers with activated terminal groups on a silicon substrate. As the temperature increased and approached the LCST, the water CA on the surface increased to approximately 30°. Upon UV light irradiation, azobenzene in the copolymer brush isomerized from the *trans* form to the more polar *cis* form. This process caused the LCST to increase by 4 °C.

Colorless spiropyran, which contains a closed ring structure, changes reversibly to colored merocyanine by ring opening; merocyanine has both zwitterionic and uncharged structures (Saragi et al. 2007). The carbon-oxygen bond in the pyran ring is cleaved upon UV light irradiation and can reversibly reform the pyran ring upon visible light irradiation or heating (Fig. 12.25).

Various polymer brushes containing photoresponsive spiropyrans were prepared on silica substrates and particles via SI-ATRP (Bell and Piech 2006) and surface-initiated ring-opening metathesis polymerization (SI-ROMP) (Samanta and Locklin 2008). Theato et al. (Choi et al. 2012) prepared polymer brushes containing photo-responsive spiropyrans on a silica surface via SI-RAFT. Piech and Bell (2006) prepared poly(methyl methacrylate) (PMMA) brushes containing spiropyrans (P(SP-*co*-MMA)) on silica colloidal particles via surface-initiated ATRP. The spiro-

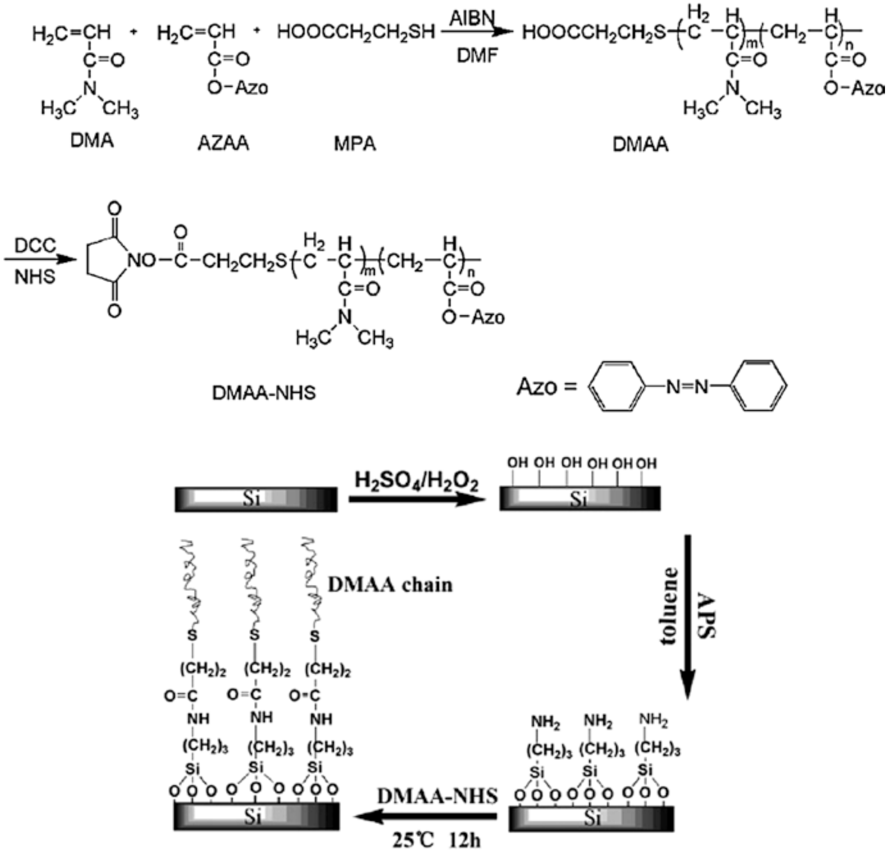

Fig. 12.24 Synthetic process of copolymer of *N,N*-dimethylacrylamide (DMAA) with *N*-hydroxysuccinimide (NHS)-activated terminal groups and preparation process of the DMAA-grafted silicon surface. (Copyright 2006, reproduced from Yuan et al. (2006) with permission from ACS)

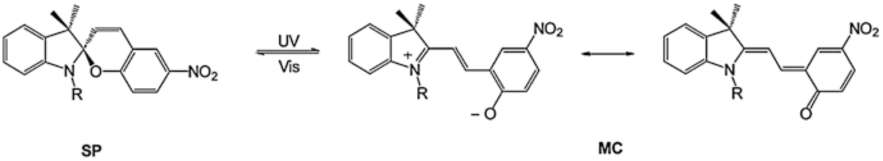

Fig. 12.25 Reversible transformation of isomeric structures of ring-closed colorless spiropyran (SP) and two canonical open forms, zwitterionic and uncharged, of colored merocyanine (MC). (Copyright 2014, reproduced from Dübner et al. (2014) with permission from ACS)

pyran moiety in the brush reversibly changed to zwitterionic merocyanine and then regained its spiropyran form due to the thermal back-reaction. The existence of free and associated merocyanine in the polymer brush was confirmed by spectroscopic analysis in organic solvent. Zhou et al. (2014) reported a fluorinated gradient copolymer containing spiropyran grafted on an etched silicon substrate with a programmed design feeding technique using an SI-ATRP “grafting from” method. Photoresponsive switchable surface wettability of the gradient brush copolymer containing spiropyran on etched silicon was achieved.

In the above methods, spiropyran-containing monomers were first prepared; then, the monomers were introduced into the brushes by copolymerization using a “grafting from” method. Dübner et al. (2014) reported the preparation of patterned poly(glycidyl methacrylate) (PGMA) brushes on a fluoropolymer substrate by extreme ultraviolet (EUV) irradiation; the spiropyran moiety was introduced into the side chains. The surface wettability was altered by UV-induced spiropyran/merocyanine isomerization. The water CA of the surface changed upon UV light irradiation in the range of 15° for PGMA, depending on the spiropyran content.

12.2.2.5 Electric Field-Responsive Surfaces

A “grafting from” approach can be used to prepare polymer brushes on planar substrates and particle surfaces that endow these surfaces with electrical properties. Polymer brushes containing pendent ferrocene groups were prepared on a gold substrate surface via ATRP and “click chemistry” (Xu et al. 2010). The physical properties of the modified gold surface were characterized by cyclic voltammetry, X-ray photoelectron spectroscopy (XPS), and water CA measurements. β-Cyclodextrin polymers could be reversibly and repeatedly loaded and unloaded on the substrate by redox reactions on the surface of the gold electrode (Fig. 12.26). The β-cyclodextrin polymers could be loaded on the polymer brushes due to host-guest interactions between the pendent β-cyclodextrin and ferrocene groups. The β-cyclodextrin polymers were repeatedly unloaded by oxidation of the ferrocenyl groups and reloaded by reduction.

Schwartz et al. (2010) synthesized carbazole-functionalized isocyanides that were polymerized on a substrate surface using a “grafting from” approach to obtain polymer brushes up to 150 nm thick with well-defined helical structures. The electronic properties of the materials grafted on the polyisocyanide brushes were studied with Kelvin probe force microscopy (KPFM) and electroabsorption.

Wei et al. prepared poly(9-(2-(4-vinyl(benzyloxy)ethyl)-9H-carbazole)) (PVBEC) brushes on a silicon surface via SI-ATRP (Wei et al. 2011). At a voltage of −2.1 V, conductance switching was observed in a memory device based on the PVBEC brushes. The prepared device demonstrated good memory properties at ON/OFF current ratios up to 10^5 and could endure 10^6 read cycles at pulse voltages of under −1.0 V.

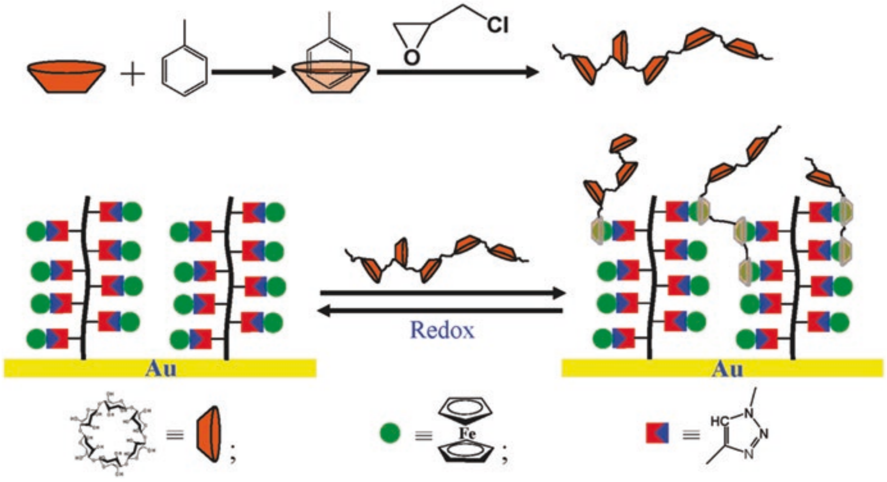

Fig. 12.26 Redox-controlled reversible loading of β-cyclodextrin polymers on a gold substrate with surface-grafted and ferrocene-functionalized polymer brushes. (Copyright 2010, reproduced from Xu et al. (2010) with permission from ACS)

12.2.2.6 Multi Stimuli-Responsive Surfaces

Dual-stimuli-responsive surfaces can be prepared from random copolymer brushes composed of thermo-responsive NIPAM and pH-responsive acrylic acid (AA). Xia et al. (2006) prepared a temperature- and pH-responsive surface by fabricating random copolymer (P(NIPAM-*co*-AA)) brushes on a rough etched silicon substrate using SI-ATRP. The composition of AA in the copolymer brushes was 3 mol%. The AA units endowed the brushes with pH-responsive properties. The LCST for the copolymer brushes was controlled by changing the pH. The LCST could be controlled from 21 to 45 °C depending on the pH value.

Dual-stimuli-responsive block copolymer brushes have also been prepared. Wang et al. (2007) prepared block copolymer brushes that were responsive to both temperature and pH stimuli on a silicon surface. Firstly, poly(2-hydroxyethyl methacrylate)-*block*-PNIPAM (PHEMA-*b*-PNIPAM) brushes were prepared by SI-ATRP on the silicon substrate surface. The pendent hydroxyl groups in the PHEMA block were reacted with excess succinic anhydride to prepare the poly(2-succinyloxyethy methacrylate)-*block*-PNIPAM (PSEM-*b*-PNIPAM) brushes. The pH- and temperature-responsive behaviors of the brushes were studied using atomic force microscopy (AFM). At acidic pH values, the thermo-responsive behavior of the polymer brushes was no longer observed because hydrogen bonds formed between the pendent carboxylic acid and amide groups, lowering the LCST of the polymer brushes. Under basic conditions, the thickness of the polymer brushes decreased with increasing temperature from 25 to 50 °C due to the disappearance of the hydrogen bonding interactions following ionization of the pendent carboxylic acid groups. Poly(methacrylic acid)-*block*-PNIPAM (PMAA-*b*-PNIPAM) brushes were prepared using a surface-initiated photoiniferter-mediated photopolymerization technique (Rahane et al. 2008). The thickness of the PMAA-*b*-PNIPAM brushes varied depending on pH, temperature, and ionic strength; the brushes were studied using ellipsometry to measure the changes in the thickness of the solvated layer.

12.3 Characterization of Stimulus-Responsive Surface/Interface

12.3.1 Spectroscopic Methods

12.3.1.1 Fourier Transform Infrared Spectroscopy (FT-IR)

For stimulus-responsive surfaces, FT-IR is mainly used to identify surface functional groups and confirm coverage with molecules to be immobilized. Being capable of in situ determining molecular orientation and intermolecular bonding, FT-IR is also utilized to characterize solution-phase structural behavior of bulk stimulus-responsive polymers, providing important information on intra- and intermolecular bonding and disordering of surface molecules responding to stimulus (Katsumoto et al. 2002; Ide et al. 2003; Woods and Bain 2014). However, the behavior of stimulus-responsive polymers immobilized on solid surfaces has rarely been characterized in situ, presumably owing to the inherent limitations of this method. Even for attenuated total reflection (ATR) FT-IR, which is commonly used for surface analysis, the IR radiation penetrates the substrate (crystal) deep enough to sample bulk materials, with the specific contribution of the surface thin layer being difficult to extract. Moreover, the absorption of bulk liquids in the range of interest also complicates measurements.

Popa et al. (2010) analyzed the thermoresponsive behavior of carboxy-terminated PNIPAM deposited on a Si surface using single-beam sample reference ATR spectroscopy, wherein a single-beam spectrometer is converted into a pseudo-double-beam ATR or transmission spectrometer by mechanically controlling the vertical displacement of the internal reflection element so that the sample and reference spectra are measured quasi-simultaneously. This technique features enhanced compensation of strong background absorption, benefitting surface layer analysis.

In the above investigation, increasing solution temperature induced the emergence of a particular PNIPAM absorption at 1653 cm^{-1}, which was attributed to the amide I C=O group involved in intramolecular hydrogen bonding (Fig. 12.27a), suggesting that the high-temperature collapsed globule conformation of PNIPAM originates from the increasing number of intramolecular hydrogen bonds involving the above C=O groups. On the other hand, the shift of the amide II band to lower wavenumbers (1556–1532 cm^{-1}) implied backbone configuration modification. This configuration modification is also suggested by the emergence of a positive peak at 2972 cm^{-1} with increasing temperature, which was attributed to asymmetric

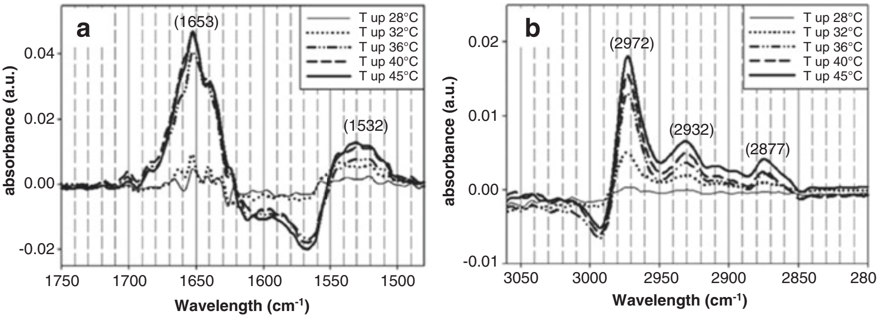

Fig. 12.27 Spectra of amide I/II (**a**), and methyl/methylene (**b**) optical regions of grafted PNIPAM recorded at 28, 32, 36, 40, and 45 °C. (Adapted with permission from Popa et al. (2010). Copyright (2007) American Chemical Society)

C–H stretching vibrations. Based on the temperature lag of these signal changes, the authors suggested that hydrogen bond formation/disruption and backbone configuration modification contribute to the collapse of PNIPAM brushes in different ways.

Infrared reflection absorption spectroscopy (IR-RAS) is another useful method for analyzing thin layers on solid surfaces, in particular, highly reflective surfaces (mainly metals). In this method, IR light is reflected onto the substrate at a certain grazing incidence angle, and changes in the substrate reflectance spectrum accompanying adsorption are measured. The reflected parallel, or p-polarized, light provides information on specific functional groups with bonds perpendicular to the reflective surface, allowing this method to be applied even to molecular-order surface layers.

Lego et al. (2010) applied IR-RAS along with AFM and contact angle measurements to characterize the pH response of covalently surface-grafted PAA brushes. In this work, spectra of PAA grafted on a silicon wafer in air were obtained after 15-min immersion in pH 6 and pH 9 solutions and subsequent drying. A characteristic –COOH stretching peak (1725 cm^{-1}) was observed at pH 6, whereas that of COO^- (1580 cm^{-1}) was not detected. As the pH was increased to 9, the COOH/COO^- peak intensity ratio decreased, confirming that PAA brushes existed in an undissociated state at pH 6, being ionized at pH 9.

12.3.1.2 Nuclear Magnetic Resonance (NMR) Spectroscopy

NMR spectroscopy is one of the most powerful methods for analyzing chemical compounds because it can determine chemical structure and mobility using one set of analytical tests. In many cases, NMR is used to identify the chemical structure from a combination of chemical shift data and spin-spin splitting. The other application for NMR is investigation of mobility of the molecules, which can be applied to characterization of stimulus-responsive surface chemistry of solid substrates.

Fujii and coworkers conducted ^{1}H NMR studies on polystyrene (PS) particles carrying pH-responsive poly[2-(diethylamino)ethyl methacrylate] (PDEAEMA) hairs (PDEAEMA-PS particles) dispersed in aqueous media (Fujii et al. 2012a). The protonated and solvated nature of the PDEAEMA hairs of the PDEAEMA−PS particles in acidic solution was indicated due to high mobility in aqueous media; at pH 3, a broad signal due to the protonated PDEAEMA chains was observed at 1.0–1.7 ppm (due to the methyl protons of the diethyl amino group). In contrast, this signal was not observed at pH 10, since the PDEAEMA chains are in their neutral, nonsolvated form and mobility is restricted at this pH.

Magnetic resonance imaging (MRI) is one of the powerful noninvasive diagnostic imaging methods. The imaging is accomplished by encoding the NMR signals so that the spatial distribution of the nuclei causing the signals can be investigated. Important progress in this research field is ^{19}F MRI technique, which uses fluorinated compounds as the contrast agents. This technique can produce high-contrast images, since there is no endogenous ^{19}F in the body. Chujo and coworkers used SiO_2 nanoparticles coated with water-soluble perfluorinated cubic octameric polyhedral oligomeric silsesquioxanes (POSS) for monitoring enzymatic activity (Fig. 12.28) (Tanaka et al. 2008). Here, amino groups on perfluorinated POSS were covalently linked to the amino groups on the silica nanoparticles via the phosphordiamidate linker which can be cleaved by the enzymatic digestion of alkaline phosphatase. When the perfluorinated POSS exists on the SiO_2 nanoparticle surface, the NMR signal is hardly detected due to an acceleration of the transverse relaxation time and an anisotropy of the spin toward the external magnetic fields; the molecular mobility of the POSS should be highly restricted and the NMR signals from the probe can be suppressed. After release of the probe, triggered by an enzymatic reaction, the NMR signals are detected with good sensitivity. Therefore, the enzyme activity can be detected by the enhancement of the signal intensity of ^{19}F NMR. The same group developed sophisticated SiO_2 nanoparticle-based molecular probes which quantitatively monitor enzymatic activity with simultaneous signal increases in ^{19}F NMR and fluorescence (Tanaka et al. 2011).

12.3.1.3 Sum-Frequency Generation Spectroscopy (SFG)

SFG is a surface vibrational spectroscopy technique invented in the late 1980s, exhibiting highly surface-specific sensitivity (Shen 1989) and being able to analyze almost any liquid interface. Unsurprisingly, SFG spectroscopy has already found extensive applications, being a particularly useful and versatile tool for in situ characterization of surface thin layers in solution, as exemplified by its use in investigations dealing with liquid structures at solid surfaces (Bain 1995), electrochemistry (Tadjeddine and Peremans 1996), and biological systems (Vogel 1996).

During SFG analysis, a sample is irradiated with two input laser beams, a pulsed tunable IR beam and a pulsed visible beam, with frequencies ω_{IR} and ω_V, respectively. These beams overlap in the chosen medium, generating an output signal at a frequency of $\omega_S = \omega_{IR} + \omega_V$. Despite corresponding to a second-order nonlinear opti-

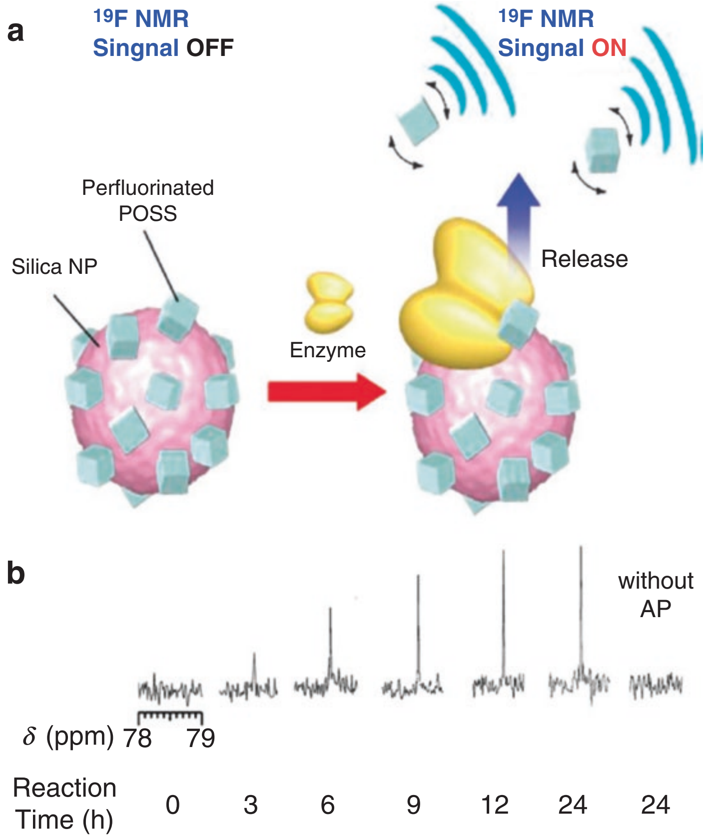

Fig. 12.28 (**a**) Scheme illustrating monitoring enzymatic activity using SiO_2 nanoparticles coated with water-soluble perfluorinated cubic octameric polyhedral oligomeric silsesquioxanes (POSS). (**b**) ^{19}F NMR spectra of perfluorinated POSS-coated SiO_2 nanoparticles with a diameter of 150 nm in enzymatic hydrolysis with alkaline phosphatase. (Reproduced from Tanaka et al. (2008) with permission from Royal Society of Chemistry)

cal process, and thus being forbidden in media with inversion symmetry in the electric-dipole approximation, SFG is allowed at surfaces or interfaces where the inversion symmetry is broken (Shen 1994). In addition, a resonant enhancement of SFG signal intensity occurs when ω_{IR}, ω_V, or ω_S approaches the surface resonance frequency. Thus, SFG spectroscopy is a highly surface- and interface-specific probing method providing important information on the orientation and conformation of surface molecules and, under certain conditions, even surface structure, and is ideal for studying the dynamic structural behavior of stimulus-responsive molecules on smart surfaces. However, the number of studies employing this method is still relatively small.

Chen et al. (2005) conducted an in situ SFG analysis of a temperature-responsive PNIPAM-grafted surface to characterize its hydration property changes, also using

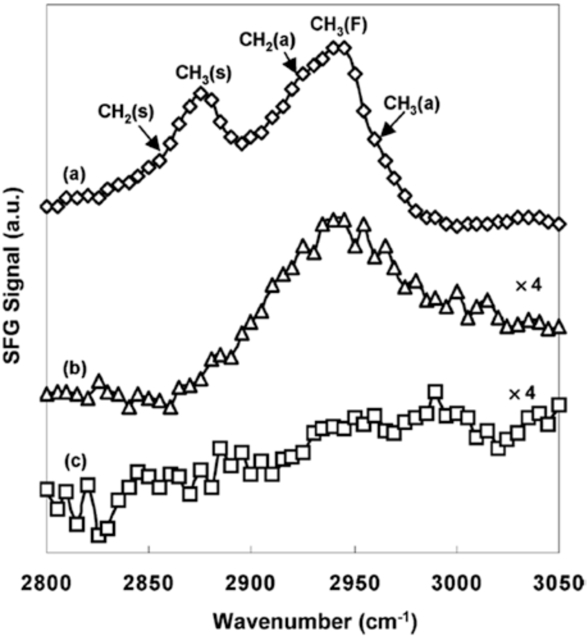

Fig. 12.29 SFG spectra of PNIPAM in (**a**) air at room temperature, (**b**) pure water at 37 °C, and (**c**) pure water at room temperature (25 °C). (Reprinted with permission from Cheng et al. (2005). Copyright (2005) American Chemical Society)

other techniques such as time-of-flight secondary-ion mass spectrometry (ToF-SIMS), contact angle measurement, and AFM. In this work, SFG spectra of the CH stretching region were acquired in water at room temperature and 37 °C (Fig. 12.29). In the latter case, a broad peak was observed between 2900 and 2980 cm^{-1}, representing a combination of CH$_2$ asymmetric stretch, CH$_3$ Fermi resonance, and CH$_3$ asymmetric stretch peaks. Conversely, no specific peaks were observed in this region at room temperature, indicating a disordered orientation of the hydrophobic isopropyl groups of PNIPAM, which pointed away from the surface normal. Based on these and other data, it was hypothesized that above the LCST, globular-shaped PNIPAM chains orient their hydrophobic groups outward to maximize hydrogen bonding underneath the surface, whereas hydrophobic isopropyl groups are bent inward, allowing amide groups and water to engage in hydrogen bonding at room temperature. Additionally, Miyamae et al. (2007) utilized SFG spectroscopy to estimate the orientational angles of isopropyl groups in PNIPAM chains in D$_2$O at 20 and 50 °C, revealing that the main chain orientation was drastically affected by temperature due to the shrinking of these chains induced by dehydration across the LCST.

Wu et al. (2016) used SFG spectroscopy to evaluate the pH-responsive behavior of positively charged poly[2-(methacryloyloxy)ethyl trimethylammonium chloride] (PMETAC) and negatively charged poly(3-sulfopropylmethacrylate potassium) (PSPMA) brushes, which were prepared by SI-ATRP. The PMETAC surface becomes more hydrophobic with increasing pH, and the SFG intensity changes of peaks at 3000–3800 cm^{-1} (interfacial water) and at 1220 cm^{-1} (C–O stretching in the –C(=O)OR side group) suggest the absence of hydrogen bonding between grafted chains at pH 2. These hydrogen bonds between hydroxide and carbonyl groups of neighboring chains gradually form with increasing pH, weakening interactions between PMETAC brushes and water molecules and thus inducing the dehydration of the brushes. Conversely, an opposite phenomenon was observed for PSPMA brushes, i.e., the desorption of water leading to interchain hydrogen bond cleavage was observed with increasing pH. However, hydrogen bond reorganization with decreasing pH exhibited a relatively weaker influence on brush hydration than that observed for PMETAC, presumably due to the different functional groups present in these brushes.

12.3.2 Radiation Methods

12.3.2.1 Small Angle X-Ray Scattering (SAXS)

SAXS uses elastic X-ray scattering to detect and characterize molecular shape and structure in the molecular weight range 5 kDa-100 MDa, or characteristic distances within colloidal or porous materials up to a lengthscale of 150 nm. A monochromatic x-ray beam, on either a laboratory-scale instrument or a synchrotron source with much higher flux, is incident on the sample. The x-rays are scattered and the scattering pattern collected at the detector. The scattering pattern consists of a plot of intensity versus scattering angle. Analysis of the scattering pattern can reveal particle size and shape distribution for colloidal solids, or nano-microstructure for soft matter samples such as concentrated surfactant phases, polymer or protein solutions. Responsive materials can be characterized through analysis of both native and triggered sample states.

For example, SAXS has been used to study the pH-responsive assembly of a series of cationic calix[4]arene-based lipids (Fujii et al. 2012b). As shown in Fig. 12.30, at low pH in the protonated state of the amine headgroup, the lipid was found to form spherical micelles. Upon increasing the pH and concomitant deprotonation of the headgroup, the lipid underwent a sphere-to-cylinder or sphere-to-cylinder-to-vesicle transition depending on the length of the alkyl chains. The SAXS patterns yielded the characteristic size and shape together with high monodispersity. In a monoolein/water bicontinous diamond cubic phase, Angelov et al. demonstrated both the thermal and hydration response of the lipid mesostructure using SAXS to characterise the swelling and collapse of the aqueous channel dimensions (Angelov et al. 2007).

The thermally triggered release of glucose as a model hydrophilic drug from phytantriol and glyceryl monooleate-based lipid mesophases was studied using SAXS by Fong and coworkers (Fong et al. 2009). As shown in Fig. 12.31, the SAXS pattern changes from a bicontinous cubic phase (Q_2) to a reverse hexagonal phase (H_2) over a narrow temperature range. The triggered release of glucose from the mesophase was shown to be reversible in vitro and the accompanying in vivo

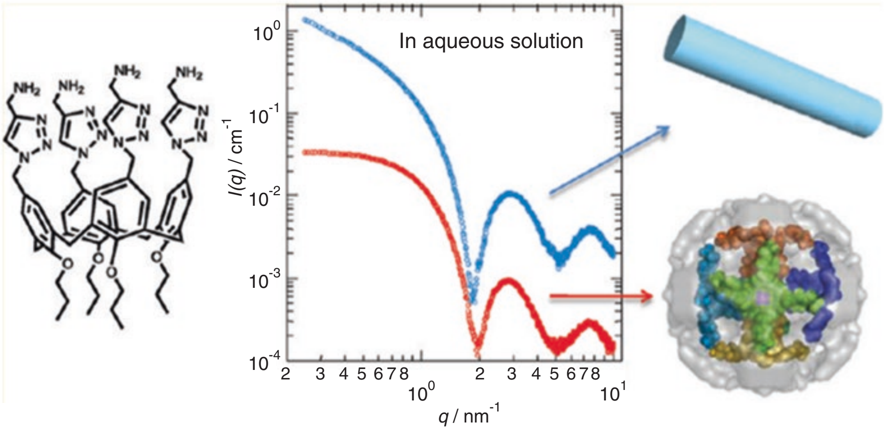

Fig. 12.30 SAXS curves at low pH (red) and high pH (blue) for the calix[4]arene lipid with propyl chain. (Copyright 2011, reproduced from Fujii et al. (2012b) with permission from the American Chemical Society)

Fig. 12.31 SAXS profiles for the phytantriol +3% vitamin E acetate cubic phase system in excess water with increasing temperature. Q_2 indicates the bicontinuous cubic phase and H_2 refers to a reverse hexagonal phase. Numbers in parentheses indicate the Miller indices (h,k,l) for the reflecting planes in the sample giving rise to the peak in intensity vs scattering vector. (Copyright 2009, reproduced from Fong et al. (2009) with permission from Elsevier)

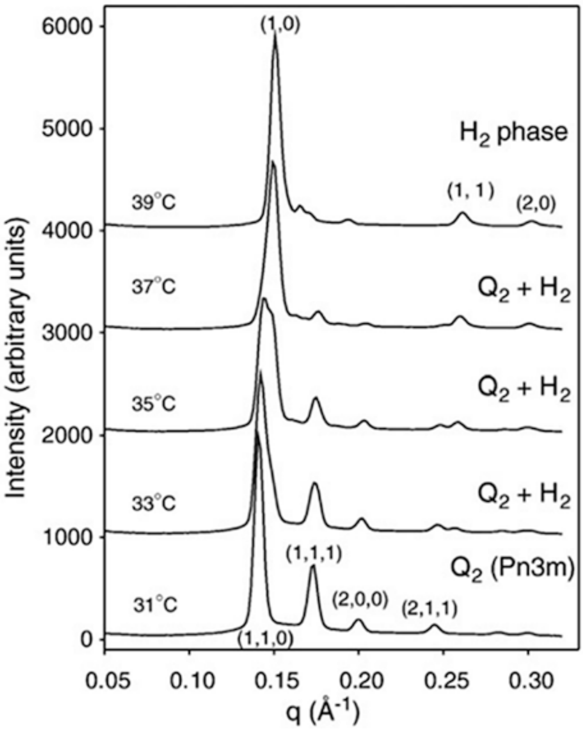

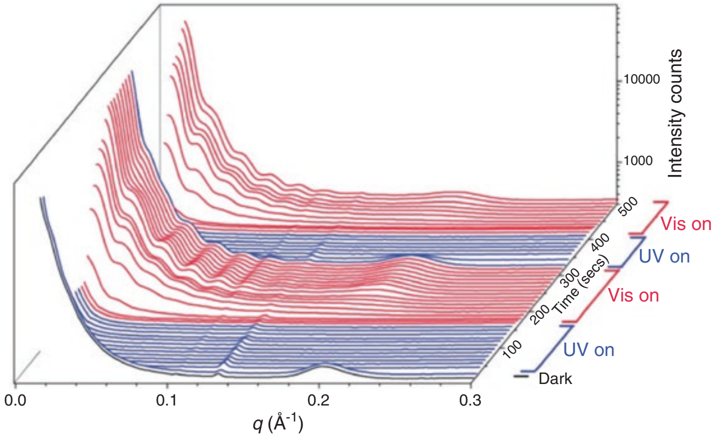

Fig. 12.32 Time resolved synchrotron SAXS patterns for the C8-Azo-TPC in n-dodecane (1.0 wt%) upon UV light (365 nm, 200 mW/cm^2) exposure and visible light (38 mW/cm^2) at 25 °C. (Copyright 2014, reproduced from Yang et al. (2014) with permission from the RSC)

response in rats could be induced through application of an external heat pack. A follow-up time-resolved SAXS study demonstrated that a heat, light or pH response can be used to control the drug release (Fong et al. 2016).

The stimulus response of small molecule gelators has also been investigated by SAXS. An azobenzene based organogelator exhibited rapid and reversible transformations from gel to solution in a range of hydrophobic solvents (Yang et al. 2014). The triggers demonstrated were heat, UV light and applied shear. Figure 12.32 shows the reversible photoresponsive structural rearrangement of 4-chlorocarbonyl-benzoic acid 4′-(4″-octyloxy-phenylazo)-benzyl ester (C8-Azo-TPC) in *n*-dodecane. In a macrocyclic hydrogelator, Hwang et al. demonstrated the reversible thermally induced assembly of the macrocyclic subunits into fibrils using SAXS (Hwang et al. 2007). While in a tyrosine-based metallo-hydrogel, Basak and coworkers showed self-healing gelation which was also attributed reversible π-π stacking into fibrils (Basak et al. 2014).

Stimulus-responsive polymeric gelators have also been characterized using SAXS. A synthetic muscle based on a pH-responsive block copolymer was shown to repeatedly perform a work function with the gel nanostructure assessed using SAXS (Howse et al. 2006). Frisman and coworkers reported a nanostructured hydrogel based on a conjugate of protein and poloxamer for tissue engineering (Frisman et al. 2011). SAXS was used to assess the thermoresponsive properties while rheology was used to characterize the mechanical properties in each state. Each of these studies demonstrates the suitability of SAXS for the interrogation of nano- or mesostructural variation upon the application of a stimulus to soft matter samples.

12.3.2.2 Small Angle Neutron Scattering (SANS)

SANS uses elastic neutron scattering to detect and characterize structures on the lengthscale 1–100 nm. A neutron beam is incident on the sample which is frequently an aqueous solution or dispersion. The neutrons are scattered as a result of interactions with the nuclei or unpaired electrons (magnetic scattering). The information gained is the scattering intensity as a function of the momentum transfer, Q. The sample is characterized in Fourier (reciprocal) space where large Q values relate to small objects and vice versa. While similar to SAXS, SANS has the advantage of sensitivity to light elements and potential for isotopic contrast matching. A unique feature is the very different scattering length densities of hydrogen and deuterium which permits parallel analysis using contrast matching to probe different sample zones such as the core and the shell of a diblock copolymer micelle sample. This approach makes SANS ideal for the characterization of soft matter at the mesoscale such as micelles, vesicles and bicontinuous phases, particularly those composed of synthetic macromolecules or biomacromolecules. Responsive materials can be characterized through analysis of both native and triggered sample states.

For example, SANS has been used to study the thermoresponsive micellization of poly(methyl methacrylate) (PMMA)-*b*-PNIPAM copolymers above and below the LCST of the PNIPAM as shown in Fig. 12.33 (Tang et al. 2006). At 28 °C, the diblock copolymer formed micelles with very small PMMA cores and extended diffuse PNIPAM shells which was modelled as a star polymer conformation. At 36 °C, the micelle size increased as the PNIPAM became dehydrated and aggregation was observed. At high concentration gelation occurred. Similarly the thermoresponsive micellization of block and gradient copolymers of 2-ethoxyethyl vinyl ether and 2-methoxyethyl vinyl ether has been characterized by SANS and modelled with a core-shell geometry (Okabe et al. 2006).

Chécot et al. reported the SANS study of polypeptide-based diblock copolymer reversible micellization and vesicle formation. The SANS data were modelled as either a core-shell micelle or a hollow vesicle complete with membrane thickness. The stimuli in this study were both pH and ionic strength. The authors noted the remarkable salt stability afforded by the polypeptides compared to classical poly-

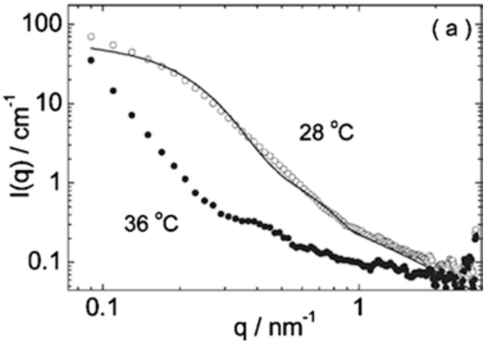

Fig. 12.33 SANS curves of 0.5 wt% D_2O solutions of a PMMA-*b*-PNIPAM copolymer above and below the LCST of PNIPAM. (Copyright 2006, reproduced from Tang et al. (2006) with permission from the Wiley)

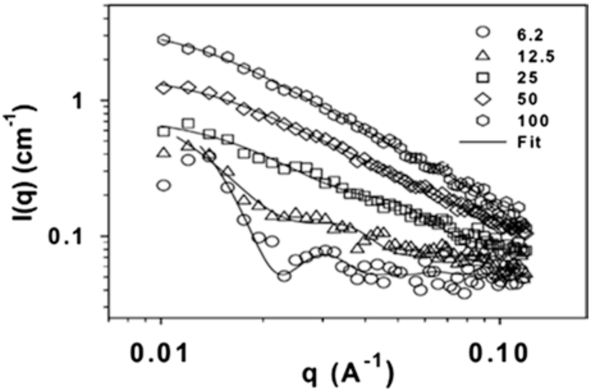

Fig. 12.34 SANS scattering intensity of rec1-resilin solutions as a function of q at 25 °C. The data sets (6.5, 12.5, 25 mg/mL) were fitted with a core-shell sphere model. However, a monodisperse, right circular cylinder with a core-shell scattering length density profile was used to fit the more concentrated solutions (50 and 100 mg/mL). (Copyright 2011, reproduced from Dutta et al. (2011) with permission from Wiley)

electrolytes (Chécot et al. 2005). The complex response of the resilin mimetic elastic protein rec1-resilin has also been investigated by SANS (Dutta et al. 2011). This genetically engineered protein exhibits an LCST, an upper critical solution temperature and pH-responsive behaviors. As shown in Fig. 12.34, a core-shell sphere or cylindrical model can be fitted to the protein conformation in solution as a function of concentration.

SANS has also proved to be a valuable tool for studying soft matter gels. Stieger et al. reported that the segment density of PNIPAM microgels was non-uniform and instead it exhibits a radial decay. The result is that the solvent-swollen particles below the LCST have a diffuse surface surrounding a more densely cross-linked internal core (Stieger et al. 2004). Diblock copolymers consisting of a thermoresponsive block and a hydrophilic block were studied by Sugihara et al. (2004) The temperature trigger for micelle formation and/or physical gelation was tunable via the block degrees of polymerization. Rheological character of the gel phases observed was explained by the SANS data which revealed the formation of a body-centred-cubic microlattice of close-packed spherical micelles. Bolamphiphile gels which exhibited temperature, concentration and pH-responses were reported by Meister and coworkers (2007). SANS measurements were modelled as nanofibers which supported the accompanying macroscopic rheology and dynamic light scattering. Eastoe and colleagues reported a novel photo-responsive organogel composed of a stilbene-containing gemini surfactant dissolved in toluene (Eastoe et al. 2004). Incident UV irradiation was the trigger for the gel-to-sol transition as shown in Fig. 12.35. Finally, SANS has been used to probe the temperature-induced gelation of perfluorodecalin-in-water emulsions stabilized by poly(NIPAM-*co*-methoxypoly(ethylene glycol) methacrylate (PEGMA)) (Koh and Saunders 2005). Above the LCST of PNIPAM an aqueous solution of this copolymer forms a disper-

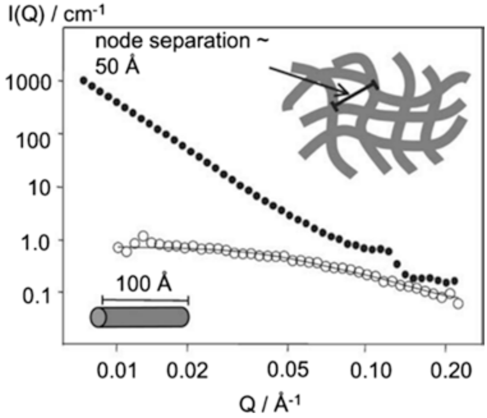

Fig. 12.35 SANS data for the photo-responsive organogel before (•) and after irradiation (°). The latter is fitted to a cylindrical micelle model with radius of 13 Å. (Copyright 2004, reproduced from Eastoe et al. (2004) with permission from the RSC)

sion of aggregates which resemble microgel particles. These aggregates undergo sticky collisions which lead to gel formation between the oil droplets of the emulsion.

Each of these studies demonstrates that SANS is highly suitable to probe the conformation of stimulus-responsive molecules in solution or dispersion.

12.3.2.3 Ellipsometry

Ellipsometry is an optical technique that uses changes in the polarization state of a reflected light beam to probe a surface. The addition of a thin film of soft matter changes the optical properties of the entire surface, and thus changes in the polarization state may be used to determine properties such film refractive index or thickness. A typical instrument measures the ellipsometric parameters Ψ and Δ, the amplitude ratio and phase difference respectively of the incident and reflected beam. Similar to techniques such as neutron reflectometry, ellipsometry is an indirect method and as such modelling of the experimentally measured values of Ψ and Δ must be undertaken to generate the film properties. This is usually an under-defined problem and so assumptions may be required; for example, the researcher often needs to assume a refractive index for a soft matter film to be able to calculate a film thickness. The use of a high precision goniometer to record ellipsometric data at multiple angles of incidence can alleviate this problem, but this is generally not possible for samples immersed in liquid as most commercial fluid cells have fixed optical windows so a single angle only is possible. Newer spectroscopic ellipsometers use light sources able to deliver a spectral range from infrared through to ultraviolet, and as such are able to directly measure, for example, the refractive index of a soft matter film immersed in liquid. Modelling of ellipsometric data may produce a volume fraction profile normal to the interface, though usually at lower resolution than profiles possible from neutron reflectometry experiments. The reader is directed to Edmondson et al. for an explanation of a number of modelling approaches and a comparison of their effectiveness in modelling a layer of poly(2-(methacryloyloxy) ethyl phosphorylcholine) (PMPC) (Edmondson et al. 2010).

A great advantage of ellipsometry over techniques such as neutron reflectometry is the high temporal resolution that may be achieved. Cheesman and coworkers used a combination of ellipsometry and quartz crystal microbalance with dissipation monitoring (QCM-D) to investigate the pH response of polybasic PDEAEMA brushes (Cheesman et al. 2013). The use of a complementary technique in this way offers great insight that is not possible using ellipsometry alone. For example, QCM-D is sensitive to changes in polymer conformation at the periphery of the brush that may not be observed in ellipsometry, however ellipsometry usually offers better temporal resolution. In this work Cheeseman and coworkers showed cyclical swelling and collapse of a PDEAEMA brush as the pH was repeatedly changed from pH 4 to pH 9 respectively; below and above the pK_a of PDEAEMA. By comparing the ellipsometric thickness of the brush immersed in aqueous solution to a dry thickness, they were able to show that the PDEAEMA brush was still quite well-solvated even when collapsed at pH > pK_a. They also demonstrated that the swelling and collapse transitions were not simple reflections of each other; the collapse transition (~10 min) took considerably long than swelling (~1 min) (Fig. 12.36). Corresponding QCM-D data showed the same phenomenon, and indicated the difference was exacerbated with increasing brush thickness.

Subsequent work from the same group investigated the pH response of a family of tertiary amine methacrylate based polymers brushes (Willott et al. 2015a), as well as their response to changes in background salt concentration and identity (Willott et al. 2015b). The response of a PDEAEMA brush, and its more hydrophilic dimethyl (PDMAEMA) and more hydrophobic diisopropyl (PDPAEMA) analogues was studied across the full pH range from well above the respective brush pK_a (collapsed), to well below the pK_a (swollen), and back to the collapsed state (Willott et al. 2015a). Here, equilibrium ellipsometry data clearly showed the influ-

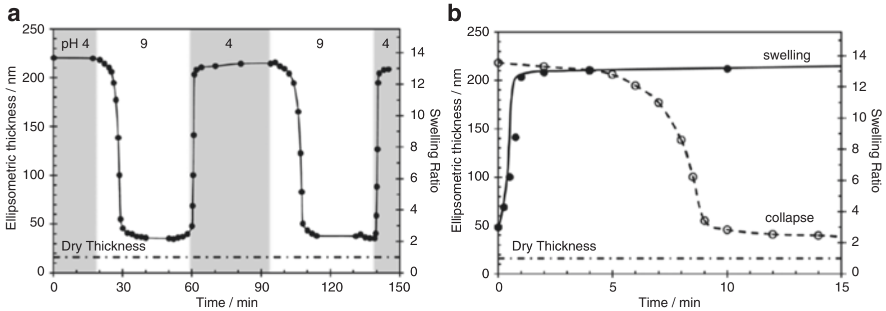

Fig. 12.36 Solvated brush thickness and corresponding swelling ratios derived from in situ ellipsometry on a PDEAEMA brush-modified wafer. (**a**) Solvated brush thickness as the pH was cycled between pH 9 (white) and 4 (shaded), and (**b**) comparison of the brush swelling and collapse kinetics. Brush = 16 nm dry thickness. (Reproduced from Cheesman et al. (2013) with permission from the Royal Society of Chemistry)

ence of the inherent hydrophobicity of the brush. The most hydrophobic PDPAEMA brush exhibited a sharp morphological transition around its pK_a, whereas the PDEAEMAEMA and PDMAEMA brushes responded over a much broader pH range. These two brushes also showed hysteretic behavior, with a higher pH required to induce collapse than swelling. The swelling state of this family of brushes well below their pK_a, in aqueous solution of potassium salts, was also shown to be a complex combination of the brush hydrophobicity and anion concentration and identity. Potassium salts of acetate (strongly kosmotropic), nitrate (mildly chaotropic) and thiocyanate (strongly chaotropic) were used to span the Hofmeister series. PDMAEMA was swollen in all salts at concentrations below 1 mM, while PDEAEMA and PDPAEMA were collapsed. At 10 mM concentration, all brushes were swollen in all salts, except for PDPAEMA in thiocyanate due to specific interactions between the hydrophobic brush and strong chaotrope. At 500 mM salt, the presence of the kosmotropic acetate ion allowed all brushes to remain swollen, while nitrate induced some collapse and thiocyanate significantly collapsed all brushes.

The ellipsometric technique may also be used to study thin films of soft matter in vapor phase environments. Fielding and coworkers investigated the response of a PDPAEMA brush to the conditions of the surrounding vapor phase, in particular the exposure to acidic HCl vapor (Fielding et al. 2011). Comparison between a dry unprotonated brush and a dry protonated brush clearly demonstrated the protonate brush responded to exposure to acidic vapor, swelling by more than 50% (Fig. 12.37).

12.3.2.4 Neutron Reflectometry (NR)

NR utilizes the reflection of a highly-collimated beam of incident neutrons from a surface to non-destructively probe the structure normal to the interface. The neutrons are scattered by the nuclei present, so neutron reflectometry is sensitive to not just atomic number but also isotopic substitution via the scattering length. The technique may be applied to the air/solid, air/liquid and liquid/solid interfaces, and is compatible with most common methods of applying a chemical or physical stimulus; flow-through cells, temperature control, electrochemical cells and optical windows are available on most instruments. Features on the length scale of 1–150 nm (10–1500 Å) are readily accessible with most neutron reflectometers.

The reflectivity, R (unitless), is measured as a function of momentum transfer, Q (Å^{-1}), which is itself a function of the wavelength of the neutrons, λ, and the incident angle, θ. In the case of specular reflection, when the angle of incidence equals the angle of reflection, the reflectivity is sensitive to variations in the scattering length density normal to interface. In the simplest case of a single slab of material at the interface, *e.g.* a spin-coated polymer film, reflections from the two interfaces present result in periodic oscillations in the data, so-called Kiessig fringes. When either interface is less well-defined or has high roughness, as in the case of a polymer brush in liquid, the fringes are less distinct and the reflectivity profile becomes relatively featureless. However, as the reflection is dependent on the scattering

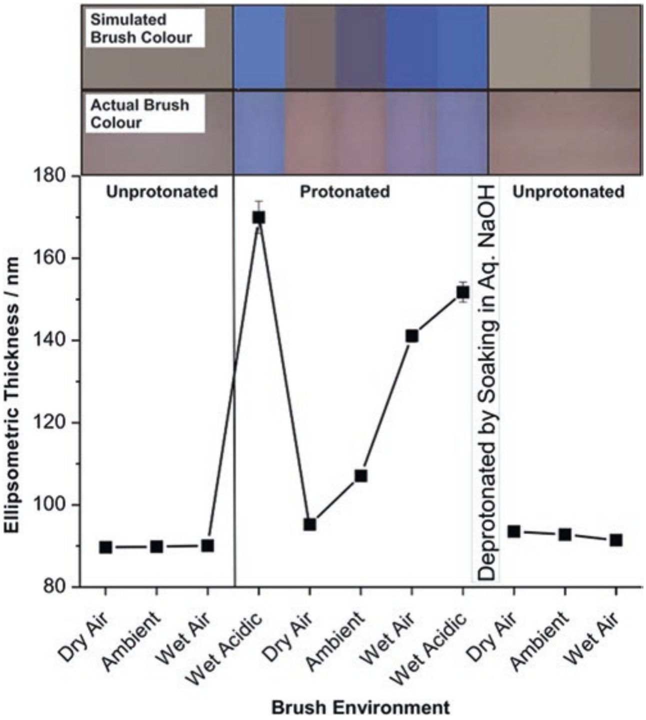

Fig. 12.37 Ellipsometric thickness as a function of surrounding vapor phase for a PDPAEMA brush grown from anionic polyelectrolyte initiator adsorbed on to an aminated silicon wafer. Both Δ and Ψ parameters were monitored to ensure that equilibrium had been attained, followed by thickness measurements via a spectroscopic scan. To show the colorimetric response to the vapor phase, images of an approximately 70 nm thick sample undergoing the same sequence of vapor treatments were recorded using a digital camera and optical microscope. Colors were modelled as detailed in the experimental section assuming a 70 nm initial brush thickness, and swelling ratios identical to that reported by ellipsometry for the 90 nm sample. (Reproduced from Fielding et al. (2011) with permission from the Royal Society of Chemistry)

length density (SLD) differences between the materials present it is possible to selectively deuterate parts of the system to highlight these features; for example, deuteration of one polymer only in a layer-by-layer lamellar structure. Also for this reason most experiments with hydrogenous soft matter are performed in deuterium dioxide (D_2O). To use reflectivity data to understand the structure of soft matter at an interface the researcher will (a) propose a structure (or volume fraction profile), (b) calculate an SLD profile, which is then (c) converted to a theoretical reflectivity profile and (d) compared to the measured data. This iterative process is continued until a satisfactory match is obtain between the experimental and theoretical curves.

Due to the time required to collect high quality data, which may be of the order of hours depending on instrument and experimental SLD differences, NR is mainly used to determine equilibrium structures in responsive soft matter systems. For example, Geoghegan and coworkers reported the volume fraction profiles of two

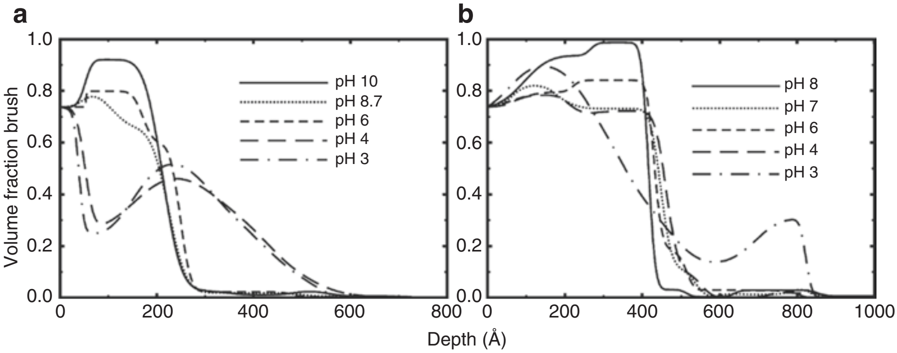

Fig. 12.38 Volume fraction profiles as a function of aqueous solution pH for PDEAEMA brushes of (**a**) 13 nm and (**b**) 27 nm dry thickness grafted from silicon blocks as measure by neutron reflectometry. (Reproduced from Geoghegan et al. (2006) with permission from Royal Society of Chemistry)

PDEAEMA brushes grafted from silicon blocks at solution pH values below and above the pK_a of PDEAEMA (~7.5) (Geoghegan et al. 2006). These data show the brushes exist as a collapsed single slab at pH > pK_a, but display a more complicated volume fraction profile when pH < pK_a (Fig. 12.38). At pH 3, i.e. far below the pK_a, both brushes show a depletion region close to the silicon substrate, where the volume fraction of polymer is a local minimum. This was attributed by the authors to the energy of self-repulsion between the charged monomer residues in the brush. At the periphery of the brush this self-repulsion is less, due to the presence of the bulk solvent, and results in a region of higher polymer volume fraction.

Geoghegan and coworkers also reported a depletion region close to the substrate for brushes of the more hydrophilic PDEAEMA analogue PDMAEMA (Tomlinson et al. 2009). Maglianetti and coworkers used a sapphire substrate to probe the pH response of PDMAEMA brushes using NR; the similarity in SLD of sapphire and D_2O enhances the sensitivity of the reflectivity curve to the hydrogenous polymer brush (Moglianetti et al. 2010). The reported data again showed the single slab of polymer at pH > pK_a and a depletion layer close to the substrate when pH < pK_a despite an overall more extended profile.

More recently Murdoch and coworkers used a combination of NR and numerical self-consistent field theory (nSCF) to study the pH and specific ion response of brushes of a more hydrophobic analogue of PDEAEMA; PDPAEMA (Murdoch et al. 2016a). Cycling of pH above and below the brush pK_a in 10 mM KNO_3 aqueous solution showed reversible switching between a collapsed and extended brush morphology respectively. Further, this work investigated the influence of the concentration of three different anions spanning the Hofmeister series on the behavior of the PDPAEMA brush below the pK_a, Fig. 12.39. In the presence of the mildly chaotropic nitrate anion the brush was swollen at concentrations from 1–100 mM, while it was collapsed below and above this range. At low salt concentration, the pK_a within the brush is shifted so as to reduce the overall charge while at high salt

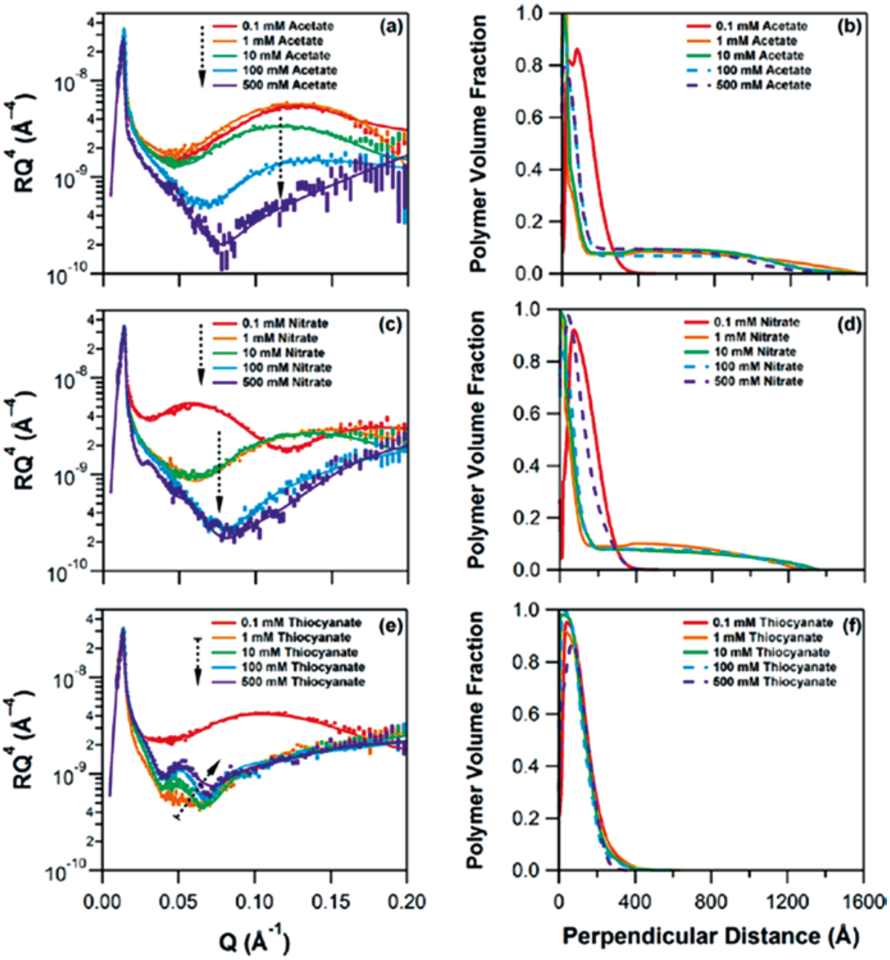

Fig. 12.39 Measured neutron reflectivity data (**a, c, e**) and corresponding volume fraction profiles (**b, d, f**) for the PDPAEMA brush immersed in 0.1–500 mM solutions of (**a, b**) potassium acetate, (**c, d**) potassium nitrate, and (**e, f**) potassium thiocyanate, all at pH 4.5 (in D_2O). Solid lines in (**a, c, e**) are fits to the experimental data. The height of the data points in (**a, c, e**) corresponds to the uncertainty of the measurement (±1 standard deviation). (Reproduced from Murdoch et al. (2016a) with permission from the American Chemical Society)

concentrations the free solution ions screen the electrostatic repulsion within the brush. The highly kosmotropic acetate anion did not interact as strongly with the PDPAEMA brush, and thus the brush remained swollen up to an acetate concentration of 500 mM. On the other hand, the chaotropic thiocyanate anion specifically interacts with the hydrophobic residues within the PDPAEMA brush, and the NR data showed a collapsed volume fraction profile at all concentrations. The results of the nSCF simulations showed the inclusion of a single interaction parameter analogous to anion hydrophilicity qualitatively captured the main features of the NR data.

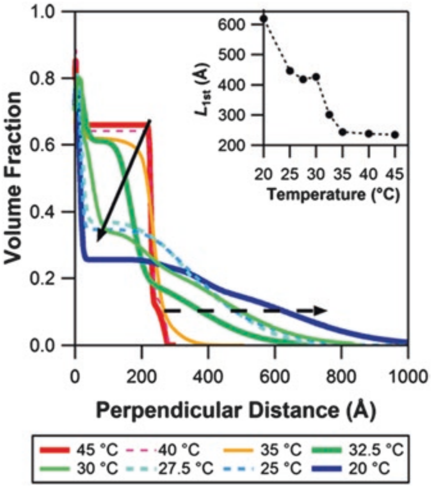

Fig. 12.40 Fitted volume fraction profiles for a PNIPAM brush immersed in D_2O as a function of sample temperature. Solid lines highlight examples of the collapsed (45 °C), vertically phase separated (between 35 and 30 °C), and swollen regimes (20 °C). Arrows are provided to guide the eye and correspond to a decrease in temperature. The inset plot at the top right presents the average brush thickness determined from twice the first moment of the volume fraction profile as a function of solution temperature. (Reproduced from Murdoch et al. (2016b) with permission from the American Chemical Society)

Subsequently, Murdoch and coworkers used NR to study specific ion effects on the thermoresponsive behavior of brushes of PNIPAM (Murdoch et al. 2016b) and poly(di(ethyleneglycol) methyl ether methacrylate) ($PMEO_2MA$) (Murdoch et al. 2017). For PNIPAM brushes in water the use of neutron reflectometry is able to provide direct evidence for a vertical phase separation within the structure of the brush (Fig. 12.40) during the transition from well-solvated at low temperatures to collapsed and poorly-solvated at temperatures above the LCST. This can only be inferred using other techniques such as QCM-D, ellipsometry and contact angle from differences in the LCST measured by these methods for the same brush; see for example Humphreys et al. (2016). Furthermore, the use of NR showed that in the presence of kosmotropic acetate or chaotropic thiocyanate anions the effect was not a simple modulation of the brush behavior around the LCST to lower or higher temperature respectively. The volume fraction profiles demonstrated that the presence or otherwise of vertical phase separation was influenced by the identity of the anions present, with thiocyanate broadening the LCST transition.

Lauw and coworkers used NR to determine the structure of the ionic liquid (IL) [C_4mpyr][NTf_2] at the gold interface as a function of applied potential (Lauw et al. 2012). Whilst the difference in the reflectivity profiles measured at −1595 mV, −895 mV and + 905 mV were subtle, careful analysis of the data revealed distinct differences in the IL nanostructure. At close to the point of zero charge (pzc) for the system (−895 mV) the layer nearest the gold substrate was a thin, compact layer exhibiting an excess of the $[C_4mpy]^+$ cation. At the more negative applied potential this layer was comprised entirely of cations, while the positive applied potential still showed a surface excess of cations. The reader is referred to the work of Lauw et al. as an example of the sophisticated modelling methods that may be applied to analyze NR data.

Another intriguing avenue for the use of neutron reflectometry in studying the response of soft matter systems is the application of a physical stimulus. For example, Prescott and coworkers from University of Bristol have pioneered the development of a cell that allows an external pressure to be applied to soft matter in an NR experiment. An example of this technique is the study of the interpenetration of polymer brushes in response to confinement under pressure (Abbott et al. 2016). Here the self-interaction of brushes of neutral poly(ethylene oxide) (PEO), and between PEO and weakly basic PDMAEMA, forced into overlap has been studied as a function of the applied pressure using NR and compared to nSCF calculations. Selective deuteration of one brush greatly enhanced the quality of the NR experiment, which show that two neutral brushes do not interpenetrate; either two PEO brushes or PEO and PDMAEMA above its pK_a. However, when the PDMAEMA is charged in solution below its pK_a significant interpenetration with a PEO brush was observed. The nSCF calculations reproduced the significant features of the NR data, and further predict the interpenetration of the two polymer brushes in response to an external pressure can by finely tuned around the pK_a of the weakly basic brush.

12.3.2.5 Light Scattering Methods

The scattering of light by macromolecules and colloidal systems has been used for many years to probe the behavior of these systems. From simple turbidity measurements to assess stability, to static light scattering for molecular weight determination or dynamic light scattering for hydrodynamic size determination the utility of light scattering to studying soft matter is broad.

Light passing through a fluid is scattered whenever it encounters a region of different dielectric constant; for example a colloidal particle. A simple method that utilizes this phenomenon is the monitoring of suspension stability using light transmittance, or conversely absorbance. In their seminal paper detailing the synthesis of PNIPAM microgels Pelton and Chibante used light scattering, via the measurement of absorbance, to measure the LCST of the microgel latex particles (Pelton and Chibante 1986). Yow and Biggs used a combined light transmission and centrifugation technique to investigate the stability and compressive rheology of suspension of polystyrene colloidal particles stabilized by the temperature responsive polyPEGMA (PPEGMA) as a function of temperature and added ionic strength (Yow and Biggs 2013). They found that below the LCST of the stabilizing PPEGMA the addition of increasing concentrations of potassium chloride resulted in particle aggregation and the formation of increasingly open and weak flocs. Above the LCST the particles were aggregated at all added salt concentrations and the suspension exhibited rapid settling.

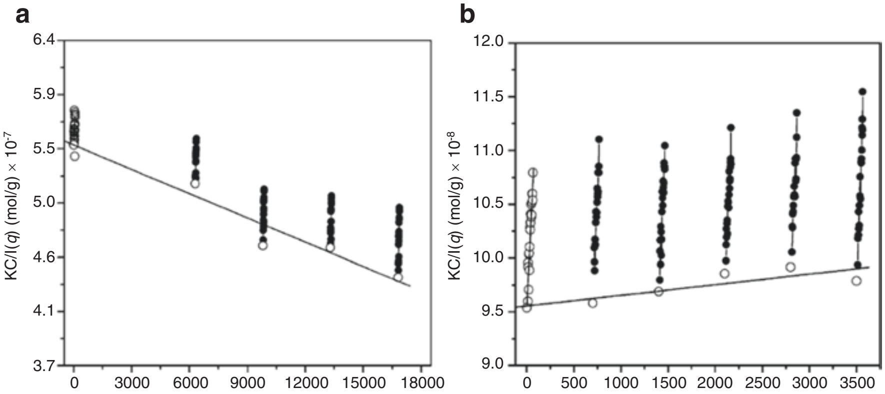

Fig. 12.41 Typical Zimm plots (KC/I(q) as a function of q^2) obtained from micellar solutions of (**a**) $PMPC_{30}$-*b*-$PDPAEMA_{30}$ and (**b**) $PMPC_{30}$-*b*-$PDPAEMA_{60}$. (Reproduced from Giacomelli et al. (2006) with permission from the American Chemical Society)

Static light scattering (SLS) measures the angular dependence of the time-averaged intensity of light scattered from particles. In the case of small colloidal particles, or macromolecules, the data may be analyzed using well-known theories to generate a Zimm, Berry or Guinier plot and so determine the root mean-square radius of hydration, $R_g^{21/2}$, and the molar mass. An SLS measurement requires careful measurement of the scattering vector, q, at multiple angles. This can be achieved by a single detector mounted on a high-precision goniometer, though this requires a very stable sample, or as a simultaneous measurement with multiple detectors. Giacomelli and coworkers used a combination of static and dynamic light scattering (DLS) to investigate the pH-induced micellization of diblock copolymers of PMPC and PDPAEMA, PMPC-*b*-PDPAEMA (Giacomelli et al. 2006). SLS measurements of the micelles were used to determine the R_g and molecular weight of micelles of two copolymers with different PDPAEMA block lengths, Fig. 12.41. By comparison to the molecular weight of the respective unimers, the authors calculated the aggregation number, N_{agg}, of the micelles to be 130 and 500 for $PMPC_{30}$-*b*-$PDPAEMA_{30}$ and $PMPC_{30}$-*b*-$PDPAEMA_{60}$ respectively.

Dynamic light scattering (DLS) monitors the time dependence of the scattering pattern by analysing the time auto-correlation function as a function of the delay time. In simplistic terms this approach compares the scattering pattern between short time intervals and in doing so accesses information regarding the dynamics of the dispersion. By far the most common application is the measurement of particle size distributions through the calculation of the hydrodynamic radius, R_H, from the measured diffusion coefficient, D, using the Stokes-Einstein equation:

$$R_H = \frac{k_B T}{6\pi\eta_0 D} \tag{12.1}$$

where k_B is Boltzmann's constant, T the absolute temperature and η_0 the viscosity of the solvent. This analysis carries with it all the assumptions underpinning the Stokes-Einstein equation, such as solid, spherical particles moving with low Reynolds number, and this may not be applicable in all circumstances. Modern "benchtop" DLS instruments usually measure the light scattering at a single angle, which is sufficient for DLS analysis. However it should be noted that DLS data is intensity weighted, and since for most samples large particles scatter more intensely the DLS measurement is naturally biased toward larger particles. Measurement software of most modern instruments automatically account for this. In addition, the calculated value of R_H will usually be larger than comparable measurements from, for example, microscopy techniques as solvent and dissolved molecules that move with the particle contribute to the scattering.

DLS measurements provide an excellent method to investigate the responsive nature of soft matter systems. Liu and Armes (Liu and Armes 2002) and Webber and coworkers (Webber et al. 2005a) used DLS to demonstrate micellization of zwitterionic poly(4-vinyl benzoic acid-*block*-poly(2-(diethylamino)ethyl methacrylate) (PVBA-*b*-PDEAEMA) and weakly basic PDMAEMA-*block*-PDEAEMA (PDMAEMA-*b*-PDEAEMA) diblock copolymers respectively. Liu and Armes showed the presence of polymeric micelles at high and low pH, while at intermediate pH the charge balance of the two blocks was such that the system was unstable. The DLS measurements of Webber and coworkers further revealed the influence of selectively quaternizing the corona-forming PDMAEMA block, with the R_H of the micelles reducing as the degree of quaternization was increased (Fig. 12.42).

The response of polymeric stabilizing layers on colloidal particles may also be monitored using DLS. Cheesman and coworkers used surface-initiated activators

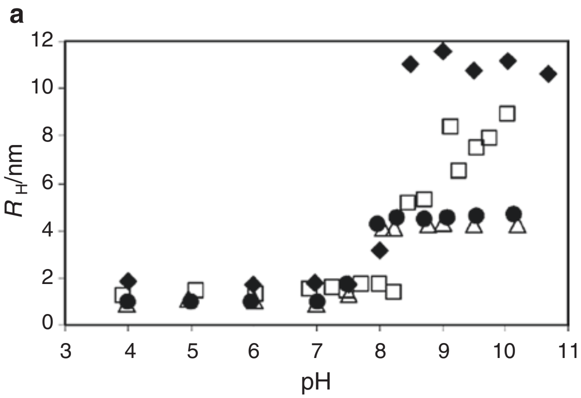

Fig. 12.42 Calculated hydrodynamic radius as a function of pH for 500 ppm, 10^{-2} M KNO_3 aqueous solutions of the diblock copolymers (◆) 0qPDMAEMA-*b*-PDEAEMA, (□) 10qPDMAEMA-*b*-PDEAEMA, (●) 50qPDMAEMA-*b*-PDEAEMA and (△) 100qPDMAEMA-*b*-PDEAEMA. "Xq" represents the targeted degree of quaternization of the PDMAEMA block. (Reproduced from Webber et al. (2005b) with permission from the Royal Society of Chemistry)

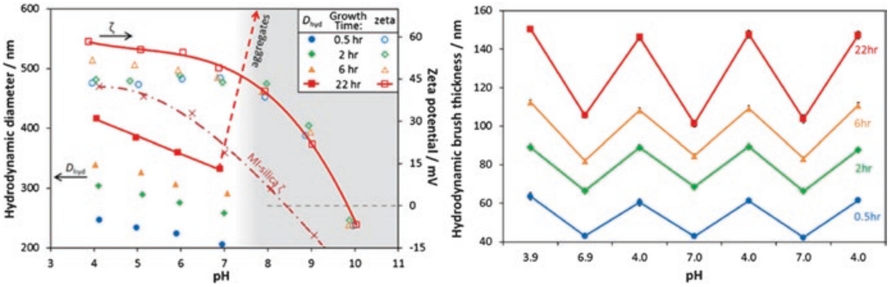

Fig. 12.43 (Left) Hydrodynamic diameter and zeta potential of PDEAEMA brush-modified particles as a function of pH. The shaded area denotes hybrid particle aggregation, the cross symbols and chained line are the zeta potential of the macroinitiator-modified silica (MI-silica). The hydrodynamic diameters of the unmodified silica and MI-silica were 124 ± 4 and 126 ± 3 nm, respectively. (Right) Hydrodynamic brush thicknesses of PDEAEMA brush-modified particles as the pH was cycled between 4 and 7. (Reproduced from Webber et al. (2005b) with permission from the Royal Society of Chemistry)

regenerated by electron transfer atom transfer radical polymerization to synthesize brushes of PDEAEMA from silica particles (Cheesman et al. 2012). DLS measurements were used to monitor the growth kinetics of the polymer brushes and to demonstrate the pH responsive nature of the stabilising PDEAEMA brush (Fig. 12.43 left). The data clearly show the thickness of the brush decreases as the solution pH is raised near to the pK_a value of PDEAEMA; ~7.3. Above this pH the inherent hydrophobicity of the PDEAEMA brush causes the particles to aggregate. The authors also used DLS measurements to show the brushes could be repeatedly swollen and collapsed in response to cycling the pH of the solution (Fig. 12.43 right).

12.3.2.6 Laser Diffraction

Laser diffraction is a method of measuring particle size that takes advantage of the angular variation in the scattering of light by particles of different size. The technique is able to measure particles in the range of submicron to millimetre in size and is compatible with flow through geometries that enable high sample rates. Laser diffraction instruments measure the intensity and angle of light scattered from particles in a dispersion and utilize advanced Mie theory, or the simpler Fraunhofer approximation, to determine particle size. Use of Mie theory requires knowledge of the optical properties of the solids, in particular both the imaginary and real components of the refractive index, and the refractive index of the solvent. The Fraunhofer approximation does not require this level of information, but is only suitable to larger particles (generally above 20–50 μm). Many modern commercial instruments based on laser diffraction have two lasers of different wavelength to increase the range of particle size measurable, as well as cells to measure particles dispersed in the gas phase; i.e. dry powder samples.

The wide particle size range accessible by laser diffraction and the flexibility of the measurement set up has led to its use across a broad spectrum of research areas.

For example, Barea and coworkers used laser diffraction to monitor the evolution of a pH responsive polymer coating on egg phosphatidyl-choline (EPC) and cholesterol (CH) based liposomes (Barea et al. 2010). Addition of Eudragit S100 pH responsive polymer resulted in an increase in particle size from 7.7 to 22.0 μm, up to a polymer concentration of 0.025% w/v, after which the particle size did not change. At polymer concentrations greater than this the ζ-potential was also observed to change from positive to negative, as a result of excess adsorption of the polymer causing charge reversal. The release of a model drug, vitamin B12, was shown to be retarded by the presence of the Eudragit S100 coating at solution pH 1.4 and 6.3, but not at pH 7.8, confirming the pH responsive nature of the polymer coating was able to influence the behavior of the liposomes.

Thompson and coworkers used laser diffraction to compare the efficacy of vermicious (worm-like) and spherical thermoresponsive diblock copolymer nanoparticles as Pickering emulsifiers (Thompson et al. 2015). Measuring the size of the *n*-dodecane emulsion droplets dispersed in water the authors showed the drops decreased in size with increased nanoparticle concentration and increased in size with water volume fraction. Upon heating to 95 °C the emulsions were observed to demulsify due to morphological changes of the nanoparticles. Further demonstrating the wide applicability of the laser diffraction technique, Lentacker and coworkers measured the particle size distributions of microbubbles coated and stabilized by poly(allylamine hydrochloride) (PAH) (Lentacker et al. 2006). These polymer-coated microbubbles were studied as an analogue of microbubble-based contrast agents for medical ultrasonography applications. Here the authors showed the as-prepared microbubbles exhibited a narrow size distribution, with the majority of bubbles less than 5 μm in size, and that coating with PAH had little influence on the distribution.

Fujii and coworkers studied the influence of particle shape and aqueous solution pH on the use of hydroxyapatite (HAp) nanoparticles as stabilizers for Pickering emulsions (Fujii et al. 2007). Nanoparticles with spherical, rod- and fiber-shaped morphologies were used to stabilize methyl myristate oil-in-water emulsions. The spheres had an average diameter of 40 nm, the rods short and long axis lengths of 80 and 410 nm respectively, and the fibers 100 and 2320 nm axis lengths. The nanoparticles formed stable oil-in-water emulsions when the pH was greater than 7.7, and the emulsion droplet size increased dependent on particle shape in the order: fiber > rod > sphere (Fig. 12.44). The emulsions were shown to respond to changes in aqueous phase pH, with rapid demulsification when the pH was below 6, due to the dissolution of the HAp particle stabilizers. The emulsification-demulsification cycle was reversible when the pH was cycled between 10 and 1 respectively, due to the precipitation and dissolution of the HAp. The authors used laser diffraction to show the emulsion droplet diameters at high pH ranged from 47 to 154 μm.

Laser diffraction was used by Fujii and coworkers to characterize the pH-responsive nature of polystyrene (PS) latex particles stabilized by PDEAEMA (Fujii et al. 2011a). Dried PDEAEMA-PS particles were further used to prepare liquid marbles of volume 15 μL to 2 mL via the rolling method. In aqueous solution at pH 3 and 10 the particle size of PDEAEMA-PS dispersions was measured to be 470 nm and 8.0 μm respectively (Fig. 12.45). The greater size at pH 10 was attributed to flocculation of the particles since the pH is above the pK_a of the stabilizing

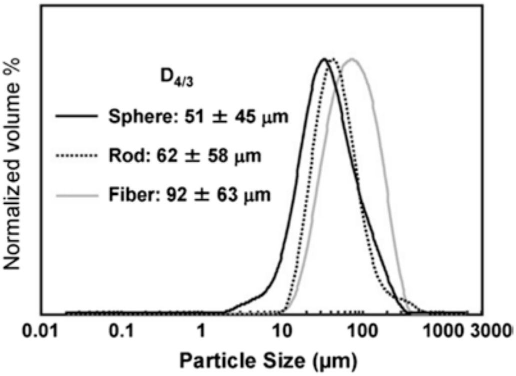

Fig. 12.44 Laser diffraction droplet size distributions of a methyl myristate-in-water emulsion prepared at pH 6–7 spherical, rod-shaped or fiber-shaped HAp particle dispersion. (Reproduced from Fujii et al. (2007) with permission from Elsevier)

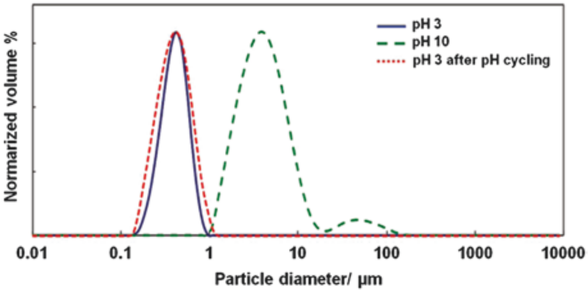

Fig. 12.45 Laser diffraction particle size distribution curves obtained for PDEAEMA-PS latex particles at pH 3 and 10. The dotted curve shown at around 0.1 μm was obtained after pH cycling (from pH 3 to 10 and back to pH 3). (Reproduced from Fujii et al. (2011a) with permission from the American Chemical Society)

PDEAEMA. The authors also confirmed that with repeated cycling of the pH the particles were able to flocculate then redisperse. This pH-dependent behavior of the PDEAEMA-PS particles was translated to their ability to stabilize water-based liquid marbles. Above the PDEAEMA pK_a liquid marbles were able to be formed, with their lifetime increasing with pH. However below the pK_a of the PDEAEMA the (hydrophilic) particles could not stabilize liquid marbles.

12.3.3 Other Methods

12.3.3.1 Atomic Force Microscopy (AFM)

Imaging

Since its invention in 1984 by Binnig et al. (1986), AFM has gained a firm position in surface imaging as one of the most powerful techniques for observing matter down to the molecular, or even atomic scale. In AFM, a probe tip attached to the end of a microfabricated cantilever is scanned over a sample. The cantilever bends upwards and downwards, following the surface undulations of the sample, which are detected with a photodiode by the deflections of the laser beam reflected from the back of the cantilever. Surface images are obtained by mapping the displacement of the cantilever. This optical lever method creates a particular advantage of AFM over other imaging techniques; i.e., AFM is compatible with different environmental conditions, including liquids. AFM can also utilize operation methods such as the intermittent- and non-contact modes, in which the cantilever oscillates during scanning, that enable soft surfaces to be observed with limited damage. Thus, AFM is a desirable tool for the in situ characterization of morphological changes in the surface polymer layers induced by application of stimulus, which can be difficult to observe using other techniques.

Using AFM imaging, Ishida and Biggs (Ishida and Biggs 2007a) visualized successfully in situ the transition of thermoresponsive PNIPAM chains grafted on a silica plate from a brush-like to mushroom-like state across the LCST in water. As shown in Fig. 12.46, the AFM images of the PNIPAM layer grafted onto a flat substrate did not show any features at temperatures below the LCST, whereas a large number of domain structures with a characteristic size of ~100 nm appeared on the surface above the LCST. These images indicate the transformation of the PNIPAM layer from stretched, brush-like state to a collapsed, mushroom-like state across the LCST. AFM imaging also facilitated observation of salt-induced structural changes in grafted PNIPAM chains in sodium sulfate solutions (Ishida and Biggs 2007b).

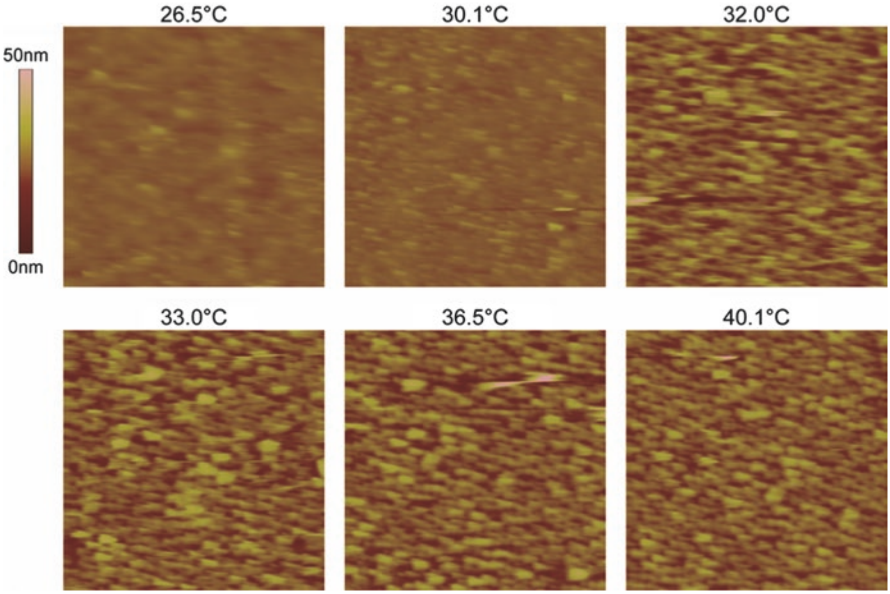

Fig. 12.46 AFM images ($2 \times 2\ \mu m^2$) of a PNIPAM layer grafted on silicon wafer in water. Images were obtained at 26.5, 30.1, 32.0, 33.0, 36.5 and 40.1 °C. (Reprinted with permission from Ishida and Biggs (2007b). Copyright (2007) American Chemical Society)

Brunsen et al. (2012) observed similar structural changes driven by solution pH for poly(2-(methacryloyloxy)ethylphosphate) (PMEP) grafted on silica. The authors found that the nanoscopic domains of the collapsed PMEP chains on the surface at pH 3 changed to fully extended at pH 8. This change was attributed to the electrostatic repulsion between the PMEP chains arising as a result of their ionization at pH 8 (Ishida and Biggs 2007b). Sakai et al. have visualized successfully the irreversible adsorption of pH-responsive cationic diblock copolymer micelles consisting of different amino methacrylate blocks on silica/aqueous solution interface, which permitted surface wettability switching as a function of pH (Sakai et al. 2006b).

The molecular weight and density of grafted chains affect the structural transformations of stimulus-responsive polymers grafted on solid surfaces significantly, and these parameters have also been probed by AFM imaging. Ishida and Biggs (2010) investigated the phase transition behavior of PNIPAM layers grafted using atom transfer radical polymerization (ATRP) at three different grafting densities with the same molecular weight. AFM imaging in water showed that the transition behavior of the grafted PNIPAM chains was abrupt across the LCST for the low-density surface, and became more moderate as the polymer graft density increased (Fig. 12.47). The authors suggested that the degree of lateral chain aggregation as a result of the grafting density alters the magnitude of structural changes driven by temperature. In contrast, Plunkett et al. (2006) pointed out that the structural changes are less pronounced at lower grafting densities when the molecular weight of the grafted chains is low, thus corroborating that both molecular weight and grafting density are important parameters driving the temperature-dependent response of PNIPAM brushes.

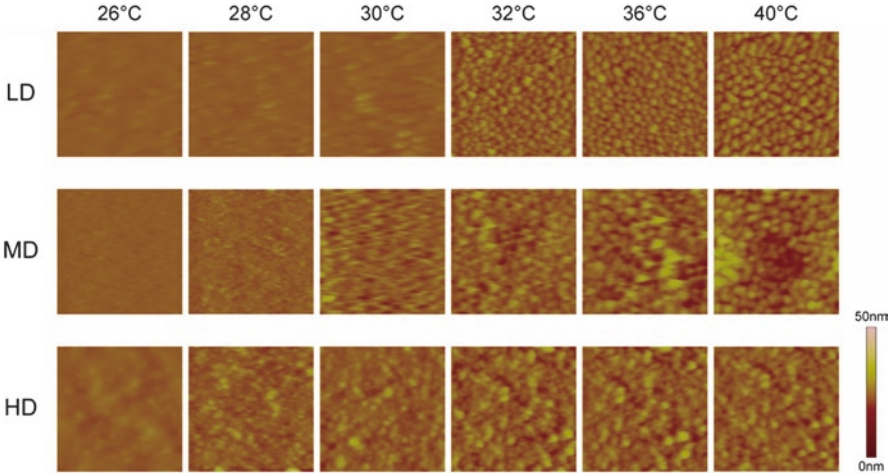

Fig. 12.47 AFM images (1 × 1 μm^2) of a PNIPAM layer on silicon wafer with low (LD), middle (MD) and high (HD) grafting densities obtained in water. Images were obtained at 26, 28, 30, 32, 36 and 40 °C. Grafting densities for the LD, MD and HD surfaces are 0.018, 0.071 and 0.361 molecule/nm^2, respectively. (Reprinted with permission from Ishida and Biggs (2010). Copyright (2010) American Chemical Society)

Interaction Force Measurements

In addition to surface imaging, AFM can be used to measure the interaction forces between the probe tip and the sample substrate. Since the probe and the substrate can be scanned vertically (z-direction), the tip–substrate interaction force during the scan is evaluated by measuring the vertical deflection of the cantilever. This method enables the measurement of interaction forces as a function of surface distance at a resolution down to a few piconewtons.

Force-distance curves between an AFM tip and a stimulus-responsive polymer layer have often been used to estimate in situ the structural changes in the layer produced as a result of the application of a stimulus. In this case, the main interaction force that is analyzed is the steric force acting between the AFM tip and polymer brushes on the sample when they comes into contact. Kidoaki et al. (2001) were the first to measure the interaction forces between an AFM tip and a PNIPAM layer grafted on a glass substrate. As shown in Fig. 12.48, the authors found that the force curve exhibited a steric repulsion from stretched PNIPAM chains acting from a long-range distance (100–200 nm) at 25 °C. On the other hand, the range of repulsion decreased significantly at 40 °C, thus confirming a heat-induced collapse of the

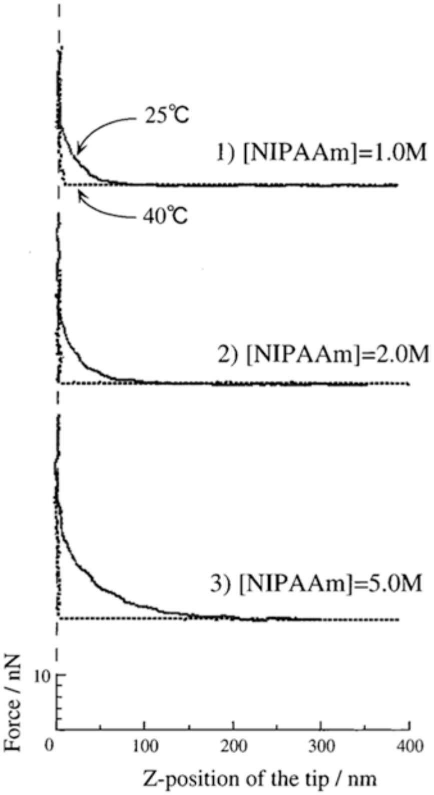

Fig. 12.48 Force curves measured between PNIPAM grafted surfaces and a AFM tip on approach: solid curves, 25 °C; dashed curves, 40 °C. Data for the surfaces different chain lengths (PNIPAM was polymerized different monomer concentration at 1.0, 2.0 and 5.0 M) are shown. (Reprinted with permission from Kidoaki et al. (2001). Copyright (2001) American Chemical Society)

PNIPAM layer. Murdoch et al. (2016b) utilized the force measurements between an AFM tip and a PNIPAM layer, with complementary neutron reflectometry (NR) and quartz crystal microbalance with dissipation monitoring (QCM-D) measurements, to examine the influence of salt identity and concentration on the structural changes in the PNIPAM layer.

For a pH-responsive polymer, Fujii et al. (2011b) measured the interaction force of PDEAEMA chains attached onto PS particles against an AFM tip, and found that the interaction force exhibited a steric repulsion caused by the flexible, PDEAEMA-rich layer on PS at pH 3. In contrast, however, a short-range attractive force was observed at a pH of 10, instead of a repulsive force. This transformation in the force curve indicates a clear structural change in the PDEAEMA arising as a result of protonation-deprotonation; flexible hydrated PDEAEMA layer at lower pH collapses to be more rigid layer at high pH by the deprotonation.

The intermolecular forces acting between polymer chains and specific molecules like proteins have also been studied by AFM. In order to measure the forces between polymer chains and molecules such as proteins, the molecules of interest are attached directly onto the AFM tip via physical and chemical adsorption, and the interaction force between the tip and the polymer layers is measured. This method is often utilized to evaluate the ability of polymer layers to attach/detach biomolecules in response to stimulus.

The PNIPAM–protein interaction measured using this method (Kidoaki et al. 2001; Cho et al. 2005; Cole et al. 2010) is generally repulsive at temperatures well below the LCST, but tends to be attractive at temperatures around and above the LCST. This tendency is particularly common when proteins are employed in the force measurements. The repulsive force at low temperatures is caused by a combination of steric force of stretched chains and repulsion between hydrated chains and protein molecules. By contrast, the dehydration of PNIPAM chains renders them more hydrophobic and induces hydrophobic interaction with the hydrophobic regions of proteins, thus resulting presumably in a net attractive force.

By attaching a micrometer-sized particle onto the end of the cantilever, often called the “colloid probe” (Ducker et al. 1991), one can also measure the surface forces between a specific macroscopic particle and the target substrate. The force measurements using such a colloid probe have been utilized to evaluate how stimulus-responsive surfaces interact with particulate materials, monitoring specifically the attachment and detachment of target materials. The force measurements between a PNIPAM-grafted substrate and a hydrophobized silica particle (Ishida and Kobayashi 2006) revealed the presence of strong repulsive forces between their surfaces at temperatures below the LCST, arising as a result of the steric repulsion caused by the hydrated chains of the polymer substrate. Above the LCST, on the other hand, strong attractive forces due to the hydrophobic attraction were observed, thus indicating that switching between repulsive and attractive forces can allow the attachment and detachment of hydrophobic particulate materials.

12.3.3.2 Quartz Crystal Microbalance (QCM)

QCM is a high-resolution mass sensing technique that utilizes the piezoelectric nature of quartz. A QCM crystal consists of a thin quartz disk between a pair of gold electrodes. Application of an oscillating electric field across the crystal induces an acoustic wave that propagates in a direction perpendicular to the crystal surface. Increasing the mass adsorbed or attached to the surface of a QCM crystal will decrease the resonant frequency (f) of the crystal with nanogram sensitivity. This decrease can be modelled using the Sauerbrey equation for thin uniform elastic coatings. If energy loss accompanies the sample oscillation, then the process is said to be inelastic and the film will dissipate energy (ΔD). The kinetics and equilibrium viscoelastic behavior of a responsive polymer adsorbed to, or grafted from a QCM crystal can be readily monitored in situ using an instrument also equipped with dissipation monitoring: a QCM-D.

For example, QCM-D has been used to study the pH-responsive behavior of selectivity quaternized PDMAEMA-*b*-PDEAEMA micellar films electrostatically adsorbed at the silica-aqueous solution interface (Sakai et al. 2007). They found that the more quaternized the polybasic diblock copolymer was, the more strongly the molecules were adsorbed onto the negatively charged silica surface. By cycling the pH between 9 and 4, they showed that the copolymer was reversibly pH-responsive. Specifically, as the solution pH was lowered to 4, the adsorbed copolymer layer became more swollen with solvent as it was protonated and as a result became more hydrophilic.

This technique has also been used by Howard et al. to study the pH-response of electrosterically-stabilized PDEAEMA microgels adsorbed at the silica-aqueous solution interface (Howard et al. 2010). It was determined that the kinetics of the microgel collapse was slower than its swelling transition. The initial swelling at pH 4.6 resulted in desorption of some microgel since the coupled mass decreased. Also, the dissipation increased which suggested that the film took up water. When the pH was switched to 8.4 the dissipation dropped significantly; which corresponded to the collapse of the film. The coupled mass also dropped as water was expelled from the film. Subsequent pH cycles were reversible. By plotting ΔD vs Δf, these workers were able to evaluate the viscoelastic properties of the film (Fig. 12.49). An increase in the slope of the plot corresponds to a more viscous film. Upon initial adsorption, and after the first swelling cycle, the collapsed film at pH 8.4 was elastic in nature. However, on subsequent cycles during which the adsorbed mass was constant, the collapsed film was more viscous in nature and behaved more like the swollen film at pH 4.6 but with less entrained water.

Ishida and Biggs investigated the thermoresponse of PNIPAM brushes grafted to a silica surface as a function of grafting density using QCM-D (Ishida and Biggs 2010). PNIPAM undergoes a conformational change around its LCST of ~32 °C. In aqueous solution at temperatures below the LCST, the PNIPAM chains hydrate and as a result swell and stretch. Above the LCST the chains collapse due to dehydration. For the low density brushes, Δf is seen to drop sharply in Fig. 12.50 in the vicinity of the LCST. This unexpected behavior was attributed to more effective

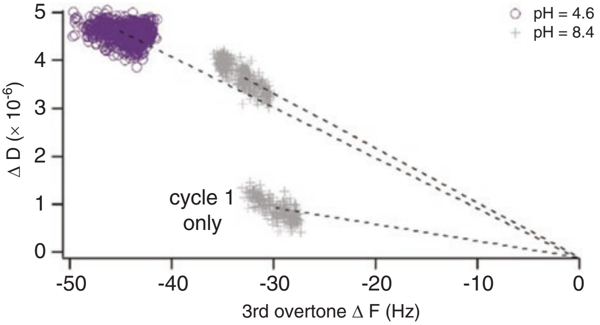

Fig. 12.49 ΔD vs Δf at pH 4.6 (purple circles) and pH 8.4 (grey crosses). The slope of line through the origin is a measure of viscoelasticity of the film and is independent on the adsorbed mass. (Copyright 2010, reproduced from Howard et al. (2010) with permission from the ACS)

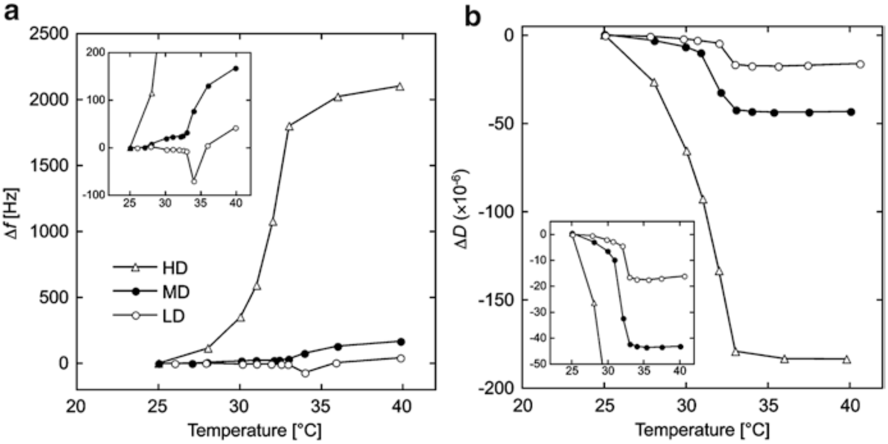

Fig. 12.50 Changes in (**a**) frequency and (**b**) dissipation as a function of temperature for PNIPAM brushes grafted to a silica-coated QCM crystal at low (LD), medium (MD) and high (HD) grafting densities. The insets reveal the behavior at enlarged scales. (Copyright 2010, reproduced from Ishida and Biggs (2010) with permission from the ACS)

coupling with the oscillating crystal upon the dehydration and collapse of the PNIPAM chains. This effect caused an increase in the 'effective' mass measured by the instrument (drop in Δf) which was greater than the initial mass loss by dehydration for the film. After reaching a minimum in Δf at 34 °C, Δf was observed to increase steeply as temperature was increased further, as expected. This complex behavior was not observed for the medium- and high-density PNIPAM brushes. Both brushes show positive increases in Δf with increasing temperature. Decreases in the dissipation around the LCST suggest a strong aggregation of the PNIPAM chains leading to a collapsed, more elastic layer.

The pH-response of PDMAEMA brushes formed by grafting premade thiol-functionalized PDMAEMA chains onto gold has been studied using QCM-D by Nordgren and Rutland (Nordgren and Rutland 2009). At room temperature and at pH 3, the PDMAEMA brush was highly swollen. Switching to pH 11 saw the brush desolvate and collapse reaching a steady-state within 5 min of the pH change. The pH-response was confirmed to be reversible at either a fixed temperature below or above the LCST. Subsequently, Cheesman et al. studied the pH-induced swelling and collapse of four PDEAEMA brushes of increasing molecular weight (Cheesman et al. 2013). Complementary work was performed by Willott et al. in a later comparative study of increasing hydrophobicity in the family PDMAEMA, PDEAEMA and PDPAEMA (Willott et al. 2015a). In all of these studies the ionic strength and salt type was controlled at 10 mM potassium nitrate. Fig. 12.51a shows the measured frequency response for four PDEAEMA brushes of increasing dry brush thickness as a function of solution pH (Cheesman et al. 2013). As the pH was lowered the measured frequency decreased reflecting the increased solvation of the brushes as they became more charged. Larger magnitude frequency responses were observed for the thicker brushes suggesting that they entrained more solvent. Multiple pH cycles demonstrate that the viscoelastic nature of the swollen state relative to the collapsed brush is independent of brush thickness as shown in Fig 12.51b.

The specific anion response of poly(2-methacryloyloxy)-ethyl-trimethylammonium (PMETAC) brushes to a range of sodium salt solutions was recently reported by Kou and coworkers as a function of ionic strength (Kou et al. 2015). Figure 12.52 shows the frequency response of the PMETAC brush-coated QCM sensor. The magnitude of brush collapse incrementally increased as a function of

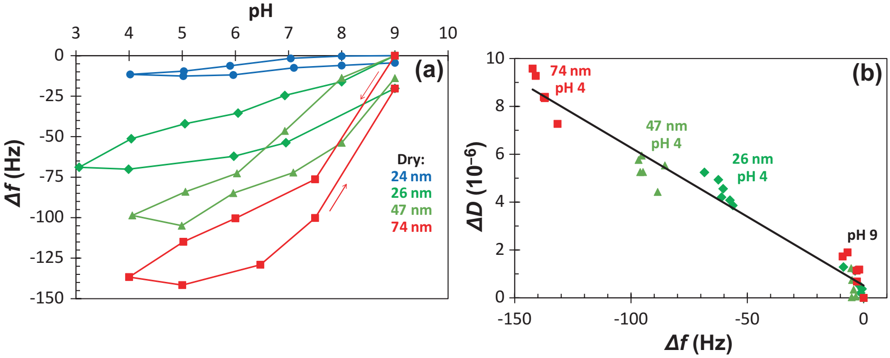

Fig. 12.51 (**a**) Change in QCM frequency response for the third overtone, normalized at pH 9, during initial hydration of four PDEAEMA brushes of different dry brush thickness as the pH was incrementally acidified and then returned to pH 9 in 10 mM potassium nitrate. Arrows indicate the chronology of all the experiments. (**b**) Change in dissipation vs frequency response for the 26–74 nm brushes for the fifth overtone. Both dissipation and frequency are normalized to the values at pH 9. The dashed line highlights the common viscoelastic nature of the three brushes. (Copyright 2013, reproduced from Cheesman et al. (2013) with permission from the Royal Society of Chemistry)

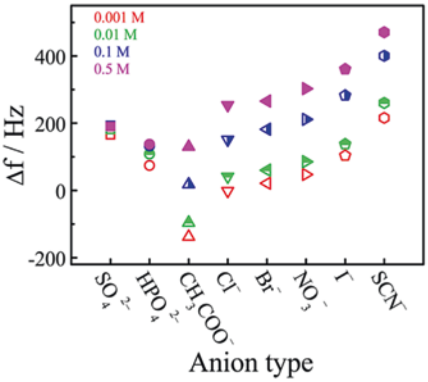

Fig. 12.52 Change in frequency for the third overtone, normalized to the frequency response measured for a PMETAC brush immersed in a range of sodium salt solution at concentrations of 1 mM (red, open symbols), 10 mM (green half up-filled symbols), 100 mM (blue, half right-filled symbols) and 500 mM (pink, filled symbols). The chaotropic nature of the anion increases from left to right. (Copyright 2015, reproduced from Kou et al. (2015) with permission from the American Chemical Society)

solution ionic strength. Moreover, the degree of brush collapse was more pronounced for the chaotropic anions. These anions are highly polarizable and are poorly solvated which means they can form stronger interactions with the quaternary ammonium residues of the brush. As a consequence, the direct ion-pairing interaction results in a decrease in the hydration of the anions and hence a lower solvation (higher Δf value) of the grafted PMETAC chains. Similarly strong Hofmeister anion effects have also been reported in the PDMAEMA, PDEAEMA, PDPAEMA brush family (Willott et al. 2015b). Strong Hofmeister cation effects have been reported in the conformational response of poly(sodium styrenesulfonate) brushes as the solvent is changed from water to methanol (Wang et al. 2014).

Each of these studies demonstrates that QCM-D is an excellent tool for gaining insight regarding the conformation of polymeric materials at the solid-liquid interface and how this changes in response to solution-based triggers such as pH, salt concentration or identity, or an external trigger such as temperature.

12.3.3.3 Contact Angle

Contact angle analysis is probably the simplest and easiest way to evaluate changes in the properties of stimulus-responsive surfaces. According to Young's equation (12.2), the contact angle θ of a liquid droplet against a flat surface is related to interfacial tensions as follows:

$$\gamma_{\mathrm{LV}}\cos\theta = \gamma_{\mathrm{SL}} - \gamma_{\mathrm{SV}}, \tag{12.2}$$

where γ_{LV}, γ_{SL}, and γ_{SV} represent interfacial tensions between liquid-vapor, solid-liquid, and solid-vapor respectively. Stimulus-responsive surfaces exhibit changes mainly in their surface free energy, which is related to γ_{SL} and γ_{SV}, and thus the contact angle θ changes depending on it.

The sessile drop method is the most popular technique used to measure the contact angle. In this method, one simply places a liquid droplet on a sample plate and measures the angle of the tangential line of the liquid against the plate using a goniometer or image analysis. There are two additional techniques used commonly to evaluate the contact angle, namely the captive bubble method, in which a macroscopic bubble is attached to a sample plate in a liquid and its angle is measured; and the Wilhelmy plate technique, in which a plate is immersed in a liquid and the weight of the plate is measured.

The wettability switching of various stimulus-responsive surfaces has been evaluated by contact angle measurements. Surfaces covalently grafted with PNIPAM, i.e., the most popular temperature-responsive surface, generally exhibit a reversible change in contact angle as a function of temperature, usually with large and almost discontinuous changes around the LCST (Yakushiji et al. 1998; Balamurugan et al. 2003; He et al. 2007). The variation in the contact angle, however, depends intricately on factors such as the molecular weight, density, and structure of the PNIPAM grafted on surfaces. Yakushiji et al. (1998) found that while a surface grafted with PNIPAM chains with freely mobile ends showed an advancing contact angle (θ_A) of 21° at 5 °C and 70° at 40 °C, this difference in θ_A broadened to 24° at 5 °C and 93° at 40 °C when the surface was grafted with chains with a looped conformation (Fig. 12.53). The authors also revealed that the surface bearing PNIPAM chains

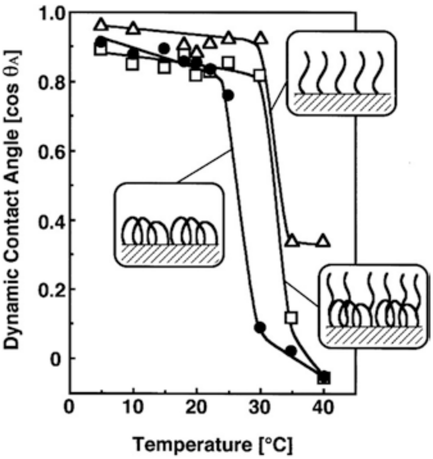

Fig. 12.53 Temperature-dependent changes in the advancing contact angle determined for three types of PNIPAM-covered surfaces. Open triangles, closed circles, and open squares represent the data for surfaces grafted with PNIPAM chains with freely mobile ends, looped conformation, and a mixture of both, respectively. (Reprinted with permission from Yakushiji et al. (1998). Copyright (2010) American Chemical Society)

with both conformations exhibited large and discontinuous changes in θ_A with a narrower temperature range and at higher temperatures. On the other hand, dense PNIPAM brushes prepared using a “grafting-from” method such as the ATRP tend to display a narrow range of contact angles, which is reported to be ~10–30° (Balamurugan et al. 2003; He et al. 2007). This can be explained by the fact that only the polymer segments in the outermost region of the brush are solvated and segments within the brush layer are less solvated at low temperatures when the brush density is high. Cross-linking of the grafted polymer can in contrast increase the range of contact angle variation on going from hydrophilic to hydrophobic. Liang et al. showed that a surface bearing PNIPAM cross-linked with *N,N′*-methylenebisacrylamide exhibited complete hydrophilicity (advancing contact angle $\theta_A = 0°$) below 25 °C, and became highly hydrophobic ($\theta_A = 92°$) above 40 °C (Liang et al. 2000). Copolymerization is often used to alter the switching temperature by changing the solubility (i.e., LCST) of the brush (Cunliffe et al. 2003).

For pH-responsive surfaces, Wilson and Whitesides (Wilson and Whitesides 1988) created an anthranilate amide-modified polyethylene carboxylic acid surface and found that the surface exhibits exceptionally large wettability variation with pH; the advancing contact angle changes from 110° at pH 1 to 33° at pH 12. Utilizing polymer brushes to create pH-responsive surfaces is another popular method, and the polymers commonly employed include PAA (Burtovyy and Luzinov 2008), poly(vinyl pyridine) (Lu et al. 2013), and tertiary amine methacrylate polymers (Willott et al. 2015a; Lei et al. 2014). Sakai et al. have reported that not only tethered polymers but also diblock copolymer micelles adsorbed on surfaces can be used to switch the surface contact angle using pH (Sakai et al. 2006b).

Photo-induced wettability changes have been investigated for quite a long time now. Photo-responsive surfaces have been produced using molecules such as spiropyran (Hayashida et al. 1986; Rosario et al. 2002), azobenzene (Siewierski et al. 1996), and pyrimidine (Abbott et al. 1999). Using spiropyran-amine, Kessler et al. (2011) created the surface with the highest light-induced switching of contact angle on a flat surface, which was 48° when irradiated with UV light ($\lambda = 365$ nm) and 78° when exposed to visible light ($\lambda > 400$ nm). In the case of a spiropyran-functionalized surface, the spiropyran molecule isomerizes through a ring-opening process into a polar, zwitterionic merocyanine structure when exposed to UV light, thus making the surface hydrophilic.

Normally, the maximum contact angle that can be obtained by modifying the surface with closely packed hydrophobic molecules is estimated to be 110–120°. Essentially the only way to create hydrophobic surfaces with even larger contact angles involves modification of surface structure. It is now well known that micro/nano-scale surface roughness enhances surface hydrophobicity and hydrophilicity, and is often referred to as the “lotus effect”. Typically, when the contact angle with a flat surface, θ_f, is greater than 90°, the same surface with enhanced structure has a contact angle much greater than θ_f, whereas if the value of θ_f is below 90°, the contact angle decreases far below θ_f. By exploiting this effect, superhydrophobic (contact angle >150°) or superhydrophilic (contact angle almost 0°) surfaces can be created.

Recently, the development of smart surfaces capable of switching their wettability to a large extent has been achieved by modifying such microfabricated surfaces with stimulus-responsive molecules. Similar to the flat surfaces mentioned above, this technique can permit the creation of surfaces responsive to external stimuli such as temperature (Yu et al. 2011; Sun et al. 2004; Chen et al. 2009), pH (Zhang et al. 2008; Stratakis et al. 2012), and light irradiation (Groten et al. 2012). In terms of obtaining surfaces with very high hydrophobicity and hydrophilicity, the morphology of the substrate structure plays an essential role. As suggested in the theory presented by Cassie and Baxter (1944), the structures that provide the highest hydrophobicity/hydrophilicity enhancement are those that have the smallest surface area in contact with the liquid and the largest area in contact with air such as porous surfaces. Microscopic pyramidal arrays (Stratakis et al. 2012), pillar arrays (Yu et al. 2011; Chen et al. 2009), and microgrooves (Sun et al. 2004) are among the structures that fulfill these conditions. Stratakis et al. used a silicon surface with artificially structured conical asperities with an average size of ~10 μm and a spacing of few μm in-between to graft on pH-responsive PDPAEMA (Stratakis et al. 2012). The created pH-responsive surface exhibited excellent reversible switching of surface wettability from superhydrophilicity (i.e., almost zero contact angle at pH 2.5) to superhydrophobicity (i.e., contact angle of more than 150° at pH 8.5), as shown in Fig. 12.54.

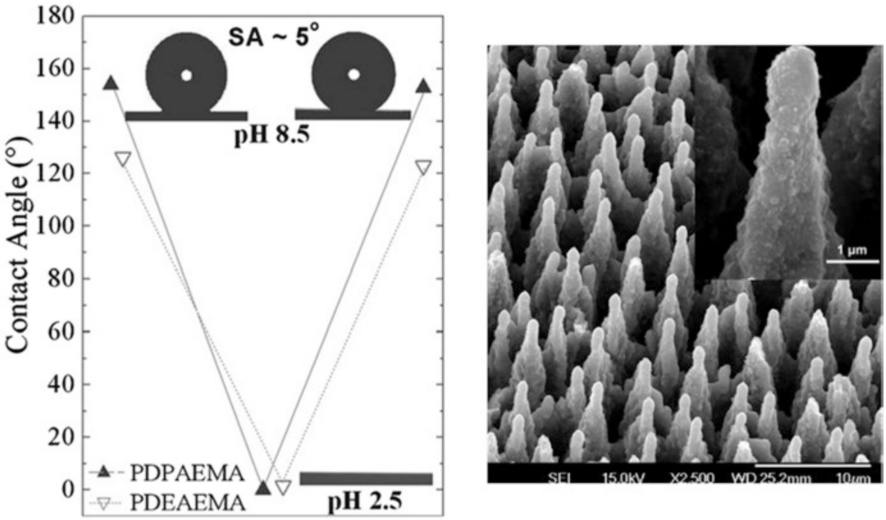

Fig. 12.54 (Left) Contact angles and images of water droplets residing on the PDPAEMA functionalized hierarchically structured surface following immersion at pH 8.5, pH 2.5 (complete wetting), and again at pH 8.5. The contact angle values for the PDEAEMA functionalized surface at pH 10 and pH 3 are also shown. (Right) SEM image of the PDPAEMA brush functionalized, artificially-structured surface. (Adapted from Stratakis et al. (2012) with permission of The Royal Society of Chemistry)

12.3.3.4 Surface Charge

The charge of a surface, or interface, plays an important role in determining the behavior and characteristics of a colloidal system. The magnitude of the charge influences the wettability of the surface, among other properties, while the sign of the charge is critically important to the adsorption, or otherwise, of ionic surfactants or polyelectrolytes. Additionally, the surface charge (or ζ-potential) of colloidal particles is a key parameter in the electrical double layer theory that forms one half of the standard Derjaguin-Landau-Verwey-Overbeek model of colloidal inter-particle forces.

The ζ-potential of a planar surface is often determined by measuring the streaming potential, or streaming current, of the surface. When an electrolyte solution is passed over the surface ions associated with the surface within the electrical double layer are sheared and translated along the surface. This charge separation results in a streaming potential, that can then be converted to a ζ-potential if the physical dimensions of the surface are well known. The surface charge of large, irregular shaped particles and even fibres may be measured using streaming potential by creating a plug of sample in a cylindrical cell. Sakai et al. used streaming potential measurements to investigate the adsorption of PDMAEMA-*b*-PDEAEMA diblock copolymer micelles to a silica surface (Sakai et al. 2006b). They were able to show that the adsorbed film responding reversibly to repeated cycling of solution pH between 4 and 9, even when the unadsorbed polymer was removed from the bulk solution, with the surface becoming highly positively charged below the pK_a (Fig. 12.55). Streaming potential is also routinely used to monitor the build-up of polyelectrolyte multilayers, such as Richert and coworkers in their study of cell interactions with multilayers of poly(L-lysine) and poly(L-glutamic acid) (Richert et al. 2002).

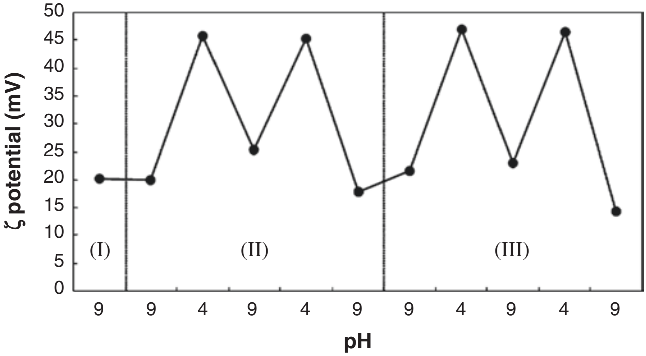

Fig. 12.55 The ζ-potential as a function of solution pH for a PDMAEMA-*b*-PDEAEMA micellar thin film adsorbed on silica. The ζ-potential was measured (I) in the presence of unadsorbed copolymer at pH 9, (II) during pH cycling in the presence of unadsorbed copolymer, and (III) during pH cycling after the removal of unadsorbed copolymer. (Reproduced from Sakai et al. (2006b) with permission from the American Chemical Society)

The ζ-potential of particles is usually measured by the principle of electrophoresis, where a charged particle suspended in a conducting medium will move in the presence of an applied electric field. The velocity at which the particle moves is measured as a function of the magnitude of the applied electric field. The measured electrophoretic mobility can then be converted to a ζ-potential using, for example, the Smoluchowski theory, that assumes the particle diameter is large compared to the Debye length, κ^{-1}, of the solution. This technique is therefore constrained by the method used to measure the particle velocity. Many modern instruments utilize laser light scattering to track the particle motion, and are thus limited to suspensions of low concentration, well-dispersed particles in the range of a few nanometres to tens of microns, though for larger particles a simple optical microscope may be used. The electroacoustic method applies a high frequency oscillating electric field to the suspension and measured the resultant ultrasound wave. This wave is then analyzed to determine the dynamic electrophoretic mobility and so the ζ-potential. The method has the advantage of being compatible with suspensions with very high volume fraction of suspended particles.

Measurement of the ζ-potential was used by Biggs and coworkers to confirm the layer-by-layer nature of the adsorption of oppositely charged copolymer micelles on silica particles (Biggs et al. 2007). Silica particles were first coated with PDMAEMA-*b*-PDEAEMA micelles, then micelles of PDEAEMA-*block*-poly(methacrylic acid) (PDEAEMA-*b*-PMAA), where the PDEAEMA block formed the core in each case. The measured ζ-potential alternated between positive (PDMAEMA outer layer) and negative (PMAA) as expected (Fig. 12.56).

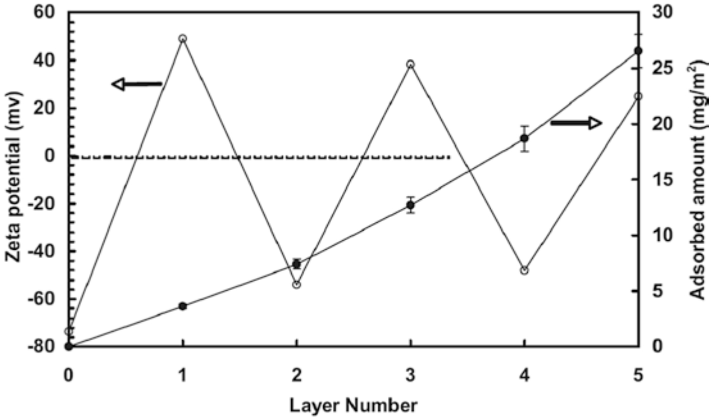

Fig. 12.56 Measured ζ-potential and adsorbed amount as a function of layer number for the alternate adsorption of PDMAEMA-*b*-PDEAEMA then PDEAEMA-*b*-PMAA micelles on silica particles. (Reproduced from Biggs et al. (2007) with permission from Wiley Publishing)

The ζ-potential of particles may also be used, often in conjunction with dynamic light scattering measurements, to demonstrate the micellization of pH-responsive copolymers. Liu and Armes studied the solution behavior of the zwitterionic copolymer poly(4-vinyl benzoic acid)-*block*-PDEAEMA (PVBA-*b*-PDEAEMA) (Liu and Armes 2002). Light scattering showed the presence of copolymer micelles at high and low pH, with a region of aggregation at intermediate pH. Measurement of the ζ-potential confirmed the micelles at low pH were cationic, and thus consisted of a core of (weakly acidic) PVBA and corona of (weakly basic) PDEAEMA. At high pH the anionic micelles had a PDEAEMA core and PVBA corona. The stability of a suspension of colloidal particles, particularly when a pH-responsive polymeric steric stabilizer is employed, may be predicted using ζ-potential measurements. Cheesman and coworkers measured the ζ-potential of silica particles with a surface-grown brush of PDEAEMA (Cheesman et al. 2012). A combination of DLS and ζ-potential measurements showed that the brush-modified particles aggregated at solution pH values greater than 7.3 despite the ζ-potential being greater than +40 mV in magnitude, Fig. 12.57. The authors attribute this behavior to the inherent hydrophobicity of the PDEAEMA polymer overcoming the remaining charge.

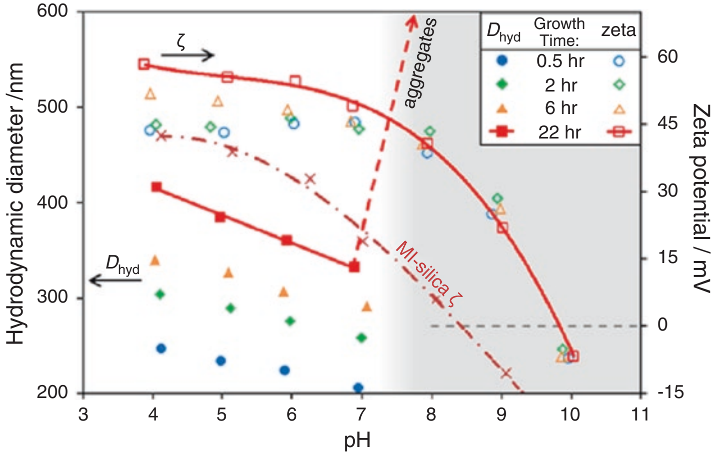

Fig. 12.57 Hydrodynamic diameter (closed symbols) and ζ-potential (open symbols) of PDEAEMA brush-modified particles as a function of pH. The shaded area denotes hybrid particle aggregation, the cross symbols and chained line are the zeta potential of the macroinitiator-modified silica (MI-silica). (Reproduced from Cheesman et al. (2012) with permission from the American Chemical Society)

12.4 Application of Stimulus-Responsive Surfaces/Interfaces

12.4.1 Pressure-Sensitive Adhesives (PSAs)

PSAs are typically made from viscoelastic polymer materials that instantly adhere to solid surfaces through van der Waals forces (without covalent bonding) when close contact is made under the application of light pressure (Satas 1989; Zosel 1992). PSAs have found their applications ranging from simple tapes and labels to adhesives in automobile, aerospace and electronic industries (Léger and Creton 2008; Wang et al. 2006; Crosby and Shull 1999; Toyama et al. 1973). Emerging applications of PSAs include transdermal drug delivery (Tan and Pfister 1999) and adherent feet for climbing robots (Daltorio et al. 2005; Murphy et al. 2006). PSAs require an optimum balance of viscous and elastic properties for good adhesion; adhesion is weak when the PSA materials are either too solid-like or too liquid-like. Therefore, it is possible to control the tack adhesion properties by tuning their viscous and elastic properties by external stimulus. Here, the stimulus-responsive PSAs which change surface adhesive properties by external stimulus are introduced.

Dar and coworkers described an approach to form stimulus-responsive PSAs that are activated by thermal energy (Dar et al. 2007). This approach was realized by formation of films that show non-adhesive properties at ambient conditions and change irreversibly into PSA upon activation using heat as a stimulus. In order to develop this system, PSA latex particles with a 'core-shell' morphology consisting of low-glass transition temperature (T_g) PSA polymer core and high-T_g stabilizer shell were synthesized. Here, the core is copolymer of 2-ethyl hexylacrylate, *n*-butyl acrylate, methyl methacrylate and 2-hydroxy ethyl acrylate and the shell is acrylic acid-based copolymer which has higher surface energy compared to the core component. The aqueous dispersion of these latex particles was dried at ambient conditions to form latex films with a well-defined morphology with the PSA core encapsulated by a protective matrix of polymeric stabilizer. The films formed at temperatures below the T_g of the stabilizer show non-tacky character at ambient conditions, which is due to the formation of a stabilizer-rich layer at the air-film interface. This stabilizer-rich surface morphology is not thermodynamically stable but kinetically trapped, and is disrupted when the temperature is elevated above the T_g of the protective polymeric stabilizer. The thermodynamically-driven softening of the stabilizer layer eliminates the kinetic barrier against diffusion, which induces rearrangement of the phases. The lower surface energy of the PSA core component drives its migration to cover the air-film surface, and the stabilizer shell component with the higher surface energy goes into bulk phase. This rearrangement to mini-

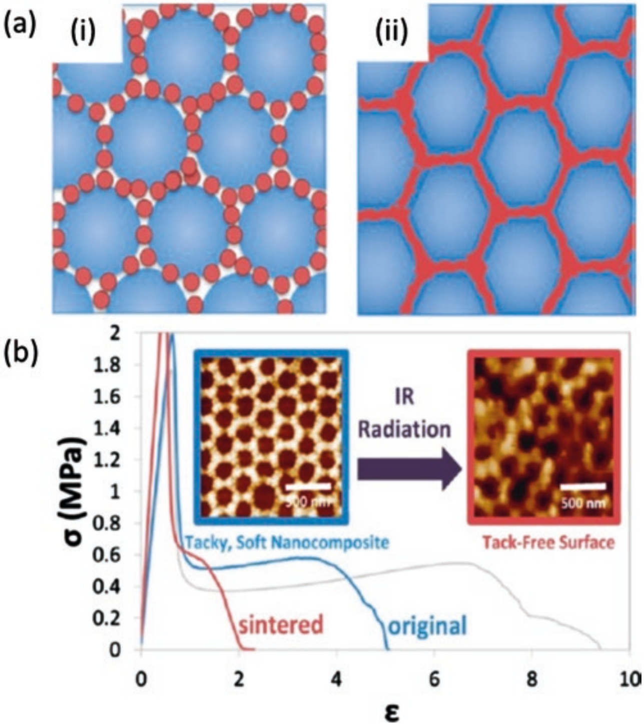

Fig. 12.58 (**a**) Two-dimensional graphical representation of a two-phase hard/soft particle blend. Hard nanoparticles (red) create a percolating network in the larger soft particles (blue). (i) Before sintering, the particles are separate but in physical contact. (ii) After sintering, the particles are fused into a rigid network. (**b**) Representative probe tack curves illustrate the effect of the sintering optimal NP blends. Insets show evolution of the nanostructure of nanocomposite PSAs obtained after sintering, as shown in AFM phase images of the air interface. (Reproduced from Gurney et al. (2012) with permission from the American Chemical Society)

mize surface energy leads to a tacky film surface. Once the films express the tack, it is retained permanently; when the temperature is lowered to ambient conditions again, there is no driving force to revert to the original morphology.

Keddie and coworkers developed nanocomposite PSAs whose tack can be switched off by thermal trigger (Gurney et al. 2012, 2013) (Fig. 12.58). The nanocomposite PSA comprises hard methacrylic nanoparticles (50 nm diameter) blended with a colloidal dispersion of larger PSA particles (270 nm). In blends of colloidal particles with different sizes, the continuous phase is determined by the relative size ratios and volume fractions of the constituents. In general, smaller particles can pack around larger particles efficiently to create a continuous percolating phase at lower volume concentrations. When the hard methacrylic nanoparticles are added to a PSA the viscoelastic balance can be optimized, and the tack adhesion energy increases to more than 200% of its initial value. When the optimized nanocomposites are heated above the T_g of the nanoparticles (130 °C), the nanoparticles sinter together to create a reinforcing rigid network structure, which switches off adhesion and reduces the tack energy by 90%. The hard nanoparticles are concentrated in the near-surface region of the latex film, possibly because of capillary-driven flow. The loss of the tack adhesion energy after sintering is explained by an increase in the elastic modulus at the film surface. The tack adhesion energy was also significantly reduced after heating using IR radiation for times as short as 30 s. Placing an opaque mask (such as coins or a plate with holes) in contact with the adhesive during exposure to the IR radiation created patterned adhesive regions with a spatial resolution of at least 2 mm (Gurney et al. 2013). Compared to adhesive systems that rely on melting transitions or cross-linking reactions, the switchable nanocomposite described simply uses conventional colloidal particles, which is likely to be much more cost-effective.

PSAs are commonly applied in the form of a thin layer on a substrate or spraying droplets. Although the PSA tapes and spray droplets are useful materials, it is difficult to apply them to confined and intricate spaces due to their high viscosity. Fujii and coworkers introduced a new concept for synthesizing PSA powder based on liquid marble technology (Fig. 12.59). PSA powder consists of particles with a PSA core and a hard $CaCO_3$ nanoparticle shell morphology, shows no adhesion in its

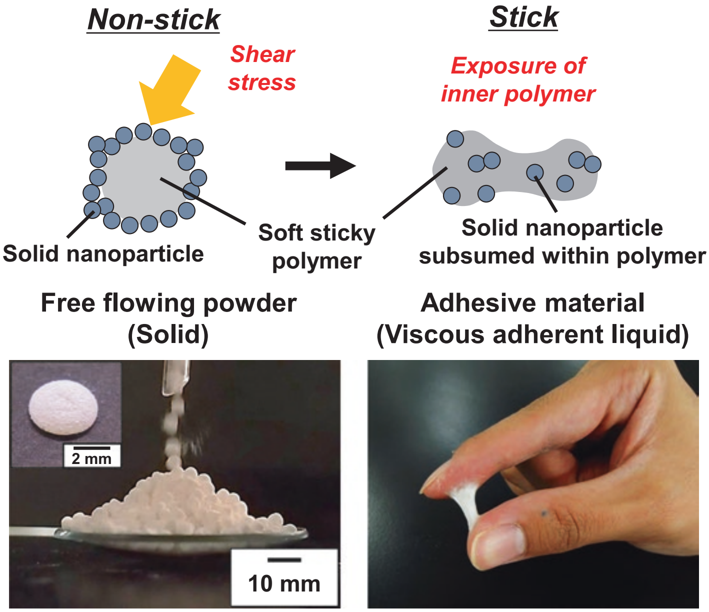

Fig. 12.59 Schematic representation of pressure-sensitive adhesion (PSA) powder consisting of particles with soft sticky polymer core and hard nanoparticle shell morphology. After application of shearing stress, adhesion nature appeared because of outflow of inner soft polymer from the hard particles shell. Digital images of such PSA materials are also shown. The PSA shows no adhesion in its original form and flows like a powder. (Inset shows single PSA particle.) The adhesion nature is only apparent after application of shear stress. (Reproduced from Fujii et al. (2016) with permission from the RSC)

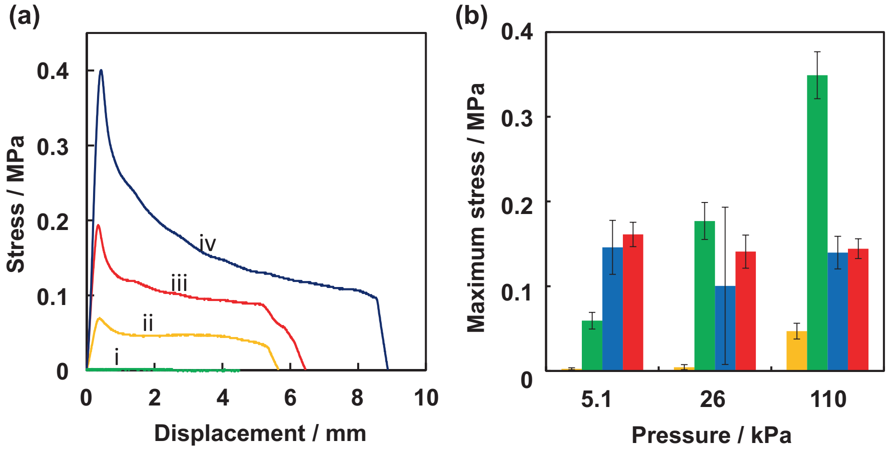

Fig. 12.60 (**a**) Stress-displacement tack curves obtained for PSA liquid marble: (i) before and (ii–iv) after kneading. Pressure applied to PSA liquid marbles: (i, ii) 5.1, (iii) 26 and (iv) 110 kPa. (**b**) Relationship between pressure applied to PSA materials and maximum stress in tack measurement. Samples: Liquid marble PSA (left bar) before and (left center bar) after kneading, (right center bar) PBA latex film with a thickness of 45 μm and (right bar) commercially available PSA tape (Scotch® Magic™ Tape 810). (Reproduced from Fujii et al. (2016) with permission from the RSC)

original form and flows like a powder. Only after application of shear stress is the adhesive nature evident. Adhesion is induced by rupture of the nanoparticle coating of the powder and outflow of the inner soft polymer. The PSA powder should be particularly useful in bonding in confined and intricate spaces, where sticky polymeric materials are difficult to apply (*e.g.* fastening screws and cracking of walls) due to their high viscosity. Figure 12.60 shows representative stress-distance (S-D) tack curves measured using the probe tack tester. The pressures applied on the samples were controlled to be 5.1×10^3 Pa, 2.6×10^4 Pa and 1.1×10^5 Pa. In the curve for the dried PSA liquid marble before application of shear stress, negligible stress ($< 2.0 \times 10^{-3}$ MPa) was detected (curve i). The liquid marbles behave as non-sticky powder. The $CaCO_3$ nanoparticles had negligible tack, and their presence at the liquid marble surface inhibits contact between the adhesive poly(*n*-butyl acrylate) (PBA) and the glass and probe substrates. After kneading the liquid marble, stress reached a maximum point immediately after test initiation and then decreased gradually extending over a long range. The failure mode was a cohesive failure (curves ii–iv). Scanning electron microscopy studies confirmed little presence of the $CaCO_3$ nanoparticles on the surface of the kneaded PSA material, which indicates that PBA component was exposed at the surface and almost all the $CaCO_3$ nanoparticles were subsumed within PBA matrix after application of shear stress, so the PBA component came into contact with the glass and probe substrates. Maximum stress measured for dried PSA liquid marbles, PBA latex film and commercially available PSA tape (Scotch® Magic™ Tape 810) are shown in Fig. 12.60b, respectively. The PBA latex film showed lower maximum stress compared to those of liquid marbles. This should be due to the difference in contact area between PBA component and the substrates; the contact area between PBA latex film (45 μm thickness) and the substrate was smaller than that between liquid marble (approximately 1 mm thickness) and substrate. Larger contact area could be attained thanks to thicker flowable PBA layer in the case of PSA powder after application of shear stress, but on the other hand full contact of PBA component with substrate cannot be attained in the case of PBA latex film because of thinner PBA film thickness and incomplete parallel alignment of probe and substrate.

12.4.2 Controlled Lubrication

The use of soft matter to modify and control the adhesion of solid surfaces is a well-researched field that is routinely used in many industrial and commercial products; for example, the use a polymer steric layer to stabilise paint pigments. However lateral forces, or the lubrication, between two sliding surfaces may also be controlled by the presence of soft matter. Such layers may consist of small molecule surfactants or high molecular weight polymers, and can be adsorbed, chemically grafted to, or indeed synthesized directly from the solid interface. In this section we will detail some examples from the literature of the use of soft matter to alter, and is some cases fine tune, the lubrication between surfaces.

Feiler and co-workers used AFM to study dynamic normal and lateral forces between two silica surfaces coated with a random copolymer of acrylamide and [3-(2-methylpropionamide)propyl]trimethylammonium chloride (AM-MAPTAC) (Feiler et al. 2003). The cationic MAPTAC units comprised 1% of the monomer residues and the molecular weight was 900,000 $g \cdot mol^{-1}$. The authors showed the measured normal forces were strongly dependent on the approach (or retract) velocity of a silica particle with an adsorbed AM-MAPTAC coating toward (or from) a similarly coated planar silica substrate, with significant hysteresis evident at large velocities. This was attributed to hydrodynamic interactions as a result of the presence of the polyelectrolyte layer, and was not evident at sufficiently slow speeds. The adsorbed polyelectrolyte also modified the lateral (frictional) forces measured by AFM (Fig. 12.61). For a given scan rate (relative velocity between the two surfaces) as the applied normal load is increased a critical load is reached, above which the measured friction force increases at a higher rate. Interestingly, as the applied load is decreased the change in friction force remains linearly dependent. Thus at low applied loads the lubricity of the polymer coating is lower during the unloading cycle, which the authors attribute to metastable deformation of the polymer layer. Further, normal forces measured after conducting a friction loop are lower than when measured prior, revealing further evidence of a change within the polyelectrolyte layer as a consequence of the friction measurement. Finally, the authors observed an interesting influence on the effect of scan rate on lubrication depending on the presence or otherwise of the AM-MAPTAC layer. In the case of bare silica

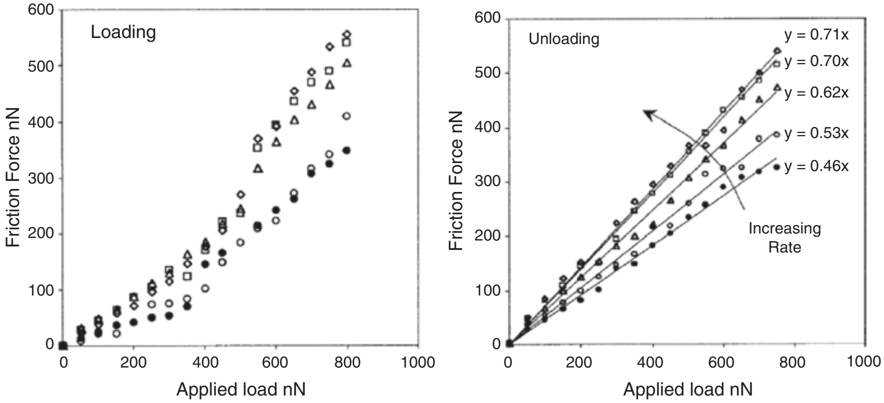

Fig. 12.61 Friction as a function of scan rate during (left) loading and (right) unloading between AM-MAPTAC coated silica surfaces. The scans were conducted in the following order: 1 Hz (open circles), 2 Hz (open triangles), 5 Hz (open diamond), 10 Hz (open squares), 1 Hz (solid circles). (Reproduced from Feiler et al. (2003) with permission from the American Chemical Society)

surfaces the friction coefficient decreased as the scan rate was increased, while this dependence was reversed for two silica surfaces coated with the polymer. Indeed, in the presence of the polymer the friction coefficient is smaller at low scan rates than bare surfaces, whereas it is greater it high scan rates. The authors attribute this effect to hydrodynamics within the brush layers as the slide past each other, similar to the effect observed for normal forces.

AFM was also used to study the contact mechanics of a zwitterionic poly(2-(methacryloyloxy)ethylphosphorylcholine) (PMPC) brush at the nanoscale (Zhang et al. 2013). Measurement of the friction force when the layer was immersed in water, methanol, ethanol and 2-propanol demonstrated direct dependence on the solvent quality. The PMPC layer proved most lubricious in methanol (good solvent), then water and ethanol, while the highest friction was measured in 2-propanol which is a poor solvent for PMPC. Furthermore, in solvents where significant adhesion was measured between the tip and polymer layer (water and ethanol) a non-linear friction-load relationship was observed. The friction response of the PMPC layer to added electrolyte was also investigated using aqueous NaCl solutions. The adhesion between the tip and the layer was seen to reduce with increased salt concentration, due to the screening of the cationic and anionic components of the brush. As seen with the molecular solvents, those aqueous electrolyte solutions that had significant adhesion also displayed non-linear friction-load relationship. To explain these contact mechanics data the authors invoked a two-component model of friction in these systems; a load dependent term that is related to the motion of the tip through the polymer brush, and an area dependent term that is due to shearing. When this shear term is negligible the friction-load relationship is linear, however as the shear term begins to dominate the friction no longer changes linearly with applied load.

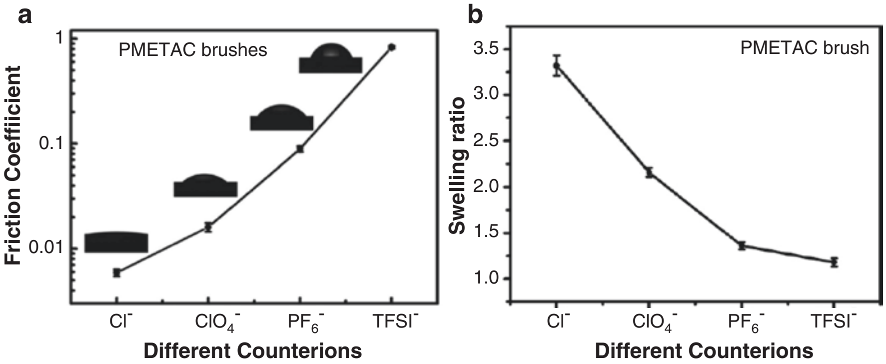

Fig. 12.62 (**a**) Changes in friction coefficients and wettability (inserted images) corresponding to PMETAC brush on silica substrates when the counterions are Cl^-, ClO_4^-, PF_6^-, and $TFSI^-$. (**b**) Corresponding swelling ratios. The height was measured by AFM using patterned brushes on gold substrates and swelling ratio was calculated as h_{wet}/h_{dry}. (Reproduced from Wei et al. (2013) with permission from the American Chemical Society)

Wei and co-workers have detailed a comprehensive study on the use of different ion species to control lubrication in polycationic, polyanionic and polyzwitterionic brushes (Wei et al. 2013). A pin-on-disk reciprocating tribometer was used to measure the macroscopic friction between a polydimethylsiloxane (PDMS) hemisphere (the “pin”) and brushes of cationic poly(2-(methacryloyloxy)-ethyltrimethylammonium chloride) (PMETAC), anionic poly(3-sulfopropyl methacrylate potassium salt) (PSPMA) or poly(methylacrylic acid sodium) (PMAA) and zwitterionic poly(2-(methacryloyloxy)-ethyl)dimethyl(3-sulfopropyl)ammonium hydroxide (PSBMA). In addition, the authors used AFM and quartz crystal microbalance with dissipation monitoring (QCM-D) to investigate the swelling and collapse of the brushes in response to the presence of different counterions, and correlated this with the friction findings. For example, in the case of the cationic (PMETAC) brush the addition of either Cl^-, ClO_4^-, PF_6^- or bis(trifluoromethanesulfonimide) ($TFSI^-$) had a significant influence on the magnitude of the measured friction coefficient (Fig. 12.62a). The effect on friction was rationalised by comparison to the “swelling ratio” of the brush in each anion (Fig. 12.62b), defined as the thickness of the brush when immersed in the electrolyte solution divided by the dry brush thickness. It is clear from the data in Fig. 12.62 that when the PMETAC brush is in the collapsed state the friction coefficient is enhanced. The authors observed this relationship between brush thickness and lubricity for all brushes characterised even when, in the case of the PMAA brush, the swelling/collapse was driven by pH changes.

A combination of AFM and QCM-D was also used by Nordgren and Rutland in their study on the dual-response of poly(2-(dimethylamino)ethyl methacrylate) (PDMAEMA) brushes grafted to gold substrates (Nordgren and Rutland 2009). Free PDMAEMA in bulk solution is both pH responsive, with an apparent pK_a of 7.0–7.5, and thermoresponsive, with a LCST of 40–50 °C; though the LCST itself

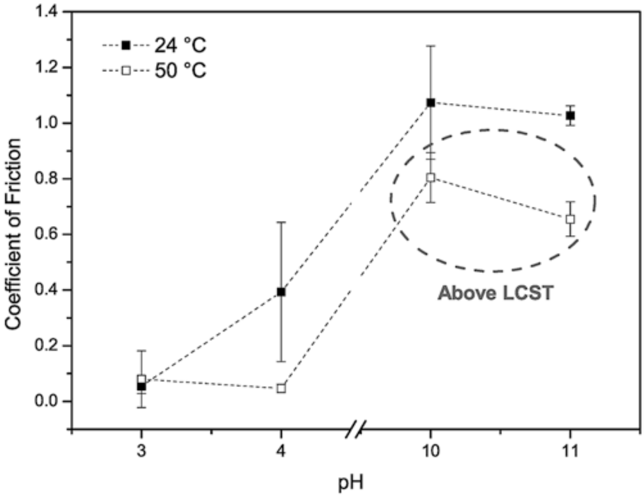

Fig. 12.63 Friction coefficient as a function of solution pH between PDMAEMA brushes grafted to gold surface at 24 °C (closed squares) and at 50 °C (open squares). The dashed lines have been added to guide the eye. (Reproduced from Nordgren and Rutland (2009) with permission from the American Chemical Society)

is pH dependent. QCM-D measurements at 24 °C clearly showed the PDMAEMA brush was swollen at pH 3 (< pK_a) and collapsed at pH 11 (> pK_a) as expected, and that at both pH values the brush was more collapsed at 50 °C. The most extended state was thus pH 3 and 24 °C, while the most collapsed was pH 11 and 50 °C, which was corroborated by normal force measurements. Consistent with the work of Wei and co-workers (Wei et al. 2013), the friction coefficients measured by AFM were found to be dependent on the swollen/collapsed state of the PDMAEMA brush (Fig. 12.63). The brush was the most lubricious in its most swollen state, with the friction coefficient increasing as the brush collapsed. Interestingly, the authors observed the friction coefficient to then reduce, i.e. the brush became more lubricating, when the most collapsed state was reached. The authors attributed this unexpected result to a smoother sliding surface at the brush periphery due to the complete collapse of the brush.

12.4.3 Sensors and Actuators

Stimulus responsive materials offer many avenues for application in the expanding world of sensors and actuators. A number of proven triggers are available including pH, temperature and light. Sensors can be based on either vapor or solution detection of the analyte. The response can be a simple switch or indeed provide a quantitative measure of the analyte. The triggered response can result in the soft matter responding in a controlled manner to invoke movement or dimensional changes that can be harnessed as the basis of an actuator. Moreover, the response can be tailored to capture or release a target active molecule in the form of a dye, flavour or drug. In this section we will detail some examples from the literature of the use of responsive soft matter to a range of stimuli which can be harnessed for sensing or actuator applications.

12.4.3.1 pH Responsive Surfaces

The pH responsive nature of adsorbed and grafted layers of polymers at solid interfaces have been deployed for applications such as acidic vapor sensing (Fielding et al. 2011), encapsulation and release (Schatz et al. 2008; Fitzgerald et al. 2008), optical sensors (Fitzgerald et al. 2008), pH and gas sensitive liquid marble stabilisers (Christau et al. 2014; Fujii et al. 2011a), and as pH-sensitive "gates" in microfluidic devices.

Fielding and co-workers synthesized brushes of the tertiary amine methacrylates poly(2-(diethylamino)ethyl methacrylate) (PDEAEMA) and poly(2-(diisopropylamino)ethyl methacrylate) (PDPAEMA) directly from silicon surfaces using atom transfer radical polymerisation (ATRP) (Fielding et al. 2011). These weakly basic polymers have pK_as of 7.3 and 6.3 respectively for free PDEAEMA and PDPAEMA in solution. Ellipsometric measurements confirmed the pH-responsive nature of the brushes when immersed in aqueous solution and repeated cycling of the pH above and below the respective pK_a demonstrated that both brushes were robust to multiple reversible responses. Of particular note in this study was the response of a "dry" PDPAEMA brush to changes in the overlying vapor phase (Fig. 12.64). Ellipsometric measurement of the brush thickness on exposure to dry, ambient and humid (or "wet") air showed no change in PDPAEMA brush thickness. Upon exposure to humid air with HCl vapor the brush swelled significantly. After this initial exposure to acidic vapor the brush was more responsive, demonstrating reversible collapse (humid air) and swelling (humid air with HCl vapor). The authors also observed distinct changes in the color of the PDMAEMA coated surface as the brush swelled and collapsed, and these correlated well with predicted color changes. The authors state the brush must be sufficiently thick to readily observe the color change, but such behavior could be readily deployed in a chemical-specific gas sensor.

Silica particles coated in a layer of PDMAEMA$_{106}$-*b*-PDEAEMA$_{25}$ were used by Schatz and co-workers to demonstrate pH-stimulus capture and release of a hydrophobic moiety (Schatz et al. 2008). Fluorescence spectroscopy and DLS measurements confirmed the copolymer reversibly formed micelles when the aqueous solution pH was increased above 8 and that hydrophobic pyrene partitioned into the cores. Adsorption of the micelles to highly negatively charged silica at pH 9 resulted in a reduction in the magnitude of the ζ-potential, from −75 mV to −5 mV. Cycling of the pH from 9 to 3.5 showed successive charge reversal indicating the polymer was not completely desorbed from the interface. Monitoring of the I_1/I_3 ratio for

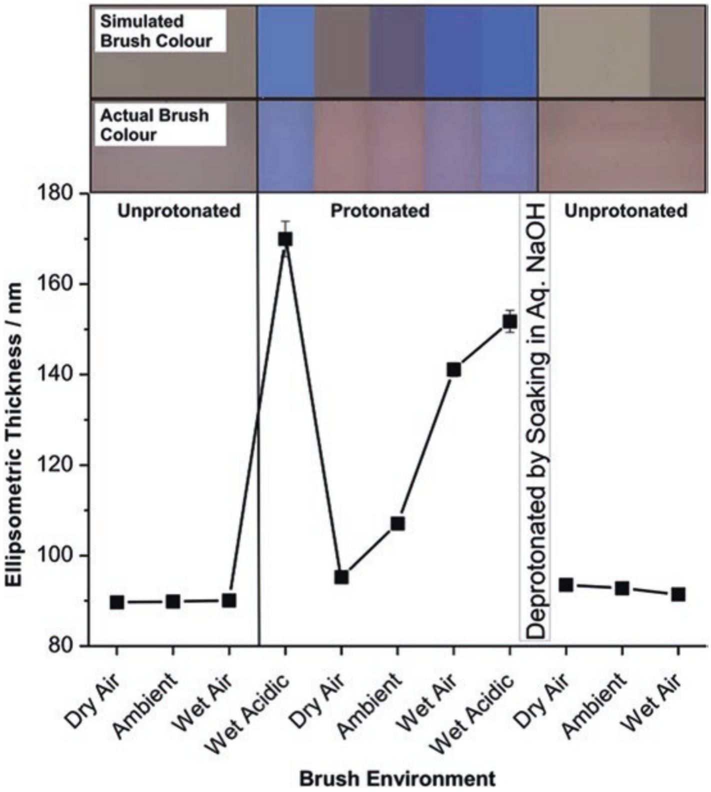

Fig. 12.64 Ellipsometric thickness as a function of surrounding vapor phase of a PDPAEMA brush exposed to different vapor phases. To show the colorimetric response to the vapor phase, images of an approximately 70 nm thick sample undergoing the same sequence of vapor treatments were recorded using a digital camera and optical microscope. (Reproduced from Fielding et al. (2011) with permission from the American Chemical Society)

pyrene fluorescence indicated that particle-adsorbed micelles do not take up as much pyrene as free solution micelles at high pH, and that the release at low pH is also hindered from the surface micelles; that is some pyrene remains bound within the adsorbed film. This difference notwithstanding, optical and fluorescent light microscopy clearly show the uptake-release-uptake of pyrene into adsorbed PDMAEMA$_{106}$-*b*-PDEAEMA$_{25}$ micelles as the pH is cycled from 9.0–3.5–9.0 (Fig. 12.65). In a similar study, Fitzgerald et al. demonstrated pH-responsive reversible capture and release of pyrene from PDPAEMA and PDEAEMA microgel films adsorbed on particulate silica (Fitzgerald et al. 2008). Given the inherent advantages of particle suspensions in terms of solids loading, specific surface area and processability, these colloidal systems offer an intriguing prospect for a reversible capture and release application.

A brush of PDMAEMA polymer was also used by Christau and co-workers for brush/particle hybrids interacting with gold nanoparticles (AuNPs) (Christau et al.

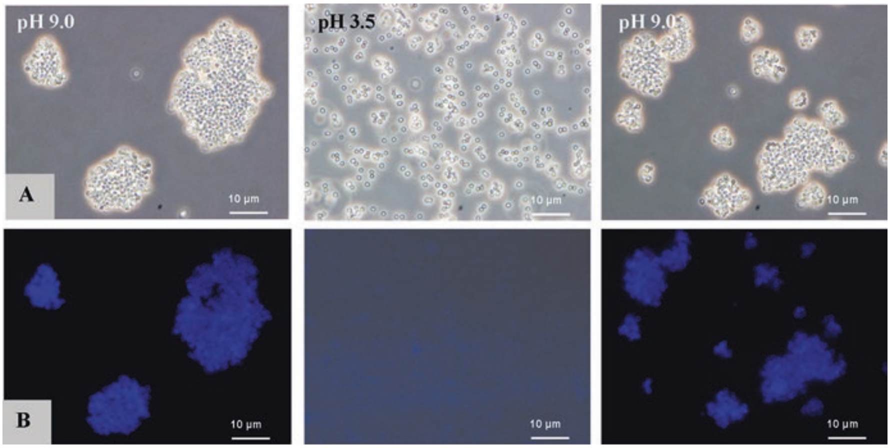

Fig. 12.65 (**a**) Conventional and (**b**) fluorescent light microscopy images of PDMAEMA$_{106}$-*b*-PDEAEMA$_{25}$ copolymer coated silica particles. Micrographs show both the pyrene encapsulation and the colloid stability when the pH was successively adjusted at 9.0, 3.5, and again 9.0. (Reproduced from Schatz et al. (2008) with permission from the American Chemical Society)

2014). Gold nanoparticles exhibit surface plasmon resonance which is dependent on, among other properties, not only particle size and shape but also their separation. Incorporation of AuNPs into a stimulus-responsive brush opens the potential for the development of optical sensors. In this particular work the authors focussed on the influence of polymer grafting density on the final distribution of the AuNPs within the brush. At very low grafting densities, in the so-called mushroom regime, the AuNPs are sparsely distributed and particle uptake is low, attributed to a lack of polymer matrix. As the grafting density is increased so is the loading of AuNPs, with X-ray reflectometry measurements indicating that the AuNPs are distributed throughout the brush normal to the interface. At very high grafting density the uptake of AuNPs is again reduced, as the AuNPs are not able to penetrate that brush and can only form a monolayer at the periphery. Whilst this work is developing these brushes for optical sensor applications, the implications of the results for the deployment of polymer brushes in targeted capture/release, in particular on maximising captive loading, is clear.

Fujii and co-workers reported the use of pH-responsive polymeric particles to stabilise liquid marbles (Fujii et al. 2011a, 2012a), and their response to an acidic liquid (Fujii et al. 2011a) or vapor phase (Fujii et al. 2012a). Sub-micrometre size polystyrene (PS) particles were synthesized with a stabilising layer of PDEAEMA. X-ray photocorrelation spectroscopy (XPS) confirmed the PDEAEMA chains were present at the surface of the latex particle, while laser diffraction measurements showed the expected solution pH-dependent behavior; the particles were well-dispersed at pH 3 (< pK_a of PDEAEMA) and aggregated at pH 10 (> pK_a of PDEAEMA). The mechanical integrity of liquid marbles, prepared from water droplets at pH 2 or 10 and stabilized by the PDEAEMA-PS particles, was tested

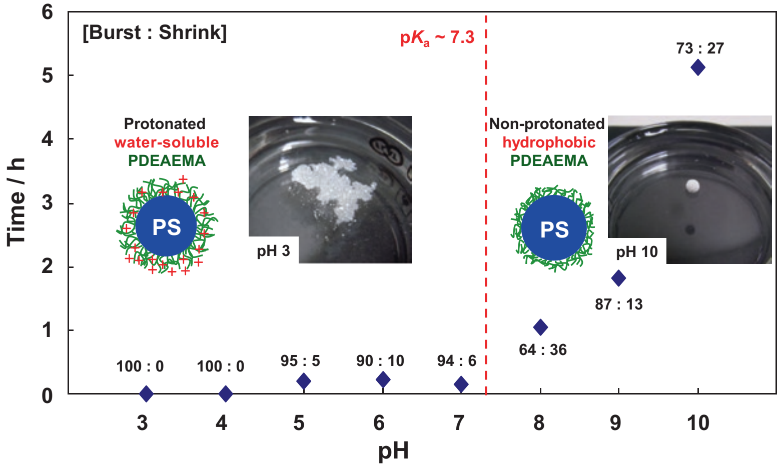

Fig. 12.66 Mean lifetime of 15 μL liquid marbles stabilized by PDEAEMA-PS latex particles on the surface of liquid water at various pH values. The percentages of liquid marbles that burst and shrink are shown next to the individual data points. (Reproduced from Fujii et al. (2011a) with permission from the American Chemical Society)

using a custom-built device that allowed marbles to fall from a predetermined height. It was noted that marbles formed from pH 2 water were less robust as they disintegrated at a lower fall height than marbles prepared at pH 10. The marbles were transferred to the surface of liquid water to test their response to the pH of this bulk phase (Fig. 12.66). When the pH of the bulk water was lower than the pK_a of PDEAEMA the marble disintegrated almost immediately, while marble lifetimes of up to 5 h were measured at higher pH values.

Fujii and co-workers later demonstrated that liquid marbles stabilized by PDEAEMA-PS particles will respond to exposure to an acidic vapor phase (Fujii et al. 2012a). When placed on a glass substrate under a saturated water vapor phase the marbles were stable for up to 18 hours, eventually shrinking due to the slow evaporation of the inner water. However, when exposed to an acidic (HCl) vapor phase the marbles "burst" within a few seconds (Fig. 12.67). This was attributed to protonation of the PDEAEMA chains, which made the PDEAEMA-PS particle hydrophilic. The particles then dispersed into the inner water droplet and the marble was no longer stabilized. These data demonstrate the ability to use stimulus-responsive particles to create liquid marbles under certain conditions only, and that these marbles may be subsequently used for targeted release of actives or as environmental sensors.

A pH responsive gradient polymer brush was used by Ionov and co-workers to control solvent wetting in a microfluidic device, effectively creating a chemical "gate" within the capillary (Ionov et al. 2006). The capillaries were coated with a gradient brush comprising poly(acrylic acid) (PAA) and the weakly basic poly(2-vinylpyridine) (P2VP), with varying relative compositions of the two monomers in

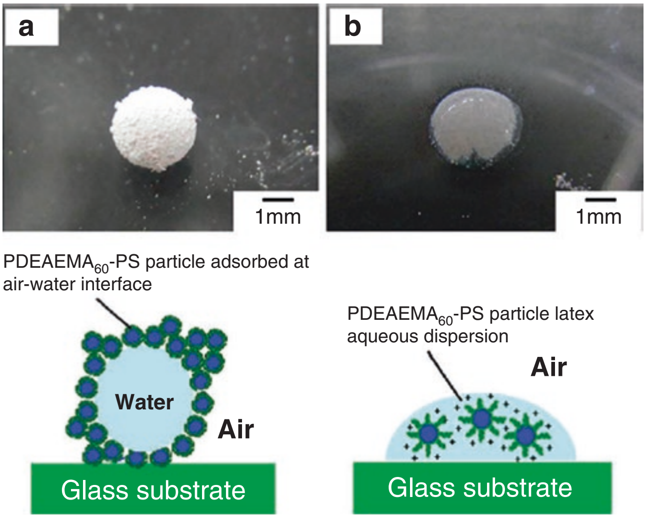

Fig. 12.67 An aqueous liquid marble stabilized by PDEAEMA-PS particles (**a**) before and (**b**) after exposure to an acidic vapor phase. (Reproduced from Fujii et al. 2012a) with permission from the American Chemical Society)

different capillaries. The Laplace equation tells us that liquid wetting (or rise) within a capillary is determined by the contact angle; the authors show the water contact angle on the PAA-*mix*-P2VP is both composition and pH dependent. When the polymer layer is PAA rich the contact angle is low at low pH, due to charging of the acrylic acid residues, and the contact angle increases as pH rises. The opposite is seen when the layer is P2VP rich, as expected due to protonation of vinylpyridine residues. Interestingly, at pH 5 the contact angle is nearly independent of the layer composition. Used in conjunction with capillaries pre-loaded with an “analyte”, the authors demonstrate the ability to dispense different amounts of the analyte due to the controlled rise of water.

12.4.3.2 Thermoresponsive Surfaces

Many polymers exhibit temperature dependent solubility; that is, they are thermoresponsive. Usually the polymer is soluble at low temperatures but becomes insoluble above an LCST. The behavior is readily translated to surfaces, either as adsorbed layers or surface-synthesized brushes, and may be manifest by changes in layer thickness, wettability or adhesion. Perhaps the most studied thermoresponsive polymer, either in free solution or surface bound, is poly(*N*-isopropylacrylamide) (PNIPAM), though even polymers more commonly associated with pH-responsiveness such as PDMAEMA and PDEAEMA exhibit an LCST.

The group of von Klitzing and Genzer have used both PDMAEMA and PNIPAM to study the uptake of AuNPs in their development of optical sensors (Yenice et al. 2015; Christau et al. 2016). Three PDMAEMA brushes of varying thickness were synthesized directly from silicon wafers, and the thermoresponsive nature of the brushes confirmed via ellipsometry and AFM indentation measurements, with an LCST of 40–45 °C. The brushes were then immersed in a solution of 13 nm diameter AuNPs to allow for uptake. Subsequent AFM indentation measurements indicated the AuNP loaded polymer brushes had lost their thermoresponsive behavior as no change in brush thickness was observed in the range 25 to 65 °C. The authors considered this to be the result of steric crowding and decreased conformational entropy within the brush and an increase in hydrophilicity due to the AuNP uptake. The loss of thermoresponsive behavior was not observed in an earlier study by Chen and co-workers, who prepared AuNP loaded PDMAEMA brushes for use as temperature controlled catalysts (Chen et al. 2014). However, this earlier study prepared the AuNP in situ within the brush so the particle size was much smaller (~3 nm) and the brushes were grafted from 130 nm diameter silica particles. It would be expected, therefore, that the effects of lowered entropy and steric crowding would be much less in this case.

When gold nanoparticles were loaded into a PNIPAM brush the thermoresponsive behavior was retained, and the film exhibited temperature dependent color changes (Christau et al. 2016). In this case the AuNPs were either coated with citrate anions (AuNP-citrate) or stabilized with 12-mercaptododecanoic acid ligands (AuNP-MDA), and the temperature induced color change was dependent on which type of particle was present. Neutron reflectometry showed the hydrophilic AuNP-citrate particles penetrate deeper in to the PNIPAM than the relatively hydrophobic AuNP-MDA particles that were localized at the brush periphery. In the case of the AuNP-citrate, increasing the temperature above the brush LCST resulted in a red-shift as the particles are forced in to closer proximity in the collapsed brush. A blue-shift was observed for AuNP-MDA due to greater (hydrophobic) particle mobility in the collapsed (and hydrophobic) brush above the LCST. Further, the color shift of the AuNP-citrate system was reproducible over 6 heating/cooling cycles while the magnitude of the blue-shift in the AuNP-MDA system was significantly reduced after the first cycle as a result of the rearrangement of the particles within the brush.

Thermally induced color changes with AuNP loaded PNIPAM microgels have also been studied (Gawlitza et al. 2013). The loaded microgels were prepared by mixing dispersions of the citrate-stabilized nanoparticle and microgels, and the influence of AuNP concentration and degree of microgel crosslinking was investigated. Dynamic light scattering demonstrated that the microgels retained their thermoresponsive behavior upon uptake of the AuNPs, though at the two lower degrees of cross-linking the extent of swelling was significantly reduced when AuNPs were loaded. For a given degree of cross-linking the surface plasmon resonance coupling was enhanced with higher particle loading, so the magnitude of the wavelength shift to higher values was greater. The loading efficiency of the AuNPs decreased with increased cross-linking, as the mesh size of the microgel is reduced preventing AuNP ingress. In the higher particle loading regime UV-Vis spectra reveal the presence of a second peak, or shoulder, at higher wavelengths that becomes more pronounced as the microgel shrinks. This second peak is a result of the close proximity of the AuNPs, less than ~5 nm.

Microgels of PNIPAM-*co*-PAA were developed as humidity sensors by Islam and Serpe (Islam and Serpe 2014). A thin, flexible substrate was coated with Cr, as an adhesive layer, then Au. A solution of the (anionic) microgels was then spread across the substrate and allowed to dry for 2 hours and incubated at 30 °C overnight to promote film formation. A solution of cationic poly-(diallyldimethylammonium chloride) (PDADMAC) was spread on the substrate neutralizing the anionic charge of the microgels. As the PDADMAC layer dries the device curls up due to the electrostatic bonding within the layer and the tight binding of the microgel layer to the substrate (Fig. 12.68). When exposed to a humid environment water vapor is adsorbed within the polymer film and the device flattens, or "opens out". This extent of device curling can be fine-tuned by the degree of humidity; the authors connected small weights to the device and showed the mass supported by the device varied linearly with humidity. This mechanical actuation is repeatable over many cycles and the authors propose that this device could be used as a low cost humidity sensor.

Thermoresponsive microgels that display a linear change in hydrodynamic radius as a function of solution temperature have been proposed as a new class of high precision nanoactuators (Zeiser et al. 2012). Core-shell microgels comprising a core of poly(*N*-*iso*-propylmethacrylamide) (PNIPMAM) and a shell of poly(*N*-*n*-propylacrylamide) (PNNPAM) were synthesized in a two-step procedure. The morphology of the microgels were chosen such that the LCST of the core (PNIPMAM, LCST = ~44 °C) was greater than the shell (PNNPAM, LCST = ~21 °C). The thermoresponse of the PNIPMAM cores only was shown to be dependent on the degree

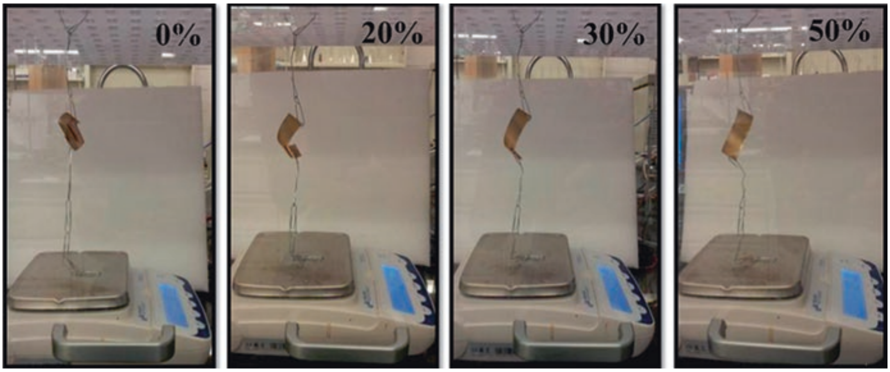

Fig. 12.68 A PNIPAM-*co*-PAA microgel-based actuator hanging in a humidity controlled chamber with paperclips attached. As the humidity was increased the polymer layer swelled causing the actuator to open up, adding more of the paperclips to the balance pan and subsequently increasing the measured mass. (Reproduced from Gawlitza et al. (2013) with permission from the Royal Society of Chemistry)

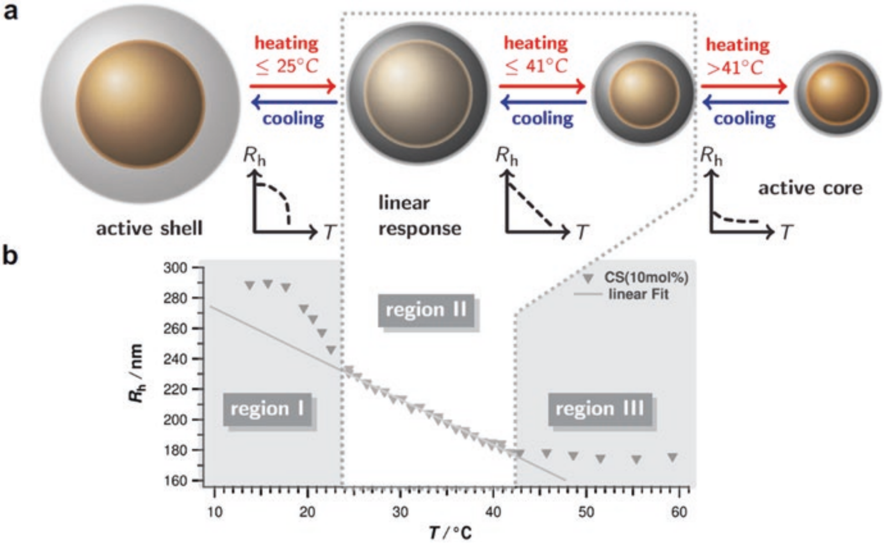

Fig. 12.69 (**a**) Schematic illustration of a core-shell microgel that undergoes reversible swelling and collapse. (**b**) Hydrodynamic radius as a function of temperature of a core-shell microgel system with 10 mol% cross-linked PNIPMAM cores. In region I the shell undergoes restricted collapse, region II covers the linear swelling behavior and in region III the core is further collapsed. (Reproduced from Zeiser et al. (2012) with permission from Elsevier)

of cross-linking, with higher degree of cross-linking resulting in a smaller magnitude of size change. The nature of the radius/temperature relationship for the cores was broadly similar to those seen for other, e.g. PNIPAM-based, microgels; a slow decrease in radius as the temperature approaches the LCST, followed by a rapid transition around the LCST, and finally region above the LCST where the microgels are essentially full collapsed. When translated to the core-shell microgel particle, however, the radius/temperature relationship is more complicated due to the individual responses of the two polymers, Fig. 12.69. Of most interest is the region between the LCST of the shell and core; i.e. between ~21 °C and 44 °C. In this region, labelled “region II” in Fig. 12.69, the radius of the core-shell microgel changes *linearly* with temperature. The authors further show that the gradient of this region, that is the sensitivity of the response, is controlled by the degree of cross-linking of the core. The highly controlled nature of this linear response makes these microgels a particularly exciting prospect for a new class of nanoactuators.

12.4.3.3 Photoresponsive Surfaces

A built-in photoresponse offers exciting prospects for liquid marble actuation and controlled-release. For example, ultraviolet irradiation has been demonstrated to disintegrate spiropyran-stabilized aqueous liquid marbles as attributed to the isomerisation to the more hydrophilic merocynanine (Nakai et al. 2013). Tang and coworkers reported the linear motion of a metallic liquid marble in hydrogen peroxide solutions propelled by oxygen bubbles formed when the photocatalytic WO_3 particulate coating is irradiated with ultraviolet light (Tang et al. 2013) (Fig. 12.70). For example in 15% H_2O_2 the velocity of the marble was recorded to be 4.58 mm/min. Fujii and coworkers demonstrated the light-driven transportation of liquid marbles and the on-demand and on-site disruption of them by an external stimulus to release the inner materials. Furthermore, it was demonstrated that the liquid marble can be used as light-driven towing engine to carry loads (Paven et al. 2016). UV irradiation has also been demonstrated to trigger the rupture of aqueous liquid marbles stabilized by novel magnetic core-polymer shell particles (Zhang et al. 2012). The additional functionality of the magnetic cores in the stabilising particles means that magnetic manipulation of the marbles is viable for delivery of the marbles to the site of desired rupture and release of internal payload.

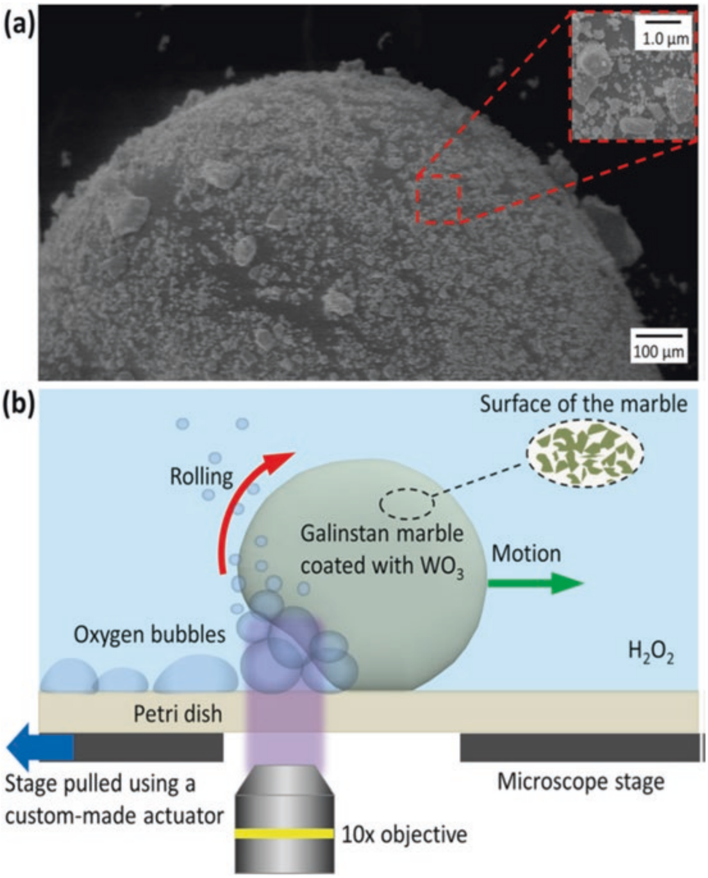

Fig. 12.70 (**a**) SEM image of a metallic liquid marble consisting of a galinstan droplet encapsulated in a coating of 80 nm WO_3 nanoparticles. (**b**) Schematic of the mechanism of light-induced motion of the marble. (Reproduced from Tang et al. (2013) with permission from American Institute of Physics)

12.4.3.4 Copolymer Systems

The use of copolymers is an attractive route to novel stimulus-responsive applications. For instance, a bilayer actuator was reported by Bassik and coworkers as shown in Fig. 12.71 (Bassik et al. 2010). The structure consisted of hydrogel bilayers of PNIPAM, PAA and polyethylene oxide diacrylate (PEODA). The hydrogels were spin-cast and then patterned by photolithography. By combining materials with optimal swelling responses, bilayer structures were triggered via changes in pH and ionic strength to actuate into 3D structures such as the hinge shown in Fig. 12.71. This study highlights a way to design and fabricate actuator polymeric hinges. A second application of stimulus-responsive copolymer surfaces lies in the colorimetric sensor for hydrogen peroxide reported by Han et al. which is based on the surface plasmon resonance of AgNPs (Han et al. 2015). Here PNIPAM-*co*-PAA microgels containing multiple AgNPs were demonstrated to be selective for H_2O_2 in complex media. Specifically, in the presence of hydrogen peroxide, the magnitude of the surface plasmon resonance dramatically decreased in a linear fashion over the concentration range of 0.30–3.00 μM. The stimulus responsive microgels provide a robust microenvironment for the AgNP that would otherwise be rather unstable.

12.4.3.5 Lipid Mesophases

The temperature-induced release of the model hydrophilic drug, glucose from phytantriol and glyceryl monooleate-based lipid mesophases has been reported (Fong et al. 2009). As shown in Fig. 12.72, the release of glucose from a phytantriol bicontinous cubic phase (Q_2) occurs at a controlled rate at 30 °C, but is prevented from release after the thermoresponsive phase transition to a reverse hexagonal phase (H_2) at 40 °C. The triggered release of glucose from the mesophase was shown to be reversible in vitro and the analogous in vivo response in rats could be induced by contact with an external heat pack. In a later study, Fong and coworkers reported the successful triggered controlled release through photoresponse, pH-response and thermoresponse from lipid mesophases (Fong et al. 2016). Thus these soft matter systems provide exciting prospects for the controlled release of pharmaceuticals.

12.4.4 Drug Delivery

The Mobil corporation discovered hexagonally ordered mesoporous silica in 1992 (Kresge et al. 1992; Beck et al. 1992) Mesoporous silica nanoparticles (MSNs) have attracted a large interest because of their high surface area (700–1200 m^2/g), uniform pore size (2–50 nm), and biocompatibility characteristics (Stein et al. 2000). Conventional MSNs (e.g., MCM-41 and SBA-15) do not present stimuli-responsive properties. This disadvantage can be overcome by grafting stimuli-responsive polymer brushes onto the surface of MSNs (Radu et al. 2004; Yu et al. 2005; Zhu et al.

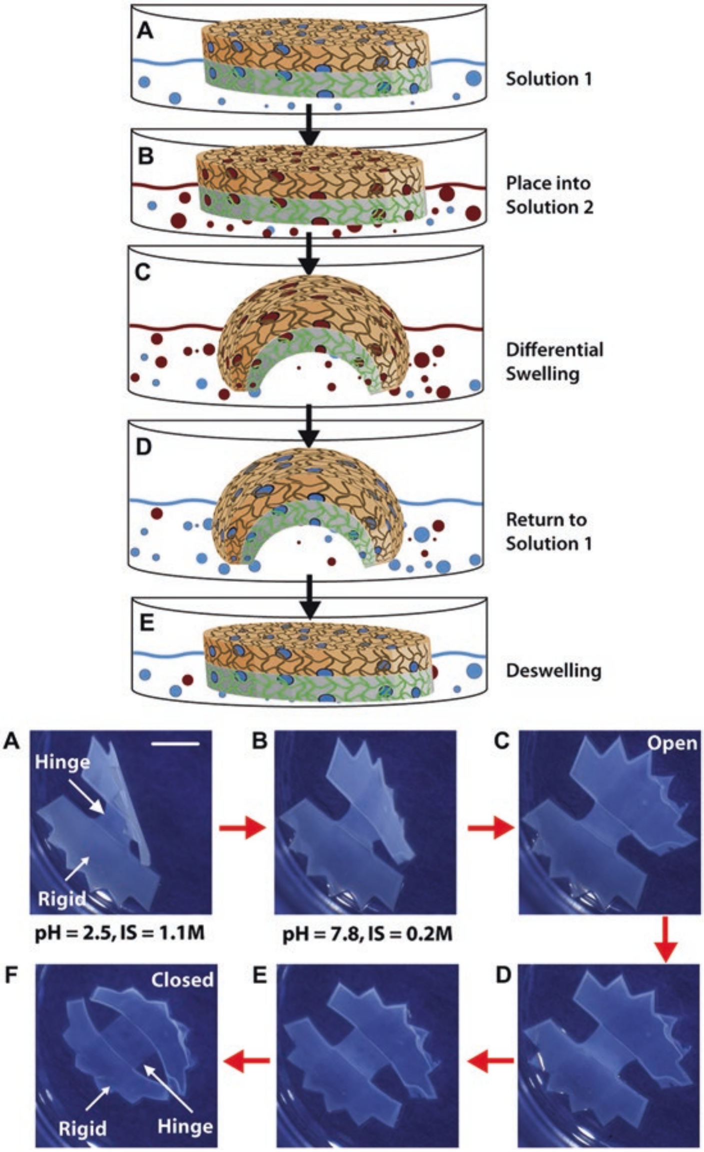

Fig. 12.71 (Top) Schematic of the bilayer actuation mechanism. A: A hydrogel bilayer is equilibrated in aqueous solution 1 with specific pH and ionic strength. B: It is transferred to solution 2 which has different pH and ionic strength. C: Gel 1 swells in response to the environmental changes while Gel 2 does not swell, causing the bilayer to fold. D: The bilayer is transferred back into solution 1. E: Gel 1 deswells in response to the environmental changes and the bilayer unfolds. (Bottom) Venus flytrap-shaped actuator constructed from rigid segments with a NIPAm-AAc/PEODA bilayer hinge folding in response to changes in pH and ionic strength. Reversible folding occurred when the hinge was transferred from a pH 2.5/1.1 M solution to a pH 7.8/0.2 M solution. The scale bar is 3 mm. (Reproduced from Bassik et al. (2010) with permission from Elsevier)

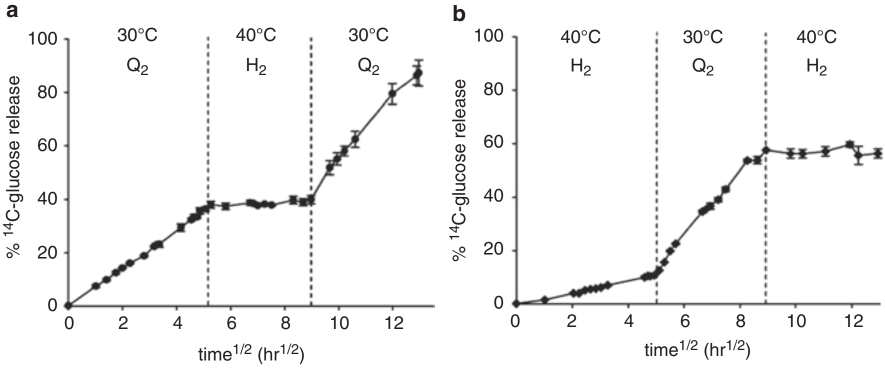

Fig. 12.72 Controlled release of glucose into phosphate buffered saline from phytantriol+3% vitamin E acetate with changing temperature. The temperature was switched as shown and triggered the transition between a bicontinous cubic phase (Q_2) and a reverse hexagonal phase (H_2). (Reproduced from Fong et al. (2009) with permission from Elsevier)

2005; Fu et al. 2003; Hong et al. 2008). MSNs are typically used as drug containers, and polymer grafting is employed as a stimuli-responsive switch. Since the system is sensitive to physiological conditions (e.g., pH and temperature), the necessary amount of drug in released in response to these stimuli. Stimulus-responsive polymer chains are grafted to the surface of MSNs to control the transport of encapsulated guest molecules. Thermo-responsive polymers such as PNIPAM are grafted to MSNs via “grafting from” approaches coupled with atom transfer radical polymerization (ATRP) (Yang et al. 2008; Zhou et al. 2007) and reversible addition/fragmentation chain transfer (RAFT) radical polymerization (Chung et al. 2008) along with “grafting to” methods (You et al. 2008).

Sun et al. reported that PAA can be grafted on the exterior surface of MSNs via RAFT radical polymerization (Hong et al. 2009). Xu et al. prepared PMAA-coated MSNs by co-polymerization of methacrylic acid (MAA) with vinyl triethoxylsilane (VTES) (Gao et al. 2009). MAA and VTES were used to prepare the pH-responsive random copolymer, with MAA serving as the pH-responsive unit and VTES acting as the anchoring group to graft the copolymer onto MSNs. The pendent triethoxysilyl group in the VTES unit can specifically bind with the surface silanol groups of MSNs. These two pH-responsive polymer-grafted MSN materials are carriers and the pH-responsive shells serve as smart nano-valves. The pH-responsive polymers can control the uptake and release processes of guest molecules. These MSNs show similar release behaviors. In basic solutions, the pores are open and the drug can be released as a result of the expansion of the polymer chains. On the other hand, in acidic solutions, compact polymer chains close the pores and confine the drug to this region.

Sun et al. prepared PDEAEMA-coated MSNs via ATRP coupling following a “grafting from” approach (Fig. 12.73) (Sun et al. 2010). At neutral or alkaline pH conditions, PDEAEMA does not dissolve in water because of the deprotonation of the pendent diethylamino groups, and the uncharged polymer chains collapse as a

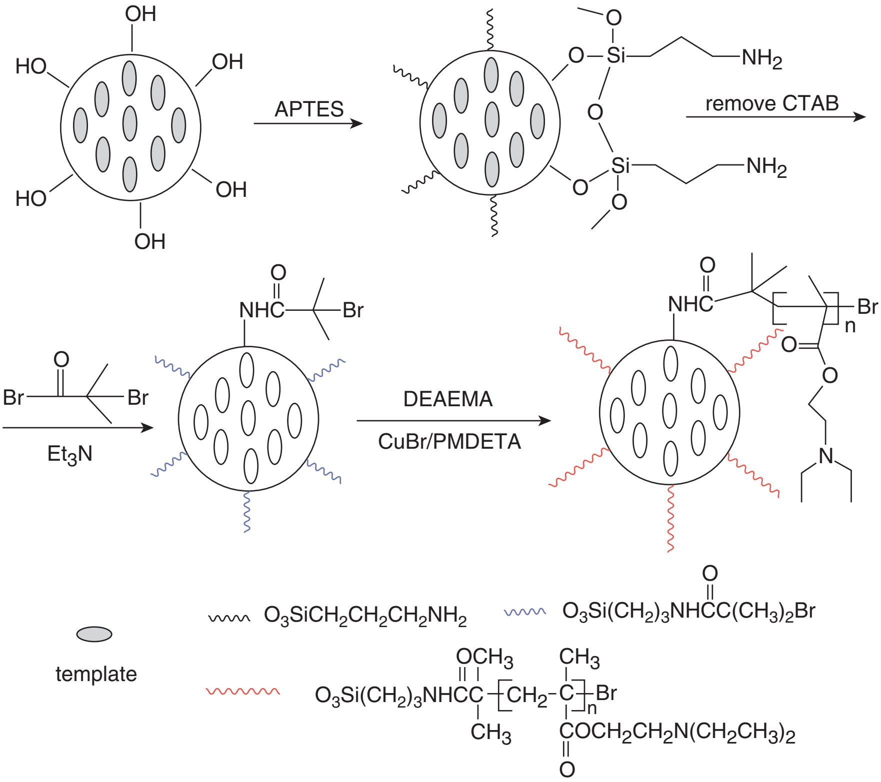

Fig. 12.73 Synthetic route of PDMAEMA-functionalized mesoporous silica nanoparticles (MSNs) via atom transfer radical polymerization (ATRP) with a "grafting from" approach. (Copyright 2010, reproduced from Sun et al. (2010) with permission from the ACS)

result of hydrophobic interactions. On the other hand, in acidic solutions, PDEAEMA can dissolve in water because of the protonation of the pendent diethylamino groups, and the protonated chains shifted to an expanded conformation (Lee et al. 1999). The pK_a value of PDEAEMA is ca. pH = 7–8 (Chen et al. 2003). pH-Responsive PDEAEMA chains grafted on MSNs can serve as a switch material to control the opening and closing processes of the pores. The PDEAEMA chains grafted on MSNs act as a good gatekeeper to control the access to the pores by a pH-responsive open–close mechanism. Thus, in acidic aqueous solutions, the guest molecules are rapidly released from the PDEAEMA-grafted MSNs, whereas this process is nearly suppressed in alkaline aqueous solutions. This weak acid-triggered release system is potentially suitable for the controlled release of anticancer reagents, given the acidity of cancerous tissues.

Lai et al. prepared a light-responsive nanogated ensemble based on a light-responsive polymer grafted on MSNs (Fig. 12.74) (Lai et al. 2010). A random copolymer of poly(*N*-isopropylacrylamide-*co*-2-nitorobenzyl acrylate) (poly (NIMAMNBAE)) containing photocleavable hydrophobic 2-nitorobenzyl groups

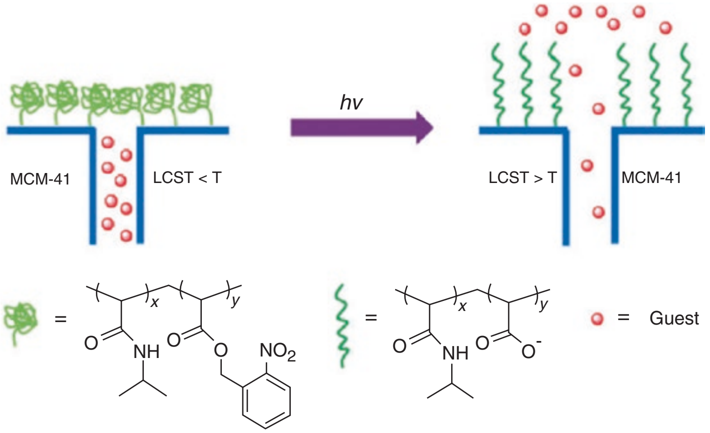

Fig. 12.74 Light-responsive nanogated ensemble based on a polymer-grafted mesoporous silica. (Copyright 2010, reproduced from Lai et al. (2010) with permission from the RSC)

has a LCST below 37 °C. The light-responsive moieties present in the thermo-responsive polymers provide these materials with a unique property of modulating its phase state upon UV light irradiation at a chosen temperature (Shimoboji et al. 2002; Jiang et al. 2008). The random copolymer was grafted onto MSNs by a "grafting to" approach. When poly(NIMAMNBAE) is in a collapsed state, the gate is closed such that the guest molecules are stored in the pores. Upon UV light irradiation, the pendent hydrophobic 2-nitorobenzyl group is photo-cleaved to generate hydrophilic acrylate with higher LCST. Therefore, the polymer chains change to an expanded conformation opening the gate and allowing the release of the encapsulated guest molecules into the bulk water phase. The LCST of the grafted random copolymer is 14 °C before UV light irradiation. Therefore the nano-valve is closed, encapsulating the guest molecules within the pores of MSNs. Upon UV light irradiation, the hydrophobic 2-nitorobenzyl group is cleaved, thereby increasing the LCST of the resulting copolymers to 46 °C. Therefore, the polymer changed its phase state at 37 °C and the encapsulated guest molecules are released from the copolymer-grafted MSNs.

Superparamagnetic iron oxide nanoparticles (SPIONs) have received a great deal of interest owing to their potential in biomedical applications such as drug delivery (Kohler et al. 2005), magnetic resonance imaging (MRI) (Bonnemain 1998; Kroft and de Roos 1999; Blasberg 2003; Baghi et al. 2005; Martina et al. 2005), and hyperthermia therapy (Gupta and Gupta 2005; Ito et al. 2004). The direct use of SPIONs as in vivo MRI contrast agents leads to biofouling of the particle surface in blood plasma and the formation of aggregates that are quickly sequestered by cells of the reticular endothelial system (RES) such as macrophages (Rogers and Basu 2005). Some natural and synthetic polymers have been employed to modify the surface of SPIONs, thereby enhancing their functions. These polymers are dextran (Kaufman et al. 2003; Berry et al. 2004), poly(ethylene glycol) (PEG) (Kohler et al.

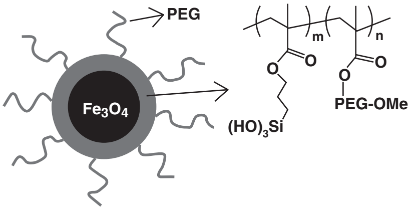

poly(TMSMA-*r*-PEGMA)@SPION

Fig. 12.75 Schematic diagram of the polymer-coated superparamagnetic iron oxide nanoparticle (SPION) and the chemical structure of the PEG-silane copolymer poly(TMSMA-*r*-PEGMA). (Copyright 2006, reproduced from Lee et al. (2006) with permission from the ACS)

2004; Zhang et al. 2002b), and poly(vinylpyrrolidone) (PVP) (D'Souza et al. 2004). These polymers are biocompatible and result in long blood-circulating SPIONs. Lee et al. (2006) prepared antifouling polymer-coated SPIONs as magnetic resonance contrast agents. SPIONs were coated with a random copolymer (poly(TMSMA-*r*-PEGMA)) containing a surface anchoring moiety (i.e., silane group) and a protein-resistant moiety (PEG), which was prepared by random copolymerization of (trimethoxysilyl) propyl methacrylate and PEG methacrylate (Fig. 12.75). The sizes of the polymer-coated SPIONs were constant even after 24 h of incubation in a 10% serum containing a cell culture medium, thereby indicating that proteins do not adsorb on their surface. The polymer-coated SPIONs were able to detect tumors in vivo by MRI and can be potentially used as efficient cancer diagnostic probes.

12.4.5 Cell Culture

Biomedical engineering is one of the ideal fields of application for surfaces that possess properties that can be switched using external stimuli. In particular considerable progress has been achieved to date in the design of materials for cell culture. Hydration-dehydration switching of stimuli-responsive polymer chains is expected to allow control over spontaneous attachment-detachment of cells when they are grafted on solid surfaces such as cell culture dishes. Such a surface can allow noninvasive harvesting of cultured cells and removal of cells merely by changing environmental stimuli, which presents a significant advantage compared to conventional methods such as mechanical scraping or enzymatic removal of cells that can have adverse impact on cells.

The stimulus-responsive system most promising for biomedical engineering is a thermo-responsive material based on PNIPAM attached on solid surfaces. PNIPAM is an ideal polymer for use in cell culture engineering because its LCST is around 32 °C in aqueous solutions, which is close to the natural temperature of the human body. Another merit of PNIPAM is its sharp transition from a hydrophilic state to a hydrophobic state across the LCST. The surface bearing PNIPAM molecules

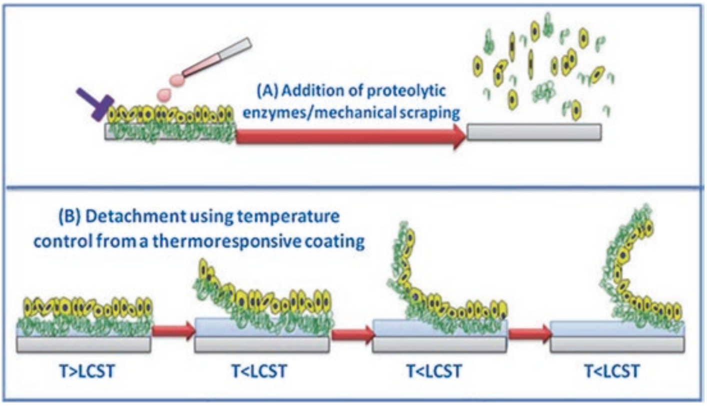

Fig. 12.76 Schematic representation of temperature-responsive culture dishes. (**a**) Conventional trypsinization to remove the cell sheet can have a possible adverse impact on the cell sheet for cell recovery. (**b**) Cells harvested from temperature-responsive dishes are recovered as intact sheets by simple temperature reduction below LCST. (Adapted from Nash et al. (2012) with permission of The Royal Society of Chemistry)

become hydrophobic, thus allowing cells to attach when the temperature is above 32 °C, i.e., a temperature at which cells normally proliferate. Once the temperature is decreased below 32 °C, the surface changes to hydrophilic, thereby allowing cells to detach. The LCST of PNIPAM can be further altered by copolymerization with either hydrophilic or hydrophobic monomer units for broader application.

Cell sheet technology using thermo-responsive polymer-grafted cell culture materials has emerged as a novel approach in regenerative medicine (Fig. 12.76). Okano's group pioneered this technology, developing a cell-sheet transplantation method utilizing a PNIPAM-grafted culture dish (Yamada et al. 1990). On this culture dish, cells are allowed to develop to a confluent sheet via cell-cell junctions above 32 °C. Subsequently, the cell sheet is collected from the culture dish at a temperature well below the LCST without the need for an enzymatic treatment. By transplantation of the resulting cell sheets into subcutaneous tissues, the authors successfully confirmed long-term survival and growth of pulsatile myocardial tissue, thereby enabling myocardial tissue regeneration (Shimizu et al. 2006). The direct transplantation of cultured cell sheets has been also applied to many other tissue recoveries, including corneal epithelia (Nishida et al. 2004), periodontal ligament (Iwata et al. 2009), myoblast cells (Memon et al. 2005), and esophageal epithelia (Ohki et al. 2006).

A variety of methods have been applied to grafting PNIPAM onto solid surfaces to create cell culture materials. Electron beam (EB) polymerization is one of the most frequently employed methods. This technique presents a significant advantage as it allows PNIPAM layers to be grafted onto engineering plastic such as PS, which is one of the most commonly utilized cell culture materials (Tekin et al. 2011; Akiyama et al. 2004). Plasma polymerization (Pan et al. 2001; Rayatpisheh et al. 2012) and UV irradiation (von Recum et al. 1999) are also promising simple and fast methods for conducting graft polymerization. Recently, a spin-coating technique has been successfully utilized for the deposition of PNIPAM onto surfaces without the need for expensive equipment such as EB or plasma reactor (Patel et al. 2012; Dzhoyashvili et al. 2016). Patel et al. have developed a method to graft PNIPAM onto silica-based surfaces by blending a small amount of 3-aminopropyltriethoxysilane with PNIPAM, which enhances the retention of PNIPAM on the surface (Patel et al. 2012).

The basic mechanisms of cell attachment to and detachment from culture dishes are suggested as follows (Cole et al. 2009). Above the LCST, the collapsed state of the PNIPAM layer allows cells to adhere on the surface via the adsorption of cell adhesive proteins residing in serum, and to spread in order to proliferate. As well as its hydrophobicity, the collapsed conformation of PNIPAM chains supports cell attachment and works as a good scaffold for cell growth. On the other hand, both the cell-PNIPAM interactions and the cellular morphological changes driven by the cytoskeletal action seem to play an important role in the detachment of cells from surfaces (Okano et al. 1995). Upon cooling, the hydration of PNIPAM chains reduces the adhesion of cells to surfaces. As a consequence, cells adopt a less flattened, spread morphology, which drives their detachment from the surface. The detachment process proceeds until the cells no longer adopt the spread morphology.

In these attachment and detachment processes, the grafting amount and grafting density of the polymer are thought to play significant roles. A series of studies have reported that thin PNIPAM layers with a few tenths of nanometres tend to have excellent attachment/detachment ability (Akiyama et al. 2004; Mizutani et al. 2008), though there are some results that do not support these observations (Dzhoyashvili et al. 2016). A possible explanation why thin layers are good for cell attachment is that the thicker the layer becomes, the more hydrated is the outermost region of the PNIPAM layer, which makes the cells unable to attach to the surface (Akiyama et al. 2004). If grafting density is altered, the property of the exposed base material on which the polymer layers are formed also affects considerably the cell attachment/detachment characteristics (Nagase et al. 2011).

Light is another useful stimulus that can produce switchable cell attachment-detachment for responsive surfaces. The largest merit of using light as a switching stimulus is that one can control its spatial and temporal resolution quite easily. Light-induced cell attachment and detachment have been achieved using photoresponsive molecules, for example spiropyran (Higuchi et al. 2004; Edahiro et al. 2005) and azobenzene (Auernheimer et al. 2005). Higuchi et al. (2004) observed UV-light induced detachment of cells from a glass plate coated with a copolymer of nitrobenzospiropyran and methyl methacrylate, whereas the cells remained adhered to the plate when exposed to visible light (Fig. 12.77). The proposed mechanism for this detachment can be explained by the irradiation with UV light, which caused the spiropyran to isomerize to a polar hydrophilic zwitterionic conformation, which allowed the cells to detach from the surface. On the other hand, the spiropyran adopts a nonionic state when exposed to visible light, with a hydrophobic surface comprised of methyl methacrylate blocks that promote cell attachment.

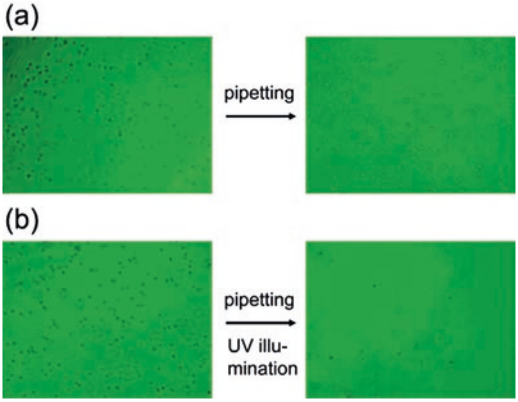

Fig. 12.77 Mesenchymal stem (KUSA-A1) cells on a glass plate coated with a copolymer of nitrobenzospiropyran and methyl methacrylate before and after pipetting 1 mL of DMEM media (**a**) under visible light and (**b**) after the irradiation with UV light. (Reprinted with permission from Higuchi et al. (2004). Copyright (2004) American Chemical Society)

To date, only a few studies have been conducted using pH-responsive systems for cell culture as a result of the limited range of pH (~6.8–7.4) that can be used for harvesting cells. Chen et al. used chitosan to attach/detach cells in response to a change in pH (Chen et al. 2012). The authors have shown that 90% of HeLa cells attached and spread well on the chitosan at pH 6.99 and 7.20, and detached within 1 h by increasing the pH to 7.65. In this case, the chitosan surface becomes positively charged as a result of protonation when the solution pH is lower than 7.4, i.e., the isoelectric point of chitosan, thereby allowing the adsorption of the negatively charged extracellular fibronectin protein. At pH 7.65, the deprotonation of the chitosan surface causes desorption of fibronectin, resulting in the detachment of cells.

12.5 Concluding Remarks

Although the concept of stimulus-responsiveness has been known for many years, the last two decades have especially witnessed tremendous progress in this field. Surfaces/interfaces that respond to external stimuli represent one of the most emerging and active scientific research areas and have a number of unexplored commercial applications. This evolving research field faces lots of exciting challenges regarding the design, fabrication and engineering of the surfaces/interfaces.

The selections of solid substrates and gases/liquids are important factors during the development of stimulus-responsive surfaces/interfaces. It is possible to introduce stimuli to the surfac-es/interfaces from both the solid substrate and the gases/liquids phases. External stimulus-induced chemical reactions at surfaces/interfaces will be a critical research topic.

One of the important extensions of the research area is the development of surfaces/interfaces capable of responding to multiple stimuli and resulting in one or more responses in a controllable and predictable fashion. Multi-responsive surfaces/interfaces that respond to more than two stimuli are extraordinarily functional, because they can provide extra tools to tune their properties finely under a complex environment such as the biological systems in a cooperative manner.

The development of new monomers and polymers with stimulus-responsive character is particularly important. The multi-responsive monomers will allow the straightforward preparation of complex systems in a one-step and one-pot manner. The development of methods for characterizing the stimulus-responsive surfaces/interfaces is also crucial. Our understanding of the mechanism of formation, dynamics of stimulus-responsive behaviors is substantially incomplete. Advances in characterization methods are expected to elucidate the relationships among the fabrication, structure and properties of the surfaces and to inspire their design philosophies toward reliable intelligent surfaces/interfaces.

While there are many exciting challenged facing this continually evolving field and there are myriad opportunities in design, synthesis and engineering of stimuli-responsive materials, nature provides endless inspiration. Interdisciplinary research is crucial to continue developing science and engineering of the stimulus-responsive surfaces/interfaces.

References

Abbott S, Ralston J, Reynolds G, Hayes R (1999) Reversible wettability of photoresponsive pyrimidine-coated surfaces. Langmuir 15:8923–8928

Abbott SA, de Vos WM, Mears LLE, Skoda M, Dalgliesh R, Edmondson S, Richardson RM, Prescott SW (2016) Switching the interpenetration of confined asymmetric polymer brushes. Macromolecules 49:4349–4357

Abrakhi S, Péralta S, Fichet O, Teyssié D, Cantin S (2013) Poly(azobenzene acrylate-*co*-fluorinated acrylate) spin-coated films: influence of the composition on the photo-controlled wettability. Langmuir 29:9499–9509

Advicula RC, Brittain WJ, Caster KC, Ruhe J (2004) Polymer brushes. Wiley, Hoboken

Agrawal M, Rueda JC, Uhlmann P, Müller M, Simon F, Stamm M (2012) Facile approach to grafting of poly(2-oxazoline) brushes on macroscopic surfaces and applications thereof. ACS Appl Mater Interfaces 4:1357–1364

Ahn SK, Kasi RM, Kim SC, Sharma N, Zhou YX (2008) Stimuli-responsive polymer gels. Soft Matter 4:1151–1157

Akiyama Y, Kikuchi A, Yamato M, Okano T (2004) Ultrathin poly(*N*-isopropylacrylamide) grafted layer on polystyrene surfaces for cell adhesion/detachment control. Langmuir 20:5506–5511

Angelov B, Angelova A, Garamus VM, Lebas G, Lesieur S, Ollivon M, Funari SS, Willumeit R, Couvreur P (2007) Small-angle neutron and x-ray scattering from amphiphilic stimuli-responsive diamond-type bicontinuous cubic phase. J Am Chem Soc 129:13474–13479

Auernheimer J, Dahmen C, Hersel U, Bausch A, Kessler H (2005) Photoswitched cell adhesion on surfaces with RGD peptides. J Am Chem Soc 127:16107–16110

Azzaroni O, Brown AA, Huck WTS (2006) UCST wetting transitions of polyzwitterionic brushes driven by self-association. Angew Chem Int Ed 45:1770–1774

Azzaroni O, Brown AA, Huck WTS (2007) Tunable wettability by clicking counterions into polyelectrolyte brushes. Adv Mater 19:151–154

Baghi M, Mack MG, Hambek M, Rieger J, Vogl T, Gstoettner W, Knecht R (2005) The efficacy of MRI with ultrasmall superparamagnetic iron oxide particles (USPIO) in head and neck cancers. Anticancer Res 25:3665–3670

Bain CD (1995) Sum-frequency vibrational spectroscopy of the solid/liquid interface. J Chem Soc Faraday Trans 91:1281–1296

Balamurugan S, Mendez S, Balamurugan SS, O'Brien MJ, López GP (2003) Thermal response of poly(*N*-isopropylacrylamide) brushes probed by surface plasmon resonance. Langmuir 19:2545–2549

Barea MJ, Jenkins MJ, Gaber MH, Bridson RH (2010) Evaluation of liposomes coated with a pH responsive polymer. Int J Pharm 402:89–94

Basak S, Nanda J, Banerjee A (2014) Multi-stimuli responsive self-healing metallo-hydrogels: tuning of the gel recovery property. Chem Commun 50:2356–2359

Bassik N, Abebe B, Laflin K, Gracias D (2010) Photolithographically patterned smart hydrogel based bilayer actuators. Polymer 51:6093–6098

Beck JS, Vartuli JC, Roth WJ, Leonowicz ME, Kresge CT, Schmitt KD, Chu CTW, Olson DH, Sheppard EW, McCullen SB, Higgins JB, Schlenker JL (1992) A new family of mesoporous molecular sieves prepared with liquid crystal templates. J Am Chem Soc 114:10834–10843

Bell NS, Piech M (2006) Photophysical effects between spirobenzopyran-methyl methacrylate-functionalized colloidal particles. Langmuir 22:1420–1427

Berry CC, Wells S, Charles S, Aitchison G, Curtis AS (2004) Cell response to dextran-derivatised iron oxide nanoparticles post internalization. Biomaterials 25:5405–5413

Bialk M, Prucker O, Rühe J (2002) Grafting of polymers to solid surfaces by using immobilized methacrylates. Colloids Surf A Physicochem Eng Asp 198-200:543–549

Biggs S, Sakai K, Addison T, Schmid A, Armes SP, Vamvakaki M, Bütün V, Webber GB (2007) Layer-by-layer formation of smart particle coatings using oppositely charged block copolymer micelles. Adv Mater 19:247–250

Binnig G, Quate CF, Gerberl C (1986) Atomic force microscope. Phys Rev Lett 56:930–933

Blasberg RG (2003) Molecular imaging and cancer. Mol Cancer Ther 2:335–343

Bonnemain B (1998) Superparamagnetic agents in magnetic resonance imaging: physicochemical characteristics and clinical applications a review. J Drug Target 6:167–174

Brown P, Butts CP, Eastoe J (2013) Stimuli-responsive surfactants. Soft Matter 9:2365–2374

Brunsen A, Díaz C, Pietrasanta LI, Yameen B, Ceolín M, Soler-Illia GJAA, Azzaroni O (2012) Proton and calcium-gated ionic mesochannels: phosphate-bearing polymer brushes hosted in mesoporous thin films as biomimetic interfacial architectures. Langmuir 28:3583–3592

Burtovyy R, Luzinov I (2008) Reversibility of pH-induced dewetting of poly(vinyl pyridine) thin films on silicon oxide substrate. Langmuir 24:5903–5910

Cassie ABD, Baxter S (1944) Wettability of porous surfaces. Trans Faraday Soc 40:546–551

Chaimberg M, Cohen Y (1994) Kinetic modeling of free-radical graft polymerization. AICHE J 40:294–311

Chécot F, Brûlet A, Oberdisse J, Gnanou Y, Mondain-Monval O, Lecommoandoux S (2005) Structure of polypeptide-based diblock copolymers in solution: stimuli-responsive vesicles and micelles. Langmuir 21:4308–4315

Cheesman BT, Willott JD, Webber GB, Edmondson E, Wanless EJ (2012) pH-responsive brush-modified silica hybrids synthesized by surface-initiated ARGET ATRP. ACS Macro Lett 1:1161–1165

Cheesman BT, Smith EG, Murdoch TJ, Guibert C, Webber GB, Edmondson S, Wanless EJ (2013) Polyelectrolyte brush pH-response at the silica-aqueous solution interface: a kinetic and equilibrium investigation. Phys Chem Chem Phys 15:14502–14510

Chen XY, Randall DP, Perruchot C, Watts JF, Patten TE, von Werne T, Armes SP (2003) Synthesis and aqueous solution properties of polyelectrolyte-grafted silica particles prepared by surface-initiated atom transfer radical polymerization. J Colloid Interface Sci 257:56–64

Chen L, Liu M, Bai H, Chen P, Xia F, Han D, Jiang L (2009) Antiplatelet and thermally responsive poly(*N*-isopropylacrylamide) surface with nanoscale topography. J Am Chem Soc 131:10467–10472

Chen T, Ferris R, Zhang J, Ducker R, Zauscher S (2010) Stimulus-responsive polymer brushes on surfaces: transduction mechanisms and applications. Prog Polym Sci 35:94–112

Chen Y-H, Chung Y-C, Wang I-J, Young T-H (2012) Control of cell attachment on pH-responsive chitosan surface by precise adjustment of medium pH. Biomaterials 33:1336–1342

Chen J, Xiao P, Gu J, Han D, Zhang J, Sun A, Wang W, Chen T (2014) A smart hybrid system of Au nanoparticle immobilized PDMAEMA brushes for thermally adjustable catalysis. Chem Commun 50:1212–1214

Cheng X, Canavan HE, Stein MJ, Hull JR, Kweskin SJ, Wagner MS, Somorjai GA, Castner DG, Ratner BD (2005) Surface chemical and mechanical properties of plasma-polymerized *N*-isopropylacrylamide. Langmuir 21:7833–7841

Chiefari J, Chong YK, Ercole F, Krstina J, Jeffery J, Le TPT, Mayadunnne RTA, Meijs GF, Moad CL, Moad G, Rizzardo E, Thang SH (1998) Living free-radical polymerization by reversible addition-fragmentation chain transfer: the RAFT process. Macromolecules 31:5559–5562

Cho EC, Kim YD, Cho K (2005) Temperature-dependent intermolecular force measurement of poly(*N*-isopropylacrylamide) grafted surface with protein. J Colloid Interface Sci 286:479–486

Choi J, Schattling P, Jochum FD, Pyun J, Char K, Theato P (2012) Functionalization and patterning of reactive polymer brushes based on surface reversible addition and fragmentation chain transfer polymerization. J Polym Sci A 50:4010–4018

Christau S, Möller T, Yenice Z, Genzer J, von Klitzing R (2014) Brush/gold nanoparticle hybrids: effect of grafting density on the particle uptake and distribution within weak polyelectrolyte brushes. Langmuir 30:13033–13041

Christau S, Möller T, Brose F, Genzer J, Soltwedel O, von Klitzing R (2016) Effect of gold nanoparticle hydrophobicity on thermally induced color change of PNIPAM brush/gold nanoparticle hybrids. Polymer 98:454–463

Chung PW, Kumar R, Pruski M, Lin VSY (2008) Temperature responsive solution partition of organic-inorganic hybrid poly(*N*-isopropylacrylamide)-coated mesoporous silica nanospheres. Adv Funct Mater 18:1390–1398

Coessens V, Pintauer T, Matyjaszewski K (2001) Functional polymers by atom transfer radical polymerization. Prog Polym Sci 26:337–377

Cole MA, Voelcker NH, Thissen H, Griesser HJ (2009) Stimuli-responsive interfaces and systems for the control of protein–surface and cell–surface interactions. Biomaterials 30:1827–1850

Cole MA, Voelcker NH, Thissen H, Horn RG, Griesser HJ (2010) Colloid probe AFM study of thermal collapse and protein interactions of poly(*N*-isopropylacrylamide) coatings. Soft Matter 6:2657–2667

Corbierre MK, Cameron NS, Sutton M, Mochrie SGJ, Lurio LB, Rühm A, Lennox RB (2001) Polymer-stabilized gold nanoparticles and their incorporation into polymer matrices. J Am Chem Soc 123:10411–10412

Corbierre MK, Cameron NS, Lennox RB (2004) Polymer-stabilized gold nanoparticles with high grafting densities. Langmuir 20:2867–2873

Crosby AJ, Shull KR (1999) Adhesive failure analysis of pressure-sensitive adhesives. J Polym Sci Polym Phys 37:3455–3472

Currie EPK, Sieval AB, Fleer GJ, Cohen Stuart MA (2000) Polyacrylic acid brushes: surface pressure and salt-induced swelling. Langmuir 16:8324–8333

Cunliffe D, Alarcon CD, Peters V, Smith JR, Alexander C (2003) Thermoresponsive surface-grafted poly(*N*-isopropylacrylamide) copolymers: effect of phase transitions on protein and bacterial attachment. Langmuir 19:2888–2899

D'Souza AJ, Schowen RL, Topp EM (2004) Polyvinylpyrrolidone–drug conjugate: synthesis and release mechanism. J Control Release 94:91–100

Daltorio KA, Horchler AD, Gorb S, Ritzmann RE, Quinn RD (2005) A small wall-walking robot with compliant, adhesive feet. Proc Int Conf Intell Robots Syst:3648–3653

Dar YL, Yuan-Huffman W, Shah S, Huang D, Xiao A (2007) Thermally activated pressure-sensitive adhesives. J Adhes Sci Technol 21:1645–1658

Datta P, Genzer J (2013) Computer simulation of template polymerization using a controlled reaction scheme. Macromolecules 46:2474–2484

Datta P, Genzer J (2016) "Grafting through" polymerization involving surface-bound monomers. Polym Chem 54:263–274

de Gennes PG (1980) Conformations of polymers attached to an interface. Macromolecules 13:1069–1075

Denes FS, Manolache S (2004) Macromolecular plasma-chemistry: an emerging field of polymer science. Prog Polym Sci 29:815–885

Dübner M, Spencer ND, Padeste C (2014) Light-responsive polymer surfaces via postpolymerization modification of grafted polymer-brush structures. Langmuir 30:14971–14981

Ducker WA, Senden TJ, Pashley RM (1991) Direct measurement of colloidal forces using an atomic force microscope. Nature 353:239–241

Dutta NK, Truong MY, Mayavan S, Choudhury NR, Elvin CM, Kim M, Knott R, Nairn KM, Hill AJ (2011) A genetically engineered protein responsive to multiple stimuli. Angew Chem Int Ed 50:4428–4431

Dzhoyashvili NA, Thompson K, Gorelov AV, Rochev YA (2016) Film thickness determines cell growth and cell sheet detachment from spin-coated poly(*N*-isopropylacrylamide) substrates. ACS Appl Mater Interfaces 8:27564–27572

Eastoe J, Sánchez-Dominguez M, Wyatt P, Heenan RK (2004) A photo-responsive organogel. Chem Commun:2608–2609

Edahiro J, Sumaru K, Tada Y, Ohi K, Takagi T, Kameda M, Shinbo T, Kanamori T, Yoshimi Y (2005) In situ control of cell adhesion using photoresponsive culture surface. Biomacromolecules 6:970–974

Edmondson S, Nguyen NT, Lewis AL, Armes SP (2010) Co-nonsolvency effects for surface-initiated poly(2-(methacryloyloxy)ethyl phosphorylcholine) brushes in alcohol/water mixtures. Langmuir 26:7216–7226

Ejaz M, Yamamoto S, Ohono K, Tsujii Y, Fukuda T (1998) Controlled graft polymerization of methyl nethacrylate on silicon substrate by the combined use of the Langmuir-Blodgett and atom transfer radical polymerization techniques. Macromolecules 31:5934–5936

Emilsson G, Schoch RL, Feuz L, Höök F, Lim RYH, Dahlin AB (2015) Strongly stretched protein resistant poly(ethylene glycol) brushes prepared by grafting-to. ACS Appl Mater Interfaces 7:7505–7515

Fazli Y, Kulani E, Khezri K, Alijani H (2015) PMMA-grafted silica aerogel nanoparticles via in situ SR&NI ATRP: grafting through approach. Micropor Mesopor Mat 214:70–79

Feiler A, Plunkett MA, Rutland MW (2003) Atomic force microscopy measurements of adsorbed polyelectrolyte layers. 1. Dynamics of forces and friction. Langmuir 19:4173–4179

Fielding LA, Edmondson S, Armes SP (2011) Synthesis of pH-responsive tertiary amine methacrylate polymer brushes and their response to acidic vapour. J Mater Chem 21:11773–11780

Fischer H (1997) The persistent radical effect in “living” radical polymerization. Macromolecules 30:5666–5672

Fischer H, Radom L (2001) Factors controlling the addition of carbon-centered radicals to alkenes-an experimental and theoretical perspective. Angew Chem Int Ed Engl 40:1340–1371

Fitzgerald PA, Dupin D, Armes SP, Wanless EJ (2007) In situ observations of adsorbed microgel particles. Soft Matter 3:580–586

Fitzgerald PA, Amalvy JI, Armes SP, Wanless EJ (2008) Film-forming microgels for pH-triggered capture and release. Langmuir 24:10228–10234

Fong W-K, Hanley T, Boyd BJ (2009) Stimuli responsive liquid crystals provide ‘on-demand’ drug delivery in vitro and in vivo. J Control Release 135:218–226

Fong W-K, Hanley TL, Thierry B, Hawley A, Boyd BJ, Landersdorfer CB (2016) External manipulation of nanostructure in photoresponsive lipid depot matrix to control and predict drug release in vivo. J Control Release 228:67–73

Frisman I, Shachaf Y, Seliktar D, Bianco-Peled H (2011) Stimulus-responsive hydrogels made from biosynthetic fibrinogen conjugates for tissue engineering: structural characterization. Langmuir 27:6977–6986

Fu Q, Rama-Rao GV, Ista LK, Wu Y, Andrzejewski BP, Sklar LA, Ward ST, López GP (2003) Control of molecular transport through stimuli-responsive ordered mesoporous materials. Adv Mater 15:1262–1266

Fujii S, Okada M, Furuzono T (2007) Hydroxyapatite nanoparticles as stimulus-responsive particulate emulsifiers and building block for porous materials. J Colloid Interface Sci 315:287–296

Fujii S, Suzaki M, Armes SP, Dupin D, Hamasaki S, Aono K, Nakamura Y (2011a) Liquid marbles prepared from pH-responsive sterically stabilized latex particles. Langmuir 27:8067–8074

Fujii S, Suzaki M, Nakamura Y, Sakai K, Ishida N, Biggs S (2011b) Surface characterization of nanoparticles carrying pH-responsive polymer hair. Polymer 51:6240–6247

Fujii S, Aono K, Suzaki M, Hamasaki S, Yusa S, Nakamura Y (2012a) pH-responsive hairy particles synthesized by dispersion polymerization with a macroinitiator as an inistab and their use as a gas-sensitive liquid marble stabilizer. Macromolecules 45:2863–2873

Fujii S, Sanada Y, Nishimura T, Akiba I, Sakurai K (2012b) A stimulus-responsive shape-persistent micelle bearing a calix[4]arene building block: reversible pH-dependent transition between spherical and cylindrical forms. Langmuir 28:3092–3101

Fujii S, Sawada S, Nakayama S, Kappl M, Ueno K, Shitajima K, Butt HJ, Nakamura Y (2016) Pressure-sensitive adhesive powder. Mater Horiz 3:47–52

Gao Q, Xu Y, Wu D, Sun Y, Li X (2009) pH-responsive drug release from polymer-coated mesoporous silica spheres. J Phys Chem C 113:12753–12758

Gawlitza K, Turner ST, Polzer F, Wellert S, Karg M, Mulvaney P, von Klitzing R (2013) Interaction of gold nanoparticles with thermoresponsive microgels: influence of the cross-linker density on optical properties. PCCP 15:15623–15631

Geoghegan M, Ruiz-Pérez L, Dang CC, Parnell AJ, Martin SJ, Howse JR, Jones RAL, Golestanian R, Topham PD, Crook CJ, Ryan AJ, Sivia DS, Websterc JRP, Menelled A (2006) The pH-induced swelling and collapse of a polybase brush synthesized by atom transfer radical polymerization. Soft Matter 2:1076–1080

Georges MK, Veregin RPN, Kazmaier PM, Hamer GK (1990) Narrow molecular weight resins by a free-radical polymerization process. Macromolecules 26:2987–2988

Giacomelli C, Le Men L, Borsali R, Lai-Kee-Him J, Brisson A, Armes SP, Lewis AL (2006) Phosphorylcholine-based pH-responsive diblock copolymer micelles as drug delivery vehicles: light scattering, electron microscopy, and fluorescence experiments. Biomacromolecules 7:817–828

Gong P, Wu T, Genzer J, Szleifer I (2007) Behavior of surface-anchored poly(acrylic acid) brushes with grafting density gradients on solid substrates: 2. Theory. Macromolecules 40:8765–8773

Groten J, Bunte C, Rühe J (2012) Light-induced switching of surfaces at wetting transitions through photoisomerization of polymer monolayers. Langmuir 28:15038–15046

Gupta AK, Gupta M (2005) Synthesis and surface engineering of iron oxide nanoparticles for biomedical applications. Biomaterials 26:3995–4021

Gurney RS, Dupin D, Nunes JS, Ouzineb K, Siband E, Asua JM, Armes SP, Keddie JL (2012) Switching off the tackiness of a nanocomposite adhesive in 30 s via infrared sintering. ACS Appl Mater Interfaces 4:5442–5452

Gurney RS, Dupin D, Siband E, Ouzineb K, Keddie JL (2013) Large-area patterning of the tackiness of a nanocomposite adhesive by sintering of nanoparticles under IR radiation. ACS Appl Mater Interfaces 5:2137–2145

Han D-M, Zhang QM, Serpe MJ (2015) Poly(*N*-isopropylacrylamide)-co-(acrylic acid) microgel/Ag nanoparticle hybrids for the colorimetric sensing of H_2O_2. Nanoscale 7:2784–2789

Hawker CJ, Bosman AW, Harth E (2001) New polymer synthesis by nitroxide mediated living radical polymerizations. Chem Rev 101:3661–3688

Hayashida S, Sato H, Sugawara S (1986) Photo-induced wettability change in films containing spiropyran microcrystals. Polym J 18:227–235

He Q, Küller A, Grunze M, Li JB (2007) Fabrication of thermosensitive polymer nanopatterns through chemical lithography and atom transfer radical polymerization. Langmuir 23:3981–3987

Henze M, Mädge D, Prucker O, Rühe J (2014) "Grafting through": mechanistic aspects of radical polymerization reactions with surface-attached monomers. Macromolecules 47:2929–2937

Higaki Y, Fröhlich B, Yamamoto A, Murakami R, Kaneko M, Takahara A, Tanaka M (2017) Ion-specific modulation of interfacial interaction potentials between solid substrates and cell-sized particles mediated via zwitterionic, super-hydrophilic poly(sulfobetaine) brushes. J Phys Chem B 121:1396–1404

Higuchi A, Hamamura A, Shindo Y, Kitamura H, Yoon BO, Mori T, Uyama T, Umezawa A (2004) Photon-modulated changes of cell attachments on poly(spiropyran-*co*-methyl methacrylate) membranes. Biomacromolecules 5:1770–1774

Hill MR, Carmean RN, Sumerlin BS (2015) Expanding the scope of RAFT polymerization: recent advances and new horizons. Macromolecules 48:5459–5469

Hirotsu T, Isayama M (1989) Water-ethanol separation by pervaporation through plasma-graft-polymerized membranes of 2-hydroxyethyl methacrylate with acrylic acid or methacrylic acid. J Membr Sci 45:137–154

Hong CY, Li X, Pan CY (2008) Smart core-shell nanostructure with a mesoporous core and a stimuli-responsive nanoshell synthesized via surface reversible addition-fragmentation chain transfer polymerization. J Phys Chem C 112:15320–15324

Hong CY, Li X, Pan CY (2009) Fabrication of smart nanocontainers with a mesoporous core and a pH-responsive shell for controlled uptake and release. J Mater Chem 19:5155–5160

Hoogenboom R (2009) Poly(2-oxazoline)s: a polymer class with numerous potential applications. Angew Chem Int Ed 48:7978–7994

Howard SC, Craig VSJ, Fitzgerald PA, Wanless EJ (2010) Swelling and collapse of an adsorbed pH-responsive film-forming microgel measured by optical reflectometry and QCM. Langmuir 26:14615–14623

Howse JR, Topham P, Crook CJ, Gleeson AJ, Bras W, Jones RAL, Ryan AJ (2006) Reciprocating power generation in a chemically driven synthetic muscle. Nano Lett 6:73–77

Huang HQ, Penn LS (2005) Dense tethered layers by the “grafting-to” approach. Macromolecules 38:4837–4843

Huang H, Penn LS, Quirk RP, Cheong TH (2004) Kinetics of sequential tethering in formation of mixed layers. Macromolecules 37:5807–5813

Humphreys BA, Willott JD, Murdoch TJ, Webber GB, Wanless EJ (2016) Specific ion modulated thermoresponse of poly(*N*-isopropylacrylamide) brushes. Phys Chem Chem Phys 18:6037–6046

Husseman M, Eva Malmström EE, McNamara M, Mate M, Mecerreyes D, Benoit DG, Hedrick JL, Mansky P, Huang E, Russell TP, Hawker CJ (1999) Controlled synthesis of polymer brushes by “living” free radical polymerization techniques. Macromolecules 32:1424–1431

Hwang I, Jeon WS, Kim H-J, Kim D, Kim H, Selvapalam N, Fujita N, Shinkai S, Kim K (2007) Cucurbit[7]uril: a simple macrocyclic pH-triggered hydrogelator exhibiting guest-induced stimuli-responsive behaviour. Angew Chem 119:214–217

Ide M, Mori T, Ichikawa K, Kitano H, Tanaka M, Mochizuki A, Oshiyama H, Mizuno W (2003) Structure of water sorbed into poly(MEA-*co*-HEMA) films as examined by ATR-IR spectroscopy. Langmuir 19:429–435

Idota N, Kikuchi A, Kobayashi J, Akiyama Y, Sakai K, Okano T (2006) Thermal modulated interaction of aqueous steroids using polymer-grafted capillaries. Langmuir 22:425–430

Inoue M, Fujii S, Nakamura Y, Iwasaki Y, Yusa S (2011) pH-responsive disruption of ‘liquid marbles’ prepared from water and poly(6-(acrylamide)hexanoic acid)-grafted silica particles. Polym J 43:778–784

Ionov L, Houbenov N, Sidorenko A, Stamm M, Minko S (2006) Smart microfluidic channels. Adv Funct Mater 16:1153–1160

Ishida N, Biggs S (2007a) Direct observation of the phase transition for a poly(*N*-isopropylacryamide) layer grafted onto a solid surface by AFM and QCM-D. Langmuir 23:11083–11088

Ishida N, Biggs S (2007b) Salt-induced structural behavior for poly(*N*-isopropylacryamide)grafted onto solid surface observed directly by AFM and QCM-D. Macromolecules 40:9045–9052

Ishida N, Biggs S (2010) Effect of grafting density on phase transition behavior for poly(*N*-isopropylacryamide) brushes in aqueous solutions studied by AFM and QCM-D. Macromolecules 43:7269–7276

Ishida N, Kobayashi M (2006) Interaction forces measured between poly(*N*-isopropylacrylamide) grafted surface and hydrophobic particle. J Colloid Interface Sci 297:513–519

Islam M, Serpe MJ (2014) Poly(*N*-isopropylacrylamide) microgel-based thin film actuators for humidity sensing. RSC Adv 4:31937–31940

Ito A, Kuga Y, Honda H, Kikkawa H, Horiuchi A, Watanabe Y, Kobayashi T (2004) Magnetite nanoparticle-loaded anti-HER2 immunoliposomes for combination of antibody therapy with hyperthermia. Cancer Lett 212:167–175

Iwata H, Oodate M, Uyama Y, Amemiya H, Ikeda Y (1991) Preparation of temperature-sensitive membranes by graft polymerization onto a porous membrane. J Membr Sci 55:119–130

Iwata T, Yamato M, Tsuchioka H, Takagi R, Mukobata S, Washio K, Okano T, Ishikawa I (2009) Periodontal regeneration with multi-layered periodontal ligament-derived cell sheets in a canine model. Biomaterials 30:2716–2723

Jakubowski W, Matyjaszewski K (2005) Activator generated by electron transfer for atom transfer radical polymerization. Macromolecules 38:4139–4146

Jhon YK, Bhat RR, Jeong C, Rojas OJ, Szleifer I, Genzer J (2006) Salt-induced depression of lower critical solution temperature in a surface-grafted neutral thermoresponsive polymer. Macromol Rapid Commun 27:697–701

Jiang X, Lavender C, Woodcock J, Zhao B (2008) Multiple micellization and dissociation transitions of thermo- and light-sensitive poly(ethylene oxide)-*b*-poly(ethoxytri(ethylene glycol) acrylate-*co*-*o*-nitrobenzyl acrylate) in water. Macromolecules 41:2632–2643

Johnson CH, Moad G, Solomon DH, Spurling TH, Vearing DJ (1990) The application of supercomputers in modeling chemical reaction kinetics: kinetic simulation of ‘quasi-living’ radical polymerization. Aust J Chem 43:1215–1230

Jonas AM, Glinel K, Oren R, Nysten B, Huck WTS (2007) Thermo-responsive polymer brushes with tunable collapse temperatures in the physiological range. Macromolecules 40:4403–4405

Kalajahi MS, Asl VH, Sadabad FB, Razin SR, Mamaqani HR (2011) Properties of PMMA/carbon nanotubes nanocomposites prepared by “grafting through” method. Polym Compos 33:215–224

Kamigaito M, Ando T, Sawamoto M (2004) Metal-catalyzed living radical polymerization. Chem Rev 4:3689–3746

Kato M, Kamigaito M, Sawamoto M, Higshimura T (1995) Polymerization of methyl methacrylate with the carbon tetrachloride/dichlorotris-(triphenylphosphine) ruthenium(II)/methylaluminum bis(2,6-di-*tert*-butylphenoxide) initiating system: possibility of living radical polymerization. Macromolecules 28:1721–1723

Katsumoto Y, Tanaka T, Sato H, Ozaki Y (2002) Conformational change of poly(*N*-isopropylacrylamide) during the coil-globule transition investigated by attenuated total reflection/infrared spectroscopy and density functional theory calculation. J Phys Chem A 106:3429–3435

Kaufman CL, Williams M, Ryle LM, Smith TL, Tanner M, Ho C (2003) Superparamagnetic iron oxide particles transactivator protein-fluorescein isothiocyanate particle labeling for in vivo magnetic resonance imaging detection of cell migration: uptake and durability. Transplantation 76:1043–1046

Kessler D, Jochum FD, Choi J, Char K, Theato P (2011) Reactive surface coatings based on polysilsesquioxanes: universal method toward light-responsive surfaces. ACS Appl Mater Interfaces 3:124–128

Kidoaki S, Ohya S, Nakayama Y, Matsuda T (2001) Thermoresponsive structural change of a poly(*N*-isopropylacrylamide) graft layer measured with an atomic force microscope. Langmuir 17:2402–2407

Kingshott P, Thissen H, Griesser HJ (2002) Effects of cloud-point grafting, chain length, and density of PEG layers on competitive adsorption of ocular proteins. Biomaterials 23:2043–2056

Kizhakkedathua JN, Kumara KR, Goodman D, Brooks DE (2004) Synthesis and characterization of well-defined hydrophilic block copolymer brushes by aqueous ATRP. Polymer 45:7471–7489

Klajn R (2014) Spiropyran-based dynamic materials. Chem Soc Rev 43:148–184

Koh AYC, Saunders BR (2005) Small-angle neutron scattering study of temperature-induced emulsion gelation: the role of sticky microgel particles. Langmuir 21:6734–6741

Kohler N, Fryxell GE, Zhang M (2004) A bifunctional poly(ethylene glycol) silane immobilized on metallic oxide-based nanoparticles for conjugation with cell targeting agents. J Am Chem Soc 126:7206–7211

Kohler N, Sun C, Wang J, Zhang M (2005) Methotrexate-modified superparamagnetic nanoparticles and their intracellular uptake into human cancer cells. Langmuir 21:8858–8864

Kolb HC, Finn MG, Sharpless KB (2001) Click chemistry: diverse chemical function from a few good reactions. Angew Chem Int Ed 40:2004–2021

Kou R, Zhang J, Wang T, Liu G (2015) Interactions between polyelectrolyte brushes and hofmeister ions: Chaotropes versus kosmotropes. Langmuir 31:10461–10468

Kresge CT, Leonowicz ME, Roth WJ, Vartuli JC, Beck JS (1992) Ordered mesoporous molecular sieves synthesized by a liquid-crystal template mechanism. Nature 359:710–712

Kroft LJ, de Roos A (1999) Blood pool contrast agents for cardiovascular MR imaging. J Magn Reson Imaging 10:395–403

Kwak Y, Goto A, Tsujii Y, Muata Y, Komatsu K, Fukuda T (2002) A kinetic study on the rate retardation in radical polymerization of styrene with addition-fragmentation chain transfer. Macromolecules 35:3026–3029

Lai J, Mu X, Xu Y, Wu X, Wu C, Li C, Chen J, Zhao Y (2010) Light-responsive nanogated ensemble based on polymer grafted mesoporous silica hybrid nanoparticles. Chem Commun 46:7370–7372

Laible R, Hamann K (1980) Formation of chemically bound polymer layers on oxide surfaces and their role in colloidal stability. Adv Colloid Interf Sci 13:65–99

Laroussi M, Akan T (2007) Arc-free atmospheric pressure cold plasma jets: a review. Plasma Process Polym 4:777–788

Lauw Y, Horne MD, Rodopoulos T, Lockett V, Akgun B, Hamilton WA, Nelson ARJ (2012) Structure of [C4mpyr][NTf2] room-temperature ionic liquid at charged gold interfaces. Langmuir 28:7374–7381

Lee AS, Gast AP, Bütün V, Armes SP (1999) Characterizing the structure of pH dependent polyelectrolyte block copolymer micelles. Macromolecules 32:4302–4310

Lee H, Lee E, Kim DK, Jang NK, Jeong YY, Jon S (2006) Antibiofouling polymer-coated superparamagnetic iron oxide nanoparticles as potential magnetic resonance contrast agents for in vivo cancer imaging. J Am Chem Soc 128:7383–7389

Léger L, Creton C (2008) Adhesion mechanisms at soft polymer interfaces. Philos Trans R Soc 366:1425–1442

Lego B, Skene WG, Giasson S (2010) Swelling study of responsive polyelectrolyte brushes grafted from mica substrates: effect of pH, salt, and grafting density. Macromolecules 43:4384–4393

Lei H, Wang M, Tang Z, Luan Y, Liu W, Song B, Chen H (2014) Control of lysozyme adsorption by pH on surfaces modified with polyampholyte brushes. Langmuir 30:501–508

Lentacker I, De Geest BG, Vandenbroucke RE, Peeters L, Demeester J, De Smedt SC, Sanders NN (2006) Ultrasound-responsive polymer-coated microbubbles that bind and protect DNA. Langmuir 22:7273–7278

Li J, Chen XR, Chang YC (2005) Preparation of end-grafted polymer brushes by nitroxide-mediated free radical polymerization of vaporized vinyl monomers. Langmuir 21:9562–9567

Li D, Jones GL, Dunlap JR, Hua F, Zhao B (2006) Thermosensitive hairy hybrid nanoparticles synthesized by surface-initiated atom transfer radical polymerization. Langmuir 22:3344–3351

Li DX, He Q, Cui Y, Wang KW, Zhang XM, Li JB (2007a) Thermosensitive copolymer networks modify gold nanoparticles for nanocomposite entrapment. Chem Eur J 13:2224–2229

Li DX, Cui Y, Wang KW, He Q, Yan XH, Li JB (2007b) Thermosensitive nanostructures comprising gold nanoparticles grafted with block copolymers. Adv Funct Mater 17:3134–3140

Li D, He Q, Yang Y, Möhwald H, Li J (2008a) Two-stage pH response of poly(4-vinylpyridine) grafted gold nanoparticles. Macromolecules 41:7254–7256

Li DJ, Dunlap JR, Zhao B (2008b) Thermosensitive water-dispersible hairy particle-supported Pd nanoparticles for catalysis of hydrogenation in an aqueous/organic biphasic system. Langmuir 24:5911–5918

Liang L, Rieke PC, Liu J, Fryxell GE, Young JS, Engelhard MH, Alford KL (2000) Surfaces with reversible hydrophilic/hydrophobic characteristics on cross-linked poly(*N*-isopropylacrylamide) hydrogels. Langmuir 16:8016–8023

Liu S, Armes SP (2002) Polymeric surfactants for the new millennium: a pH-responsive, zwitterionic, schizophrenic diblock copolymer. Angew Chem Int Ed 41:1413–1416

Liu F, Urban MW (2010) Recent advances and challenges in designing stimuli-responsive polymers. Prog Polym Sci 35:3–23

Lu Y, Zhuk A, Xu L, Liang X, Kharlampieva E, Sukhishvili SA (2013) Tunable pH and temperature response of weak polyelectrolyte brushes: role of hydrogen bonding and monomer hydrophobicity. Soft Matter 9:5464–5472

Ma QG, Wooley KL (2000) The preparation of t-butyl acrylate, methyl acrylate, and styrene block copolymers by atom transfer radical polymerization: precursors to amphiphilic and hydrophilic block copolymers and conversion to complex nanostructured materials. J Polym Sci Polym Chem 38:4805–4820

Ma QG, Remsen EE, Kowalewski T, Wooley KL (2001) Two-dimensional, shell-cross-linked nanoparticle arrays. J Am Chem Soc 123:4627–4628

Martina MS, Fortin JP, Menager C, Clement O, Barratt G, Grabielle-Madelmont C, Gazeau F, Cabuil V, Lesieur S (2005) Generation of superparamagnetic liposomes revealed as highly efficient MRI contrast agents for in vivo imaging. J Am Chem Soc 127:10676–10685

Matsuda T, Ohya S (2005) Photoiniferter-based thermoresponsive graft architecture with albumin covalently fixed at growing graft chain end. Langmuir 21:9660–9665

Matyjaszewski K (2012) Atom transfer radical polymerization (ATRP): current status and future perspectives. Macromolecules 45:4015–4039

Matyjaszewski K, Xia J (2001) Atom transfer radical polymerization. Chem Rev 101:2921–2990

Meister A, Bastrop M, Koschoreck S, Garamus VM, Sinemus T, Hempel G, Drescher S, Dobner B, Richtering W, Huber K, Blume A (2007) Structure-property relationship in stimulus-responsive bolaamphiphile hydrogels. Langmuir 23:7715–7723

Memon IA, Sawa Y, Fukushima N, Matsumiya G, Miyagawa S, Taketani S, Sakakida SK, Kondoh H, Aleshin AN, Shimizu T, Okano T, Matsuda H (2005) Repair of impaired myocardium by means of implantation of engineered autologous myoblast sheets. J Thorac Cardiovasc Surg 130:1333–1341

Mendes PM (2008) Stimuli-responsive surfaces for bio-applications. Chem Soc Rev 37:2512–2529

Minko S, Patil S, Datsyuk V, Simon F, Eichhorn KJ, Motornov M, Usov D, Tokarev I, Stamm M (2002) Synthesis of adaptive polymer brushes via “grafting to” approach from melt. Langmuir 18:289–296

Miyamae T, Akiyama H, Yoshida M, Tamaoki N (2007) Characterization of poly(*N*-isopropylacrylamide)-grafted interfaces with sum-frequency generation spectroscopy. Macromolecules 40:4601–4606

Mizutani A, Kikuchi A, Yamato M, Kanazawa H, Okano T (2008) Preparation of thermoresponsive polymer brush surfaces and their interaction with cells. Biomaterials 29:2073–2081

Moglianetti M, Webster JR, Edmondson S, Armes SP, Titmuss S (2010) Neutron reflectivity study of the structure of pH-responsive polymer brushes grown from a macroinitiator at the sapphire−water interface. Langmuir 26:12684–12689

Möller M, Matyjaszewski K (eds) (2012) Polymer science: a comprehensive reference. Elsevier, Amsterdam

Murdoch TJ, Willott JD, de Vos WM, Nelson A, Prescott SW, Wanless EJ, Webber GB (2016a) Influence of anion hydrophilicity on the conformation of a hydrophobic weak polyelectrolyte brush. Macromolecules 49:9605–9617

Murdoch TJ, Humphreys BA, Willott JD, Gregory KP, Prescott SW, Nelson A, Wanless EJ, Webber GB (2016b) Specific anion effects on the internal structure of a poly(*N*-isopropylacrylamide) brush. Macromolecules 49:6050–6060

Murdoch TJ, Humphreys BA, Willott JD, Prescott SW, Nelson A, Webber GB, Wanless EJ (2017) Enhanced specific ion effects in ethylene glycol-based thermoresponsive polymer brushes. J Colloid Interface Sci 490:869–878

Murphy M, Tso WW, Tanzini M, Sitti M (2006) Waalbot: an agile small-scale wall climbing robot utilizing pressure sensitive adhesives. Proc Int Conf Intell Robots Syst:3411–3416

Murthy KS, Ma QG, Remsen EE, Kowalewski T, Wooley KL (2003) Thermal shaping of shell-crosslinked (SCK) nanoparticles, facilitated by nanoconfinement of fluid-like cores. J Mater Chem 13:2785–2795

Nagase K, Kobayashi J, Kikuchi A, Akiyama Y, Kanazawa H, Okano T (2007) Interfacial property modulation of thermoresponsive polymer brush surfaces and their interaction with biomolecules. Langmuir 23:9409–9415

Nagase K, Kobayashi J, Kikuchi AI, Akiyama Y, Kanazawa H, Okano T (2008a) Effects of graft densities and chain lengths on separation of bioactive compounds by nanolayered thermoresponsive polymer brush surfaces. Langmuir 24:511–517

Nagase K, Kobayashi J, Kikuchi A, Akiyama Y, Kanazawa H, Okano T (2008b) Preparation of thermoresponsive cationic copolymer brush surfaces and application of the surface to separation of biomolecules. Biomacromolecules 9:1340–1347

Nagase K, Watanabe M, Kikuchi A, Yamato M, Okano T (2011) Thermo-responsive polymer brushes as intelligent biointerfaces: preparation via ATRP and characterization. Macromol Biosci 11:400–409

Nakai K, Fujii S, Nakamura Y, Yusa S (2013) Ultraviolet-light-responsive Liquid Marbles. Chem Lett 42:586–588

Nash ME, Healy D, Carroll WM, Elvira C, Rochev YA (2012) Cell and cell sheet recovery from pNIPAm coatings; motivation and history to present day approaches. J Mater Chem 22:19376–19389

Nishida K, Yamato M, Hayashida Y, Watanabe K, Maeda N, Watanabe H, Yamamoto K, Nagai S, Kikuchi A, Tano Y, Okano T (2004) Functional bioengineered corneal epithelial sheet grafts from corneal stem cells expanded ex vivo on a temperature-responsive cell culture surface. Transplantation 77:379–385

Nordgren N, Rutland MW (2009) Tunable nanolubrication between dual-responsive polyionic grafts. Nano Lett 9:2984–2990

Oh JK, Kim K, Matyjaszewski K (2006) Preparation of poly(oligo(ethylene glycol) monomethyl ether methacrylate) by homogeneous aqueous AGET ATRP. Macromolecules 39:3161–3167

Ohki T, Yamato M, Murakami D, Takagi R, Yang J, Namiki H, Okano T, Takasaki K (2006) Treatment of oesophageal ulcerations using endoscopic transplantation of tissue-engineered autologous oral mucosal epithelial cellsheets in a canine model. Gut 55:1704–1710

Ohno K, Koh K, Tsujii Y, Fukuda T (2003) Fabrication of ordered arrays of gold nanoparticles coated with high-density polymer brushes. Angew Chem Int Ed 42:2751–2754

Ohno K, Akashi T, Huang Y, Tsujii Y (2010) Surface-initiated living radical polymerization from narrowly size-distributed silica nanoparticles of diameters less than 100 nm. Macromolecules 43:8805–8812

Okabe S, Seno K-I, Kanaoka S, Aoshima S, Shibayama M (2006) Micellization study on block and gradient copolymer aqueous solutions by DLS and SANS. Macromolecules 39:1592–1597

Okano T, Yamada N, Okuhara M, Sakai H, Sakurai Y (1995) Mechanism of cell detachment from temperature-modulated, hydrophilic-hydrophobic polymer surfaces. Biomaterials 16:297–303

Pan YV, Wesley RA, Luginbuhl R, Denton DD, Ratner BD (2001) Plasma polymerized *N*-isopropylacrylamide: synthesis and characterization of a smart thermally responsive coating. Biomacromolecules 2:32–36

Pasparakis G, Vamvakaki M (2011) Multiresponsive polymers: nano-sized assemblies, stimuli-sensitive gels and smart surfaces. Polym Chem 2:1234–1248

Patel NG, Cavicchia JP, Zhang G, Zhang Newby BM (2012) Rapid cell sheet detachment using spin-coated pNIPAAm films retained on surfaces by an aminopropyltriethoxysilane network. Acta Biomater 8:2559–2567

Paven M, Mayama H, Sekido T, Butt H-J, Nakamura Y, Fujii S (2016) Light-driven delivery and release of materials using liquid marbles. Adv Funct Mater 26:3199–3206

Pelton RH, Chibante P (1986) Preparation of aqueous latices with *N*-isopropylacrylamide. Colloids Surf 20:247–256

Piech M, Bell NS (2006) Controlled synthesis of photochromic polymer brushes by atom transfer radical polymerization. Macromolecules 39:915–922

Plunkett KN, Zhu X, Moore JS, Leckband DE (2006) PNIPAM chain collapse depends on the molecular weight and grafting density. Langmuir 22:4259–4266

Popa AM, Angeloni S, Bürgi T, Hubbell JA, Heinzelmann H, Pugin R (2010) Dynamic perspective on the function of thermoresponsive nanopores from in situ AFM and ATR-IR investigations. Langmuir 26:15356–15365

Pyun J, Kowalewski T, Matyjaszewski K (2003) Synthesis of polymer brushes using atom transfer radical polymerization. Macromol Rapid Commun 24:1043–1059

Radu DR, Lai CY, Wiench JW, Pruski M, Lin VSY (2004) Gatekeeping layer effect: a poly(lactic acid)-coated mesoporous silica nanosphere-based fluorescence probe for detection of amino-containing neurotransmitters. J Am Chem Soc 126:1640–1641

Rahane SB, Floyd JA, Metters AT, Kilbey SMII (2008) Swelling behavior of multiresponsive poly(methacrylic acid)-*block*-poly(*N*-isopropylacrylamide) brushes synthesized using surface-initiated photoiniferter-mediated photopolymerization. Adv Funct Mater 18:1232–1240

Raula J, Shan J, Nuopponen M, Niskanen A, Jiang H, Kauppinen EI, Tenhu H (2003) Synthesis of gold nanoparticles grafted with a thermoresponsive polymer by surface-induced reversible-addition-fragmentation chain-transfer polymerization. Langmuir 19:3499–3504

Rayatpisheh S, Li P, Chan-Park MB (2012) Argon-plasmainduced ultrathin thermal grafting of thermoresponsive pNIPAm coating for contractile patterned human SMC sheet engineering. Macromol Biosci 12:937–945

Richert L, Lavalle P, Vautier D, Senger B, Stoltz J-F, Schaaf P, Voegel J-C, Picart C (2002) Cell interactions with polyelectrolyte multilayer films. Biomacromolecules 3:1170–1178

Rizzardo E (1987) Living free radical polymerization. Chem Aust 54:32

Rogers WJ, Basu P (2005) Factors regulating macrophage endocytosis of nanoparticles: implications for targeted magnetic resonance plaque imaging. Atherosclerosis 178:67–73

Rosario R, Gust D, Hayes M, Jahnke F, Springer J, Garcia AA (2002) Photon-modulated wettability changes on spiropyran-coated surfaces. Langmuir 18:8062–8069

Sakai K, Smith EG, Webber GB, Schatz C, Wanless EJ, Bütün V, Armes SP, Biggs S (2006a) Comparison of the adsorption of cationic diblock copolymer micelles from aqueous solution onto mica and silica. Langmuir 22:5328–5333

Sakai K, Smith EG, Webber GB, Baker M, Wanless EJ, Bütün V, Armes SP, Biggs S (2006b) Characterizing the pH-responsive behavior of thin films of diblock copolymer micelles at the silica/aqueous solution interface. Langmuir 22:8435–8442

Sakai K, Smith EG, Webber GB, Baker M, Wanless EJ, Bütün V, Armes SP, Biggs S (2007) pH-responsive behavior of selectively quaternized diblock copolymers adsorbed at the silica/aqueous solution interface. J Colloid Interface Sci 314:381–388

Samanta S, Locklin J (2008) Formation of photochromic spiropyran polymer brushes via surface-initiated, ring-opening metathesis polymerization: reversible photocontrol of wetting behavior and solvent dependent morphology changes. Langmuir 24:9558–9565

Sanjuan S, Perrin P, Pantoustier N, Tran Y (2007) Synthesis and swelling behavior of pH-responsive polybase brushes. Langmuir 23:5769–5778

Saragi TPI, Spehr T, Siebert A, Fuhrmann-Lieker T, Salbeck J (2007) Spiro compounds for organic optoelectronics. Chem Rev 107:1011–1065

Sarsabili M, Parvini M, Kalajahi MS, Anzabi PG (2013) In situ reversible addition-fragmentation chain transfer polymerization of styrene in the presence of MCM-41 nanoparticles: comparing "grafting from" and "grafting through" approaches. Adv Polym Technol 32:21372

Satas D (1989) Handbook of pressure sensitive adhesives, 3rd edn. Van Nostrand Reinhold, New York

Schatz C, Smith EG, Armes SP, Wanless EJ (2008) Reversible pH-triggered encapsulation and release of pyrene by adsorbed block copolymer micelles. Langmuir 24:8325–8331

Schwartz E, Lim E, Gowda CM, Liscio A, Fenwick O, Tu G, Palermo V, de Gelder R, Cornelissen JJLM, Van Eck ERH, Kentgens APM, Cacialli F, Nolte RJM, Samorì P, Huck WTS Rowan AE

(2010) Synthesis, characterization, and surface initiated polymerization of carbazole functionalized isocyanides. Chem Mater 22:2597–2607

Seino M, Yokomachi K, Hayakawa T, Kikuchi R, Kakimoto MA, Horiuchi S (2006) Preparation of poly(*N*-isopropylacrylamide) grafted silica bead using hyperbranched polysiloxysilane as polymer brush and application to temperature-responsive HPLC. Polymer 47:1946–1952

Serpe MJ, Jones CD, Lyon LA (2003) Layer-by-layer deposition of thermoresponsive microgel thin films. Langmuir 19:8759–8764

Serpe MJ, Kim J, Lyon LA (2004) Colloidal hydrogel microlenses. Adv Mater 16:184–187

Serpe MJ, Yarmey KA, Nolan CM, Lyon LA (2005) Doxorubicin uptake and release from microgel thin films. Biomacromolecules 6:408–413

Shen YR (1989) Surface properties probed by second-harmonic and sum-frequency generation. Nature 337:519–525

Shen YR (1994) Surfaces probed by nonlinear optics. Surf Sci 299/300:551–562

Shimizu T, Sekine H, Isoi Y, Yamato M, Kikuchi A, Okano T (2006) Long-term survival and growth of pulsatile myocardial tissue grafts engineered by the layering of cardiomyocyte sheets. Tissue Eng 12:499–507

Shimoboji T, Ding ZL, Stayton SP, Hoffman AS (2002) Photoswitching of ligand association with a photoresponsive polymer-protein conjugate. Bioconjug Chem 13:915–919

Siewierski LM, Brittain WJ, Petrash S, Foster MD (1996) Photoresponsive monolayers containing in-chain azobenzene. Langmuir 12:5838–5844

Sobani M, Asl VH, Kalajahi NS, Mamaqani HR, Langari SAM, Khezri K (2013) “Grafting through” approach for synthesis of polystyrene/silica aerogel nanocomposites by in situ reversible addition fragmentation chain transfer polymerization. J Sol-Gel Sci Technol 66:337–344

Stein A, Melde BJ, Schroden RC (2000) Hybrid inorganic-organic mesoporous silicates-nanoscopic reactors coming of age. Adv Mater 12:1403–1419

Stevens MJ, Plimptom SJ (1998) The effect of added salt on polyelectrolyte structure. Eur Phys J B 2:341–345

Stieger M, Richtering W, Pedersen JS, Lindner P (2004) Small angle neutron scattering study of structural changes in temperature sensitive microgel colloids. J Chem Phys 120:6197–6206

Stratakis E, Mateescu A, Barberoglou M, Vamvakaki M, Fotakis C, Anastasiadis SH (2012) From superhydrophobicity and water repellency to superhydrophilicity: smart polymer-functionalized surfaces. Chem Commun 46:4136–4138

Stuart MAC, Huck WTS, Genzer J, Muller M, Ober C, Stamm M, Sukhorukov GB, Szleifer I, Tsukruk VV, Urban M, Winnik F, Zauscher S, Luzinov I, Minko S (2010) Emerging applications of stimuli-responsive polymer materials. Nat Mater 9:101–113

Sugihara S, Hashimoto K, Okabe S, Shibayama M, Kanaoka S, Aoshima S (2004) Stimuli-responsive diblock copolymers by living cationic polymerization: precision synthesis and highly sensitive physical gelation. Macromolecules 37:336–343

Sun TL, Wang GJ, Feng L, Liu BQ, Ma YM, Jiang L, Zhu DB (2004) Reversible switching between superhydrophilicity and superhydrophobicity. Angew Chem Int Ed 43:357–360

Sun JT, Hong CY, Pan CY (2010) Fabrication of PDEAEMA-coated mesoporous silica nanoparticles and pH-responsive controlled release. J Phys Chem C 114:12481–12486

Tadjeddine A, Peremans A (1996) Vibrational spectroscopy of the electrochemical interface by visible infrared sum-frequency generation. Surf Sci 368:377–383

Tan HS, Pfister WR (1999) Pressure-sensitive adhesives for transdermal drug delivery systems. Pharm Sci Technol Today 2:60–69

Tanaka K, Kitamura N, Naka K, Chujo Y (2008) Multi-modal ^{19}F NMR probe using perfluorinated cubic silsesquioxane coated silica nanoparticles for monitoring enzymatic activity. Chem Commun:6176–6178

Tanaka K, Kitamura N, Chujo Y (2011) Bimodal quantitative monitoring for enzymatic activity with simultaneous signal increases in ^{19}F NMR and fluorescence using silica nanoparticle-based molecular probes. Bioconjug Chem 22:1484–1490

Tang T, Castelletto V, Parras P, Hamley IW, King SM, Roy D, Perrier S, Hoogenboom R, Schubert US (2006) Thermo-responsive poly(methyl methacrylate)-*block*-poly(*N*-isopropylacrylamide) block copolymers synthesized by RAFT polymerization: Micellization and gelation. Macromol Chem Phys 207:1718–1726

Tang X, Tang S, Sivan V, Zhang W, Mitchell A, Kalantar-Zadeh K, Khoshmanesh K (2013) Photochemically induced motion of liquid metal marbles. Appl Phys Lett 103:174104-1–174104-4

Taylor W, Jones RAL (2010) Producing high-density highmolecular-weight polymer brushes by a "grafting to" method from a concentrated homopolymer solution. Langmuir 26:13954–13958

Taylor W, Jones RAL (2013) Protein adsorption on wellcharacterized polyethylene oxide brushes on gold: dependence on molecular weight and grafting density. Langmuir 29:6116–6122

Tekin H, Sanchez JG, Tsinman T, Langer R, Khademhosseini A (2011) Thermoresponsive platforms for tissue engineering and regenerative medicine. AICHE J 57:3249–3258

Thompson KL, Fielding LA, Mykhaylyk OO, Lane JA, Derry MJ, Armes SP (2015) Vermicious thermo-responsive Pickering emulsifiers. Chem Sci 6:4207–4214

Tomlinson MR, Cousin F, Geoghegan M (2009) Creation of dense polymer brush layers by the controlled deposition of an amphiphilic responsive comb polymer. Polymer 50:4829–4836

Toyama M, Ito T, Nukatsuka H, Ikeda M (1973) Studies on tack of pressure-sensitive adhesive tapes: on the relationship between pressure-sensitive adhesion and surface energy of adherends. J Appl Polym Sci 17:3495–3502

Treat ND, Ayres N, Boyes SG, Brittain WJ (2006) A facile route to poly(acrylic acid) brushes using atom transfer radical polymerization. Macromolecules 39:26–29

Tsarevski NV, Sumerlin BS (eds) (2013) Fundamentals of controlled/living radical polymerization. Royal Society of Chemistry, London

Tsujii Y, Ohno K, Yamamoto S, Goto A, Fukuda T (2006) Structure and properties of high-density polymer brushes prepared by surface-initiated living radical polymerization. Adv Polym Sci 197:1–45

Urban MW (ed) (2011) Handbook of stimuli-responsive materials. Wiley-VCH, Weinheim

Vogel V (1996) What do nonlinear optical techniques have to offer the biosciences? Curr Opin Colloid Interface Sci 1:257–263

von Recum HA, Okano T, Kim SW, Bernstein PS (1999) Maintenance of retinoid metabolism in human retinal pigment epithelium cell culture. Exp Eye Res 69:97–107

Wang JS, Matyjaszewski K (1995) Controlled/"living" radical polymerization. Halogen atom transfer radical polymerization promoted by a cu(I)/cu(II) redox process. Macromolecules 28:7901–7910

Wang T, Lei CH, Dalton AB, Creton C, Lin Y, Sun YP, Fernando KAS, Manea M, Asua JM, Keddie JL (2006) Waterborne, nanocomposite pressure-sensitive adhesives with high tack energy, optical transparency, and electrical conductivity. Adv Mater 18:2730–2734

Wang X, Xiao X, Wang X, Zhou J, Li L, Xu J (2007) Reversibly switchable double-responsive block copolymer brushes. Macromol Rapid Commun 28:828–833

Wang T, Long Y, Liu L, Wang X, Craig VSJ, Zhang G, Liu G (2014) Cation-specific conformational behavior of polyelectrolyte brushes: from aqueous to nonaqueous solvent. Langmuir 30:12850–12859

Webber GB, Wanless EJ, Bütün V, Armes SP, Biggs S (2002) Self-organized monolayer films of stimulus-responsive micelles. Nano Lett 2:1307–1313

Webber GB, Wanless EJ, Armes SP, Tang Y, Li Y, Biggs S (2004) Nano-anemones: stimulus-responsive copolymer-micelle surfaces. Adv Mater 16:1794–1798

Webber GB, Wanless EJ, Armes SP, Biggs S (2005a) Tunable diblock copolymer micelles–adapting behavior via subtle chemical modifications. Faraday Discuss 128:193–209

Webber GB, Wanless EJ, Armes SP, Biggs S (2005b) Tunable diblock copolymer micelles–adapting behaviour *via* subtle chemical modifications. Faraday Discuss 128:193–209

Wei QS, Ji J, Shen JC (2008) Synthesis of near-infrared responsive gold nanorod/PNIPAAm core/shell nanohybrids via surface initiated ATRP for smart drug delivery. Macromol Rapid Commun 29:645–650

Wei Y, Gao D, Li L, Shang S (2011) Memory effect in polymer brushes containing pendent carbazole groups. Polymer 52:1385–1390

Wei Q, Cai M, Zhou F, Liu W (2013) Dramatically tuning friction using responsive polyelectrolyte brushes. Macromolecules 46:9368–9379

Willott JD, Humphreys BA, Murdoch TJ, Edmondson S, Webber GB, Wanless EJ (2015a) Hydrophobic effects within the dynamic pH-response of polybasic tertiary amine methacrylate brushes. Phys Chem Chem Phys 17:3880–3890

Willott JD, Murdoch TJ, Humphreys BA, Edmondson S, Webber GB, Wanless EJ (2015b) Anion-specific effects on the behavior of pH-sensitive polybasic brushes. Langmuir 31:3707–3717

Wilson MD, Whitesides GM (1988) The anthranilate amide of "polyethylene carboxylic acid" shows an exceptionally large change with pH in its wettability by water. J Am Chem Soc 110:8718–8719

Woods DA, Bain CD (2014) Total internal reflection spectroscopy for studying soft matter. Soft Matter 10:1071–1096

Wu T, Gong P, Szleifer I, Vlček P, Šubr V, Genzer J (2007) Behavior of surface-anchored poly(acrylic acid) brushes with grafting density gradients on solid substrates: 1. Experiment. Macromolecules 40:8756–8764

Wu T, Zhang YF, Wang XF, Liu SY (2008) Fabrication of hybrid silica nanoparticles densely grafted with thermoresponsive poly(*N*-isopropylacrylamide) brushes of controlled thickness via surface-initiated atom transfer radical polymerization. Chem Mater 20:101–109

Wu B, Wang X, Yang J, Hua Z, Tian K, Kou R, Zhang J, Ye S, Luo Y, Craig VSJ, Zhang G, Liu G (2016) Reorganization of hydrogen bond network makes strong polyelectrolyte brushes pH-responsive. Sci Adv 2:e1600579

Wuelfing WP, Gross SM, Miles DT, Murray RW (1998) Nanometer gold clusters protected by surface-bound monolayers of thiolated poly(ethylene glycol) polymer electrolyte. J Am Chem Soc 120:12696–12697

Xia F, Feng L, Wang S, Sun T, Song W, Jiang W, Jiang L (2006) Dual-responsive surfaces that switch between superhydrophilicity and superhydrophobicity. Adv Mater 18:432–436

Xu FJ, Zhong SP, Yung LYL, Tong YW, Kang ET, Neoh KG (2006) Thermoresponsive comb-shaped copolymer-Si (100) hybrids for accelerated temperature-dependent cell detachment. Biomaterials 27:1236–1245

Xu LQ, Wan D, Gong HF, Neoh KG, Kang ET, Fu GD (2010) One-pot preparation of ferrocene-functionalized polymer brushes on gold substrates by combined surface-initiated atom transfer radical polymerization and “click chemistry”. Langmuir 26:15376–15382

Yakushiji T, Sakai K, Kikuchi A, Aoyagi T, Sakurai Y, Okano T (1998) Graft architectural effects on thermoresponsive wettability changes of poly(*N*-isopropylacrylamide)-modified surfaces. Langmuir 14:4657–4662

Yamada N, Okano T, Sakai H, Karikusa F, Sawasaki Y, Sakurai Y (1990) Thermo-responsive polymeric surfaces; control of attachment and detachment of cultured cells. Makromol Chem Rapid Commun 11:571–576

Yamago S (2009) Precision polymer synthesis by degenerative transfer controlled/living radical polymerization using organotellurium, organostibine, and organobismuthine chain-transfer agents. Chem Rev 109:5051–5068

Yang Y, Yan X, Cui Y, He Q, Li D, Wang A, Fei J, Li JJ (2008) Preparation of polymer-coated mesoporous silica nanoparticles used for cellular imaging by a “graft-from” method. Mater Chem 18:5731–5737

Yang R, Peng S, Hughes TC (2014) Multistimuli responsive organogels based on a reactive azobenzene gelator. Soft Matter 10:2188–2196

Yenice Z, Schön S, Bildirir H, Genzer J, von Klitzing R (2015) Thermoresponsive PDMAEMA brushes: effect of gold nanoparticle deposition. J Phys Chem B 119:10348–10358

Yim H, Kent MS, Satija S, Mendez S, Balamurugan SS, Balamurugan S, Lopez GP (2004) Study of the conformational change of poly(*N*-isopropylacrylamide)-grafted chains in water with neutron reflection: molecular weight dependence at high grafting density. J Polym Sci B Polym Phys 42:3302–3310

Yim H, Kent MS, Mendez S, Lopez GP, Satija S, Seo Y (2006) Effects of grafting density and molecular weight on the temperature-dependent conformational change of poly(*N*-isopropylacrylamide) grafted chains in water. Macromolecules 39:3420–3426

Yoshida M, Lahann J (2008) Smart nanomaterials. ACS Nano 2:1101–1107

You YZ, Kalebaila KK, Brock SL, Oupicky D (2008) Temperature-controlled uptake and release in PNIPAM-modified porous silica nanoparticles. Chem Mater 20:3354–3359

Yow HN, Biggs S (2013) Probing the stability of sterically stabilized polystyrene particles by centrifugal sedimentation. Soft Matter 9:10031–10041

Yu AM, Wang YJ, Barlow E, Caruso F (2005) Mesoporous silica particles as templates for preparing enzyme loaded biocompatible microcapsules. Adv Mater 17:1737–1741

Yu Q, Li X, Zhang Y, Yuan L, Zhao T, Chen H (2011) The synergistic effects of stimuli-responsive polymers with nano-structured surfaces: wettability and protein adsorption. RSC Adv 1:262–269

Yuan W, Jiang G, Wang J, Wang G, Song Y, Jiang L (2006) Temperature/light dual-responsive surface with tunable wettability created by modification with an azobenzene-containing copolymer. Macromolecules 39:1300–1303

Yusa S, Fukuda K, Yamamoto T, Iwasaki Y, Watanabe A, Akiyoshi K, Morishima Y (2007) Salt effect on the heat-induced association behavior of gold nanoparticles coated with poly(*N*-isopropylacrylamide) prepared via reversible addition-fragmentation chain transfer (RAFT) radical polymerization. Langmuir 23:12842–12848

Zeiser M, Freudensprung I, Hellweg T (2012) Linearly thermoresponsive core-shell microgels: towards a new class of nanoactuators. Polymer 53:6096–6101

Zhang Q, Remsen EE, Wooley KL (2000) Shell cross-linked nanoparticles containing hydrolytically degradable, crystalline core domains. J Am Chem Soc 122:3642–3651

Zhang Q, Clark CG, Wang M, Remsen EE, Wooley KL (2002a) Thermally-induced (re)shaping of Core−Shell Nanocrystalline particles. Nano Lett 2:1051–1054

Zhang Y, Kohler N, Zhang M (2002b) Surface modification of superparamagnetic magnetite nanoparticles and their intracellular uptake. Biomaterials 23:1553–1561

Zhang MM, Liu L, Zhao HY, Yang Y, Fu GQ, He BL (2006) Double-responsive polymer brushes on the surface of colloid particles. J Colloid Interface Sci 301:85–91

Zhang Q, Xia F, Sun T, Song W, Zhao T, Liu M, Jiang L (2008) Wettability switching between high hydrophilicity at low pH and high hydrophobicity at high pH on surface based on pH-responsive polymer. Chem Commun:1199–1201

Zhang L, Cha D, Wang P (2012) Remotely controllable liquid marbles. Adv Mater 24:4756–4760

Zhang Z, Morse AJ, Armes SP, Lewis AL, Geoghegan M, Leggett GJ (2013) Nanoscale contact mechanics of biocompatible polyzwitterionic brushes. Langmuir 29:10684–10692

Zhang S, Vi T, Luo K, Koberstein JT (2016) Kinetics of polymer interfacial reactions: polymer brush formation by click reactions of alkyne end-functional polymers with azide-functional substrates. Macromolecules 49:5461–5474

Zhao B, Brittain WJ (2000) Polymer brushes: surface-immobilized macromolecules. Prog Polym Sci 25:677–710

Zhou Z, Zhu S, Zhang D (2007) Grafting of thermo-responsive polymer inside mesoporous silica with large pore size using ATRP and investigation of its use in drug release. J Mater Chem 17:2428–2433

Zhou YN, Li JJ, Zhang Q, Luo ZH (2014) Light-responsive smart surface with controllable wettability and excellent stability. Langmuir 30:12236–12242

Zhu YF, Shi JL, Shen WH, Dong XP, Feng JW, Ruan ML, Li YS (2005) Stimuli-responsive controlled drug release from a hollow mesoporous silica sphere/polyelectrolyte multilayer core-shell structure. Angew Chem Int Ed 44:5083–5087

Zosel A (1992) Chapter 4. In: Satas D (ed) Advances in pressure sensitive adhesive technology, vol 1. Satas & Associates, Warwick

Chapter 13
Liquid Manipulation

Daisuke Ishii

Abstract Liquid manipulation is very important for micro and nano fluidic devices and an intelligent bio interface. Micro droplet transfer on high adhesion superhydrophobic surfaces has been reported in recent years. By using the superhydrophobic metal–polymer co-existing surfaces possessing different adhesion properties, micro droplet transfer between superhydrophobic surfaces was achieved. Water micro droplets were transferred from a low-adhesion superhydrophobic surface to a middle-adhesion superhydrophobic surface via a high-adhesion superhydrophobic surface without any mass loss. Droplet after transferring possessed high water contact angle over 150°. These moving processes were performed repeatedly. These droplet handlings on the adhesion superhydrophobic surfaces will be expected for fluidic devises with energy saving.

Water transport was achieved by using open channel with liquid selectivity and design flexibility inspired by a coastal animal. The animal has pairs of legs on which open-air capillary structures uptake water spontaneously using interfacial free energy. After surface modifications, the artificial open channels were able to transport a variety of liquids against gravity by the synergetic effect of surface chemistry and structure, and the surface energy contrast induced by partial modifications let a certain liquid spread through on specific areas of the channel. In addition, these wetting properties and shapes of the liquid channels were found to be overwritten over multiple times with a set of surface modifications. These rewritable open channels with liquid selectivity are applicable to a wide variety of microstructure surfaces, opening the way for its application of reusable microfluidics and lab-on-a-chip devices.

Keywords Superhydrophobicity · Self-organization · Water adhesion · wettability · liquid spreading

---

D. Ishii (✉)
Department of Life Science and Applied Chemistry, Graduate School of Engineering,
Nagoya Institute of Technology, Nagoya, Aichi, Japan
e-mail: ishii.daisuke@nitech.ac.jp

A. Hozumi et al. (eds.), *Stimuli-Responsive Dewetting/Wetting Smart Surfaces and Interfaces*, Biologically-Inspired Systems 11,
https://doi.org/10.1007/978-3-319-92654-4_13

13.1 Droplet Transfer on High Adhesion Superhydrophobic Surfaces

Droplet manipulations mimicking behaviors on plant or insect surfaces such as lotus leaf effect (Barthlott and Neinhuis 1997; Neinhuis and Barthlott 1997) are now interesting because simple surface structures provide amazing functionalities. Superhydrophobic surfaces which have the water contact angle larger than or near 150° are much paid attention, since its good water repellent property is used various applications in coating and electronic technologies (Zhang et al. 2008). Many researchers have been reported to obtain strong water repellent surface such as a hydrophobic fractal surface (Onda et al. 1996) and a nanopin array surface (Hosono et al. 2005). Recently several reports were published about water droplet adhesion superhydrophobic surfaces mimicked by gecko's feet (Cho and Choi 2008) and rose petals (Feng et al. 2008). These adhesion properties were caused by van der Waals' force on large real surface area against small apparent surface area or nano-scaled rough surfaces in micro-scaled dimple structures. However, it was difficult to control these adhesion forces by reason of origin of the surface structures.

In first chapter, it is introduced to a superhydrophobic metal-polymer co-existing (MP) surface with different droplet adhesion properties. The adhesive superhydrophobic MP surfaces were composed of hydrophobic hexagonally polystyrene pillar arrays made from a self-organized honeycomb-patterned polystyrene film (Yabu et al. 2005) and hydrophilic metal-domes deposited by nickel electroless plating. Numeric density of the nickel dome that controls adhesion property on the superhydrophobic surface was adjusted by temperature of a catalytic Pd salt and cationic polymer mixture solution for electroless plating. Droplet manipulations such as a transfer and a separation were achieved by using the MP surface possessing different water adhesion force. Micro droplet handling by control of wettability is important for further understanding of superhydrophobic surfaces and application in microfluidic devices.

The MP surface composed of hydrophobic hexagonally polymer pillar arrays dotted with metal micro-domes was fabricated by electroless plating for honeycomb-patterned polymer films and peeling process (Fig. 13.1). According to the previous report (Karthaus et al. 2000), the honeycomb films were prepared by casting a chloroform solution of 10:1 mixture of polystyrene (**PS**; $M_w = 280{,}000\ \mathrm{g\ mol^{-1}}$) and synthesized amphiphilic copolymer (**CAP**; $M_w = 270{,}000\ \mathrm{g\ mol^{-1}}$) on a glass substrate with hexagonally condensed water droplet arrays. The honeycomb film was soaked in a catalytic mixture solution containing $0.010\ \mathrm{mol\ dm^{-3}}$ poly(allylamine hydrochloride) (**PAH**; $M_w = 15{,}000\ \mathrm{g\ mol^{-1}}$) and $0.010\ \mathrm{mol\ dm^{-3}}$ $PdCl_2$ at 25 °C. The catalytic solution was gradually heated to 30 C, 45 °C, and 60 °C, respectively, and kept for 10 min under horizontal shaking at 10 rpm. Treated honeycomb films were immersed in a nickel plating bath at 25 °C containing $0.10\ \mathrm{mol\ dm^{-3}}$ $Ni(H_2PO_2)_2 \cdot 6H_2O$, $0.19\ \mathrm{mol\ dm^{-3}}$ H_3BO_3, $0.030\ \mathrm{mol\ dm^{-3}}$ CH_3COONa and $0.0098\ \mathrm{mol\ dm^{-3}}$ $(NH_4)_2SO_4$ without any rinse and drying (Ishii et al. 2006). Then the plating bath including the treated honeycomb film was heated to 70 °C and kept for 2 h with no stirring. After several time rinses with distilled water at 50 °C and natural drying, a nickel layer

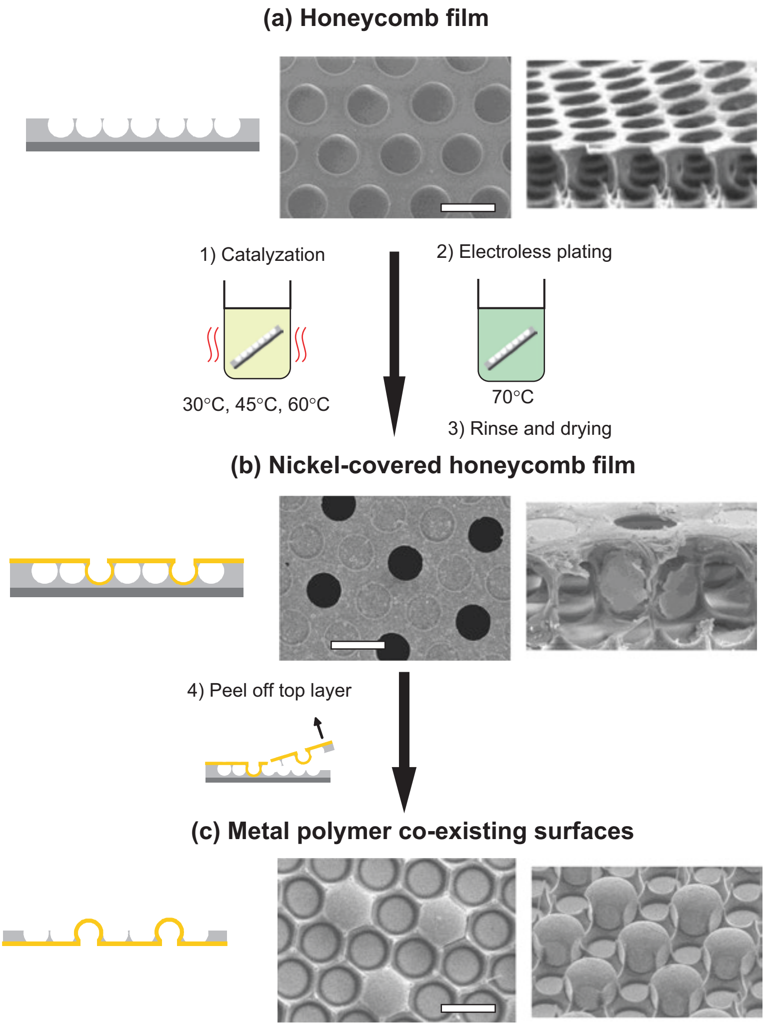

(a) Honeycomb film

(b) Nickel-covered honeycomb film

(c) Metal polymer co-existing surfaces

Fig. 13.1 Schematic illustrations of a preparation method of MP surfaces. SEM images of top (left) and tilt (right) views of (**a**) a honeycomb film, (**b**) a nickel-covered honeycomb film fabricated by immersion in the catalytic mixture solution at 45 °C, and (**c**) a MP surface fabricated by peeling off a top layer of the nickel-covered honeycomb film (Scale bar: 10 μm)

was covered on the honeycomb film. After electroless plating, metallic faces of the nickel-covered honeycomb films were adhered on an acryl substrate of 2.0 mm in a thickness by an epoxide resin adhesive (Araldite®). After heating at 70 °C for 2 h, a lower half layer of the nickel-covered honeycomb film was peeled off from the acryl substrate. A water contact angle (WCA) to 3 mg water droplet on a surface was measured by contact angle meter. A sliding angle (SA) was measured to tilt the surfaces with a micro-droplet of 5 mg. Density of the metal micro-dome was calculated by means of low-magnified SEM images.

SEM images of a honeycomb film, a nickel covered honeycomb film fabricated by immersion in the catalytic solution at 45 °C, and a MP surface fabricated by immersion in the catalytic solution at 45 °C are inserted in Fig. 13.1a. An average diameter of a honeycomb hole was about 7 μm. A nickel-covered honeycomb film possessing some pores, which were dotted in whole of the honeycomb film, were obtained after nickel electroless plating via the catalytic mixture solution immersion process. A tilted SEM image shown in a right column of Fig. 13.1b clears that the pores were openings of micro mono vessels. When the temperature of the catalytic mixture solution was changed low (30 °C) and high (60 °C), the quantity of the pores was decreasing and increasing, respectively. In general, wettability of almost surfaces including the PS honeycomb film is influenced by a solution temperature. Because the surface tension of all solutions is represented by function of the solution temperature. This result indicates that the quantity of the pores was dependent of wettability of the catalytic mixture solution to the honeycomb film. In the case of immersion in the catalytic solution at low temperature, wettability of the honeycomb film was low, so that the quantity of the pores of the nickel-covered honeycomb film was a few. On the other hand, in the case of immersion in the one at high temperature, the quantity of the pores was much because of good wettability to the honeycomb film. The quantity of the pore of the nickel-covered honeycomb film was easily changed by the catalytic mixture solution temperature. The MP surfaces after peel off the bottom half of the nickel-covered honeycomb film were composed of superhydrophobic PS pillar arrays dotted with hydrophilic nickel micro-domes as shown in Fig. 13.1c . The nickel micro-dome was a reverse side of the micro mono vessel in the nickel-covered honeycomb film. This result anticipates that density of the nickel dome to the honeycomb hole is controlled indirectly by the catalytic mixture solution temperature. Figure 13.2 shows SEM images of the MP surfaces having different density of the nickel dome. The nickel dome density of the MP

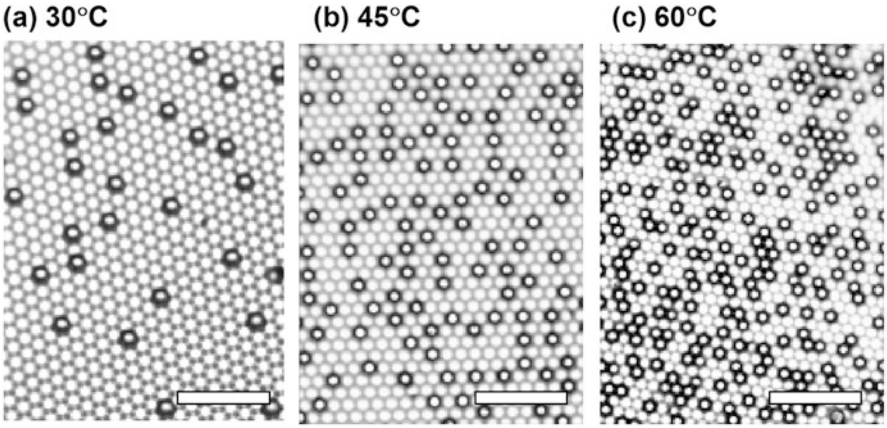

Fig. 13.2 SEM images of the superhydrophobic metal–polymer surfaces fabricated by using the catalytic mixture solution at (**a**) 30 °C, (**b**) 45 °C, and (**c**) 60 °C. The black dots indicate the nickel domes (Scale bar: 100 μm)

surface fabricated by using the catalytic mixture solution at 30 °C, 45 °C, and 60 °C was about 3%, 15%, and 25%, respectively. The difference of the nickel dome density was directly efficient to surface properties such as a surface wettability and an adhesion property because of change of balance between hydrophilicity and hydrophobicity.

A water droplet adhesion property was measured by a water contact angle (WCA) and a sliding angle (SA). The MP surface with nickel dome density of 3% possessed a WCA of 155° and a SA of fewer than 5°, and was abbreviated as a low-adhesion MP surface. The MP surface with dome density of 15% possessed a WCA of 150° and a SA of 30° (a middle-adhesion MP surface). The MP surface with dome density of 25% possessed a WCA of 145° and a not measured SA because the droplet adhered the surface when turned upside down (a high-adhesion MP surface). As the dome density was increasing, the WCA was decreasing and the SA was increasing, which means that the hydrophilic nickel domes gave the adhesion behaviors. This result made clear that the adhesion property was controlled by the quantity of the nickel dome easily changed by the catalytic mixture solution temperature for electroless plating.

Water micro droplet transfer was attempted by using the MP surfaces with different adhesion properties as shown in Fig. 13.3. A water droplet of 5 mg on the low-

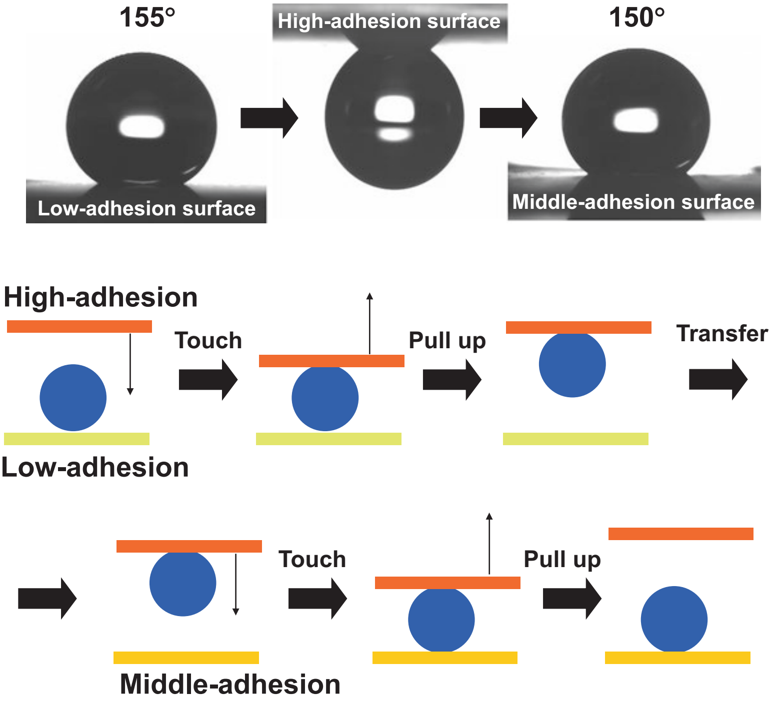

Fig. 13.3 Droplet transfer of 5.0-mg water droplet from the low-adhesion MP surface to the middle-adhesion MP surface via the high-adhesion MP surface and schematic model of a micro-droplet transfer by using the MP surfaces with different adhesion properties

adhesion MP surface was carried with the high-adhesion MP surface by means of pulling off after slight contact from above. However, in the case of the middle-adhesion MP surface, a water droplet did not remove from the low-adhesion MP surface. On the other hand, the high-adhesion MP surface was not caught a water droplet on the middle-adhesion MP surface from above. These results suggest that the adhesion force of the high-adhesion MP surface was stronger than that of the low-adhesion MP surface plus gravity on the water droplet, and weaker than that of the middle-adhesion MP surface plus gravity on the water droplet. By using this difference, the water droplet was transferred from the low-adhesion MP surface to the middle-adhesion MP surface via the high-adhesion MP surface. After transfer, the water droplet on the middle-adhesion MP surface was sliding when the surface was tilted at about 30°. A droplet transfer reported in the past is from a superhydrophobic surface to a hydrophilic surface via an adhesion superhydrophobic surface (Cho and Choi 2008). Therefore, after transfer, the water droplet is spreading, and is unable to be handled. The novel transfer method in this report remains a droplet shape after transfer, so that the droplet was handily manipulated again. These behaviors were useful to microfluidic devices, bio interfaces, and micro-reactors.

13.2 Droplet Sensing on High Adhesion Superhydrophobic Surfaces

Water droplet pinning on a novel superhydrophobic hybrid surface was controlled by a gradient structure of metal domes in polymer pillar arrays. The MP surface was fabricated by electroless plating and simple peeling of a self-organized honeycomb-patterned polymer film. The area number density of metal domes controlled water droplet adhesion on the superhydrophobic hybrid surface. The gradient in the number density of metal domes on the hybrid surface was formed by continuously changing the temperature of the solution during the plating process. The polystyrene-based honeycomb-patterned porous film (Fig. 13.1a) was set vertically in a vial containing 10 mL of an aqueous catalyst solution at 50 °C. Then, 40 mL of the catalyst solution at 25 °C was gradually added to the vial at 2.5 mL s^{-1}. Lastly, the honeycomb film was transferred from the catalyst solution to a plating bath (Fig. 13.4). The metal-coated honeycomb film was cleaved to reveal metal–polymer hybrid structures and a polymer pillar array. The metal deposited in the honeycomb holes constitutes the metal domes within the polymer nano-pillar array.

The area number density of metal domes on the hybrid surface was changed in accordance with the temperature of the catalyst solution. The temperature of the catalyst solution was gradually decreased from 50 °C to 30 °C by adding catalyst solution at 25 °C. The honeycomb films were highly wettable by the high-temperature solution because of its low surface tension. Once the honeycomb holes were wetted by the solution, the solution could not escape from the holes because of the high interfacial energy between the solution and the surface of the hole. A composite micrograph of the hybrid surface shows the gradient in the number density of

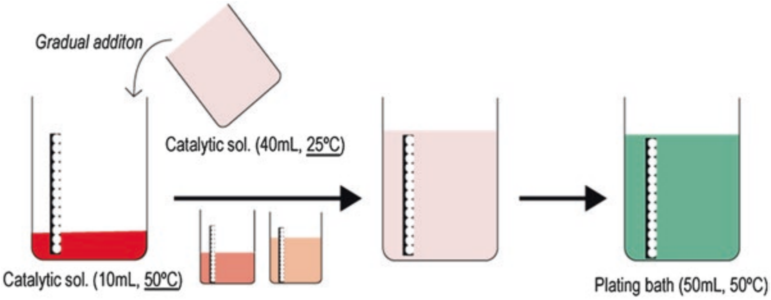

Fig. 13.4 Preparation method of the superhydrophobic metal–polymer hybrid surface having a gradient in the number density of metal domes by metallization process involving gradual temperature change of the aqueous catalyst solution

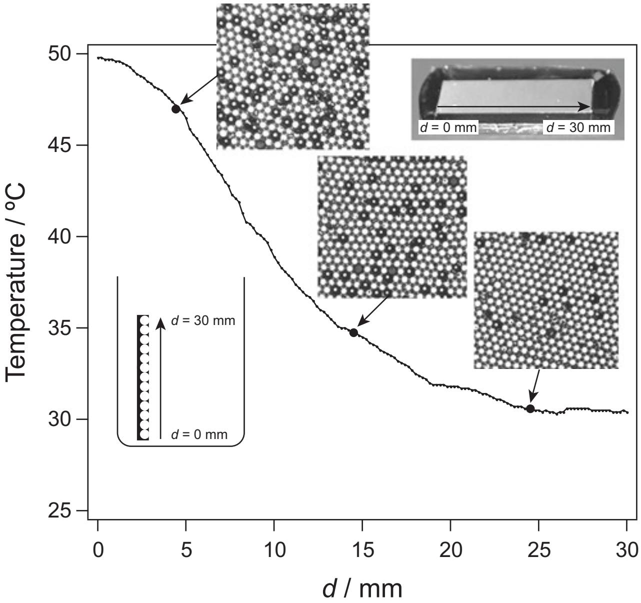

Fig. 13.5 Gradient in the areal number density of metal domes (*N*) of the superhydrophobic metal–polymer hybrid surface. Temperature change of the catalyst solution in the vial with vertical-fixed honeycomb film by gradual addition of 40 mL of catalyst solution at 25 °C at a rate of 2.5 mL s^{-1} into the initial 10 mL of catalyst solution at 50 °C. The position at $d = 30$ mm is the top of honeycomb-patterned porous film

metal domes (Fig. 13.5). Through the plating process, the substrate was modified such that the number density of metal domes (*N*) was low at the top ($d = 30$ mm) and high at the bottom ($d = 0$ mm). The relationships between contact angle and *N* at different positions (*d*) along the hybrid surface were investigated. As *d* increased from the top of substrate ($d = 30$ mm), *N* substantially decreased from about 3000 to 100 mm^{-2}. The contact angle of the hybrid surface slightly increased from 141°

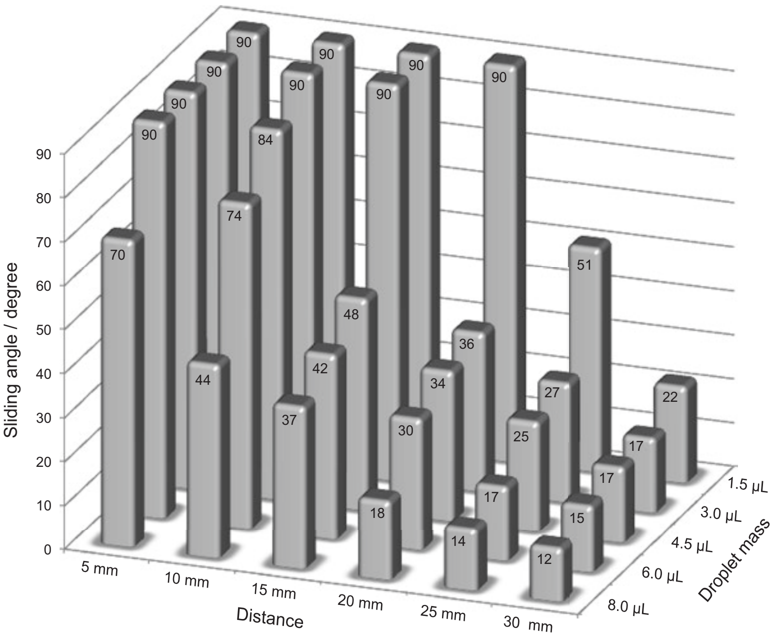

Fig. 13.6 Adhesive force gradient (AFG) of the superhydrophobic metal–polymer hybrid surface. Sliding angles of water droplets of various masses on the hybrid surface plotted versus position *d*. "Adhesion" indicates that the water droplet does not slide off the surface at a tilt angle greater than 90°

to 162° with increasing *d*. These results show that a gradient in the number density of metal domes was obtained by continuous changing the catalyst solution temperature, and the resulting hybrid surface remained highly hydrophobicity even where *N* was large.

The metal domes have good affinity for water, and thus affect the adhesion properties of water microdroplets on the hybrid surface. Sliding angle, which is a measure of the adhesion strength of a droplet, was investigated to elucidate the dependence of adhesion strength on position along the substrate. In Fig. 13.6, the sliding angles of water droplets of various masses are plotted versus position *d* along the hybrid surface having a gradient in the number density of metal domes. Sliding angle decreased with decreasing *d* for a given water droplet mass, but increased with decreasing water droplet mass for a given *d*. Notably, a small water droplet situated at a position with high *N* adhered to the surface when the substrate was turned upside down; in other words, the adhesive force was greater than the gravitational force acting on the droplet. The pinning location of the water droplets moved further down the substrate as the water droplet mass was increased.

The adhesive force at each position along the hybrid surface was calculated as follows:

$$F = mg\sin\theta_{\mathrm{SA}}$$

where F is the adhesive force, θ_{SA} is the sliding angle, m is the mass of water droplet, and g is the acceleration due to Earth's gravity. From the value of F, the adhesive force of a single metal dome of 9.0 μm in diameter (F_{dome}) was calculated as

$$F_{dome} = F / S(m) N(d)$$

where $S(m)$ is the apparent contact area with a water droplet of a given mass m, and $N(d)$ is the area number density of metal domes at position d. $S(m)$ was measured from the projection of the water droplet onto the hybrid surface. F_{dome} was nearly constant at 7.3 ± 0.9 nN, regardless of position (d) and water droplet mass (m). These results indicate that the adhesive force was regulated by only the number density of metal domes (N). In other words, the hybrid surface having a gradient in the number density of metal domes had an adhesive force gradient (AFG) acting on the water droplet.

The location-selective pinning of a water droplet on the AFG hybrid surface was measured. The relationship between the pinning location and water droplet mass was examined through the sliding behavior of water droplets of various masses, which were dropped onto the AFG hybrid surface (d = 30 mm) with a slope of 20° (Fig. 13.7). The 20 mg water droplet passed over the entire length of the AFG hybrid surface. In contrast, droplets of 15 mg or less slid and were then pinned on the AFG hybrid surface. The pinning location became closer to the starting position as the droplet volume was decreased. The pinning location on the tilted AFG hybrid surface acts as an invisible gate for the sliding water droplets, dividing the surface into a sliding area and an adhesion area. The gate location could be accurately estimated

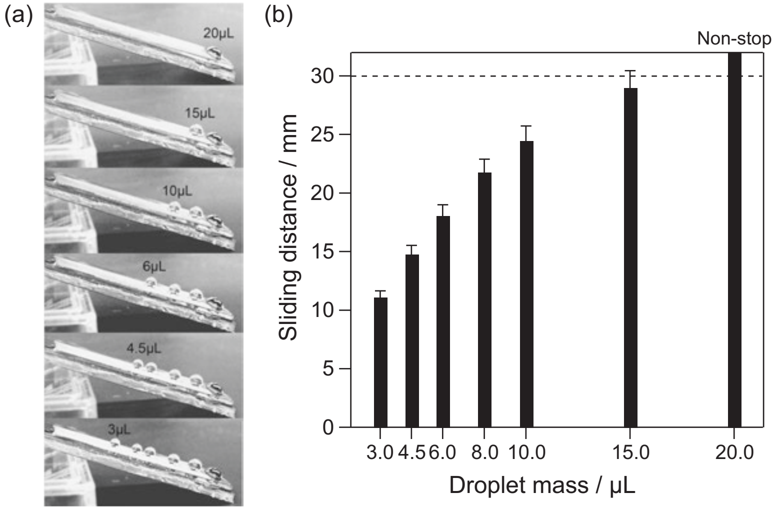

Fig. 13.7 Invisible gates for the sliding water droplets on the tilted AFG hybrid surface with slope of 20°. (**a**) Sliding and pinning behavior of water droplets of various masses. The pinning location acts as an invisible gate for the sliding water microdroplet. (**b**) Sliding distance was plotted to the various mass of water droplet

from the water droplet's equation of motion. When the droplet was placed on a substrate at a higher tilt angle, the gate location was farther from the starting position, owing to the larger gravitational potential energy of the water droplet. Droplet volume and substrate tilt angle govern gate location on the AFG hybrid surface. Moreover, further tilting the substrate or adding water to a droplet induces a pinned water droplet to start sliding again. This study provides the first demonstration of location-selective pinning of a sliding water droplet on a metal–polymer hybrid surface having a gradient in the adhesive force that acts on the water droplet.

13.3 Overwritable Liquid Selective Open Channel

A coastal animal, *Ligia extotica*, was set as a biological model. It has pairs of legs on which open-air capillary structures uptake water spontaneously to its gill using interfacial free energy (Horiguchi et al. 2007) (Fig. 13.8a). SEM observations revealed the water channels are composed of micron-sized blades oriented in parallel lines (Fig. 13.8b). Within a certain range of high surface energy, the channels on the legs were able to transport water against gravity without letting the water out of the channels (Ishii et al. 2013). This passive-energy transport system could be reproduced by the optimization of microstructures and chemical composition on surface (Tani et al. 2014). This biomimetic liquid transport system not only has no need of external pressure, unlike conventional closed capillary systems, but also

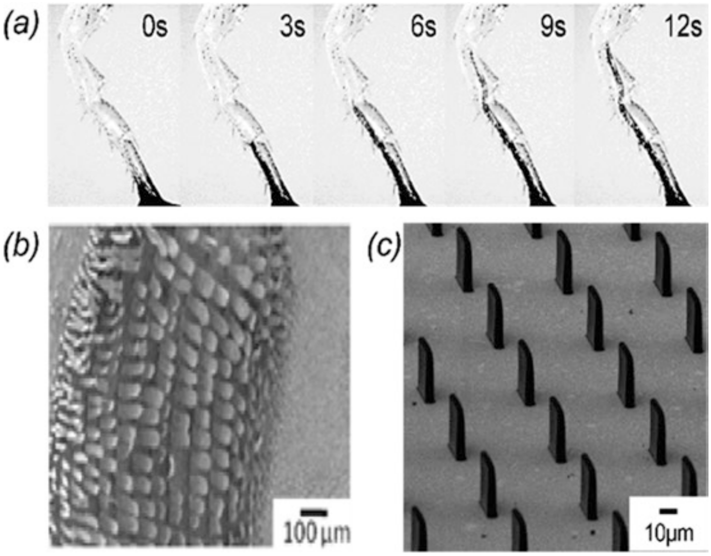

Fig. 13.8 (**a**) Water transport on a leg of Ligia exotica. SEM images of open capillary structures (**b**) on a leg of Ligia exotica and (**c**) fabricated on a silicon substrate by photolithography

accessibility to the channels from outside which enables inter-channel liquid transport and ease of cleaning.

A series of open channels composed of micro-scaled arrays of epoxy blades on silicon wafer mimicking those surface structures of the animal is fabricated by photolithography (Fig. 13.8c). These open channels are composed of two elements: silicon wafer substrate and numerous blades made of SU-8, an epoxy-based photoresist. 30 min of VUV/O_3 treatment was enough to render both of silicone wafer and SU-8 wettable to water as well as to oil since the process creates high surface energy functional groups such as carbonyl and hydroxyl groups on utmost surface. When the tip of the open channel treated by VUV/O_3 comes into contact with the horizontal surface of a liquid pool, the liquid spontaneously rises on the surface and forms TCL on its propagating front (Fig. 13.9). The measured position of the TCL as a function of time qualitatively follows the Washburn model. The imbibition height z scaled as $z \sim t^{1/2}$. This dynamics is observed in typical capillary rise (Tani et al. 2015). The forest of blades on the channel makes TCL tortuous along with the

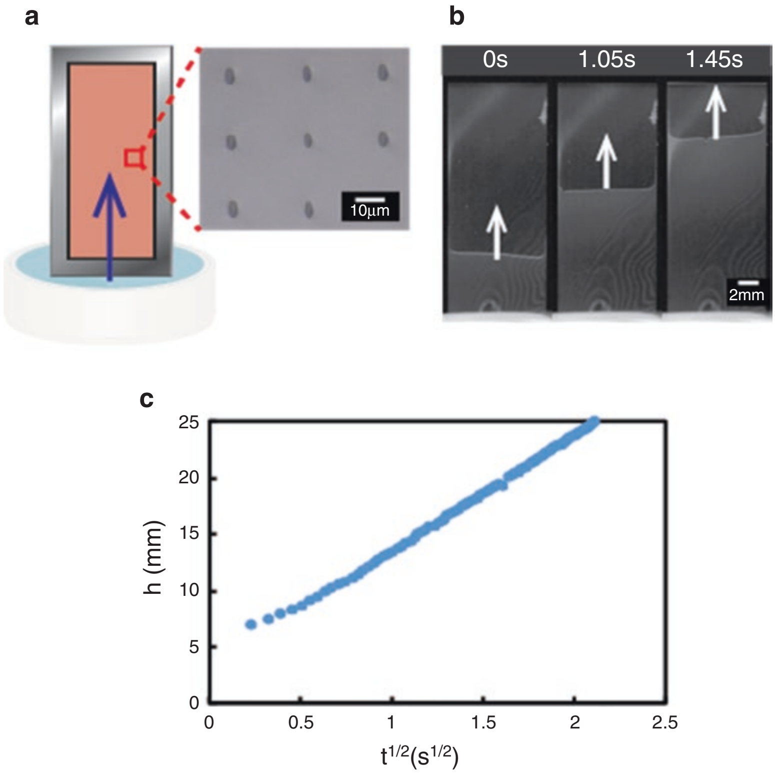

Fig. 13.9 Directional water transport against gravity on open channel. (**a**) Schematic of experimental setup. Water transport begins once the tip of an open channel (magnified photograph) immersed in water. (**b**) Image sequence of water transport on an open channel. (**c**) Height of the rise (h) vs square root of elapsed time (t)

topography of surface (Wenzel state), which elongates the length of TCL and enhances the innate wettability of surface. It enables the spontaneous liquid transport against gravity.

While VUV/O_3 treatment is useful when it comes to rendering the open channel completely wettable to any liquid and transport them, chemical vapor deposition (CVD) treatment with alkylsilanes disables certain types of liquids from being transported on the channel. Two types of alkylsilanes, triethoxymethylsilane (TEMS) and heptadecafluorodecyltrimethoxysilane (FAS-17), were adapted for tuning the surface chemistry. Firstly, as-prepared open channels are modified by VUV/O_3 treatment for 10 min so as to be reactive to these alkylsilanes. After the treatment, each sample were immediately placed with a glass vial containing 10 μL of either two types of alkylsilanes into a PFA container in a nitrogen atmosphere with less than 10% relative humidity. The container was sealed with a cap and then heated at 95 °C for a certain period of time in an oven. Finally, the treated sample was rinsed with ethanol and water, and then dried. Static contact angles on SU-8 substrate and silicon wafer treated with CVD were measured. Surfaces modified with FAS-17 (heated for 60 min) show relatively high static CAs due to the presence of perfluorinated alkyl chains on the outermost surface with low surface energy. On the open channels modified with FAS-17, silicone oil as well as water were completely repelled and not transported. In addition, no minute droplet sticks to the surface after the open channel was pulled out from the liquid pool. On the other hand, the open channels modified with TEMS (heated for 40 min), while repellency similar to those modified with FAS-17, were fully wettable to the droplets of silicone oil (Wenzel state) and exclusively transport silicone oil against gravity when immersed into a reservoir of silicone oil. This radical difference of wetting properties is achieved by the elongated TCL. The longer torturous TCL intersects with more of the surface of the open channel, which results in enhancement of innate wetting properties. The CAs of water on TEMS treated silicone wafer and SU-8 were relatively high (≥ 70 °), while those of silicone oil were low (<30 °). The microstructure of open channels reinforces the original wetting properties and leads to liquid selective transport against gravity.

By selectively modifying specific region on the open channels, wetting patternings were also achieved. Introducing a photomask into the setup of VUV/O_3 treatment, water flows on directly irradiated area of the channel without spreading over the areas that were not exposed to the direct irradiation (Fig. 13.10a). With this method, highly designed liquid channels for both of oil and water could be written. Silicone oil wets the central region modified with TEMS without leaking through to edge regions modified with FAS-17 (Fig. 13.10b), however, water on any part of this surface is completely repelled. Silicone oil has much lower surface energy than water, therefore, the TEMS modified central region, which have higher surface energy than FAS-17 modified edge regions, drives silicone oil thermodynamically to wet and spread on the channels and rise against gravity.

Moreover, this liquid transport system characterized by liquid and regional selectivity was found to gain “rewritability” by CVD of alkylsilanes following VUV/O3 treatment. The surfaces modified by CVD regain its wetting properties over multiple times (Fig. 13.11). This result indicates it is possible to “write” open channels

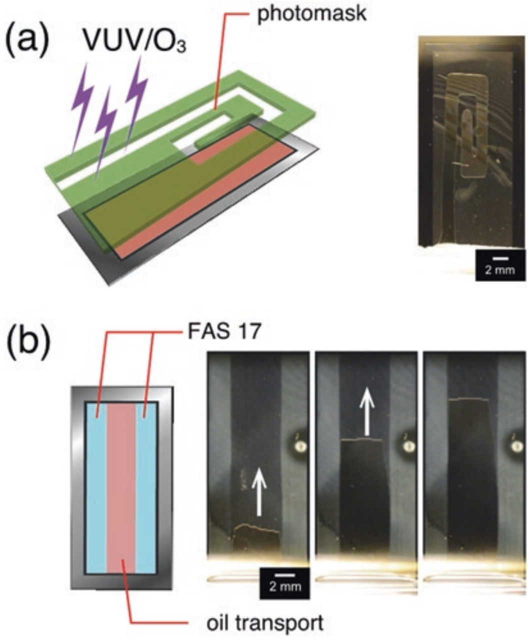

Fig. 13.10 (**a**) The area highly treated with VUV/O_3 was able to transport water without leaking out to non-treated area. (**b**) Schematic of an open channel partially treated with CVD of FAS-17 and image sequence of silicone oil transport. The central area exclusively transports oil without leaking out to FAS-17 treated area

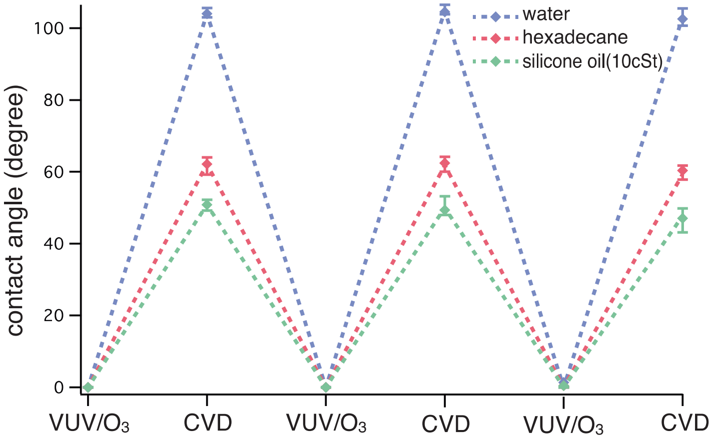

Fig. 13.11 Static contact angles of water (blue line), n-hexadecane (red line) and silicone oil (10 cSt) on silicon wafer modified by VUV/O_3 and CVD of FAS-17 (heated for 1 day) over 3 times

exclusive to specific liquids, and overwrite different channels with different wetting properties after the reset of the former wetting properties by a set of modifications (VUV/O_3 and CVD) on the entire surface. These rewritable open channels with liquid selectivity are simple and applicable to a wide variety of microstructure surfaces, opening the way for its application of many devices handling minute amounts of liquids, such as Lab-on-a-chip.

13.4 Liquid Transport by Modified Open Channel

Open-air channels composed of micro-sized arrays of epoxy blades on silicon wafer inspired from the wharf roach were fabricated by photolithography. These open-air channels were composed of numerous epoxy blades. Sample parameter is summarized in Table 13.1. The area of an open-air channel is 25 mm (height) × 10 mm (width) and the width of an epoxy blade is 2 μm. Pitch interval (*PI*) between two blades in water spreading in long axis of a blade (LA) direction and line width (*LW*) between two blades in short axis of a blade (SA) direction are fixed at 50 μm of all samples. Samples are divided into three groups of the slit length (*SL*; 25, 50, 100 μm) of an epoxy blade. Another parameter *S*, we call shift step, is defined as an indicator of arrangement patterns shift distance *d* (Fig. 13.12). A maximum value of *S* is set 0.50.

To achieve completely wetting state for water, the surfaces of channels were irradiated by a vacuum VUV treatment (500 ± 20 Pa, 20 min) with an excimer lamp, which the process generates hydrophilic groups with high surface free energy such as carboxyl and hydroxyl groups on the surfaces. The hydrophilic channel was set vertically (Fig. 13.13a) or horizontally (Fig. 13.13c). A bottom of the channel was contacted with a water pool. Water spontaneously transported in LA or SA direction and form three-phase contact line (TCL) on its propagating front (Fig. 13.13b and d). The transport behaviors of each sample were recorded and the measured position of the TCL as a function of time *t* (Fig. 13.13e, f) follows the Washburn's model.

Table 13.1 Relationship of shift distance: d [μm] and shift step: S

	Sample number															
	a1		a2		a3		a4		a5		a6		a7		a8	
Sample group	*d*	*S*	*d*	*S*	*d*	*S*	*d*	*S*	*d*	*S*	*d*	*S*	*d*	*S*	*d*	*S*
SL 25 μm	0	0	10	0.13	20	0.27	25	0.33	30	0.40	37.5	0.50	–	–	–	–
SL 50 μm	0	0	10	0.10	20	0.20	30	0.30	40	0.40	50	0.50	–	–	–	–
SL 100 μm	0	0	10	0.067	20	0.13	30	0.20	40	0.27	50	0.33	60	0.40	75	0.50

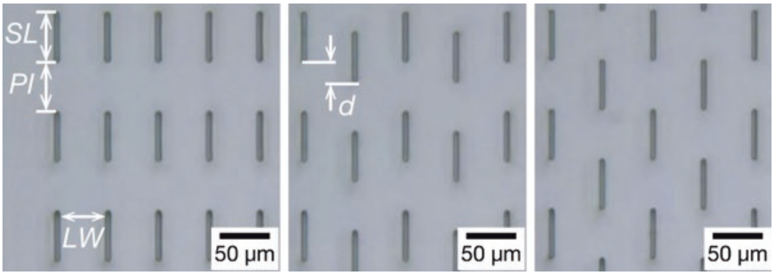

Fig. 13.12 Optical microscope images of a series of channels with a quantifiable shift of arrangement patterns

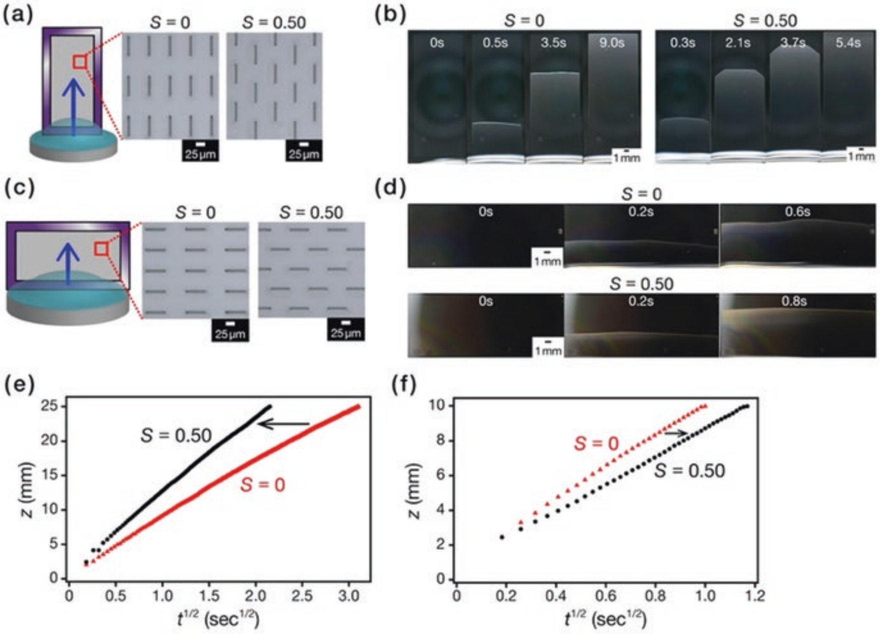

Fig. 13.13 Capillary rise of the channels of *S* = 0 and 0.50 in (**a**, **b**, and **e**) LA direction and (**c**, **d**, and **f**) SA direction. (**a** and **c**) Schematic models of experiment. (**b** and **d**) Image sequences of water transport. (**e** and **f**) Imbibition height *z* plotted to square root time

The imbibition height z scaled as $z \sim t^{1/2}$. This dynamics is observed in typical capillary rise (Tani et al. 2015).

The values of transport velocity D are plotted to the shift step S (Fig. 13.14). The D values in LA direction of each non-shift pattern (S = 0) were almost the same. Transport velocities in LA direction accelerated with increase of the S value, which indicates that a quantifiable shift of blades induced improvement of the transport velocity. Shift of arrangement patterns produced narrow gap area (Fig. 13.14d). Longer length of SL effectively affected acceleration of the transport velocity. When the total amounts of the gap area of the channels with SL = 25 µm of over S = 0.33 were the same, the transport velocity was not accelerated with increase of the S value. In particular, it was interested in improvement of the transport velocity of the channels with SL = 100 µm of over S = 0.33. The contacting time of TCL to the next blades was shortened by closing gap area. In the case of no-gap channels of S = 0.33 and 0.40, the transport velocities in LA direction were almost the same. Amazingly, the no-gap channel of S = 0.50 transported rapidly compared with the no-gap channels of S = 0.33 and 0.40. This result could be explained by assumption of oblique-directional gap area (Fig. 13.14e). Large tilting angle a (S = 0.50) contributed to narrow the oblique-directional gap area and to produce straight flow paths with the oblique direction, resulting drastic improvement of the transport velocity.

In the latter of water transport in LA direction, the shapes of TCL were formed two types depending on arrangement of blade patterns on the surfaces. The TCL

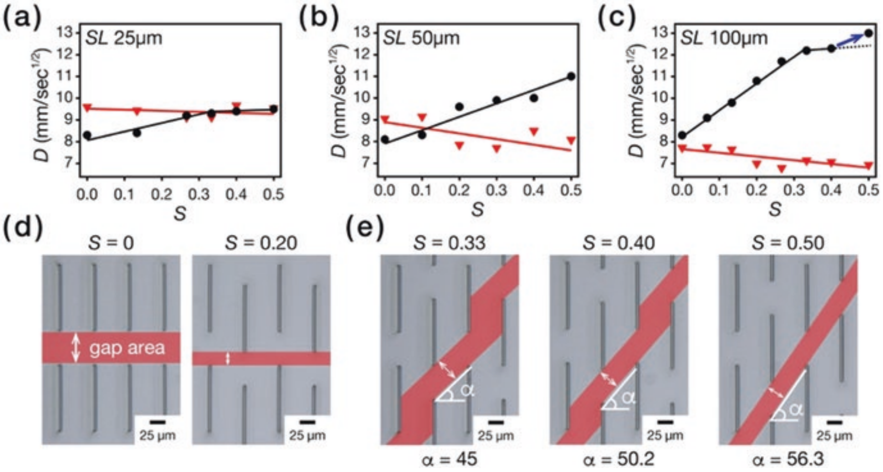

Fig. 13.14 Transport velocities plotted to the shift step *S* in the channels of (**a**) *SL* = 25 μm, (**b**) *SL* = 50 μm, and (**c**) *SL* = 100 μm. Black circles and red triangles indicate water transport in LA and SA directions, respectively. Optical images of the samples of *SL* = 100 μm (**d**) with and (**e**) without gap area. The values indicate tilting angle

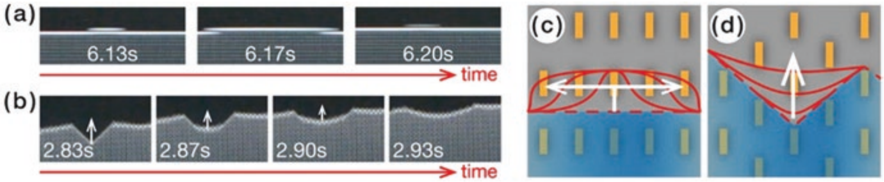

Fig. 13.15 (**a** and **b**) Time sequence of propagation of TCLs and (**c** and **d**) schematic illustrations of the TCLs in the channels of (**a** and **c**) *S* = 0 and (**b** and **d**) *S* = 0.50

propagating towards horizontal direction was observed in the default channels of *S* = 0 (Fig. 13.15a, c). On the other hand, the length of TCL in the no-gap channels of *S* = 0.50 with *SL* = 50 and 100 μm was elongated vertically by the surface topography and often formed valleys pulling up their bottoms (Fig. 13.15b, d). The TCLs of other gap patterns like the channels of *S* = 0.33 and 0.40 seemed to propagate horizontally and vertically. This hybrid propagation indicates that continuous vertical pulling up contributes strongly to improvement of transport velocity in LA direction, and long length of TCL increases the driving force of water transport.

Transport velocity in SA direction declined slightly with increasing of the *S* values (red line of Fig. 13.15a–c). The TCL was towards horizontal direction like the default gap patterns of *S* = 0 in LA direction. In the case of water transport in SA direction, the constant value of *LW* can be replaced gap area in all channels. Therefore it is estimated that the transport velocity is the same. However, when the *SL* got long, the rate of decline was large. This result indicates that the flow paths from bottom to top of the channel dominate the transport velocity in SA direction. The default gap patterns of $S = 0$ possessed the vertical flow paths in SA direction. On the other hand, the no-gap channels of $S = 0.50$ never make the vertical flow paths in SA direction, and form the oblique flow paths. Finally we conclude that the inhibition of water transport in SA direction and continuous vertical pulling up of TCL in LA direction produce rapid transport system of the bio-inspired patterned surfaces.

Two features induced this phenomenon: (1) the narrow gap area accelerated TCL contact to next blades and produced strong driving force. In the no-gap channels, the gap areas formed oblique flow paths. (2) The length of TCL elongated by the topography of micropatterned surface enhances the intrinsic wettability of surface, that is, driving force. Novel approach of shift arrangement patterns on surface will be useful for developing efficient capillary-driven devices in various fields in the future. To completely understand this behavior, however, measurement of liquid spreading on a microscopic scale is necessary.

References

Barthlott W, Neinhuis C (1997) Purity of the sacred lotus, or escape from contamination in biological surfaces. Planta 202:1–8

Cho WK, Choi IS (2008) Fabrication of hairy polymeric films inspired by geckos: wetting and high adhesion properties. Adv Funct Mater 18:1089–1096

Feng L, Zhang Y, Xi J, Zhu Y, Wang N, Xia F, Jiang L (2008) Petal effect: a superhydrophobic state with high adhesive force. Langmuir 24:4114–4119

Horiguchi H, Hironaka M, Meyer-Rochow VB, Hariyama T (2007) Water uptake via two pairs of specialized legs in Ligia exotica (Crustacea, isopoda). Biol Bull 213:196–203

Hosono E, Fujihara S, Honma I, Zhou H (2005) Superhydrophobic perpendicular nanopin film by the bottom-up process. J Am Chem Soc 127:13458–13459

Ishii D, Nagashima T, Udatsu M, Sun RD, Ishikawa Y, Kawasaki S, Yamada M, Iyoda T, Nakagawa M (2006) Pd−promoted Ni−P electroless deposition on a hydrogen-bonded molecular surface of a supramolecular fibrous template. Chem Mater 18:2152–2158

Ishii D, Horiguchi H, Hirai Y, Yabu H, Matsuo Y, Ijiro K, Tsujii K, Shimozawa T, Hariyama T, Shimomura M (2013) Water transport mechanism through open capillaries analyzed by direct surface modifications on biological surfaces. Sci Rep 3:3024

Karthaus O, Maruyama N, Cieren X, Shimomura M, Hasegawa H, Hashimoto T (2000) Water-assisted formation of micrometer-size honeycomb patterns of polymers. Langmuir 16:6071–6076

Neinhuis C, Barthlott W (1997) Characterization and distribution of water-repellent, self-cleaning plant surfaces. Ann Bot 79:667–677

Onda T, Shibuichi S, Satoh N, Tsujii K (1996) Super-water-repellent fractal surface. Langmuir 12:2125–2127

Tani M, Ishii D, Ito S, Hariyama T, Shimomura M, Okumura K (2014) Capillary rise on legs of a small animal and on artificially textured surfaces mimicking them. PLoS One 9(5):e96813

Tani M, Kawano R, Kamiya K, Okumura K (2015) Towards combinatorial mixing devices without any pumps by open-capillary channels: fundamentals and applications. Sci Rep 5:10263

Yabu H, Takebayashi M, Tanaka M, Shimomura M (2005) Superhydrophobic and lipophobic properties of self-organized honeycomb and pincushion structures. Langmuir 21:3235–3237

Zhang X, Shi F, Niu J, Jiang Y, Wang Z (2008) Superhydrophobic surfaces: from structural control to functional application. J Mater Chem 18:621–633

Chapter 14
Material-Independent Surface Modification Inspired by Principle of Mussel Adhesion

Soo Hyeon Lee and Haeshin Lee

Abstract Mussels' unique ability to adhere virtually any surfaces of materials underwater has drawn significant attention to scientists and engineers. This chapter will introduce a new concept of surface chemistry called polydopamine that can functionalize virtually any material surfaces. Polydopamine (PD) is a uniquely adaptable and simple surface functionalization method, being the first single step material-independent surface chemistry when it was first reported in 2007 (Lee H, Dellatore SM, Miller WM, Messersmith PB, Science 318:426–430, 2007). Understanding this surface chemistry is essential for the next chapter 15 for explaining a general strategy to incorporate stimuli-sensitive properties at a surface level. We compare PD coatings to other commonly employed surface modification methods, followed by an account of how approaches to PD deposition have evolved from the original 'recipe' to the current state-of-the-art PD preparation methods.

Keywords Mussel-inspired surface modification · Surface functionalization · Mussel adhesion protein · Material-independent · Polydopamine · Polynorepinephrine · Catechol

14.1 Introduction

Mussels exhibit strong adhesiveness to virtually all types of inorganic and organic surfaces in a wet environment. This interesting adhesion feature has drawn significant interest from researchers in a variety of research fields. Polydopamine/polynorepinephrine nanoscale adhesive films, inspired by the amino acid composition of mussel adhesive proteins, can be generated by oxidative self-polymerization of the corresponding monomer called dopamine and norepinephrine in the alkaline

---

S. H. Lee · H. Lee (✉)
Department of Chemistry, Korea Advanced Institute of Science and Technology (KAIST), Daejeon, Republic of Korea
e-mail: haeshin@kaist.ac.kr

A. Hozumi et al. (eds.), *Stimuli-Responsive Dewetting/Wetting Smart Surfaces and Interfaces*, Biologically-Inspired Systems 11,
https://doi.org/10.1007/978-3-319-92654-4_14

aqueous condition. They mimic the intrinsic adhesive properties of mussels, showing material-independent (i.e. any materials) surface coating properties. Polydopamine or polynorepinephrine coated surfaces, in turn, can serve as secondary reaction substrates through catechol redox chemistry or covalent bond formation with amine/ thiol functional groups. Besides self-polymerization, commercially available polymers can be engineered by catechol amine conjugation, resulting in universal adhesive materials to be useful for surface modification. Importantly, the purpose of this chapter is to provide scientific background for next chapter for stimuli-sensitive surface coatings. This nature-inspired surface modification is an efficient and versatile platform, which can be applied for the development of various bio/energy materials and novel hybrid materials.

14.2 Overview of Mussel Adhesive Proteins

Mussels strongly bind to the marine surface such as rocks and moss using a series of their byssal threads. In contrast to conventional industrial adhesives, losing their adhesiveness in a wet condition, mussel adhesive protein exhibits a strong adhesion capacity in an aqueous environment. Moreover, it can bind to virtually all types of surfaces including metal/nonmetal/organic polymer/inorganic materials. For example, mussel adhesive protein can bind even to polytetrafluoroethylene (PTFE), which has been known to be antifouling surface. Lee et al. analyzed mussel adhesive proteins to identify the underlying mechanism of this particular adhesion process (Lee et al. 2007, 2011). Mefp-3 (Mytilus edulis foot protein-3) is found at the interface between mussel pads and surfaces. The analysis of amino acid compositions revealed that approximately 20% of total amino acids in this protein are 3,4-dihydroxy-L-phenylalanine (dopa). Dopa is well-known for a dopamine precursor and a norepinephrine intermediate compound produced by post-translational modification of tyrosine. As shown in Fig. 14.1, dopa content in Mefp-3 is

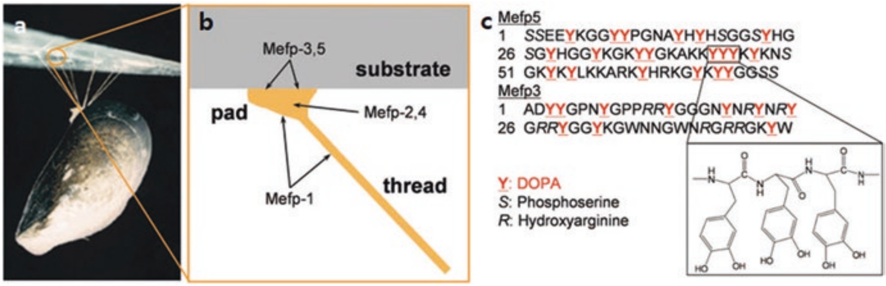

Fig. 14.1 Biodistribution and amino acid composition of mussel adhesive protein. (**a**) Photograph showing the byssal threads of mussel attaching to a glass surface. (**b**) Biodistribution of Mefps (Mytilus edulis foot proteins) in the byssal threads. (**c**) Amino acid composition of Mepf-3 and -5, containing a high dopa content, and the chemical structure of dopa. (Adapted with permission from Lee et al. (2006), copyright 2006 the National Academy of Sciences)

extraordinarily higher than other amino acids, such as glycine, asparagine, tryptophan, and others. This result suggests that dopa plays an important role to the adhesive ability of mussel protein. Mefp-5, another adhesive interface protein of mussels, contains dopa with a high proportion (28%). Noticeably, lysine locates next to dopa with a high proportion compared to other amino acids, suggesting that dopa and lysine synergistically contribute to the wet-resistant adhesions.

Lee, Scherer, and Messersmith reported the adhesion force of dopa to the titanium dioxide (Ti) and gold (Au) surfaces at a single molecule level for the first time (Lee et al. 2006). An atomic force microscopy (AFM) tip containing a single dopa residue was used to measure the "pull-off force", which is the force required to detach the dopa-modified cantilever from the surface. The single dopa pull-off experiment on Ti surfaces demonstrated that catechol forms coordination bond with the metal core, exhibiting nearly 750 pN with full reversibility in binding/unbinding cycles (Fig. 14.2a–c). In contrast, dopa reacts with primary amines on amine-functionalized surfaces to form the covalent bond, exhibiting irreversible covalent reaction with ~ 2 nN force Fig. 14.2d (middle curve). In pull-off experiments carrying out at pH 8.3 (which is similar to marine environment) and 9.7 (which can induce catechol oxidation) with Ti surface, a bimodal force distribution consisting of 150–250 pN and 700–800 pN was observed. Since the low-force signal appeared only under the oxidizing condition, it is conceivable that the high-force and the low-force signals attribute to the coordination interaction of Ti surface with dopa (Fig. 14.2b, the chemical structure on the AFM tip shown right) and dopa-quinone (Fig. 14.2b, the chemical structure shown left), respectively. Considering all data explained together that dopa contains a catechol group, dopa can strongly adhere to various surfaces by forming coordination/covalent bonds.

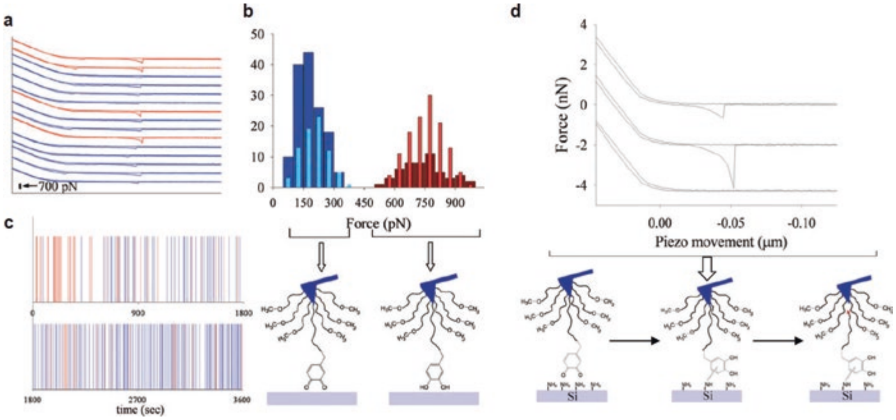

Fig. 14.2 (**a–c**) Coordination bond between dopa and titanium surface. Different biomodal force signals of dopa (red) and dopa-quinone (blue) suggests that oxidation of dopa reduces adhesion capacity. (**d**) Covalent bond formation between dopa and organic surface containing primary amines via a Michael-type addition reaction. (Adapted with permission from Lee et al. (2006), copyright 2006 the National Academy of Sciences)

14.3 The First Material-Independent Surface Chemistry: Polydopamine Coating

Dopamine is a single molecule (Mw. 153 Da) containing catechol and primary amine functional group. Identification of dopamine is inspired by the aforementioned chemical structure shown in Fig. 14.1c in which dopa with a catechol side chain and lysine with a primary amine group exists nearly 50% of total amino acid composition. H. Lee et al. demonstrated that dopamine oxidation process can functionalize virtually any types of material surfaces as well as any morphology of materials including 0, 1, 2, and 3 dimension regardless of porosity (Lee et al. 2007). Substrates can be simply dipped into an aqueous dopamine solution at pH 8.5 (marine pH) and polydopamine film can be spontaneously generated on the substrate surface by oxidative self-polymerization of dopamine (Fig. 14.3) (Waite 2008; Hong et al. 2011a). Dopamine releases two electrons to be dopamine-quinone, and the amine existed in the dopamine-quinone rapidly reacts with the catechol to form leukodopamine-chrome (Fig. 14.3b). Finally, further oxidation forms an important intermediate 5,6-dihydroxyindole. After this, no more intra-molecular oxidation occurs but rather inter-molecular polymerization between 5,6-dihydroxyindole is found.

Importantly, polydopamine-mediated surface modification facilitates a secondary treatment of surface. Polydopamine film layer on the surface carries catechol functional group, which possesses redox activity. Therefore, polydopamine film can reduce metallic ions and immobilize the resulting metal nanoparticles on the surface due to non-specific adhesiveness of polydopamine. In addition, catechol can form a covalent bond with primary amine group. Therefore, various molecules containing primary amine groups can be introduced on the surface through secondary treatment. As shown in Fig. 14.4, polydopamine coating enables super-hydrophobic surface coating in an aqueous condition to increase of hydrophilicity (Kang et al. 2010). For example, polyethylene (PE) layer was coated by polydopamine and applied for Li-ion batteries separators (Ryou et al. 2011).

Since polydopamine-mediated surface modification method was firstly introduced, various methods to control the deposition rate have been reported. The simplest method is to directly dip the substrates to be coated into a Tris solution containing dopamine at pH 8.5 using oxygen from the air as a dopamine oxidant. Another method to coat not only in alkaline conditions but also in neutral or acidic aqueous media is to use ammonium persulfate as a dopamine oxidant. With this method, alkaline corrosive or pH-sensitive materials, which had been considered unsuitable for polydopamine-mediated surface modification in an alkaline media, were successfully coated with polydopamine (Wei et al. 2010). Bersmann et al. reported Cu^{2+} as dopamine self-polymerization oxidant and this process can be performed in acidic aqueous media (pH 4.5). In their study, the coating thickness increased continuously more than 70 nm while the maximum coating thickness with original coating method in an alkaline solution was only 40–50 nm (Bernsmann et al. 2011). According to UV-Vis spectrophotometry analysis, however, the film

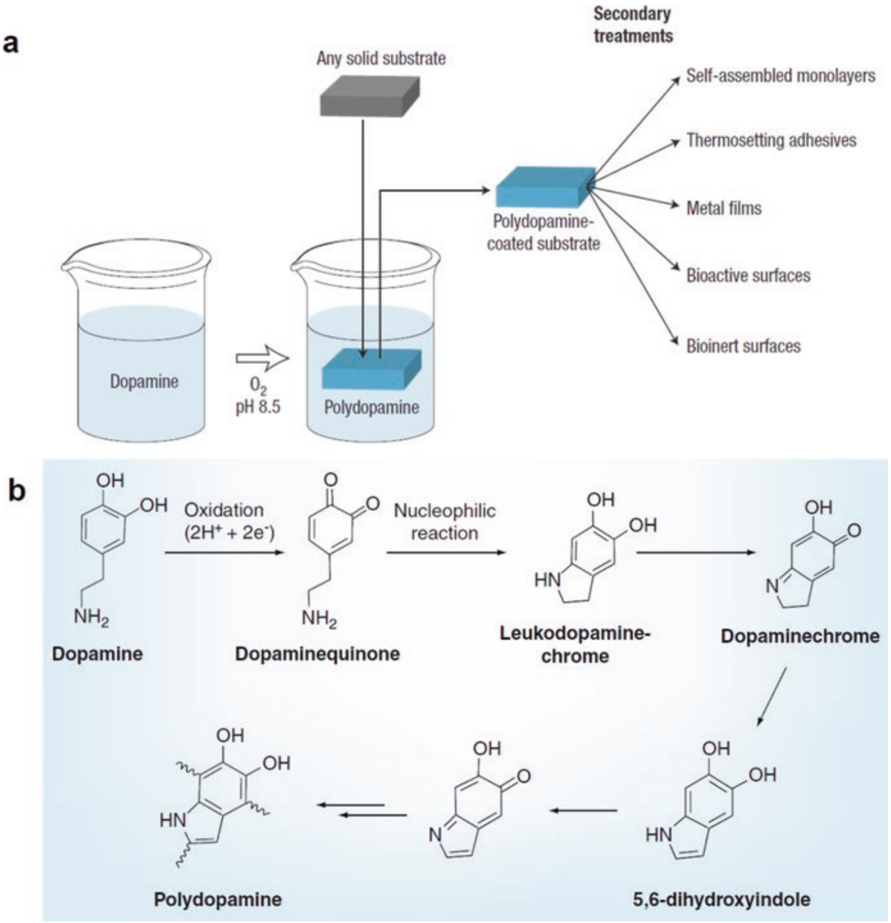

Fig. 14.3 (**a**) Self-polymerization of dopamine for surface modification and secondary treatment. (Adapted with permission from Waite (2008), copyright 2008 Nature Publishing Group). (**b**) Chemistry of polydopamine formation. (Adapted with permission from Hong et al. (2011a), copyright 2011 Future Medicine Ltd.)

prepared with Cu^{2+} media showed the different absorption spectrum compared to one prepared in an alkaline media probably due to the specific interaction between Cu^{2+} and catechol. Natalio et al. demonstrated the inorganic catalyst-mediated dopamine coating in the absence of oxidants (Natalio et al. 2011). In this study, V_2O_5 nanowire was considered as a biomimetic material of vanadium haloperoxidase and used as an inorganic catalyst to produce polydopamine at a neutral pH condition. Taken together, polydopamine coating can be achieved using various oxidants at different pH conditions in controlling the coating thickness. This technical progress enables polydopamine to be considered as a universe surface modification material for diverse applications.

Fig. 14.4 (**a**) Scheme of polydopamine surface coating. (**b**) Polyethylene membrane before (left) and after (right) polydopamine coating. (Adapted with permission from Ryou et al. (2011), copyright 2011 Wiley-VCH Verlag GmbH & Co. KGaA)

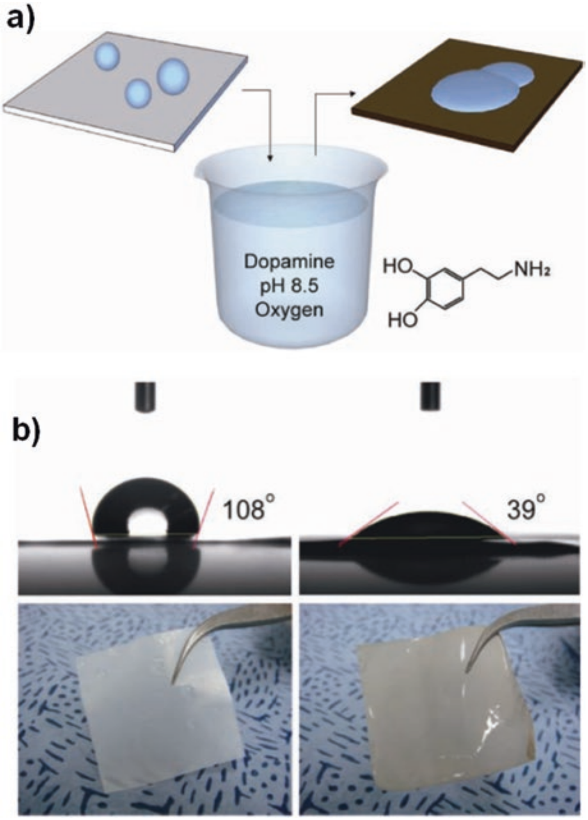

14.4 Toxicity of Polydopamine Coating

Adhesive biomaterials can provide a new direction of biomedical technology, such as tissue adhesive pad and adhesive drug delivery patch, etc., which can replace to surgical treatments. The development of cell or tissue compatible materials is crucial in the artificial tissue regeneration field. To date, many biomaterials have suffered from the difficulties to maintain a strong adhesive ability in the aqueous environment, such as in the body. Polydopamine possesses a prominent potential in the development of various biomaterials and medical devices not only due to its strong adhesion property in wet conditions but also due to biocompatibility.

Cytotoxicity of polydopamine coating has been investigated with various in vitro cell culture experiments. Chan Beum Park and colleagues demonstrated that osteoblast, MC3T3-E1, and PC12 cell lines attached and grew on various surfaces, e.g., polyethylene, polytetrafluoroethylene, silicon rubber, and polydimethylsiloxane, after polydopamine-mediated surface coating, showing a higher survival rate compared to the cells growing on non-treated control surfaces (Fig. 14.5) (Ku et al. 2010a).

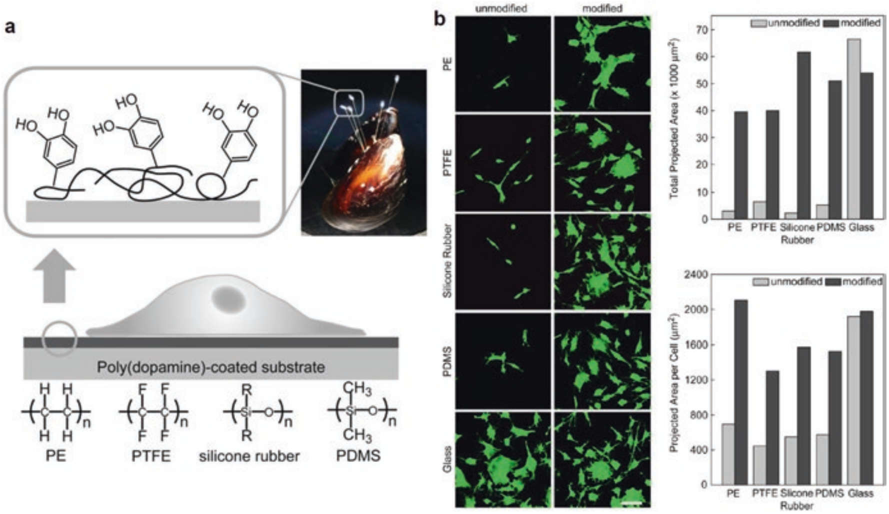

Fig. 14.5 (**a**) Scheme of cell adhesion on the substrates modified by mussel-inspired polydopamine. (**b**) Analysis of cell adhesion capacity before and after polydopamine surface modification on various substrates. (Adapted with permission from Ku et al. (2010a), copyright 2010 Elsevier)

Another group also showed that polydopamine coating on poly(l-lactide-co-ε-caprolactone) surface enhanced the adhesion of C2C12 myoblast cell line (Shin et al. 2011). Like on the 2D plate, polydopamine surface modification on the polymeric nanofibers enhanced the adhesion and viability of human umbilical vein endothelial cells (HUVECs), suggesting that these cell-adhesive polymeric nanofibers can be used as prosthetic scaffolds for vascular grafts (Ku and Park 2010). Considering that polydopamine coating can improve the cell adhesion without eliciting cytotoxicity, Ku et al. demonstrated a simple cell patterning method using polydopamine. Polydopamine coated surface was prepared using conventional photolithography and various cell lines, e.g., fibrosarcoma HT1080, mouse preosteoblast MC3T3-E1, and mouse fibroblast NIH-3T3, were able to grow in polydopamine modified region (Ku et al. 2010b).

As aforementioned, polydopamine coating materials were reported to be non-cytotoxic in vitro mammalian cell culture systems. However, in vivo toxicity of polydopamine is rather unexplored. Hong et al. evaluated firstly in vivo toxicity of polydopamine (Fig. 14.6) (Hong et al. 2011a). Quantum dot (QD), which is an inorganic nanomaterial known to exhibit in vivo toxicity, was modified with polydopamine and was intravenously administered into mice. Injection of QD with bare surface caused the blood immunogenicity, resulting to decrease lymphocytes and increase both neutrophils and monocytes. The level of leukocytes in the mice treated with polydopamine coated QD was not changed compared to control group without any treatment. Besides QD, poly-L-lactic acid (PLLA) with polydopamine coating was implanted to mice, and the adhesion of macrophages and foreign body giant cells on the PLLA surface was monitored. In vivo immune response decreased

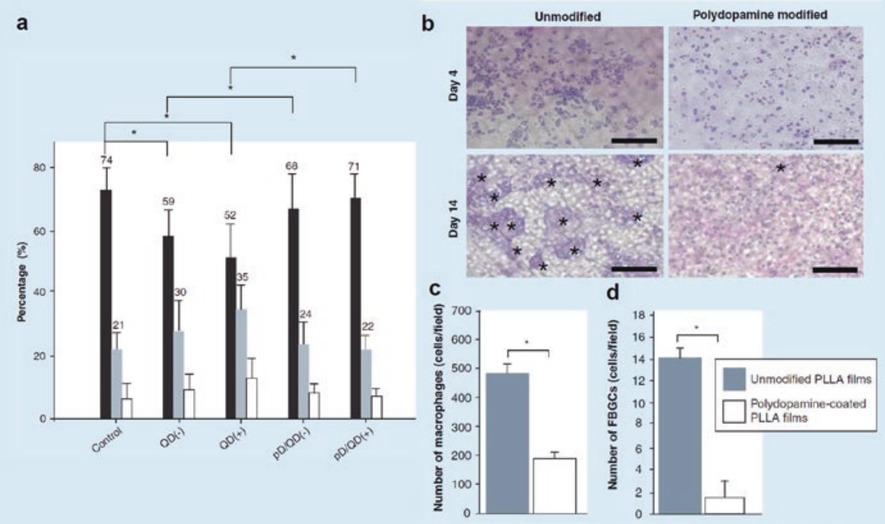

Fig. 14.6 Biocompatibility test with polydopamine coated quantum dot (**a**) and poly(l-lactic acid) (PLLA) surfaces (**b–d**). (**a**) A quantitative analysis of leukocytes in blood after intravenous injection of polydopamine coated quantum dots to mice. Black, gray, and white bars represent lymphocytes, neutrophils, and monocytes, respectively. (**b**) Morphology visualization of adherent immune cells on the PLLA surface before (left) and after (right) polydopamine coating by Wright staining. Asteriks indicate foreign body giant cells (FBGCs). (**c**, **d**) A quantitative analysis of adhered macrophage (**c**) and FBGCs (**d**) on PLLA films. (Adapted with permission from Hong et al. (2011a), copyright 2011 Future Medicine Ltd.)

significantly on the surface PLLA surface with polydopamine coating compared to the PLLA surface without polydopamine coating. These results indicate that polydopamine surface modification does not activate any immune responses and indeed attenuates the in vivo toxicity of injected or implanted materials due to masking the surface of materials with biocompatible polydopamine nanolayers.

14.5 Polydopamine-Mediated Secondary Surface Derivatization

Polydopamine formed by dopamine oxidation intrinsically exhibits a certain degree of redox activity. This redox activity facilitates to reduce metal ions to be metal nanoparticles, which are immobilized on the adhesive polydopamine surface (on-surface synthesis). Unlike the previous methods to synthesize metal nanoparticles, this metal nanoparticle on-surface synthesis method does not use any surfactants and reducing agents but utilize only polydopamine reducing power. Compared to the previous methods which require the additional surface modifications and synthetic materials to immobilize nanoparticles, polydopamine-mediated

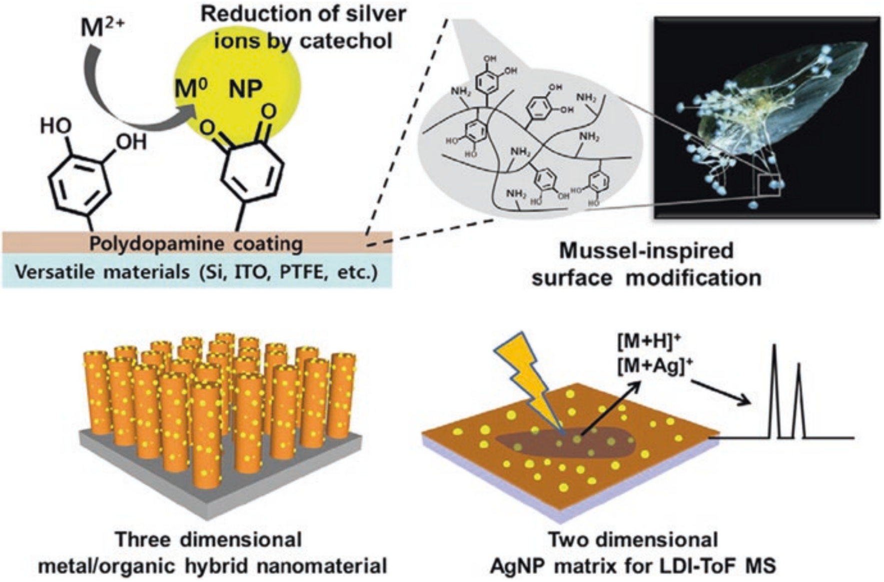

Fig. 14.7 Scheme of secondary surface derivatization on polydopamine coated surfaces: formation/immobilization of metal nanoparticles and the application of this metal/organic hybrid nanomaterial for LDI ToF-MS. (Adapted with permission from Hong et al. (2011b), copyright 2011 IOP Publishing Ltd.)

immobilization of metal nanoparticles is a simple and versatile method (Fig. 14.7). Au nanoparticles synthesized on the polydopamine surface can be applied for biosensor and hybrid nanowire fabrication. For example, polydopamine coated indium-tin oxide (ITO) glass facilitated formation and immobilization of Au nanoparticles on the glass surface and this material was applied for the electrochemical immunosensor (Wang et al. 2011). Another studies showed a hybrid organic-inorganic nanowires by synthesizing Au nanoparticles on the surface of polydopamine coated carbon nanotubes (Fei et al. 2008) and Ag nanocables (Min et al. 2010).

There are also several studies demonstrating various applications with silver nanoparticles (Ag) synthesized on the polydopamine surface. Sureshkumar et al. developed the magnetic Ag nanocomposite possessing antibacterial activity by synthesizing Ag nanoparticles on the surface of polydopamine coated bacterial cellulose nanofibers which contain magnetite nanoparticles (Sureshkumar et al. 2010). Long et al. demonstrated a facile method to fabricate conductive thin films with Ag nanoparticles on polymeric substrates (Long et al. 2011). Hong et al. demonstrated a new concept metallic matrix for laser desorption/ionization time-of-flight mass spectrometry (LDL-ToF MS) with on-surface synthesized Ag nanoparticles (Hong et al. 2011b). Differing from the previous reports using metal nanoparticles as matrix-assisted laser desorption/ionization time-of-flight mass spectrometry (MALDI-ToF MS) matrix, the sample to be analyzed does not need to be mixed with metallic nanoparticles in this platform. Instead, the samples can be simply loaded on the Ag nanoparticle immobilized matrix before analysis. Besides Au and Ag nanoparticles, several metal nanoparticles, such as Pt, and Pd, were also synthesized on various surfaces and applied for surface catalysts (Ye et al. 2010; Ryoo et al. 2011). This metal nanoparticle on-surface synthesis is a novel surface modification method resulting to provide diverse functionalities on the surface.

Apart from redox property, polydopamine coated surface exhibits the chemical reactivity with catechol group, which can form the covalent bond with primary amine groups via Michael addition reaction. This platform can be applied for the immobilization of various biomaterials, such as protein, biopolymers, polysaccharide, etc., to substrates. Various proteins have been immobilized on polydopamine coated surfaces. For example, trypsin (Lee et al. 2009), amylase (Sureshkumar and Lee 2011), and lipase (Ren et al. 2011) showed their intrinsic enzymatic activities after surface immobilization. Immunosensor platform was demonstrated by immobilizing antibodies such as IgG (Spillman 2011) and anti-sulfate-reducing bacteria (SRB) (Wan et al. 2011) and inducing specific antigen-antibody recognitions. Some proteins were immobilized on polydopamine coated substrates to enhance cell attachment. Bovine serum albumin (BSA) was immobilized onto polydopamine deposited diamond-like carbon surfaces, exhibiting good hemocompatibility and cytocompatibility to PC12 cell line (Tao et al. 2009, 2011). In addition, vascular endothelial growth factor (VEGF) (Poh et al. 2010) and bone morphogenetic protein-2 (BMP-2) (Lai et al. 2011) were immobilized on polydopamine coated titanium substrates to promote the differentiation of mesenchymal stem cells for revascularization and bone osseointegration, respectively. Anti-biofoulant membrane was fabricated by grafting amine-functionalized PEG onto polydopamine coated surfaces (McCloskey et al. 2010; Pop-Georgievski et al. 2011). Heparin was immobilized on polydopamine coated polyethylene (Jiang et al. 2010) and polyvinylidene fluoride (PVDF) (Zhu et al. 2009) surfaces via chemical reactions, which can be applied for blood contacting implants.

14.6 Polydopamine-Mediated Superhydrophobic Surface Modification and Microfluidics Applications Thereof

Non-wetting property of superhydrophobic surfaces has limited their chemical modification. Material-independent polydopamine coating platform can applied for superhydrophobic surfaces modification. Kang et al. represented a simple coating method to convert superhydrophobic surfaces to hydrophilic surfaces by dipping the substrates into a weak alkaline dopamine solution, resulting to dramatically decrease the water contact angle from 150° to 40° (Fig. 14.8) (Kang et al. 2010). Although plasma treatment with argon and oxygen gas has been considered as a versatile tool to increase hydrophilicity of superhydrophobic surfaces, it can enhance temporarily surface wettability and permanent hydrophilic surface modification remains still challenging. Therefore binding of chemically stable polydopamine on superhydrophobic surfaces to change their hydrophilicity has a great advantage.

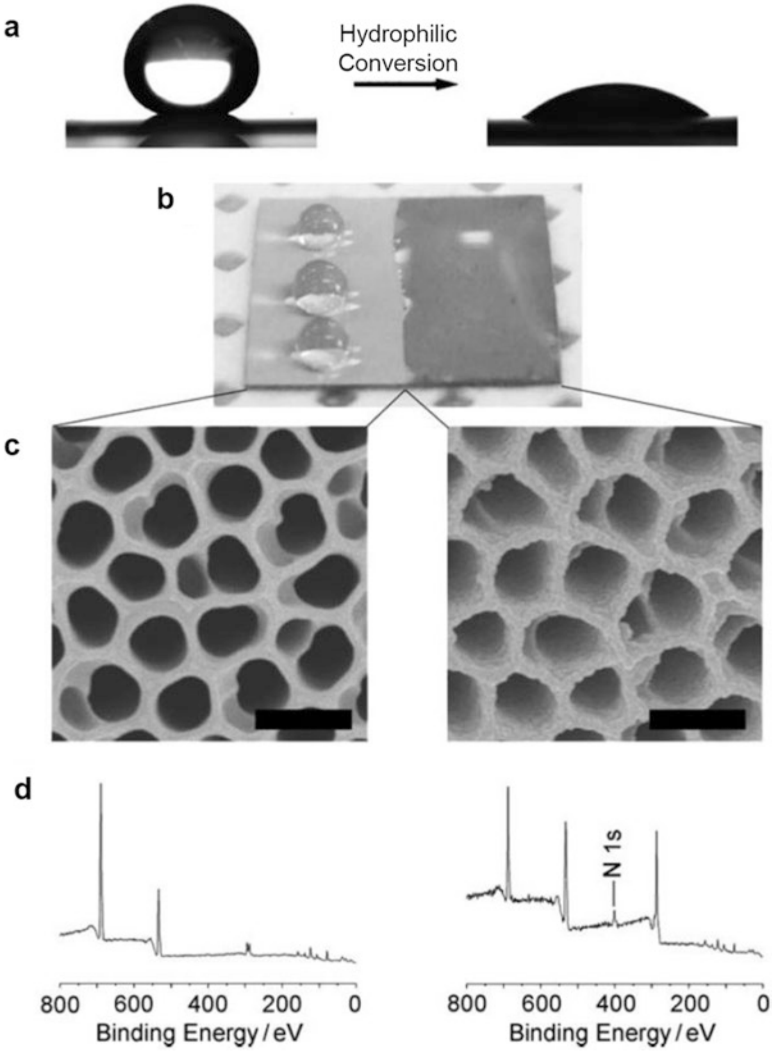

Fig. 14.8 Polydopamine functionalized superhydrophobic surfaces. Contact angle images (**a**), wetting properties (**b**), SEM images (**c**), and XPS spectra (**d**) of superhydrophobic surface before and after polydopamine coating. (Adapted with permission from Kang et al. (2010), copyright 2010 Wiley-VCH Verlag GmbH & Co. KGaA)

Recently You et al. reported a new polydopamine-based microfluidic system, named polydopamine microfluidic device (You et al. 2012). This device was fabricated by generating polydopamine-microlines (60 μm) on superhydrophobic aluminum oxide surfaces by polydopamine coating via photolithography. The Y-shape patterning of hydrophilic kinked polydopamine-microlines can confine the droplet movement and chemical reactions along the polydopamine coated regions

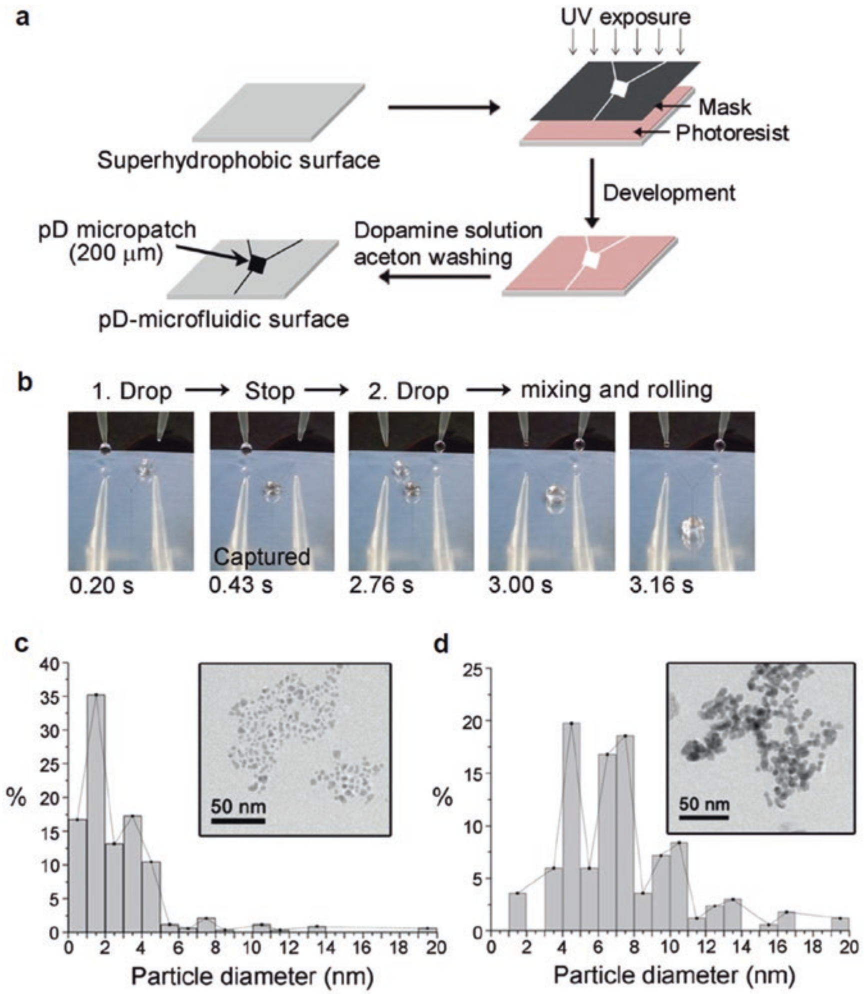

Fig. 14.9 Fabrication of polydopamine-based microfluidic device. (**a**) Manufacturing process of polydopamine coated micropatch for microfluidic system. (**b**) Novel strategy to enhance the mixing efficiency of micro-droplets using Y-shape patterning of kinked polydopamine-microlines. (**c**, **d**) Size distribution of Au nanoparticles synthesized by polydopamine microfluidic device (**c**) and bulk mixing (**d**). (Adapted with permission from You et al. (2012), copyright 2012 Wiley-VCH Verlag GmbH & Co. KGaA)

(Fig. 14.9). Contrast to conventional microfluidic devices equipped with high-cost micropump, this device is a pump-free and gravity-based system which does not require an energy input to control the flow of droplets. This study demonstrated that polydopamine microfluidic device can serve as an efficient micro-reactor for nanoparticle synthesis with a higher yield compared to the typical bulk reaction. Synthesis of Au nanoparticles, a typical rapid reaction, was performed using this system. As a result, more homogenous and smaller nanoparticles were obtained in the comparison of bulk reaction. Another application of this device is to observe structural change of proteins in real-time, which is useful for protein folding studies. You et al. monitored the real-time denaturation of photoactive yellow protein (PYP) after mixing with guanidine on polydopamine-microline by colorimetric analysis (You et al. 2012).

14.7 Polynorepinephrine-Mediated Surface Functionalization

Kang et al. reported that polynorepinephrine can be applied for material-independent surface modification (Kang et al. 2009). Like dopamine, norepinephrine exhibits a surface adhesive property in alkaline aqueous media and facilitates secondary surface derivatization with catechol redox activity and covalent formation with primary amine functional groups. Due to the presence of the alkyl hydroxyl group in norepinephrine, polynorepinephrine coated surface can be continued to perform the surface-initiated ring-opening polymerization (ROP) (Fig. 14.10). For example, biodegradable polymer such as poly-ε-caprolactone (PCL) can be synthesized on the polynorepinephrine coated surface.

Despite widespread studies concerning polydopamine coated surfaces, polynorepinephrine-mediated surface modification has not been yet widely investigated. Haeshin Lee and colleagues demonstrated a facile method of graphene oxide surface modification and its secondary surface derivatization with polynorepinephrine (Kang et al. 2011). Since carbon nanocomposites, such as carbon nanotube, graphene, and graphene oxide, have received much attention as new materials exhibiting excellent electrical and mechanical properties, this study has a particular

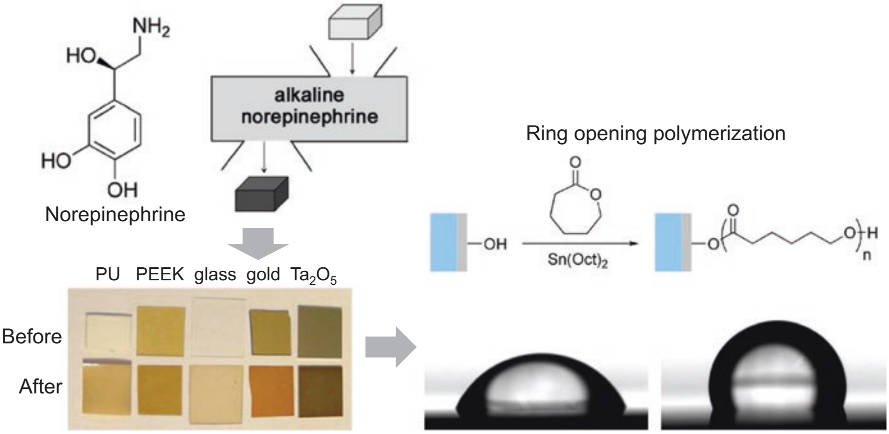

Fig. 14.10 Material-independent surface modification by norepinephrine and secondary modification by ring-opening polymerization of ε-caprolactone. (Adapted with permission from Kang et al. (2009), copyright 2009 American Chemical Society)

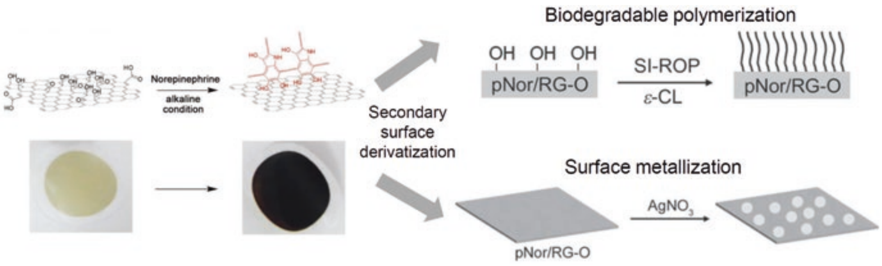

Fig. 14.11 Polynorepinephrine (pNor) coated graphene oxide surface (RG-O) and its secondary surface derivatization. (Adapted with permission from Kang et al. (2011), copyright 2011 Wiley-VCH Verlag GmbH & Co. KGaA)

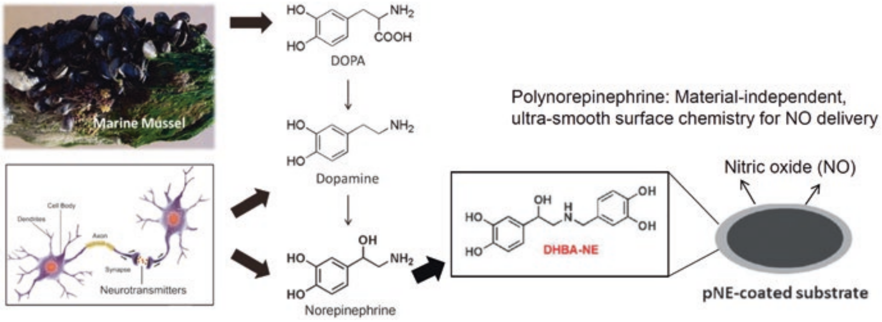

Fig. 14.12 Nitric oxide reservoir system using polynorepinephrine coated substrates. (Adapted with permission from Hong et al. (2013), copyright 2013 Wiley-VCH Verlag GmbH & Co. KGaA)

significance for proposing a versatile platform for surface functionalization of graphene composites. As shown in Fig. 14.11, polynorepinephrine coated reduced graphene film was fabricated by oxidizing norepinephrine on the graphene oxide surface. And PCL grafting and Ag nanoparticle formation/immobilization was performed via ROP and catechol-mediated metallization, respectively.

During self-polymerization of norepinephrine, a new catecholamine intermediate, 3,4-dihydroxybenzaldehyde (DHBA), is generated. This molecule contains an aldehyde functional group which can react with remaining norepinephrine in the solution, resulting to form another new catecholamine intermediate called DHBA-NE. Hong et al. found that DHBA-NE remaining in the polynorepinephrine coating layer plays an important role to decrease the surface roughness and prevent the formation of large aggregates which have been considered as drawbacks of catecholamine surface chemistry, especially with polydopamine (Hong et al. 2013). To develop a novel nitric oxide (NO) reservoir, a NO releasing compound, diazeniumdiolate, was conjugated to secondary amine of DHBA-NE located in polynorepinephrine layer of nanoparticles. As a nano-depot to facilitate the controlled release of NO in the body, this system has a great potential for biomedical applications (Fig. 14.12).

14.8 Catechol-Containing Adhesive Polymers

Differing from surface modification with self-polymerized dopamine, catechol-containing adhesive polymers have been investigated by conjugating dopamine to commercially available polymers. For example, catechol-conjugated polyethylenimine (PEI-C) can form a stable intermolecular bonding due to the interaction between primary amines and catechol groups (Fig. 14.13) (Lee et al. 2008). This material can facilitate layer-by-layer (LBL) assembly using PEI cationic character and secondary chemical reaction on primary amine or catechol moieties (Kim et al. 2012). Lee et al. synthesized PEI-C and demonstrated its remarkable surface modification ability with various surfaces, such as poly(tetrafluoroethylene) (PTFE), polyethylene (PE), poly(ethylene terephthalate) (PET), and polycarbonate (PC) (Lee et al. 2008). By adding hyaluronic acid-catechol (HA-C) to PEI-C coated surface, LBL assembly was performed (Fig. 14.14). Positive charge of PEI and negative charge of HA facilitated LBL deposition with a high efficacy and polydopamine alone is not suitable for this application. These hybrid polymers possess not only their intrinsic characters but also catechol property, enabling the reduction of Ag ions to synthesize Ag particles (Fig. 14.15). Kim et al. formulated sticky virus by simply mixing virus with PEI-C for spatially patterned gene delivery (Fig. 14.16) (Kim et al. 2012). Adhesive property of catechol on the virus surface enables virus to be immobilized on the surface and positively charged PEI facilitates the intracellular delivery of virus, resulting to spatially control the gene expression on substrates, such as cell sheet.

Recently a simple method to prepare water-soluble chitosan by catechol conjugation was presented (Kim et al. 2013). High molecular weight chitosan can be dissolved only in acidified solutions in which primary amine groups can be proton-

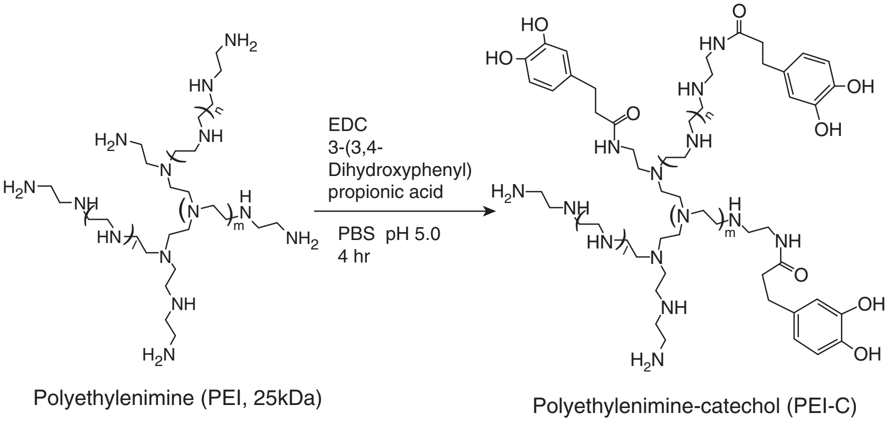

Fig. 14.13 Synthesis of catechol-containing polymer. (Adapted with permission from Lee et al. (2008), copyright 2008 Wiley-VCH Verlag GmbH & Co. KGaA)

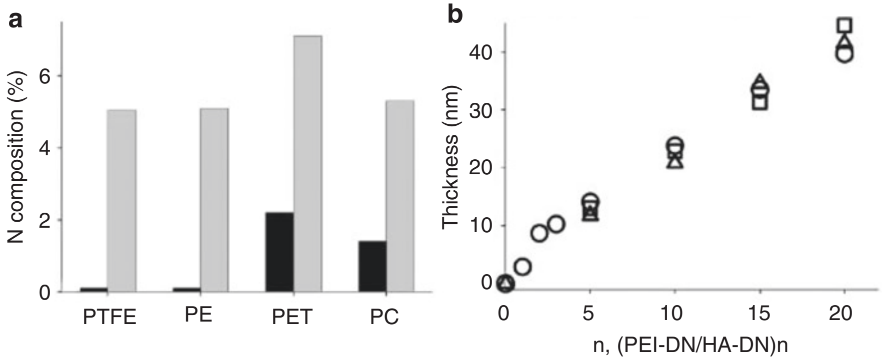

Fig. 14.14 Material-independent LBL assembly using PEI-catechol (PEI-C). (**a**) XPS analysis to confirm the increase of nitrogen composition after PEI (black) or PEI-C (gray) coating. (**b**) Measurement of film thickness after PEI-C/ hyaluronic acid-catechol (HA-C) adsorption on SiO*x*, Au, and PMMA (circles, triangles, and squares, respectively). (Adapted with permission from Lee et al. (2008), copyright 2008 Wiley-VCH Verlag GmbH & Co. KGaA)

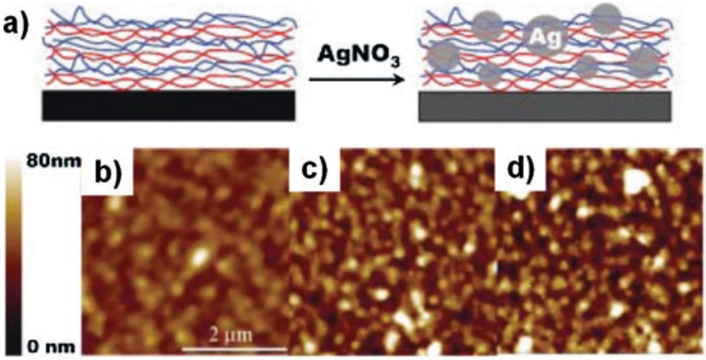

Fig. 14.15 (**a**) Schematic illustration of Ag nanoparticle formation on LBL films coated with PEI-C/HA-C. (**b–d**) AFM images of LBL film coated with PEI-C/HA-C after incubating in 1 mM AgNO$_3$ solution for 0 min (**b**), 30 min (**c**), and 18 h (**d**). (Adapted with permission from Lee et al. (2008), copyright 2008 Wiley-VCH Verlag GmbH & Co. KGaA)

ated to enhance the solubility while it is precipitated in aqueous solutions at neutral pH due to its intermolecular hydrogen bonding. Despite various beneficial properties of chitosan (low toxicity, biodegradability, antibacterial activity, etc.), this solubility issue limits its applications for biomaterials and, therefore, many research groups have investigated to solve this problem. In chitosan-catechol conjugates, hydrophilic catechol can disturb chitosan intermolecular binding, resulting to increase dramatically chitosan solubility. While unmodified chitosan with high molecular weight (approximately 100 kDa) was hardly dissolved at a pH higher than 2, catechol conjugated chitosan was easily solubilized at pH 7. At a pH higher than 7, catechol conjugated chitosan rapidly formed hydrogels by interaction of

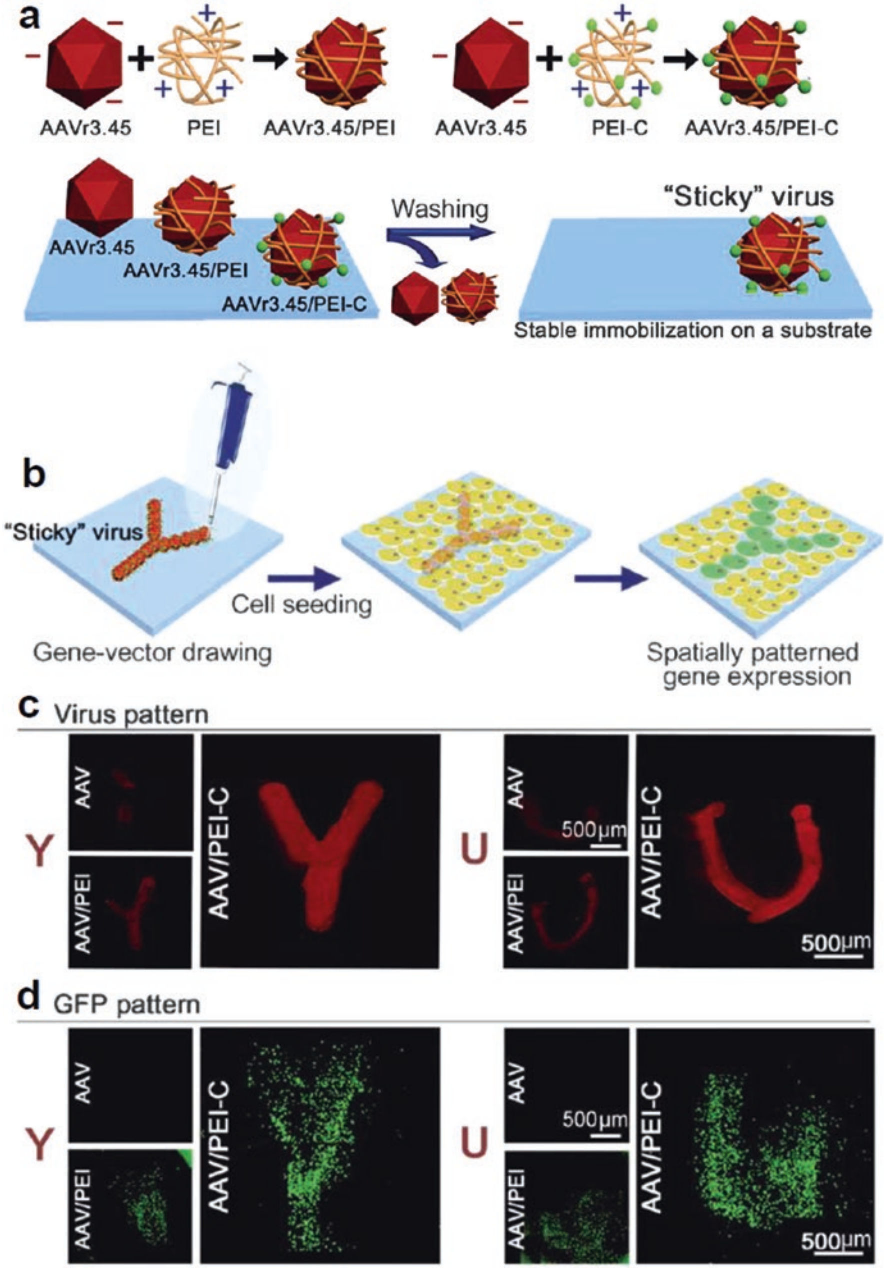

Fig. 14.16 (**a, b**) Schematic illustrations of adhesive virus formulation by PEI-C coating (**a**), and viral patterning and patterned gene expression (**b**) using sticky virus. **c, d)** Resultant viral pattern (**c**) and patterned GFP expression (**d**). (Adapted with permission from Kim et al. (2012), copyright 2012 Wiley-VCH Verlag GmbH & Co. KGaA)

oxidized catechol with primary amine groups in chitosan. Moreover this catechol modified chitosan obtains the adhesive property, which is useful for surface modifications.

14.9 Conclusion

Polydopamine- or polynorepinephrine-mediated surface modification using the mussel adhesive protein-inspired chemical group is a novel surface functionalization platform which can be applied for virtually any types of material surfaces. These coating materials enable the secondary surface derivatization, such as metal nanoparticle synthesis/immobilization or covalent bond formation with primary amine functional groups. Catechol-conjugated polymers, which exhibit surface adhesive properties, can be also applied for surface modification materials. This mussel-inspired surface modification can contribute to develop various bio/energy materials and novel hybrid materials.

References

Bernsmann F, Ball V, Addiego F, Ponche A, Michel M, Gracio JJ, Toniazzo V, Ruch D (2011) Dopamine-melanin film deposition depends on the used oxidant and buffer solution. Langmuir 27:2819–2825

Fei B, Qian B, Yang Z, Wang R, Liu WC, Mak CL, Xin JH (2008) Coating carbon nanotubes by spontaneous oxidative polymerization of dopamine. Carbon 46:1795–1797

Hong S, Kim KY, Wook HJ, Park SY, Lee KD, Lee DY, Lee H (2011a) Attenuation of the in vivo toxicity of biomaterials by polydopamine surface modification. Nanomedicine (Lond) 6:793–801

Hong S, Lee JS, Ryu J, Lee SH, Lee DY, Kim DP, Park CB, Lee H (2011b) Bio-inspired strategy for on-surface synthesis of silver nanoparticles for metal/organic hybrid nanomaterials and LDI-MS substrates. Nanotechnology 22:494020

Hong S, Kim J, Na YS, Park J, Kim S, Singha K, Im GI, Han DK, Kim WJ, Lee H (2013) Poly(norepinephrine): ultrasmooth material-independent surface chemistry and nanodepot for nitric oxide. Angew Chem Int Ed Engl 52:9187–9191

Jiang J-H, Zhu L-P, Li X-L, Xu Y-Y, Zhu B-K (2010) Surface modification of PE porous membranes based on the strong adhesion of polydopamine and covalent immobilization of heparin. J Memb Sci 364:194–202

Kang SM, Rho J, Choi IS, Messersmith PB, Lee H (2009) Norepinephrine: material-independent, multifunctional surface modification reagent. J Am Chem Soc 131:13224–13225

Kang SM, You I, Cho WK, Shon HK, Lee TG, Choi IS, Karp JM, Lee H (2010) One-step modification of superhydrophobic surfaces by a mussel-inspired polymer coating. Angew Chem Int Ed Engl 49:9401–9404

Kang SM, Park S, Kim D, Park SY, Ruoff RS, Lee H (2011) Simultaneous reduction and surface functionalization of graphene oxide by mussel-inspired chemistry. Adv Funct Mater 21:108–112

Kim E, Song IT, Lee S, Kim JS, Lee H, Jang JH (2012) Drawing sticky adeno-associated viruses on surfaces for spatially patterned gene expression. Angew Chem Int Ed Engl 51:5598–5601

Kim K, Ryu JH, Lee DY, Lee H (2013) Bio-inspired catechol conjugation converts water-insoluble chitosan into a highly water-soluble, adhesive chitosan derivative for hydrogels and LbL assembly. Biomater Sci 1:783–790

Ku SH, Park CB (2010) Human endothelial cell growth on mussel-inspired nanofiber scaffold for vascular tissue engineering. Biomaterials 31:9431–9437

Ku SH, Ryu J, Hong SK, Lee H, Park CB (2010a) General functionalization route for cell adhesion on non-wetting surfaces. Biomaterials 31:2535–2541

Ku SH, Lee JS, Park CB (2010b) Spatial control of cell adhesion and patterning through mussel-inspired surface modification by polydopamine. Langmuir 26:15104–15108

Lai M, Cai K, Zhao L, Chen X, Hou Y, Yang Z (2011) Surface functionalization of TiO2 nanotubes with bone morphogenetic protein 2 and its synergistic effect on the differentiation of mesenchymal stem cells. Biomacromolecules 12:1097–1105

Lee H, Scherer NF, Messersmith PB (2006) Single-molecule mechanics of mussel adhesion. Proc Natl Acad Sci U S A 103:12999–13003

Lee H, Dellatore SM, Miller WM, Messersmith PB (2007) Mussel-inspired surface chemistry for multifunctional coatings. Science 318:426–430

Lee H, Lee Y, Statz AR, Rho J, Park TG, Messersmith PB (2008) Substrate-independent layer-by-layer assembly by using mussel-adhesive-inspired polymers. Adv Mater 20:1619–1623

Lee H, Rho J, Messersmith PB (2009) Facile conjugation of biomolecules onto surfaces via mussel adhesive protein inspired coatings. Adv Mater 21:431–434

Lee BP, Messersmith PB, Israelachvili JN, Waite JH (2011) Mussel-inspired adhesives and coatings. Annu Rev Mater Res 41:99–132

Long Y, Wu J, Wang H, Zhang X, Zhao N, Xu J (2011) Rapid sintering of silver nanoparticles in an electrolyte solution at room temperature and its application to fabricate conductive silver films using polydopamine as adhesive layers. J Mater Chem 21:4875–4881

McCloskey BD, Park HB, Ju H, Rowe BW, Miller DJ, Chun BJ, Kin K, Freeman BD (2010) Influence of polydopamine deposition conditions on pure water flux and foulant adhesion resistance of reverse osmosis, ultrafiltration, and microfiltration membranes. Polymer 51:3472–3485

Min Z, Xihao Z, Xiwen H, Langxing C, Yukui Z (2010) Preparation and characterization of polydopamine-coated silver core/shell nanocables. Chem Lett 39:552–553

Natalio F, Andre R, Pihan SA, Humanes M, Wever R, Tremel W (2011) V2O5 nanowires with an intrinsic iodination activity leading to the formation of self-assembled melanin-like biopolymers. J Mater Chem 21:11923–11929

Poh CK, Shi Z, Lim TY, Neoh KG, Wang W (2010) The effect of VEGF functionalization of titanium on endothelial cells in vitro. Biomaterials 31:1578–1585

Pop-Georgievski O, Popelka Š, Houska M, Chvostová D, Proks V, Rypáček F (2011) Poly(ethylene oxide) layers grafted to dopamine-melanin anchoring layer: stability and resistance to protein adsorption. Biomacromolecules 12:3232–3242

Ren Y, Rivera JG, He L, Kulkarni H, Lee D-K, Messersmith PB (2011) Facile, high efficiency immobilization of lipase enzyme on magnetic iron oxide nanoparticles via a biomimetic coating. BMC Biotechnol 11:63

Ryoo H-I, Lee JS, Park CB, Kim D-P (2011) A microfluidic system incorporated with peptide/Pd nanowires for heterogeneous catalytic reactions. Lab Chip 11:378–380

Ryou M-H, Lee YM, Park J-K, Choi JW (2011) Mussel-inspired polydopamine-treated polyethylene separators for high-power Li-ion batteries. Adv Mater 23:3066–3070

Shin YM, Lee YB, Shin H (2011) Time-dependent mussel-inspired functionalization of poly(L-lactide-co-varepsilon-caprolactone) substrates for tunable cell behaviors. Colloids Surf B Biointerfaces 87:79–87

Spillman SD (2011) Increased cross-platform microarray data set correlation via substrate-independent nanofilms. Anal Chem 83:5592–5597

Sureshkumar M, Lee C-K (2011) Polydopamine coated magnetic-chitin (MCT) particles as a new matrix for enzyme immobilization. Carbohydr Polym 84:775–780

Sureshkumar M, Siswanto DY, Lee C-K (2010) Magnetic antimicrobial nanocomposite based on bacterial cellulose and silver nanoparticles. J Mater Chem 20:6948–6955

Tao C, Yang S, Zhang J, Wang J (2009) Surface modification of diamond-like carbon films with protein via polydopamine inspired coatings. Appl Surf Sci 256:294–297

Tao C, Zhang J, Yang S (2011) Preparation and biocompatibility of BSA monolayer on silicon surface. J Nanosci Nanotechnol 11:5068–5074

Waite JH (2008) Mussel power. Nat Mater 7:8–9

Wan Y, Zhang D, Wang Y, Qi P, Hou B (2011) Direct immobilisation of antibodies on a bioinspired architecture as a sensing platform. Biosens Bioelectron 26:2595–2600

Wang G, Huang H, Zhang G, Zhang X, Fang B, Wang L (2011) Dual amplification strategy for the fabrication of highly sensitive interleukin-6 amperometric immunosensor based on polydopamine. Langmuir 27:1224–1231

Wei Q, Zhang F, Li J, Li B, Zhao C (2010) Oxidant-induced dopamine polymerization for multifunctional coatings. Polym Chem 1:1430–1433

Ye W, Hu H, Zhang H, Zhou F, Liu W (2010) Multi-walled carbon nanotube supported Pd and Pt nanoparticles with high solution affinity for effective electrocatalysis. Appl Surf Sci 256:6723–6728

You I, Kang SM, Lee S, Cho YO, Kim JB, Lee SB, Nam YS, Lee H (2012) Polydopamine microfluidic system toward a two-dimensional, gravity-driven mixing device. Angew Chem Int Ed Engl 51:6126–6130

Zhu L-P, Yu J-Z, Xu Y-Y, Xi Z-Y, Zhu B-K (2009) Surface modification of PVDF porous membranes via poly(DOPA) coating and heparin immobilization. Colloids Surf B Biointerfaces 69:152–155

Chapter 15
Stimuli-Responsive Mussel-Inspired Polydopamine Material

Mikyung Shin, Younseon Wang, and Haeshin Lee

Abstract The first material-independent surface chemistry called polydopamine coating was introduced in Chap. 14. Surface properties for a given material can be controlled by the coating. Therefore, one can provide stimuli-responsiveness on a surface level by co-immobilization of chemical moieties that are sensitive to light, pH, temperature, or humidity when performing polydopamine coating. Alternatively, covalent conjugations of stimuli-responsive functional groups to dopamine hydrochloride result in preparations of series of dopamine derivatives. One-step coating of these derivatives becomes general methods to incorporating stimuli-responsive properties on virtually any material surfaces. This chapter provides detail information on this topic.

Keywords Polydopamine · Surface chemistry · Light-sensitive · pH-sensitive · Temperature-sensitive · Humidity-sensitive · Stimuli-responsiveness

15.1 Introduction

The first material-independent surface chemistry called polydopamine coating was introduced in 2007. It was inspired by the adhesive nature of catechols and amines in mussel adhesive proteins. For the materials versatility in surface functionalization ranging metal oxide, noble metals, low energy surfaces such as poly(tetrafluoroethylene), poly(dimethylsiloxane), polystyrene, poly(lactic-co-glycolic) acid, polycarbonate, polycaprolactone, graphene/graphene oxide, carbon nanotube, and various 3D porous materials, polydopamine has emerged as one of the most powerful tools available. Broad potentials in the biomedical, energy, consumer, industrial, military, and other sectors demonstrated by polydopamine coatings have been demonstrated. It is important to mention that polydopamine coating

---

M. Shin · Y. Wang · H. Lee (✉)
Department of Chemistry, Korea Advanced Institute of Science and Technology (KAIST), Daejeon, Republic of Korea
e-mail: haeshin@kaist.ac.kr

A. Hozumi et al. (eds.), *Stimuli-Responsive Dewetting/Wetting Smart Surfaces and Interfaces*, Biologically-Inspired Systems 11,
https://doi.org/10.1007/978-3-319-92654-4_15

often becomes a complementary tool with another well-known method called layer-by-layer deposition. For example, catechol or catecholamine moieties which are the building blocks of polydopamine, have been chemically tethered or end-functionalized to polymers for uses in layer-by-layer assembly.

There are important external stimuli such as temperature, pH, light, humidity, and others, and their chemical motifs can be adaptable with polydopamine. Thus, the stimuli-responsive properties can potentially be applied to any type of surface chemistry and any shapes of materials of not only flat substrates but nano-/micro-particles and 3D porous materials. In this chapter, we describe the current state of the art in polydopamine-mediated stimuli-sensitive coating methods by polydopamine itself or in the form of combination with polydopamine/layer-by-layer depositions.

15.2 Temperature Responsiveness *vs* Polydopamine

Polydopamine is a heterogeneous polymeric compound with a conjugated system composed of phenol rings or phenol-indole rings with alternating single (C-C) and double (C=C) bonds (Fig. 15.1a). In the conjugated system, the total electron resonance depends on the molecular weight distribution. Thus, polydopamine shows broad absorption across the entire range of light from the ultraviolet (UV)/visible

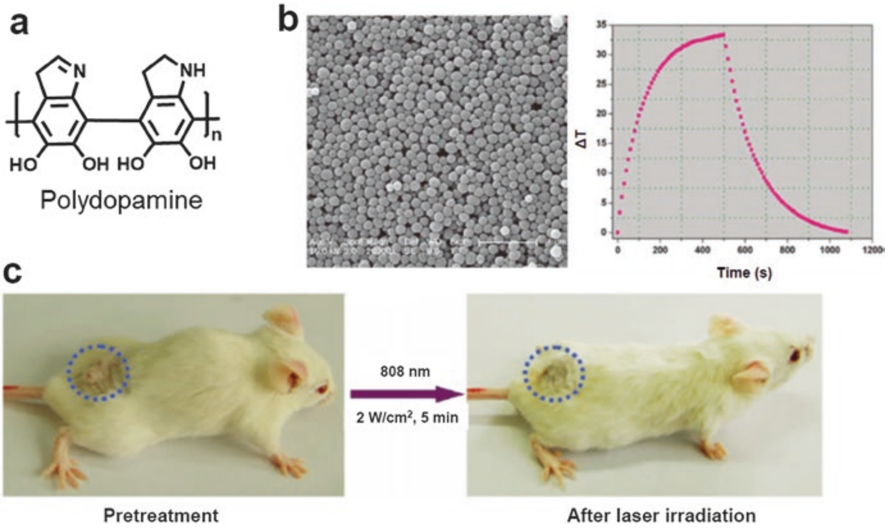

Fig. 15.1 (**a**) Chemical structure of polydopamine. (**b**) Size and morphology of polydopamine nanoparticles (left) and their heat generation properties under 808 nm laser irradiation (right). (**c**) Inhibition of tumor growth after intratumoral injection of polydopamine nanoparticles followed by laser irradiation. (Adapted with permission from Liu et al. (2013), copyright 2013 Wiley-VCH Verlag GmbH & Co. KGaA)

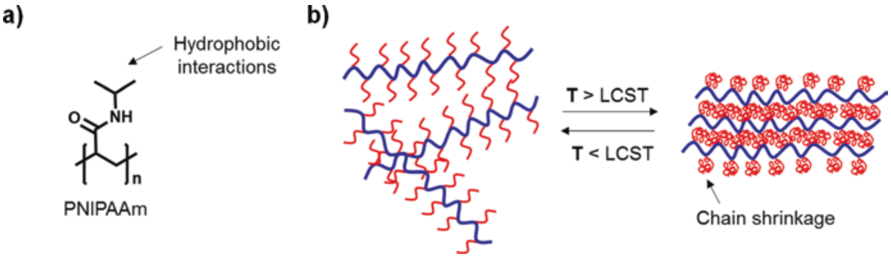

Fig. 15.2 (**a**) Chemical structure of PNIPAAm. (**b**) Schematic illustration of the dependence of the PNIPAAm chain mobility on the LCST

region to the near infrared (NIR) region. For this reason, the compound appears dark-brown or black color. It is true that the NIR absorption of polydopamine results in the generation of heat. In 2013, Lu et al. were the first to report NIR photothermal therapy using the heat generated by polydopamine (Liu et al. 2013). In this study, polydopamine nanoparticles with an average size of 70 nm were used for the photothermal treatment of tumors (Fig. 15.1b, left). The temperature of the nanoparticles increased up to approximately 58 °C after 500 seconds of irradiation by a 808 nm laser (Fig. 15.1b, right). After intratumoral injection, the heat generated by the nanoparticles efficiently inhibited tumor regrowth (Fig. 15.1c). Furthermore, after intravenous injection, the nanoparticles accumulated in the tumor sites without any long-term toxicity.

In this way, the heat generation capability of polydopamine under NIR irradiation is outstanding. Furthermore, these properties can be combined with a temperature-responsive system using conventional temperature-sensitive polymers, such as poly(N-isopropylacrylamide) (PNIPAAm) (Fig. 15.2a). For example, temperature-responsive PNIPAAm hydrogels can be simply designed. The temperature responsiveness of PNIPAAm is caused by the rapid phase separation from aqueous solution when the solution is heated to a critical temperature called the lower critical solution temperature (LCST). As the temperature gradually increases from ambient conditions, the polymeric chain mobility of PNIPAAm also increases. Simultaneously, the mobility of the water molecules solvating the side chains of isopropyl acrylamide increases. Above a critical temperature of 32 °C in pure water, the transient dissociation of water molecules close to the isopropyl groups occurs, which results in chain shrinkage of PNIPAAm through hydrophobic interactions between the isopropyl groups (Fig. 15.2b) (Hoffman 2013). Therefore, the PNIPAAm hydrogels exhibit temperature-responsive release profile of encapsulated compounds above the LCST.

Recently, Xiong Lu and colleagues introduced polydopamine nanoparticles into PNIPAAm hydrogel networks (Fig. 15.3a) (Han et al. 2016). This temperature/light sensitive controlled release system combined the polymeric temperature sensitivity and the NIR absorption of polydopamine followed by heat generation (Fig. 15.3b and 15.3c). The hydrogels showed phase transitions and volume shrinkage in response to NIR irradiation. The polydopamine nanoparticles acted as highly

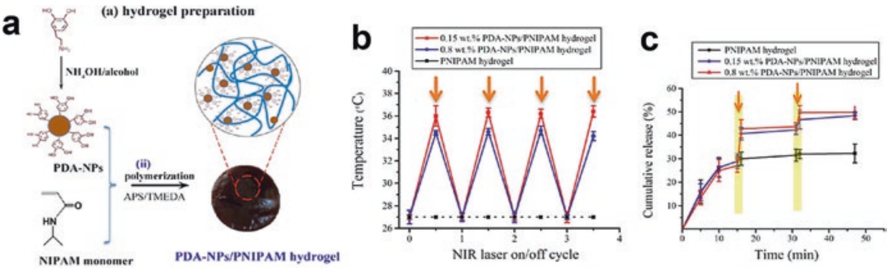

Fig. 15.3 (**a**) Schematic illustration of the polydopamine nanoparticle-incorporated PNIPAAm hydrogel system. (**b**) Temperature changes of the hydrogels as a function of the NIR irradiation ON/OFF cycle. (**c**) Profile of drug release from the hydrogels under NIR irradiation (yellow box) and without the laser. (Adapted with permission from Han et al. (2016), copyright 2016 American Chemical Society)

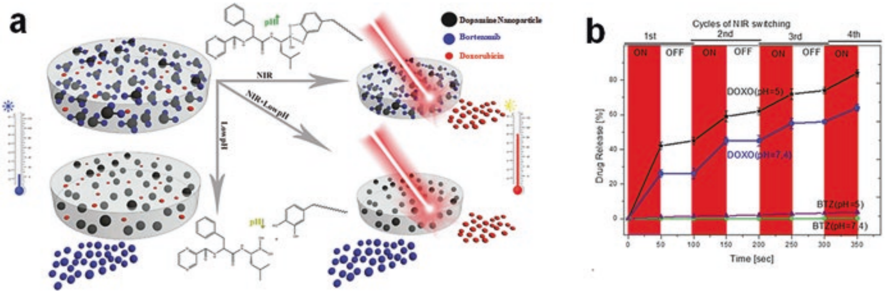

Fig. 15.4 (**a**) Multiple stimuli (pH and NIR)-responsive polydopamine/PNIPAAm-co-PAAm hydrogels for dual drug release. (**b**) Profile of dual drug release from the hydrogel stimulated by an acidic pH (pH 5) or NIR irradiation. (Adapted with permission from GhavamiNejad et al. (2016a), copyright 2016 Springer Nature)

effective internal heat generating agents, providing bioactive adhesion sites for cell attachment, growth factor immobilization, and tissue adhesion.

Furthermore, it has been reported that polydopamine nanoparticles incorporated in PNIPAAm-co-poly(acrylamide) (PAAm) hydrogels exhibited a new trend in the drug release profile (GhavamiNejad et al. 2016a). For stimuli-responsive dual drug delivery, two different drugs, doxorubicin and bortezomib (BTZ), were encapsulated in the hydrogels (Fig. 15.4a). The boronate in BTZ was bound to the catechol groups (main adhesive moieties) displayed on the polydopamine nanoparticles, which were incorporated into the hydrogel network. Unbound doxorubicin was also spontaneously loaded in the hydrogel through its swelling properties. Under NIR irradiation, the heat generated by the polydopamine nanoparticles caused shrinkage of the polymer chains, releasing the doxorubicin because it was not bound to the nanoparticles (Fig. 15.4b). In addition, BTZ was gradually released in acidic conditions (pH 5) through the pH-dependent dissociation of the bond between the catechol and boronate.

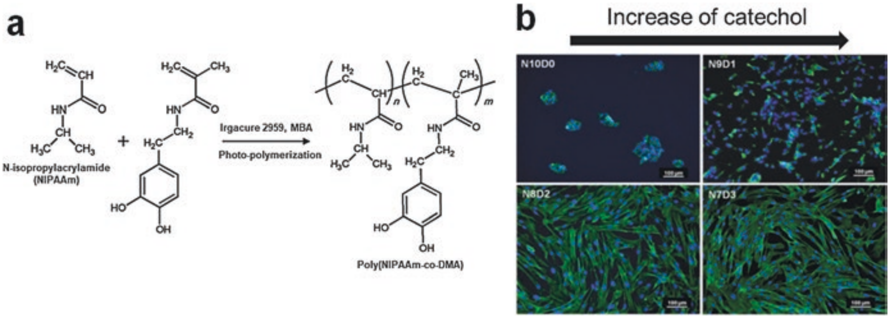

Fig. 15.5 (**a**) Synthesis of the copolymer, PNIPAAm, containing catechol (PNIPAAm-Ca). (**b**) Increase in cell attachment to the surface of the PNIPAAm-Ca hydrogels depending on catechol content. (Adapted with permission from Kim et al. (2016a), copyright 2015 Royal Society of Chemistry)

In addition to the studies focused on the catechol groups of polydopamine nanoparticles, important adhesive moieties of polydopamine have been directly conjugated to a variety of temperature-responsive polymers (Ai et al. 2014; Kim et al. 2016a; Vatankhah-Varnoosfaderani et al. 2014; GhavamiNejad et al. 2016b). For example, PNIPAAm hydrogels containing catechol (PNIPAAm-Ca) were synthesized by free radical photo-polymerization (Fig. 15.5a) (Kim et al. 2016a). In this study, the hydrogel showed unique properties of enhanced mechanical strength and improved cell attachment and spreading on the surface (Fig. 15.5b). The increase in the number of catechol groups present in the hydrogels also decreased the inherent LCST and swelling ratio of PNIPAAm.

Furthermore, the hydrogels using PNIPAAm-Ca and poly(ethylene glycol) triacrylate showed dense crosslinking at 37 °C, wet-resistant adhesion, and biocompatibility (Ai et al. 2014). The mechanical strength of these temperature-responsive catechol-containing hydrogels could be enhanced by introducing additives such as reduced graphene oxide, which interacted with the polar groups of the polymeric chains via hydrogen bonds (GhavamiNejad et al. 2016b). Similarly to the study on the polydopamine-incorporated system for dual drug release by multiple stimuli (GhavamiNejad et al. 2016a), PNIPAAm-Ca can form a cis-diol/boron complex with boron-containing compounds (i.e., H_3BO_3), resulting in gelation (Vatankhah-Varnoosfaderani et al. 2014). The hydrogels respond to both temperature and pH due to the catechol-boron intermolecular interactions.

Other widely used temperature-sensitive polymers are the block copolymers of poly(propylene oxide)-poly(ethylene oxide) (PPO-PEO). In general, the PPO blocks are physically associated through intermolecular hydrophobic interactions. When the temperature gradually increases, the PPO blocks drive sol-to-gel transitions, and the PEO blocks undergo dehydration followed by gelation. Thus, tethering catechols onto the amphiphilic block copolymers can impart temperature responsiveness as well as interfacial adhesion and cohesive cross-linking functions (Fig. 15.6) (Barrett et al. 2013). Although the polymeric solution was prepared at or

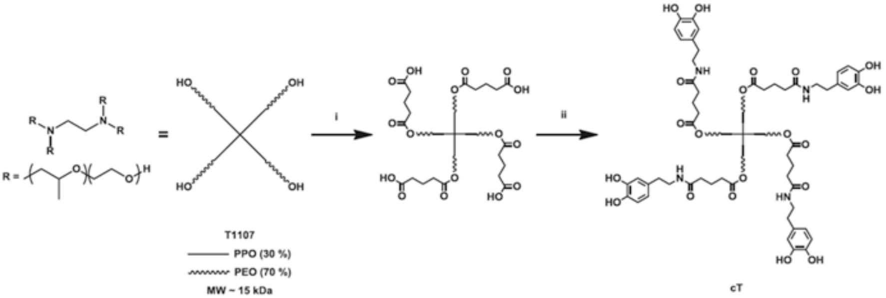

Fig. 15.6 Catechol-tethered PPO-PEO copolymers. (Adapted with permission from Barrett et al. (2013), copyright 2013 Wiley-VCH Verlag GmbH & Co. KGaA)

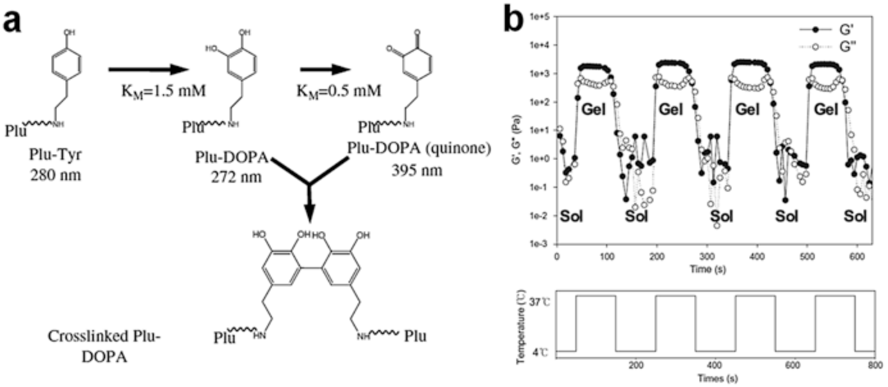

Fig. 15.7 (**a**) Crosslinking of catechol-conjugated Pluronic through an enzymatic reaction. (**b**) Temperature-reversible sol-gel transition of the Pluronic-catechol hydrogels over four cycles of alternating the temperature between 4 and 37 °C. (Adapted with permission from Lee et al. (2011), copyright 2010 Elsevier Ltd)

below room temperature, gelation occurred through catechol oxidation. Moreover, at physiological temperature (37 °C), the gels exhibited volume shrinkage, improved toughness compared to the analogous PEO-based gels, and wet-resistant tissue adhesiveness derived from the catechol groups.

The catechol groups can also be conjugated with another form of PEO-PPO-PEO triblock copolymers, such as Pluronic. Park et al. reported a variety of drug delivery formulations of micelles and hydrogels using catechol-conjugated Pluronic prepared by enzyme-mediated reactions (Lee et al. 2011). In that study, when Pluronic was tethered to tyramine instead of catechol groups, tyrosinase-mediated oxidative conversion from tyrosine to dopa/dopaquinone resulted in temperature-responsive formulations (Fig. 15.7a). These hydrogels showed reversible sol-gel transitions as the temperature was alternated between 4 and 37 °C (Fig. 15.7b). In addition, substantial erosion followed by controlled release of the macromolecules was observed as a function of time.

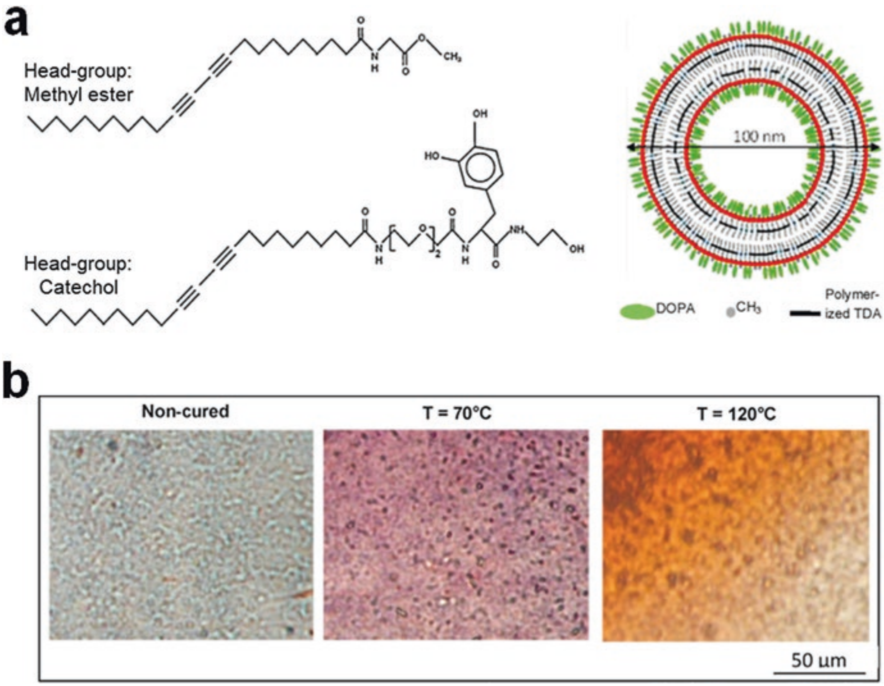

Fig. 15.8 (**a**) Chemical structure of peptide amphiphiles containing head groups of methyl ester or catechol (left), and schematic illustration of their vesicular structure (right). (**b**) Colorimetric changes of the vesicles after heating. (Adapted with permission from Samyn et al. (2014), copyright 2013 Elsevier Ltd.)

To design temperature-sensitive and bioadhesive polymers, catechols were terminally tethered as side chains to hyperbranched poly(amino acid)s (Lu et al. 2016). Pluronic was used as an initiator for the polymerization, resulting in temperature sensitivity. The adhesive strength of these copolymers increased at physiological temperature (37 °C) as a function of time and remained constant after 720 min. Moreover, the polymers showed enzymatic degradability and non-cytotoxicity.

There is one interesting approach in which catechol-functionalized polymeric vesicles showed colorimetric sensing properties that responded to changes in the temperature (Samyn et al. 2014). These vesicles were synthesized by photoinduced polymerization of amphiphilic monomers containing a tail of diacetylenic acid with a head group of methyl ester or catechol (Fig. 15.8a). Although the color changes after heating from 30 to 120 °C mainly resulted from the polymerized diacetylenes (Fig. 15.8b), the presence of the catechol head affected the vesicular stability and led to an irreversible color transition by adhesion. This study shows a fundamental and stable sensing concept using catechol-based interfacial adhesion.

In addition, another interesting approach using catechol adhesion and temperature responsiveness is the biomimetic adhesion inspired by the adhesion of mussels and the gluing mechanism of sandcastle worms (Shao and Stewart 2010). The

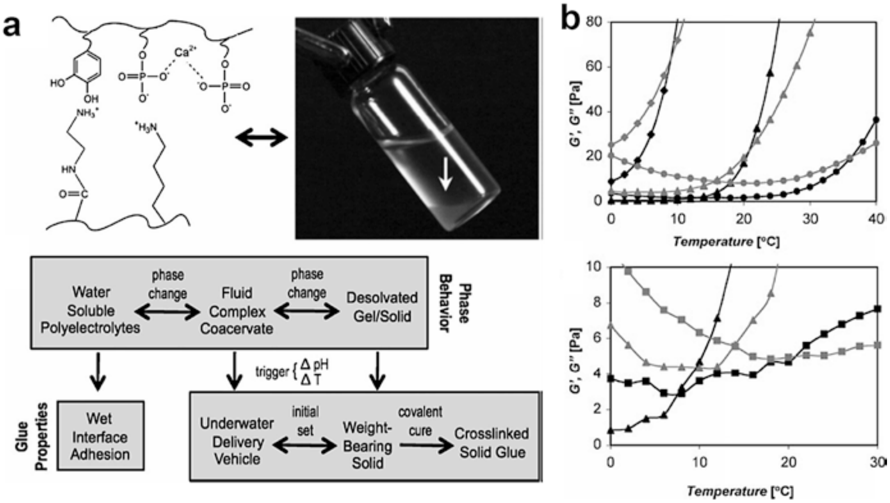

Fig. 15.9 (**a**) Complex coacervate composed of catechol-tethered polyphosphate and aminated gelatin and its phase transition diagram. (**b**) Temperature-dependent phase transitions of the complexes containing calcium ions (top) or magnesium ions (bottom). (Adapted with permission from Shao and Stewart (2010), copyright 2013 Wiley-VCH Verlag GmbH & Co. KGaA)

sandcastle worm is assembled using a proteinaceous adhesive composed of oppositely charged proteins and cations. Thus, catechol-tethered polyelectrolytes can show strong adhesion properties. Stewart et al. reported complex adhesion based on catechol-tethered polyphosphate, polyaminated gelatin, and cations (i.e., Ca^{2+} and Mg^{2+}) (Fig. 15.9a). The authors found that the complex showed a pH-dependent phase transition from a water-soluble polyelectrolyte to a coacervate (at pH 5.0) and a hydrogel (at pH 7.4). In addition, with increases in the cation-to-polyphosphate ratios (to Ca^{2+} ratios greater than 0.15 and Mg^{2+} ratios greater than 0.8), a temperature-dependent phase change was observed. Although the details of the cation ratio are dependent on the type of cation, the sol-to-gel crossover temperature decreased with increasing cation ratio (Fig. 15.9b). This study demonstrated for the first time that a catechol/cation/polyelectrolyte complex exhibits both strong wet-adhesion and temperature-dependent phase transitions analogous to those of typical temperature-responsive polymers.

All of these studies demonstrate that the catechol-polymerized form of polydopamine enhances the heat generation in response to light, and catechol-conjugated temperature-sensitive polymers exhibit sol-gel transitions as well as mussel-inspired adhesive properties as a function of temperature. The degree of catechol conjugation affects the inherent LCST of the temperature-responsive polymer. In addition, the covalent crosslinking of dicatechol results in a dense polymeric network and a low swelling ratio of the hydrogels.

15.3 Light-Responsive Mussel-Inspired Polydopamine

As mentioned in the previous section, polydopamine has a π-π conjugated system that absorbs all light from the UV region to the visible and NIR regions, resulting in charge transfer and semi-conducting properties (Liu et al. 2013). Thus, polydopamine can be useful for developing photoresponsive/optoelectronic devices (Nam et al. 2014). In 2014, a study on mussel-inspired organic phototransistors based on a polydopamine thin film was reported for the first time (Fig. 15.10a). The phototransistor exhibited a high photoresponsivity upon light irradiation as well as high photocurrent generation at low voltage (Fig. 15.10b).

Similarly to the strategies for temperature-responsive systems, catechol can be introduced into the polymeric backbone through light-triggered polymerization or degradation. For example, catechol and acrylate-containing poly(ethylene glycol) (PEG)-based polymers were crosslinked via a free radical mechanism with UV irradiation, resulting in bioadhesives (Zhang et al. 2015). In addition, polymers contain-

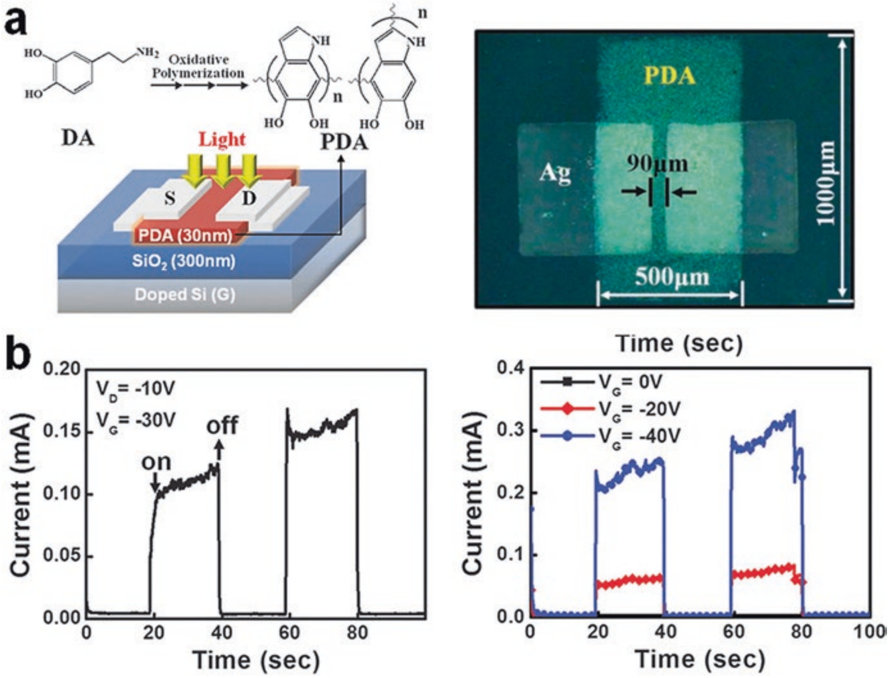

Fig. 15.10 (**a**) Mussel-inspired phototransistor consisting of a polydopamine thin film coated on a Si/SiO$_2$ substrate. (**b**) Photoresponse of the phototransistor to light irradiation for 20 seconds (left). Photoswitching properties at a constant drain voltage as a function of the gate voltage for 20 seconds. (Adapted with permission from Nam et al. (2014), copyright 2013 Royal Society of Chemistry)

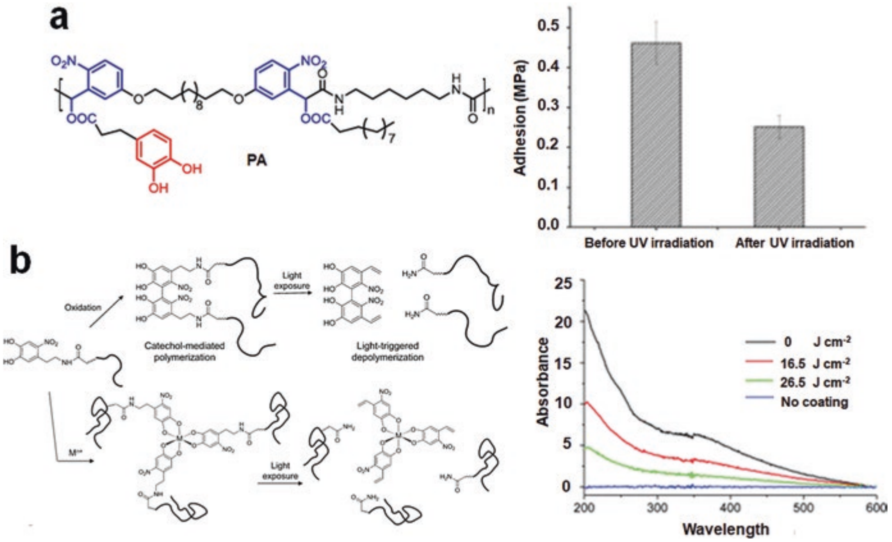

Fig. 15.11 (**a**) Chemical structure of a catechol-containing UV-dismantlable adhesive (left) and its adhesive force after UV irradiation. (Adapted with permission from (Wang et al. 2015), copyright 2015 Elsevier Ltd.) (**b**) Chemical bonding induced by oxidation of catechol, the coordination complex between catechol and a metal, and debonding under light irradiation. (Adapted with permission from Shafiq et al. (2012), copyright 2012 Wiley-VCH Verlag GmbH & Co. KGaA)

ing o-nitrobenzyl ester linkages and catechol groups exhibited adhesiveness and UV-induced cleavable properties (Fig. 15.11a) (Wang et al. 2015). Nitrodopamine, one of the catechol derivatives, has a photocleavable functional group in the form of the o-nitrophenyl ethyl moiety. Thus, catechol-mediated polymerization as well as light-triggered degradation properties were observed (Fig. 15.11b) (Shafiq et al. 2012). Biocompatible materials with wide uses in multiple medical applications have been actively developed to date.

White et al. also reported that a polyacrylamide hydrogel with catechol-metal coordination bonds and diphenyliodonium chloride as a photoacid generator showed a sol-gel transition in response to UV light (Fig. 15.12) (White et al. 2013).

A photoresponsive copolymer containing catechol and azobenzene derivatives has been developed. The azo compound exhibited cis-trans conformational changes under UV exposure. Thus, these catechol/azo functional group-incorporated materials could be used for surface-independent modification capable of controlling the sliding and adhesion states of water droplets with light (Fig. 15.13) (Wu et al. 2014).

Furthermore, there is another interesting study using catechol-containing methacrylates (Kim et al. 2016b). In this study, the polymer was carbonized under strongly acidic conditions, forming fluorescent nanoparticles (Fig. 15.14). The catechol groups displayed on the nanoparticles interacted with TiO_2 via coordination bonds, which increased the photocatalytic activity of TiO_2 due to formation of a

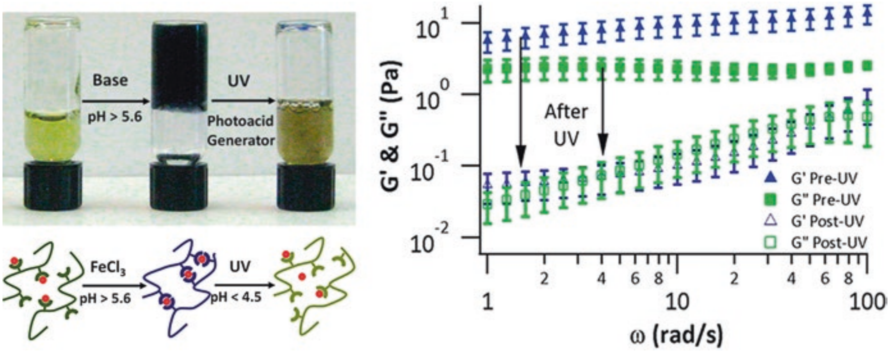

Fig. 15.12 UV-triggered sol-gel transition of a polyacylamide-catechol hydrogel containing the photoacid generator diphenyliodonium chloride. (Adapted with permission from White et al. (2013), copyright 2013 American Chemical Society)

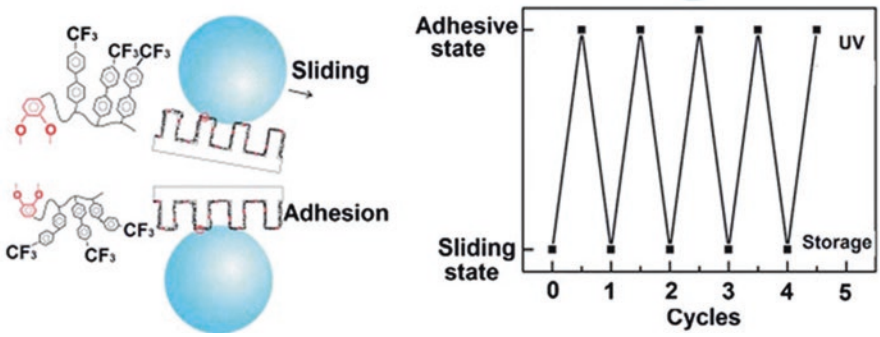

Fig. 15.13 Schematic illustration of the water droplet sliding motion during the adhesive state transformation of catechol-containing photoresponsive polymers and interchangeable cycles of the state. (Adapted with permission from Wu et al. (2014), copyright 2014 Royal Society of Chemistry)

large band gap through the catechol coordination. This study also showed changes in the light responsiveness through catechol-involved reactions.

Tyrosine is a biological amino acid precursor for forming catechol residues (i.e., Dihydroxyphenylalanine (DOPA). The enzymatic reaction is a representative of the mechanism for the conversion of tyrosine to DOPA. In addition to the enzyme-mediated reaction, the photomediated oxidation of tyrosine is also possible (Tanaka and Iwasaki 2016). Thus, the photooxidation of tyrosine to DOPA and the newly generated ability to adhere onto the substrate can be useful for biomolecular patterning with light irradiation (Fig. 15.15).

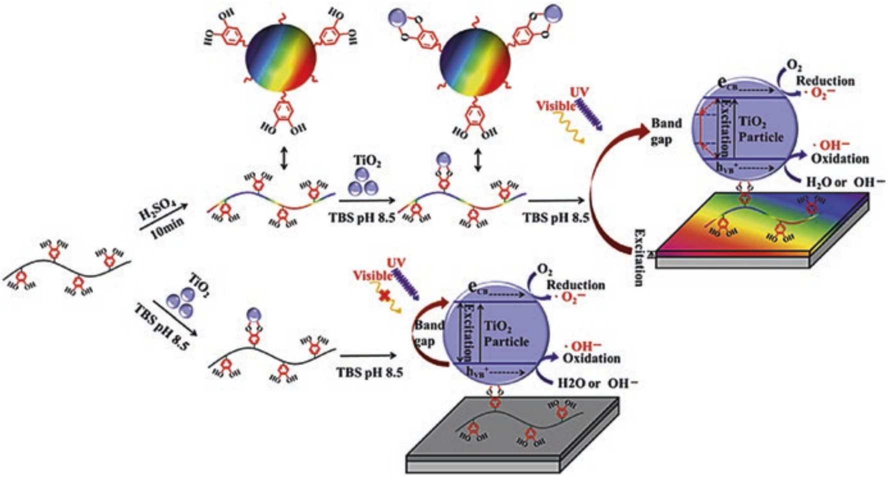

Fig. 15.14 Schematic illustration of the energy position and visible light photocatalytic mechanism of the catechol-methacrylate fluorescent/TiO_2 surface under visible light irradiation. (Adapted with permission from Kim et al. (2016b), copyright 2016 Elsevier Ltd.)

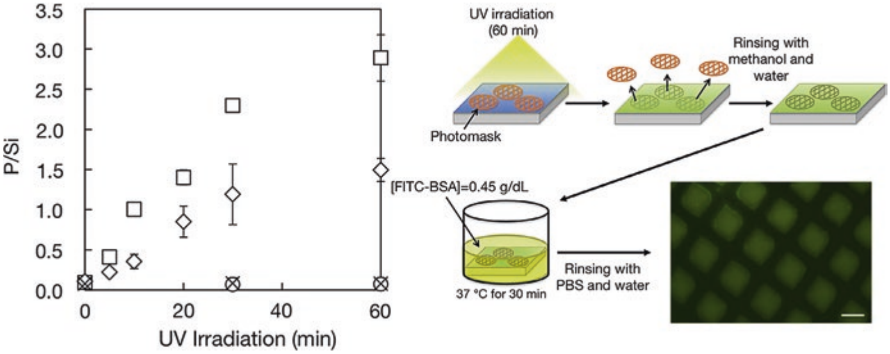

Fig. 15.15 Increase in the phosphorus composition by adhesion of zwitterionic 2–methacryloyloxyethyl phosphorylcholine (MPC)-DOPA polymers as a function of UV irradiation time (left). Photoassisted preparation of protein microarrays and a fluorescence image exhibiting the patterned adsorption of fluorescein-tagged albumin. (Adapted with permission from Tanaka and Iwasaki (2016), copyright 2016 Elsevier Ltd.)

15.4 Humidity-Sensitive and Responsive Materials

Polydopamine can be coated on the surface of any material to change its physical and chemical properties. Hydrophobic surfaces modified with polydopamine become hydrophilic, which improves the wettability of the surface. For example, gold nanoparticles are one of the promising materials for chemical and biochemical sensors due to their larger surface-to-volume ratio relative to that of other materials.

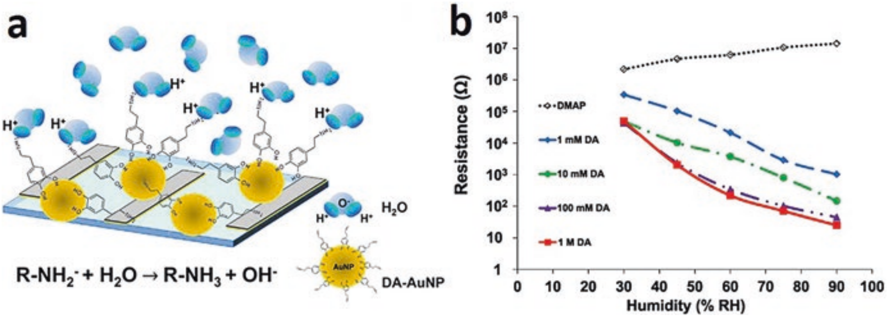

Fig. 15.16 (**a**) Enhancement of moisture adsorption via introduction of a polydopamine coating on gold nanoparticles (Au NPs). (**b**) Resistance of the humidity sensor coated with Au NPs modified with different concentrations of dopamine. (Adapted with permission from Lee et al. (2014), copyright 2013 Elsevier Ltd.)

However, the hydrophobic surface of gold nanoparticles should be modified with hydrophilic molecules to be used as humidity-sensing materials (Lee et al. 2014). When polydopamine is coated on gold nanoparticles, the amine groups and hydroxyl groups of polydopamine can interact with water via hydrogen bonds (Fig. 15.16a). As a result, the enhanced affinity for water from the polydopamine coating provides the humidity sensor with more sensitive performance. In addition, the sensitivity improves as the concentration of dopamine increases (Fig. 15.16b), which means that the interior of the polydopamine layer as well as its surface interacts with water molecules by absorbing moisture.

The hydration of the polydopamine layer imparts conductive properties. The structure of polydopamine is similar to that of eumelanin, a natural bio-pigment in the human body, which is a heterogeneous macromolecule composed of oligomeric and polymeric indol units of 5,6-dihydroxyindole (DHI) and 5,6-dihydroxyindole-2-carboxylic acid (DHICA) monomers (d'Ischia et al. 2013). This indole-connected form is similar to the structure of polyindole, which is a conductive polymer. As a result, eumelanin shows the characteristics of a semiconductor under thermal, light, and moisture stimuli (Capozzi et al. 2006; Baraldi et al. 1979; Mostert et al. 2012). Like eumelanin, polydopamine also exhibits semiconductor properties when exposed to moisture. The polydopamine film was formed at the air/solution interface with the aid of a base such as aniline or under high pH conditions rather than mild pH conditions. The strong alkaline conditions reduce the aggregation of the polydopamine oligomers during the synthesis of polydopamine and generate a structure more similar to that of polyindole (Wu et al. 2015; Wu and Hong 2016). When the interfacial film was transferred onto gold electrodes (Fig. 15.17a), the polydopamine thin film showed different conductivities based on the degree of hydration and the thickness of the film. The resistance of the electrode was reduced by increasing the humidity, which means that increased hydration provided higher conductivity (Fig. 15.17b). In addition, the humidity sensor modified with the polydopamine thin film exhibited ultrasensitive responses with a response time of 5–7 s

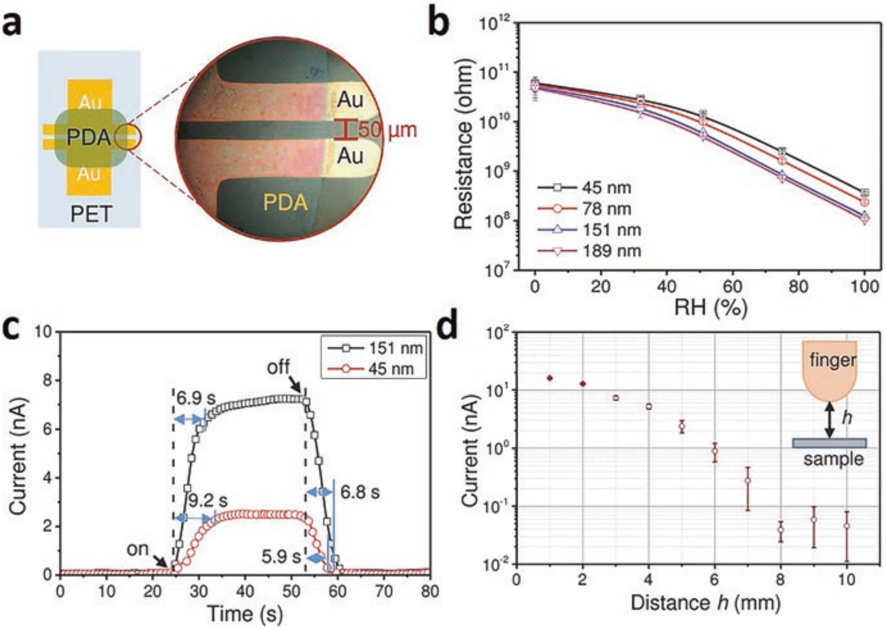

Fig. 15.17 (**a**) Polydopamine thin film transferred onto gold electrodes. (**b**) Changes in the resistance for different thicknesses of the polydopamine film as a function of the relative humidity (RH). (**c**) Response and recovery times of humidity sensors with different film thicknesses (black: 151 nm and red: 45 nm). (**d**) Changes in the current as a function of the distance between the fingertip and the polydopamine film. (Adapted with permission from Wu et al. (2015), copyright 2015 WILEY-VCH Verlag GmbH & Co. KGaA, Weinheim)

and a recovery time of 6–9 s (Fig. 15.17c). These characteristics are superior to the those of humidity sensors composed of inorganic materials, such as VS_2 nanosheets (response and recovery times of 30–40 and 12–50 s, respectively) and SnO_2 nanowires (response and recovery times of 120–170 and 20–60 s, respectively). This ultrasensitive humidity sensor can be applied as a touchless position sensor (Fig. 15.17d).

The conductivity of polydopamine results from oxidation of the dopamine molecules as well as the structure of polydopamine (Wünsche et al. 2015). DHI, the hydroquinone form of oxidized dopamine, can be reversibly oxidized to quinone imine (QI) (Fig. 15.18a). Both electrons and protons can be transported in the hydrated polydopamine film during the reversible redox reaction. The protons migrate and accumulate at the negative electrode under the presence of an electric field, which creates a pH gradient between the electrodes. The semiquinone (SQ^-) species near the positive electrode are oxidized by the pH gradient (Fig. 15.18b). As a result, the current of the Pd electrode increases more when both electrons and protons are provided by exposure to H_2 than when only electrons are provided (Fig. 15.18c).

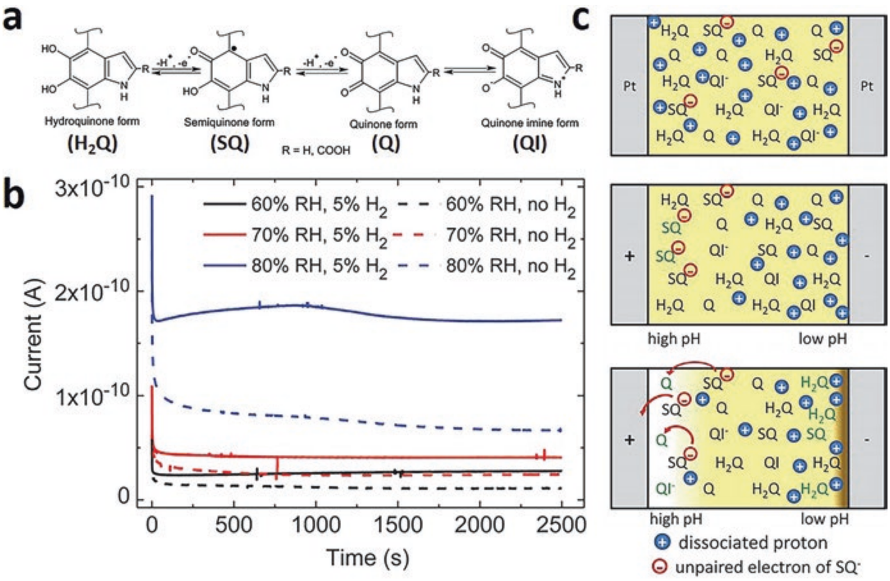

Fig. 15.18 (**a**) Different redox forms of the DHI intermediates during the formation of polydopamine. (**b**) Illustration of the migration of the various redox forms of DHI and protons between electrodes and the oxidation of SQ^- by the pH gradient. (**c**) Changes in the current at different relative humidities (black lines: 60%, red lines: 70%, and blue lines: 80%) with H_2 gas treatment (with H_2 gas: solid lines and without H_2 gas: dotted lines). (Adapted with permission from Wünsche et al. (2015), copyright 2015 American Chemical Society)

The hydroscopic nature of polydopamine particles causes reversible changes in the structural coloration of the polydopamine layer with changes in the humidity (Xiao et al. 2016). In nature, some materials (e.g., butterfly scales, bird feathers, and beetle elytra) undergo structural changes in their nanostructures for camouflage in response to external stimuli (i.e., changes in the environment). Similarly, the arrangement of self-assembled polydopamine particles changes as the polydopamine layer absorbs different amounts of moisture in response to changes in the humidity (Fig. 15.19a). The swelling of the polydopamine particles causes their rearrangement and structural change, which results in changes in the refractive index. Polydopamine films with different colors can be prepared, as the thicknesses of (274 ± 11) nm and (602 ± 17) nm give blue and red films, respectively. When the humidity increases from 10% to 90%, the blue and red films turn green (Fig. 15.19b). The original color of the polydopamine layer is recovered when the humidity is reduced to 10%. The dynamic color changes of the polydopamine layer occur quickly (within 20 s), allowing for its application as a humidity sensor based on the optical properties (Fig. 15.19c).

In addition, the humidity affects the interactions between the catechol functional groups and transition metals (Tofan-Lazar et al. 2013). The absorbance of the adsorbed catechol molecules on a 1% solid $FeCl_3$ surface was measured under a gas

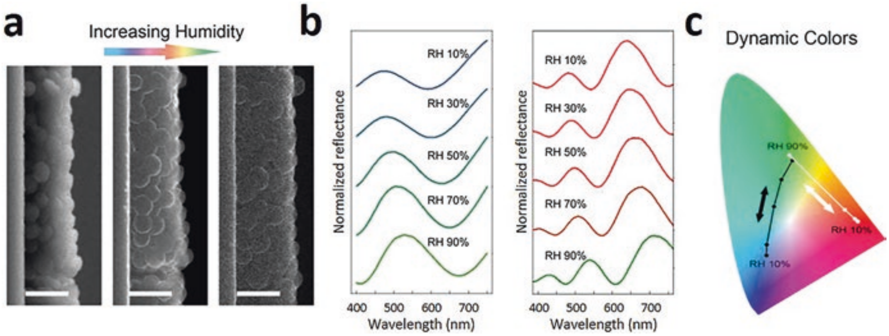

Fig. 15.19 (**a**) Thickness and arrangement of a polydopamine film depending on the humidity. (**b**) Absorbance of visible light by the polydopamine film according to changes in the relative humidity. (**c**) Dynamic color change of the polydopamine film over a wide range of relative humidity changes. (Adapted with permission from Xiao et al. (2016), copyright 2016 American Chemical Society)

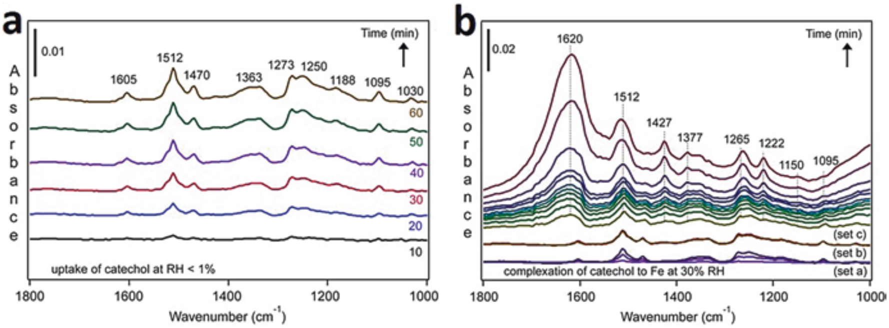

Fig. 15.20 (**a**) Absorbance of catechols adsorbed on solid $FeCl_3$ under a gas atmosphere (RH < 1%). (**b**) Absorbance of catechols interacting with the surface of $FeCl_3$ under 30% RH. (Adapted with permission from Tofan-Lazar et al. (2013), copyright 2013 American Chemical Society)

atmosphere (i.e., dry conditions, RH < 1%) and 30% RH (Fig. 15.20a, b) for 1 hour. Fig. 15.20a shows that Fe(III) could not form complexes with catechol because the catechol was protonated and could only molecularly adsorb to the $FeCl_3$ surface under the gas atmosphere (dry conditions). On the other hand, the peaks of catechol below 1600 cm^{-1} in Fig. 15.20b increased because the surface water improved the mobility of Fe(III) and helped to form the catechol-Fe complex. As a result, the interfacial water under humid conditions facilitated the interaction between catechol molecules and transition metal complexes and stabilized the catechol-metal complex via hydrogen bonding networks at the gas/solid interface. These results can help to explain the interfacial chemistry between catechol functional groups of the proteins in marine creatures and the wet surface with transition metals.

15.5 Conclusion

In this chapter, a variety of functionalization techniques regarding incorporation of polydopamine-based stimuli-responsive at a surface level were explained. Interface functionalizations of polydopamine for photothermal therapy (light responsiveness), catechol/azo conjugates for water sliding surface, and surface patternings by tyrosine-to-dopa oxidation by light illuminations are introduced. The authors envision that it is likely that the family of polydopamine and related coatings will be widely implemented in biomedical, energy, consumer products, agricultural, military and other sectors. Finally, important challenges facing the field in the future are better understanding of polydopamine formation mechanisms and elucidation of the chemical structure of polydopamine, enhancement of mechanical robustness of polydopamine.

References

Ai Y, Nie J, Wu G, Yang D (2014) The DOPA-functionalized bioadhesive with properties of photocrosslinked and thermoresponsive. J Appl Polym Sci 131:41102

Baraldi P, Capelletti R, Crippa PR, Romeo N (1979) Electrical characteristics and electret behavior of melanin. J Electrochem Soc 126:1207–1212

Barrett DG, Bushnell GG, Messersmith PB (2013) Mechanically robust, negative-swelling, mussel-inspired tissue adhesives. Adv Healthc Mater 2:745–755

Capozzi V, Perna G, Carmone P, Gallone A, Lastella M, Mezzenga E, Quartucci G, Ambrico M, Augelli V, Biagi PF, Ligonzo T, Minafra A, Schiavulli L, Pallara M, Cicero R (2006) Optical and photoelectronic properties of melanin. Thin Solid Films 511-512:362–366

d'Ischia M, Wakamatsu K, Napolitano A, Briganti S, Garcia-Borron JC, Kovacs D, Meredith P, Pezzella A, Picardo M, Sarna T, Simon JD, Ito S (2013) Melanins and melanogenesis: methods, standards, protocols. Pigment Cell Melanoma Res 26:616–633

GhavamiNejad A, SamariKhalaj M, Aguilar LE, Park CH, Kim CS (2016a) pH/NIR light-controlled multidrug release via a mussel-inspired nanocomposite hydrogel for chemo-photothermal cancer therapy. Sci Rep 6:33594

GhavamiNejad A, Hashmi S, Vatankhah-Varnoosfaderani M, Stadler FJ (2016b) Effect of H2O and reduced graphene oxide on the structure and rheology of self-healing, stimuli responsive catecholic gels. Rheol Acta 55:163–176

Han L, Zhang Y, Lu X, Wang K, Wang Z, Zhang H (2016) Polydopamine nanoparticles modulating stimuli-responsive PNIPAM hydrogels with cell/tissue adhesiveness. ACS Appl Mater Interfaces 8:29088–29100

Hoffman AS (2013) Stimuli-responsive polymers: biomedical applications and challenges for clinical translation. Adv Drug Deliv Rev 65:10–16

Kim Y-J, Tachibana M, Umezu M, Matsunaga YT (2016a) Bio-inspired smart hydrogel with temperature-dependent properties and enhanced cell attachment. J Mater Chem B 4:1740–1746

Kim YK, Sharker SM, In I, Park SY (2016b) Surface coated fluorescent carbon nanoparticles/TiO2 as visible-light sensitive photocatalytic complexes for antifouling activity. Carbon 103:412–420

Lee SH, Lee Y, Lee SW, Ji HY, Lee JH, Lee DS, Park TG (2011) Enzyme-mediated cross-linking of Pluronic copolymer micelles for injectable and in situ forming hydrogels. Acta Biomater 7:1468–1476

Lee H-C, Wang C-Y, Lin C-H (2014) High-performance humidity sensors utilizing dopamine biomolecule-coated gold nanoparticles. Sensors Actuators B Chem 191:204–210

Liu Y, Ai K, Liu J, Deng M, He Y, Lu L (2013) Dopamine-melanin colloidal nanospheres: an efficient near-infrared photothermal therapeutic agent for in vivo cancer therapy. Adv Mater 25:1353–1359

Lu D, Zhang Y, Li T, Li Y, Wang H, Shen Z, Wei Q, Lei Z (2016) The synthesis and tissue adhesiveness of temperature-sensitive hyperbranched poly(amino acid)s with functional side groups. Polym Chem 7:1963–1970

Mostert AB, Powell BJ, Pratt FL, Hanson GR, Sarna T, Gentle IR, Meredith P (2012) Role of semiconductivity and ion transport in the electrical conduction of melanin. Proc Natl Acad Sci U S A 109:8943–8947

Nam HJ, Cha J, Lee SH, Yoo WJ, Jung DY (2014) A new mussel-inspired polydopamine phototransistor with high photosensitivity: signal amplification and light-controlled switching properties. Chem Commun (Camb) 50:1458–1461

Samyn P, Shroff K, Prucker O, Rühe J, Biesalski M (2014) Colorimetric sensing properties of catechol-functional polymerized vesicles in aqueous solution and at solid surfaces. Colloids Surf A Physicochem Eng Asp 441:242–254

Shafiq Z, Cui J, Pastor-Perez L, San Miguel V, Gropeanu RA, Serrano C, del Campo A (2012) Bioinspired underwater bonding and debonding on demand. Angew Chem Int Ed Engl 51:4332–4335

Shao H, Stewart RJ (2010) Biomimetic underwater adhesives with environmentally triggered setting mechanisms. Adv Mater 22:729–733

Tanaka M, Iwasaki Y (2016) Photo-assisted generation of phospholipid polymer substrates for regiospecific protein conjugation and control of cell adhesion. Acta Biomater 40:54–61

Tofan-Lazar J, Situm A, HA A-A (2013) DRIFTS studies on the role of surface water in stabilizing catechol-iron(III) complexes at the gas/solid interface. J Phys Chem A 117:10368–10380

Vatankhah-Varnoosfaderani M, Hashmi S, GhavamiNejad A, Stadler FJ (2014) Rapid self-healing and triple stimuli responsiveness of a supramolecular polymer gel based on boron–catechol interactions in a novel water-soluble mussel-inspired copolymer. Polym Chem 5:512–523

Wang Y-Z, Li L, Du F-S, Li Z-C (2015) A facile approach to catechol containing UV dismantlable adhesives. Polymer 68:270–278

White EM, Seppala JE, Rushworth PM, Ritchie BW, Sharma S, Locklin J (2013) Switching the adhesive state of catecholic hydrogels using phototitration. Macromolecules 46:8882–8887

Wu T-F, Hong J-D (2016) Synthesis of water-soluble dopamine–melanin for ultrasensitive and ultrafast humidity sensor. Sensors Actuators B Chem 224:178–184

Wu Y, Liu Z, Liang Y, Pei X, Zhou F, Xue Q (2014) Photoresponsive superhydrophobic coating for regulating boundary slippage. Soft Matter 10:5318–5324

Wu T-F, Wee B-H, Hong J-D (2015) An ultrasensitive and fast moisture sensor based on self-assembled dopamine–melanin thin films. Adv Mater Interfaces 2:1500203

Wünsche J, Deng Y, Kumar P, Di Mauro E, Josberger E, Sayago J, Pezzella A, Soavi F, Cicoira F, Rolandi M, Santato C (2015) Protonic and electronic transport in hydrated thin films of the pigment eumelanin. Chem Mater 27:436–442

Xiao M, Li Y, Zhao J, Wang Z, Gao M, Gianneschi NC, Dhinojwala A, Shawkey MD (2016) Stimuli-responsive structurally colored films from bioinspired synthetic melanin nanoparticles. Chem Mater 28:5516–5521

Zhang H, Zhao T, Newland B, Duffy P, Annaidh AN, O'Cearbhaill ED, Wang W (2015) On-demand and negative-thermo-swelling tissue adhesive based on highly branched ambivalent PEG–catechol copolymers. J Mater Chem B 3:6420–6428

Index

A. Hozumi et al. (eds.), *Stimuli-Responsive Dewetting/Wetting Smart Surfaces and Interfaces*, Biologically-Inspired Systems 11,
https://doi.org/10.1007/978-3-319-92654-4